Universidad de Alcalá
COMISIÓN DE ESTUDIOS OFICIALES
DE POSGRADO Y DOCTORADO

ACTA DE EVALUACIÓN DE LA TESIS DOCTORAL

Año académico 2017/18

DOCTORANDO: **FERNANDEZ CRUZA, JORGE**
D.N.I./PASAPORTE: ******246**

PROGRAMA DE DOCTORADO: **D441-ELECTRÓNICA: SISTEMAS ELECTRÓNICOS AVANZADOS. SISTEMAS INTELIGENTES**
DPTO. COORDINADOR DEL PROGRAMA: **ELECTRÓNICA**
TITULACIÓN DE DOCTOR EN: **DOCTOR POR LA UNIVERSIDAD DE ALCALÁ**

En el día de hoy 18/01/18, reunido el tribunal de evaluación nombrado por la Comisión de Estudios Oficiales de Posgrado y Doctorado de la Universidad y constituido por los miembros que suscriben la presente Acta, el aspirante defendió su Tesis Doctoral, elaborada bajo la dirección de **JORGE JAIME CAMACHO SOSA DIAS // CARLOS FRITSCH YUSTA.**

Sobre el siguiente tema: *AUTOENFOQUE EN IMAGEN ULTRASÓNICA*

Finalizada la defensa y discusión de la tesis, el tribunal acordó otorgar la CALIFICACIÓN GLOBAL[1] de (**no apto, aprobado, notable** y **sobresaliente**): SOBRESALIENTE

Alcalá de Henares, 18 de ENERO de 2018

EL PRESIDENTE
Fdo.: ÁLVARO HERNÁNDEZ ALONSO

EL SECRETARIO
Fdo.: GUSTAVO SUTTER CAPRISTO

EL VOCAL
Fdo.: ALBERTO IBÁÑEZ RODRÍGUEZ

Con fecha 24 de enero de 2018 la Comisión Delegada de la Comisión de Estudios Oficiales de Posgrado, a la vista de los votos emitidos de manera anónima por el tribunal que ha juzgado la tesis, resuelve:

☒ Conceder la Mención de "Cum Laude"
☐ No conceder la Mención de "Cum Laude"

La Secretaria de la Comisión Delegada

FIRMA DEL ALUMNO,
Fdo.: JORGE FERNÁNDEZ CRUZA

---

[1] La calificación podrá ser "**no apto**" "**aprobado**" "**notable**" y "**sobresaliente**". El tribunal podrá otorgar la mención de "cum laude" si la calificación global es de sobresaliente y se emite en tal sentido el voto secreto positivo por unanimidad.

Universidad
de Alcalá
**COMISIÓN DE ESTUDIOS OFICIALES
DE POSGRADO Y DOCTORADO**

En aplicación del art. 14.7 del RD. 99/2011 y el art. 14 del Reglamento de Elaboración, Autorización y Defensa de la Tesis Doctoral, la Comisión Delegada de la Comisión de Estudios Oficiales de Posgrado y Doctorado, en sesión pública de fecha 24 de enero, procedió al escrutinio de los votos emitidos por los miembros del tribunal de la tesis defendida por *FERNANDEZ CRUZA, JORGE*, el día 18 de enero de 2018, titulada *AUTOENFOQUE EN IMAGEN ULTRASÓNICA*, para determinar, si a la misma, se le concede la mención "cum laude", arrojando como resultado el voto favorable de todos los miembros del tribunal.

Por lo tanto, la Comisión de Estudios Oficiales de Posgrado **resuelve otorgar** a dicha tesis la

MENCIÓN "CUM LAUDE"

Alcalá de Henares, 31 de enero de 2018
EL PRESIDENTE DE LA COMISIÓN DE ESTUDIOS
OFICIALES DE POSGRADO Y DOCTORADO

Juan Ramón Velasco Pérez

Copia por e-mail a:
Doctorando: FERNANDEZ CRUZA, JORGE
Secretario del Tribunal: GUSTAVO SUTTER CAPRISTO. Profesor Contratado Doctor. Dpto. Tecnología Electrónica y de las Comunicaciones. Univ. Autónoma de Madrid
Director/a de Tesis: JORGE JAIME CAMACHO SOSA DIAS // CARLOS FRITSCH YUSTA

Universidad
de Alcalá

ESCUELA DE DOCTORADO
Servicio de Estudios Oficiales de Posgrado

DILIGENCIA DE DEPÓSITO DE TESIS.

Comprobado que el expediente académico de D./Dª JORGE FERNÁNDEZ CRUZA reúne los requisitos exigidos para la presentación de la Tesis, de acuerdo a la normativa vigente, y habiendo presentado la misma en formato: ☒ soporte electrónico ☐ impreso en papel, para el depósito de la misma, en el Servicio de Estudios Oficiales de Posgrado, con el nº de páginas: 282 se procede, con fecha de hoy a registrar el depósito de la tesis.

Alcalá de Henares a 27 de OCTUBRE de 2017

Aurora Juárez Abril

Fdo. El Funcionario

Programa de Doctorado en Electrónica
Sistemas Electrónicos Avanzados. Sistemas Inteligentes

Autoenfoque en imagen ultrasónica

Tesis Doctoral presentada por:

Jorge Fernández Cruza

Directores:
Dr. Jorge Camacho Sosa Dias
Dr. Carlos Fritsch Yusta

Alcalá de Henares, 2017

Universidad
de Alcalá

DEPARTAMENTO DE ELECTRÓNICA
Escuela Politécnica Superior
28805 Alcalá de Henares (Madrid)
Teléfonos: 91 885 65 40 Fax: 91 885 65 91
eldep@depeca.uah.es

UNIVERSIDAD DE ALCALÁ, PATRIMONIO DE LA HUMANIDAD

Dr. Jorge Camacho Sosa Dias, Doctor Contratado del CSIC,

Dr. Carlos Fritsch Yusta, Investigador Científico del CSIC,

Dr. Raúl Mateos Gil, Profesor Titular de la Universidad de Alcalá

INFORMAN : Que la Tesis Doctoral titulada “**Autoenfoque en imagen ultrasónica**”, presentada por D. Jorge Fernández Cruza y realizada bajo nuestra dirección y tutela, dentro del campo **tecnología de ultrasonidos**, reúne los méritos de calidad y originalidad para optar al Grado de Doctor.

Alcalá de Henares, 25 de Octubre de 2017

Como director/directores:

Como tutor:

Fdo.:Jorge Camacho Sosa Dias

Fdo: Carlos Fritsch Yusta

Fdo.: Raúl Mateos Gil

Universidad
de Alcalá

DEPARTAMENTO DE ELECTRÓNICA
Escuela Politécnica Superior
28805 Alcalá de Henares (Madrid)
Teléfonos: 91 885 65 40   Fax: 91 885 65 91
eldep@depeca.uah.es

Dr. D. Manuel Mazo Quintas, coordinador de la Comisión Académica del Programa de Doctorado "ELECTRÓNICA: Sistemas Electrónicos Avanzados, Sistemas Inteligentes".

INFORMA: Que la Tesis Doctoral titulada "Autoenfoque en imagen ultrasónica", presentada por D. Jorge Fernández Cruza, dirigida por los doctores D. Jorge Camacho Sosa Dias y D. Carlos Fritsch Yusta, y tutelada por el doctor D. Raúl Mateos Gil cumple con todos los requisitos científicos y metodológicos para ser defendida ante un tribunal.

Alcalá de Henares, 24 de octubre de 2017

Fdo.: Manuel Mazo Quintas

A Juana, Jose y Juan Antonio, que, aunque no les veamos,
su bondad, alegría, y cariño a los demás, viven en nosotros.

Agradecimientos

En la típica cena de congreso dónde abundan los asiáticos y los europeos tienden a juntarse (mejor aún si son del sur), contaba un griego que, en la universidad dónde él daba clases, la gente no pagaba por estudiar. La cosa funcionaba de otra manera, cuando terminaban, la deuda que habían contraído se pagaba con parte del sueldo en sus primeros años de trabajo.

No sé si este es un modelo bueno o no, pero lo que sí que se es que aunque aquí no se nos exige parte de nuestro sueldo, muchos de nosotros tenemos una gran deuda, al menos una deuda moral. Tenemos una deuda con la sociedad, y con sus padres y abuelos que han creado un escenario en el que puedas vivir con ciertas garantías. Una deuda con profesores, con gente que te ha cuidado, amigos que se han preocupado por ti y que te han aconsejado y te han hecho como eres. Una deuda impagable con tus padres, que te lo han dado todo.

Probablemente, esas personas no vayan a recibir nada de mí, ni lo esperan, pero sigo teniendo una deuda que espero devolver en otros. Así que es el momento de dejar de recibir y empezar a devolver y seguir con esta cadena de favores o estafa piramidal inversa. Espero estar a la altura.

Y en concreto, a quien más tengo que agradecer esta ayuda “a fondo perdido” es a mis directores, Carlos y Jorge, por toda su dedicación y mucho más que ayuda a esta tesis y a los trabajos anteriores que la componen. Gracias en especial a José Miguel, que aparte de ser un compañero genial, ha puesto su trabajo e ilusión en que todo esto no se quede en un montón de palabras y figuras en un fondo blanco. ¡Te prometo que veremos todo esto funcionando! Y gracias también de antemano a Ricardo, en el que confío que con su extraordinario trabajo conseguirá que todo este esfuerzo e ilusión por parte de los cuatro, hayan merecido la pena. Gracias también a todos los compañeros del CSIC, sobre todo por esos años tan buenos en Arganda, y como ya dije en aquel momento, “no creo que tenga otro trabajo como este”. Y aunque yo siga en lo mismo, ya no es lo mismo. ¡Que tengamos todos mucha suerte!

Gracias a mi padre, por enseñarme con 14 años lo que era un biestable. Sin eso, este trabajo habría sido imposible ¡hay más de 200.000 en este trabajo (Tabla 2.3)! Quien iba a decir entonces que iba a usar tantos. Y a mi madre por darme todo sin reservas, hacerme como soy y aguantarme todos estos años… ¡y los que quedan! Este trabajo también es vuestro.

Muchas gracias Rosa, porque siempre creíste en mí y siempre me animaste la que más a que llegara aquí. Gracias Kapi, porque me has escuchado siempre a pesar de los rollos que te he

metido con este tema y además porque todo lo que hemos estudiado, lo hemos hecho al lado.
Gracias Eva, por enseñarme que un transductor de 2,093MHz resuena alegre con un transductor de 2,637 MHz, pero que resuena triste con otro de 2,489MHz.

Y gracias Pot y Cholo, por hacerme sentir parte de vuestra familia y que siempre os habéis preocupado por lo que hago, a pesar de que alguno sigue pensando que hago *sonotones*.

¡Gracias!

Resumen

A diferencia de la imagen óptica, donde el autoenfoque es actualmente una función prácticamente estándar, la imagen ultrasónica carece hasta el presente de esta capacidad, que sería especialmente útil en el ámbito de la Evaluación No Destructiva (END). Esta memoria resume los trabajos de investigación desarrollados para dotar de esta capacidad a la imagen ultrasónica a alta velocidad.

Esta disfunción se debe a múltiples razones, destacando la diferencia entre cómo se realiza el enfoque en las imágenes óptica y ultrasónica. Para la imagen óptica, se varía la distancia focal de la lente y/o la apertura del diafragma; en cualquier caso, hay que ajustar un número reducido de parámetros y la calidad del enfoque se puede determinar con funciones sencillas que evalúan la nitidez (*sharpness*). En el caso de la imagen ultrasónica existen, al menos, tantos focos como píxeles en la imagen, debiendo ajustarse centenares de parámetros (retardos) para enfocar en cada uno de ellos. No es posible realizar una función de enfoque análoga al caso óptico, sino que es preciso considerar la física de propagación del ultrasonido y la estrategia seguida para formar la imagen.

La inspección de componentes por ultrasonidos se realiza, actualmente, con sistemas de imagen *phased array*, versión industrial de los ecógrafos médicos. En ambos casos se utiliza un *array* con decenas o centenares de pequeños transductores piezoeléctricos que se controlan individualmente para enfocar y deflectar el haz ultrasónico en emisión y recepción. Pero, mientras que en medicina el *array* está en contacto con el cuerpo, que es flexible, en la industria se suele interponer un medio acoplante entre el array y el componente a inspeccionar. Cuando la pieza no es plana o cilíndrica, se utiliza agua como medio acoplante, que se adapta a su forma y proporciona un medio continuo y de baja atenuación para la transmisión del sonido.

En estas condiciones existen dos medios de propagación, lo que dificulta la determinación de los retardos de enfoque por efectos de la refracción. Como en estas condiciones no existen fórmulas cerradas que faciliten su cálculo, hasta la fecha se han venido utilizando procesos iterativos computacionalmente costosos que impiden la modificación rápida del enfoque cuando varía la geometría de la pieza (por ejemplo, durante la realización de un barrido). Estas razones han impedido el desarrollo de técnicas de autoenfoque efectivas.

Esta Tesis aporta tres técnicas que, junto al cálculo en tiempo real de los parámetros de enfoque y un soporte arquitectural de imagen a ultra-alta velocidad, están entre las primeras aproximaciones reales para solucionar el problema del autoenfoque en imagen ultrasónica. De hecho, una de ellas (AUTOFOCUS) ha sido patentada y transferida a la industria, que la comercializa en equipos *phased array* con esta capacidad.

La memoria describe las motivaciones, fundamentos, aproximaciones conocidas al problema así como las dificultades y las soluciones investigadas. Una segunda parte incluye las publicaciones más relevantes donde se han comunicado los resultados, contrastando los teóricamente esperados con los experimentalmente obtenidos.

Abstract

Different from optics, where auto-focusing is a standard feature, ultrasonic imaging has so far lacked this capability, which would be especially useful in the Non-Destructive-Testing field (NDT). The research work presented in this PhD thesis is aimed to provide ultra-fast ultrasound imaging with auto-focus capability.

This limitation is due to multiple reasons, but mainly because the differences between the auto-focusing process in optics and ultrasound. In optics, the lens focal distance and/or the aperture are changed; In any case, just a few parameters have to be adjusted and based on simple mathematical functions that evaluate the image sharpness. In the case of the ultrasonic image, there are at least as many foci as pixels in the image, and hundreds of parameters (delays) must be adjusted to focus on each pixel. An auto-focus approach equivalent to the optics case is not possible, and it is necessary to consider the propagation physics of the ultrasound and the strategy followed to form the image.

Ultrasonic inspection of parts and components is currently performed with *phased array* imaging systems, the industrial version of medical ultrasound echography. In both cases, the tens to hundreds of small piezoelectric transducers in an array are individually controlled to focus and steer the beam, both in emission and reception. But while in medicine the array is in contact with the tissue, which is flexible, for industry applications some coupling material is placed between the array and the component under inspection. When the part is not flat or cylindrical, water is used for coupling, which adapts to the component shape and provides a continuous medium with low attenuation for the wave propagation.

Under these conditions there are two propagation media, which complicates the focusing delays calculation because of refraction. Since there are no closed mathematical formulations in this case, computationally expensive iterative processes must be followed for delay calculation, which prevent the rapid modification of the beamforming parameters when the component geometry changes during the scan. These reasons have limited the development of effective self-focusing techniques.

This PhD Thesis proposes three techniques that, along with the real-time calculation of the focusing parameters and an ultra-high speed imaging architecture, are among the first attempts for the auto-focusing problem in ultrasound imaging. In fact, one of them

(AUTOFOCUS) has been patented and transferred to the industry, for a company that nowadays commercializes phased array equipment with this feature.

This book describes the motivations, fundaments and the prior state of the art, along with the proposed methods and solutions. Then the most relevant publications are presented, where the research results are disclosed.

Índice general

Índice de Figuras

Índice de tablas

Lista de símbolos y acrónimos

$\Delta\alpha$	Dispersión angular del haz
ΔT	Intervalo de tiempo entre instantes de muestreo en la dirección de propagación
Δx	Resolución lateral en el plano de la imagen
Δy	Resolución lateral en el plano perpendicular al array
Δz	Resolución axial
η	Relación del nivel eficaz de los lóbulos de cuantización al lóbulo principal
θ	Ángulo de propagación respecto a la normal a la interfaz
θ_F	Ángulo de deflexión
λ	Longitud de onda
μ	Relación entre el período de la señal recibida y la resolución de los retardos
μ_f	Valor medio de la textura de fondo de la imagen
μ_q	Valor medio de la textura en la zona de interés (quiste, tumor, etc.)
ρ	Densidad
σ	Desviación estándar de las fases de los datos de apertura
σ_0	Desviación estándar de una distribución uniforme entre $-\pi$ y π
σ_f^2	Desviación estándar de la textura de fondo de la imagen
σ_q^2	Desviación estándar de la textura en la zona de interés (quiste, tumor, etc.)
τ_{iF}	Retardo de focalización del elemento *i* al foco F
v	Resolución de los retardos de focalización como fracción del periodo de muestreo
φ	Ángulo de deflexión para conseguir incidencia normal en AVSI
(x_{Ck}, z_{Ck})	Coordenadas del centro de la sub-apertura *k* en AVSI
(x_E, z_E)	Coordenada del punto de entrada al material
(x_{Ek}, z_{Ek})	Coordenadas de las fuentes virtuales en AVSI
(x_i, y_i, z_i)	Coordenadas del elemento *i* de un array
(x_F, y_F, z_F)	Coordenadas del foco
$A_i(k)$	Señal recibida por el elemento *i*

A-Scan	Señal recibida por un elemento o conformada en una dirección
A/D	Conversor Analógico-Digital
AFE	Analog Front End
ARM	Advanced RISC Machine
ASIC	Application Specific Integrated Circuit
AVSI	Automatic Virtual Source Imaging
B	Ancho de banda relativo
B-Scan	Imagen formada por una colección de A-Scans
c	Velocidad del sonido
c_{agua}	Velocidad de propagación en el agua
c_{biol}	Velocidad de propagación en el tejido blando
c_L	Velocidad de propagación de ondas longitudinales
c_T	Velocidad de propagación de ondas transversales
CAD	Computed Aided Design
CAT	Compensación Atenuación-Tiempo
CCD	Charged Coupled Device
CCF	Circular Coherence Factor
CNR	Contraste a Ruido
CPU	Central Processing Unit
CR	Contraste
CUDA	Compute Unified Device Architecture
c_1	Velocidad de propagación en el medio en contacto con el array
c_2	Velocidad de propagación en la pieza o el material a inspeccionar
C-Scan	Imagen de máxima amplitud a partir de un conjunto de B-Scans
d	Distancia entre elementos de un array (pitch)
D	Tamaño o Apertura de un array
DDF	Dynamic Depth Focusing
DDR	Double Data Rate
D_{ik}	Distancia entre elementos emisor y receptor en la detección de la superfici en pitch-catch
DMA	Direct Memory Access
D-Scan	Imagen de tiempo de vuelo a partir de un conjunto de B-Scans

E	Elemento emisor en AVSI
EADS	European Aeronautic Defence and Space
END	Evaluación No Destructiva
F	Tasa de imágenes
FFLC	Fast Focal Law Computing
FMC	Full Matrix Capture
FPGA	Field Programmable Gate Array
f_R	Frecuencia central del transductor o array
f_S	Frecuencia de muestreo
$f(x)$	Función que describe la superficie de la interfaz entre dos medios
$f'(x)$	Derivada primera de la función que describe la superficie del material
$f''(x)$	Derivada segunda de la función que describe la superficie del material
G	Punto de entrada al material
GPU	Graphics Processor Unit
GTX	Gigabit Tranceiver
HLS	High Level Symthesis
$H(\cdot)$	Transformada de Hilbert
K	Número de muestras recibidas por cada elemento del array
I_F	Imagen TFM
I_{iF}	Imagen parcial TFM al emitir con el elemento i
L	Número de líneas de la imagen
L_F	Profundidad de foco a -3dB
LSF	Lateral Spread Function
LVDS	Low-Voltage Differential Signaling
M	Número de elementos activos de una subapertura
N	Número de elementos del array
O	Centro del array
OWI	Omnidirectional Wave Imaging
p	Grado del polinomio de ajuste de la interfaz
P	Punto de incidencia normal en AVSI
PAUT	Phased Array for Ultrasound Testing
PCI	Phase Coherence Imaging

PSF	Point Spread Function
PWI	Plane Wave Imaging
PWPCI	Plane Wave Phase Coherence Imaging
$P(x, z)$	Coordenadas de un pixel de la imagen
Q_i	Código de enfoque del elemento i
R	Cantidad de líneas conformadas en paralelo
RD	Rango dinámico
R_i	Distancia desde el elemento i a la interfaz
$\vec{r}_{iF}$	Vector del elemento i al foco F
R_F	Distancia desde el centro del array al foco
$s(k)$	Señal conformada después de aplicar los retardos de focalización
SAFT	Synthetic Aperture Focusing
SAUL	Self-Adaptive Ultrasonic Technique
SCF	Sign Coherence Factor
SoC	System On Chip
SSP	Split Spectrum Processing
STA	Synthetic Transmit Aperture
T_{ABik}	Tiempo de vuelo en pitch-catch entre el emisor i y el receptor k
t_{adq}	Tiempo de adquisición de un A-Scan
t_{AF}	Tiempo de vuelo desde el elemento A al foco F
T_{Ai}	Tiempo de vuelo en pulso-eco al elemento emisor i
TDTE	Time-Domain Topological Energy
TGC	Time Gain Control
TFM	Total Focusing Method
t_i	Tiempo de ida y vuelta desde el elemento i a la interfaz
t_{iF}	Tiempo de vuelo desde el elemento i al foco F
t_{ijF}	Tiempo de vuelo desde el emisor i al foco F y de vuelta al receptor j
t_{iv}	Tiempo de vuelo en ida y vuelta
t_k	Constante de ajuste del elemento k para el cálculo del array virtual
TMS	Técnica de Muestreo Selectivo
T_R	Período de la señal recibida
T_S	Intervalo entre muestras

t_{VF}	Tiempo de vuelo desde el elemento virtual V al foco F
T_X	Resolución de los retardos de focalización
U	Distancia del límite del campo cercano
UCI	Unidad de Control e Interfaz
UFAF	Ultra-Fast Auto-Focusing
VCF	Vector Coherence Factor
V_k	Derivada del tiempo de vuelo para el foco k
x	Coordenada espacial a lo largo del array
z	Coordenada espacial normal al transductor (dirección de propagación)
y	Coordenada espacial perpendicular al array y a la dirección de propagación
Z	Impedancia acústica
z_{max}	Distancia máxima en la imagen

Planteamiento

La imagen ultrasónica ha evolucionado mucho en las dos últimas décadas, tanto por los avances de la tecnología microelectrónica como por el hallazgo de métodos innovadores para la formación de la imagen acústica. Entre ellos, por su relación con este trabajo y la innovación que representan respecto a la tecnología convencional de imagen ecográfica *phased array*, cabe citar: imagen ultra-rápida [Montaldo, 2009], imagen con onda plana [Le Jeune, 2016], nuevas formulaciones para *TFM* (*Total Focusing Method*) [Zhang, 2010], elastografía cuantitativa [Tanter, 2014], conformación ultra-rápida con coherencia de fase [Cruza, 2017], tomografía ultrasónica [Rouyer, 2010] y autoenfoque para Evaluación No Destructiva (*END*) [Cruza, 2013]. Todas estas innovaciones recientes han abierto líneas de investigación y han dado lugar a nuevas aplicaciones en imagen ultrasónica.

Esta Tesis Doctoral forma parte de los esfuerzos dirigidos a encontrar nuevos métodos y aplicaciones de imagen ultrasónica y, concretamente, en técnicas de autoenfoque e imagen a alta velocidad para aplicaciones en *END*.

Objetivos

El principal objetivo de esta Tesis Doctoral ha sido **investigar métodos y tecnologías para obtener imágenes acústicas auto-enfocadas**. Un segundo aspecto ha sido **investigar técnicas que faciliten la obtención de imágenes de calidad competitiva con los mejores estándares, pero a muy alta velocidad**. Por último, se ha prestado una especial atención a la tecnología necesaria para cubrir las necesidades de autoenfoque e imagen ultrasónica a alta velocidad, con el **desarrollo de nuevas arquitecturas de formación de imagen en paralelo**. En el ámbito de la END, donde es más útil, un sistema de imagen ultrasónica auto-enfocada ha de obtener automáticamente las leyes focales adaptadas a la geometría actual array-acoplante-pieza para producir la mejor imagen posible.

En esta situación no serían necesarias ni la actual descripción CAD de la geometría, ni tener que capturar la geometría de la pieza antes de la inspección, ni definir *a priori* las posiciones de los focos o calcular leyes focales, ni considerar posibles desviaciones geométricas por tolerancias de fabricación o durante la inspección real. El proceso de autoenfoque debe ser automático y adaptado a la geometría actual para resultar útil al operador. Además de facilitar su la labor, simplificaría la preparación de las inspecciones y mejoraría la capacidad de detección y evaluación de defectos. El ahorro de tiempo y esfuerzos supondría una notable reducción de costes, y la mejora de la capacidad de detección un aumento en la fiabilidad de las inspecciones.

Sorprende que, a pesar de su indudable interés, una función de **“autoenfoque”**, habitual en los sistemas de imagen óptica, **esté ausente en todas las realizaciones conocidas de imagen ultrasónica** y, en particular, en los sistemas para END. **Sólo en los últimos años se han empezado a buscar soluciones a este problema**.

Las razones para esta carencia son varias. Para empezar, el enfoque de una imagen óptica y de una ultrasónica se basa en mecanismos muy diferentes. La imagen óptica se enfoca variando la distancia focal de las lentes y, a veces, el tamaño de apertura (diafragma), tratando de optimizar alguna función de nitidez (*sharpness*). Esto es, el enfoque requiere ajustar muy pocos parámetros.

En cambio, para enfocar la imagen ultrasónica, hay que determinar y aplicar un conjunto de *retardos* que corresponden a la posición espacial de cada muestra o pixel[1] de la imagen (*ley focal*). Una ley focal contiene N retardos (uno por cada elemento del array) y son necesarias tantas leyes focales como muestras o píxeles contenga la imagen ultrasónica. Abordar la optimización simultánea de N variables por cada muestra (N ~128) en una imagen con millones de muestras es un proceso inviable.

Además, las imágenes ultrasónicas en END suelen estar afectadas por la refracción del sonido al atravesar distintas interfases, en muchos casos de geometría desconocida, lo que complica enormemente el proceso de enfoque. Un símil óptico a este problema podría ser el de obtener una imagen no distorsionada del fondo de una piscina corrigiendo el efecto que generan las ondas en la superficie del agua, para lo cual habría que estimar la posición de la superficie en cada punto (desconocida y variable en el tiempo) y corregir localmente la refracción para eliminar la distorsión del fondo. Aun así, la complejidad seguiría siendo menor que la que supone generar una imagen ultrasónica, dado que esta última se obtiene a

---

[1] El concepto “muestra” se suele asociar a la metodología *phased array*, y el de “pixel” a la *TFM*.

todas las profundidades en el material inspeccionado, no sólo en un plano como sería el caso del fondo de la piscina en el símil propuesto.

La solución a estos problemas hay que encontrarla considerando la física de propagación del pulso ultrasónico. Si el medio es homogéneo y se opera por contacto, el problema es trivial, quedando reducido a calcular los tiempos de vuelo nominales desde cada elemento del array a cada muestra en la imagen. Este procedimiento es rápido, pues se realiza con fórmulas cerradas que proporcionan las leyes focales óptimas. La geometría es fija de modo que, una vez calculadas, las leyes focales permanecen invariables. Además, para el enfoque dinámico en medios homogéneos, se han propuesto múltiples circuitos que calculan los retardos de enfoque para cada canal durante la propia adquisición de señal.

El problema real aparece cuando se interpone un medio de acoplamiento entre array y pieza, que es el caso más frecuente en las aplicaciones de imagen ultrasónica para END. En realidad, en esta situación, los problemas son varios:

1. Cuando se conoce la geometría, sólo hay que calcular las leyes focales atravesando la interfaz entre dos medios considerando la refracción. Como para determinar los tiempos de vuelo en esta situación no existen fórmulas cerradas, la solución ha de buscarse por métodos numéricos iterativos aplicando, por ejemplo, el *principio de Fermat*: encontrar la trayectoria más rápida desde cada elemento a cada foco pasando por algún punto en la interfaz, considerando la velocidad de propagación en cada medio.

2. Incluso en este caso no resulta práctico calcular la ley focal para cada muestra de la imagen, tanto por el gran volumen de datos que exigirían las leyes focales como por el tiempo de cálculo necesario. Sería mucho más conveniente disponer de circuitos de cálculo que evaluaran las leyes focales conforme se fueran necesitando durante el proceso de formación de la imagen en tiempo real. Sin embargo, se han hecho múltiples propuestas de circuitos de este tipo para medios homogéneos, pero ninguno de ellos sirve cuando hay varios medios de propagación, como es el caso habitual en END.

3. Además, el caso de mayor interés para el autoenfoque se da cuando se desconoce la geometría o no se conoce con la suficiente precisión. Es aquí cuando la función de autoenfoque resulta de la máxima utilidad. Por un lado, haciendo innecesarias las descripciones geométricas CAD o el *escaneo previo* de la pieza (con láser, cámaras, etc.) que permitan su estimación. Por otro, facilitando la obtención de la imagen óptima en la

situación transductor-pieza actual, cuando ambos elementos no están mecánicamente ligados.

4. La operación de una función de autoenfoque en tiempo real, con altas tasas de imagen o, al menos, sin impactar en la tasa estándar de imágenes, demanda arquitecturas innovadoras que permitan la adquisición y procesamiento a alta velocidad. Este aspecto, incorporado a las aplicaciones médicas desde hace décadas, no se ha considerado para END por la diversidad de configuraciones y por las complicaciones que introduce la refracción entre dos medios de propagación.

La falta de soluciones para estos problemas ha retrasado la introducción de una función de autoenfoque en imagen ultrasónica. Cada uno de ellos es un reto en sí mismo y el presente trabajo de investigación es una aproximación al objetivo propuesto: **determinar algoritmos, arquitecturas y estrategias que realicen el *autoenfoque de la imagen ultrasónica en tiempo real y a alta velocidad***, tema que da título y contenido a la presente Tesis Doctoral.

1 Antecedentes

1.1 Breve reseña histórica

La imagen ultrasónica se ha utilizado en los ámbitos clínico e industrial durante décadas, compartiendo métodos, técnicas y tecnologías en ambos sectores. En aplicaciones industriales, la Evaluación No Destructiva (*END*) de materiales por ultrasonidos se remonta a los trabajos de Sergei Y. Sokolov hacia 1928. A partir del efecto piezoeléctrico descubierto por los hermanos Curie en 1880 y, utilizando cristales de cuarzo a ambos lados del material, Sokolov transmitió ondas ultrasónicas y sugirió, por primera vez, la posibilidad de detectar defectos internos por una mayor atenuación de la señal recibida (técnica de "*transmisión*", Figura 1.1.a).

La técnica "*pulso-eco*" se desarrolló posteriormente, cuando lo permitió la tecnología. En este caso un único transductor actúa como emisor y receptor de los ecos producidos en el medio (Figura 1.1.b). Los ecos se originan en los cambios de *impedancia acústica* que

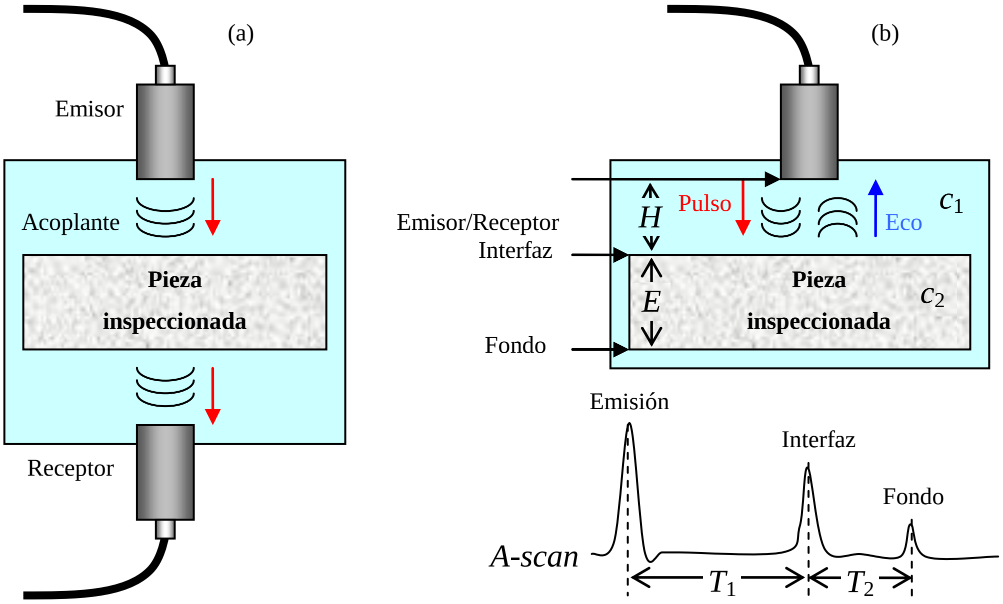

Figura 1.1 - a) Técnica de transmisión, con transductores emisor y receptor separados; b) Técnica pulso-eco, donde el mismo transductor actúa como emisor y receptor, mostrando la traza o A-scan.

aparecen a lo largo de la propagación del sonido, como por ejemplo en grietas, poros u otro tipo de discontinuidades, así como en las interfases de las piezas. La impedancia acústica es el producto de la densidad del material ρ por la velocidad de propagación del ultrasonido c.

Los primeros instrumentos basados en estas ideas registraban en un osciloscopio la traza o *A-scan* (*A* de *amplitud*) de los ecos recibidos desde el *disparo* del transductor [Firestone, 1940]. Esta técnica se ha mantenido desde hace casi ochenta años y se continúa utilizando en buena parte de las inspecciones para END por ultrasonidos.

Conociendo la velocidad de propagación y midiendo el tiempo en el que se recibe el eco, se puede determinar su ubicación. En el ejemplo de la Figura 1.1.b la distancia del transductor a la interfaz es $H = c_1 T_1 / 2$ y el espesor de la pieza es $E = c_2 T_2 / 2$, donde la división por 2 tiene en cuenta que los pulsos ultrasónicos recorren el doble de distancia (ida y vuelta por ser pulso-eco) y los tiempos T_1 y T_2 son los indicados en el *A-scan* mostrado en la figura.

La técnica pulso-eco se introdujo también con posterioridad en el ámbito clínico. Las primeras imágenes *B-scan* (*B* de *brillo*) se obtuvieron con exploración manual usando un transductor monoelemento. Las trazas *Ascan* consecutivas se mostraban yuxtapuestas en una pantalla de alta persistencia, mientras que la amplitud de los ecos modulaba el brillo [Wild, 1952]. Este método rudimentario requería cierta destreza para sincronizar el movimiento manual del transductor con la formación de la imagen, aunque poco después se añadió un brazo mecánico con posición codificada. A finales de los 60's y principios de los 70's, se obtuvieron las primeras imágenes *Bscan* en tiempo real utilizando transductores oscilantes o giratorios [Krause, 1969], [Griffith, 1974], dando lugar a los primeros equipos comerciales de *ecografía médica* (sistemas *Vidoson* de Siemens, referencia histórica en [Levi, 1997]).

A mediados de los 70 se introducen los *arrays* ultrasónicos, que cambiarían radicalmente la forma de generar las imágenes [Macowski, 1975]. En esta década se desarrollarán las principales bases teóricas de la formación de imagen ultrasónica *phased array* a semejanza del radar, determinando sus limitaciones y posibilidades [Steinberg, 1976], [Macowski, 1979], [Kino, 1987]. Desde entonces y, hasta bien entrada la década de los 90, los nuevos desarrollos se dirigirían al sector clínico por las dificultades de aplicación y coste para END.

Un array está formado por N transductores de pequeño tamaño, donde N oscila entre 16 para aplicaciones simples, hasta varios centenares, o incluso miles, para imagen de alta resolución y 3D. Controlados individualmente con retardos aplicados a las señales emitidas y recibidas, se puede orientar (*deflectar*) y concentrar (*enfocar*) el haz ultrasónico por medios electrónicos y sin movimientos mecánicos. Los *retardos de enfoque y deflexión* compensan las diferencias en el tiempo de vuelo del ultrasonido desde cada elemento a la posición del foco o viceversa, proceso que se denomina *conformación del haz* o *beamforming*. El conjunto de los *N retardos de enfoque* para los *N* elementos del array para un foco determinado en emisión o recepción a distancia R_F en la dirección θ_F, se denomina *ley focal*.

Los retardos de enfoque en emisión hacen que los pulsos generados por los diferentes elementos lleguen simultáneamente al foco, donde se suman constructivamente para proporcionar la máxima intensidad de campo ultrasónico. Sólo puede crearse una ley focal en emisión, ya que una vez emitidos los pulsos no se puede modificar su trayectoria.

Análogamente, en recepción, los retardos de enfoque alinean en fase las señales recibidas por los diferentes elementos con una procedencia común (el foco), de forma que puedan sumarse *coherentemente*. En el caso del enfoque dinámico, los retardos aplicados en recepción se modifican dinámicamente haciendo que el foco coincida en cada instante con el frente del pulso ultrasónico emitido. De este modo el Ascan adquirido está enfocado a todas las profundidades, lo que proporciona máxima resolución, relación señal/ruido y rango dinámico en el modo *phased array*.

La denominación *phased array* procede del ámbito del *radar*, donde un conjunto de antenas (*array de antenas*) emite con *diferentes fases* para crear un *haz de radiofrecuencia* en la dirección deseada, y donde la *apertura* es el tamaño (*D*) del array, $D = N \cdot d$, siendo *d* la distancia entre elementos (*pitch*). Esta terminología se ha mantenido para los arrays de transductores ultrasónicos, aunque en radar se opera en *campo lejano* (distancias >> *D*), mientras que en ultrasonidos el rango de distancias no pasa de algunas aperturas (*campo cercano*). La distancia al array que establece la frontera entre ambas regiones es:

$$U = D^2 / 4\lambda \qquad (1)$$

donde $\lambda = c / f_R$ es la longitud de onda, c la velocidad de propagación y f_R la frecuencia central del array. De este modo:

a) Se puede conformar *en recepción* un haz ultrasónico que viaja a la velocidad del sonido manteniéndolo enfocado a lo largo de toda su propagación si se modifican dinámicamente los retardos de enfoque (*enfoque dinámico en recepción*). En emisión no es posible, ya que una vez emitido el pulso ultrasónico con una configuración de retardos, queda completamente determinada su propagación.

b) Al obtenerse la imagen ultrasónica en la región del campo cercano no son posibles ciertas simplificaciones. Por ejemplo, en radar se puede suponer que el reflector está situado a la misma distancia de todas las antenas, variando únicamente el ángulo con el que se observa (*deflexión*). Esto no es posible en el caso de la imagen ultrasónica si se quiere obtener una buena resolución en la imagen.

c) Mientras que el radar opera en un medio homogéneo con velocidad de propagación constante, en muchas aplicaciones ultrasónicas se interpone un medio para acoplar el sonido entre el array y el objeto inspeccionado. La existencia de dos o más medios con velocidades de propagación diferentes obliga a considerar la refracción.

Si bien las bases teóricas para la formación de imagen ultrasónica con arrays quedó establecida en la década de los 70's, el desarrollo de la tecnología electrónica correspondiente tardó bastantes años. El proceso de conformación ultrasónica no es trivial, en especial para realizar el enfoque dinámico en tiempo real (imagen enfocada a todas las profundidades) y la tecnología electrónica necesaria era costosa y voluminosa por aquella época.

1.2 Propagación de las ondas ultrasónicas

Las ondas ultrasónicas para imagen las genera un transductor emisor haciendo uso del efecto piezoeléctrico. Se emite un pulso de corta duración, cuyas características principales son la frecuencia central f_R y el ancho de banda B relativo. El pulso ultrasónico es una vibración mecánica que se propaga por el medio material al que se acopla el transductor. Las vibraciones tienen dos direcciones principales: *ondas de compresión o longitudinales*, en la de propagación y *ondas de cizalla o transversales* donde las oscilaciones son perpendiculares a la dirección de propagación. Cada uno de estos modos se propaga con su propia velocidad, c_L para las longitudinales y c_T para las transversales.

En medios biológicos las velocidades son muy diferentes (tres órdenes de magnitud, $c_L \approx$ 1540 m/s y $c_T \approx 2$ m/s) y, en particular, las ondas transversales se atenúan muy rápidamente.

Así, excepto para algunas aplicaciones de *elastografía* que evalúan la rigidez de los tejidos internos (módulos elásticos) a partir de la velocidad de las ondas transversales [Bercoff, 2004], su presencia se ignora y se supone que sólo existen las longitudinales. Lo más frecuente es, además, considerar que se propagan con velocidad constante (medio homogéneo), excepto en ciertas aplicaciones que miden las sutiles variaciones de velocidad en el medio que se utilizan para el diagnóstico [Mast, 2000].

En los sólidos pueden coexistir ondas longitudinales y transversales, con $c_L \sim 2\ c_T$. En metales $c_L \sim 6000$ m/s, en plásticos y *composites* de matriz plástica, $c_L \sim 3000$ m/s. Estas son cifras orientativas, extraídas de [Krautkrämer, 1990]. A diferencia del caso clínico, ambas velocidades son comparables y las transversales no se atenúan tanto.

También es común suponer que los transductores se comportan como pistones, esto es, la oscilación es simultánea en todos los puntos de su superficie. Este movimiento produce inicialmente ondas de compresión, aunque en realidad también genera transversales como efecto de la difracción en el borde del transductor. Por otra parte, cualquier discontinuidad en la propagación del pulso ultrasónico produce ondas de ambos tipos. Como se ha mencionado, en una inspección ultrasónica para END de materiales sólidos hay que contar con la presencia de ondas longitudinales y transversales. Con frecuencia estas últimas, que son más lentas, contaminan las indicaciones de las longitudinales.

En cada discontinuidad del material desde el punto de vista acústico, se producen efectos de *reflexión* (generación de ecos), *refracción* (cambio de dirección del haz) y *difracción* (re-emisión omnidireccional en los bordes). Las “discontinuidades” son cambios de *impedancia acústica*, determinada por el producto de la densidad ρ y la velocidad de propagación de las ondas longitudinales en el material, $Z_L = \rho \cdot c_L$. Así, una grieta, un taladro o una interfaz entre dos medios de propagación diferentes representan cambios de impedancia acústica que dan lugar, en principio, a los tres efectos mencionados.

Para la detección de defectos se observan las indicaciones debidas a la reflexión o a la difracción, mientras que la refracción se utiliza de forma indirecta para generar ondas transversales a partir de las longitudinales que produce el transductor o que se propagan por un acoplante líquido. Por otra parte, como se expondrá, la refracción complica la obtención de imágenes ultrasónicas.

El estudio de la propagación de un pulso ultrasónico requeriría una representación en 5 dimensiones: las tres coordenadas espaciales, más el tiempo, indicando la amplitud del *campo*

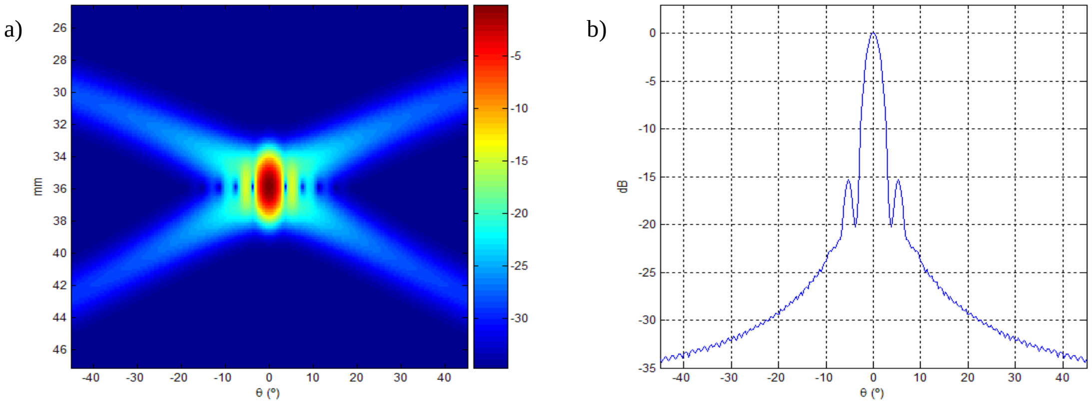

Figura 1.2 - a) Campo con foco en z_F=36 mm, deflexión θ_F = 0º, array de f_R=5MHz, B=40%, N=32 elementos, d=0.6 mm, en función del ángulo (eje horizontal) y profundidad (eje vertical); b) Patrón lateral en dB.

ultrasónico con una quinta dimensión. Como no es posible esta representación, a lo largo de los años se han ido aceptando, convencionalmente, dos formas básicas de visualización:

a) Campo ultrasónico: representación en dos dimensiones espaciales de la amplitud *máxima* del ultrasonido que se obtiene *en algún instante de tiempo*, representando la amplitud con una escala de colores o tonos de gris. Convencionalmente ***z*** es la coordenada normal al transductor (dirección de propagación), ***x*** es la coordenada a lo largo de un array lineal e ***y*** es perpendicular a ambas.

b) Patrón axial o lateral del campo: Representa la proyección del campo ultrasónico (amplitud del ultrasonido) en función del ángulo de deflexión. Muestra el lóbulo principal en la dirección deflectada, cuya anchura determina la resolución lateral y sus lóbulos laterales que limitan el rango dinámico de la imagen.

La Figura 1.2.a muestra el campo ultrasónico creado por un array de f_R = 5 MHz, B=40%, N = 32 elementos, d=0.6 mm, con un foco a distancia $R_F = 0.5D$, ángulo de deflexión θ_F = 0º. La Figura 1.2.b, representa el patrón lateral en función de θ, en dB normalizado al máximo.

La primera representa la respuesta al impulso del sistema de imagen (o PSF, del inglés *Point Spread Function*), que es la que se formaría si hubiera un reflector puntual ideal en el foco. En esta figura se observa el *lóbulo principal* (la región de mayor intensidad, en rojo) cuya longitud y anchura determinan la *resolución axial y lateral*, respectivamente, así como unos *lóbulos laterales* en forma de “alas de mariposa” que limitan el rango dinámico de la imagen al producir señales en lugares donde no debería haber indicaciones. La Figura 1.2.b representa la proyección sobre el eje horizontal (ángulo θ) del máximo de la amplitud del campo que muestra la Figura 1.2.a, denominado patrón lateral o *LSF* (del inglés *Lateral Spread Function*).

1.3 Tecnología

Los *sistemas phased array ultrasónicos* emiten y reciben *haces enfocados en emisión y en recepción* para obtener las líneas de una imagen, que puede ser sectorial si los haces se generan a intervalos angulares (Figura 1.3.a), o lineal si los haces son paralelos a intervalos del paso entre elementos, utilizando un subconjunto de N_S elementos que se desplazan en cada disparo a lo largo del array (Figura 1.3.b). El primer caso puede utilizar todos los elementos del array para generar cualquier número de líneas de imagen, mientras que con el barrido lineal, el número máximo de líneas es $L_{max} = N\text{-}N_S$.

En emisión, el disparo se *retrasa* en cada elemento para que los pulsos ultrasónicos lleguen simultáneamente al foco. En recepción, enfoque y deflexión se realizan *retrasando* las señales recibidas para compensar las diferencias de recorridos desde cada punto en la línea de imagen a cada elemento.

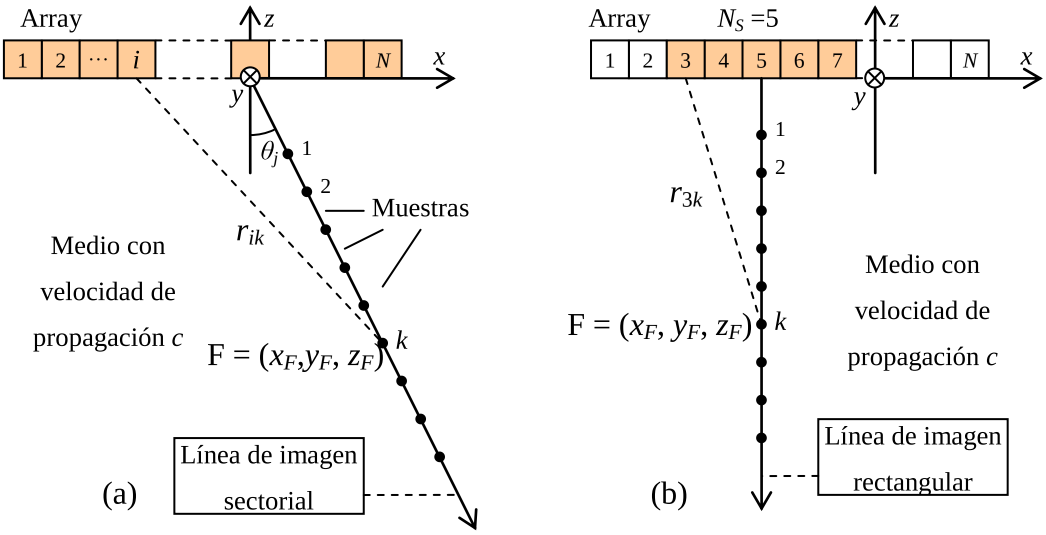

Figura 1.3 - Imágenes *phased array*: a) *sectorial* con barrido angular y ángulo de deflexión θ_j para la línea *j*; b) *barrido lineal* con deflexión 0º, línea obtenida con una subapertura del array (elementos 3 al 7).

En resumen, enfoque y deflexión se realizan introduciendo *retardos* en las excitaciones de los elementos en emisión o en las señales registradas por estos en recepción. Desde el punto de vista de los retardos de enfoque, emisión y recepción son procesos análogos. Esto es, los retardos aplicados para crear un foco en emisión son iguales a los que se introducen en recepción para enfocar en ese mismo punto.

Con referencia a la Figura 1.3, que supone un medio homogéneo con velocidad de propagación *c*, el tiempo de tránsito t_{iF} desde el elemento *i* del array en (x_i, y_i, z_i) a un foco genérico F situado en (x_F, y_F, z_F), tanto en barrido angular como lineal, es:

$$t_{iF} = \frac{|\vec{r}_{iF}|}{c} = \frac{\sqrt{(x_i - x_F)^2 + (y_i - y_F)^2 + (z_i - z_F)^2}}{c}, \tag{2}$$

siendo $\vec{r}_{iF}$ el vector entre el elemento *i* y el foco F. Los *N* retardos τ_{iF} aplicados a las señales de los elementos del array, $1 \le i \le N$, para que lleguen simultáneamente a un foco genérico F (enfoque en emisión) o para alinear en fase las que procedan de F (enfoque en recepción) son:

$$\tau_{iF} = \max_{1 \le i \le N}(t_{iF}) - t_{iF}, \quad 1 \le i \le N \tag{3}$$

Es obvio que la suma del tiempo de vuelo y del retardo es $t_{iF} + \tau_{iF} = \max(t_{iF}) = \text{constante}$ para todos los elementos *i* (“simultaneidad”).

El conjunto de retardos τ_{iF} se denomina *ley focal* para el foco en F, que puede ser utilizada para crear un foco *en emisión* y/o *en recepción* en dicha posición. Los retardos de enfoque incluyen implícitamente la deflexión del haz al considerar las coordenadas (x_F, y_F, z_F) del foco. Los focos en emisión y recepción son independientes y pueden ubicarse en diferente posición.

A este proceso se le denomina *conformador de retardo y suma* expresando que, una vez alineadas en tiempo/fase, las señales recibidas se suman *coherentemente*, esto es, interfieren constructivamente sólo las que proceden del foco. Al conjunto de *N* muestras ya retrasadas y antes de la suma coherente se le denomina *datos de apertura*. Aplicando el proceso de retardo y suma (o, para simplificar, *de enfoque*) a todas las muestras en cada línea (denominado *enfoque dinámico estricto*), se obtiene una imagen enfocada en toda su extensión y profundidad. Este proceso requiere mantener la información de fase, por lo que las señales individuales se adquieren y procesan en radiofrecuencia o señal analítica (compleja) hasta realizar la suma coherente.

Las primeras tecnologías *phased array* en tiempo real proporcionaban imágenes ultrasónicas conmutando líneas de retardo analógicas o semi-analógicas (*CCDs*) para deflectar y enfocar el haz con un único foco en emisión y pocos en recepción, llegando a alcanzar tasas de 15-20 imágenes/s [Maslak, 1979], [Manes, 1988]. La tecnología electrónica de la época no permitía el enfoque dinámico estricto por las dificultades de conmutar rápidamente un gran número de líneas de retardo que eran voluminosas, introducían artefactos de conmutación y distorsionaban las señales. Además, era difícil obtener la resolución temporal requerida para evitar los *lóbulos de cuantización* de los retardos [Peterson, 1984]. Estos lóbulos aparecen por falta de resolución temporal y limitan el rango dinámico de la imagen.

La introducción de conversores A/D de coste limitado y frecuencias de muestreo suficientes para las señales ultrasónicas (varios MHz) permitió superar estos problemas en la década de los 90's, realizando conformadores de retardo y suma totalmente digitales [Karaman, 1993], [Thomenius, 1996], [Lee, 2005].

El canal ultrasónico asociado a cada elemento del array dispone, en emisión, de un *púlser* o excitador de alta tensión (típicamente ~100V, flancos de < 5 ns). En recepción, cada canal incluye una protección, un amplificador de banda ancha (típicamente ≥ 20 MHz, ganancia variable con la distancia entre 0 y 60 dB), bajo nivel de ruido (típicamente < 1 nV/√Hz), un filtro anti-aliasing y un conversor A/D con una resolución típicamente ≥ 12 bits y frecuencia de muestreo de hasta 50 MHz, para transductores de 1 a 20 MHz (Figura 1.4).

Las muestras adquiridas son procesadas digitalmente para introducirles los retardos de enfoque con la resolución requerida, manteniendo la tasa de muestreo más baja posible compatible con el criterio de Nyquist.

La inclusión de conversores A/D en el pre-procesador o *front-end* facilitó el *enfoque dinámico* (*DDF=Dynamic Depth Focusing*), que modifica continuamente la ley focal de recepción para situar el foco sobre el frente de ondas [Song, 1990], [Steinberg, 1992]. El enfoque dinámico es estándar desde entonces en ecografía médica y se va introduciendo progresivamente para END. El *enfoque dinámico estricto* sitúa un foco en cada muestra del *Ascan* conformado.

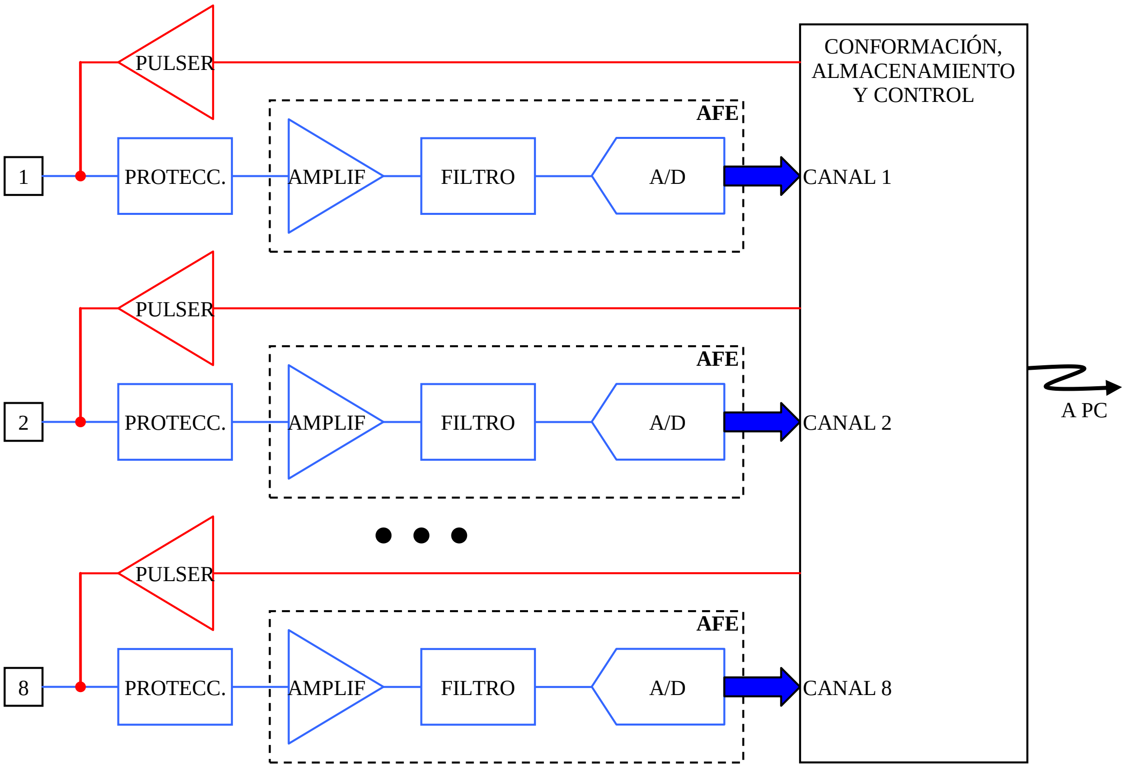

Figura 1.4 - Esquema de un sistema de ecografía convencional. En rojo, circuito de emisión. En azul, circuito de recepción. En cajas con trazos, electrónica integrada en un AFE.

La tecnología digital es la única que se mantiene en la actualidad. Incluso se han desarrollado dispositivos específicos para imagen ultrasónica (*Analog Front End*, AFE) que integran todo el procesamiento analógico en recepción de varios canales (bloque a trazos en Figura 1.4).

El hardware del *front-end* es común para dos estrategias diferentes de formación de imagen:

1. Conformación en tiempo real *phased array.*
2. Conformación por técnicas de apertura sintética o TFM (*Total Focusing Method*).

1.3.1 Conformación phased *array*

La tecnología *phased array* construye la imagen línea a línea durante la adquisición de señal. Tras aplicar los *retardos de enfoque*, se obtienen los *datos de apertura* sobre los que se realiza la *suma coherente*. Esta operación puede implementarse en ASICs o FPGAs y en tiempo real para obtener cada línea de la imagen a la velocidad de propagación del ultrasonido. Una imagen típica puede tener 200 líneas, así que para obtener 25 imágenes/s (tiempo real) es necesario adquirir y procesar (*conformar*) al menos 5000 líneas o *A-scan* por segundo, con miles de muestras cada uno.

Un equipo convencional de ecografía (médica o industrial) tiene entre 64 y 256 canales. Para obtener imágenes en tiempo real, hay que operar a tasas de adquisición y procesamiento de entre 6.4 y 25.6 GB/s para una frecuencia de muestreo de 50 MHz con dos bytes por muestra. En el intervalo entre muestras (20 ns) hay que obtener y aplicar un nuevo juego de retardos a las señales recibidas para operar con enfoque dinámico estricto. Con la tecnología actual, es complicado realizar este proceso con una implementación *software* sobre un procesador de propósito general, siendo la transferencia de datos la mayor limitación.

El conjunto de retardos $\{\tau_{ik}\}, 1 \leq i \leq N$ que crean un foco en la muestra k de una línea de la imagen, $1 \leq k \leq K$, se aplican a las muestras de la señal $A_i(k)$ recibida por el elemento i del array. Sumando estos valores se obtiene la muestra k de salida:

$$s(k) = \sum_{i=1}^{N} A_i[k - \tau_{ik}] \tag{4}$$

Extendiendo este proceso de retardo y suma a las muestras registradas por todos los canales con $1 \leq k \leq K$, $1 \leq i \leq N$, la secuencia s(k) de salida se obtiene con enfoque dinámico estricto. En este caso es importante conocer con qué resolución hay que determinar y aplicar los retardos de enfoque.

Como la resolución de los retardos no es infinita, aparecen unos lóbulos denominados de *cuantización de retardos* que afectan a la calidad de la imagen, emborronando el fondo y reduciendo su rango dinámico. La relación del nivel eficaz o rms de estos lóbulos al del lóbulo principal está dado por [Peterson, 1984]:

$$\eta \approx \frac{\pi}{\mu\sqrt{6N}} \qquad \mu >> 1 \tag{5}$$

donde μ es la relación entre el periodo de la señal recibida T_R y la resolución T_X de los retardos. Para que η sea menor que la mitad del fondo de ruido del array ($1/N$), debe verificarse [Fritsch, 2010]:

$$\mu = \frac{T_R}{T_X} \geq 2\pi\sqrt{\frac{N}{6}}, \qquad T_X \leq \frac{T_R}{2\pi}\sqrt{\frac{6}{N}} \tag{6}$$

El valor de μ dado por (6) proporciona un límite para la resolución T_X y, por tanto, para el error con el que deben calcularse los retardos de enfoque. En efecto, no es de esperar que los retardos que intervienen en (4) sean un múltiplo entero del periodo de muestreo. Así, para un array con N=128 elementos, resulta μ=29. Si la frecuencia es f_R = 5 MHz (T_R = 200 ns), la resolución de los retardos y/o el error con los que se calcula debe ser menor que 6.9 ns.

Es interesante destacar lo siguiente: Para un ancho de banda relativo de hasta el 100% se considera suficiente una frecuencia de muestreo 4 veces superior a la del array para verificar el criterio de Nyquist, esto es, f_S=20 MHz si f_R = 5 MHz. Sin embargo, la resolución temporal que demandan los retardos ($T_X \leq$ 6.9 ns) es la que corresponde a una frecuencia de muestreo de 145 MHz. No hay contradicción con el teorema de Nyquist, pues muestreando a 20 MHz se dispone de toda la información para reconstruir la señal. El retardo con la resolución requerida se puede conseguir interpolando o, como se realiza en la práctica, sobre-muestreando las señales adquiridas antes de realizar la suma coherente.

1.3.2 Técnicas de apertura sintética y TFM

Una implementación alternativa a la técnica *phased array* adquiere, tras realizar un *disparo omnidireccional* (con un único elemento, por ejemplo, o con un subconjunto de elementos y una ley focal divergente que crea una fuente virtual [Sutcliffe, 2012c]), las N trazas registradas por los elementos, cada una de ellas con K muestras (juego completo de datos).

A partir del juego completo de datos con N x K muestras obtenido tras un disparo, se forma una *imagen de baja resolución*, pues la emisión fue omnidireccional. Repitiendo el proceso cambiando el emisor a lo largo de la apertura, se generan N imágenes cuya suma proporciona una imagen de alta resolución, enfocada en emisión y recepción.

Para realizar el enfoque en cada píxel de la imagen, se calcula el tiempo de vuelo desde el emisor i al píxel y de éste a cada receptor j. La suma de ambos es el tiempo de vuelo total del pulso ultrasónico t_{ij} desde que se emitió hasta que llegó al receptor (Figura 1.5):

$$t_{ijF} = \frac{r_{iF} + r_{jF}}{c} \tag{7}$$

El valor I_{iF} de la imagen de baja resolución en F cuando emite el elemento i es:

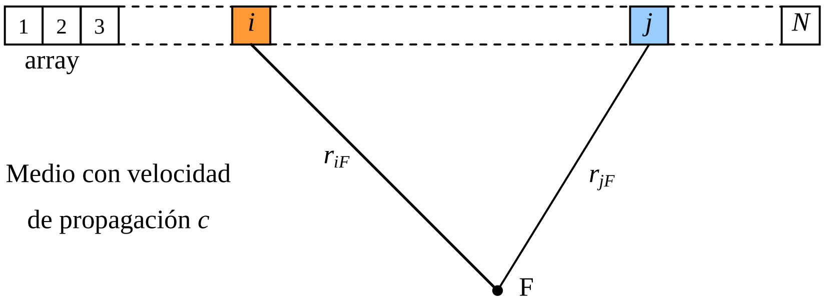

Figura 1.5 - Esquema de principio de la técnica TFM. El elemento *i* es el emisor y el *j* el receptor. Para cada pixel F de la imagen se calculan el tiempo de vuelo desde el emisor a F y al receptor para determinar el instante de llegada de la señal procedente de F al receptor.

$$I_{iF} = \left| \sum_{j=1}^{N} A_{ij}(t_{ijF}) \right| \tag{8}$$

donde |·| es el módulo del argumento y $A_{ij}(t_{ijF})$ es el valor complejo del A-scan recibido por el elemento *j* en el instante t_{ijF} cuando emitió el elemento *i*. Se opera con la señal analítica (compleja) para mantener la información de fase hasta realizar la suma coherente.

Los tiempos de vuelo t_{ijF} deben determinarse con la misma resolución que en el caso anterior para evitar lóbulos de cuantización. La ecuación (8) se aplica a todos los píxeles F para obtener cada imagen de baja resolución. Ahora, variando el elemento emisor, se realiza un máximo de *N* disparos omnidireccionales, que proporcionan otras tantas imágenes de baja resolución, cuya suma en radiofrecuencia o señal compleja da la imagen final. El valor final en el pixel F es:

$$I_F = \left| \sum_{i=1}^{N} \sum_{j=1}^{N} A_{ij}(t_{ijF}) \right| \tag{9}$$

Con cada disparo desde el elemento seleccionado como emisor se adquieren simultáneamente los *N* A-scan recibidos por todos los elementos, formando una matriz de *N* x *K* muestras (*K* muestras por A-scan). Tras realizar los *N* disparos omnidireccionales seguidos de la adquisición de *N* x *K* muestras cada uno, se dispone de una matriz completa con N^2 x *K* datos, denominada *Full Matrix Capture* o *FMC*. Tras determinar por geometría los tiempos de vuelo (7) y calcular las señales analíticas interpoladas para conseguir la resolución temporal necesaria, se extraen y suman los valores que corresponden a cada píxel como indica (9).

La imagen final está enfocada en todos los píxeles en emisión y recepción, ya que se han tenido en cuenta los tiempos de vuelo desde cada emisor a cada píxel y a cada receptor. En la actualidad se considera que la imagen *TFM* es el estándar de calidad, especialmente en resolución, aunque todavía no alcanza la relación señal/ruido y cadencias de imagen de la técnica *phased array*.

Generalmente *TFM* se aplica por software, con CPUs o GPUs, por lo que no requiere un hardware especializado, aparte del genérico mostrado en la Figura 1.4. La técnica se conoció inicialmente como *Synthetic Aperture Focusing Technique* o *SAFT*, *Synthetic Transmit Aperture* o STA y otras variantes.

De especial importancia es la metodología *monoestática* que utiliza el mismo elemento para emitir y recibir, siendo la más sencilla que permite operar en tiempo real desde hace décadas [Kino, 1980], [Frazier, 1998], [Stepinski, 2007].

Las técnicas de apertura sintética han tenido una gran aceptación [Corl, 1978], [Kino, 1980], [Gehlbach, 1981], [Karaman, 1995], [Lockwood, 1998], [Gammelmark, 2003], [Nikolov, 2005]. En épocas más recientes y, exclusivamente en el ámbito de END, se ha propuesto y aceptado la denominación *Total Focusing Method* o *TFM* para la misma técnica [Holmes, 2005], nombre que se mantendrá en este trabajo.

Evidentemente la posibilidad de operar con *TFM* por software en tiempo real depende de la capacidad de procesamiento de la plataforma que ejecute el algoritmo, aunque el mayor problema suele ser transferir las N x K muestras adquiridas tras cada disparo. Por ejemplo, si $N = 128$, $K = 4$ Kmuestras de 2 Bytes, hay que transferir 1MB/disparo. La imagen final se obtiene de N disparos, esto es, de procesar un volumen de 128 MB.

En estas condiciones, alcanzar una tasa F=25 imágenes/s requiere una velocidad de transferencia sostenida superior a los 3.2 GB/s. Actualmente se alcanza con algunos estándares de PCI Express y otros, aunque también hay que contar el tiempo de procesamiento y de transferencia de las imágenes finales. En cualquier caso, se han obtenido ciertos resultados sobre plataformas multi-CPU y GPUs [Romero, 2009], [Lambert, 2012] y, más recientemente, con FPGAs [Njiki, 2013], [Le Jeune, 2015].

No obstante, en la práctica, sólo existe un equipo comercial que implemente la técnica TFM en tiempo real para arrays con un número limitado de elementos ($N \leq 64$) e imágenes de tamaño moderado (65 Kpíxeles) [M2M, 2016].

1.4 La imagen ultrasónica en el ámbito industrial

Desde hace 8 décadas se utilizan *transductores monoelemento*, tanto en pulso-eco como en transmisión, para crear imágenes por barrido mecánico, tanto de forma automática como manual (Figura 1.6). La yuxtaposición de los *Ascan* adquiridos por un transductor monoelemento forma una imagen *Bscan*. Una forma alternativa registra la amplitud máxima y su posición dentro de una ventana temporal definida dentro de cada *Ascan*, produciendo imágenes *Cscan* (amplitud) o *Dscan* (posición). Estas imágenes dan una visión global de la presencia de defectos en la pieza, que pueden analizarse posteriormente con mayor detalle si se almacenan todos los *Bscan* [Krautkrämer, 1990]. En el ámbito clínico se utilizan casi exclusivamente imágenes *Bscans*.

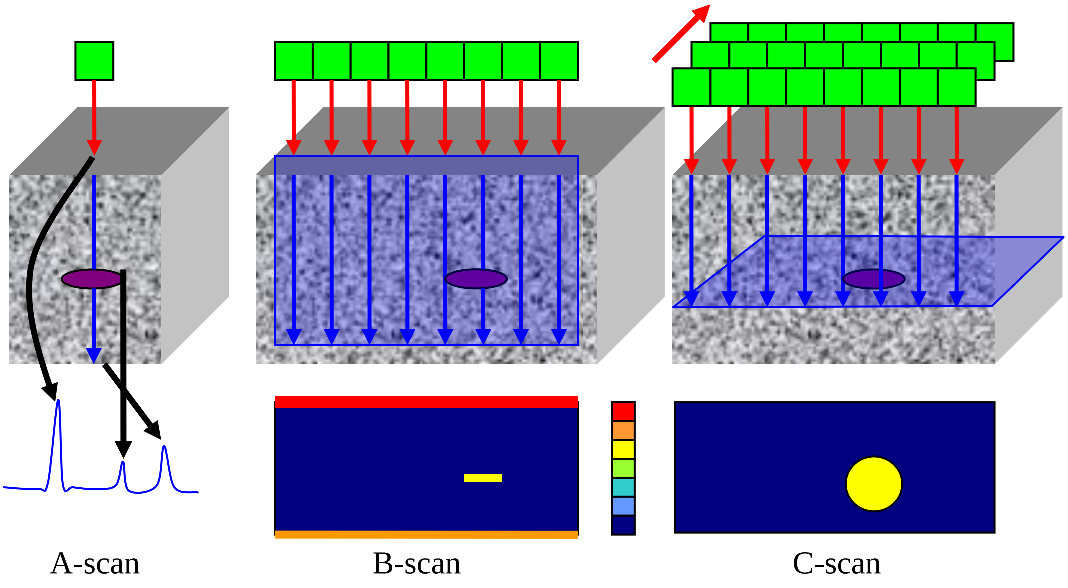

Figura 1.6 - Modalidades Ascan, Bscan y Cscan, monoelementos y arrays. El Ascan es una traza de ecos. El Bscan se forma por la yuxtaposición de múltiples Ascan codificando la amplitud con colores. El Cscan representa el máximo de la amplitud en una rodaja a cierta profundidad.

El barrido mecánico, se mantiene en la actualidad para transductores monoelemento y arrays. Un monoelemento obtiene en cada posición de barrido un *Ascan*, es decir, una línea de un *Bscan* y un único píxel del *Cscan* o *Dscan*. La inspección de componentes grandes puede requerir horas con sistemas automáticos basados en transductores monoelemento.

Por el contrario, un equipo *phased array* produce en cada posición una imagen *Bscan* con cierto número L de líneas ($L \approx 100$ para $N=128$ elementos), reduciendo proporcionalmente el tiempo de exploración y, consecuentemente, los costes asociados. Este último aspecto animó, sin duda, el desarrollo de los primeros equipos de imagen ultrasónica para END.

La imagen ultrasónica había demostrado ser una potente herramienta de diagnóstico en medicina, con las ventajas de ser no invasiva ni utilizar radiación ionizante. Sin embargo, su introducción en el ámbito industrial para la Evaluación No Destructiva (END) de componentes fue muy posterior, cuando la tecnología *phased array* ya había madurado en el ámbito clínico. Entre las razones que justifican este retraso se encuentran:

a) En medicina la región a inspeccionar es de extensión limitada, la superficie de contacto (piel) se adapta perfectamente a la forma redondeada del transductor y el medio se puede considerar homogéneo. En END la región de interés suele ser extensa, sobre componentes rígidos de geometría variable y casi nunca en contacto directo con el transductor, sino a través de un medio de acoplamiento. La presencia de varios medios de propagación complica la obtención de las *leyes focales*, mientras que es trivial en las aplicaciones médicas o en las muy escasas de END por contacto (ecuaciones 2 y 3).

b) En el ámbito médico, los ecógrafos vienen pre-programados de fábrica, con posiciones de los focos, leyes focales y otros parámetros. En una aplicación de END es el operador quien debe determinar estos parámetros para cada componente a inspeccionar, algo que no siempre es intuitivo y requiere un nivel formativo superior.

c) Los ecógrafos clínicos se fabrican de forma masiva y su coste se ha ido reduciendo. Además, la tecnología y su operación, son similares en las diversas especialidades médicas. En cambio, los equipos para END deben tener una gran versatilidad para adaptarse a muy diferentes aplicaciones, el mercado es más reducido y cada aplicación es diferente y debe ser preparada cuidadosamente antes de realizar la inspección.

d) La existencia de normas establecidas en END, generalmente basadas en transductores monoelemento, no siempre son trasladables a la imagen *phased array*. Este hecho sigue obstaculizando la introducción de la tecnología de imagen ultrasónica para END.

La complejidad y coste de la tecnología de imagen ultrasónica ha retrasado la introducción de la técnica *phased array* con enfoque dinámico hasta finales de los 90's y la de *TFM* hasta mediada la primera década del 2000 para aplicaciones de END.

1.5 Caracterización de la imagen

Ciertas características de la imagen relacionadas con su calidad son comunes a las aplicaciones médicas y de END. Las principales son: *resolución*, *dispersión angular, profundidad de foco, contraste*, *rango dinámico* y *tasa de visualización*. Salvo indicación expresa, la formulación se debe a [Kino, 1987].

Resolución: La *resolución* es la capacidad para separar en la imagen dos reflectores puntuales próximos entre sí. La imagen ultrasónica no es isótropa y hay que distinguir entre resolución axial Δz y lateral Δx y/o Δy. Una excepción es la imagen ultrasónica compuesta de ángulo completo (360º) que, para ciertas aplicaciones, presenta una resolución prácticamente isótropa [Hansen, 2008], [Medina, 2015].

Resolución axial Δz **:** medida a lo largo del eje de propagación, está determinada por la longitud del pulso ultrasónico, inversamente proporcional al ancho de banda relativo B del transductor, de frecuencia f_R. Llamando $\lambda = c / f_R$ la longitud de onda, está dada por:

$$\Delta z \approx 2\lambda / B \tag{10}$$

Resolución lateral Δx o Δy Se mide en dirección transversal a la de propagación y está determinada por la anchura del lóbulo principal del array. Es función del tamaño de la apertura $D=N\cdot d$, donde N es el número de elementos y d la distancia entre ellos, del ángulo de deflexión θ_f y de la distancia al foco R_f:

$$\Delta x \approx R_f \frac{\lambda}{D\cos\theta_f} = 2\left.\frac{R_f}{N\cos\theta_f}\right|_{d=\lambda/2} \tag{11}$$

Dispersión angular del haz $\Delta\alpha$: Es el ángulo cubierto por el haz ultrasónico emitido (o recibido) por una apertura de tamaño *D*. Entre ceros del lóbulo principal es:

$$\Delta\alpha \approx \frac{2\lambda}{D} \tag{12}$$

La dispersión angular del haz ultrasónico es importante en este trabajo porque se utiliza en dos de las técnicas de autoenfoque propuestas (AVSI y AVSI-TFM).

Profundidad de foco o longitud focal L_F: Definida como el rango en la dirección axial en el que la amplitud del campo cae menos de 3 dB respecto a su máximo valor en el foco situado a distancia R_F, dada por:

$$L_F = 7.1\lambda\left(\frac{R_f}{D}\right)^2 \tag{13}$$

Contraste (*CR*) y contraste a ruido (*CNR*): Por otra parte el *contraste* de la imagen es el cociente de los valores medios de amplitud en el fondo de la imagen μ_f y en la región de interés μ_q. Expresado en dB el contraste es [Turnbull, 1992]:

$$CR = -20\log_{10}\frac{\mu_q}{\mu_f} \tag{14}$$

El Contraste a Ruido (*CNR*) proporciona una medida de la *visibilidad* de los diferentes tejidos o indicaciones y es la relación entre el contraste y la desviación estándar de la textura de imagen y de fondo [Karaman, 1995]:

$$CNR = \frac{CR}{\sqrt{\sigma_q^2 + \sigma_f^2}} \tag{15}$$

Rango dinámico (*RD*): El máximo rango dinámico *RD* de la imagen es la relación de la amplitud del lóbulo principal en el foco, donde se suman coherentemente *N* señales, y en otro punto donde sólo exista señal de un elemento, esto es, $RD=N/1$, que en dB es:

$$RD_{dB} = 20\log(N)\ \text{dB} \tag{16}$$

Por ejemplo, si $N = 128$, $RD_{dB} = 42$ dB. En *TFM*, donde coinciden los focos de emisión y recepción, el rango dinámico alcanza $RD=N^2$ dado que se suman coherentemente N^2 señales (84 dB para $N=128$).

La presencia de lóbulos laterales limita el rango dinámico, aunque su efecto puede reducirse mediante técnicas de apodización o modulación de la amplificación de cada elemento a lo largo de la apertura con una ventana determinada (Hamming, Hanning, Blackman, etc.). La apodización reduce los lóbulos laterales a costa de perder resolución lateral [Szabo, 2004].

Por otra parte, los sistemas de imagen ultrasónica incluyen una función de compensación de la atenuación con el tiempo o CAT, denominada también Time-Gain Control (TGC), que modifica dinámicamente el factor de amplificación de las señales recibidas en función de la profundidad, tratando de mantener el nivel de la señal dentro del rango dinámico del conversor A/D. Con esto es normal alcanzar rangos dinámicos en el entorno de los 100 dB con respecto al ruido equivalente de entrada del amplificador.

Un aspecto frecuentemente olvidado en relación con la compensación TGC es que, al depender el coeficiente de atenuación de la frecuencia con un exponente >1, las señales van perdiendo las componentes de mayor frecuencia en su propagación y, por tanto, se reducen la resolución axial y la lateral.

Tasa de imágenes (F): Número de imágenes por segundo. Para obtener una imagen hasta una profundidad zmax en un medio homogéneo con velocidad de propagación c, el tiempo de tránsito del ultrasonido en ida y vuelta (pulso-eco) es:

$$t_{iv} = 2z_{\max} / c \tag{17}$$

El tiempo necesario para adquirir los datos de la imagen es:

$$\begin{aligned} t_{adq} &= 2Lz_{\max} / c \quad \text{phased array} \\ t_{adq} &= 2Nz_{\max} / c \quad \text{TFM} \end{aligned} \tag{18}$$

La máxima tasa de imágenes es la inversa de t_{adq}. Para una imagen *phased array* de *L*=200 líneas, en tejido biológico (*c*=1540 m/s) y una profundidad de 100 mm, la máxima tasa de imágenes es *F*= 38.5 imágenes/s. En acero (c≈ 6000 m/s) y, por contacto, la tasa de imágenes podría aumentar hasta *F*=150 imágenes/s. En *TFM*, si *N*=128 elementos y se opera por contacto, la máxima tasa de imágenes *teórica* sería de unas 230 imágenes/s, aunque difícilmente se alcanza la décima parte de este valor con la tecnología actual.

La máxima tasa de imágenes es una **limitación impuesta por la velocidad de propagación del ultrasonido, que sólo se puede superar mediante la formación de**

Tabla 1.1 - Requisitos de la imagen ultrasónica

Característica	**Medicina**	**END - industrial**
Resolución	Alta: 0.5 a 1 mm	Alta: 0.5 a 2 mm
Contraste	Alto: > 40 dB	Medio: > 30 dB
Rango dinámico	Alto: > 80 dB	Medio: > 50 dB
Tasa de imágenes	> 25 s^{-1} (ecografía clásica) > 300 s^{-1} (ecocardiografía) > 1000 s^{-1} (elastografía)	> 25 s^{-1} (inspecciones manuales) > 300 s^{-1} (inspecciones automáticas) > 1000 s^{-1} (ferrocarril, aeronáutica)

múltiples líneas de la imagen en paralelo, uno de los aspectos abordados en este trabajo de investigación.

La Tabla 1.1 muestra, en resumen y de forma cualitativa, las diferentes necesidades en las aplicaciones médicas e industriales con algunos valores orientativos. En general, la imagen médica es algo más exigente que la de END, especialmente en cuanto a rango dinámico.

1.6 Factores diferenciales en las aplicaciones de ecografía.

La ecografía comparte tecnología y métodos de formación de la imagen tanto en aplicaciones médicas como industriales. Sin embargo, existen diferencias entre ambas aplicaciones que, en ciertos casos, han condicionado el presente trabajo de investigación.

a) **Leyes focales:**

MEDICINA: El medio de propagación del ultrasonido en el ámbito médico es tejido biológico, que habitualmente se considera *homogéneo* con *velocidad de propagación constante* y próxima a la del agua (c_{agua} ≈ 1480 m/s a 20ºC, c_{biol} ≈ 1540 m/s). La inspección se realiza por *contacto* del array con la piel, que se adapta a la forma del transductor. Por consiguiente, existe *un único medio de propagación*, sin efectos de *refracción* en la interfaz entre dos medios. Acústicamente el tejido se asimila a un líquido por lo que, en la práctica, sólo se propagan *ondas longitudinales* o de compresión.

Estas características facilitan el cálculo de las leyes focales con *fórmulas cerradas* dadas por las ecuaciones (2) y (3), repetidas aquí donde $c \approx 1540$ m/s. Para el elemento i del array y un foco genérico en F (x_F, y_F, z_F),

$$t_{iF} = \frac{|\vec{r}_{iF}|}{c} = \frac{\sqrt{(x_i - x_F)^2 + (y_i - y_F)^2 + (z_i - z_F)^2}}{c}, \qquad \text{(2-rep)}$$

$$\tau_{iF} = \max_{1 \le i \le N}(t_{iF}) - t_{iF}, \quad 1 \le i \le N \qquad \text{(3-rep)}$$

Todos los parámetros son conocidos *a priori*, así que los N retardos $\{\tau_{iF}\}$ que forman la ley focal para cada foco se podrían precalcular y almacenar, pero ni siquiera esto es necesario. Con enfoque dinámico, hay que modificar continuamente la ley focal para seguir al pulso ultrasónico en su propagación. Sería un problema almacenar todos los retardos requeridos para el enfoque dinámico estricto, tantos como muestras se adquieran por el número de elementos. Hay que tener en cuenta, además, que para operar en tiempo real todos los canales han de tener acceso a la información de sus retardos respectivos, por lo que es difícil compartir una memoria común para todos los canales.

Para evitar estas dificultades, diversos autores propusieron circuitos de cálculo de las leyes focales que se integran en el control de cada canal de forma descentralizada y operan en tiempo real [Jeon, 1994], [Bae, 1998], [Feldkämper, 2000].

Desafortunadamente los circuitos de enfoque conocidos *sólo son válidos si el array está en contacto con un medio homogéneo, de velocidad constante*.

END-INDUSTRIAL: En el ámbito industrial apenas se hacen inspecciones con el transductor en contacto directo con el componente, tanto para evitar el desgaste de la superficie del array como para incidir con ángulos determinados. Es más habitual disponer una *suela o cuña* de material plástico bajo el transductor, adaptada a la geometría de la pieza.

Si el componente es irregular o grande se opera por *inmersión*, que puede ser total o local, donde el agua acopla el ultrasonido a la pieza a la vez que se adapta a su geometría. La inmersión local se realiza introduciendo los transductores en boquillas especiales, a las que se suministra un flujo continuo de agua durante el barrido.

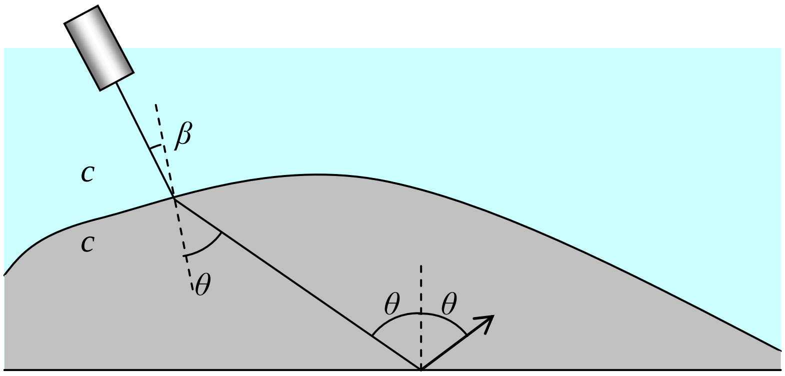

Figura 1.7 - Propagación en dos medios con velocidades c_1 y c_2. Ley de Snell: refracción en la interfaz entre ambos medios y reflexión en el fondo de la pieza (2º medio).

Así pues, en END, existen generalmente *dos medios de propagación*: el acoplante (plástico, agua, etc.) y el material de la pieza. Al propagarse las ondas ultrasónicas por dos medios con velocidades diferentes han de tenerse en cuenta los efectos de la *refracción*. Entre las consecuencias destacan que los tiempos de vuelo elementos-focos *no pueden calcularse mediante fórmulas cerradas*, como cuando se opera por contacto, y *tampoco son válidos los circuitos de enfoque conocidos*.

Además, debido a la refracción, en END ni siquiera es posible definir trayectorias del ultrasonido *sin considerar la geometría de la interfaz entre ambos medios*. La *ley de Snell* indica, a partir de las velocidades de propagación en acoplante (c_1) y pieza (c_2) y del ángulo de propagación respecto a la normal a la interfaz (θ) que se desea, cuál debe ser el ángulo incidente β, también respecto a la normal en el punto de incidencia (Figura 1.7):

$$\sin\beta = (c_1 / c_2)\sin\theta \tag{19}$$

Ahora bien, dado que la emisión de cada elemento del array es prácticamente omnidireccional, *¿en qué punto de la interfaz debe incidir para que el haz refractado pase por el foco*? Esta información es **crítica para conocer el tiempo de vuelo elemento-interfaz-foco, considerando cada tramo con su velocidad de propagación**, tanto para *phased array* como para *TFM*.

Aunque, a primera vista, el problema parece simple, no existe una formulación cerrada que permita abordarlo y hay que recurrir a métodos numéricos[2]. Se utilizan *técnicas basadas en el principio de Fermat* (búsqueda del camino más rápido) que se aproximan a la solución mediante *algoritmos iterativos* [Parrilla, 2007], [Long, 2009], [Drinkwater, 2009], [Suttcliffe, 2012a], [Le Jeune, 2015]. **Para realizar un enfoque dinámico estricto el proceso ha de repetirse con cada muestra del Ascan adquirido y para cada elemento del array**.

Al margen del tiempo *de cálculo*, **la solución sólo se puede encontrar si se *conoce la geometría de la interfaz* con la suficiente precisión**. Esto sólo está asegurado si se trabaja con cuñas o suelas rígidas como medios de acoplamiento, pero no en las inspecciones por inmersión o por contacto con suelas flexibles, donde las posiciones relativas entre los elementos del array y la pieza pueden variar. En estos casos se parte de una *descripción CAD del componente* y/o *se escanea para determinar su geometría*, por ejemplo, mediante sistemas láser [Santamaría, 2015]. Esta representación *se combina* con la del array para calcular el conjunto de leyes focales *adaptadas a la geometría actual*, aunque el procedimiento es engorroso y, en ocasiones, difícil de realizar en inmersión.

Las herramientas de cálculo de leyes focales para END se han basado mayoritariamente en programas de simulación de campo, con diversas aproximaciones: respuesta espacial al impulso [Buiochi, 2004], propagación de ondas monocromáticas [Ibañez, 2010] o técnicas de trazado de rayos (*raytracing*) [Richard 2010]. Las herramientas de simulación de campo permiten, por otra parte, verificar la corrección de las leyes focales calculadas.

El tiempo de cómputo no es despreciable, por lo que rara vez se usa el enfoque dinámico estricto, limitando el cálculo de leyes focales a algunos puntos en cada línea. Incluso así, habitualmente no pueden evaluarse en tiempo real, por lo que es preciso preparar con antelación las inspecciones.

En estas situaciones **las funciones de auto-enfoque que se proponen en esta Tesis Doctoral podrían resultar muy útiles**.

---

[2] La excepción es una interfaz plana, cuya solución se encuentra resolviendo una ecuación de 4º grado con un algoritmo que, además, tampoco es más rápido que los métodos iterativos [Parrilla, 2008].

b) Modos de propagación e indicaciones espurias:

Como se ha mencionado, en tejidos biológicos y, a efectos prácticos de la imagen, puede considerarse que sólo existen ondas longitudinales por comportarse como un líquido[3]. La situación es diferente en sólidos (END), donde pueden coexistir varios modos de propagación, cada uno de ellos con una velocidad diferente.

Los modos de propagación más importantes para este trabajo son las ya mencionadas ondas longitudinales (o de compresión) y transversales (o de cizalla). De hecho, en cada discontinuidad (interfaz, defecto, pared, etc.), se producen ambos modos, que se mezclan y pueden dar lugar a imágenes confusas por sus diferentes velocidades de propagación. Por ejemplo, una grieta produce ecos longitudinales que llegan al transductor antes que los del modo transversal, dando lugar a una doble indicación. Otros modos también presentes en sólidos son las ondas superficiales y, para ciertas combinaciones de frecuencia y espesor, ondas dispersivas en las que varía su velocidad de propagación con la frecuencia [Rose, 2004].

Las leyes focales deben calcularse no sólo para una geometría determinada sino, también, para un tipo de onda y velocidad de propagación [Drinkwater, 2006]. De este modo se atenúan las indicaciones debidas a otros modos de propagación, aunque no se eliminan completamente. También existen interferencias por otras causas como reverberaciones, ecos geométricos, sonido residual, etc. De hecho, en ocasiones, las indicaciones de ciertos defectos reales pueden llegar a ser de menor amplitud que las espurias.

La técnica de *Imagen por Coherencia de Fase* (*Phase Coherence Imaging, PCI*), desarrollada por nuestro grupo [Camacho, 2009], suprime en gran parte las indicaciones espurias y otras asociadas a las limitaciones físicas de los arrays ultrasónicos reales (tamaño de apertura, distancia entre elementos, etc.), como son los lóbulos laterales y de rejilla. En realidad, la *PCI* atenúa cualquier indicación que no proceda del foco.

---

[3] En realidad, los tejidos biológicos son medios viscoelásticos en los que sí pueden propagarse ondas transversales o de cizalla. Pero éstas son mucho más lentas, de menor amplitud que las longitudinales y se atenúan muy rápidamente, por lo que, a efectos de la imagen habitual, pueden ignorarse.

Este resultado ha permitido **desarrollar una nueva metodología de imagen ultra-rápida y de alta calidad con cadencias de imagen muy superiores a las actuales**, que forma parte de los resultados de esta Tesis Doctoral [Cruza, 2017].

c) Rango dinámico, resolución y tasa de imágenes

MEDICINA: La imagen médica exige un elevado rango dinámico, ~80 dB, que permita visualizar simultáneamente señales débiles y fuertes en escala logarítmica. Casi todos los equipos de ecografía disponen de apodización dinámica o estática para aumentar el rango dinámico de las imágenes con ciertas pérdidas de resolución [Szabo, 2004]. Por otra parte, delimitar y medir estructuras biológicas con precisión requiere una elevada resolución [Gooding, 2010]. En términos generales la resolución lateral y el rango dinámico mejoran al operar con mayor número de elementos, mientras que la resolución axial mejora con un mayor ancho de banda y mayor frecuencia del transductor, pero la atenuación puede limitar la profundidad máxima de la imagen en este caso.

En tejidos blandos la atenuación está típicamente en el rango de 0.5 a 1 dB/cm/MHz. La señal de un transductor de 5 MHz a una profundidad de 10 cm (20 cm en ida y vuelta) se atenúa hasta en 100 dB, lo que dificulta obtener imágenes de calidad. Las frecuencias más altas (10-20 MHz) se reservan para imágenes de órganos superficiales (ojos, piel, etc.), las medias (5-10 MHz) para tejidos intermedios (ecocardiografía) y las bajas (2 a 5 MHz) para tejidos más profundos (ginecología, abdomen, etc.).

Por otra parte algunas aplicaciones (ecocardiografía, elastografía, etc.) requieren altas tasas de imagen, por encima de las 1000 imágenes por segundo [Bercoff, 2004], que demandan alternativas ultra-rápidas de adquisición y formación de la imagen.

END-INDUSTRIAL: En las aplicaciones de imagen ultrasónica para END la resolución también es muy importante, tanto en sentido axial como en lateral. La máxima resolución se obtiene enfocando en emisión y recepción en cada punto de la imagen mediante la técnica *TFM*, considerada la referencia de resolución. Sin embargo, *TFM* tiene peor relación señal/ruido y demanda mayor potencia de cálculo que la técnica *phased array*. En la práctica, sólo existe una realización física que opere en tiempo real para $N \leq 64$ elementos e imágenes de hasta 65 Mpixels, sin autoenfoque [M2M, 2016].

Este tema ha sido investigado en esta Tesis Doctoral proponiendo una nueva técnica de autoenfoque adaptada a la técnica *TFM* [Cruza, 2016a].

Disponer de un elevado rango dinámico también es importante para END, en especial para inspeccionar materiales con ruido de grano y de alta atenuación (aleaciones y soldaduras de aceros austeníticos, composites, etc.). En estos casos, la mayor limitación está en el ruido de fondo que, junto con la aparición de indicaciones geométricas de mayor nivel, puede enmascarar la presencia de pequeños defectos.

A lo largo de los años se han desarrollado métodos de diversidad espacial y frecuencial para reducir los niveles de ruido de grano, siendo la más conocida la técnica *Split Spectrum Processing* (SSP) [Newhouse, 1982] que analiza las señales en múltiples bandas dentro del espectro del transductor.

Estos métodos requieren una sintonía crítica de diversos parámetros para mejorar la relación señal/ruido de grano. La Imagen por Coherencia de Fase (*PCI*) mencionada anteriormente proporciona un método robusto y libre de parámetros para la cancelación automática de ruido de grano en tiempo real [Camacho, 2011a], [Dasel, 2014].

En las aplicaciones de END no se suele utilizar la apodización, pues es más importante la resolución que el rango dinámico. Esto se debe a que las imágenes se proporcionan en escala lineal, con un rango limitado a los 25-30 dB. La técnica *PCI* también ayuda a mejorar, simultáneamente, resolución lateral y rango dinámico al reducir el nivel de los lóbulos laterales [Camacho, 2009].

Como en el caso médico, la END demanda una elevada tasa de imágenes sólo en ciertas aplicaciones. En particular la inspección automática de componentes grandes, donde un array manejado por un robot realiza un barrido y adquiere imágenes Bscan a intervalos regulares. El tiempo de inspección es importante para reducir los costes y el número de instalaciones requeridas para inspeccionar el 100% de la producción, particularmente en sectores como el aeronáutico y aeroespacial.

Asimismo, el sector ferroviario demanda la END automática de infraestructuras, en particular carriles, a alta velocidad (> 80 Km/h). En la actualidad este proceso se realiza con algunos transductores monoelemento y una resolución espacial limitada. Para obtener una imagen cada 10 mm, el sistema ultrasónico debería proporcionar tasas superiores a las

2000 imágenes/s, una capacidad que está muy lejos de la tecnología comercial disponible en la actualidad.

El aumento de la tasa de imágenes también ha formado parte de los objetivos y resultados de esta Tesis Doctoral.

1.7 Carencias.

A pesar de que la imagen ultrasónica ha mantenido una evolución constante, eso no impide que existan ciertas carencias y limitaciones que, progresivamente, van siendo superadas con resultados de la investigación y nuevos desarrollos.

Entre las carencias que han sido abordadas en este trabajo deben citarse:

- **La falta de técnicas de autoenfoque que eviten los problemas asociados al cálculo y programación de leyes focales**, en especial con un medio de acoplamiento.
- **La escasez de propuestas para producir imágenes ultrasónicas con o sin auto-enfoque a ultra-alta velocidad**, como demandan cada vez más aplicaciones.
- **La necesidad de nuevas arquitecturas y métodos numéricos para acelerar, tanto el cálculo de las leyes focales, como de producir imágenes.**

Los efectos de algunas de estas carencias se muestran con un ejemplo a continuación.

La Figura 1.8.izq muestra la imagen ultrasónica de una pieza cilíndrica con taladros. Pero una ligera desviación geométrica pieza-array produce una imagen carente de significado (Figura 1.8.dcha). Está reconocido que una mera desviación de 1º produce importantes pérdidas en la imagen [Chatillon, 2009].

El problema es común en piezas de formas no uniformes, que hay que inspeccionar por inmersión y que pueden desviarse o modificar ligeramente su forma. Actualmente, **la única alternativa es el escaneo previo de la pieza**, normalmente por medios ópticos (láser-cámara) para, una vez detectada su geometría, poder calcular las *leyes focales adaptadas* [Cuevas, 2015]. Ciertamente esta operación ni es sencilla ni fiable cuando el componente se encuentra sumergido. En los últimos años, ha surgido el interés por resolver este problema pendiente,

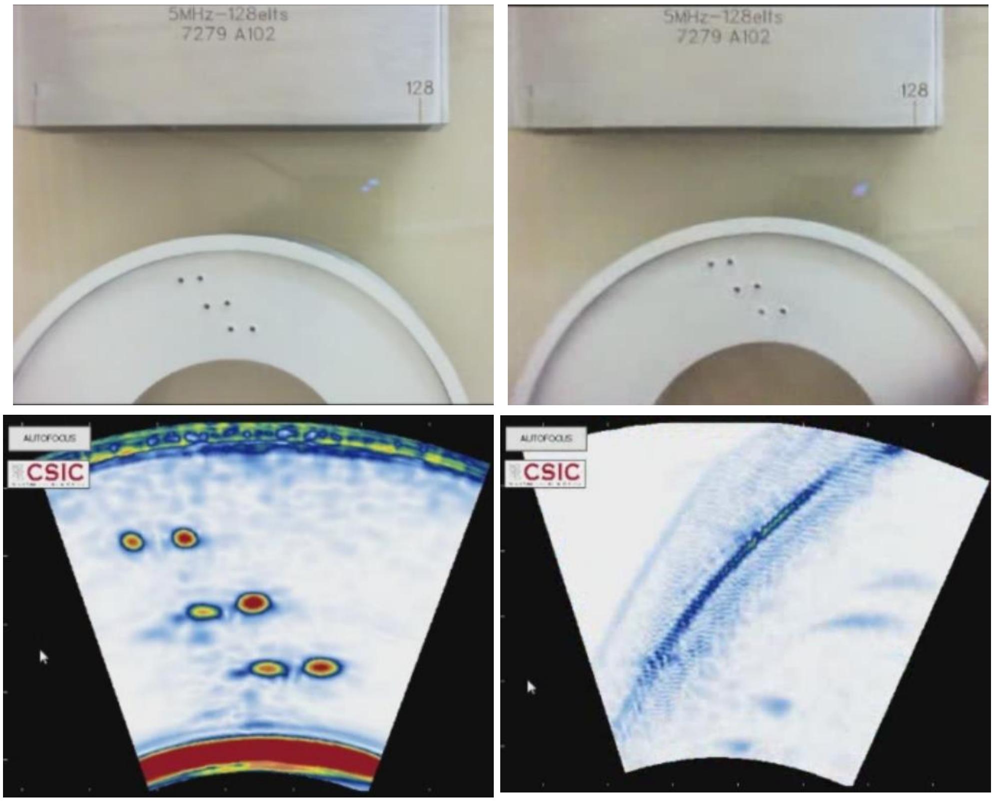

Figura 1.8 - Inspección de una pieza cilíndrica con un conjunto de taladros. Izquierda: geometría adaptada pieza-array, produce una imagen correcta. Derecha: geometría ligeramente desviada. En esta última desaparecen las indicaciones de los taladros y las interfases.

sobre todo en el sector industrial que es al que más afecta, con algunas alternativas que merece la pena reseñar brevemente.

Por otra parte, se está demandando un aumento de velocidad en los procesos automáticos de inspección no destructiva, que sólo pueden cubrirse con nuevos métodos de imagen a alta velocidad. Las disponibilidades tecnológicas animan a cubrir ambas necesidades.

La solución pasa por **encontrar técnicas adaptadas a la geometría actual del componente que produzcan imágenes enfocadas a todas las profundidades en un tiempo compatible con las velocidades de exploración requeridas** evitando el uso de medios diferentes de los utilizados para adquirir las imágenes ultrasónicas. Esto sólo es abordable con sistemas de imagen de muy altas prestaciones, basados en las disponibilidades tecnológicas actuales.

1.8 Aproximaciones previas al autoenfoque

Si el array se sitúa en contacto con el objeto a inspeccionar (Figura 1.9), el cálculo de leyes focales es trivial como ha sido expuesto, mediante la aplicación de las fórmulas cerradas (2) y (3).

Por tanto, no es de extrañar que se hayan propuesto *arrays flexibles* que se adaptan a la superficie de la pieza a inspeccionar, Figura 1.10.a [Casula, 2004], [Toullelan, 2008], o membranas flexibles adaptadas a una cuña convencional que realizan una función análoga, Figura 1.10.b [Long, 2007b].

Sin embargo, estas realizaciones sólo son válidas para inspecciones manuales a baja velocidad, para evitar daños al array o a la membrana. En el primer caso, la posición de los elementos se obtiene con ayuda de perfilómetros integrados en el dispositivo. En el caso de la membrana, no se ha dado ningún método para medir su deformación, por lo que se producen grandes errores en la estimación de la geometría.

Una evolución de la suela deformable es la integración de un array en el interior de un

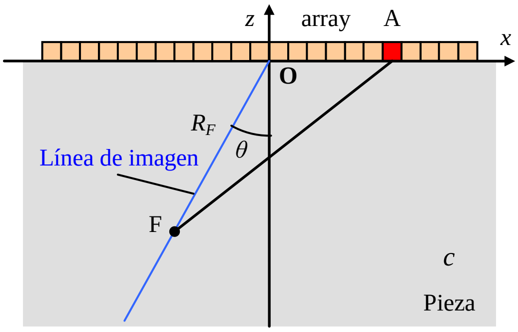

Figura 1.9 - Esquema de una inspección por contacto array-pieza, sin acoplante interpuesto.

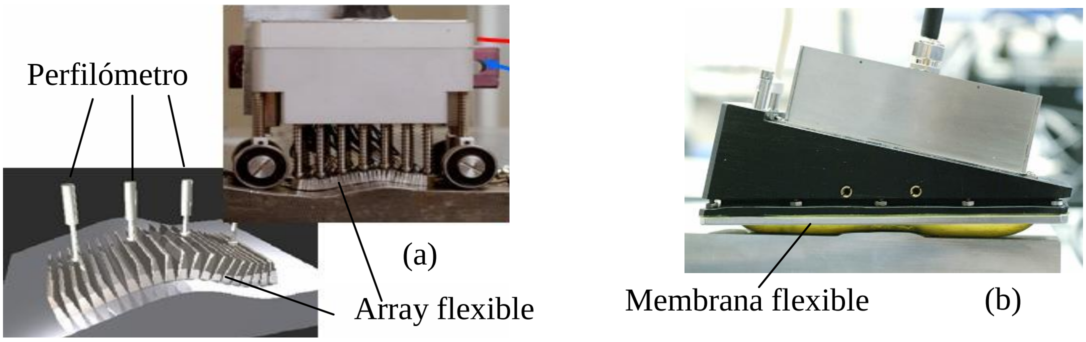

Figura 1.10 - Acoplamientos flexibles para inspección por contacto de superficies irregulares: a) array flexible [Toullelan, 2008], b) suela deformable [Long, 2007b].

Figura 1.11 - Integración de un array dentro de un rodillo de superficie flexible [Rapidscan, 2017].

rodillo de material flexible, cuyo plano de imagen contiene a la generatriz que está en contacto con la pieza. En este caso, las leyes focales pueden estar pre-calculadas, suponiendo que la deformación del rodillo es pequeña, usándose más bien como método de acoplamiento seco en componentes planos o con muy baja curvatura (Figura 1.11).

Los componentes de geometría más compleja requieren que la inspección se realice por inmersión. En estas condiciones, la refracción que produce el cambio de medio de propagación complica el cálculo de las leyes focales. No sólo esto, sino que no es trivial posicionar un array y una pieza de geometría compleja en inmersión con la precisión requerida para el enfoque dinámico estricto. Por esta razón una función de autoenfoque debería operar sin conocimiento previo de la geometría del componente, adaptándose a ella de forma automática.

Para evitar esta dificultad se han propuesto algunas aproximaciones que, aunque no todas pueden considerarse de auto-enfoque, al menos facilitan la obtención de imágenes válidas para la detección y evaluación de ciertos defectos. Las más destacables son:

- *PAUT* (*Phased Arrays for Ultrasound Testing*), desarrollada por EADS (European Aeronautic Defence and Space) para piezas aeronáuticas. Realiza un primer disparo con todos los elementos del array para generar una onda plana, registra los tiempos de llegada del primer eco y re-dispara el array con unos retardos inversos (Figura 1.12). Esto produce un frente de ondas *paralelo* a la interfaz con lo que el ultrasonido incide perpendicularmente en la pieza [Ithurralde, 2006]. Obviamente PAUT no facilita el enfoque dinámico al carecer de información de la geometría de la interfaz pero, al entrar con incidencia normal, permite detectar defectos planos y paralelos a la interfaz, aunque es difícil dimensionarlos con un haz ultrasónico tan ancho.

- *PAINTBRUSH* + *TDTE* (*Time-Domain Topological Energy*), descritas en [Dominguez, 2010a] y [Dominguez, 2010b]. Paintbrush es similar a PAUT en el sentido de que emite y recibe con onda plana. La pobre resolución lateral del método se suple con el algoritmo TDTE que realiza una inversión temporal de los datos registrados y su ajuste por simulación con los proporcionados por una pieza de referencia. Resulta computacionalmente costoso, con unos tiempos para formar la imagen con GPU entre 45 y 600 segundos en función del espesor del componente [Dominguez, 2010a].

- *SAUL* (*Self-Adaptive Ultrasonic Technique*). Es una extensión de la técnica *PAUT* para superficies de geometrías más complejas [Robert, 2012a], [Robert, 2012b]. La técnica genera un primer frente de ondas plano cuyos ecos se utilizan para calcular las

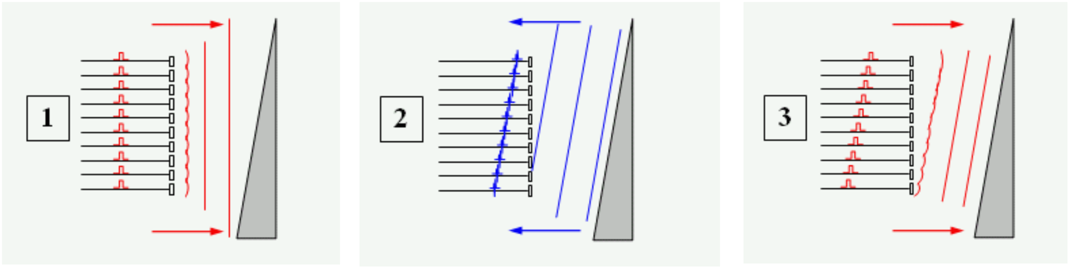

Figura 1.12 - Técnica PAUT para generar onda plana paralela a la interfaz: 1) Emisión onda plana paralela al array, 2) recepción del eco de la interfaz, 3) Re-emisión con retardos invertidos respecto a los del primer eco recibido en el paso anterior. Gráfico de [Ithurralde, 2006].

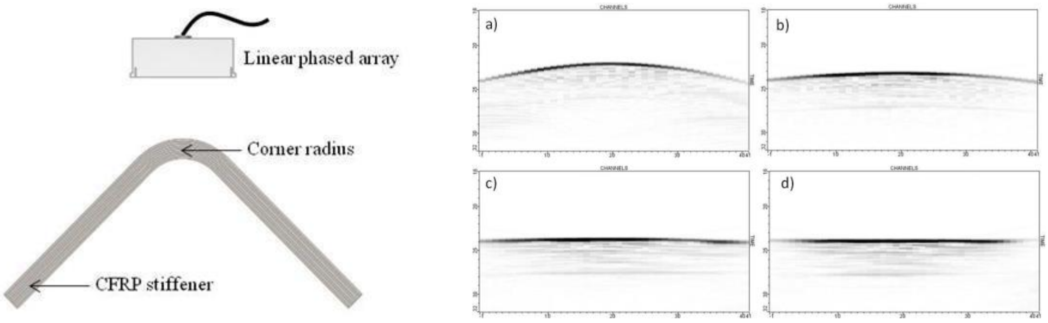

Figura 1.13 - Esquema de operación de SAUL: El frente de ondas emitido se va adaptando a la forma de la interfaz en disparos sucesivos (4 en este caso). A la derecha la imagen adquirida de un laminado sólido de fibra de carbono ([Robert, 2012a]).

leyes focales en emisión para el siguiente disparo, tratando de equilibrar los tiempos de llegada del eco de la interfaz.

Repitiendo el proceso, en tres o cuatro disparos consecutivos el frente de ondas se adapta a la geometría de la interfaz, de modo que, al final, el ultrasonido penetra en la pieza con incidencia normal (Figura 1.14).

SAUL facilita la detección de defectos en estructuras laminadas, pero difícilmente puede dimensionarlos al carecer de enfoque dinámico. De hecho, la resolución lateral es muy baja, de modo que no podría separar dos defectos próximos entre sí que estuvieran ubicados a la misma profundidad. Una vez detectado un defecto, puede dimensionarse por otros medios.

La técnica se comercializa y se aplica en la inspección de laminados sólidos de fibra de carbono.

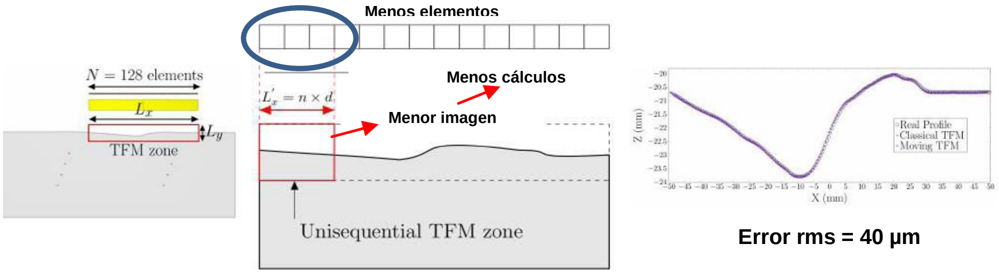

Figura 1.14 - Técnica ADAPT-TFM. Primero obtiene una imagen TFM móvil con una subapertura, que se usa para extraer el perfil. De éste se calculan por Fermat los tiempos de vuelo emisor-interfaz-pixel-interfaz-receptor para obtener la imagen por TFM [Le Jeune, 2015].

- *ADAPT-TFM* (*Adaptive Imaging with the Total Focusing Method*) [Le Jeune, 2015]. Esta técnica, adecuada para inspecciones por inmersión, genera dos imágenes *TFM* (Figura 1.14). La primera considera un medio homogéneo (sólo agua), que detecta la geometría de la interfaz. Para reducir el tiempo de cálculo se opera con una pequeña subapertura y, además, las imágenes parciales son pequeñas, agilizando el proceso de obtención del perfil de la pieza.

  Para la segunda imagen se calculan, por aplicación del principio de Fermat y métodos iterativos, los tiempos de vuelo a los píxeles considerando la geometría detectada. Es un auténtico método de auto-enfoque, con el inconveniente de ser bastante costoso en tiempo de cálculo, lo que limita la tasa de imágenes.

Aparte de estas ideas, no se ha encontrado en la literatura especializada más propuestas o alternativas que faciliten la obtención de imagen ultrasónica sin conocimiento a priori de la geometría array-pieza.

2 Aportaciones

Aunque nuestro grupo también ha participado en la producción de antecedentes para abordar los problemas descritos, esta sección resume las aportaciones más destacables que forman parte de esta Tesis Doctoral.

2.1 Técnicas de autoenfoque propuestas en esta Tesis

Los trabajos que forman parte de esta Tesis Doctoral han seguido una línea muy diferente a otras aproximaciones anteriores, lo que ha permitido desarrollar varias alternativas para la generación de imagen ultrasónica autoenfocada, de calidad y a alta velocidad. De forma muy resumida, las principales aportaciones para la imagen ultrasónica autoenfocada que han dado lugar a algunas de las publicaciones incluidas en esta memoria, han sido:

- **AUTOFOCUS [Cruza, 2013]**. Propone tres innovaciones: a) estimación de la geometría array-interfaz por métodos ultrasónicos, b) cálculo de un array virtual que elimina los problemas asociados a la refracción, c) circuito que implementa el enfoque dinámico estricto en tiempo real con leyes focales adaptadas a la geometría.

- **UFAF [Cruza, 2015a]**, *Ultra Fast Auto-Focusing*, calculador ultra-rápido de leyes focales para autoenfoque. Complementa a la técnica *AUTOFOCUS* proporcionando un hardware que calcula los parámetros del circuito de autoenfoque a alta velocidad. Con FPGAs de tamaño moderado y arrays de 128 elementos, se pueden alcanzar tasas superiores a las 300 imágenes por segundo sin conocimiento previo de la geometría, corrigiendo las leyes focales en cada imagen.

- **AVSI-TFM [Cruza, 2016a]**, *Autofocused Virtual Source Imaging by TFM*. Genera *L* fuentes virtuales en la interfaz enfocando sobre ella con diferentes subaperturas en emisión y recepción. Ni calcula ni necesita una representación geométrica de la interfaz, sino únicamente las coordenadas del punto de incidencia normal desde cada subapertura. Estas se calculan con medidas ultrasónicas y las mismas fórmulas cerradas propuestas para AUTOFOCUS.

Una vez formadas las *L* fuentes virtuales sobre la interfaz, la técnica *TFM* genera la imagen usando las fuentes virtuales como elementos de un array. Una de las mayores ventajas de esta técnica es que las fuentes virtuales se generan "en contacto" con la pieza, evitando de forma natural los problemas asociados a la refracción.

Una alternativa más simple que *AVSI-TFM* es componer la imagen mediante técnicas de apertura sintética monoestática, donde emisor y receptor coinciden en la misma fuente virtual [Camacho, 2015]. La técnica, denominada simplemente *AVSI*, tampoco requiere conocer la geometría de la interfaz y es muy rápida. Demostramos que *AVSI* proporciona imágenes autoenfocadas de alta resolución en tiempo real, utilizando un equipamiento estándar, multiplexado, aunque con una relación señal/ruido menor que la *AVSI-TFM*.

- **PWPCI [Cruza, 2017]**, *Plane-wave Phase Coherence Imaging*. Este método proporciona una elevada tasa de imágenes sin sacrificar su calidad. Se basa en la emisión de ondas planas, en general con una diversidad de ángulos que conforman imágenes de baja resolución. Su composición y procesamiento con coherencia de fase mejora la calidad de las imágenes hasta hacerlas indistinguibles de las *TFM* de referencia, **pero a tasas hasta dos órdenes de magnitud superiores que las alcanzadas actualmente con *TFM***.

Este conjunto de aportaciones facilita la obtención de imágenes auto-enfocadas tanto con técnicas *phased array* (AUTOFOCUS) como *TFM* (AVSI-TFM, AVSI). Para evitar los problemas causados por la refracción en la interfaz con *phased array*, se ha desarrollado la **teoría y método de cálculo del *array virtual* que opera en un único medio**. Para *TFM* se han propuesto las alternativas AVSI-TFM y AVSI que también operan en un único medio.

Un factor importante para la operación en tiempo real ha sido el **diseño y desarrollo de circuitos con bajo uso de recursos hardware que, asociados a cada canal, realizan el enfoque dinámico estricto en tiempo real y con alta resolución temporal**. Por primera vez, junto con el array virtual, estos circuitos han posibilitado obtener imagen con propagación en dos medios y en tiempo real (durante la adquisición de señal).

En la actualidad estamos finalizando el diseño y realización del **hardware que podrá integrar todas las técnicas aquí presentadas y, además, la formación de imagen en**

paralelo. Este sistema, basado en FPGAs Kintex y SoCs Zynq, inicia una nueva generación de equipos de imagen ultrasónica para END de muy altas prestaciones.

2.1.1 Técnicas Autofocus y AVSI para autoenfoque

En principio, un enfoque automático y simultáneo con la generación de imagen, debe realizar dos operaciones antes de la adquisición de datos (AUTOFOCUS):

I. Estimar la geometría de la interfaz acoplante-pieza obteniendo su representación analítica $z = \mathrm{f}(x)$ para calcular las leyes focales.

II. Calcular las leyes focales adaptadas a la geometría estimada y programarlas en el sistema de adquisición de señales.

Por otra parte, también es posible prescindir del cálculo de la representación analítica de la interfaz, como hacen las propuestas *AVSI* y *AVSI-TFM*. En estas alternativas,

I. Sólo es necesario encontrar las coordenadas en la interfaz de las fuentes virtuales.

II. La imagen se forma mediante técnicas de apertura sintética utilizando las fuentes virtuales como elementos de un array virtual en contacto con el componente.

En ningún caso hay que re-evaluar ni leyes focales ni posiciones de las fuentes virtuales si no cambia la geometría. Los cambios de geometría se detectan por las desviaciones de los puntos de incidencia normal en la interfaz, procedimiento rápido basado en fórmulas cerradas, que puede implementarse fácilmente en hardware o en el procesador de un SoC.

En resumen, la principal diferencia entre *AUTOFOCUS* y las técnicas *AVSI* es que en el primer caso se evalúa una función representativa de la geometría de la interfaz, mientras que en *AVSI* se sitúan las fuentes virtuales sobre la interfaz sin necesidad de estimar su forma.

Otra diferencia es su operación en tiempo real: *AUTOFOCUS* y *AVSI* pueden ejecutarse en cualquier sistema *phased array*, independientemente del número de canales disponibles en recepción. *AVSI-TFM* requiere un sistema con *N* canales emisores y *N* receptores simultáneos, así como un procesador de altas prestaciones para formar la imagen *TFM*.

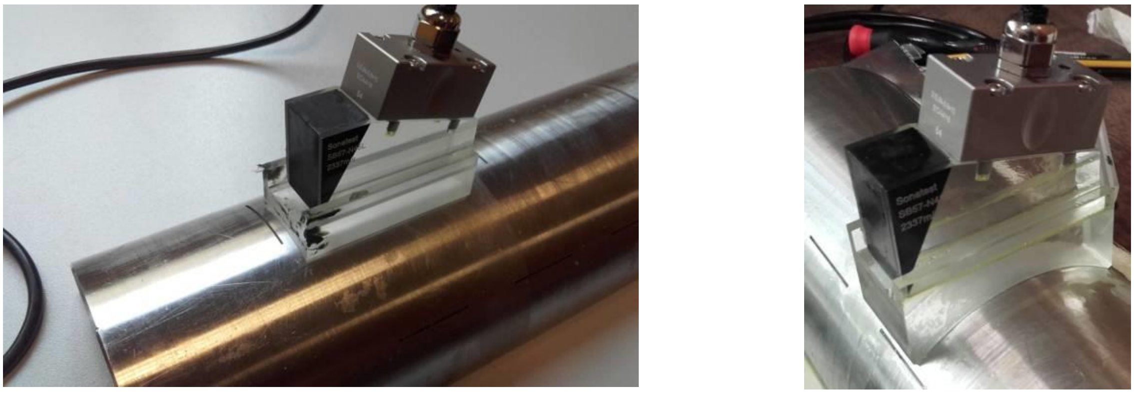

Figura 2.1 - Inspección de geometrías simples con cuñas o suelas adaptadas y leyes focales fijas.

2.1.2 Estimación de la geometría de la interfaz.

Para inspeccionar componentes de forma conocida y constante se utiliza una suela o cuña de material plástico cuya forma se adapta a la pieza. Las leyes focales se precalculan por Fermat u otro método y se mantienen indefinidamente, ya que la geometría no cambia. Esta práctica es habitual para la inspección de cilindros o planos, utilizando gel acoplante entre cuña y pieza para eliminar el aire y mejorar el acoplamiento (Figura 2.1).

El mayor problema surge cuando no se conoce la geometría de la pieza, es demasiado complicada para utilizar una suela fija o se conoce con precisión limitada, como sucede frecuentemente al inspeccionar piezas de forma arbitraria por inmersión. En muchos casos la inmersión es local, mediante el suministro de un flujo continuo de agua entre el transductor y el componente.

La Figura 2.2 muestra algunos ejemplos de estas situaciones, frecuentes en el sector aeronáutico, generación de energía, plantas químicas, centrales nucleares, etc.

Para el cálculo de las leyes focales, **no sólo es necesario conocer la geometría de la pieza, sino la del array-pieza**. La esquina superior izquierda de la Figura 2.2.a muestra un ejemplo donde se conoce la geometría circular de la pieza, pero no la posición relativa del array con la suficiente precisión. Algunos autores han ideado técnicas para reconocer la posición de cada uno de los elementos de un array flexible (Figura 1.10) a partir de la propia imagen, pero con un gran coste computacional [Roy, 2000], [Hunter, 2010], [Hunter, 2011].

Figura 2.2 - Situaciones en las que, o es difícil conocer la geometría exacta, o la forma y/o radios de curvatura del componente cambian con la región inspeccionada. No pueden usarse cuñas fijas.

Incluso en estos casos los errores son relativamente grandes, por lo que su utilización queda restringida a situaciones en las que basta obtener imágenes aproximadas.

La inversión temporal proporciona imágenes enfocadas automáticamente al reflector de mayor amplitud en la imagen [Fink, 1989]. Su generalización para el enfoque en múltiples reflectores utiliza técnicas iterativas [Prada, 1991], [Prada, 1997]. En cualquier caso, se trata de métodos complejos de gran carga computacional, cuya aplicación ha quedado restringida al ámbito académico.

Más recientemente se ha propuesto obtener una estimación de la geometría mediante la técnica ADAPT-TFM descrita anteriormente. Esta alternativa crea, con una subapertura, una imagen de pequeñas dimensiones debajo del propio array, limitando el número de píxeles para reducir el tiempo de cálculo de la geometría array-pieza. La subapertura se desplaza a lo largo del array para cubrir con imágenes en varios disparos toda la región bajo el array. El perfil se obtiene por la máxima amplitud de las señales en cada una de las imágenes adquiridas, utilizándose para evaluar los tiempos de vuelo por aplicación del principio de Fermat con métodos iterativos. El error máximo reportado es de 80 µm para un array de N=128 elementos, frecuencia f_R = 2 MHz ($\lambda \approx 0.75$ mm en agua).

La primera aproximación para la obtención de una representación analítica precisa de la interfaz entre acoplante y pieza fue realizada por nuestro grupo en [Camacho, 2014a]. En este trabajo se propusieron tres técnicas, que estiman la geometría con los mismos medios (array y equipo electrónico) que se utilizan para adquirir y formar la imagen. Las técnicas son de *pulso-eco*, *pitch-catch* y *onda plana*, cada una de ellas con sus requisitos y propiedades, como se describen a continuaición.

2.1.2.1 Técnica pulso-eco para estimar la geometría

Cada uno de los elementos del array se utiliza en pulso-eco como un transductor individual, obteniendo con cada disparo el tiempo de vuelo al punto más próximo de la interfaz (Figura 2.3), esto es, el que corresponde al primer eco registrado.

El tiempo de vuelo del ultrasonido en ida y vuelta t_i para el elemento i proporciona las distancias R_i elemento-interfaz que definen N circunferencias tangentes a la interfaz. En el punto de tangencia, la incidencia del ultrasonido es normal a la interfaz (Figura 2.4):

$$R_i = c_1 t_i / 2 \tag{20}$$

Para los elementos i e i + 1, considerando que los segmentos E_iP_i y $E_{i+1}P_{i+1}$ son prácticamente paralelos:

$$\sin \varphi_i = \frac{R_i - R_{i+1}}{d} = \frac{c_1}{2d}(t_i - t_{i+1}) \quad 1 \le i \le N-1 \tag{21}$$

siendo d la distancia entre elementos. Si (x_{Ai}, z_{Ai}) son las coordenadas del elemento i del

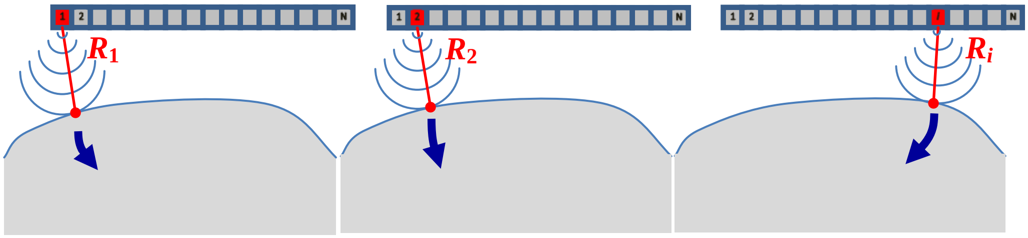

Figura 2.3 - Esquema para la obtención de la interfaz por pulso-eco. Cada elemento del array actúa como emisor y receptor, detectando el punto más próximo de la interfaz a distancia R_i.

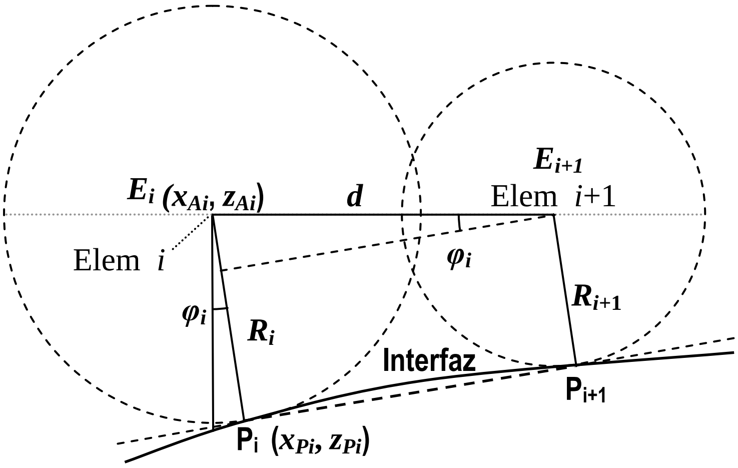

Figura 2.4 - Geometría para el cálculo de las coordenadas de los puntos P_i en la interfaz.

.

array, las del punto P_i en la interfaz se obtienen mediante:

$$\begin{aligned} x_{Pi} &= x_{Ai} + R_i \sin \varphi_i \\ z_{Pi} &= z_{Ai} - R_i \cos \varphi_i \end{aligned} \qquad 1 \le i \le N-1 \tag{22}$$

Así, con *N* disparos se obtienen las coordenadas de *N*-1 puntos en la interfaz (Figura 2.5).

Con este conjunto de puntos, basta **realizar un ajuste a un polinomio o función** para obtener una representación analítica de la interfaz $z = f(x)$. Conviene anticipar que ***las técnicas AVSI y AVSI-TFM utilizan* (20) a (22) *para ubicar las fuentes virtuales***, sin necesidad de realizar ningún ajuste a una función.

El mayor inconveniente del método es que requiere múltiples disparos y adquisiciones del

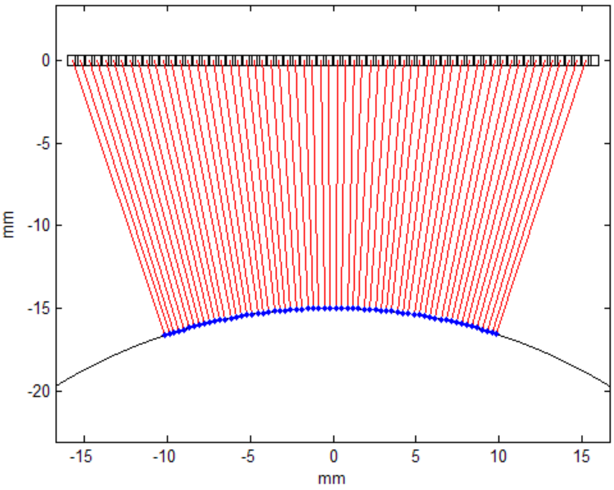

Figura 2.5 - Detección de puntos de la interfaz (azul) con la técnica pulso-eco.

tiempo de vuelo. Por ejemplo, considerando una columna de agua entre array y pieza de 15 mm en promedio, son necesarios al menos 20 μs para cada medida que, para N = 128, resulta 2.6 ms. Este tiempo no es despreciable y puede reducir la tasa de imágenes. En la práctica, puede limitarse el número de puntos que intervienen en la función de ajuste, lo que reduce el número de emisiones.

A cambio de este inconveniente, la técnica pulso-eco puede utilizarse virtualmente con cualquier tecnología, ya que sólo requiere emitir y recibir por un único canal para cada medida. Otras propuestas más rápidas, como las que se describen a continuación, requieren la adquisición de señales en paralelo.

2.1.2.2 Estimación de la geometría por pitch-catch

En este caso se elige un elemento como emisor y cierto número M de elementos a cada lado como receptores. La Figura 2.6 muestra un ejemplo, con N = 64, en el que se eligen tres emisores ubicados en los elementos {11, 32, 53}. Estos emisores tienen M=10 receptores a cada lado, cada uno de ellos proporcionando un punto de la interfaz con el algoritmo que se describe a continuación. Con sólo 3 disparos se obtienen, en este ejemplo, 60 puntos de la interfaz.

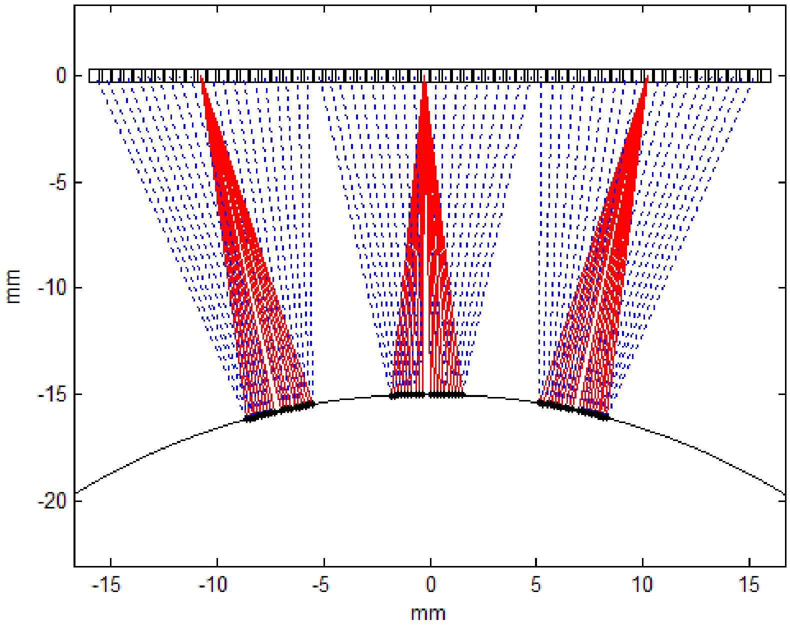

Figura 2.6 - Operación en pitch-catch. Un emisor (rojo) para múltiples receptores (azul) a ambos lados.

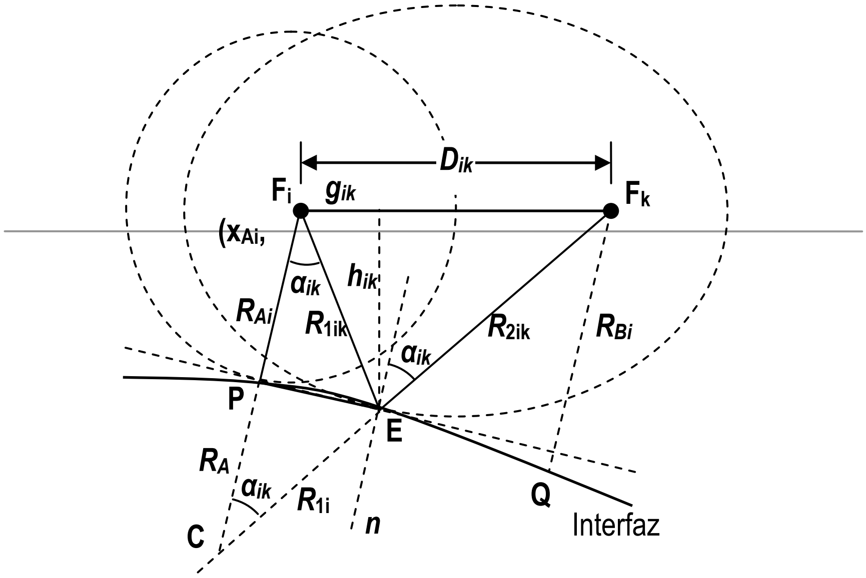

Figura 2.7 - Geometría para calcular las coordenadas del punto E en la interfaz.

Para calcular las coordenadas de los puntos detectados en la interfaz se utiliza la geometría mostrada en la Figura 2.7 para los elementos *i* (emisor) y *k* (receptor), cuya distancia $D_{ik}=(k-i)\cdot d$.

En este caso se mide el tiempo de vuelo T_{Ai} en pulso-eco al elemento emisor *i* en (x_{Ai}, z_{Ai}), y en pitch-catch del emisor a la interfaz y al receptor T_{ABik}:

$$\begin{aligned} T_{Ai} &= 2R_{Ai}/c_1 \\ T_{ABik} &= (R_{1ik}+R_{2ik})/c_1 \end{aligned} \tag{23}$$

El tiempo T_{Ai} define una circunferencia con centro en (x_{Ai}, z_{Ai}) y radio R_{Ai}. El tiempo T_{ABik} define una elipse con focos en los elementos *i* y *k*, verificándose:

$$\begin{aligned} R_{Ai} &= c_1 T_{Ai}/2 \\ R_{ABik} &= R_{1ik}+R_{2ik} = c_1 T_{ABik} \end{aligned} \tag{24}$$

Suponiendo que las pendientes de la normal a la interfaz en E y P son iguales[4], el ángulo de incidencia α_{ik} es igual al que forma el rayo reflejado en E hacia F_k, los triángulos PEF_i y PEC son iguales y $PC = PF_i = R_{Ai}$ y $EC = EF_i = R_{1ik}$. Aplicando el teorema del coseno a F_iCF_k,

$$D_{ik}^2 = 4R_{Ai}^2 + (R_{1ik}+R_{2ik})^2 - 4R_{Ai}(R_{1ik}+R_{2ik})\cos\alpha_{ik} \tag{25}$$

$$\cos\alpha_{ik} = \frac{4R_{Ai}^2 + R_{ABik}^2 - D_{ik}^2}{4R_{Ai}R_{ABik}} \tag{26}$$

---

[4] La condición es que el radio de curvatura de la pieza no sea demasiado pequeño.

Sustituyendo $R_{Ai} = R_{1ik} \cos\alpha_{ik}$ se obtiene:

$$R_{1ik} = \frac{4R_{Ai}^2 R_{ABik}}{4R_{Ai}^2 + R_{ABik}^2 - D_{ik}^2} \tag{27}$$

donde todas las variables del término a la derecha son conocidas. Así,

$$R_{2ik} = R_{ABik} - R_{1ik} \tag{28}$$

Los segmentos g_{ik} y h_{ik} verifican:

$$h_{ik}^2 = R_{1ik}^2 - g_{ik}^2 = R_{2ik}^2 - (D_{ik} - g_{ik})^2 \tag{29}$$

$$\begin{aligned} g_{ik} &= \frac{R_{1ik}^2 - R_{2ik}^2 + D_{ik}^2}{2D_{ik}} \\ h_{ik} &= \sqrt{R_{1ik}^2 - g_{ik}^2} \end{aligned} \tag{30}$$

y las coordenadas (x_{Eik}, z_{Eik}) del punto E son:

$$\begin{aligned} x_{Eik} &= x_{Ai} + g_{ik} \\ z_{Eik} &= z_{Ai} - h_{ik} \end{aligned} \tag{31}$$

En el caso de menor extensión, M=1, se obtienen 2 puntos de la interfaz por cada 3 elementos, utilizando el central como emisor. En el caso extremo, con M=N/2-1 y un único disparo se obtienen N-2 puntos de la interfaz. Sin embargo la reducción de la sensibilidad angular de los elementos impone un límite para esta posibilidad si N es grande.

2.1.2.3 Estimación de la geometría por onda plana

También es posible estimar la geometría de la interfaz con un único disparo simultáneo de todos los elementos del array, que produce una onda plana (Figura 2.8). Se puede observar en esta figura que sólo vuelven al array los ecos producidos por parte de la onda plana emitida, cuya extensión es igual a la del array.

Se utiliza la geometría de la Figura 2.9 para determinar las coordenadas del punto P (x_i, z_i), cuyo eco es recibido por el elemento i del array. Teniendo en cuenta que $z_i < 0$,

$$R_i - z_i = c_1 T_i \tag{32}$$

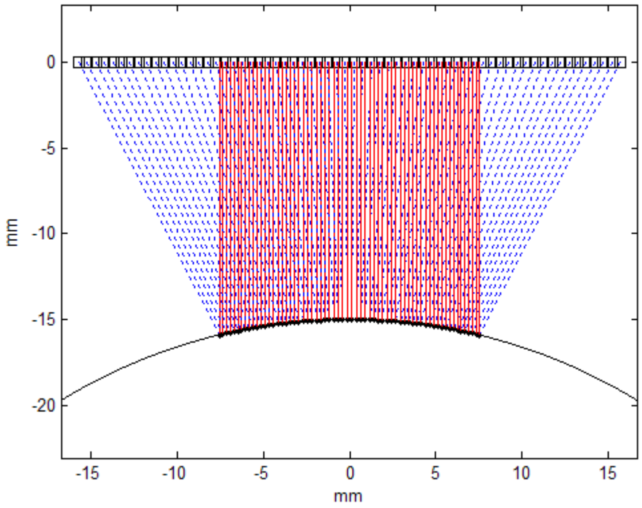

Figura 2.8 - Emisión con onda plana. Las reflexiones en la interfaz llegan a los *N* elementos del array. De la medida de estos tiempos de vuelo se deducen las coordenadas de *N* puntos de la interfaz.

El lugar geométrico para los posibles puntos P está dado por:

$$\sqrt{(x-x_{Ai})^2+z^2}-z=c_1T_i \tag{33}$$

$$z=\frac{(x-x_{ai})^2}{2c_1T_i}-\frac{c_1T_i}{2} \tag{34}$$

Como esta parábola y la interfaz son tangentes en P, sus pendientes son iguales:

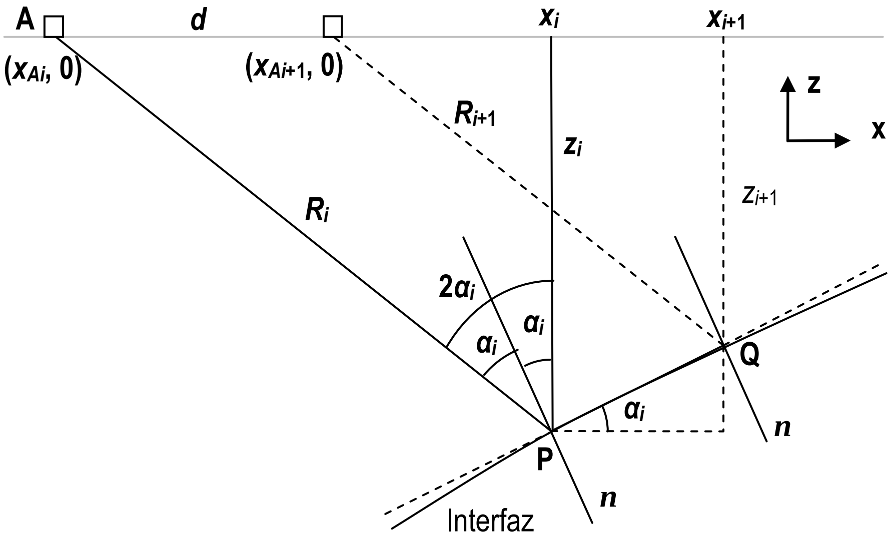

Figura 2.9 - Geometría para calcular las coordenadas de P en la interfaz por onda plana.

$$\frac{dz}{dx} = \frac{x - x_{ai}}{c_1 T_i} = \tan\alpha_i \tag{35}$$

Aplicando la ley de Snell en P, los ángulos incidentes y reflejados son iguales a α_i. Entonces,

$$\begin{aligned} z_i &= -R_i \cos 2\alpha_i \\ x_i &= x_{Ai} + R_i \sin 2\alpha_i \end{aligned} \tag{36}$$

Sustituyendo en (32),

$$R_i = \frac{c_1 T_i}{1 + \cos 2\alpha_i} \tag{37}$$

Con $\Delta L_i = c_1(T_{i+1} - T_i)$ y suponiendo que las normales a la interfaz en P y Q son paralelas,

$$R_{i+1} - R_i = \frac{c_1(T_{i+1} - T_i)}{1 + \cos 2\alpha_i} = \frac{\Delta L_i}{1 + \cos 2\alpha_i} \tag{38}$$

De (36),

$$\begin{aligned} \Delta z_i &= z_{i+1} - z_i = \frac{-\cos 2\alpha_i}{1 + \cos 2\alpha_i} \Delta L_i \\ \Delta x_i &= x_{i+1} - x_i = d + \frac{\sin 2\alpha_i}{1 + \cos 2\alpha_i} \Delta L_i \end{aligned} \tag{39}$$

Después de algunas manipulaciones matemáticas, se obtienen las siguientes ecuaciones:

$$\tan\alpha_i = \frac{\Delta z_i}{\Delta x_i} = \frac{(\tan^2\alpha_i - 1)\Delta L_i}{2(d + \Delta L_i \tan\alpha_i)} \tag{40}$$

$$\Delta L_i \tan^2\alpha_i + 2d \tan\alpha_i + \Delta L_i = 0 \tag{41}$$

Resolviendo esta ecuación para obtener $\tan\alpha_i$ y sustituyendo en (42) se obtiene $x = x_i$ con cuyo resultado se obtiene z=z_i de (41). Repitiendo este proceso para todos los elementos $1 \le i \le N$ se obtienen las coordenadas de N puntos de la interfaz a partir de un único evento de disparo y adquisición simultánea con fórmulas cerradas.

2.1.2.4 Resumen de métodos y tratamiento de medidas atípicas.

El objetivo de los métodos anteriores es obtener un conjunto de coordenadas en la interfaz que se pueden utilizar para ajustar a una función determinada por mínimos cuadrados. Con anterioridad se habían propuesto ciertas técnicas para la estimación de perfiles mediante medidas ultrasónicas de rango, mayoritariamente dirigidas a aplicaciones de percepción y/o robótica [Barshan, 2000], [Barshan, 2001]. En general los métodos válidos para robótica carecen de la precisión requerida para el cálculo de leyes focales adaptadas, del orden de centésimas de mm.

Cuando la forma de la interfaz es totalmente desconocida, se sugiere el ajuste a un polinomio de grado p a las medidas P_i, con valores $2 \leq p \leq 5$. Esto facilita la generalización del ajuste y evita que una medida espuria (*outlier*) invalide la estimación. Para una interfaz plana el ajuste se hará a un polinomio de primer grado, $p = 1$ (recta de regresión). Finalmente, si se conoce que la geometría es circular (cilíndrica), el ajuste se hará a una circunferencia (en 2D), siguiendo alguno de los métodos descritos en [Umbach, 2003].

Las técnicas descritas son robustas para curvaturas moderadas (radio de curvatura > D). La precisión de la interfaz calculada es, en promedio, mejor que la de una medida aislada. Si la frecuencia de muestreo es suficiente, la representación analítica $z = f(x)$ **permite calcular las leyes focales adaptadas a la geometría array-pieza actual con mayor o igual fiabilidad que con descripciones CAD**, pues consideran las posibles desviaciones presentes. Por otra parte, **los métodos descritos se basan en fórmulas cerradas**, cuya evaluación es muy rápida en los computadores actuales. En particular, hay que destacar la ausencia de procesos iterativos para la búsqueda de soluciones.

Los *outliers* son medidas atípicas alejadas de los valores verdaderos, que pueden ser debidas a un impulso de ruido, captura de datos erróneos (de otra región), adquisición en zonas con baja relación señal/ruido, etc. La presencia de estos valores atípicos afecta negativamente a los ajustes por mínimos cuadrados, así que es importante realizar su detección y eliminación del juego de datos utilizado para ajustar la función que describe la geometría.

Hay diversos criterios para eliminar estas medidas atípicas, pero en esta aplicación son particularmente importantes:

a) Evitar que el final de la excitación impulsiva contamine las medidas.

b) Definir una amplitud mínima de señal para evitar el ruido.

c) Aplicar técnicas estándar de eliminación basados en medidas de dispersión, test de Tukey y otros [Ben-Gal, 2005].

d) Identificar y eliminar indicaciones causadas por reverberaciones y/o ecos geométricos conocidos, que pueden generar series de puntos consecutivos próximos entre sí pero alejados de la interfaz.

Es importante que la detección de medidas atípicas sea un proceso rápido y, preferiblemente, ejecutado en el propio sistema de adquisición para no penalizar la cadencia de imágenes.

2.2 Enfoque por hardware en tiempo real.

Las ecuaciones (2) y (3) proporcionan los retardos de enfoque cuando se opera por contacto con medios homogéneos. Cada muestra de la imagen requiere un juego de retardos o ley focal, que han de expresarse con suficiente resolución - ecuación (6) - y que se aplican simultáneamente a cada canal en recepción. Así, para realizar el enfoque dinámico estricto en un sistema con N canales, hay que proporcionar N retardos en cada periodo de muestreo. Valores típicos son: intervalo entre muestras T_S =20 ns y una resolución de los retardos $T_X \leq$ 6.9 ns si N=128. Para un retardo máximo $N \cdot T_S$ = 2.56 μs, la representación numérica de cada retardo requiere al menos 9 bits.

En la práctica, se utiliza una versión más compacta de los retardos de enfoque. Nuestro grupo desarrolló la *Técnica de Muestreo Selectivo* (*TMS*) que, en promedio, codifica la información de enfoque dinámico con menos de 1 bit/foco [Fritsch, 2006]. La *TMS* aprovecha que, a partir de cierto rango, el intervalo ΔT entre los instantes de muestreo en un determinado canal para conformar una muestra de salida, verifica:

$$T_S - \frac{T_S}{v} \leq \Delta T \leq T_S \qquad (42)$$

donde v es una constante arbitraria que establece la resolución temporal de los retardos como una fracción del periodo de muestreo T_S. Esto significa que se puede mantener el enfoque en todas las muestras con un error temporal inferior a T_S / v modificando el intervalo de muestreo en cada canal (operación con tasa de muestreo variable).

La técnica elige entre dos posibles estados para suministrar la muestra siguiente: la que corresponde a un periodo de muestreo entero T_S o la adelantada una fracción $1/v$ del periodo de muestreo, $T_S - T_S/v$. La elección se realiza con un código de enfoque Q_i de un único bit por foco. En general, los intervalos entre muestras no son múltiplos del periodo de muestreo y se obtienen por interpolación con *filtros de retardo fraccional* [Laasko, 1996].

En *TMS* los focos se separan, al menos, la profundidad de foco, manteniendo entre focos un muestreo uniforme a intervalos T_S. Esto equivale a compartir un único código de enfoque entre todas las muestras dentro de la profundidad de foco. En promedio, *TMS* requiere menos de 1 bit/muestra y, a pesar de ello, realiza el enfoque dinámico estricto.

Aunque la *TMS* usa la memoria de forma muy eficiente, se conocen diversas alternativas para realizar el enfoque dinámico en tiempo real por hardware, con circuitos especializados que van calculando las leyes focales o los instantes de muestreo durante la adquisición. Las primeras aproximaciones se basaron en el algoritmo del punto medio utilizado en gráficos de computador mediante circuitos relativamente complejos, que requerían programar muchos parámetros para su operación [Jeon, 1994].

Una variante de la técnica anterior proporcionó el retardo variable requerido por el enfoque dinámico [Bae, 1998], mientras que en otras aproximaciones se redujo el consumo de recursos hardware [Feldkämper, 2000]. Otra alternativa obtiene un reloj de muestreo de periodo no uniforme para adaptarse a los retardos requeridos y utilización con conversores ΔΣ [Lie, 2005]. Finalmente, en [Alexandru, 2010], se describe un circuito de enfoque con un número reducido de recursos hardware.

El circuito de enfoque en tiempo real descrito en [Cruza, 2013] y mostrado esquemáticamente en la Figura 2.10, **constituye otra aportación de esta Tesis**. S*ólo requiere programar dos parámetros* iniciales (registros R y B, el registro D se inicializa a cero), facilitando una rápida re-programación en un proceso de auto-enfoque cuando cambia la geometría. Además, utiliza muy pocos recursos hardware de las FPGAs actuales: 4 sumadores, 1 multiplicador y un selector para calcular el siguiente código de enfoque. El máximo error temporal es $\varepsilon < T_S / v$, pudiendo elegirse arbitrariamente bajo aumentando *v*, si bien esto afectaría al rango mínimo en que es aplicable.

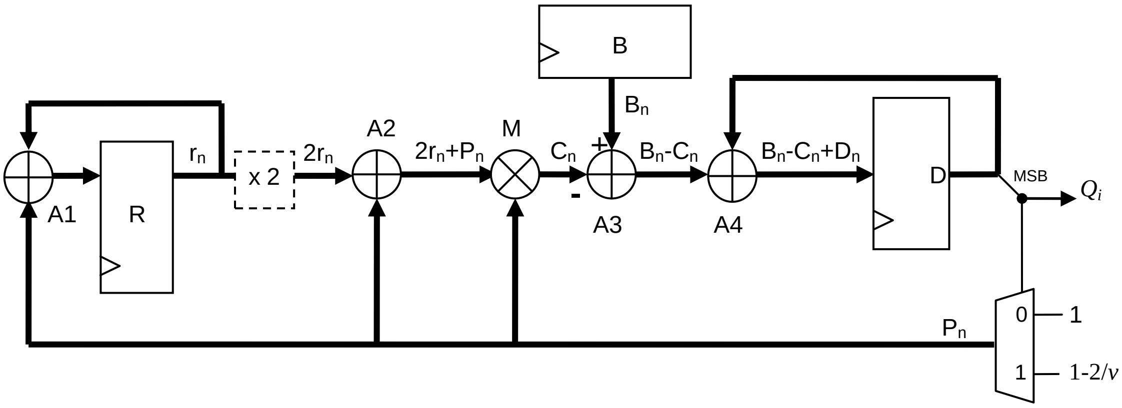

Figura 2.10 - Calculador de códigos de enfoque Q_n con resolución arbitraria T_S/v.

Conjuntamente con el circuito, se propone un algoritmo que determina y carga los valores iniciales de los registros R y B antes de iniciar la adquisición. Este es un proceso rápido realizado por software con fórmulas cerradas.

Iniciada la adquisición de señal, el circuito calcula, para cada muestra i, el código Q_i de enfoque que le corresponde, realizando efectivamente el enfoque dinámico estricto. Este circuito y la metodología para su utilización ha sido patentado [Fritsch, 2012] y transferido a la empresa Dasel, que lo integra en su tecnología SITAU.

2.3 Cálculo de leyes focales con propagación en dos medios

En END es habitual operar con un medio de acoplamiento interpuesto entre array y pieza. La Figura 2.11 muestra ejemplos donde se interpone una cuña rígida de plástico (a), o agua como medio de acoplamiento del ultrasonido entre el array y la pieza (b).

En estas condiciones existen dos velocidades de propagación (c_1 y c_2) que corresponden a la del acoplante y a la de la pieza, respectivamente. En phased array las líneas de imagen parten del centro del array en O y entran en la pieza en los puntos H formando un ángulo θ con la normal en ese punto.

Análogamente, para alcanzar el foco F desde el elemento A, hay que atravesar la interfaz por el punto G. El problema es determinar sus coordenadas para cada foco y elemento, de modo que se puedan calcular los tiempos de vuelo elemento-foco y, de estos, las leyes focales según (3).

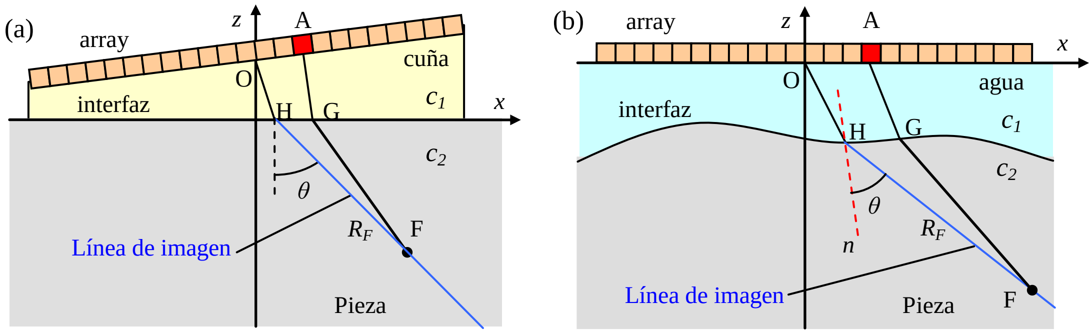

Figura 2.11 - a) Inspección de una pieza plana con una cuña interpuesta; b) Inspección de una pieza de geometría arbitraria por inmersión en agua.

Tradicionalmente este problema se ha abordado buscando el camino más rápido entre A y F (principio de Fermat) para encontrar las coordenadas del punto de entrada G (o H, con un proceso análogo para el rayo principal):

$$t_{AF} = \frac{|\vec{x}_A - \vec{x}_G|}{c_1} + \frac{|\vec{x}_G - \vec{x}_F|}{c_2} = \text{mínimo} \tag{43}$$

Exclusivamente para una interfaz plana con y_G=0, z_G=0, derivando e igualando a cero (43), la coordenada desconocida x_G es la solución a la ecuación de 4º grado [Parrilla, 2008]:

$$Ax_G^4 + Bx_G^3 + Cx_G^2 + Dx_G + E = 0\,, \tag{44}$$

donde todos los coeficientes se obtienen de parámetros conocidos, implícitos en la ecuación de partida (43). Hay algoritmos que resuelven esta ecuación por el método de Ferrari [Nickalls, 2009] pero, en el caso general, la interfaz no es plana, por lo que es preciso encontrar una solución alternativa.

Pues bien, aunque se han hecho esfuerzos para generalizar el proceso anterior a una interfaz de geometría arbitraria, los algoritmos propuestos son complejos y muy costosos en tiempo de cálculo, del orden de 6 ms/pixel [Weston, 2011]. Teniendo en cuenta que una imagen puede tener centenares de miles de píxeles, esta no sería una alternativa práctica.

Una metodología diferente que se utiliza habitualmente, muestrea la interfaz a intervalos pequeños determinando, para cada foco y para cada elemento, cuál de las posibles muestras de la interfaz está en el camino más rápido (Figura 2.12).

Weston realizó un análisis de diferentes algoritmos para una interfaz plana, incluyendo la búsqueda *iterativa* del punto de entrada, la solución *numérica* a la ecuación de 4º grado y el método *analítico* `roots.m` proporcionado por Matlab. El método numérico requirió menos

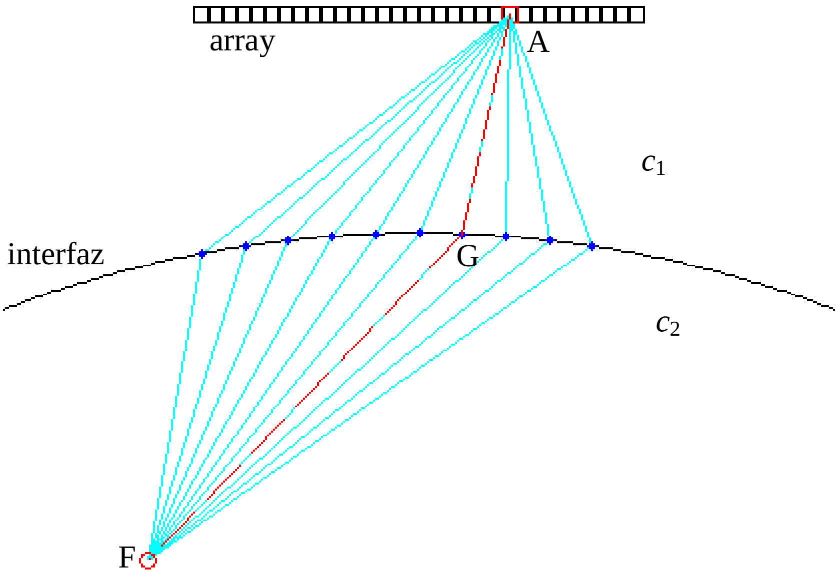

Figura 2.12 - Aplicación del principio de Fermat: búsqueda del camino más rápido de A a F probando todos los posibles a través de una interfaz muestreada. Se destaca en rojo la solución.

tiempo (1.5 ms) que el analítico (2.5 ms) y, sobre todo, que el iterativo (entre 20 y 960 ms dependiendo del intervalo de discretización de 50 a 1 μm, respectivamente).

Aunque el método iterativo es el más lento, no hay otra alternativa para interfases de geometría arbitraria. En cualquier caso, en [Cruza, 2015a] se proporciona una técnica para determinar de forma óptima el intervalo de discretización de la interfaz, esto es, el intervalo de muestreo que garantiza una determinada precisión en los tiempos de vuelo calculados.

Por otra parte, como la búsqueda exhaustiva consume mucho tiempo, frecuentemente se limita el cálculo de leyes focales a unos pocos focos por cada línea de imagen [Liang, 2010]. Esto impide realizar el enfoque dinámico estricto, importante para los procedimientos de eliminación de indicaciones espurias basados en la coherencia de fases [Cruza, 2017].

Entre las aproximaciones al problema de enfoque con interfases arbitrarias, nuestro grupo propuso en el pasado la técnica *Fast Focal Law Computing (FFLC-SW)*, que resuelve la ecuación (44) por software. *FFLC-SW* utiliza el método de Newton-Raphson [Traub, 1982] modificado para calcular el índice al punto de entrada en una interfaz discretizada a intervalos arbitrariamente pequeños, comenzando desde la región más alejada al array, de muestra en muestra y de forma recurrente.

Para la muestra k de la interfaz en (x_k, z_k), la pendiente es $m_k = (z_{k+1} - z_k)/(x_{k+1} - z_k)$. Denominando V_k a la derivada del tiempo de vuelo desde un elemento del array en (x_A, z_A) a

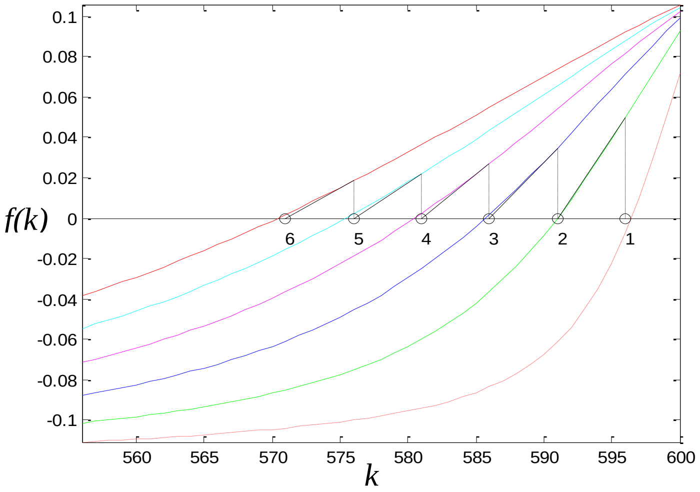

Figura 2.13 - Cálculo recurrente con la técnica *FFLC-SW* del índice al punto de entrada en una interfaz muestreada: La solución siguiente se obtiene del resultado de la anterior en la primera iteración.

un foco en (x_F, z_F) pasando por la interfaz en (x_k, z_k) e igualando a cero resulta [Parrilla, 2007], [Parrilla, 2008];

$$V_k = \frac{1}{c_1}\frac{(x_k - x_A) + m_k(z_k - z_A)}{\sqrt{(x_k - x_A)^2 + (z_k - z_A)^2}} + \frac{1}{c_2}\frac{(x_k - x_F) + m_k(z_k - z_F)}{\sqrt{(x_k - x_F)^2 + (z_k - z_F)^2}} = 0 \tag{45}$$

La aplicación del método de Newton-Raphson a esta ecuación proporciona el índice k para la solución por aproximaciones sucesivas:

$$k_{i+1} = k_i - \mathrm{round}\left(\frac{V_k}{V_{k+1} - V_k}\right) \tag{46}$$

Los resultados de la primera iteración en *FFLC-SW* son prácticamente equivalentes a los de la búsqueda exhaustiva, pero se obtienen en un tiempo de uno a dos órdenes de magnitud inferior a los reportados en [Weston, 2011]. La Figura 2.13 muestra la evolución del algoritmo para las primeras muestras, empezando por la más alejada al array, donde el resultado k_i se utiliza como dato inicial para evaluar el índice k_{i+1} de la siguiente muestra.

El método se ha utilizado durante años para evaluar las leyes focales con enfoque dinámico estricto para la tecnología *phased array* SITAU transferida por nuestro grupo a la empresa DASEL. El tiempo medio de cálculo está en el entorno de 5 µs/foco·elemento en un PC.

Para una imagen de 200 líneas, cada una de ellas con 2K muestras y un array de 128 elementos, el tiempo de cálculo de las leyes focales con la técnica *FFLC-SW* para enfoque dinámico estricto es de unos 260 segundos (algo más de 4 minutos), un orden de magnitud más rápida que otras alternativas, pero obviamente, insuficiente para realizar una operación de autoenfoque adaptativa a cambios en la geometría. Esto se consiguió finalmente con la propuesta *UFAF* (*Ultra Fast Auto-Focusing*) descrita posteriormente [Cruza, 2015a].

2.4 Eliminar los problemas que causa la refracción.

Por primera vez y, con este trabajo, **se ha considerado la posibilidad de eliminar la refracción en los cálculos de leyes focales**, esto es, **convertir el problema en uno trivial de propagación a través de un único medio homogéneo**. La idea original fue calcular un *array virtual* tal que, operando en el segundo medio y, por tanto, sin refracción, produjera unos tiempos de vuelo a los focos en las imágenes *phased array* equivalentes a los obtenidos con los métodos tradicionales [Cruza, 2012a], [Cruza, 2013]. Más tarde se generalizó el método para su aplicación en TFM [Cruza, 2016b].

Un avance posterior ha sido obviar la refracción, creando fuentes virtuales sobre la superficie del componente, que actúan como un array en contacto con la pieza. Son las técnicas AVSI y AVSI-TFM que también forman parte de este trabajo [Camacho, 2015], [Cruza, 2016a].

2.4.1 El array virtual

La Figura 2.14 muestra un ejemplo con un *array lineal* de 32 elementos, $f = 5$ MHz y $d = \lambda / 2$ (en gris) para inspeccionar por inmersión en agua (c_1 = 1480 m/s) una pieza con forma parabólica y velocidad de propagación c_2 = 6200 m/s (aluminio). El *array virtual* equivalente (en negro), calculado para el rayo principal (en rojo) con una deflexión de 30º respecto a la normal, tiende a adaptarse a la forma de la interfaz.

En un sistema de imagen 2D, que es el caso más habitual, las coordenadas (x_V, z_V) de un elemento del array virtual que se corresponde con el del array real en (x_A, z_A) se obtienen igualando los tiempos de vuelo a dos focos en la línea de imagen.

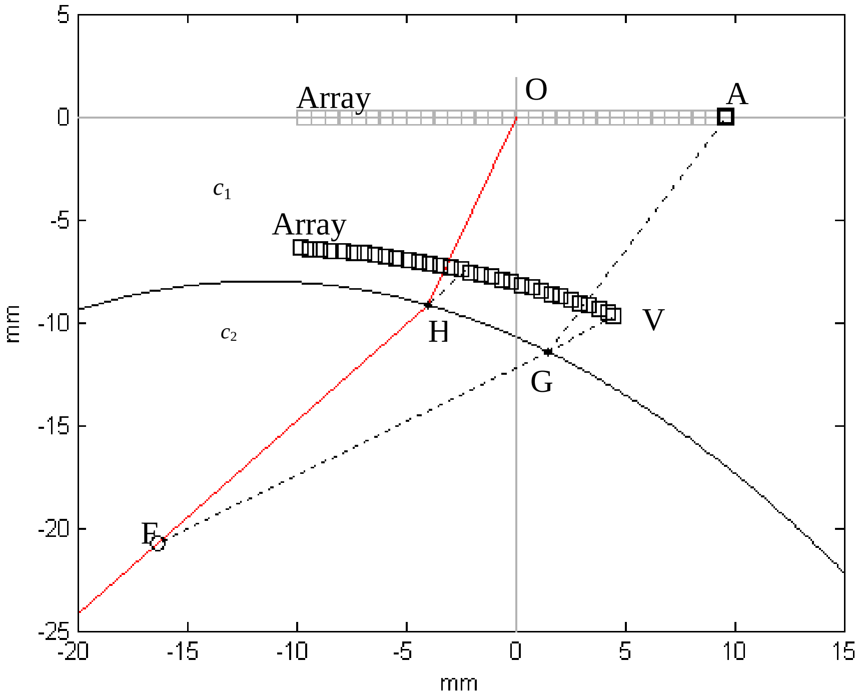

Figura 2.14 - Array real (gris) y array virtual (negro). Rayo principal (——) y rayos al foco F desde el elemento real pasando por la interfaz y desde el virtual (- - -).

El tiempo de vuelo de un elemento del array real A al foco en F se calcula como la suma del tiempo de vuelo hasta G con velocidad c_1 más el tiempo de vuelo de G a F con velocidad c_2:

$$t_{AF} = \frac{AG}{c_1} + \frac{GF}{c_2} \tag{47}$$

El problema es encontrar las coordenadas del punto G de entrada en la interfaz. Habitualmente se aplica el principio de Fermat para encontrar el tiempo de vuelo t_{AF} que corresponde al camino más rápido de A a F. Con el array virtual, este tiempo está dado por:

$$t_{VF} = \frac{VF}{c_2} + t_K \tag{48}$$

donde t_K es una constante para todos los focos en el rayo principal que se calcula a partir del invariante de Abbe [Cruza, 2012a]:

$$t_K = t_{AG}\left(1 - \frac{c_1^2}{c_2^2}\right) \tag{49}$$

Para obtener las coordenadas de los elementos del array virtual se eligen dos focos, uno en las proximidades de la interfaz y otro alejado. Típicamente, si $R_{\max}$ es el rango máximo de la imagen, la distancia R_A al foco F_A se elegirá en $0.05R_{\max} \le R_A \le 0.1R_{\max}$ y para F$_B$, el más alejado, en $0.5R_{\max} \le R_B \le R_{\max}$. Tras obtener por Fermat los tiempos de vuelo t_{FA} y t_{FB} de los elementos a estos focos, las coordenadas del array virtual se encuentran haciendo $t_{VF} = t_{AF}$ para F$_A$ y F$_B$, esto es:

$$\begin{aligned} t_{FA} &= t_{VFA} + t_{AG}\left(1 - \frac{c_1^2}{c_2^2}\right) \\ t_{FB} &= t_{VFB} + t_{AG}\left(1 - \frac{c_1^2}{c_2^2}\right) \end{aligned} \qquad (50)$$

Al calcular los tiempos de vuelo t_{FA} y t_{FB} a F$_A$ y F$_B$ por Fermat se determina también t_{AG}. Las coordenadas (x_V, z_V) de los elementos virtuales son las raíces del sistema:

$$\begin{aligned} \frac{\sqrt{(x_V - x_{FA})^2 + (z_V - z_{FA})^2}}{c_2} + t_K &= t_A \\ \frac{\sqrt{(x_V - x_{FB})^2 + (z_V - z_{FB})^2}}{c_2} + t_K &= t_B \end{aligned} \qquad (51)$$

Obviamente el error, o diferencia de tiempo de vuelo con respecto al cálculo por Fermat, es nulo a las distancias R_A y R_B donde se encuentran los focos de referencia (Figura 2.15, distancias normalizadas al tamaño *D* de la apertura). Entre estos focos el error está acotado,

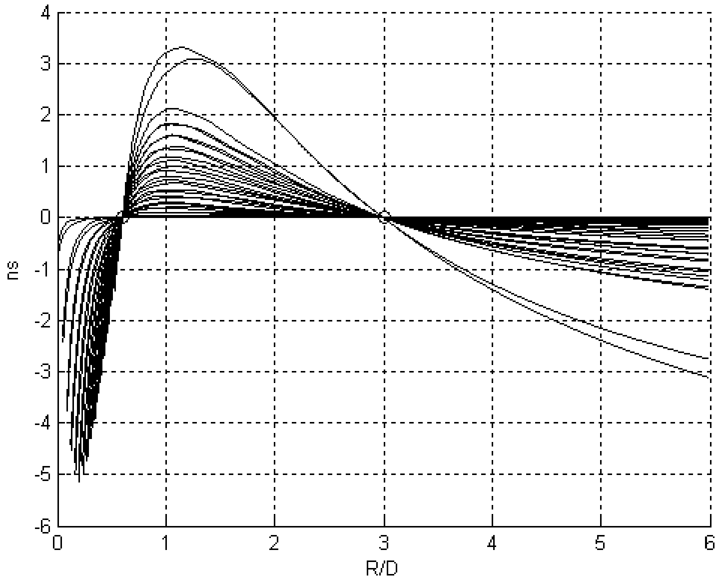

Figura 2.15 - Diferencias en el tiempo de vuelo para todas las muestras del rayo principal entre el cálculo del array virtual y el convencional por Fermat, en función de la distancia normalizada *R/D*.

creciendo lentamente más allá de R_B y de forma más rápida entre 0 y R_A.

Para un array con N = 128 elementos y frecuencia de 5 MHz, se obtuvo que la resolución temporal debe ser $T_X \leq 6.9$ ns (ecuación 6). Los errores absolutos mostrados en la Figura 2.15 son inferiores a esta cifra, por lo que es de esperar que apenas influyan en la imagen. Además, en END no es tan importante maximizar el contraste, por lo que el requisito anterior puede relajarse. En la práctica se pueden aceptar errores temporales mayores, siempre que el error cuadrático medio global se mantenga acotado y en el entorno del valor requerido para T_X.

El array virtual proporciona una alternativa para calcular tiempos de vuelo y leyes focales equivalentes, pero sin las complicaciones de la refracción. De hecho, **posibilita por primera vez la utilización de circuitos de enfoque hardware en tiempo real para obtener imágenes con enfoque dinámico estricto cuando hay dos medios de propagación**.

2.4.2 Aceleración del cálculo del array virtual

La técnica *UFAF* (*Ultra-Fast Auto-Focusing*) que hemos propuesto recientemente, resuelve el principal problema para el cálculo rápido del array virtual: encontrar los tiempos de vuelo a los dos focos de referencia F_A y F_B [Cruza, 2015a].

UFAF ha sido completamente desarrollada en hardware con herramientas HLS (High Level Synthesis). Combina los algoritmos de *Newton-Raphson* [Traub, 1982], *regula falsi* [Dowell, 1971] e *Illinois* [Ford, 1995] para obtener la solución a la ecuación (43), concretamente a su derivada igualada a cero, que proporciona una ecuación del tipo $f(x)=0$. Inicialmente, *UFAF* aplica *Newton-Raphson* para, a partir de una primera solución x_0, obtener las siguientes como:

$$x_{k+1} = x_k - \frac{f(x_k)}{f'(x_k)}, \quad k = 0,1,2,... \tag{52}$$

La convergencia del algoritmo de *Newton-Raphson* es muy rápida, pero no está garantizada. La determinación de una situación de no convergencia se basa en:

- Algún x_k queda fuera del intervalo $[\min(x_A, x_F), \max(x_A, x_F)]$, esto es, la solución no se encuentra entre las abcisas del elemento y foco.
- Tras cierto número de iteraciones, no se ha encontrado una solución.

- La derivada de $f(x)$ es negativa: $f'(x_k) < 0$, indicando que x_k es solución para un máximo, no un mínimo.

Si se detecta alguna de estas condiciones, la técnica UFAF conmuta automáticamente al algoritmo *Illinois*, que es una variante del conocido como *regula falsi*. Estos algoritmos siempre convergen si f(x) es continua, pues la solución está en el intervalo $U_k = [a_k, b_k]$, donde $f(a_k)$ y $f(b_k)$ tienen signos opuestos. La nueva aproximación a la solución se obtiene por interpolación lineal entre los puntos $[a_k, f(a_k)]$ y $[b_k, f(b_k)]$ mediante:

$$x_{k+1} = \frac{b_k f(a_k) - a_k f(b_k)}{f(a_k) - f(b_k)} \tag{53}$$

El siguiente intervalo U_{k+1} queda definido por x_{k+1} y el valor a_k o b_k que proporcione un valor de la función $f(\cdot)$ de signo opuesto al de $f(x_{k+1})$.

La técnica *UFAF* se implementa de forma muy eficiente en los SoCs estado del arte, como los de la familia Zynq [Xilinx, 2017b]. Estos dispositivos incluyen procesadores ARM y lógica programable que pueden realizar aplicaciones hardware + software. El procesador obtiene puntos de la interfaz mediante alguno de los métodos pulso-eco, pitch-catch u onda plana descritos anteriormente, ajusta por mínimos cuadrados el polinomio f(x) que representa a la interfaz y obtiene los coeficientes de sus derivadas primera y segunda, f'(x) y f''(x).

La lógica programable implementa en hardware el núcleo central de UFAF, el calculador de tiempos de vuelo mediante los algoritmos descritos. El calculador de tiempos de vuelo utiliza cierto número de recursos, ya que debe operar con aritmética en coma flotante estándar de 32 bits (simple precisión). La Tabla 2.1 muestra los recursos utilizados al implementar los algoritmos de *Fermat*, *Newton-Raphson*, *Illinois* y una combinación de estos sobre una Zynq XC-7Z020-1C indicando, entre paréntesis, el porcentaje sobre los disponibles.

Tabla 2.1 - UFAF. Recursos utilizados en función del algoritmo (XC-7Z020-1C)

Recursos	Fermat	Newton	Illinois	Newton + Illinois
LUTs	5247 (10%)	11603 (22%)	8785 (17%)	10988 (21%)
Registros	5318 (5%)	11310 (11%)	11250 (11%)	12470 (12%)
RAMB18	44 (16%)	44 (16%)	44 (16%)	44 (16%)
DSP48	20 (9%)	41 (19%)	30 (14%)	43 (20%)

Tabla 2.2 - Número de iteraciones y tiempos de ejecución (ms) por imagen (32 Kfocos) sobre distintos soportes.

	Fermat	**Newton+Illinois**
Número medio de iteraciones	8.7	1.8
Tiempo en Core i-7 (ms)	50	19
Tiempo en ARM (ms)	397	148
Tiempo en hardware (ms)	21.6	3.3
Máximo error temporal (ns)	0.11	0.48

La búsqueda de Fermat utiliza aproximadamente la mitad de recursos que las otras alternativas. Vale la pena destacar que el número de recursos adicionales requeridos para implementar ambos métodos (Newton e Illinois) es bajo, como consecuencia de la reutilización de bloques ya implementados.

En cuanto a la velocidad de operación, la Tabla 2.2 compara la ejecución en tres soportes: software en un PC con procesador Core i-7, software en el ARM y hardware. Los parámetros de la aplicación son: array de 128 elementos, imagen de 128 líneas y 2 focos/línea como requiere el cálculo del array virtual, esto es, un total de 32 K cálculos de tiempos de vuelo por imagen.

La búsqueda de Fermat es unas 18 veces más rápida por hardware que en el ARM, aunque sólo 2 veces más que en el Core i-7. Ciertamente, en esta última situación, habría que contabilizar el tiempo de transferencia de datos desde el sistema de ultrasonidos (*front-end*) al computador. En el caso del ARM no es necesaria la transferencia de datos, pues se adquieren sobre los recursos directamente accesibles en el hardware de adquisición (memoria DDR).

La alternativa propuesta que combina los métodos de Newton-Raphson e Illinois es la más rápida en todos los soportes. En promedio esta combinación encuentra la solución en menos de 2 iteraciones, mientras que Fermat requiere casi 9 iteraciones; en ambos casos, el error temporal está por debajo de 1 ns.

Y, ciertamente, **la implementación hardware de UFAF es la más rápida (3.3 ms/imagen), que podría proporcionar hasta 300 imágenes autoenfocadas por segundo, con enfoque dinámico estricto, un nivel no alcanzado hasta la fecha por ninguna otra propuesta**.

2.5 El proceso AUTOFOCUS

El array virtual elimina, de hecho, los problemas asociados a la refracción y opera *como si se tratara de un único medio de propagación*. De este modo, una vez calculado, se pueden cargar los parámetros del circuito de enfoque y operar en tiempo real. El cálculo del array virtual para imagen 2D, requiere conocer la función $z = \mathrm{f}(x)$ que represente al contorno de la interfaz, al menos en la región de entrada/salida del ultrasonido. Así se tienen todos los elementos para operar con autoenfoque en tiempo real. El proceso se realiza en tres etapas:

1. Estimación de la geometría por pulso-eco, pitch-catch u onda plana.
2. Cálculo del array virtual posiblemente con el acelerador hardware.
3. Programación de parámetros de los circuitos de enfoque dinámico estricto.

Este proceso, que sólo ha de ejecutarse cuando cambia la geometría del componente a inspeccionar, con el acelerador hardware es rápido. En particular, puede utilizarse para cualquier inspección por inmersión o con suela, sea o no conocida la geometría de la pieza, donde el cálculo de las leyes focales adaptadas requiere sólo algunos milisegundos.

Un hecho a destacar es que **el proceso de autoenfoque propuesto es mucho más rápido que calcular las leyes focales por cualquiera de los métodos conocidos**, como se hace en la actualidad suponiendo perfectamente conocida la geometría.

2.6 Técnicas AVSI

Las técnicas AVSI y AVSI-TFM son también de auto-enfoque, pero sortean los problemas de la propagación en dos medios evitando la refracción de forma explícita, sin requerir el cálculo del array virtual equivalente ni de una representación analítica de la interfaz.

Su operación se basa en crear cierto número de fuentes virtuales sobre la superficie de la pieza mediante el envío de haces enfocados. Para ello se realiza un barrido lineal con subaperturas de M elementos de los N del array y un paso de 1 elemento en cada disparo. La subapertura i se enfoca en emisión y recepción sobre un punto E_i de la interfaz, donde se crea una fuente virtual. De este modo se dispone de un total de $L = N - M + 1$ fuentes virtuales que actúan como un array en contacto con el componente, sin que le afecte la refracción (Figura 2.16).

El haz ultrasónico se abre al entrar en el segundo medio con velocidad de propagación $c_2 > c_1$ por refracción. Un punto P(x, z) es iluminado por cierto número de haces ultrasónicos e, idealmente, por los L generados por las fuentes virtuales. Los puntos óptimos para ubicar las fuentes virtuales $\mathrm{E_k}$ en (x_{Ek}, z_{Ek}) son los de incidencia normal en la interfaz desde el centro de cada subapertura [Camacho, 2015]. Estos se calculan mediante la técnica pulso-eco (ecs. 20 a 22), pero no es preciso realizar ajuste alguno a una función como en AUTOFOCUS.
Para crear las fuentes virtuales se utiliza foco fijo en emisión y en recepción. El tiempo de vuelo T_{ik} desde el elemento del array $\mathrm{A_i}$ en (x_{Ai}, z_{Ai}) a la fuente virtual $\mathrm{E_k}$ en (x_{Ek}, z_{Ek}) es:

$$T_{ik} = \frac{\left|\vec{r}_{Ai} - \vec{r}_{Ek}\right|}{c_1} = \frac{\sqrt{\left(x_{Ai} - x_{Ek}\right)^2 + \left(z_{Ai} - z_{Ek}\right)^2}}{c_1} \qquad (54)$$

donde únicamente interviene la velocidad de propagación c_1. De forma análoga, el tiempo de vuelo desde el centro de la subapertura $\mathrm{C_k}$ en (x_{Ck}, z_{Ck}) a la fuente virtual $\mathrm{E_k}$ es:

$$T_{Ck} = \frac{\left|\vec{r}_{Ck} - \vec{r}_{Ek}\right|}{c_1} = \frac{\sqrt{\left(x_{Ck} - x_{Ek}\right)^2 + \left(z_{Ck} - z_{Ek}\right)^2}}{c_1} \qquad (55)$$

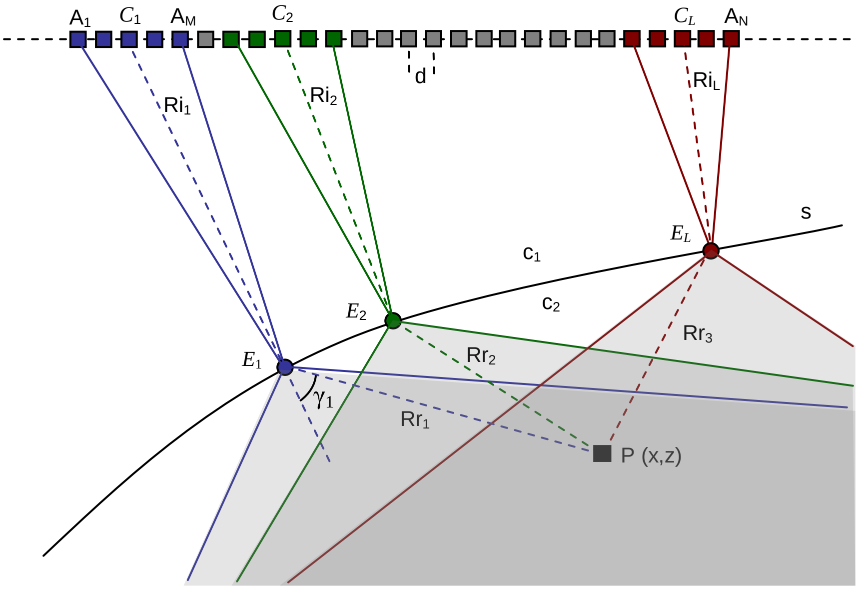

Figura 2.16 - Principio de operación de las técnicas AVSI. Cada subapertura i de M elementos con centro en C_i se enfoca en emisión y recepción en el punto E_i de la interfaz, donde crea una fuente virtual.

La ley focal para crear la fuente virtual es:

$$\tau_{ik} = T_{Ck} - T_{ik} \tag{56}$$

Todos los parámetros son conocidos para realizar el enfoque desde las subaperturas sobre las fuentes virtuales respectivas en emisión y para recibir los ecos desde esas mismas fuentes virtuales. Además, el foco es fijo en E_i, lo que reduce notablemente los requerimientos del hardware de adquisición. Esta estrategia evita las complicaciones de la refracción y, al mismo tiempo realiza el autoenfoque sin necesidad de conocimiento previo de la geometría de la pieza. Para crear la imagen se proponen dos técnicas de apertura sintética:

a) *AVSI-monoestático*, donde cada elemento del array virtual creado en la superficie de la pieza actúa como emisor y receptor [Camacho, 2015]. Este método es conocido desde hace décadas y opera en tiempo real [Kino, 1980]. Presenta una excelente resolución, aunque una relación señal/ruido pobre al usar un único elemento para emitir el pulso ultrasónico de forma no enfocada, y un rango dinámico limitado debido a su elevado nivel de lóbulos laterales.

b) *AVSI-TFM*, que utiliza una única fuente virtual en emisión y múltiples en recepción para construir un juego de datos completo tras cada emisión [Cruza, 2016a]. Con estos datos se construyen imágenes siguiendo el proceso *TFM* para obtener la imagen final de alta resolución. La enorme ventaja de *AVSI-TFM* es que el proceso *TFM* se realiza únicamente en el segundo medio, sin refracción, lo que posibilita obtener la imagen en tiempo real utilizando arquitecturas paralelas.

La Figura 2.17 compara las imágenes obtenidas con *TFM*, *AVSI-monoestática* y *AVSI-TFM* para una aplicación sencilla en la que se desconoce la geometría conjunta array-pieza [Cruza, 2016a].

En todos los casos se utilizó un array de N=128 elementos, f_R = 5 MHz, d= 0.65 mm. Las subaperturas para las técnicas AVSI fueron de M=16 elementos, con lo que el número de fuentes virtuales generadas fue L= 113 en los puntos de incidencia normal.

Se observa que el contraste (o rango dinámico) de la técnica *AVSI monoestático* es inferior a la que proporcionan *TFM* y *AVSI-TFM*, aunque la resolución es similar en todas las imágenes. Además, se observa que la técnica AVSI monoestático genera el lóbulo de rejilla característico de esta modalidad de apertura sintética, que aparece en la región de las

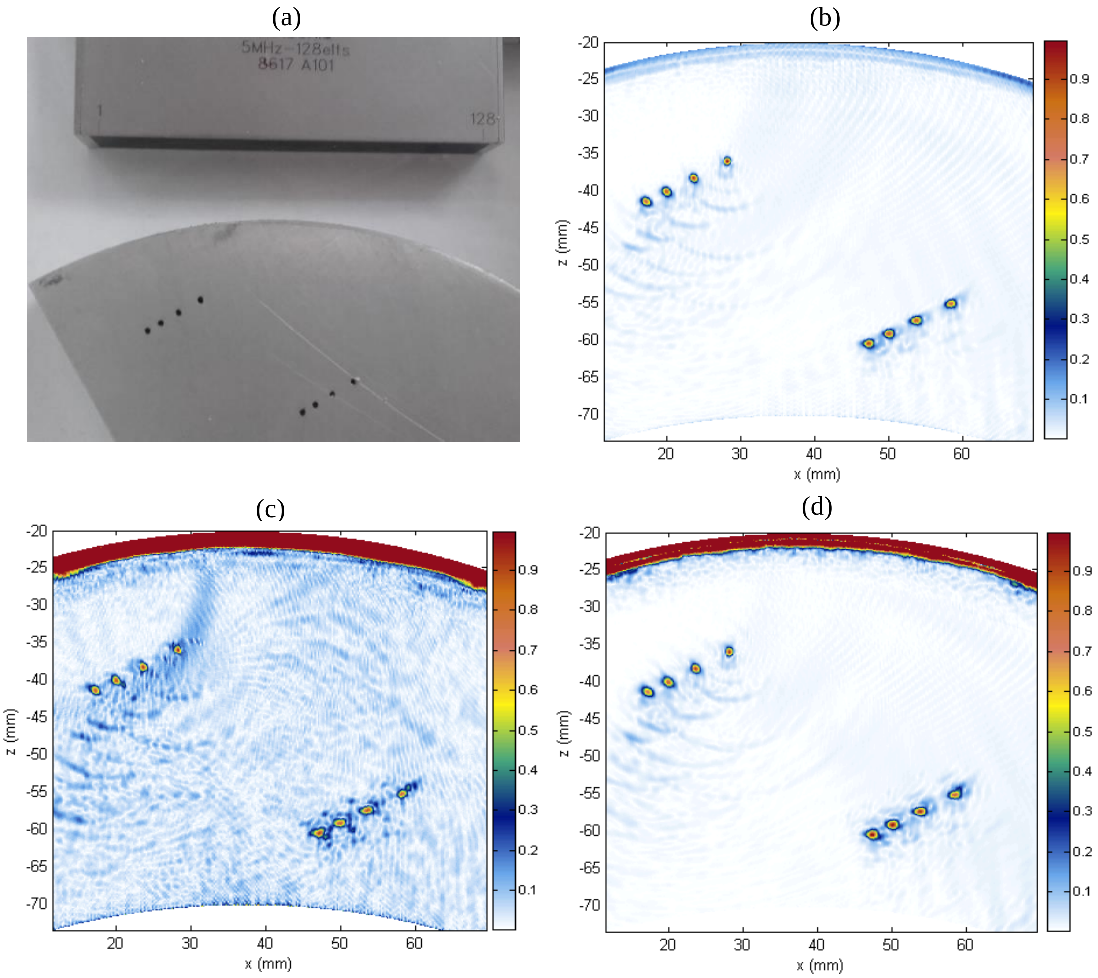
(a) (b) (c) (d)

Figura 2.17 - Comparación de imágenes: a) Geometría; b) *TFM* clásico; c) *AVSI monoestático*; d) *AVSI-TFM*.

indicaciones más próximas al array. Los resultados de las técnicas *TFM* convencional y *AVSI-TFM* son prácticamente indistinguibles, con un contraste en la región central de unos 33 dB.

La mayor diferencia entre *TFM* y *AVSI-TFM* radica en que, para obtener la imagen, la primera ha de resolver los problemas de la refracción en la interfaz, mientras que la *AVSI-TFM* carece de estos problemas por diseño, siendo una auténtica técnica de imagen autoenfocada.

Al comparar AVSI-TFM con AUTOFOCUS esta última puede aplicarse con cualquier sistema phased array, pero AVSI-TFM demanda recepción en paralelo para ser eficiente. En la actualidad el paralelismo aportado por las plataformas multi-core, multi-CPU y multi-GPU hacen posible su implementación en tiempo real, siempre que el ancho de banda entre el sistema de adquisición y el de procesamiento sea suficiente para la transferencia de datos.

2.7 Imagen acústica ultra-rápida.

Como fue expuesto, la tasa de imágenes para adquirir con tecnología convencional *phased array* imágenes de L lineas hasta una profundidad $z_{\max}$ en un medio con velocidad de propagación c está limitada por el tiempo de vuelo en ida y vuelta para cada línea:

$$t_{iv} = 2z_{\max} / c \tag{57}$$

Dependiendo de las condiciones de adquisición, la tecnología convencional *phased array* puede alcanzar tasas de 20 a 200 imágenes/s. Por otra parte, la técnica *TFM* realiza N disparos omnidireccionales, adquiere N Ascan en paralelo y construye las imágenes parciales y final por software sobre una plataforma a la que hay que suministrarle los datos adquiridos.

El tiempo dedicado a la adquisición de señal es algo menor en *TFM* que con *phased array* (siempre que el número de líneas de la imagen sea mayor que el número de elementos del array), pero los factores limitantes en *TFM* son su coste computacional y el ancho de banda necesario para transferir los datos adquiridos [Lambert, 2012]. Una implementación hardware de la técnica *TFM* alcanzó 7 imágenes por segundo para un tamaño de 120 x 120 píxeles con un array de 64 elementos [Njiki, 2013], a todas luces insuficiente para las aplicaciones de alta velocidad. La alternativa utilizada en ocasiones es adquirir las señales y almacenarlas en memoria para, posteriormente, realizar el proceso de conformación de imagen. Esta estrategia no resulta práctica para la inspección de grandes componentes.

Entre las primeras propuestas para aumentar la cadencia de imágenes está la de conformar simultáneamente P líneas a partir de una única emisión, obteniendo una tasa de imagen P veces superior [Shattuck, 1984], [Hergum, 2007]. En principio, haciendo $P = L$ se podría obtener una imagen por disparo, proporcionando tasas muy altas, del orden de $F = 30000$ imágenes/s si $z_{\max} = 100\,\text{mm}$ y $c = 6000$ m/s. En realidad no sería posible alcanzar tasas tan elevadas por la necesidad de considerar el tiempo de tránsito a través del acoplamiento y de esperar la extinción de las reverberaciones residuales.

El mayor problema de esta aproximación es la necesidad de iluminar *eficientemente* todo el espacio de interés con una *emisión omnidireccional* (*OWI = Omnidirectional Wave Imaging*). Un elemento virtual creado con las contribuciones de varios elementos proporciona mayor intensidad de sonido y mejor relación señal/ruido que un único elemento real. Sin embargo presenta otros problemas, como pérdidas de amplitud en el sentido angular, que habría que compensar [Sutcliffe, 2012b]. La ausencia de enfoque en emisión limita la resolución lateral.

Una alternativa es emitir con onda plana (*PWI =Plane Wave Imaging*), que también insonifica en su propagación toda la región de interés. En este caso la onda plana se genera con todos los elementos del array, por lo que tiene intensidad suficiente. La técnica *PAUT* descrita anteriormente es una forma de *PWI* con una única emisión. El problema es que *PAUT* tiene muy baja resolución lateral al no incluir ningún proceso de enfoque.

La técnica *Fast_Scanning* es un método *PWI* de un único disparo, desarrollado por nuestro grupo para la inspección de laminados delgados, con tasas de hasta 1000 imágenes/s [Camacho, 2014b], si bien enfocando sólo en recepción y con foco fijo.

En el ámbito clínico se desarrolló la técnica *M-PWI* (*multiple-PWI*) que emite ondas planas con diferentes orientaciones consecutivamente. Cada onda plana produce una imagen enfocada únicamente en recepción, pero la combinación de las obtenidas con múltiples orientaciones produce una imagen de calidad comparable a la del estándar *TFM* [Tanter, 2014]. Por otra parte, *M-PWI* requiere menos emisiones para obtener una calidad de imagen similar a la que proporciona una técnica *phased array* multifocal [Montaldo, 2009].

La técnica *M-PWI* también ha sido utilizada para aumentar la tasa de imágenes en END y, al mismo tiempo, mantener una calidad similar a la que proporciona el estándar *TFM* [Le Jeune, 2016]. Según los datos publicados, para arrays con N=128 elementos, mientras que *TFM* necesita 128 disparos omnidireccionales, *M-PWI* obtiene una imagen de calidad comparable con 40 disparos de onda plana. Desde luego, tanto en uno como en otro caso, es impensable obtener imágenes de calidad con un único disparo, omnidireccional o de onda plana, requiriendo del orden de N disparos en *TFM* y N/3 en *M-PWI*.

La alternativa que se propone supera esta limitación mediante la combinación de la imagen de onda plana *PWI* con la de coherencia de fase *PCI* (*Phase Coherence Imaging*), denominando esta combinación *PWPCI* (*Plane Wave Phase Coherence Imaging*). Opera con un único disparo de onda plana, enfoque dinámico en recepción y aplicación de técnicas de coherencia.

Se ha demostrado que *PWPCI* proporciona, con una única emisión, imágenes de calidad comparable la obtenida con el estándar *TFM* con N adquisiciones y formación de imágenes parciales [Cruza, 2017]. De este modo, *PWPCI* puede alcanzar, al menos en teoría, tasas de decenas de miles de imágenes por segundo, una cifra no alcanzada por ninguna otra técnica hasta el momento.

La clave de la técnica *PWPCI* es ponderar la imagen PWI obtenida con un único disparo de onda plana con la imagen de coherencia que resulta del análisis de la dispersión de las fases de los datos de apertura (señales tras aplicar los retardos de enfoque y antes de la suma coherente). Para medir esta dispersión, propusimos diversos factores de coherencia [Camacho, 2009], [Camacho, 2011b]:

1. *Factor de coherencia de fase PCF*, definido como:

$$PCF = \max\left(0\,,1-\frac{\sigma}{\sigma_0}\right) \tag{58}$$

donde σ es la desviación estándar de las fases de apertura y $\sigma_0 = \pi/\sqrt{3}$ es la desviación estándar de una distribución uniforme de las fases.

2. *Factor de coherencia de signo SCF*, definido como:

$$SCF = 1-\sqrt{1-\left[\frac{1}{N}\sum_{i=1}^{N} b_i\right]^2} \tag{59}$$

donde b_i es el signo del dato i de la apertura con posibles valores {-1, 1}.

3. *Factor de coherencia circular CCF*, definido como:

$$CCF = 1-\sqrt{\operatorname{var}\left(\frac{s_i}{|s_{ai}|}\right)+\operatorname{var}\left(\frac{\mathrm{H}[s_i]}{|s_{ai}|}\right)} \tag{60}$$

que considera la distribución circular de la fase en $(0,2\pi]$ y se calcula a partir de la señal analítica $s_a = s + j\mathrm{H}(s)$, donde s representa los datos de apertura, $\mathrm{H}(s)$ su transformada de Hilbert, j es la unidad imaginaria y $\operatorname{var}(\cdot)$ es la varianza.

4. *Factor de coherencia vectorial VCF*, que también considera la distribución circular de fases y fue propuesto recientemente en [Cruza, 2017] específicamente para *PWPCI* mediante:

$$VCF = \frac{\sqrt{\left(\sum s\right)^2 + \left(\sum[\mathrm{H}(s)]\right)^2}}{N\,|s_a|} \tag{61}$$

Una de las virtudes de *VCF* respecto a la formulación *CCF* es que evita el cálculo de varianzas, por lo que su obtención es más rápida y más fácilmente realizable en hardware. Otra ventaja es su mayor tolerancia a pequeñas variaciones de fase y, por tanto, al ruido en los datos adquiridos.

La implementación y experimentación con esta técnica, descritas en [Cruza, 2017], produjo los resultados mostrados en la Figura 2.18. Utilizando un array de *N*=64 elementos, 5 MHz sobre una probeta con taladros laterales, se compara la imagen estándar TFM obtenida con 64 disparos con la *PWPCI-SCF* adquirida con sólo un disparo. Se observa un menor ruido de fondo de la técnica *PWPCI* y una resolución similar en ambas imágenes.

2.8 Arquitecturas para imagen ultra-rápida y autoenfoque

En el ámbito de la END y para inspecciones manuales, donde se opera con una suela o cuña adaptada al componente, basta asegurar unas 30 imágenes por segundo para que el operador perciba la imagen en tiempo real y tenga una respuesta adecuada. Como ya se expuso en esta situación no es necesario el autoenfoque ya que la geometría es constante.

En inspecciones automáticas es más frecuente operar por inmersión (total o parcial), donde hay una capa de agua entre el array y el componente. Aquí es donde el autoenfoque resultaría más útil, aunque en la práctica no existen soluciones por las dificultades para adaptar las leyes focales a una geometría posiblemente cambiante durante la exploración del componente.

Así, la exploración de piezas con autoenfoque y resoluciones espaciales de 1 imagen/mm ha estado limitada a menos de 70 mm/s [Smith, 2003]. Cuando se utiliza la técnica SAUL, que se adapta para incidencia normal a la interfaz, sin auto-enfoque y con baja resolución lateral, se alcanzan los 100 mm/s con resoluciones de 1 imagen cada 2 mm y arrays de 48

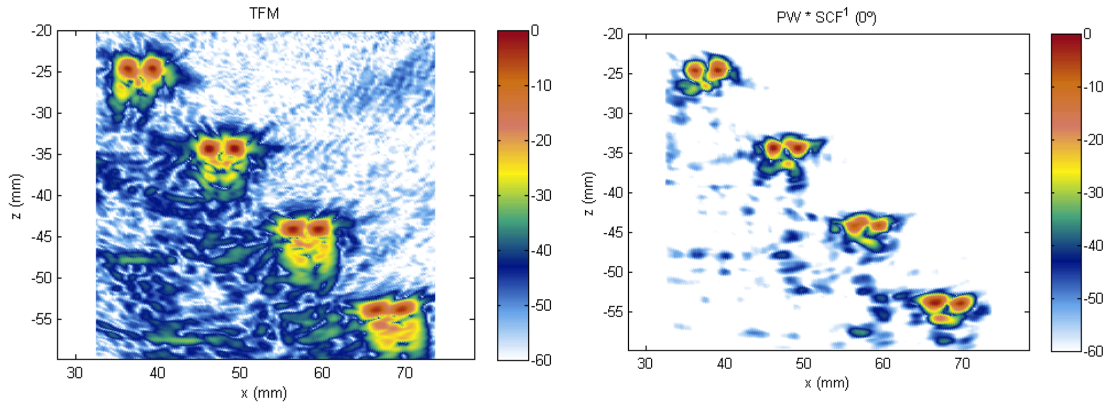

Figura 2.18 - Izquierda: imagen TFM; derecha: imagen PWPCI con SCF. Rango dinámico 60 dB.

elementos [Robert, 2012a]. En [Sutcliffe, 2012a] se alcanzaron 20 imágenes/s de pequeño tamaño (120 x 80 píxeles), con leyes focales pre-calculadas y almacenadas en memoria, cuyo cálculo requirió más de 1 hora. Finalmente, en [Sutcliffe, 2012c] se reportan 8 imágenes/s con la técnica TFM, arrays de 64 elementos e imágenes de 120 x 240 píxeles, usando GPUs y CUDA.

Por otra parte, la imagen ultra-rápida ha sido propuesta con anterioridad en el ámbito clínico, donde las leyes focales son fijas y se opera habitualmente por contacto, para obtener imágenes 3D y 4D en tiempo real [Wygant, 2006], visualizar el movimiento del corazón [Hasegawa, 2011], elastografía transitoria e imagen supersónica [Tanter, 2002], [Bercoff, 2004] y, en nuestro grupo, para tomografía ultrasónica [Camacho, 2012].

La velocidad de inspección es insuficiente para las aplicaciones más exigentes de END. Además, generalmente no realizan un verdadero autoenfoque para proporcionar la máxima calidad de imagen a todas las profundidades. Estas razones motivaron la investigación presentada en esta Tesis relativa a nuevos métodos y arquitecturas para imagen ultrasónica ultra-rápida (miles de imágenes/s), que permita incorporar la capacidad de autoenfoque en condiciones reales de la aplicación [Cruza, 2015c], [Cruza, 2017].

Una manera de abordar el problema es mediante un hardware con capacidad para almacenar gran cantidad de adquisiciones en una memoria local (p.ej. DDR3) y una conexión de gran ancho de banda (p.ej. PCI-Express) con un sistema independiente que conforme la imagen (p.ej, una plataforma con multi-CPU o GPU). Esta arquitectura tiene numerosas ventajas:

- La imagen se genera por software, lo que independiza en gran medida el diseño del hardware de adquisición y facilita la implementación de los algoritmos de formación de la imagen.

- El sistema de adquisición es relativamente sencillo, en el sentido de que no tiene que implementar el conformador en recepción. Es básicamente un sistema de excitación con conformación en emisión y adquisición de señal de todos los elementos del array en paralelo, con un ancho de banda suficiente para su almacenamiento y transferencia.

- Para la formación de la imagen se puede utilizar hardware estándar (GPUs/CPUs) con gran capacidad de procesamiento, de bajo coste y que, en general, incorpora los últimos avances tecnológicos (tecnologías de fabricación, comunicaciones, etc.).

Estas ventajas hacen que sea la alternativa más utilizada en investigación, con realizaciones comerciales para esta finalidad como usPlatform [us4us, 2007], Vantage64 [Verasonics, 2017], habiendo sido también utilizada en algún equipo médico comercial de Supersonic Imagine [Aixplorer, 2017].

Por otra parte, tienen algunas desventajas:

- Las plataformas basadas en múltiples GPU/CPU tienen un gran consumo energético, del orden de 10 veces superior que un sistema con capacidad similar de procesamiento basado en FPGAs [Berten, 2016], son relativamente grandes y requieren refrigeración. Estos aspectos limitan su utilidad en sistemas portátiles o embarcados en la robótica de inspección.

- Las latencias de procesamiento son altas y, en general, poco deterministas debido principalmente al movimiento de datos entre las memorias de los distintos agentes (hardware de adquisición, CPU y GPU) y al sistema operativo si se programa con herramientas software convencionales.

La última descarta en la práctica las arquitecturas basadas en GPU/CPU para implementar sistemas de imagen auto-enfocada que requieren modificar los parámetros de operación en bucle cerrado y tiempo real, sin admitir latencias elevadas y variables. Estrictamente, en el tiempo entre dos imágenes consecutivas, el sistema debe ser capaz de adquirir los datos, formar la imagen, detectar la superficie, recalcular las leyes focales y reprogramar el hardware de disparo y adquisición para generar la siguiente imagen.

Con estas ideas hemos desarrollado un sistema para imagen ultra-rápida y autoenfocada en tiempo real que se describe brevemente a continuación, en el que se implementarán las técnicas de imagen desarrolladas en esta tesis doctoral.

2.8.1 Sistema para imagen ultra-rápida y autoenfocada

El objetivo es implementar algoritmos de auto-enfoque en tiempo real a tasas de imagen elevadas. Por las razones apuntadas anteriormente optamos por una implementación basada en FPGAs, en lugar de un sistema de adquisición conectado a un ordenador central de procesamiento. En este sistema el control de los circuitos de emisión, la digitalización de las señales recibidas y la conformación de la imagen se realizan de forma distribuida en las FPGA del sistema, transfiriendo la imagen final a un computador de control. Además, el sistema dispone de un procesador local suficientemente potente para implementar los algoritmos de auto-enfoque ante cambios de geometría y con capacidad para reprogramar rápidamente los parámetros de adquisición en las FPGAs. Otros objetivos fueron la escalabilidad y el procesamiento distribuido. Lo primero es importante para cubrir aplicaciones que requieran distinto número de canales, algo usual en NDT. Por otra parte, el procesamiento distribuido es imprescindible para manejar el gran volumen de datos generado.

Así, el sistema está basado en módulos capaces de controlar, digitalizar y procesar 32 canales de ultrasonido (Figura 2.19.izq). Los módulos se pueden conectar entre sí mediante un bus segmentado de alta velocidad para realizar sistemas de un número ilimitado de canales en bloques de 32. La Figura 2.19.dcha muestra la instalación del módulo, conectado a un array, en una base con fuentes de alimentación y *UCI*, descrita a continuación.

Cada módulo contiene la electrónica analógica de excitación (pulsers), circuitos de protección y el front-end analógico (amplificador, filtro y conversor A/D) para 32 canales (ver Figura 2.19). Cuenta además con 1 GB de memoria DDR para almacenar el resultado de la conformación o directamente las señales recibidas, lo que permite implementar diversos modos de funcionamiento. La FPGA elegida es la XC7K160T de la serie Kintex de Xilinx, aunque la huella es compatible con los modelos XC7K325T y XC7K410T, de mayor capacidad.

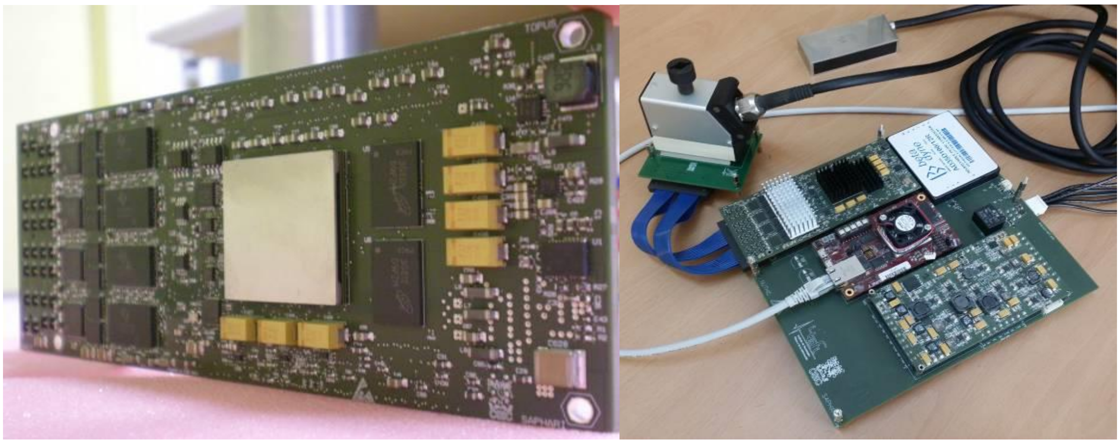

Figura 2.19 - Izquierda: Módulo de 32 canales multi-conformador basado en XC7K160T, que incluye pulsers, AFEs y 1 GB de memoria DDR-3. Derecha: integración del módulo en una placa base con fuentes de alimentación y UCI, conectado a un array, primer prototipo de un sistema de 32 canales.

Además de los módulos de procesamiento, cada sistema cuenta con una Unidad de Control e interfaz (*UCI*) que controla la adquisición, ejecuta las rutinas de auto-enfoque y realiza la comunicación con el ordenador central de almacenamiento y visualización de resultados. [Moreno, 2012]. La UCI se implementa en un módulo comercial basado en el FPGA-SoC de Xilinx ZYNQ XC7Z100, que además de una FPGA de altas prestaciones, proporciona dos procesadores ARM. Uno de ellos (CPU0) se encarga de las comunicaciones con el PC mediante GEthernet, alcanzando 90MB/s, mientras que el otro procesador (CPU1) se encarga de programar y configurar las FPGAs de los módulos y de ejecutar el programa de adquisición. Es en este procesador donde se implementan los algoritmos de auto-enfoque, utilizando herramientas avanzadas de síntesis como HLS [Cruza, 2014].

El sistema cuenta con dos buses segmentados entre las FPGAs de los diferentes módulos de procesamiento para sistemas con $N > 32$ canales. El primero, basado en 10 pares LVDS (6.4 Gb/s), se utiliza para programación de parámetros de adquisición y procesamiento y enviar las imágenes ya conformadas a la UCI, siendo la CPU1 maestra en todas las transferencias.

El segundo bus está basado en los transceptores GTX de la serie 7 de Xilinx, que proporcionan una comunicación dúplex de hasta 10 Gbps en cada sentido (en los dispositivos utilizados, *speed grade* 2). Cada módulo se conecta con el anterior con 4 GTX y con el siguiente con los 4 restantes en el chip. De esta manera, si se cierra el circuito (topología de anillo, Figura 2.20.dcha) se obtienen dos buses circulares de 40Gbps cada uno, cuyos datos circulan en sentido opuesto, lo que permite la transferencia de datos entre dos FPGA cualesquiera del sistema a 80 Gb/s si se ocupan los dos buses. En caso de no cerrar el circuito (Figura 2.20.izq), se perdería la mitad del ancho de banda disponible

El bus de alta velocidad se utiliza para transmitir las imágenes parcialmente conformadas entre las FPGAs de los módulos, ya que formar cada línea de imagen requiere información de todos los canales (Ec. 4). Para ello, cada módulo conforma las L líneas de la imagen con la información adquirida por sus 32 canales, y las envía por uno de los dos buses de 40 Gbps a la siguiente FPGA. Esta suma los resultados de conformar sus propios canales con los datos recibidos de la anterior y envía el resultado al módulo siguiente. Cuando los datos han recorrido todas las FPGAs, la imagen ya está completamente formada.

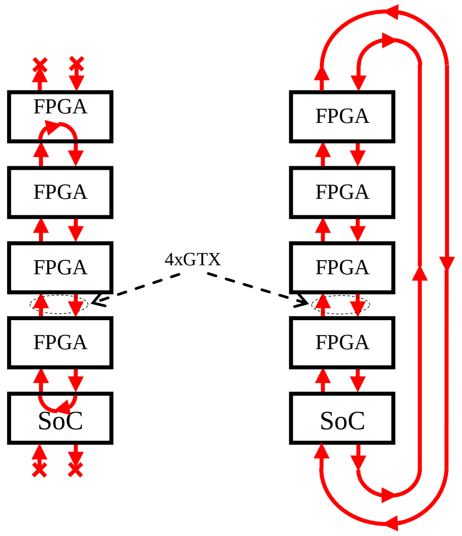

Figura 2.20 - Izquierda: Si no se cierran las conexiones entre los módulos extremos se consigue un único bus de 40 Gbps máximo. En caso de cerrarlo se opera con dos circuitos cerrados de 40Gbps, duplicando el ancho de banda.

La imagen conformada se almacena en la memoria dinámica (DDR) de los módulos, pues la memoria interna de las FPGAs es insuficiente. La imagen se divide en tantas zonas como módulos de 32 canales haya en el sistema, y cada módulo usa su DDR para almacenar su parte de la imagen. De esta manera se aprovecha no sólo la potencia de procesamiento de todas las FPGAs, sino también el ancho de banda de memoria de todos los módulos, haciendo del sistema una arquitectura de procesamiento distribuido a alta velocidad.

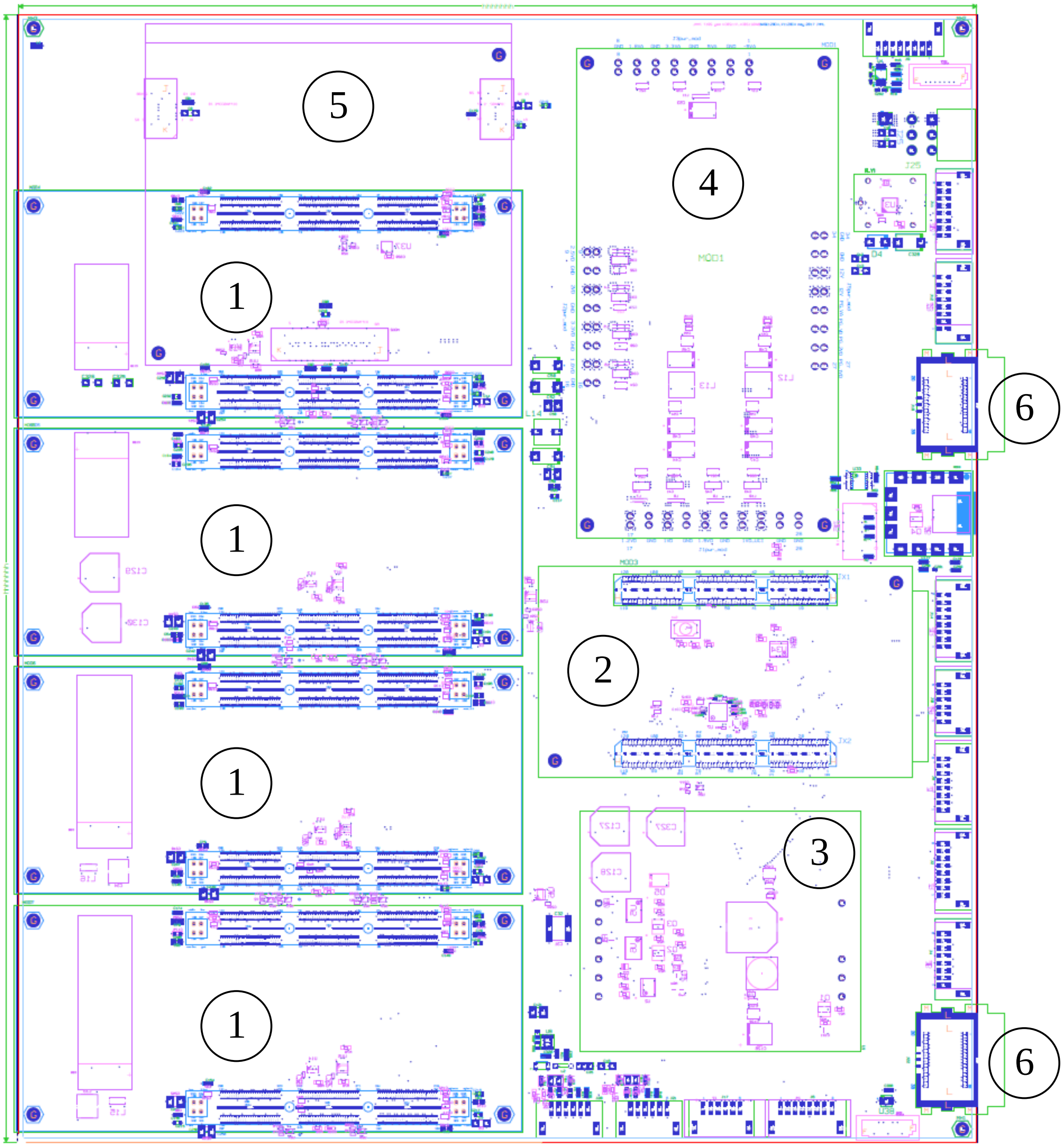

Figura 2.21 - Placa base de un sistema de 128 canales. 1- Módulos de 32 canales; 2- Módulo SoC; 3- Fuente de alta tensión; 4- Fuentes de baja tensión; 5- Ampliación con 8 canales de ultrasonido convencional [Cruza, 2010] [Cruza, 2011b]; 6- Conectores de alta velocidad.

La Figura 2.21 muestra la placa base de un sistema de 128 canales, donde se aprecian las huellas de las fuentes de alimentación, la UCI, los 4 módulos de adquisición y procesamiento de 32 canales, la fuente de alta tensión y los dos conectores de alta velocidad. Estos conectores permiten escalar el sistema interconectando placas de 128 canales y manteniendo la topología en forma de anillo sin perder velocidad de transferencia (Figura 2.22).

2.8.2 Conformador optimizado para imagen ultra-rápida

Una forma de acelerar la generación de imágenes es integrar un cierto número S de conformadores donde, cada uno de ellos, obtiene en paralelo y en tiempo real L líneas de imagen con enfoque dinámico estricto. Esto proporciona imágenes de $L{\cdot}S$ líneas en tiempo real, esto es, durante la adquisición y para una única emisión [Shattuck, 1984], [von Ramm, 1991], [Rasmussen, 2012]. Pero los retardos de enfoque requieren una elevada resolución temporal (del orden de 6.9 ns para arrays de 5 MHz, 128 elementos) y la frecuencia de muestreo, la menor compatible con el criterio de Nyquist para limitar consumo, ancho de banda y recursos internos, no proporciona esta resolución. En esta situación hay que utilizar filtros de retardo fraccional [Laasko, 1996] junto con el conformador, cuya realización con lógica distribuida en una FPGA consumiría demasiados recursos.

Por estas razones propusimos reformular las ecuaciones del conformador para adaptarlas a la arquitectura de los bloques DSP (*DSP slices*) de las FPGA estado del arte [Cruza, 2011a]. La ventaja de los *DSP slices* para implementar imagen ultrasónica en paralelo es que, al ser realizaciones específicas, su velocidad de operación es mayor que la lógica estándar (*fabric*), incluyendo un multiplicador, uno o más sumadores por celda y otras funciones. Las mayores y más avanzada FPGAs (Virtex Ultrascale+) disponen de más de 12.000 *DSP slices*.

En este trabajo [Cruza, 2011a] propusimos filtros semi-paralelos para aprovechar que la frecuencia máxima de conmutación de las celdas DSP de las FPGAs del momento (Spartan-6) era mayor que la frecuencia de muestreo. De esta manera y colocando los filtros en una arquitectura sistólica se conseguía un conformador de 32 canales usando 33 celdas DSP, comparado con las 160 que se serían necesarias sin optimización alguna. Ello permitió obtener 5 líneas en paralelo usando una FPGA de bajo coste (XC6S100T).

Sin embargo, ya en ese mismo trabajo se predecía la posible utilización de la siguiente generación de FPGAs. Una mayor experiencia en el diseño con celdas DSP y unas mejores prestaciones de la electrónica, nos han permitido subir un orden de magnitud el número de líneas en paralelo que se pueden conformar por cada FPGA.

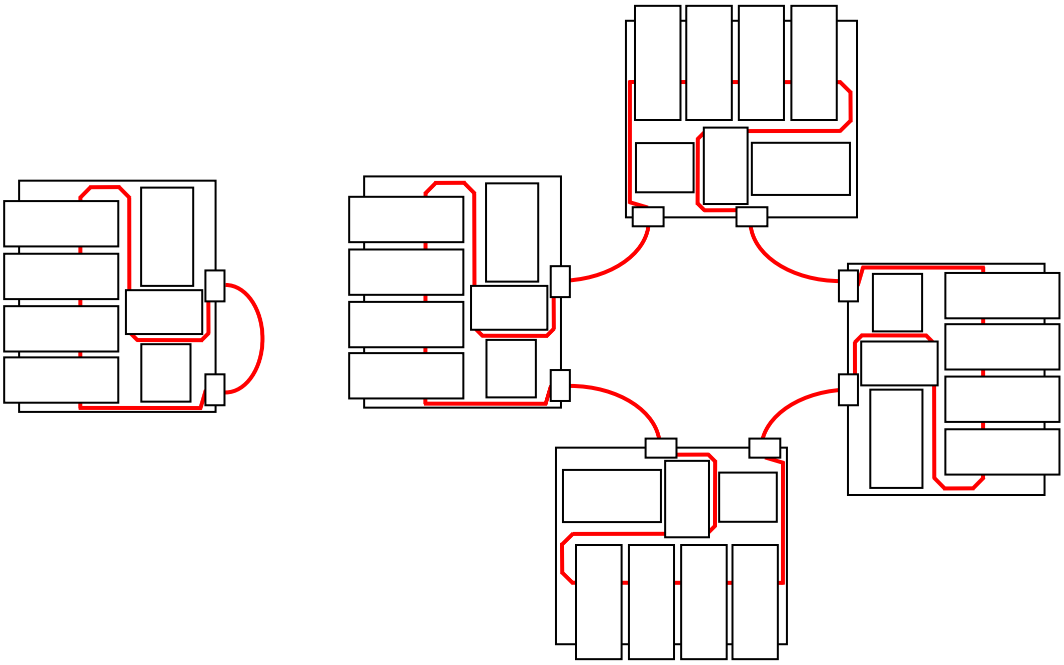

Figura 2.22 - Izquierda: Sistema de 128 canales. Derecha: Sistema de 512 canales a partir de cuatro placas de 128 canales. En línea roja los 4 enlaces bidireccionales GTX (8 pares).

Las optimizaciones realizadas en este nuevo diseño son las siguientes:

1. Optimización de la memoria: en vez de utilizar FIFOs para implementar los retardos, se emplean memorias circulares. De este modo se pueden utilizar un único bloque de memoria RAM para las distintas líneas de un mismo canal.

2. Aprovechamiento de la frecuencia de trabajo de la lógica convencional que implementa parte del circuito de enfoque. La nueva versión opera con una frecuencia f_{FOC} entre 200 y 240 MHz.

3. Aprovechamiento de la alta frecuencia de conmutación de las celdas DSP, que permiten trabajar al doble de frecuencia que la lógica distribuida, esto es, f_{DSP} entre 400 y 480 MHz. De este modo se comparte un filtro de interpolación entre dos canales, utilizando 4 celdas por cada dos canales, 64 en total para un conformador de 32 canales.

4. Al igual que en [Cruza, 2011a] se utiliza una arquitectura sistólica donde los filtros se encadenan, usando las líneas rápidas de transferencia de datos entre celdas DSP. Además, de esta manera se ahorra un sumador por cada filtro con respecto a una arquitectura en árbol.

Una ventaja de esta arquitectura es la posibilidad de conformar múltiples líneas de la imagen en paralelo (*R* líneas), esencialmente con la misma lógica mediante multiplexado en el tiempo. Si la frecuencia de operación de los circuitos de enfoque es f_{FOC} y la frecuencia de muestreo es f_S se pueden conformar por multiplexado en el tiempo,

$$R=\left[\frac{f_{FOC}}{f_S}\right]_{\downarrow}\ \text{líneas de imagen simultáneamente.} \tag{58}$$

donde $[\cdot]_{\downarrow}$ indica redondeo hacia abajo. De esta manera, con un solo conformador, se obtienen *R*=4 líneas de imagen en paralelo para f_S = 50 MHz, f_{FOC} = 200 MHz y f_{DSP} = 400 MHz. Si la frecuencia de muestreo se reduce a 10 MHz, válida para arrays de hasta 2.5 a 3.3 MHz, se pueden obtener hasta *R*=20 líneas de imagen en paralelo.

La Tabla 2.3 muestra el consumo de recursos de un único conformador y de las tres FPGAs compatibles. En negrita el recurso limitante, que para el caso de la FPGA XC7K325 son las celdas DSP. En los casos de las FPGAs XC7K160 y XC7K410, el limitante es el número de LUTs libres, ya que se ha estimado que son necesarias alrededor de 30000 LUTs

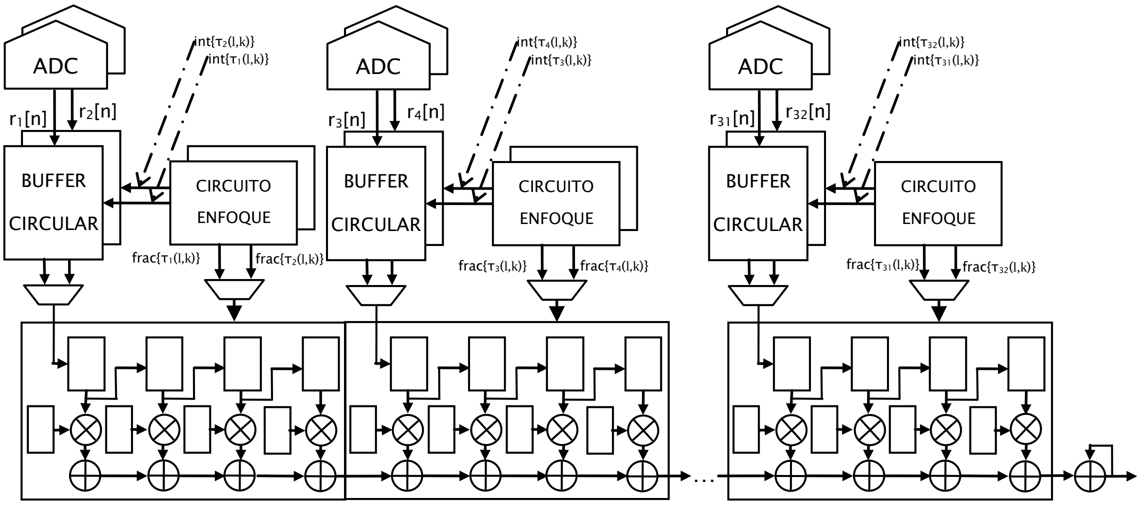

Figura 2.23 - Arquitectura sistólica que combina la interpolación de muestras para mejorar la resolución temporal con la suma coherente para 32 canales ultrasónicos, implementando un conformador.

Tabla 2.3 – Uso de recursos para un único conformador y para los que pueden albergar las tres FPGAs compatibles del diseño.

		Conformador	**XC7K160**	**XC7K325**	**XC7K410**
Nº conformadores		1	6	12	16
Líneas en paralelo (50MSPS)		4	24	48	64
Líneas en paralelo (10MSPS)		20	120	240	320
RECURSOS FPGA	**LUTs**	10778	**64668 (64.2%)**	129336 (63.2%)	**172448 (77.2%)**
	LUT as Memory	4101	24606 (71.2%)	49212 (77.2%)	65616 (72.2%)
	Registros	11812	70872 (35.2%)	141744 (35.2%)	188992 (37.2%)
	18Kb Block RAM	32+132[5]	324 (50.2%)	516 (58.2%)	644 (41.2%)
	DSPs	65	390 (65.2%)	**780 (93.2%)**	1040 (68.2%)

adicionales para implementar otros módulos como los buses internos, comunicaciones y controlador de DDR.

Sin embargo, los recursos internos de la FPGA no son el único factor limitante, ya que las líneas generadas de cada módulo se deben trasmitir al resto de módulos para que se sumen con los resultados de la conformación del resto de canales. Suponiendo que los enlaces GTX alcanzaran los 10Gbps y un rendimiento del 90%, podríamos transmitir la información de 16 conformadores con 21 bits por muestra.

El ancho de banda de memoria también es limitante ya que una vez conformada la imagen se ha de guardar en memoria dinámica. En este caso, ya que el tamaño de la imagen se divide entre los distintos módulos del sistema, cuantos más módulos, mayor ancho de banda total. Por ejemplo, un sistema de 32 canales, solo podría almacenar la información de 12 conformadores suponiendo 24 bits por muestra y un exageradamente optimista rendimiento del 96%. Sin embargo, el sistema de 128 canales podría almacenar sin problemas la información de 16 conformadores, 32 bits por muestra y utilizando solo el 43% del ancho de banda máximo de la memoria.

---

[5] Son necesarias 132 BRAMs para almacenar las leyes focales para 1024 lineas. Este consumo es fijo sin depender del número de conformadores que se implementan.

2.8.3 Características más importantes de la arquitectura propuesta

Se ha diseñado un sistema capaz de generar imagen ultra-rápida y con capacidad de auto-enfoque en tiempo real. Las ventajas de esta arquitectura distribuida basada en FPGAs y un SoC son las siguientes:

1. La arquitectura permitiría conformar hasta 64 líneas en paralelo a máxima frecuencia de adquisición (50MSPS) y hasta 320 líneas adquiriendo a 10MSPS (arrays de hasta 2.5MHz). Esto habilita al sistema para realizar imagen ultrarrápida.

2. La arquitectura es escalable en cuanto al número de canales activos, es decir, se pueden implementar igualmente sistemas de un número bajo de canales (por ejemplo 32) como de gran número de canales (por ejemplo 2048), sin perder prestaciones.

3. La arquitectura distribuida permite conformar imágenes de gran tamaño en tiempo real, sin importar el número de canales activos.

4. El sistema puede funcionar de manera autónoma, solo enviando las imágenes a un ordenador que puede ser de bajas prestaciones, ya que éste solo representa y/o almacena imágenes ya procesadas por el sistema de ultrasonidos.

5. Además, la comunicación al sistema remoto se realiza por el canal más compatible y extendido, Ethernet.

6. La presencia de memoria dinámica con un ancho de banda de hasta 59 Gbps por módulo, permite almacenar la adquisición utilizando menos de la mitad del ancho de banda de memoria dinámica disponible, con capacidad para una gran cantidad de adquisiciones.

7. Los procesadores ARM permiten ejecutar software de procesamiento de potencia moderada, útil para ciertos algoritmos de autoenfoque. Estos procesadores comparten memoria con una gran cantidad de recursos FPGA, permitiendo aceleradores hardware de gran rendimiento [Cruza, 2014].

8. Su reducido tamaño y consumo comparado con sistemas basados en procesamiento por CPU/GPU permite realizar sistemas portátiles para medicina o END, capaces de ser embarcados en la robótica de inspección.

3 Publicaciones

Esta tesis cuyos trabajos comenzaron poco después de terminar el trabajo fin de Máster, ha dado lugar a 7 trabajos publicados en revistas indexadas en JCR (4 en Q1, 2 en Q2 y una en Q3), siendo primer autor en 4 de ellas. Asimismo participo como inventor en una patente con extensión internacional, actualmente transferida. También ha dado lugar a 7 trabajos para congresos internacionales, con 6 de primer autor, y 2 nacionales, con 1 de primer autor.

En la sección 3.1, se enumeran estos trabajos, relacionándolos por sus aportaciones. En él **¡Error! No se encuentra el origen de la referencia.** se adjuntan los trabajos completos publicados por el orden de mención en 3.1.

3.1 Relación de publicaciones

El primer problema que fue abordado por nuestro grupo para el autoenfoque fue el del cálculo en tiempo real de tiempos de vuelo y leyes focales en el caso de dos medios de propagación. Las publicaciones:

- J. F. Cruza, J. Camacho, L. Serrano, C. Fritsch, “New Method for Real-time Focusing through Interfaces”, *IEEE Trans. on Ultrason. Ferroelectr. Freq. Control*, 60, 4, pp. 739-751, 2013. (JCR: IF=1.503, Q2, Citas: 10)
- J. F. Cruza, J. Camacho, J. M. Moreno, C. Fritsch, “Automatic dynamic focusing through interfaces”, *Proc. IEEE Ultrason. Symp.*, pp. 1469-1472, 2012.
- C. Fritsch, J. Camacho, J. F. Cruza, J.M. Moreno, J. Brizuela, “Array virtual para cálculo de leyes focales”, *Tecniacústica 2011, Ed. Soc. Española de Acústica*, ISBN 978-84-87985-20-1, 2011.

presentan el concepto del *array virtual* descrito en la memoria, sección 2.4.1, su implementación y pruebas de verificación.

El *array virtual*, originalmente desarrollado para *Phased Array* se extendió al caso de *TFM*, dando lugar a la siguiente publicación:

- J. F. Cruza, J. Camacho and J. M. Moreno, "Total Focusing Phased Array," *2016 IEEE International Ultrasonics Symposium (IUS),* Tours, 2016, pp. 1-4., doi: 10.1109/ULTSYM.2016.7728610

Por otra parte, el array virtual posibilitó el desarrollo de circuitos de focalización dinámica para un medio homogéneo en el caso de dos medios, publicado y patentado en

- C. Fritsch, J. F. Cruza, J. Camacho, J. M. Moreno, J. Brizuela, L. Medina, "Controlador de enfoque dinámico para sistemas de imagen ultrasónica", *Pat. ES P201230799*, 25 May 2012.

En un siguiente paso, los trabajos:

- J. Camacho, J. F. Cruza, J. Brizuela, C. Fritsch, "Automatic Dynamic Depth Focusing for NDT", *IEEE Trans. on Ultrason. Ferroelectr. Freq. Control*, 61, 4, pp. 673-684, 2014. (JCR: IF=1.512, Q2, Citas: 11)
- J. F. Cruza, J. Camacho, C. Fritsch, R. González-Bueno, R. Giacchetta, "Autofocus: Enfoque Automático para Phased Arrays", *13 Congreso Nacional de Ensayos No Destructivos*, ISBN: 978-84-606-7565-5, pp. 689-698 , 2015.

aportan un conjunto de técnicas para la obtención de la geometría de la pieza y su posición relativa respecto del array, usando como datos medidas de tiempos de vuelo con el mismo array que adquiere la imagen. Estás técnicas combinadas con las del *array virtual* aportan una potente herramienta para el autoenfoque en NDT, la función AUTOFOCUS expuesta en la sección 2.1.

Por otra parte, el *Array Virtual* reduce el problema de cálculo de tiempos de vuelo a través de una interfaz a solamente dos focos por línea pero, a pesar de ello, esta parte del algoritmo es la que consume más tiempo, dado que se basa en búsquedas iterativas.

En la publicación

- J. F. Cruza, J. Camacho, J. M. Moreno, C. Fritsch, "Ultrafast hardware-based focal law calculator for automatic focusing", *NDT & E International*, 74, pp. 1-7, 2015. (JCR: IF=1.871, Q1, Citas: 2)

se proponen varios algoritmos de cálculo que aceleran el proceso y se implementan en lógica de FPGA. Esta propuesta abrió la posibilidad de obtener todas las imágenes enfocadas en tiempo real con una tasa de imágenes autoenfocadas alta. La sección 2.4.2 describe el hardware desarrollado así como los distintos algoritmos y estrategias utilizados.

Por otro lado, los trabajos

- J. Camacho, J. F. Cruza, "Auto-Focused Virtual Source Imaging With Arbitrarily Shaped Interfaces", *IEEE Trans. on Ultrason. Ferroelectr. Freq. Control*, **62**, 11, pp. 1944-1956, 2015. (JCR: IF=2.287, Q1, Citas: 2)
- J. F. Cruza, J. Camacho, "Total Focusing Method with Virtual Sources in the presence of unknown geometry interfaces", *IEEE Trans. on Ultrason. Ferroelectr. Freq. Control*, **63**, 10, pp. 1581-1592, 2016. (JCR: IF=2.743, Q1)

presentan una novedosa técnica de imagen autoenfocada, alternativa a la anterior que no requiere obtener una representación matemática de la interfaz. Se basa en emitir y recibir enfocando en puntos de la interfaz con distintas aperturas del array, lo que elimina los problemas asociados a la refracción para el cálculo de los tiempos de vuelo.

La sección 2.6 describe las dos técnicas propuestas.

Otra aportación relevante ha sido una técnica de imagen ultra-rápida (PWPCI). Con una única emisión, enfoque dinámico en recepción y coherencia de fase instantánea obtiene miles de imágenes por segundo de calidad comparable a los mejores estándares. Se expone en la sección 2.7 y se publicó en:

- J. F. Cruza, J. Camacho, C. Fritsch, "Plane-wave phase-coherence imaging for NDE", *NDT & E International*, **87**, pp. 31-37, 2017. (JCR: IF=2.726, Q1).

Una técnica más sencilla, de emisión en onda plana y conformación en paralelo, se propuso para la inspección de grandes componentes planos en aeronáutica a alta velocidad con cierta capacidad de autoenfoque. Dada su especificidad, el nuevo método fue comunicado al 6th International Symposium on NDT in Aerospace:

- J. Camacho, J. F. Cruza, E. Cuevas, S. Hernández, "Fast Scanning: achieving high scanning velocities in the phased array inspection of aeronautic components", Proc. of the. 12-14 Nov. 2014, Madrid, Spain.

  http://www.ndt.net/events/aeroNDT2014/app/content/Paper/41_Cruza.pdf

Por último, para poder llevar todas estas técnicas de imagen a la práctica, es preciso un hardware con gran capacidad de procesamiento y que pueda modificar de manera rápida los parámetros de adquisición y procesamiento. Este hardware se describe de manera resumida en 2.8 y en las siguientes publicaciones.

- J. F. Cruza, L. Medina-Valdés, C. Fritsch, "Real time autofocusing hardware for ultrasonic imaging with interfaces", *Proc. IEEE Ultrason. Symp.*, pp. 1-**4**, 2015
- J. F. Cruza, J. Camacho, J. M. Moreno, L. Medina, "A New Architecture for Fast Ultrasound Imaging", *AIP Conf. Proc.*, **1581**, 1, pp. 1975-1982, 2014.
- J. F. Cruza, M. Pérez, J. M. Moreno, C. Fritsch, "Real time fast ultrasound imaging technology and possible applications", *43 Annual Symp. Ultrasonic Industry Association, 2014 UIA Symp.*, Ed. Physics Procedia (Elsevier), **63**, pp. 79-84, 2015
- J. F. Cruza, J. Camacho, J. Brizuela, J.M. Moreno, C. Fritsch, "Modular Architecture for Ultrasound Beamforming with FPGAs", International Congress on Ultrasonics (ICU-2011), Ed. AIP Conf. Proceedings, 1433, pp.181-184, 2012. doi: http://dx.doi.org/10.1063/1.3703166

Una de las características de la arquitectura propuesta es su escalabilidad, manteniendo sus prestaciones con independencia de la complejidad del sistema, como fue presentado en:

- J. Camacho, L. Medina, J. F. Cruza, J. M. Moreno, C. Fritsch, “Multimodal Ultrasonic Imaging for Breast Cancer Detection”, *Archives of Acoustics*, **37**, 3, pp. 253-260, 2012. (JCR: IF=0.829, Q3, Citas: 9)

3.2 Tesis por compendio de artículos

La realización de tesis por compendio de artículos requiere que al menos tres de estos trabajos se hayan publicado después de la matriculación en el programa de doctorado, que el doctorando figure como primer autor y que la revista se posicione en el primer tercio JCR, requisitos que se cumplen con los siguientes artículos:

- J. F. Cruza, J. Camacho, J. M. Moreno, C. Fritsch, “Ultrafast hardware-based focal law calculador for automatic focusing”, *NDT & E International*, 74, pp. 1-7, 2015. (JCR: IF=1.871, Q1, Citas: 2)
- J. F. Cruza, J. Camacho, “Total Focusing Method with Virtual Sources in the presence of unknown geometry interfaces”, *IEEE Trans. on Ultrason. Ferroelectr. Freq. Control*, **63**, 10, pp. 1581-1592, 2016. (JCR: IF=2.287, Q1)
- J. F. Cruza, J. Camacho, C. Fritsch, “Plane-wave phase-coherence imaging for NDE”, *NDT & E International*, **87**, pp. 31-37, 2017. (JCR: IF=2.726, Q1)

4 Conclusiones

Con la realización de este trabajo de Tesis Doctoral, “Imagen ultrasónica autoenfocada”, se han obtenido las siguientes conclusiones:

1. Se ha demostrado, teórica y experimentalmente, la posibilidad de obtener imagen ultrasónica de calidad con autoenfoque, sin conocimiento *a priori* de la geometría del componente. Esta capacidad es particularmente útil para aplicaciones de Evaluación No Destructiva de componentes con geometría compleja.

2. Se han propuesto tres técnicas ultrasónicas (pulso-eco, *pitch-catch* y onda plana) y los algoritmos correspondientes, para calcular una representación analítica de la geometría desconocida de la interfaz del componente inspeccionado. Se han verificado experimentalmente, mostrando la capacidad adaptativa de la función de autoenfoque.

3. Se ha propuesto un array virtual que elimina los problemas asociados a la refracción en la interfaz entre dos medios de propagación para el cálculo de las leyes focales. El array virtual opera en un único medio y proporciona tiempos de vuelo esencialmente equivalentes a los obtenidos al considerar la propagación con refracción.

4. Se ha propuesto la realización hardware *UFAF* (*Ultra-Fast Auto-Focusing*) que reduce en más de un orden de magnitud el tiempo de cálculo de los parámetros del circuito de enfoque, adaptados a la interfaz entre dos medios. Resuelve la ecuación de mínimo tiempo de vuelo (principio de Fermat), combinando algoritmos de Newton-Raphson e Illinois.

5. Se ha propuesto, diseñado y construido un circuito de enfoque dinámico estricto (en todas las muestras) que opera en tiempo real y consume pocos recursos hardware en una FPGA. Además, sólo requiere la inicialización de dos parámetros para suministrar códigos de enfoque con una resolución superior al periodo de muestreo.

6. Se ha propuesto y verificado experimentalmente el proceso *AUTOFOCUS* que realiza el autoenfoque para formar la imagen ultrasónica de piezas con formas desconocidas en tres pasos: 1. Estimación de la geometría, 2. Programación del circuito de enfoque, 3. Obtención de la imagen con enfoque dinámico estricto en tiempo real.

7. Se han propuesto y verificado experimentalmente otras dos técnicas de autoenfoque en componentes de geometría desconocida, basadas en la creación de fuentes virtuales sobre la superficie de las piezas y formación de imagen mediante técnicas de apertura sintética. A diferencia de *AUTOFOCUS*, estas nuevas técnicas (*AVSI* y *AVSI-TFM*) operan sin determinar una representación analítica de la interfaz entre dos medios.

8. Se ha propuesto y verificado experimentalmente la técnica *PWPCI* (*Plane-Wave Phase Coherence Imaging*) para la obtención de imagen ultrasónica dos órdenes de magnitud más rápida que con la metodología estándar *phased array*. Tras emitir una onda plana, se aplica en recepción la técnica de coherencia de fase. El conjunto obtiene una imagen de calidad, resolución y relación señal/ruido, comparables a la del estándar *TFM*.

9. Se ha propuesto una nueva arquitectura sistólica para realizar la conformación en paralelo de múltiples líneas de imagen en modo *phased array*, que utiliza de forma muy eficiente los *DSP slices* disponibles en las FPGAs estado del arte, facilitando la obtención de imagen ultrasónica a alta velocidad.

10. El conjunto de los resultados obtenidos puede representar un nuevo paradigma en imagen ultrasónica, al proporcionar la máxima calidad (no inferior a la que se obtiene con descripciones CAD de la geometría), a la máxima cadencia (en algún caso con un único disparo, varios miles de imágenes/s) y con un consumo muy limitado de recursos hardware que permiten su implementación en FPGAs de tamaño y coste moderados.

5 Trabajo futuro

A muy corto plazo, el trabajo más inmediato es finalizar el desarrollo de la nueva arquitectura e implantar todos los algoritmos que forman parte de esta Tesis Doctoral y realizar la transferencia a la industria ya comprometida. Se estima que el plazo para disponer de la nueva tecnología es de 6-8 meses.

A medio plazo (uno a tres años), utilizar la nueva tecnología en aplicaciones que demandan una alta velocidad y calidad de imagen, que ya están siendo abordadas por nuestro grupo de investigación y que, por tanto, demandan los resultados obtenidos:

- Tomografía de ángulo completo para detección precoz de cáncer de mama.
- Técnicas de imagen elastográfica sin contacto
- Inspección de grandes piezas aeronáuticas con autoenfoque a alta velocidad.

Desde el momento presente y, a más largo plazo, continuar con la línea de investigación abierta, realizando nuevas propuestas de imagen ultrasónica autoenfocada y a ultra-alta velocidad, combinada con otras técnicas conocidas y por descubrir, así como abordar sus posibles aplicaciones.

Referencias

Aixplorer, 2017	Supersonic Imagine, 2017: http://www.supersonicimagine.com/Aixplorer-R/Technology
Alexandru, 2010	R. Alexandru, “Delay controller for ultrasound receive beamformer”, U.S. Pat. 7 804 736 B2, Sep. 28, 2010.
Bae, 1998	M. Bae, “Focusing delay calculation method for real-time digital focusing and apparatus adopting the same”, US Pat. 5836881, 17 Nov. 1998.
Barshan, 2000	B. Barshan, D. Baskent, “Comparison of two methods of surface profile extraction from multiple ultrasonic range measurements”, *Meas. Sci. Technol.* **11**, pp. 833–844, 2000.
Barshan, 2001	B. Barshan, “Ultrasonic Surface Profile Determination by Spatial Voting”, *IEEE Instrumentation and Measurement Technology Conference*, pp. 583-588, 2001.
Ben-Gal, 2005	I. Ben-Gal, “Outlier detection”, en *Data Mining and Knowledge Discovery Handbook*, Ed. O. Maimon y L. Rockach, Kluwer Academic Pub., 2005.
Berten, 2016	Berten DSP, “GPUs vs FPGAs performance comparison”, White paper BWP-001, 2016, en: http://www.bertendsp.com/gpu-vs-fpga-performance-comparison/
Buiochi, 2004	F. Buiochi, O. Martínez, L. G. Ullate and F. Montero, “A Computational Method to Calculate the Longitudinal Wave Evolution Caused by Interfaces Between Isotropic Media”, *IEEE Trans. on Ultrason. Ferroelectr. Freq. Control*, 51, 2, pp. 181-192, 2004.
Bercoff, 2004	Bercoff J, Tanter M, Fink M. Supersonic shear imaging: A new technique for soft tissue elasticity mapping. *IEEE Trans Ultrason., Ferroelectr. Freq. Control*, 51, 4, pp. 396–409, 2004.
Camacho, 2006	J. Camacho, A. Ibáñez, M. Parrilla, C. Fritsch, “A Front-End Ultrasound Array Processor based on LVDS Analog-to-Digital Converters”, *Proc. IEEE Ultrason. Symp*, pp. 1631-1634, 2006.
Camacho, 2009	J. Camacho, M. Parrilla, C. Fritsch, “Phase Coherence Imaging”, *IEEE Trans. on Ultrason. Ferroelectr. Freq. Control*, **56**, 5, pp. 958-974, 2009.
Camacho, 2011a	J. Camacho, C. Fritsch, “Phase coherence imaging of grained materials”, *IEEE Trans. on Ultrason. Ferroelectr. Freq. Control*, **58**, 5, pp. 1006-1015, 2011.
Camacho, 2011b	J. Camacho, C. Fritsch, “Adaptive Beamforming by Phase Coherence Processing”, *Ultrasound Imaging*, Chap. 4, Ed. InTech, 2011, http://www.intechopen.com/books/ultrasound-imaging/
Camacho, 2012	J. Camacho, L. Medina, J. F. Cruza, J. M. Moreno, C. Fritsch, “Multimodal Ultrasonic Imaging for Breast Cancer Detection”, *Archives of Acoustics*, **37**, 3, pp. 253-260, 2012.
Camacho, 2014a	J. Camacho, J. F. Cruza, J. Brizuela, C. Fritsch, “Automatic Dynamic Depth Focusing for NDT”, IEEE Trans. on Ultrasonics, Ferroelectrics and Frequency Control, 61, 4, pp. 673-684, 2014.
Camacho, 2014b	J. Camacho, J. F. Cruza, E. Cuevas, S. Hernández, “Fast Scanning: achieving high scanning velocities in the phased array inspection of aeronautic components”, Proc. of the 6th international symposium on NDT in aerospace. 12-14 Nov. 2014, Madrid, Spain. http://www.ndt.net/events/aeroNDT2014/app/content/Paper/41_Cruza.pdf

Camacho, 2015 J. Camacho, J. F. Cruza, “Auto-Focused Virtual Source Imaging With Arbitrarily Shaped Interfaces”, *IEEE Trans. on Ultrason. Ferroelectr. Freq. Control*, **62**, 11, pp. 1944-1956, 2015.

Casula, 2004 O. Casula, C. Poidevin, G. Cattiaux and G. Fleury, “A flexible phased array transducer for contact examination of components with complex geometry”, *16th Conf. on Nondestructive Testing*, Montreal, Canada, 2004.

Chatillon, 2009 S. Chatillon, S. Mahaut and P. Dubois, “Simulation of advanced UT phased array techniques with matrix probes and dynamic settings for complex component inspections”, *Rev. QNDE*, 28, pp. 864-871, 2009.

Corl, 1978 P. D. Corl, P. M. Grant, G. S. Kino, “A digital synthetic focus acoustic imaging system for NDE”, *Proc. Ultrason. Symp.*, pp. 263-268, 1978.

Cruza, 2010 J. F.Cruza, R. González Bueno, R. Mateos, C. Fritsch, “DIFRASCOPE: Un instrumento compacto para TOFD”, *41º Congreso Nacional de Acústica* (Tecniacústica 2010), León (España), 13-15 Oct. 2010.

Cruza, 2011a J. F. Cruza, “Diseño de un conformador de haces ultrasónicos en tiempo real”, *Trabajo Fin de Maestría*, Dpto. de Electrónica, Esc. Politécnica Superior, Univ. Alcalá de Henares, Sep. 2011.

Cruza, 2011b J. F. Cruza, F. M. Sánchez, C. Fritsch, R. Mateos, ”Procesador digital de señal ultrasónica en tiempo real”, *XI Jornadas de Computación Reconfigurable y Aplicaciones* (JCRA'11), Ed. Universidad de La Laguna, ISBN 978-84-614-8814-8, 2011.

Cruza, 2012a J. F. Cruza, J. Camacho, J. M. Moreno, C. Fritsch, “Automatic dynamic focusing through interfaces”, *Proc. IEEE Ultrason. Symp.*, pp. 1469-1472, 2012.

Cruza, 2012b J. F. Cruza, J. Camacho, J. Brizuela, J.M. Moreno, C. Fritsch, “Modular Architecture for Ultrasound Beamforming with FPGAs”, *International Congress on Ultrasonics (ICU-2011)*, Ed. AIP Conf. Proceedings, **1433**, pp.181-184, 2012. doi: http://dx.doi.org/10.1063/1.3703166

Cruza, 2013 J. F. Cruza, J. Camacho, L. Serrano, C. Fritsch, “New Method for Real-time Focusing through Interfaces”, *IEEE Trans. on Ultrason. Ferroelectr. Freq. Control*, **60,** 4, pp. 739-751, 2013.

Cruza, 2014 J. F. Cruza, J. Camacho, J. M. Moreno, L. Medina, “A New Architecture for Fast Ultrasound Imaging”, *AIP Conf. Proc.*, **1581**, 1, pp. 1975-1982, 2014.

Cruza, 2015a J. F. Cruza, J. Camacho, J. M. Moreno, C. Fritsch, “Ultrafast hardware-based focal law calculador for automatic focusing”, *NDT & E International*, 74, pp. 1-7, 2015.

Cruza, 2015b J. F. Cruza, M. Pérez, J. M. Moreno, C. Fritsch, “Real time fast ultrasound imaging technology and possible applications”, *43 Annual Symp. Ultrasonic Industry Association, 2014 UIA Symp.*, Ed. Physics Procedia (Elsevier), **63**, pp. 79-84, 2015.

Cruza, 2015c J. F. Cruza, L. Medina-Valdés, C. Fritsch, “Real time autofocusing hardware for ultrasonic imaging with interfaces”, *Proc. IEEE Ultrason. Symp.*, pp. 1-**4**, 2015.

Cruza, 2016a J. F. Cruza, J. Camacho, “Total Focusing Method with Virtual Sources in the presence of unknown geometry interfaces”, *IEEE Trans. on Ultrason. Ferroelectr. Freq. Control*, **63**, 10, pp. 1581-1592, 2016.

Cruza, 2016b	J. F. Cruza, J. Camacho and J. M. Moreno, "Total Focusing Phased Array," *2016 IEEE International Ultrasonics Symposium (IUS)*, Tours, 2016, pp. 1-4. doi: 10.1109/ULTSYM.2016.7728610
Cruza, 2017	J. F. Cruza, J. Camacho, C. Fritsch, “Plane-wave phase-coherence imaging for NDE”, *NDT & E International*, **87**, pp. 31-37, 2017.
Cuevas, 2015	E.Cuevas, S. Hernández, “Soluciones basadas en robot para obtener procesos de inspección no destructiva automatizados, integrados e industriales, *13º Congreso Nacional de Ensayos No Destructivos,* Sevilla, pp. 165-177, 2015
Dasel, 2014	Dasel SL, Filtro GNR, http://www.daselsistemas.com/index.php/es/conocimientos/tecnicas-avanzadas/464-filtro-gnr, 2014.
Dominguez, 2010a	N. Dominguez, G. Ithurralde, “Ultra-Fast Ultrasonic Inspection for Aeronautical Composites Using Paintbrush Acquisitions and Data Processing on GPU”, *10th ECNDT*, NDT of transport means, 2010, http://www.ndt.net/article/ecndt2010/reports/1_10_03.pdf
Dominguez, 2010b	N. Dominguez, V. Gibiat, “Non-destructive imaging using the time domain topological energy method”, *Ultrasonics*, **50**, pp. 367-372, 2010.
Dowel, 1971	M. Dowell and P. Jarratt, “Modified regula falsi method for computing the root of an equation”, *BIT*, 11, pp. 168-174, 1971.
Drinkwater, 2006	B. W. Drinkwater, P. D. Wilcox, “Ultrasonic arrays for non-destructive evaluation: A review”, *NDT&E International*, 39, pp. 525-541, 2006.
Drinkwater, 2009	B.W. Drinkwater and A.I. Bowler, “Ultrasonic array inspection of the Clifton Suspension Bridge chain-links”, *Insight*, 51, 9, pp. 491-498, 2009.
Feldkämper, 2000	H. T. Feldkämper, R. Schwann, V. Gierenz, T. G. Noll, "Low power delay calculation for digital beamforming in handheld ultrasound systems", *Proc. IEEE Ultrason. Symp.*, 2, pp. 1763-1766, 2000.
Fink, 1989	M. Fink, C. Prada, F. Wu and D. Cassereau, “Self focusing in inhomogeneous media with “time reversal” acoustic mirrors”, *Proc. IEEE Ultrasonics Symposium*, pp. 681-686, 1989.
Firestone, 1940	F. A. Firestone, “Flaw detecting device and *measuring* instrument”, *US. Pat. 2.280.226*, 27 May 1940.
Ford, 1995	J.A. Ford, “Improved algorithms of Illinois-type for the numerical solution of nonlinear equations”, *Tech. report CSM-257*, Dept. of Computer Science, Essex Univ., Colchester (GB), 1995.
Frazier, 1998	C.H. Frazier, W. D. O'Brien: "Synthetic Aperture Techniques with a virtual source element", *IEEE Trans. on Ultrasonics, Ferroelec. and Freq. Control*, **45**, 1, pp. 196-207, 1998.
Fritsch, 2006	C. Fritsch, M. Parrilla, A. Ibañez, R. Giacchetta, O. Martinez, “The Progressive Focusing Correction Technique for Ultrasound Beamforming”, *IEEE Trans Ultrason., Ferroelectr. Freq. Control,* **53**, 10, pp. 1820-1831, 2006.
Fritsch, 2010	C. Fritsch, J. Camacho, M. Parrilla, ”New ultrasound imaging techniques with phase coherence processing”, *Ultrasonics*, 50, pp. 122-126, 2010.
Fritsch, 2012	C. Fritsch, J. F. Cruza, J. Camacho, J. M. Moreno, J. Brizuela, L. Medina, “Controlador de enfoque dinámico para sistemas de imagen ultrasónica”, *Pat. ES P201230799*, 25 May 2012.

Gehlbach, 1981: S. M. Gehlbach, R. E. Alvarez, “Digital ultrasound imaging techniques using vector sampling and raster line reconstruction”, *Ultrasonic Imaging*, 3, pp. 83-107, 1981.

Ibañez, 2010 A. Ibañez, C. Fritsch, M. Parrilla and J. Villazón, “Monochromatic Transfer Matrix method for acoustic field simulation thorough media boundaries”, *Physics Procedia*, 3, pp. 883-890, 2010.

Gammelmark, 2003 K. L. Gammelmark, J. A. Jensen, “Multielement synthetic transmit aperture imaging using temporal encoding,” *IEEE Trans. Med. Imag.*, vol. 22, pp. 552–563, 2003.

Gooding, 2010 M. J. Gooding, J. Finlay, J. A. Shipley, M. Halliwell, F. A. Duck, “Three-dimensional ultrasound imaging of mammary ducts in lactating women”, *J. Ultrasound Med*., 29, pp. 95-103, 2010.

Griffith, 1974: J. M. Griffit, W. L. Henry, “A Sector Scanner for Real-Time Two-Dimensional Echocardiography”, *Circulation*, 49, pp. 1147-1152, 1974.

Hansen, 2008 Ch. Hansen, N. Hüttebräuker, M. Hollenhorst, A. Schasse, L. Heuser, G. S-Altedorneburg, H. Ermert, “An Automated System for Full Angle Spatial Compounding in Ultrasound Breast Imaging”, *ECIFMBE 2008, IFMBE Proceedings*, 22, pp. 541–545, 2008.

Hasegawa, 2011 H. Hasegawa, H, Kanai, “High-frame-rate echocardiography using diverging transmitbeams and parallel receive beamforming”, *J. Med. Ultrasonics,* DOI 10.1007/s10396-011-0304-0, 2011.

Hergum, 2007 T. Hergum, T. Bjastad and H. Torp, “Parallel Beamforming using Synthetic Transmit Beams”, *IEEE Transactions on Ultrasonics, Ferroelectrics and Frequency Control*, **54**, 2, pp. 271–279, 2007

Holmes, 2005 C. Holmes, B. Drinkwater, P. Wilcox, “Post-processing of the full matrix of ultrasonic transmit–receive array data for non-destructive evaluation,” *NDT & E International*, 38, 8, pp. 701-711, 2005.

Hunter, 2010 A. Hunter, B. Drinkwater and P. Wilcox, “Autofocusing ultrasonic imagery for non-destructive testing and evaluation of specimens with complicated geometries”, *NDT&E International*, 43, pp. 78-85, 2010.

Hunter, 2011 A. Hunter, B. Drinkwater and P. Wilcox, “Least-Squares Estimation of Imaging Parameters for an Ultrasonic Array Using Known Geometric Image Features”, *IEEE Trans. on UFFC*, 58, 2, pp. 414-426, 2011.

Ithurralde, 2006 G. Ithurralde, “Advanced Functions of PAUT (Phased Arrays for Ultrasound Testing) in Aeronautics”, *European Congress in NDT*, ECNDT 2006 - Tu.1.1.3, pp. 1-7, 2006.

Jeon, 1994 K. Jeon, M. H. Bae, S. B. Park, S. D. Kim, "An efficient real time focusing delay calculation in ultrasonic imaging systems", *Ultrasonic Imaging*, 16, pp. 231-248, 1994.

Karaman, 1993 M. Karaman, A. Atalar, H. Köymen, "VLSI circuits for adaptive digital beamforming in ultrasound imaging", *IEEE Trans. Medical Imaging*, 12, 4, pp. 711-720, 1993.

Karaman, 1995 M. Karaman, P. C. Li, M. O’Donnell, “Synthetic Aperture Imaging for Small Scale Systems”, *IEEE Trans Ultrason., Ferroelectr. Freq. Control*, 42, 3, pp. 429-442, 1995.

Kino, 1980 G. S. Kino, D. Corl, S. Bennett, K. Peterson, “Real time synthetic aperture imaging system”, *Proc. IEEE Ultrason. Symp*., pp. 722-731, 1980.

Kino, 1987: G. S. Kino, “Acoustic waves: devices, imaging and analog signal processing”, Prentice Hall Inc., 1987.

Krause, 1969	W. E. Krause, R. E. Soldner, O. H. Kresse, “Ultrasound diagnostic apparatus”, US. Pat. 3.470.868, 7 Oct. 1969.
Krautkrämer, 1990	J. Krautkrämer, H, Krautkrämer, “Ultrasonic Testing of Materials”, *Ed. Springer-Verlag*, 1990.
Laasko, 1996	T. I. Laakso, V. Valimaki, M. Karjalainen, U.K.Laine, “Splitting the Unit Delay”, *IEEE Sig. Proc. Magazine*, pp. 30-58, Jan. 1996.
Lambert, 2012	J. Lambert, A. Pédron, G. Gens, F. Bimbard, L. Lacassagne, E. Iakovleva, “Analysis of multicore CPU and GPU toward parallelization of total focusing method ultrasound reconstruction”, *DASIP 2012 Conf. on Design and Architectures for Signal and Image Processing*, Karlsruhe, Germany, Oct 2012.
Lee, 2005	J.-Y. Lee, H. S. *Kim*, J. H. Song, J. Cho, T. K. Song, “A hardware efficient beamformer for small ultrasound scanners”, *Proc. IEEE Ultrason. Symp.*, 2, pp. 1396-1399, 2005.
Le Jeune, 2015	L. Le Jeune, S. Robert, P. Dumas, A. Membre, C. Prada, “Adaptive ultrasonic imaging with the total focusing method for inspection of complex components immersed in water”, *Rev. Progress QNDE*, 34, AIP Conf. Proc. 1650, 1037, Boise, Idaho, 2015.
Le Jeune, 2016	L. Le Jeune, S. Robert, E. Lopez Villaverde and C. Prada, “Plane wave imaging for ultrasonic non-destructive testing: generalization to multimodal imaging”, *Ultrasonics*, 64, pp. 128-138, 2016.
Levi, 1997	S. Levi, “The history of ultrasound in gynecologie 1950-1980”, *Ultrasound in Med. and Biol.*, 23, 4, pp. 481-552, 1997.
Liang, 2010	J. Liang, Z. Wang, Y. Shi, “Ultrasonic Inspection of Thick Parts with Phased Array Dynamic Focusing, *ECNDT’ 2010*, 1.3.91, 2010.
Lie, 2005	I. Lie and M. E. Tanase, “About the possibility to implement a nonuniform oversampling receive beamformer in a FPGA”, *Proc. IEEE Ultrasonics Symp.*, pp. 1404–1407, 2005.
Lockwood, 1998	G. R. Lockwood, J. R. Talman, S. S. Brunke, “Real-time Ultrasound 3D-Imaging Using Sparse Synthetic Aperture Beamforming”, *IEEE Trans Ultrason., Ferroelectr. Freq. Control*, **45**, 4, pp. 980-988, 1998.
Long, 2007a	R. Long, J. Russell, P. Cawley, “Non-Destructive Inspection of Components with irregular Surfaces using a Conformable Ultrasonic Phased Array”, *6th International Conference on NDE* in Relation to Structural Integrity for Nuclear and Pressurized Components, 2007. Disponible en: http://www.ndt.net/article/jrc-nde2007/papers/20_01-9.pdf
Long, 2007b	R. Long, P. Cawley, “Phased Array Inspection of Irregular Surfaces”, *Review of Quantitative Nondestructive Evaluation*, 26, ed. D. O. Thompson and D. E. Chimenti, pp. 814-821, 2007.
Long, 2009	R. Long, J. Rusell, P. Cawley and N. Habgood, “Ultrasonic phased array inspection of flaws on weld fusion faces using full matrix capture”, *Rev. QNDE*, 28, pp. 848-855, 2009.
Macowski, 1975	A. Macowski, “Ultrasonic array for reflection imaging”, US Pat. 3.918.024, 4 Nov. 1975.
Macowski, 1979	A. Macowski, “Ultrasonic Imaging Using Arrays”, *Proc. IEEE*, 67, pp. 484-495, 1979.
Manes, 1988	G. Manes, P. Tortoli, F. Andreuccetti, G. Avitabile, C. Atzeni, “Synchronous Dynamic Focusing for Ultrasound Imaging”, *IEEE Trans Ultrason., Ferroelectr. Freq. Control*, **35**, 1, pp. 14-21, 1988.
Maslak, 1979	S. H. Maslak, “Acoustic imaging apparatus”, US Pat. 4.140.022, 20 Feb. 1979.
Mast, 2000	T. D. Mast, "Empirical relationships between acoustic parameters in human soft tissues," *Acoustics Research Letters Online*, vol. 1, pp. 37-42, 2000.

Medina, 2015	L. Medina, J. Camacho, C. Fritsch, “A Characterization of Ultrasonic Full Angle Spatial Compounding as a Possible Alternative for Breast Cancer Screening”, *Archives of Acoustics*, 40, 3, pp. 301-310, 2015.
Montaldo, 2009	G. Montaldo, M. Tanter, J. Bercoff, N. Benech, and M. Fink, “Coherent plane-wave compounding for very high frame rate ultrasonography and transient elastography,” *IEEE Trans. Ultrason. Ferroelectr. Freq. Control*, 56, 3, pp. 489–506, 2009.
Moreno, 2012	J. M. Moreno, L. Medina, J. Brizuela, J. F. Cruza y C. Fritsch, “Unidad de Control e Interfaz”, *Jornadas de Computación Reconfigurable y Aplicaciones*, JCRA 2012, Elche, 19-21 Sept. 2012.
M2M, 2016	M2M, http://www.m2m-ndt.com/products/Spec%20Gekko.pdf, “Gekko, Phased-array flaw detector”, 2016.
Newhouse, 1982	V. L. Newhouse, N. M. Bilgutay, J. Saniie, E. S. Furgason, “Flaw-to-grain echo enhancement by split-spectrum processing”, *Ultrasonics*, 20, pp. 59-68, 1982.
Nickalls, 2009	R. W. D. Nickalls, “The quartic equation: Invariants and Euler’s solution revealed”, *Math. Gaz*, **93**, 256, pp. 66-75, 2009, http://www.nickalls.org/dick/papers/maths/quartic2009.pdf
Nikolov, 2005	M. Nikolov, V. Behar, “Analysis and optimization of synthetic aperture ultrasound imaging using the effective aperture approach”, *Int. J. Information Theory & Applications*, 12, pp. 257-265, 2005.
Njiki, 2013	M. Njiki, S. Bouaziz, A. Elouardi, O. Casula, O. Roy, “A Multi-FPGA implementation of real-time reconstruction using total focusing method”, *Proc. 2013 IEEE Int’l Conf. on Cyber Technology in Automation, Control and Intelligent systems* , pp. 468-473, May 26-29, Nanjing, China, 2013.
Parrilla, 2007	M. Parrilla, A. Ibáñez, J. Camacho, C. Fritsch, “Fast focal law computing for Non-Destructive Testing with phased arrays”, *International Congress on Ultrasonics*, paper #1228 Vienna, April 9 - 13, 2007.
Parrilla, 2008	M. Parrilla, J. Brizuela, J. Camacho, A. Ibáñez, P. Nevado, C. Fritsch, “Dynamic focusing through arbitrary geometry interfaces”, *Proc. IEEE Ultrason. Symp.*, pp. 1195-1198, 2008.
Peterson, 1984	D. K. Peterson, G. S. Kino, “Real-Time Digital Image Reconstruction: A Description of Imaging Hardware and an Analysis of Quantization Errors”, *IEEE Trans. Sonics Ultrason.*, 31, 4, pp. 337-351, 1984.
Prada, 1991	C. Prada, F. Wu, M. Fink, “The Iterative Time Reversal Mirror: A solution to self-focusing in pulse-echo mode”, *J. Acoust. S. Am*, 90, 2, pp. 119-1129, 1991.
Prada, 1997	C. Prada, M. Tanter and M. Fink, “Flaw Detection in Solid with the DORT Method”, *Proc. IEEE Ultrasonics Symposium*, pp. 679-683, 1997.
Rapidscan, 2017	Sonatest, 2017, https://sonatest.com/products/specialised-products/rapidscan
Rasmussen, 2012	M. F. Rasmussen, G. Férin, R. Dufait, J. A. Jensen, “Comparison of 3D Synthetic Aperture Imaging and Explososcan using Phantom Measurements”, *Proc. IEEE Ultrason. Symp.*, pp.113-116, 2012.
Robert, 2012a	S. Robert, O. Casula, O. Roy and G. Neau, “Real-time Inspection of Complex Composite Structures with a Self-Adaptive Ultrasonic Technique”, *18th World Conf. on Non Destructive Testing,* Durban (South Africa), 2012.
Robert, 2012b	S. Robert, O. Casula, M. Njiki and O. Roy, “Assessment of real-time techniques for ultrasonic non-destructive testing”, *Rev. Progress in Quantitative Nondestructive Evaluation*, 31, pp. 1960-1967, 2012.
Richard, 2010	D. Richard, D. Reilly, J. Berlanger, G. Maes, “Software Tools for the Design of Phased Array UT Inspection Techniques”, http://www.ndt.net/article/SimNDT2010/papers/9_Richard.pdf, 2010.

Romero, 2009: D. Romero, O. Martínez, C. J. Martín, R. T. Higuti, A. Octavio, “Using GPUS for beamforming acceleration on SAFT imaging”, *Proc. IEEE Ultrason. Symp.*, pp. 1334-1337, 2009.

Rose, 2004 J. L. Rose, “Ultrasonic waves in solid media”, *Cambridge University Press,* 2004.

Rouyer, 2010 J. Rouyer, S. Mensah, P. Lasaygues, J. P. Lefebre, “Ultrasound Tomography dedicated to Anatomical Breast Inspection”, *Proc. IEEE Ultrason. Symp*., pp. 2340-2343, 2010.

Roy, 2000 O. Roy, S. Mahaut and S. Chatillon, “Ultrasonic Inspection of Complex Geometry Component Specimen with a Smart Flexible Contact Phased Array Transducer: Modeling and Applications”, *Proc. IEEE Ultrasonics Symposium*, pp. 763-766, 2000.

Stepinski, 2007 T. Stepinski, “An implementation of synthetic aperture focusing technique in frequency domain”, *IEEE Trans. on Ultrason. Ferroelectr. Freq. Control*, 54, 7, pp. 1399-1408, 2007.

Santamaría, 2015 M.L. Santamaría, A. Morán, F. Cruces, R.Marín, F. Lasagni, C. Pérez, “Inspección automatizada de radios CFRP por ultrasonidos CFRP”, Memorias *13º Congreso Nacional de Ensayos No Destructivos*, pp. 327-333, Sevilla, 6 a 8 de mayo de 2015.

Shattuck, 1984 D. P. Shattuck, M. D. Weinshenker, S. W. Smith, and O. T. von Ramm, “Explososcan: A parallel processing technique for high speed ultrasound imaging with linear phased arrays,” *J. Acoust. Soc. Amer.*, vol. 75, no. 4, pp. 1273–1282, 1984.

Smith, 2003 R. A. Smith, J. M. Bending, L. D. Jones, T.R.C. Harman, D.I.A. Lines, “Rapid ultrasonic scan of ageing aircraft”, *Insight-Non Destructive Testing and Condition Monitoring*, **45**, 3, pp. 174-177, 2003.

Song, 1990 T. K. Song, S. B. Park, “A new phased array system for dynamic focusing and steering with reduced sampling rate”, *Ultrasonic Imaging*, 12, pp. 1-16, 1990.

Steinberg, 1976 B. D. Steinberg, “Principles of Aperture and Array System Design”, *Ed. John Wiley & Sons*, 1976.

Steinberg, 1992 B. D. Steinberg, “Digital Beamforming in Ultrasound”, *IEEE Trans. UFFC*, 39, 6, pp. 716-721, 1992.

Sutcliffe, 2012a M. Sutcliffe, M. Weston, B. Dutton and I. Cooper, “Real-time full matrix capture with auto-focusing of known geometry through dual layered media”, *NDT Conf. of BINDT*, Daventry, UK, 11-13 Sept. 2012.

Sutcliffe, 2012b M. Sutcliffe, M. Weston, P. Charlton, B. Dutton, K. Donne, “Virtual source aperture imaging for non-destructive testing”, *Insight*, 54, 7, pp. 371-379, 2012.

Sutcliffe, 2012c M. Sutcliffe, M Weston, P Charlton, B Dutton, K. Donne, “Virtual source aperture imaging for non-destructive testing”, *Insight*, **54**, 7, pp. 371-379, 2012.

Szabo, 2004 T. L. Szabo, “Diagnostic Ultrasound Imaging: Inside Out*”, Elsevier Academic Press*, Hartford, Connecticut, 2004.

Tanter, 2002 M. Tanter, J. Bercoff, L. Sandrin, M. Fink, “Ultrafast Compound Imaging for 2-D Vector Estimation: Application to Transient Elastography”. *IEEE Trans. on Ultrason. Ferroelectr. Freq. Control*, 49, 10, pp. 1363-1374. 2002.

Tanter, 2014 M. Tanter and M. Fink, “Ultrafast imaging in biomedical ultrasound”, *IEEE Trans. Ultrason. Ferroelectr. Freq. Control*, 61, 1, pp. 102-119, 2014.

Thomenius, 1996 K. E. Thomenius, “Evolution of Ultrasound Beamformers”, *Proc. IEEE Ultrason. Symp.*, pp. 1615-1622, 1996.

Toullelan, 2008 G. Toullelan, A. Nadim, O. Casula, P. Dumas, E. Abittan, L. Doudet, “Inspection of Complex Geometries using Flexible Phased-Array Transducers”, 17th World Conference on Nondestructive Testing, 2008. http://www.ndt.net/article/wcndt2008/papers/391.pdf

Traub, 1982 J. F. Traub, “Iterative methods for the solution of equations”, *Am. Math. Soc.*, Ed. Chelsea Pub. Co., New York, 1982.

Turnbull, 1992 D. H. Turnbull, P. K. Lum, A. T. Kerr, F. S. Foster, “Simulation of B-scan images from two-dimensional transducer arrays: Part I- Methods and quantitative contrast measurements”, *Ultrasonic Imaging*, 14, pp. 323-343, 1992.

Umbach, 2003 D. Umbach, K. N. Jones, “A Few Methods to Fitting Circles to Data”, *IEEE Trans. on Instrum. and Meas.*, **52**, 6, pp. 1881-1885, 2003.

us4us, 2007 http://us4us.eu/products/USPlatform/

Verasonics, 2017 Research Ultrasound System Vantage 64, http://verasonics.com/vantage-64/

von Ramm, 1991 O. T. von Ramm, S. W. Smith, and H. G. Pavy, “High-speed ultrasound volumetric imaging system—Part ii: Parallel processing and image display,” *IEEE Trans. Ultrason., Ferroelect., Freq. Contr.*, **38**, 2, pp. 109–115, 1991.

Weston, 2011 M. Weston, “Advanced Ultrasonic Digital Imaging and Signal Processing for Applications in the Field of Non-Destructive Testing”, *Ph. D. Thesis,* Univ. Manchester (UK), 2011.

Weston, 2012 M. Weston, P. Mudge, C. Davis and A. Peyton, “Time efficient auto-focussing algorithms for ultrasonic inspection of dual-layered media using Full Matrix Capture”, *NDT&E International*, 47, pp. 43-50, 2012.

Wild, 1952 J.J. Wild, J.M. Reid, “Application of Echo-Ranging Techniques to the Determination of Structure of Biological Tissues”, *Science*, 115, pp. 226-230, 1952.

Wygant, 2006 I.O. Wygant, M. Karaman, O. Oralkan, B. Khuri-Yakub, “Beamforming and hardware design for a multichannel front-end integrated circuit for real-time 3D catheter-based ultrasonic imaging”, *Medical Imaging, Proc. Spie,* 6147, 61470A-1, 2006.

Xilinx, 2017a Xilinx, “UltraScale Architecture and Product Data Sheet: Overview”, DS890, Feb. 2017, www.xilinx.com/support/documentation/data_sheets/ds890-ultrascale-overview.pdf

Xilinx, 2017b Xilinx, “Zynq-7000 All Programmable SoC Data Sheet: Overview”, DS190, Jun. 2027, en: www.xilinx.com/support/documentation/data_sheets/ds190-Zynq-7000-Overview.pdf

Zhang, 2010 J. Zhang, B.W. Drinkwater, P. D. Wilcox, A. J. Hunter, “Defect detection using ultrasonic arrays: The multi-mode total focusing method”, *NDT&E International*, **43**, pp. 123-133, 2010.

Apéndice

New Method for Real-Time Dynamic Focusing Through Interfaces

Jorge F. Cruza, Jorge Camacho, Luis Serrano-Iribarnegaray, and Carlos Fritsch, *Senior Member, IEEE*

***Abstract*—In nondestructive evaluation (NDE) a coupling medium (wedge) is frequently inserted between the array probe and the object being evaluated. In this situation, focal law computing is complicated by the refraction effects at the interface. Furthermore, there are not known techniques to perform dynamic focusing by hardware in these conditions.**

This work addresses these problems by following a two-step procedure. First, a virtual array that operates in a single medium with nearly equivalent time-of-flight to the foci is obtained. Then, simple hardware is proposed to perform dynamic focusing in real-time. It operates with arrays of any geometry as required by the virtual array in presence of arbitrarily shaped interfaces. The paper describes the theory and evaluates the timing errors of the approximations made. These errors are low enough to allow use of the new technique in most NDE and some specific medical applications. The new technique is validated by simulation and experimentally.

I. Introduction

Phased-array techniques are being applied to nondestructive evaluation (NDE) in several industrial fields. This technology offers many advantages by providing images generated by electronically scanning the part with an ultrasonic beam. Such images can be obtained with dynamic focusing, increasing sensitivity and resolution at all depths.

In emission, beam steering and focusing are achieved by controlling the delays applied to the excitation pulses. In reception, the same beam-forming principle is valid. For an *N*-element array, a reception focal law is the set of *N* delays applied to the *N* received signals before summation to generate a single focus. Ideally, every output sample should correspond to a focus along the propagation path and, hence, it should have its own set of delays values.

For homogeneous parts inspected by contact in pulse–echo mode, focal laws are obtained as the differences in the two-way time-of-flight from the array center to the focus and back to every array element. They are computed by simple geometrical considerations when the medium has a constant propagation velocity c. For an array element A at $\vec{x}_\mathrm{A}$ and a focus F at $\vec{x}_\mathrm{F}$, the time-of-flight is

$$t_\mathrm{AF} = \frac{|\vec{x}_\mathrm{A} - \vec{x}_\mathrm{F}|}{c}. \tag{1}$$

The focal law for F is the set of differences on t_AF for the N array elements and provides the focusing information for this focus. All the terms are known and, in fact, focal laws for some applications (i.e., medical imaging) can be pre-computed and stored in the beamformer hardware for real-time operation. Furthermore, this focusing information can be coded to reduce memory requirements [1]. The increase of focus depth with range has also been used to further increase the information density [2].

On the other hand, different approaches have been proposed for computing the focal laws in real-time for homogeneous media using specialized hardware. In general, these approaches are based on iteratively computing (1) from a starting point following the midpoint algorithm used in computer graphics [3]. For every channel, such a circuit requires loading 13 initial parameters in registers and is implemented with 5 adders, several multiplexers, and logic to yield a variable sampling clock that matches the arrival instant of echoes to every channel. Although it was complex, it was the first attempt to dynamically compute the focusing information.

A variant of this technique evaluates a fractional delay value (below or equal to the sampling period) that produces the variable delay required for dynamic focusing [4]. In another proposal, changes in the algorithm were introduced to reduce the power consumption of the delay calculator, using fewer hardware resources [5], and dynamic apodization was further included [6]. A different formulation of the midpoint algorithm allowed simplifying the sampling clock generator circuit for oversampled $\Delta\Sigma$ beamformers [7]. A focusing delay calculator circuit with reduced resource requirements was also proposed in [8].

However, in NDE, some wedge or coupling medium is frequently located between the array probe and the inspected object. Also, some medical imaging procedures operate in water immersion [9], [10], where the small differences in the propagation velocity of tissue and water must be taken into account. In these cases, there are two different propagation velocities (c_1 for the coupling medium and c_2 for the inspected object). The time-of-flight from the element to the focus is now

$$t_\mathrm{AF} = \frac{|\vec{x}_\mathrm{A} - \vec{x}_\mathrm{G}|}{c_1} + \frac{|\vec{x}_\mathrm{G} - \vec{x}_\mathrm{F}|}{c_2}, \tag{2}$$

Manuscript received August 10, 2012; accepted January 15, 2013. This work has been founded by the project DPI-2010-17648 of the Spanish National R&D&I Plan 2008-2011.

J. F. Cruza, J. Camacho, and C. Fritsch are with the UMEDIA group, Spanish National Research Council (CSIC), Madrid, Spain (e-mail: carlos.f@csic.es).

L. Serrano-Iribarnegaray is with the Electrical Engineering Department, Polytechnic University of Valencia, Valencia, Spain.

DOI http://dx.doi.org/10.1109/TUFFC.2013.2622

0885–3010/$25.00

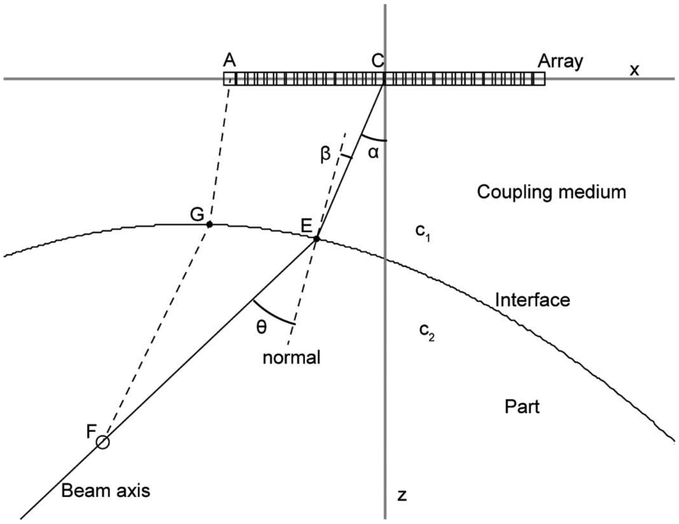

Fig. 1. Schematic of the inspection of an object with a coupling medium.

where $\vec{x}_{\mathrm{G}}$ represents the ray entry point at the interface. Rays are an idealization of the path followed by the volumetric ultrasonic pulse, but are useful for computing the focal laws. Refraction complicates this evaluation because there are no closed formulae to obtain the entry-point coordinates $\vec{x}_{\mathrm{G}}$ accurately enough for arbitrarily shaped interfaces.

This problem is frequently addressed by means of simulation tools. The most general approach solves the wave equation, but this is not a practical process. The Helmholtz model performs a simplification by considering a continuous wave [11], although a fine spatial sampling is required to get enough time resolution, which increases the computing burden [12].

Methods based on the spatial impulse response are widely used [13]. If changes of media are involved, the method can still be applied [14], but the successive convolutions at the interfaces increase the computing time. By contrast, ray-tracing methods [15] predict sound trajectories and allow computing of the focal laws with less computational cost.

In fact, ray-tracing methods are often used for the general case of arbitrarily shaped interfaces and incorporated into the simulation tools of NDE phased-array instruments [16]–[18]. However, computing time can still be an issue for focusing at all samples, so that focal laws are usually obtained only for a small set of foci [19].

From a practical point of view, Fermat's principle is frequently used, searching for the minimum time-of-flight path given by (2). In the most general case, the required fine sampling of the interface leads to long searches. However, for a plane interface and equating to zero the derivative of (2), $\vec{x}_{\mathrm{G}}$ can be exactly obtained by solving a fourth-degree equation, whose exact solution is known [20]. Our group extended this procedure to arbitrary geometry interfaces using a Newton–Raphson approach to provide a fast focal law calculator (FFLC) [21].

In addition to the time involved in this process, another requirement is that the focusing information must be stored in the beamformer. For dynamic focusing at all the samples, this is only practical by coding, as proposed in [1], [2], and [22] because as yet, there are no methods to compute focal laws in real-time for the general case of arbitrarily shaped interfaces.

This paper is a first attempt to address such a problem by following a two-step process. The first step computes a virtual array that operates in a single medium with approximately equivalent time-of-flight from the elements to the foci (Section II). In the second step, a circuit with low resource requirements performs dynamic focusing in real-time; this circuit operates with arbitrarily shaped arrays, as requires the virtual array (Section III). Section IV provides experimental results obtained with the new approach, which has been patented [23]. A short discussion and conclusions follow.

II. A Nearly Equivalent Virtual Array

A. The Conventional Approach

Fig. 1 shows the general arrangement to image certain component of arbitrary shape and propagation velocity c_2 with a phased array. Between the array and the inspected object, there is a coupling medium with propagation velocity c_1. As an example, $c_1 = 1500$ m/s, $c_2 = 6200$ m/s, the interface has a parabolic profile $z = ax^2 + bx + c$ with $a = -0.02$, $b = -0.4644$, and $c = -10.6958$. The array has $N = 32$ elements with an inter-element pitch $d = 0.62$ mm for a total aperture size $D_{\mathrm{A}} = N \cdot d = 19.8$ mm. The distance CE is approximately 10 mm.

An electronically controlled scan is performed. The scan line with an angle $\theta = -30°$ to the interface normal is shown. The coordinate origin is located at the array center C with the x-axis along its length; the z-axis points toward the propagation direction. This work refers to images in the plane $y = 0$.

The interface is defined (usually at discrete points) by the set of vectors $\vec{x} = (x, y)$ and by the normal unit vectors $\vec{n}$. Following the Snell's law, the incident angle β is given by

$$\sin\beta = \frac{c_1}{c_2}\sin\theta. \tag{3}$$

Unit vectors pointing to the array center $\vec{x}_{\mathrm{C}}$ from the interface are $\vec{v} = (\vec{x}_{\mathrm{C}} - \vec{x})/|\vec{x}_{\mathrm{C}} - \vec{x}|$. The coordinates $\vec{x}_{\mathrm{E}}$ of the main ray entry point E correspond to the interface point for which the dot product $\vec{v}_{\mathrm{E}} \cdot \vec{n}$ is closest to $\cos\beta$, that is

$$\min_{x_{\mathrm{E}}, z_{\mathrm{E}}} |\vec{v}(x_{\mathrm{E}}, z_{\mathrm{E}}) \cdot \vec{n}(x_{\mathrm{E}}, z_{\mathrm{E}}) - \cos\beta|. \tag{4}$$

Obviously, interpolation can be used to achieve a better approximation. Once the entry point coordinates $\vec{x}_E = (x_E, z_E)$ are found, the array steering angle α is given by

$$\alpha = \tan^{-1}(x_E/z_E), \tag{5}$$

which allows production of the ultrasound beam in the intended direction. The components of the unit vector in the direction of the main ray toward the part $\vec{u} = (u_x, u_z)$ can be computed from

$$\begin{aligned} \vec{u} \cdot (-\vec{n}) &= \cos\theta \\ |u| &= 1. \end{aligned} \tag{6}$$

The main ray now becomes fully described by the entry point coordinates (x_E, z_E) and the slope $m = u_z/u_x$. Now, foci can be set on the main ray, ideally at the position of every sample at spatial intervals

$$\Delta R = \frac{c_2 T_S}{2}, \tag{7}$$

where T_S is the sampling period, and the 1/2 factor is due to operation in pulse–echo mode. For a focus at F, the focal law is defined by the differences in the time-of-flight from F to every array element. The time-of-flight from element A at $\vec{x}_A$ to focus F at $\vec{x}_F$ is given by (2) (repeated here for convenience)

$$t_{AF} = t_{AG} + t_{GF} = \frac{|\vec{x}_A - \vec{x}_G|}{c_1} + \frac{|\vec{x}_G - \vec{x}_F|}{c_2},$$

where $\vec{x}_G$ represents the entry-point G of the ray from element A to focus F following the refraction law.

To evaluate this expression, $\vec{x}_G = (x_G, z_G)$ must be known. Computing these entry-point coordinates can be performed by searching the point $\vec{x}_G$ at the interface that minimizes (2), i.e., the fastest path. This yields accurate results as long as the interface is finely discretized or interpolation is used. In the latter case, an iterative procedure should be followed until the difference in t_{AF} between interpolated points is smaller than the allowed timing error. The search must be carried out for all the foci and all the elements, which may involve a considerable amount of time.

To speed up the process, it could be applied to a reduced number of primary foci. These can be appropriately chosen on the main ray with increasing intervals. The time-of-flight to samples between these foci could be obtained by interpolation. However, it is not simple to choose the optimum positions and the number of the primary foci for arbitrary interfaces and propagating media. If the interval between foci is too large, high focusing errors may be produced; if the interval is too small, computing time is again an issue. Furthermore, most delta-encoding methods require continuity on the time-of-flight derivative, an aspect that must be considered by the interpolation process. In any case, the computed delay laws, which amount for a considerable data volume, must be transferred and stored in the beamformer hardware.

For all these reasons it is desirable to find methods that allow: 1) speeding up of the focal laws computing process; 2) avoidance of using too much memory in the beamformer hardware; and 3) providing of accurate timing results for good focusing. These objectives are addressed next.

B. Defining a Nearly Equivalent Virtual Array in a Homogeneous Medium

The idea is to obtain a nearly equivalent virtual array that, operating in the second medium only (propagation velocity c_2), avoids all the problems associated with the interface and with refraction. This way, the two-media problem is converted to a single homogeneous medium case, in which the previously proposed methods and circuits for real-time computing the focal laws would be applicable. A solution to the previously considered example is anticipated in Fig. 2.

In such a figure, assuming a large curvature radius at G, the application of the Abbe's invariant (from geometric optics [24]) yields

$$|\vec{x}_{VG}| \approx \frac{c_1}{c_2} |\vec{x}_{AG}|. \tag{8}$$

Strictly speaking, G is different for F_A and F_B. However, assuming that these variations are small, the entry-point is chosen for the farthest focus at F_B. This subject is addressed later. Then, with $t_{AG} = |\vec{x}_{AG}|/c_1$ and $t_{VG} = |\vec{x}_{VG}|/c_2$,

$$t_{VG} \approx \frac{c_1^2}{c_2^2} t_{AG}. \tag{9}$$

Now, considering that the virtual array operates in the second medium with propagation velocity c_2, the time-of-flight from virtual element V to focus F is

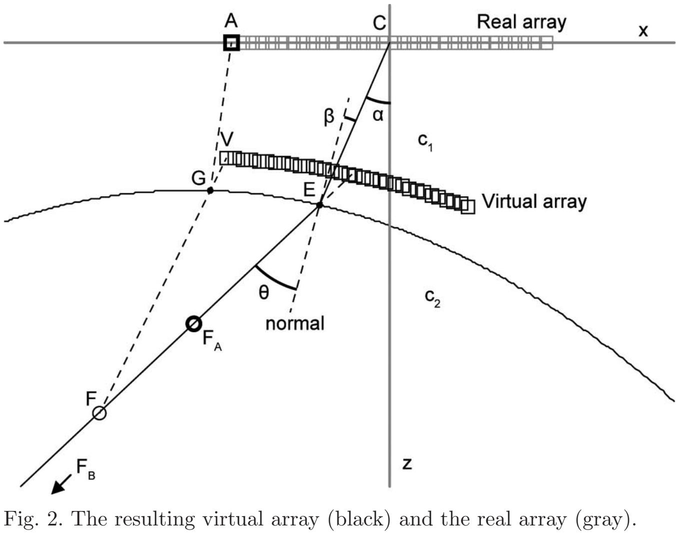

Fig. 2. The resulting virtual array (black) and the real array (gray).

$$t_{\mathrm{VF}} = \frac{|\vec{x}_{\mathrm{V}} - \vec{x}_{\mathrm{F}}|}{c_2} \approx t_{\mathrm{VG}} + t_{\mathrm{GF}}, \tag{10}$$

because $|\vec{x}_{\mathrm{V}} - \vec{x}_{\mathrm{F}}| \approx |\vec{x}_{\mathrm{V}} - \vec{x}_{\mathrm{G}}| + |\vec{x}_{\mathrm{G}} - \vec{x}_{\mathrm{F}}|$. Substitution of (9) and (10) into (2) yields:

$$t_{\mathrm{AF}} \approx t_{\mathrm{VF}} + t_{\mathrm{AG}}\left(1 - \frac{c_1^2}{c_2^2}\right). \tag{11}$$

That is, time-of-flight from a real array element A to a focus F is approximately equal to that from the corresponding virtual array element V to F plus a constant term t_{K}:

$$t_{\mathrm{K}} = t_{\mathrm{AG}}\left(1 - \frac{c_1^2}{c_2^2}\right). \tag{12}$$

The virtual array coordinates $(x_{\mathrm{V}}, z_{\mathrm{V}})$ are found by solving (11) for two foci in the range of interest: $\mathrm{F_A}$ at $(x_{\mathrm{FA}}, z_{\mathrm{FA}})$ and $\mathrm{F_B}$ at $(x_{\mathrm{FB}}, z_{\mathrm{FB}})$. The time-of-flight to these foci t_{AFA} and t_{AFB}, as well as t_{AG} for focus FB, are computed searching for the minimum of (2), in application of Fermat's principle. The equations to solve for $(x_{\mathrm{V}}, z_{\mathrm{V}})$ are:

$$\begin{aligned} \frac{\sqrt{(x_{\mathrm{V}} - x_{\mathrm{FA}})^2 + (z_{\mathrm{V}} - z_{\mathrm{FA}})^2}}{c_2} + t_{\mathrm{K}} &= t_{\mathrm{AFA}} \\ \frac{\sqrt{(x_{\mathrm{V}} - x_{\mathrm{FB}})^2 + (z_{\mathrm{V}} - z_{\mathrm{FB}})^2}}{c_2} + t_{\mathrm{K}} &= t_{\mathrm{AFB}}. \end{aligned} \tag{13}$$

By setting

$$\begin{aligned} k_{\mathrm{A}} &= c_2(t_{\mathrm{AFA}} - t_{\mathrm{K}}) \\ k_{\mathrm{B}} &= c_2(t_{\mathrm{AFB}} - t_{\mathrm{K}}) \\ K &= x_{\mathrm{FA}}^2 - x_{\mathrm{FB}}^2 + z_{\mathrm{FA}}^2 - z_{\mathrm{FB}}^2 - k_{\mathrm{A}}^2 + k_{\mathrm{B}}^2 \\ a &= \frac{K}{2(x_{\mathrm{FA}} - x_{\mathrm{FB}})} \\ b &= \frac{z_{\mathrm{FA}} - z_{\mathrm{FB}}}{x_{\mathrm{FA}} - x_{\mathrm{FB}}} \end{aligned} \tag{14}$$

and

$$\begin{aligned} A &= 1 + b^2 \\ B &= 2bx_{\mathrm{FA}} - 2ab - 2z_{\mathrm{FA}} \\ C &= x_{\mathrm{FA}}^2 + z_{\mathrm{FA}}^2 + a^2 - 2ax_{\mathrm{FA}} - k_{\mathrm{A}}^2, \end{aligned} \tag{15}$$

after some simple mathematical manipulations, the result is

$$\begin{aligned} z_{\mathrm{V}} &= \frac{-B - \sqrt{B^2 - 4AC}}{2A} \quad \text{for elements } i \le \frac{N}{2} \\ z_{\mathrm{V}} &= \frac{-B + \sqrt{B^2 - 4AC}}{2A} \quad \text{for elements } i > \frac{N}{2} \\ x_{\mathrm{V}} &= a - bz_{\mathrm{V}}. \end{aligned} \tag{16}$$

These closed formulae yield the coordinates of the virtual array elements, regardless of the interface shape. To get t_{AFA}, t_{AFB}, and t_{AG}, numerical methods must be applied to just 2 foci. After this fast process, focal laws to all the samples can be easily calculated following (1), replacing $\vec{x}_{\mathrm{A}}$ with $\vec{x}_{\mathrm{V}}$ because the virtual array operates in the second medium with constant propagation velocity c_2.

With the coordinates $\vec{x}_{\mathrm{V}} = (x_{\mathrm{V}}, z_{\mathrm{V}})$ just obtained and the value of t_{K} given by (12), the time-of-flight from element A to focus F is computed as

$$t_{\mathrm{AF}} \approx \frac{|\vec{x}_{\mathrm{V}} - \vec{x}_{\mathrm{F}}|}{c_2} + t_{\mathrm{K}}. \tag{17}$$

This is a significantly faster process than searching for the fastest ray for every focus, so that the first objective is reached. But, more important, known hardware methods that perform the dynamic focusing in real time but operate only in homogeneous media can be used. Section III presents new circuits with low resource requirements and some other advantages to perform this operation.

C. Focusing Errors

A key issue of the proposed technique is to evaluate the errors resulting from the different approximations carried out. There are two main error sources:

1) Errors produced by the consideration of t_{K} being constant when, in reality, the entry-point G and, thus, t_{AG} in (12) change with the focus position.
2) Solutions (16) of (13) are exact for $\mathrm{F_A}$ and $\mathrm{F_B}$, but only approximate at neighboring ranges.

It could be argued that, if the position of the entry-point G is considered constant, the focal laws could have been computed without obtaining the virtual array. In this case, the coordinates of G had to be computed for a single focus by numerical methods. After that, the time-of flight t_{AF} would be obtained from (2) with $\vec{x}_{\mathrm{G}}$ constant, a closed formula that would avoid iterative methods or search processes. However, such technique would produce inaccurate results at regions other than the proximities of the single focus chosen to obtain the entry-point coordinates.

By contrast, when using the virtual array approach, equations are solved for two foci at $\mathrm{F_A}$ and $\mathrm{F_B}$, where the timing errors become zero. In their proximities, small timing errors can be expected. In fact, considering a fixed entry-point for t_{K} is less important in this case, in which its value is included in the equations, due to the added degree of freedom given by the choice of the virtual array elements position.

Fig. 3 shows the timing errors for the example of Fig. 1 when $\mathrm{F_A}$ is set at $D_{\mathrm{A}}/2$ and at D_{A} from the interface; $\mathrm{F_B}$ is set at $4D_{\mathrm{A}}$ in both cases. Dynamic aperture was applied with f-number = 0.74 and errors are considered when the element becomes active. The resulting timing errors span about 8 ns, almost independently of the locations of $\mathrm{F_A}$ and $\mathrm{F_B}$ and the maximum rms error is 1.3 ns. For a 5-MHz

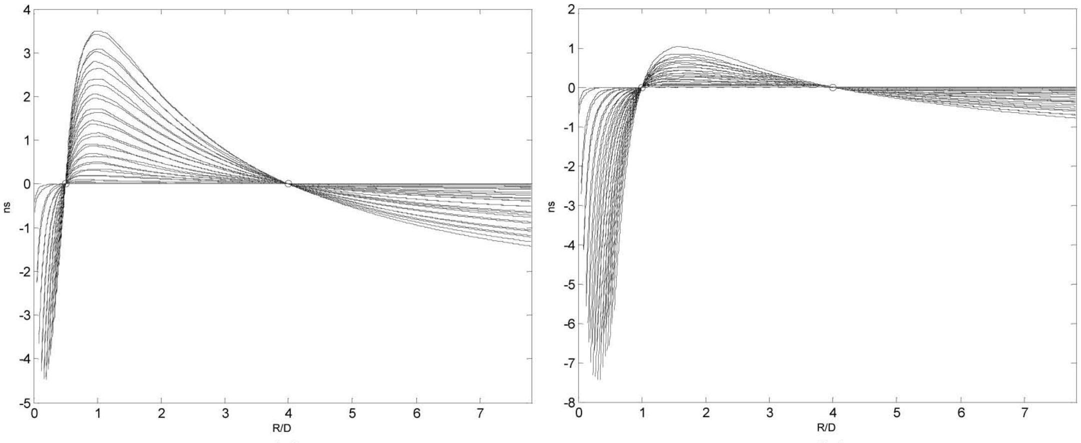

(a) (b)

Fig. 3. Timing errors in nanoseconds with the virtual array approach: (a) focus F_A at $D_A/2$ from the interface; (b) focus F_A at D_A from the interface. In both cases, focus F_B at $4D_A$ from the interface.

array, this represents less than 1/150 the signal period (a phase error of about 2.4°).

The low errors provided by this technique are explained by the automatic adjustment made by the virtual array: three parameters (t_K, x_V, and z_V) adjust the time-of-flight to foci F_A and F_B, whose position can be conveniently chosen to keep small timing errors at other locations. As a rule of thumb, F_A should be chosen near the interface, typically at a relative range $0.5 \leq R_A/D_A \leq 1$, whereas F_B should be located in the proximities of the near-field limit or at the maximum range of interest. The latter can be also used to obtain t_K, as indicated by (13). However, their positions within these ranges are not critical.

In both cases, errors decrease as the elements approach the array center. In fact, the virtual array center is located in the prolongation of the main ray because it is a solution of (14) for any two foci in the main ray. No errors are produced for any hypothetical virtual element at this position because the two-way entry-point will always be at E and t_K will be exact.

Timing errors increase slightly for higher steering angles. Fig. 4(a) shows these errors for $\theta = 45°$ and errors for $\theta = 60°$ are shown in Fig. 4(b). In both cases, the increase in the error is small (2 to 4 ns), and the rms error is practically constant (1.5 and 1.3 ns, respectively).

Although it is difficult to generalize these results for any inspection conditions, the method is robust enough to be considered a good alternative to the iterative and search processes required by conventional techniques. The next paragraph shows a similar good behavior for other geometries and propagation velocities.

D. Some Other Examples

The proposed technique has been tested with many other common configurations for NDE. Fig. 5(a) shows an example with a 15° plastic wedge ($c_1 = 2.4{\cdot}10^3$ m/s) on a plane surface aluminum component ($c_2 = 6.2{\cdot}10^3$ m/s). Focus F_A is set at range $R_A = D_A$, F_B at $R_B = 4D_A$ from the interface and the steering angle is $\theta = 45°$. Real and virtual arrays are shown, as well as the main-ray and element-ray entry-points E and G, respectively.

Fig. 5(b) shows the focusing errors as a function of the relative range R/D, resulting of the time-of-flight evalua-

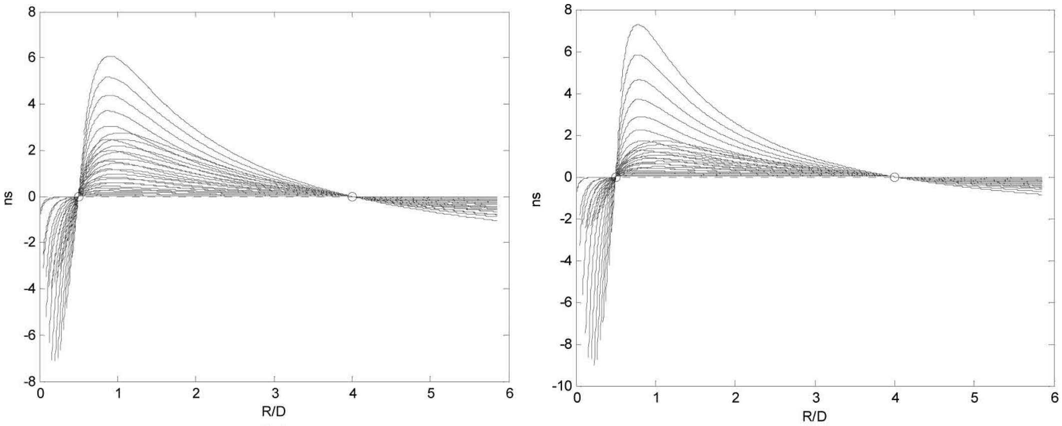

(a) (b)

Fig. 4. Timing errors in nanoseconds as a function of the steering angle: (a) $\theta = 45°$; (b) $\theta = 60°$.

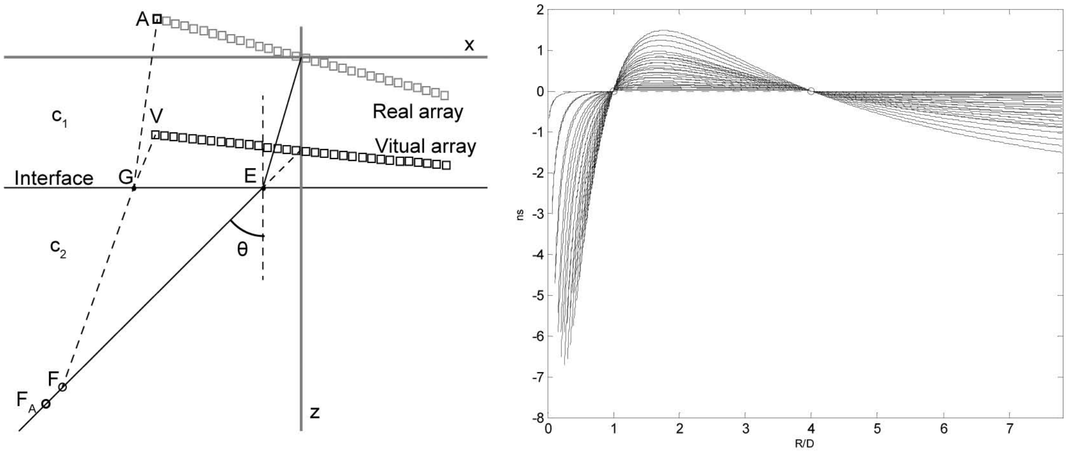

(a) (b)

Fig. 5. (a) Inspection of a planar object with a wedge; (b) timing errors in nanoseconds with the virtual array approach.

tion from the virtual elements. It can be seen that these errors are also very low in this case, less than 9 ns peak-to-peak.

Another example is shown in Fig. 6(a). Here, a cylinder of 30 mm radius of a material with $c_2 = 2.7 \cdot 10^3$ m/s is inspected by immersion using the same array. In spite of the rather awkward position of the real array, the virtual array adapts to the interface shape, which produces very small focusing errors [less than 3 ns peak-to-peak, Fig. 6(b)].

III. Real-Time Focusing Hardware

Because the virtual array operates in a single medium, any of the previously reported circuits for real-time dynamic focusing can be applied with modifications to deal with the virtual array's nonlinear geometry. Here, we describe a new circuit architecture that has several other advantages.

A. Real-Time Estimation of the Round-Trip Time-Of-Flight

To simplify the development of the new procedure, it is useful to set a local coordinates origin at the center of the virtual array. This is carried out by a simple translation:

$$x'_\mathrm{V} = x_\mathrm{V} - x_\mathrm{B}, \quad z'_\mathrm{V} = z_\mathrm{V} - z_\mathrm{B}, \tag{18}$$

where $(x_\mathrm{B}, z_\mathrm{B})$ are the previous coordinates of the virtual array center [Fig. 7(a)].

In these new coordinates, the main ray steering angle is $\phi = \tan^{-1}(u_x/u_z)$, where the components $\vec{u} = (u_x, u_z)$ are given by (6). Considering the emission from the array center, the round trip time-of-flight for a focus F located at range R_F and a virtual array element V at $(x'_\mathrm{V}, z'_\mathrm{V})$ is:

$$t_\mathrm{F} = \frac{R_\mathrm{F} + r_\mathrm{F}}{c_2}, \tag{19}$$

where

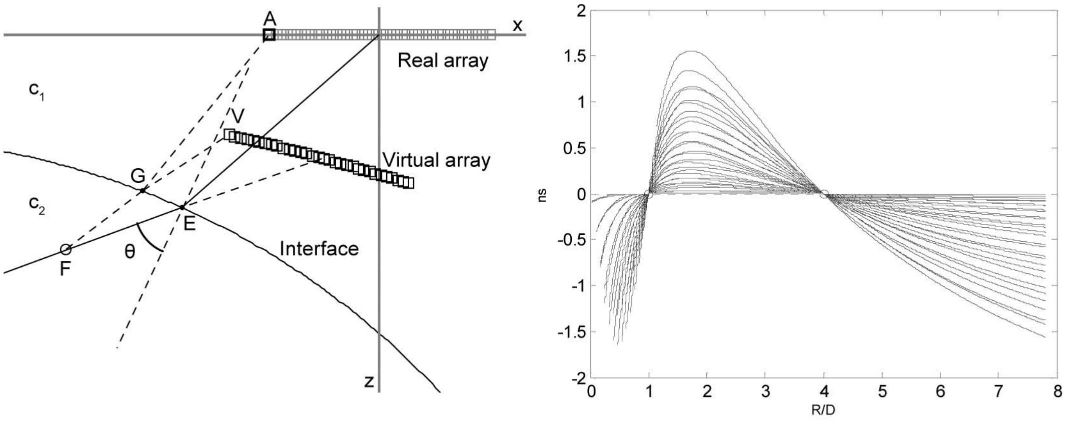

(a) (b)

Fig. 6. (a) Inspection of a cylinder of $c_2 = 2.7 \cdot 10^3$ m/s and radius 30 mm by immersion ($c_1 = 1.5 \cdot 10^3$ m/s); (b) focusing errors in nanoseconds for this arrangement using the virtual array.

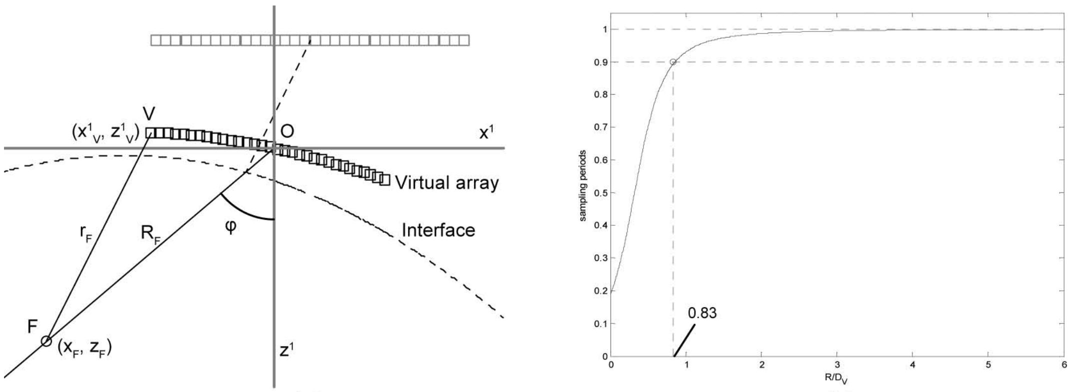

(a) (b)

Fig. 7. (a) Translation of the virtual array center to the new origin at O; (b) differences on round-trip time of flight to consecutive samples for element V in sampling periods and $v = 10$.

$$r_{\mathrm{F}} = \sqrt{R_{\mathrm{F}}^2 + x_{\mathrm{V}}'^2 + z_{\mathrm{V}}'^2 - 2R_{\mathrm{F}}(x_{\mathrm{V}}' \sin\phi + z_{\mathrm{V}}' \cos\phi)}. \qquad (20)$$

For an aperture size D_{V}, it was demonstrated [2] that, from a range R_0 given by

$$R_0 = \frac{v}{4\sqrt{v-1}} D_{\mathrm{V}}, \qquad (21)$$

the differences in the round trip time-of-flight to consecutive foci, $\Delta t_n = t_{n+1} - t_n$, satisfy

$$1 - \frac{1}{v} \le t_{n+1} - t_n < 1, \quad n \ge n_0, \qquad (22)$$

where the minimum range $n_0 = R_0/\Delta R$ and Δt_n are in sampling periods. For example, choosing $v = 10$ results in $0.9 \le \Delta t_n < 1$ from a relative range $n_0/D_{\mathrm{V}} = 0.83$. Fig. 7(b) shows these differences for element V in Fig. 7(a) as a function of relative range R/D_{V}.

On the other hand, the sampling period T_{S} defines the interval between samples ΔR given by (7). Normalizing the distances by ΔR, successive samples at $\{1{\cdot}\Delta R, 2{\cdot}\Delta R, 3{\cdot}\Delta R, \ldots\}$ become represented by the sequence $\{1, 2, 3, \ldots\}$ expressed in sampling periods, and range R_{F} at $n \cdot \Delta R$ becomes n. That is, distances are represented by the two-way time-of-flight in sampling periods as

$$n = R_{\mathrm{F}}/\Delta R, \quad r = r_{\mathrm{F}}/\Delta R, \quad x = x_{\mathrm{A}}/\Delta R, \quad z = z_{\mathrm{A}}/\Delta R. \qquad (23)$$

Then,

$$r_n = \sqrt{n^2 + x^2 + z^2 - 2n(x\sin\phi + z\cos\phi)}. \qquad (24)$$

The two-way time-of-flight (19) becomes

$$t_n = \frac{n + r_n}{2}. \qquad (25)$$

The problem is to estimate a round-trip time-of-flight $\hat{t}_n$ so that the difference with the real value t_n is lower than a fraction $1/v$, where v is any constant greater than 1:

$$|t_n - \hat{t}_n| \le 1/v. \qquad (26)$$

For $v = 10$ and assuming that the sampling rate is, at least, 4 times the fundamental frequency of the array, the timing error would be less than 1/40 the signal period, a figure that will keep the delay quantization lobes at insignificant levels (see [1]). This process could be applied from f-number ≥ 0.83.

To keep the errors within the limits of (26), a binary variable Q_n is evaluated for every sample ($Q_n = \{0, 1\}$) to get the next value $\hat{t}_{n+1}$ equal to the precedent $\hat{t}_n$ incremented by 1 or by $1 - 1/v$ if the current estimation is below or above the real value t_n, respectively:

$$Q_n = (t_n < \hat{t}_n) \qquad (27)$$

$$\hat{t}_{n+1} = \hat{t}_n + 1 - Q_n/v. \qquad (28)$$

The single-bit sequence $\{Q_n\}$ represents a variable sampling clock that acquires the signals at the instant they arrive to the element with a timing error below $1/v$. The idea of using sampling clock generators was previously proposed [25] and used with several beamforming techniques, because it provides automatic sample alignment with FIFOs ([2], [26], [27]). The requirement of a separate sampling clock for every channel was overcome with interpolation techniques that still use the focusing code Q_n to select the delay for sample n [22]. Thus, the binary sequence Q_n can be seen both as a variable sampling clock generator and as a focusing code, depending on the actual implementation. This sequence has all the information required for dynamic focusing with low timing error.

B. Algorithm for Real-Time Focusing Code Generation

Although the application of (28) keeps the absolute error below $1/v$ for all $n \ge n_0$, it requires the knowledge of the value t_n to obtain Q_n, a subject that is addressed here. From (25),

$$t_{n+1} = \frac{n+1+r_{n+1}}{2} \tag{29}$$

$$\Delta t_n = t_{n+1} - t_n = \frac{r_{n+1} - r_n + 1}{2}. \tag{30}$$

Putting this result into (22),

$$r_n + 1 - \frac{2}{v} \le r_{n+1} < r_n + 1. \tag{31}$$

The value Q_n can be also obtained by comparing r_n with its estimate $\hat{r}_n$:

$$Q_n = (r_n < \hat{r}_n). \tag{32}$$

Because r_n and $\hat{r}_n$ are both positive, Q_n can be also obtained by comparing their squares,

$$Q_n = (r_n^2 < \hat{r}_n^2), \tag{33}$$

or by the sign bit of the difference,

$$D_n = r_n^2 - \hat{r}_n^2. \tag{34}$$

Squaring (24) and setting $\alpha = x\sin\phi + z\cos\phi$ and $\beta = x^2 + z^2$,

$$r_n^2 = n^2 - 2n\alpha + \beta \tag{35}$$

$$r_{n+1}^2 = r_n^2 + 2n + H, \tag{36}$$

where $H = 1 - 2\alpha = 1 - 2(x\sin\phi + z\cos\phi)$ is constant for a given element and steering angle. Following the same rationale used for (28) and setting $P_n = 1 - 2Q_n/v$,

$$\hat{r}_{n+1} = \hat{r}_n + P_n. \tag{37}$$

Eqs. (34), (36), and (37) allow construction of a simple circuit that obtains the focusing code Q_n at every sampling clock, as shown in Fig. 8. The circuit uses 3 registers (NS, R2, and RE2), which hold the values n, r_n^2, and $\hat{r}_n^2$, respectively, 4 adders (A1 to A4), one multiplier (M), and a multiplexer.

Register NS is a counter that increments at every clock cycle. Its contents are doubled (no logic required) and added to the constant H. The R2 value r_{n+1}^2 is obtained at the next clock cycle as indicated by (36) by registering the output of adder A4.

The estimated value $\hat{r}_n$ is obtained as indicated by (37) and it is then squared by multiplier M. Subtracting this result from the contents of R2 yields the value D_n, from which the most significant bit (MSB) is extracted as the focusing code Q_n. This code is used to select the current P_n value with the multiplexer.

This circuit is attractive because its simplicity. However, it has an important drawback: the large number of bits required for registers R2 and RE2, for the data path, and for the multiplier output, because several variables are squared. For example, if the largest number n of samples is 16 Ksample, these registers should have 28 bits for the integer part and $2v$ bits for the fractional part (typically, 36 bits); the multiplier output would double this figure (72 bits!). Although some overflow handling logic can be included to reduce these requirements, this would complicate the otherwise elegant design and the mentioned advantages would be lost. Furthermore, the circuit requires presetting 3 variables (NS, R2, and RE2) during initialization.

The algorithm can be further developed to overcome these shortcomings. Squaring (37),

$$\hat{r}_{n+1}^2 = \hat{r}_n^2 + 2P_n\hat{r}_n + P_n^2. \tag{38}$$

Subtracting (38) from (36),

$$r_{n+1}^2 - \hat{r}_{n+1}^2 = (r_n^2 - \hat{r}_n^2) + 2n - 2P_n\hat{r}_n + H - P_n^2. \tag{39}$$

Now, let us set

$$\begin{aligned} B_n &= 2n + H \\ C_n &= P_n(2\hat{r}_n + P_n) \\ D_n &= r_n^2 - \hat{r}_n^2. \end{aligned} \tag{40}$$

The following iterative procedure allows these values to be computed:

$$\begin{aligned} B_{n+1} &= B_n + 2 \\ D_{n+1} &= D_n + B_n - C_n \\ \hat{r}_{n+1} &= \hat{r}_n + P_n. \end{aligned} \tag{41}$$

Finally, taking into account (33) and (34),

$$Q_n = (r_n^2 < \hat{r}_n^2) = (D_n < 0), \tag{42}$$

that is, the binary variable Q_n that adjusts the timing to keep the error below $1/v$ is just the sign of D_n, which can be iteratively computed as indicated by (41) with the help

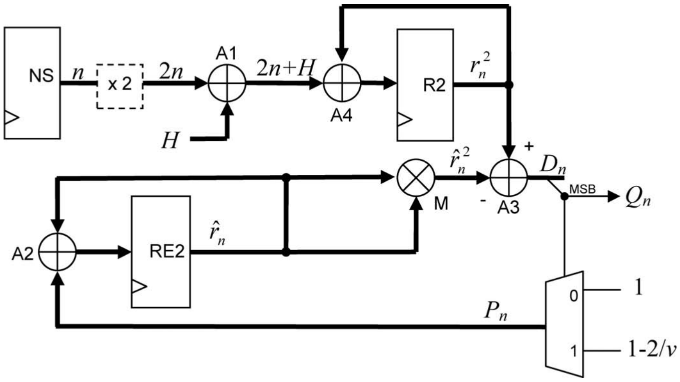

Fig. 8. A simple circuit to compute the focusing codes Q_n in real time.

of two other variables, B_n and C_n, also iteratively computed as indicated by (40).

The algorithm requires initial values and auxiliary variables that are computed off-line:

$$\begin{aligned} n_0 &= [R_0/\Delta R]_{\uparrow} \\ H &= 1 - 2(x \sin\phi + z\cos\phi) \\ \hat{r}_0 &= r_0 = r(n_0) \\ D_0 &= 0 \\ B_0 &= 2n_0 + H, \end{aligned} \qquad (43)$$

where $[\cdot]\uparrow$ represents rounding up. For the sake of completeness, some other important values, already presented, are repeated here:

$$\begin{aligned} Q_n &= (D_n < 0) \\ P_n &= 1 - 2Q_n/v \\ C_n &= P_n(2\hat{r}_n + P_n). \end{aligned} \qquad (44)$$

Note that this algorithm operates with the full aperture from sample number n_0 and greater, with $n_0 = [R_0/\Delta R]\uparrow$. Usually this is enough for most applications, because it allows operation with an f-number as low as unity for $v \leq 15$. For samples below n_0, dynamic aperture must be used and the algorithm should be applied to the active elements only, a mechanism that can be easily implemented in the beamformer.

C. An Efficient Real-Time Focusing Hardware Implementation

The algorithm expressed by (41) and (44) has a quite straightforward implementation. Fig. 9 shows the proposed hardware that includes registers R, B, and D to hold the variables $\hat{r}_n$, B_n, and D_n, respectively, four adders (A1 to A4), one multiplier (M), and a single multiplexer that handles two constants. Basically, it uses the same elements than the previous circuit, but with smaller data widths.

Registers R and B are loaded during initialization with the values r_0 and B_0 indicated in (43), whereas register D is simply cleared. The circuit operates with the sampling clock so that every sample becomes focused.

Register B is implemented as a counter that increments by 2 at every clock cycle, as expressed by (41), $B_{n+1} = B_n + 2$. This is built as a conventional counter for the most significant bits, whereas the least significant bit remains static, as preloaded.

Register R holds the actual estimation $\hat{r}_n$ which is iteratively computed at every sampling clock as $\hat{r}_{n+1} = \hat{r}_n + P_n$. Doubling this value requires no logic, because it is simply obtained by a bit shift-left operation.

The value C_n is obtained by adding P_n to $2\hat{r}_n$ and multiplying the result by P_n. Adder A3 obtains $B_n - C_n$ and adder A4 provides the input to the D register, $B_n - C_n + D_n$, to obtain the value D_{n+1} after the next sampling clock. The sign bit of D is the focusing code Q_n that handles the multiplexer to provide $P_n = 1$ when $Q_n = 0$ and $P_n = 1 - 2/v$ when $Q_n = 1$. These two values are constants and the whole circuit operates with fractional arithmetic.

Other circuits for real-time focusing avoid using multipliers, but this one follows a different approach. Although it would be a simple matter to substitute the multiplier by an adder and a multiplexer if v is a power of 2, the proposed circuit has several advantages over such implementation.

First, no restrictions apply to v, which can be freely chosen as any number greater than unity. Adjusting v to the minimum number that meets the timing constraints (28), allows reduction of R_0, which increases the useable range with full aperture. Second, the registers and data path require fewer bits than the previous version of Fig. 8 because no squares are involved in the computations. Third, current state-of-the-art FPGAs include dedicated DSP cells with multipliers and adders implemented in silicon, which save logic resources and operate at high switching frequencies.

This circuit can be implemented quite efficiently in these cells (for example, DSP-48 of Xilix FPGAs [28]). Such implementation is out of the scope of this paper, but its power efficiency exceeds that of circuits made with general logic resources. Moreover, because of the high switching rate of DSP cells, a single circuit could be shared

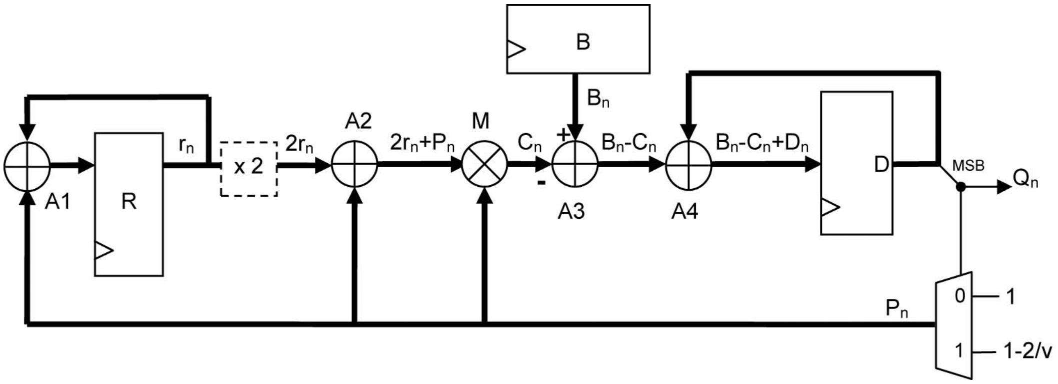

Fig. 9. Proposed circuit for the real-time evaluation of the focusing code Q_n.

among several channels by time multiplexing, further reducing the resource requirements. And, finally, because the circuit architecture is well suited for pipelining, the additional required registers can be also provided by the DSP cells.

IV. Results

Overall errors have two sources: those resulting from the approximations made to build the virtual array, analyzed in Section II, and estimation errors on the round-trip time-of-flight produced by the focusing circuit. From the initial value $\hat{t}_0 = t(n_0)$, the successive estimated values $\hat{t}_n$ are iteratively obtained from the focusing code sequence $\{Q_n\}$ by

$$\hat{t}_{n+1} = \hat{t}_n + Q_n/v. \tag{45}$$

Then, timing errors $\varepsilon = \hat{t}_n - t_n$ are computed using the reference round-trip time-of-flight t_n obtained by application of Fermat's principle with a finely discretized interface. Fig. 10(a) shows the errors produced by the focusing circuit only, with $T_\mathrm{S} = 25$ ns and $v = 4$ for element V in the virtual array of Fig. 2. These errors remain within ± 3.125 ns $= T_\mathrm{S}/2v$ of the actual time, as predicted by theory.

Fig. 10(b) shows the overall errors due to both the virtual array approximations and to the focusing circuit in dark gray. The oscillating nature of the errors due to the focusing circuit is evident and the error due to the virtual array only is overlaid in black. The maximum error is below or equal to the sum of the maximum error of both. In this case, it is bounded between -4 and $+6$ ns, approximately. This low error has little influence in the image quality for arrays with central frequency below 10 MHz.

To experimentally verify these findings, the focusing circuit was implemented in VHDL and incorporated into the SITAU-111 ultrasound system (Dasel S.L., Madrid, Spain) for 128 active channels. Because the current SITAU implementation is based on Spartan-3 devices that lack DSP cells, a single focusing circuit per channel was implemented with distributed logic.

To assess the performance of the focusing circuit, two 60° sector images of the same region of an aluminum part with 1-mm-diameter side-drilled hole (SDH) pairs were acquired. A 5-MHz, 128-element array with 0.6 mm pitch (Imasonic, Besançon, France) was used in contact with the part, and images were produced in real time with an active aperture of 32 elements. Fig. 11(a) shows the image obtained with the progressive focusing correction (PFC) technique [2], (standard SITAU firmware) that codes in a single bit the focusing information with $v = 4$. Fig. 11(b) shows the image obtained with the new technique, where the standard SITAU focusing firmware was replaced by the described focusing circuit, and the same value $v = 4$.

At first sight, it is rather difficult to find any significant difference among both images, but a detail of the very near zone obtained by positioning the array just over the nearest SDHs [Figs. 11(c) and 11(d)] reveals a slight resolution improvement of about 20% when using the proposed method. The reason is that the PFC version implemented in the SITAU system can only focus 1 out of 2 consecutive samples, reducing the number of active elements at small depths because of a larger r_0 value. On the other hand, the proposed method allows focusing at all samples, which guarantees the maximum active aperture at all depths.

Once the real-time focusing circuit was validated, a second experiment was conducted to evaluate the virtual array method's performance. The same part and array were used, but with a methacrylate wedge between them to obtain a planar interface. The wedge angle is $\alpha = 39°$ and a sector scan between $-10°$ and 80° in 0.5° steps with an active aperture of 64 elements was performed.

Figs. 12(a) and 12(b) show a schematic representation of the real array (gray squares) and the virtual array (black squares), for the extreme angles of the scan ($-10°$ and 80°, respectively). It is clearly seen how the virtual ar-

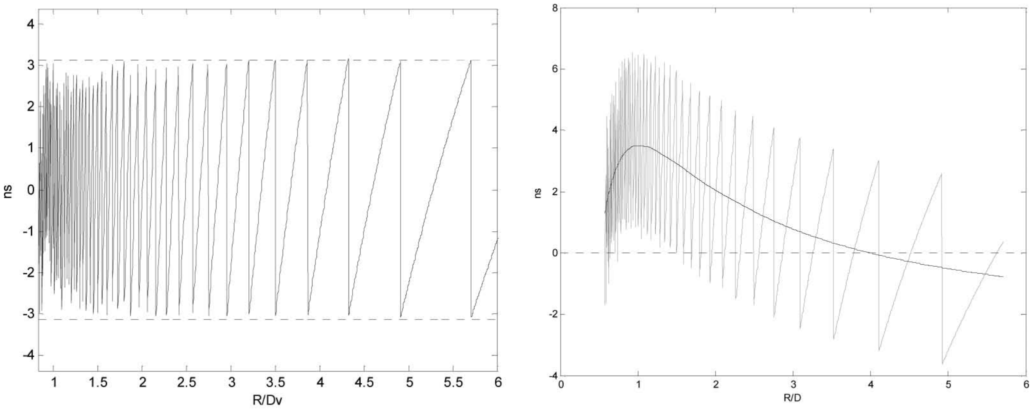

(a) (b)

Fig. 10. (a) Timing errors in nanoseconds due to the focusing circuit only for $v = 4$ and $T_\mathrm{S} = 25$ ns ($T_\mathrm{S}/2v = 3.125$ ns); (b) overall errors (dark gray) taking into account the approximations made by the virtual array and the focusing circuit; in black, the errors due to the virtual array only [errors in Fig. 4(a) for element V].

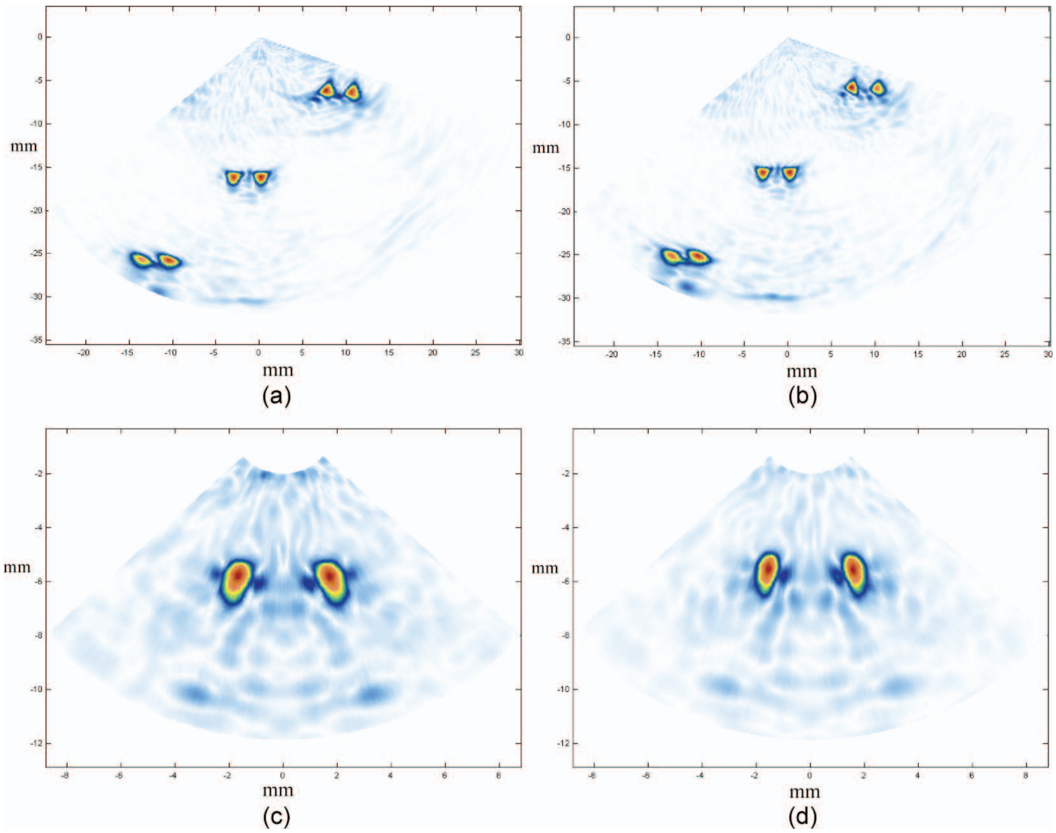

Fig. 11. Images obtained with a 32-element, 5-MHz array over an aluminum block with pairs of 1-mm-diameter side-drilled holes. (a) Using the progressive focusing correction (PFC) technique (b) with the method proposed in this work. Detail of the very near zone using (c) the PFC technique and (d) the method proposed in this work.

ray shape depends heavily on the refracted angle, which is different for each scan line. Fig. 12(c) shows the acquired image, where the three pairs of drills can be detected with the expected resolution, given by the virtual array aperture size and wavelength. Amplitude differences among them are mainly due to the angular sensitivity of the array elements and to the dependence of the transmission coefficient with the incident angle.

A third experiment with a complexly shaped interface was finally conducted. The same array was used to inspect by water immersion a cylindrical part with 100 mm curvature radius and two groups of 4 side-drilled holes of 1 mm diameter [Fig. 13(c)]. A sector scan from $-20°$ to $60°$ was performed with an active aperture of 64 elements, whose extreme scan lines are schematically represented in Figs. 13(a) and 13(b) (real array in gray and virtual array in black). Fig. 13(d) shows the obtained image, where 8 holes are clearly detected at the correct positions and with the expected resolution.

V. Discussion and Conclusions

The proposed method solves the problem of real-time computation of the focal laws when a coupling medium is inserted between the array and the inspected part. It performs strict dynamic focusing at all samples from a minimum range, which is small enough for most applications (lower than the aperture length). For smaller ranges, dynamic aperture techniques should be used.

The new method first computes a nearly equivalent virtual array that operates in the second medium only and then uses a circuit to obtain single-bit focusing codes. These codes can be directly used to acquire the echo signals (behaving as a sampling clock generator) or can be used to select the output of a fractional delay filter bank to set the appropriate delay. The circuit requires presetting only two parameters (registers R and B) per channel; the values of the parameters are evaluated from the virtual array.

This approach offers important advantages over the state-of-the-art:

1) Off-line computing time for the two required parameters is small, because the closed formulae obtained with this work provide fast processing. In particular, it is much faster than computing hundreds to thousands of focal laws.
2) Memory requirements are significantly reduced, because the preset parameters R and B typically amount to 36 to 40 bits together. No more individual focal law coding is required.

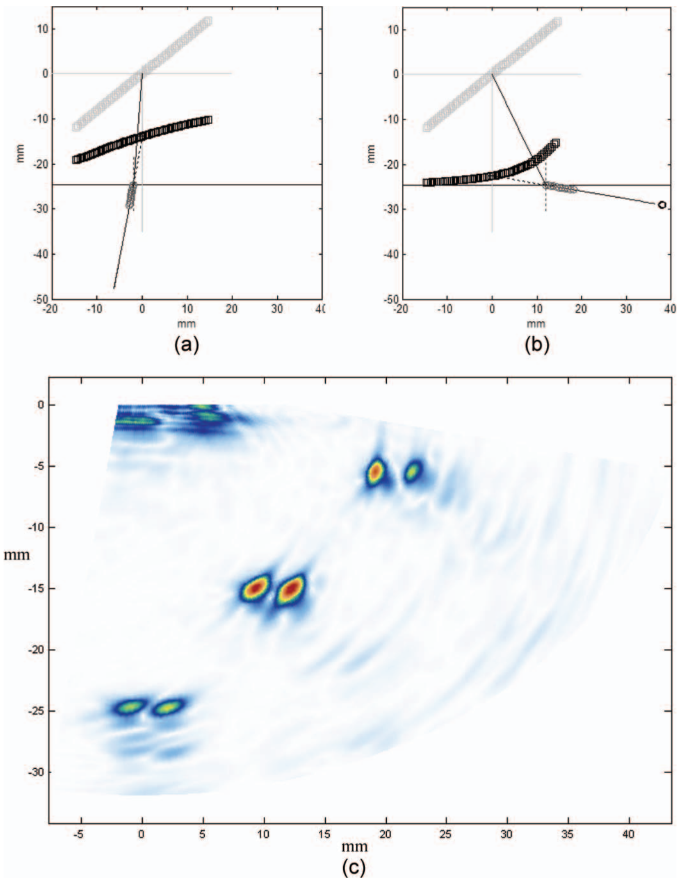

Fig. 12. Schematic representation of the real array (gray) and the virtual array (black) for the extreme angles of the scan (a) −10° and (b) 80°. (c) Image obtained with the real-time focusing circuit operating from the virtual array.

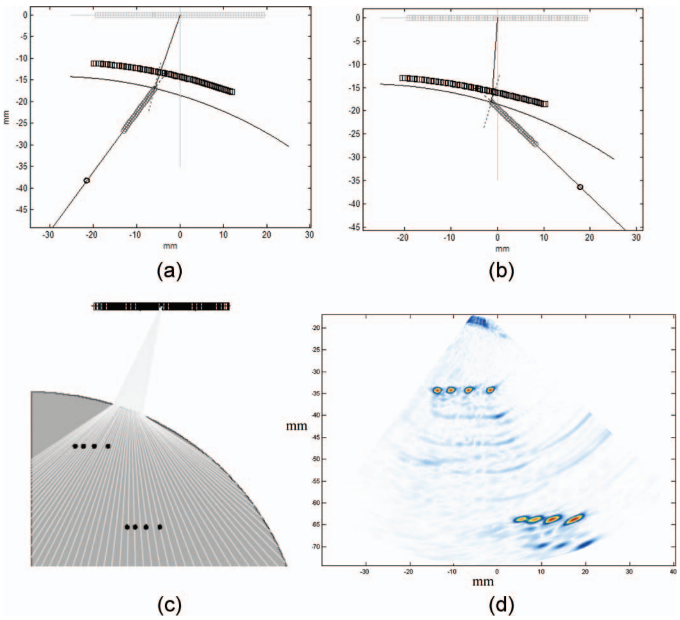

Fig. 13. Schematic representation of the real array (gray) and the virtual array (black) for the extreme angles of the scan (a) −20° and (b) 60°. (c) Schematic representation of the inspected part and scan geometry. (d) Image obtained with the real-time focusing circuit operating from the virtual array.

3) Loading the preset parameters is quite fast (a few microseconds for a 128-channel system), making the focusing circuit ready to perform dynamic focusing.
4) The proposed circuit architecture uses little logic and can take advantage of the availability of DSP cells in FPGAs to improve performance or even share logic among channels by time-multiplexing.
5) The new method operates with arbitrarily shaped interfaces as long as their curvature radius is large, because of the requirements of Abbe's invariant (say larger than 3 apertures). Obviously, the method is also valid for operation with homogeneous media, making the virtual array equal to the real array.
6) Full aperture can be used from the proximities of the virtual array and, hence, from the interface. In homogeneous media, the circuit can operate with numeric apertures (f-number) even below unity with high timing resolution, an improvement over previous works.
7) A possible extension of the proposed method is to provide an auto-focusing function. In this case, the interface is first detected and interpolated-extrapolated. Then, the virtual array is computed and the corresponding parameters are preset. Dynamic focusing will be performed without any other intervention of the operator. This function, which will be fully developed in a future work, seems especially useful for applications with small steering angles in which the distance from the array to the object is unknown or variable.

A shortcoming of the new method is that exact errors are difficult to predict analytically for arbitrarily shaped interfaces. However, it has been tested with many common NDE configurations by simulation. These included plastic wedges and immersion techniques with a water column of 10 to 40 mm, with targets of diverse materials and curvature radii, various propagation velocities in the coupling medium, etc. In all the cases, timing errors have been found to be limited to a few nanoseconds. These small errors are irrelevant for the image quality in most real-life applications.

REFERENCES

[1] D. K. Peterson and G. S. Kino, "Real-time digital image reconstruction: A description of imaging hardware and an analysis of quantization errors," *IEEE Trans. Sonics Ultrason.*, vol. 31, no. 4, pp. 337–351, 1984.

[2] C. Fritsch, M. Parrilla, A. Ibáñez, R. Giacchetta, and O. Martínez, "The progressive focusing correction technique for ultrasound beamforming," *IEEE Trans. Ultrason. Ferroelectr. Freq. Control*, vol. 53, no. 10, pp. 1820–1831, 2006.

[3] K. Jeon, M. H. Bae, S. B. Park, and S. D. Kim, "An efficient real time focusing delay calculation in ultrasonic imaging systems," *Ultrason. Imaging*, vol. 16, no. 4, pp. 231–248, 1994.

[4] M. Bae, "Focusing delay calculation method for real-time digital focusing and apparatus adopting the same," US Patent 5 836 881, Nov. 17, 1998.

[5] H. T. Feldkämper, R. Schwann, V. Gierenz, and T. G. Noll, "Low power delay calculation for digital beamforming in handheld ultrasound systems," in *Proc. IEEE Ultrasonics Symp.*, 2000, pp. 1763–1766.

[6] B. G. Tomov and J. A. Jensen, "Compact implementation of dynamic receive apodization in ultrasound scanners," *Proc. SPIE*, vol. 5373, pp. 260–271, 2004.

[7] I. Lie and M. E. Tanase, "About the possibility to implement a nonuniform oversampling receive beamformer in a FPGA," in *Proc. IEEE Ultrasonics Symp.*, 2005, pp. 1404–1407.

[8] R. Alexandru, "Delay controller for ultrasound receive beamformer," U.S. Patent 7 804 736 B2, Sep. 28, 2010.

[9] R. C. Waag and R. J. Fedewa, "A ring transducer system for medical ultrasound research," *IEEE Trans. Ultrason. Ferroelectr. Freq. Control*, vol. 53, no. 10, pp. 1707–1718, 2006.

[10] N. F. Ruiter, R. Dapp, M. Zapf, and H. Gemmeke, "A new method for grating lobe reduction for 3D synthetic aperture imaging with ultrasound computer tomography," *Proc. IEEE Ultrason. Symp.*, 2010, pp. 2372–2375.

[11] T. Huttunen, M. Malinen, J. P. Kaipio, P. J. White, and K. Hynynen, "A full-wave Helmholz model for continuous-wave ultrasound transmission," *IEEE Trans. Ultrason. Ferroelectr. Freq. Control*, vol. 52, no. 3, pp. 397–409, 2005.

[12] A. Ibañez, M. Parrilla and J. Villazón, "Simulation of ultrasonic continuous wave fields in homogeneous media with soft curved interfaces," in *9th European Conf. on NDT*, 2006, Th.3.3.1.

[13] P. R. Stepanishen, "Transient radiation from pistons in an infinite planar baffle," *J. Acoust. Soc. Am.*, vol. 49, no. 5B, pp. 1629–1638, 1971.

[14] F. Buiochi, O. Martínez, L. G. Ullate, and F. Montero, "A computational method to calculate the longitudinal wave evolution caused by interfaces between isotropic media," *IEEE Trans. Ultrason. Ferroelectr. Freq. Control*, vol. 51, no. 2, pp. 181–192, 2004.

[15] G. A. Deschamps, "Ray techniques in electromagnetics," *Proc. IEEE*, vol. 60, no. 9, pp. 1022–1035, 1972.

[16] L. Le ber, O. Roy, and N. Jazayeri, "Applications of phased array techniques to NDT of industrial structures," in *2nd Int. Conf. on Technical Inspection and NDT*, Tehran, Iran, 2008.

[17] D. Richard, D. Reilly, J. Berlanger, and G. Maes, (2010, Sep.) Software tools for the design of phased array UT inspection techniques. [Online]. Available: http://www.ndt.net/article/SimNDT2010/papers/9_Richard.pdf

[18] P. Calmon, S. Mahaut, S. Chatillon, and O. Roy, "Simulation of phased array techniques for realistic NDE configurations," in *Proc. IEEE Ultrasonic Symposium*, 2002, pp. 723–727.

[19] J. Liang, Z. Wang, Y. Shi, "Ultrasonic Inspection of thick parts with phased array dynamic focusing," in *European Conf. on NDT*, 2010, art. no. 1.3.91.

[20] R. W. D. Nickalls, "The quartic equation: Invariants and Euler's solution revealed," *Math. Gaz.*, vol. 93, no. 256, pp. 66–75, 2009, [Online]. Available: http://www.nickalls.org/dick/papers/maths/quartic2009.pdf

[21] M. Parrilla, J. Brizuela, J. Camacho, A. Ibanez, P. Nevado, and C. Fritsch, "Dynamic focusing through arbitrary geometry interfaces," in *Proc. IEEE Ultrason. Symp.*, 2008, pp. 1195–1198.

[22] J. Camacho, M. Parrilla, A. Ibáñez, and C. Fritsch, "The progressive dynamic focusing correction technique in NDE," in *Proc. IEEE Ultrason. Symp.*, 2007, pp. 1586–1589.

[23] C. Fritsch, J. F. Cruza, J. Camacho, J. M. Moreno, J. Brizuela, and L. Medina, "Controlador de enfoque dinámico para sistemas de imagen ultrasónica," Patent ES P201230799, May 25, 2012.

[24] M. Born and E. Wolf, *Principles of Optics*. Cambridge, UK: Cambridge University Press, 1997.

[25] J. H. Kim, T. K. Song, and S. B. Park, "Pipelined sampled-delay focusing in ultrasound imaging systems," *Ultrason. Imaging*, vol. 9, pp. 75–91, 1987.

[26] M. O'Donnell, M. G. Magrane, "Method and apparatus for fully digital beam formation in a phased array coherent imaging system," U.S. Patent 4 809 184, Feb. 28, 1989.

[27] T. K. Song and J. F. Greenleaf, "Ultrasonic dynamic focusing using an analog FIFO and asynchronous sampling," *IEEE Trans. Ultrason. Ferroelectr. Freq. Control*, vol. 41, no. 3, pp. 326–332, 1994.

[28] Xilinx Inc., "Xtreme DSP DSP-48A for Spartan 3A DSP FPGAs," User Guide, ug-431, 2008, [Online]. available: http://www.xilinx.com/support/documentation/user_guides/ug431.pdf

Jorge F. Cruza was born in Madrid, Spain, in 1983. He obtained the B.S. degree in telecommunication engineering in 2009 and the M.S. degree in electronics in 2011, both from the Universidad de Alcalá (UAH). He is currently Ph.D. student at UAH. Since 2010, he has been an Associate Researcher at the Acoustic and Non-Destructive Testing Center (CAENDCSIC). His research interests include high-resolution acoustic imaging, real-time beamforming, and FPGA signal processing.

Jorge Camacho was born in Montevideo, Uruguay, in 1979. He received the B.S degree in electronic engineering from the Universidad de la República, Uruguay (UdeLaR) in 2004. He received the Ph.D. degree in systems and automation engineering from the Universidad Complutense de Madrid (UCM) in 2010. Since 2005, he has been an associate researcher at the Spanish National Research Council (CSIC). His research interests include high-resolution acoustic imaging, real-time beamforming, and new imaging methods for medical and NDT applications.

Luis Serrano-Iribarnegaray was born in 1949 in Bilbao, Spain. He received the electrical and doctoral engineering degrees from the universities of Bilbao (in 1971) and Madrid (in 1978), Spain, repectively. Since 1982, he has held the chair for theory and control of electrical machines at the Universidad Politécnica de Valencia/Spain and has been the scientist responsible in Spain for various international projects on electronic control of electrical machines, supported by the European Union.

Carlos Fritsch was born in Madrid, Spain, in 1948. He obtained the M.S. degree in telecommunication engineering and the Ph.D. degree in informatics from the Universidad Politécnica de Madrid, in 1971 and 1988, respectively. Since 1972, he has been a member of the scientific staff at the Spanish National Research Council (CSIC). In the last 22 years, he has headed several research projects in the field of ultrasound technology. His research interests include digital signal processing applied to the field of ultrasound, beamforming and processing architectures, ultrasound imaging, fast focal law computing algorithms, and new methods for NDT and medical applications.

10.1109/ULTSYM.2012.0367

Automatic dynamic focusing through interfaces

J. F. Cruza, J. Camacho, J. M. Moreno, C. Fritsch

Ultrasound for Medical and Industrial Applications Group (UMEDIA)
Spanish National Research Council (CSIC)
La Poveda (Arganda del Rey), 28500 Madrid, Spain

Abstract – **An interface between the coupling medium and the inspected part is frequently found in Non Destructive Testing (NDT). When phased array technology is used, the focal laws must be obtained considering the refraction at the interface, which requires computationally intensive iterative procedures since no closed formulae exist for the general case.**

This work presents a new two-step approach. In the first step, the two propagation media scenario is converted into a single homogeneous medium by computing a *virtual array* with nearly equivalent flight times to the foci. In the second step, a *focusing hardware*, conveniently initialized, evaluates in real-time the sampling instants that correspond to the focal laws.

Focusing errors are small enough to validate the new technique for a wide range of applications. In fact, for active apertures currently used in NDT, the resolution and dynamic range are almost not affected as it is experimentally shown. Furthermore, focal law computing time is dramatically reduced by evaluating a few parameters instead of focusing delays for every output sample, element and steering direction. The instrument focal law storage requirements become significantly reduced as well.

Keywords – *Phased array*, *dynamic focusing, interfaces, NDT.*

I. INTRODUCTION

The phased array technique finds many applications in Non Destructive Testing (NDT) due to its capabilities of electronic beam steering and focusing. Dynamic focusing is being progressively included in the NDT phased array instruments due to its superior image quality.

However, dynamic focusing requires a large number of focal laws, ideally one for every output sample in the beamformed image. This demands a large amount of memory in the phased array instrument, although it can be reduced by coding [1-2]. Furthermore, in many NDT applications, there is a coupling medium (a wedge, water, etc.) between the array transducer and the inspected part, whose shape can be arbitrary.

Obtaining the focal laws for the most general case (coupling medium, geometry, etc.) is a computationally intensive process that must take into account refraction at the interface. There are not closed formulae and simulation tools or numerical iterative procedures must be used [3-5]. This usually involves a large computing time to get the focal laws for all the samples and steering angles.

This work presents a new two-step approach. In the first one, the two propagation media scenario (coupling and inspected part) is converted into a single homogeneous medium. To this purpose, a *virtual array* that operates in the second medium only is obtained. Flight times to the foci are nearly equivalent. In the second step, a *focusing hardware*, conveniently initialized, evaluates in real-time the dynamic focusing sampling instants from the virtual array. Although any of the known circuits that operate in homogeneous media for dynamic focusing could be used (for instance, [6-9]), the proposed hardware has some features that are interesting for its implementation in state-of-the-art FPGAs.

This methodology provides several advantages: a) It avoids the cumbersome process of computing focal laws through arbitrary geometry interfaces taking into account the refraction laws; b) Memory requirements in the phased array instrument are significantly reduced; c) Strict dynamic focusing (at all the output samples) is achieved in real-time; d) Parameter computing and uploading to hardware is very fast; e) the focusing hardware is simple enough to be efficiently integrated within the beamformer.

II. THE VIRTUAL ARRAY

The idea is to obtain a virtual array that, operating in the second medium only, avoids the problems associated with the refraction at the interface and provides approximately equal flight times to the foci. Fig. 1 shows the general arrangement, with an arbitrarily shaped interface between two media with sound velocities c_1 and c_2, respectively. In this figure, the resulting virtual array is also shown. Foci are located in *main rays* forming an angle θ with the normal to the interface. The incident ray has an angle β that results from the Snell's law. From these data, the steering angle α and the emission focal law can be computed.

The time-of-flight from focus F to array element A is:

$$t_F = r_{AG} / c_1 + r_{GF} / c_2 \tag{1}$$

where the difficulty is on computing the coordinates of the entry-point G. But, if the curvature radius of the interface is large enough, the application of the Abbe's invariant of geometric optics yields:

$$r_{VG} \approx r_{AG} c_1 / c_2 \tag{2}$$

With $t_{AG} = r_{AG}/c_1$ and $t_{VG} = r_{VG}/c_2$,

$$t_{VG} = (c_1^2 / c_2^2) t_{AG} \tag{3}$$

Considering that the virtual array operates in the second medium with propagation velocity c_2, $t_{VF} \approx t_{VG} + t_{GF}$. Then,

$$t_{AF} \approx t_{VF} + t_{AG}(1 - c_1^2 / c_2^2) \tag{4}$$

Thus, the time-of-flight from array element A to focus F is approximately equal to that from the corresponding virtual array element V to F plus a constant term t_K:

$$t_K = t_{AG}(1 - c_1^2 / c_2^2) \tag{5}$$

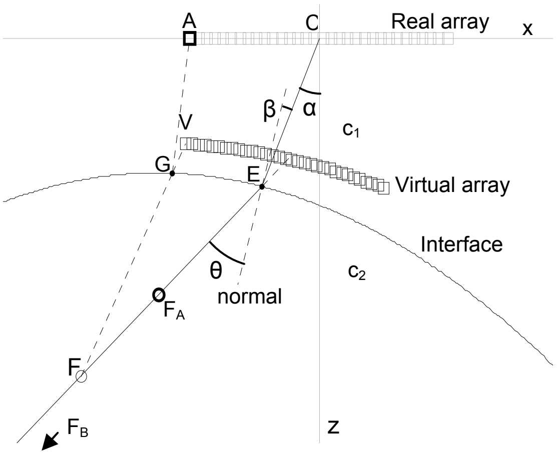

Fig. 1. Geometry. Representation of the real and virtual arrays, the latter operating in the second medium only of propagation velocity c$_2$.

The virtual array coordinates are found by solving (4) for two foci, F$_A$ and F$_B$, conveniently located in the main ray near and far from the interface, respectively. The flight times to these foci are computed searching for the minimum of (1) in application of the Fermat's principle.

III. FOCUSING HARDWARE

Setting the coordinates origin at the virtual array centre (Fig. 2), the distance r_F from virtual element at (x_V, z_V) to a focus located at (R_F, θ) is:

$$r_F = \sqrt{R_F^2 + x_V^2 + z_V^2 - 2R_F(x_V \sin\varphi + z_V \cos\varphi)} \qquad (6)$$

The sampling period T_S defines the interval ΔR between samples, $\Delta R = c_2 T_S/2$. Normalizing all the distances by ΔR, we get $n = R_F/\Delta R$=integer, $x = x_V/\Delta R$, $z = z_V/\Delta R$ and $r_n = r_F/\Delta R$:

$$r_n = \sqrt{n^2 + x^2 + z^2 - 2n(x\sin\varphi + z\cos\varphi)} \qquad (7)$$

Squaring this equation with $\alpha = x\sin\varphi + z\cos\varphi$, $\beta = x^2 + z^2$:

$$r_n^2 = n^2 - 2n\alpha + \beta \qquad (8)$$

$$r_{n+1}^2 = r_n^2 + 2n + H \qquad (9)$$

where $H = 1 - 2\alpha$ is constant for an element and steering angle.

It has been shown [2] that, for an aperture size D_V and from a minimum range R_0, the differences in the round-trip time-of-fligth to consecutive foci, $\Delta t_n = t_{n+1} - t_n$ verify:

$$1 - 1/v \le t_{n+1} - t_n < 1, \quad n \ge n_0 \qquad (10)$$

where v is a constant greater than unity, $n_0 = R_0/\Delta R$ and,

$$R_0 = vD_V/(4\sqrt{v-1}). \qquad (11)$$

For example, choosing v=10 results in $0.9 \le \Delta t_n < 1$ from a relative range R_0/D_V =0.83. The hardware must find an estimate $\hat{t}_n$ of t_n such as $|t_n - \hat{t}_n| < 1/v$, that is, a fraction of a sampling period, where:

$$t_n = (n + r_n)/2 \qquad (12)$$

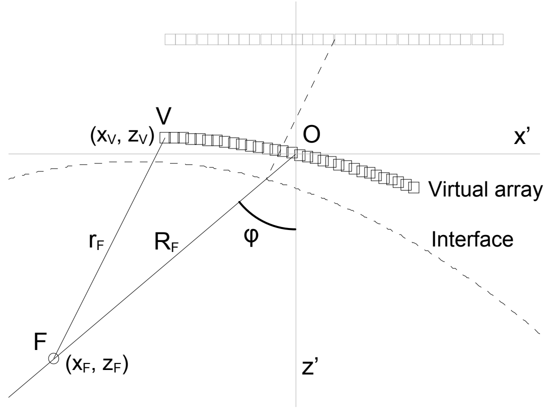

Fig. 2.- Traslation of the coordinates origin to the virtual array centre.

Substitution in (10) yields,

$$r_n + 1 - \frac{2}{v} \le r_{n+1} < r_n + 1 \qquad (13)$$

A binary variable Q_n is evaluated for every sample, $Q_n = (r_n < \hat{r}_n)$. The next estimation of r_n to keep the errors within the bounds of (10) and (13) becomes:

$$\hat{r}_{n+1} = \hat{r}_n + 1 - 2Q_n/v = \hat{r}_n + P_n \qquad (14)$$

$$\hat{r}_{n+1}^2 = \hat{r}_n^2 + 2P_n\hat{r}_n + P_n^2 \qquad (15)$$

Subtracting this equation from (9),

$$r_{n+1}^2 - \hat{r}_{n+1}^2 = (r_n^2 - \hat{r}_n^2) + 2n - 2P_n\hat{r}_n + H - P_n^2 \qquad (16)$$

Now, let us call:

$$\begin{aligned} B_n &= 2n + H \\ C_n &= P_n(2\hat{r}_n + P_n) \\ D_n &= r_n^2 - \hat{r}_n^2 \end{aligned} \qquad (17)$$

that can be iteratively computed as:

$$\begin{aligned} B_{n+1} &= B_n + 2 \\ D_{n+1} &= D_n + B_n - C_n \\ \hat{r}_{n+1} &= \hat{r}_n + P_n \end{aligned} \qquad (18)$$

Since both r_n and $\hat{r}_n$ are positive magnitudes, the binary variable Q_n can be also computed from:

$$Q_n = (r_n^2 < \hat{r}_n^2) = (D_n < 0) \qquad (19)$$

The binary variable Q_n tracks the focusing time at every sample by advancing by $1-1/v$ the sampling instant if Q_n=1 or leaving a sampling period to the next sample if Q_n=0, keeping the timing error within $\pm T_S/v$. Q_n is just the sign of D_n, whose value can be iteratively obtained from (18).

Initial values for the variables involved are set for $n = n_0$, obtained from (11) and from the definition of α, β and H. The initial value D_0 can be =0, so that only 2 parameters have to be preset for every element and steering angle.

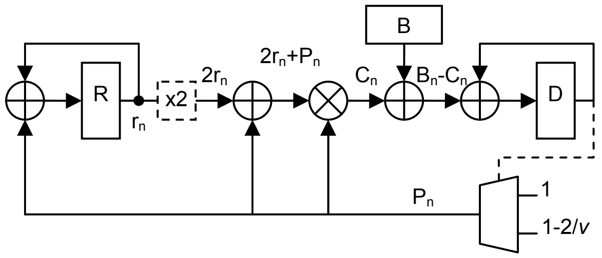

Fig. 3. Focusing hardware. Register R holds $\hat{r}_n$, counter B holds B_n and register D holds D_n. The multiplexer is controlled by the sign of D.

The circuit shown in Fig. 3 implements the algorithm described above. It has 3 registers for $\hat{r}_n$, B_n and D_n, 4 adders and a multiplier. A multiplexer provides P_n=1 or P_n=1-1/2v as required by the sign of D_n, which is the focusing code Q_n.

Not shown is a bank of fractional delay filters that produces samples at intervals 1/v the sampling period. This filter bank is controlled by Q_n, as performed in [10] to keep track of the dynamic focusing.

Note that the operation "x2" requires no logic. Although the multiplier could be easily substituted by a multiplexer and an adder if v is power of 2, it provides two advantages: first, no restrictions apply to the chosen value of v and, second, state-of-the art FPGAs include DSP cells. The architecture shown adapts well to these cells, thus avoiding the use of distributed logic, which results in lower power consumption and the possibility of sharing a single focusing circuit among several channels.

IV. PERFORMANCE

The main source of timing errors is the approximation of t_K given by (5) being constant. In fact, the entry-point G varies with the focus position, so that t_{AG} is not constant. Since the virtual element V is in the prolongation of the segment FG, its position should be modified for every focus. However, in most configurations, these variations are small enough to produce no significant errors.

Another source of error is that (4) is solved for two foci, F_A and F_B, where timing errors are zero. In their proximities it is expected that these errors are low. Setting F_A and F_B near the origin and end of the acquisition range, respectively, is a good trade off.

On the other hand, the focusing hardware has a timing error within $\pm T_S/v$ following from the algorithm derivation.

It is not easy to obtain the bounds of the timing error for the general case of arbitrarily shaped interfaces, steering angles, distance from the array, sound velocity, etc. There are too many variables involved and simulation seems the best tool to evaluate the proposed technique.

To this purpose, the reference time of flight is computed from every sample to real array elements following the Fermat's principle (fastest path), with a finely discretized interface. Then, flight times to the corresponding virtual array elements operating in the second medium only are computed. The differences are considered timing errors.

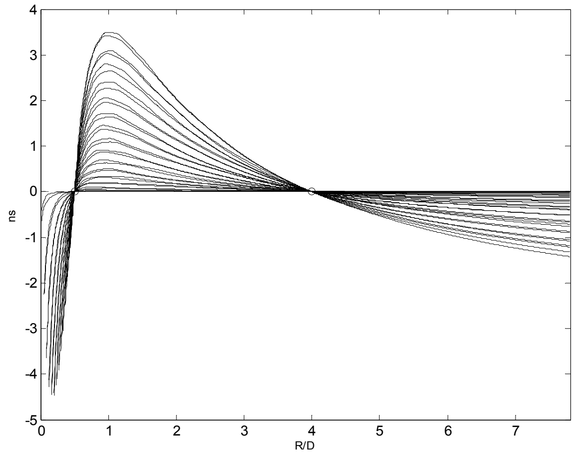

Fig. 4. Timing errors in ns with F_A at 0.5D and F_B at 4D from the interface and c_1 = 1.5 mm/μs, c_2 = 6.2 mm/μs

Fig. 4 shows the timing errors in ns for the configuration shown in Fig. 1, with c_1 = 1.5 mm/μs and c_2 = 6.2 mm/μs. The foci F_A and F_B are located at ranges 0.5D and 4D from the interface, respectively. Timing errors are null at F_A and F_B, as it was expected. In the lower ranges, errors are computed for the active elements only, by application of the active aperture given by (11).

It is seen that the maximum error up to, at least, a range of 8D is bounded within ±4 ns. This is a good figure for common situations. For a 5 MHz array, the maximum error is within 1/50 the fundamental period. In this case, with a sampling frequency of 40 MHz and v=4, the focusing circuit error will be bounded within ±6.25 ns, a similar figure. Both errors are independent and the maximum overall error will be about 10 ns, 1/20 the fundamental period.

The effect of the position of F_A is shown in Fig. 5. In this case, F_A is located at range D instead of 0.5D, while the remaining parameters are kept. Errors in the region closer to the interface increase slightly (up to nearly 8 ns) and are lower from F_A and ahead.

This has been repeated for many other configurations, including different shaped interfaces, distances, propagation velocities, steering angles, etc. In all the cases, the maximum errors were in the range of a few ns, being the example shown representative of the simulations carried out.

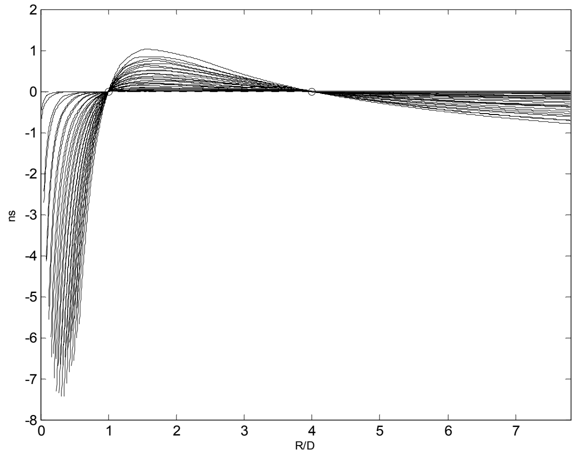

Fig. 5. Timing errors in ns with F_A at 0.5D and F_B at 4D from the interface and c_1 = 1.5 mm/μs, c_2 = 6.2 mm/μs

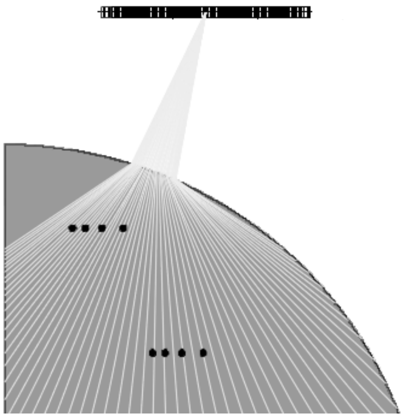

Fig. 6. Schematic for the inspection by immersion of an aluminum cylindrical part with several side-drilled holes

The focusing hardware was implemented in VHDL and integrated on a phased array instrument (SITAU-111, Dasel Sistemas, Spain). A 5MHz, 128-element array with 0.6 mm pitch (Imasonic, Besançon, France) was used to inspect by immersion an aluminum cylindrical part with a curvature radius of 100 mm. A sector scan from -20º to 60º was performed with an active aperture of 64 elements in an arrangement shown in Figure 6.

Figure 7 shows the obtained image, where 8 holes are clearly seen with their correct positions and resolution.

V. CONCLUSIONS

A new technique that provides automatic dynamic focusing in presence of interfaces has been proposed. This technique reduces the two media propagation problem to a single one with homogeneous medium in which a virtual array provides nearly equivalent flight times to the foci.

Once the problem is converted to the homogeneous case, any of the real-time focusing circuits previously described in the literature could be applied to perform a strict dynamic focusing at all the acquired samples.

However this work presents a new circuit that has some advantages. Among them, the timing resolution can be arbitrarily set and the circuit can be implemented using the DSP cells available in state-of-the-art FPGAs. The latter provides reduced power consumption. Also, a single focusing circuit can be shared among several channels by time-multiplexing, further reducing the required hardware resources.

Timing errors have been evaluated by comparing the reference time-of-flight from the foci to real array elements with those obtained with the virtual array. This process has been carried out by simulation for many different configurations (steering angles, propagation velocities, interface shape, etc.). In all cases, the errors found are within a few ns or tens of ns, which are good enough to produce high quality images and validate the approach.

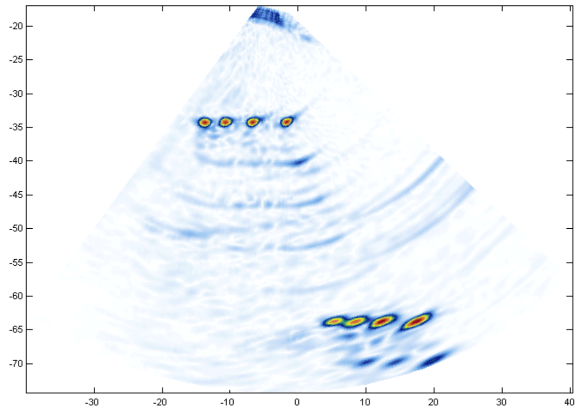

Fig. 7. Image of the SDH in the aluminum cylindrical part obtained with the virtual array concept and the proposed focusing circuit.

ACKNOWLEDGEMENTS

This work has been supported by Project DPI2010-17648 of the Spanish Ministry of Science and Innovation.

REFERENCES

[1] D. K. Peterson, G. S. Kino, “Real-Time Digital Image Reconstruction: A Description of Imaging Hardware and an Analysis of Quantization Errors”, *IEEE Trans. Sonics Ultrason.*, 31, 4, pp. 337-351, 1984.

[2] C. Fritsch, M. Parrilla, A. Ibáñez, R. Giacchetta, O. Martínez, “The Progressive Focusing Correction Technique for Ultrasound Beamforming”, *IEEE Trans. UFFC*, 53, 10, pp. 1820-1831, 2006.

[3] L. Le ber, O. Roy, N. Jazayeri, “Applications of Phased Array Techniques to NDT of Industrial Structures”, *2nd. Int’l Conf. on Technical Inspection and NDT* (TINDT’2008), Tehran, 2008.

[4] D. Richard, D. Reilly, J. Berlanger, G. Maes, “Software Tools for the Design of Phased Array UT Inspection Techniques”, *SimNDT2010*, http://www.ndt.net/article/SimNDT2010/papers/9_Richard.pdf

[5] C. Poidevin, O. Roy, S. Chatillon, G. Cattiaux, "Simulation tools for ultrasonic testing", *Proc. of the 3rd Int. Conf on NDE in relation to Structural Integrity for Nuclear and Pressurized Component*, Sevilla, 2001.

[6] K. Jeon, M. H. Bae, S. B. Park, S. D. Kim, "An efficient real time focusing delay calculation in ultrasonic imaging systems", *Ultrasonic Imaging*, 16, pp. 231-248, 1994.

[7] M. Bae, “Focusing delay calculation method for real-time digital focusing and apparatus adopting the same”, US Pat. 5836881, 17 Nov. 1998.

[8] H. T. Feldkämper, R. Schwann, V. Gierenz, T. G. Noll, "Low power delay calculation for digital beamforming in handheld ultrasound systems", *Proc. IEEE Ultrason. Symp.,* 2, pp. 1763-1766, 2000.

[9] B.G. Tomov. J.A. Jensen, “Compact implementation of dynamic receive apodization in ultrasound scanners”, *Proc. SPIE*, 5373, pp. 260-271, 2004.

[10] J. Camacho, M. Parrilla, A. Ibáñez, C. Fritsch, “The Progressive Dynamic Focusing Correction Technique in NDE”, *Proc. IEEE Ultrason. Symp*., pp. 1586-1589, 2007.

42º CONGRESO ESPAÑOL DE ACÚSTICA
ENCUENTRO IBÉRICO DE ACÚSTICA
EUROPEAN SYMPOSIUM ON ENVIRONMENTAL ACOUSTICS
AND ON BUILDINGS ACOUSTICALLY SUSTAINABLE

ARRAY VIRTUAL PARA CÁLCULO DE LEYES FOCALES

PACS: 43.35.Yb

C. Fritsch, J. Camacho, J. Fdez. Cruza, J.M. Moreno, J. Brizuela
Grupo UMEDIA (Ultrasound for Medical and Industrial Applications)
Consejo Superior de Investigaciones Científicas (CSIC)
La Poveda, 28500 Madrid, Spain
Tel: 918 711 900,
Fax: 918 717 050
E-mail: carlos@iai.csic.es; jorgecam@iai.csic.es; jorge.fernandez.cruza@iai.csic.es;
jm.moreno@csic.es; brizuela@iai.csic.es

ABSTRACT

This work presents a new technique to compute focal laws for ultrasonic inspections through interfaces. Conventional methods are computing intensive since the interface must be finely discretized to apply the refraction laws with the required accuracy. The proposed method is based on defining a virtual array that operates in the second medium only, thus avoiding the interface. Since it operates in a homogeneous medium, computing the focal laws is fast, which is especially important when dynamic focusing is used with a high number of foci.

RESUMEN

Este trabajo presenta una nueva técnica para calcular leyes focales en inspecciones a través de interfases. Los métodos convencionales son costosos en tiempo de cálculo ya que es preciso discretizar finamente la interfaz de forma que puedan aplicarse con la precisión requerida las leyes de la refracción. El método propuesto se basa en construir un array virtual que opera en el segundo medio y evita, por tanto, el paso a través de la interfaz. Al operar en un medio homogéneo, el cálculo de las leyes focales es muy rápido, aspecto de relevancia especial cuando se opera con focalización dinámica, dado el elevado número de focos.

INTRODUCCIÓN

Durante los últimos años ha aumentado la utilización de la tecnología de imagen *phased array* en el ámbito de la Evaluación No Destructiva por ultrasonidos. Las ventajas que proporciona son muchas: deflexión y enfoque del haz de forma electrónica, evitando el uso de múltiples transductores focalizados y cuñas, mejores características para la evaluación de defectos, mayor sensibilidad y mejor relación señal/ruido, entre otras.

Una mejora adicional de la calidad se consigue con focalización dinámica, proceso que permite obtener una imagen enfocada a todas las profundidades de forma automática. El enfoque se logra modificando los retardos aplicados a las señales recibidas en función de la profundidad, de forma que compensen las diferencias en los tiempos de vuelo desde cada foco a cada elemento del array. Se llama *ley focal* al conjunto de retardos para un foco determinado.

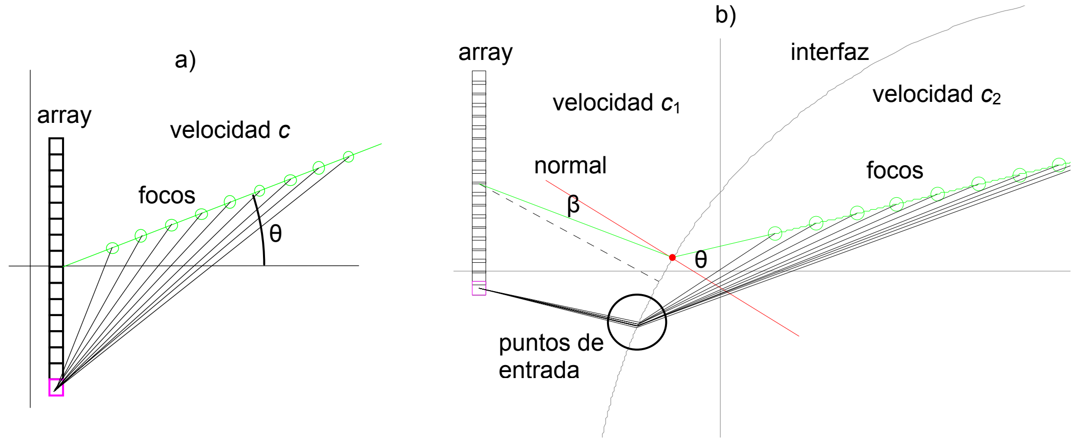

Figura 1. a) Inspección en un medio homogéneo de velocidad c; b) Inspección cuando hay dos medios de propagación con velocidades c_1 y c_2

Cuando se inspecciona un medio homogéneo como, por ejemplo, una pieza por contacto o, también, en ecografía médica (Fig. 1a), el cálculo de las leyes focales que corresponden a cada foco es simple. Si un elemento del array se ubica en (x_A, z_A), para un foco en (x_F, z_F), el tiempo de vuelo al elemento del eco producido en el foco es:

$$t_{AF} = \frac{1}{c}\sqrt{(x_A - x_F)^2 + (z_A - z_F)^2} \tag{1}$$

A partir de los tiempos de vuelo a cada foco *k*, la ley focal es el conjunto de retardos,

$$\{\tau(k)\} = T_0 - t_{AF}(k) \tag{2}$$

donde T_0 representa el tiempo de vuelo desde el centro del array (origen de tiempos). Un aspecto interesante es que existen técnicas que realizan este cálculo por hardware durante la adquisición de señal [1-2], lo que supone un coste nulo en tiempo de cálculo.

Sin embargo, con frecuencia es necesario introducir cuñas entre el *array* y la pieza o, en otros casos, se inspecciona por inmersión. En estas condiciones existen dos medios de propagación: acoplante (cuña o agua) y pieza, con velocidades de propagación c_1 y c_2, respectivamente (Fig. 1b). Para calcular las leyes focales hay que considerar los efectos de la refracción, complicando el problema para interfases de geometría arbitraria, para las que no existe una solución cerrada general. El problema es calcular t_{AF} para cada elemento y cada foco considerando que el punto de entrada del haz ultrasónico es diferente en cada caso. Hasta la fecha, no se conocen métodos para automatizar el proceso y permitir el cálculo de las leyes focales por hardware en tiempo real.

Adicionalmente, hay que calcular las leyes focales con gran precisión para evitar la generación de lóbulos de cuantización de los retardos [3]. Para un array de *N* elementos de frecuencia fundamental f_R, el error rms en los retardos T_X debe ser mejor que:

$$T_X \leq \frac{1}{2\pi f_R}\sqrt{\frac{6}{N}} \tag{3}$$

Por ejemplo, si *N*=64 y f_R = 5 MHz, resulta $T_X \leq$ 10 ns. En inmersión, este error temporal equivale, en ida y vuelta, a un recorrido de solo 7.5 µm en agua (*c* ≈ 1500 m/s).
Existen herramientas comerciales de simulación de campo que facilitan el cálculo de las leyes focales por distintos métodos [4-6], pero son lentas para realizar la focalización dinámica con la debida resolución. Por otra parte, también hemos desarrollado un método rápido de cálculo de leyes focales a través de interfases de geometría arbitraria, basado en la solución de una ecuación por Newton-Raphson sin iteraciones [7]. Aunque es una técnica sencilla y rápida, tampoco es fácil su implantación en hardware.

Este trabajo presenta un nuevo método que convierte el problema de 2 medios en otro de un único medio homogéneo, evitando por tanto el paso a través de la interfaz. Es aplicable a geometrías y velocidades en acoplante y pieza arbitrarias, dentro de las habituales. Y, sobre todo, facilita la utilización de hardware de cálculo en tiempo real de las leyes focales. La técnica se presentará después de una breve descripción de los métodos convencionales.

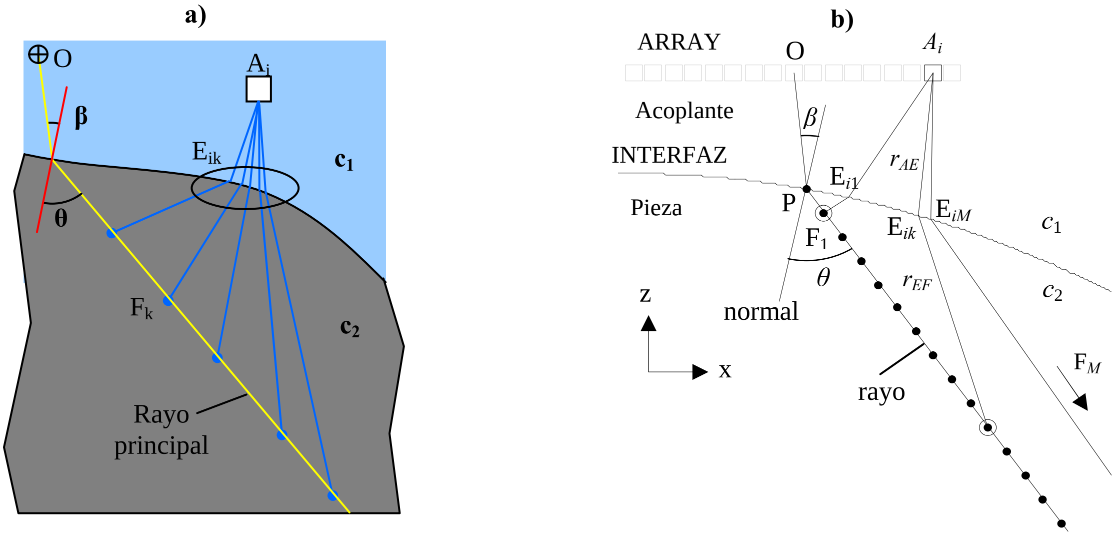

Figura 2. a) Detalle para un elemento del array y puntos de entrada al foco; b) Geometría

MÉTODO CONVENCIONAL

La Figura 2 muestra la geometría general para el cálculo de leyes focales. El proceso convencional se realiza en dos pasos:

P-1. Obtener el rayo principal que forma un ángulo con la normal θ especificado. Por conveniencia, el rayo principal pasa por el centro del array (en O), origen de tiempos. Aplicando la ley de Snell, con un índice de refracción $n=c_1/c_2$:

$$\sin\beta = \frac{c_1}{c_2}\sin\theta = n\sin\theta \qquad (4)$$

El punto de entrada del rayo principal es aquél en el que el producto escalar de los vectores unitarios $\vec{n}$ = normal, $\vec{v}$ = punto de entrada a centro del array hace $\vec{n}\cdot\vec{v} = \cos\beta$. Para su evaluación, se realiza una búsqueda en los puntos de la interfaz discretizada para localizar el que mejor aproxima la anterior igualdad.

P-2. Para cada elemento *i* del array,
para cada foco *k*,
encontrar las coordenadas (x_E, z_E) del punto de entrada E_{ik}. Aplicando el principio de Fermat, se buscará en la interfaz discretizada aquél que minimiza el tiempo de vuelo t_{AF} (camino más rápido) dado por:

$$t_{AF} = \frac{r_{AE}}{c_1} + \frac{r_{EF}}{c_2} = \frac{\sqrt{(x_A - x_E)^2 + (z_A - z_E)^2}}{c_1} + \frac{\sqrt{(x_E - x_F)^2 + (z_E - z_F)^2}}{c_2} \quad (5)$$

obteniéndose el juego de retardos por aplicación de (2).

El procedimiento es simple y preciso si se discretiza finamente la interfaz, pero muy costoso en tiempo de cálculo. El mayor problema reside en la búsqueda involucrada en el segundo paso, para muchos focos, a pesar de que hay formas de optimizar el proceso. Además, este método no es adecuado para calcular las leyes focales en tiempo real.

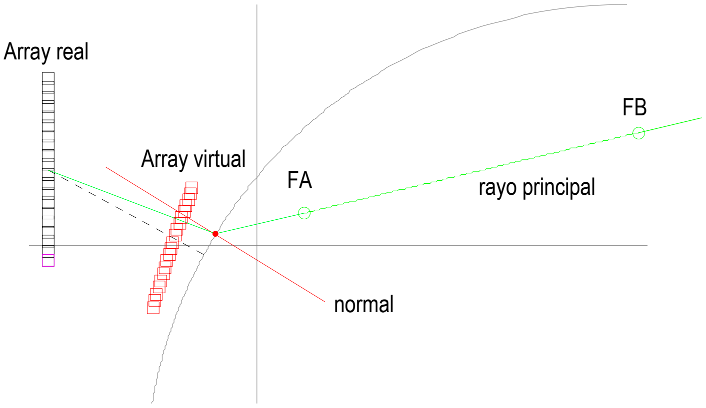

Figura 3. Ubicación del array virtual y focos FA y FB sobre el rayo principal

DETERMINACIÓN DE UN ARRAY VIRTUAL EQUIVALENTE.

Aquí se propone una técnica diferente que evita las complicaciones de la interfaz. Consiste en evaluar un *array virtual aproximadamente equivalente* en tiempos de vuelo a todos los focos situados sobre el rayo principal, considerando un medio homogéneo de velocidad c_2.

La Figura 3 muestra la solución al problema propuesto en la Figura 1b. La distribución de elementos en el array virtual no es uniforme y forma parte del problema determinar su ubicación. Para ello se eligen dos focos, uno próximo a la interfaz (FA) y otro alejado (FB), posiblemente en el límite del campo cercano $U = D^2/4\lambda_2$, siendo D el tamaño de la apertura y λ_2 la longitud de onda en el segundo medio.

Los tiempos de vuelo del array virtual al foco son:

$$t_{VF} = \frac{r_{VF}}{c_2} = \frac{\sqrt{(x_V - x_F)^2 + (z_V - z_F)^2}}{c_2} \quad (6)$$

Se postula que:

$$t_{VF} + T_A \approx t_{AF} \quad \text{para todos los focos entre FA y FB} \qquad (7)$$

donde T_A es un tiempo constante para cada elemento del array real. Sustituyendo (5) en (7) y, para un foco lejano (en el ∞),

$$T_A \approx \left(\frac{r_{AE}}{c_1} + \frac{r_{EF}}{c_2}\right) - \frac{r_{VF}}{c_2} \approx \left(\frac{r_{AE}}{c_1} + \frac{r_{EF}}{c_2}\right) - \left(\frac{r_{VE}}{c_2} + \frac{r_{EF}}{c_2}\right) \qquad (8)$$

Por el invariante de Abbe [8], $c_1 r_{AE} \approx c_2 r_{VE}$ que, sustituido en (8) proporciona,

$$T_A = \frac{r_{AE}}{c_1}(1 - n^2) \qquad (9)$$

donde r_{AE} se calcula para un foco FB en ∞ con un proceso análogo al expuesto en P-1, sustituyendo las coordenadas del centro del array por las del elemento actual.

Una vez evaluado T_A, las coordenadas (x_V, z_V) de cada elemento del array virtual, se obtienen resolviendo (7) para los focos FA y FB (dos ecuaciones y dos incógnitas). Obviamente la ecuación (7) se verificará exactamente sólo para FA y FB y de forma aproximada para el resto de focos entre ellos. Para ello se calculan previamente los tiempos t_{AF}(A) y t_{AF}(B) por aplicación del principio de Fermat (5). Al elegir FB en el ∞, sólo será necesario realizar el proceso de búsqueda para t_{AF}(A).

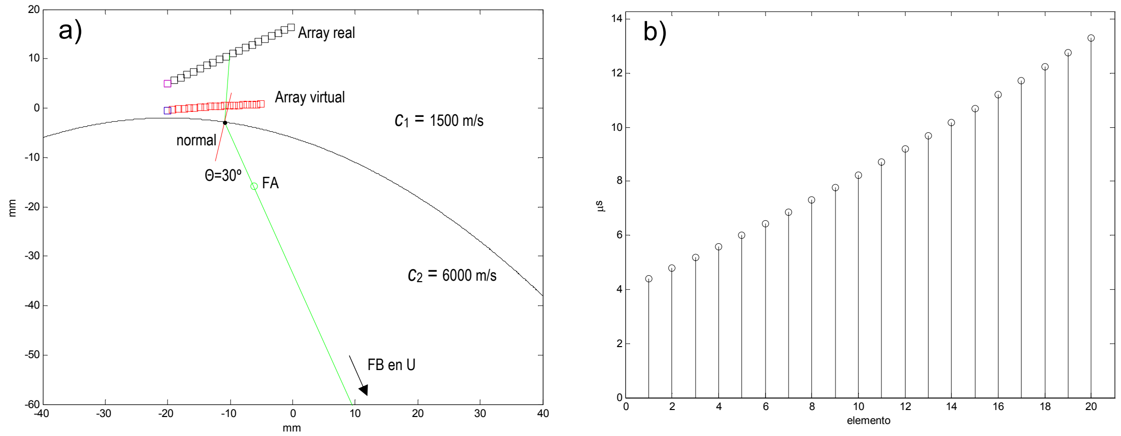

Figura 4. a) Representación geométrica de las posiciones del array real, array virtual y rayo principal; b) Valores de T_A para los diferentes elementos, µs

RESULTADOS

El aspecto más importante es evaluar los errores en el tiempo de vuelo a los diferentes focos situados entre FA y FB en el límite del campo cercano. Para ello se comparan los valores obtenidos mediante la aplicación del principio de Fermat (método convencional expuesto en los pasos P1 y P2) y una interfaz finamente discretizada con los que proporciona la nueva técnica.

La Figura 4a) muestra un ejemplo con un array de 10 MHz de *N*=20 elementos a distancias de 1.2 mm entre sí, que se utiliza para inspeccionar por inmersión (c_1 = 1500 m/s) una pieza metálica con una interfaz parabólica (c_2 = 6000 m/s). Se observa que el array real no tiene una orientación particularmente buena con respecto a la pieza, pero se trata de mostrar que la técnica funciona bien en estas condiciones.

En la Fig. 4a) también se muestran las posiciones del array virtual. Los tiempos asociados T_A se visualizan en la Fig. 4b) para este ejemplo. Se observa que son diferentes para cada elemento y aumentan con la distancia a la interfaz.

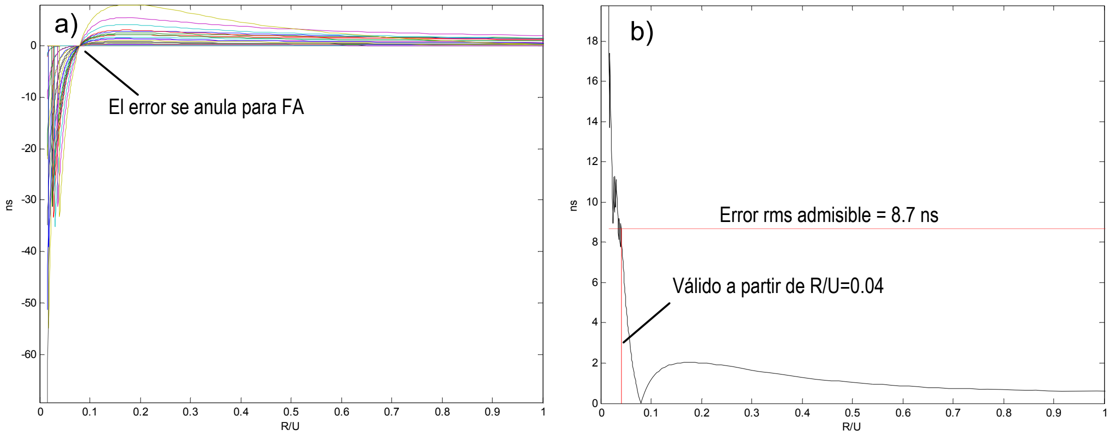

Figura 5. a) Errores en el tiempo de vuelo para todos los elementos (ns); b) Error rms (ns)

La Figura 5a) muestra los errores obtenidos como diferencias entre los calculados por aplicación del principio de Fermat y los que produce la nueva técnica en función de la distancia normalizada *R/U*. Se observa que el error se mantiene por debajo de los 8 ns en todos los casos a partir del foco FA, donde se anula para todos los elementos como cabía esperar. Como el foco FB se sitúa en el ∞, el error no se anula en el límite del campo cercano (*R/U*=1).

La Figura 5b) muestra el error *rms* en función de la profundidad normalizada R/U. Para este caso, la aplicación de (3) produce un error *rms* admisible de 8.7 ns. Se comprueba que este error no se alcanza en todo el rango a partir de *R/U* = 0.04 (a 8.6 mm desde la interfaz).

CONCLUSIONES

Se ha propuesto un nuevo método para calcular las leyes focales, particularmente adecuado para la focalización dinámica en presencia de interfases. La técnica convierte un problema de cálculo a través de la interfaz, donde hay que tener en cuenta las leyes de la refracción, en otro en el que un array virtual opera en un medio homogéneo.

A diferencia de los métodos convencionales, que requieren realizar una búsqueda del camino más rápido de propagación, la nueva técnica presenta una complejidad análoga a la de operar en un medio único, basado en puras consideraciones geométricas con expresiones cerradas. La contrapartida es que los resultados son aproximados, pero se ha comprobado que los errores en los retardos de focalización obtenidos están acotados, siendo inferiores al máximo error rms aceptable para mantener bajos lóbulos de cuantización en casi todo el rango.

El cálculo de las coordenadas del array virtual se realiza resolviendo un simple sistema de ecuaciones. Al tiempo de vuelo a cada foco calculado se le añade una constante para cada elemento del array, que se deriva del invariante de Abbe.

Una ventaja adicional proporcionada por la nueva técnica es que posibilita el cálculo de las leyes focales por hardware en tiempo real, utilizando alguno de los métodos conocidos para esta finalidad. Esta característica se obtiene por primera vez cuando existen dos medios de propagación involucrados.

AGRADECIMIENTOS

Este trabajo ha sido realizado con financiación del proyecto DPI-2010-17648 del Ministerio de Ciencia e Innovación.

REFERENCIAS

1. K. Jeon, M. H. Bae, S. B. Park, S. D. Kim, "An efficient real time focusing delay calculation in ultrasonic imaging systems", *Ultrasonic Imaging*, 16, pp. 231-248, 1994.
2. H. T. Feldkämper, R. Schwann, V. Gierenz, T. G. Noll, "Low power delay calculation for digital beamforming in handheld ultrasound systems", *Proc. IEEE Ultrason. Symp.,* 2, pp. 1763-1766, 2000.
3. D. K. Peterson, G. S. Kino, "Real-time digital image reconstruction: A description of image hardware and an analysis of quantization errors", *IEEE Trans. on Sonics and Ultrasonics*, 31, 4, pp. 337-351, 1984.
4. G. A. Deschamps, “Ray techniques in electromagnetics”, Proceedings of the IEEE, 60, 9, pp. 1022-1035, September 1972.
5. F. Buiochi et al., “A Computational Method to Calculate the Longitudinal Wave Evolution Caused by Interfaces Between Isotropic Media”, IEEE Transactions on Ultrasonics, Ferroelectrics, and Frequency Control, 51, 2, pp. 181-192, 2004.
6. M. A. Andrade, J. C. Adamowski, A. Ibañez, M. Parrilla, C. Fritsch, “Optimization of Complex Shape Part Inspections with Phased Arrays”, *Proc. IEEE Ultrasonics Symposium*, pp. 733-736, 2009.
7. M. Parrilla, J. Brizuela, J. Camacho, A. Ibáñez, P. Nevado, C. Fritsch, “Dynamic Focusing through Arbitrary Geometry Interfaces”, *Proc. IEEE Ultrasonics Symposium*, pp. 1195-1198, 2008.
8. M. Born, E. Wolf: “Principles of Optics”, *Cambridge University Press*, 1997.

Total Focusing Phased Array

Jorge F. Cruza, Jorge Camacho, Jose Miguel Moreno
Sensors and Ultrasonic Systems Department (DSSU),
Spanish National Research Council (CSIC)
Madrid, Spain
jorge.f.cruza@csic.es

***Abstract*— Phased Array (PA) uses a single focus in emission and Dynamic Depth Focusing (DDF) in reception, while Total Focusing Method (TFM) focuses every image pixel in emission and in reception. By contrast, TFM lacks the A-scan information, which is standard in PA and can be very useful for evaluation. Another issue common to both techniques is the difficulty associated with two media propagation and unknown interface geometry. A further TFM drawback is the limited image extent due to memory and time consumption.**

This work addresses these problems by proposing the new Total Focus Phased Array (TFPA) technique that combines the advantages of PA and TFM. TFPA builds A-scan lines as in PA, but focused in emission and in reception at all depths. This process is achieved in real-time by N+1 focusing hardware blocks that do not limit the length of every A-scan. Furthermore, TFPA can operate with the Virtual Array concept that avoids the problems of refraction in two propagation media applications. TFPA has many advantages: A-scan information is preserved, image is focused in emission and in reception, moderate complexity with real-time capability, no refraction issues and no limit on the depth or the number of pixels/samples in the image.

***Index Terms*—Total Focusing Phased Array, Beamforming, Emission Focusing, Real-time Ultrasonic Imaging, NDE.**

I. INTRODUCTION

THE key advantage of the Total Focusing Method (TFM) over Phased Array (PA) is that images are focused in emission and in reception, which yields the best resolution. However, this leads to a high processing burden: A 256x256 pixel image acquired with a 128-element array requires more than 8 million of TOF computations.

TFM has also other limitations. One of them is the lack of a physical beam, while many NDT standards and codes require angles and propagation modes to perform the inspections. In this sense, the conventional phased array (PA) technique shows some advantages: it generates ultrasonic beams and acquires A-scans with specific angles or sector scans, operates in real-time, even with strict Dynamic Depth Focusing (DDF) carried out by specialized circuits that compute the focusing delays in real-time [1-2]. By contrast, in TFM, the time-of-flight (TOF) from elements to image pixels are usually computed by software and stored to be used during image formation, which requires a considerable amount of time and memory [3].

However, the greater problems for TFM and PA arise in a two propagation media scenario. While for inspections in a homogeneous medium TOFs are easily computed as the ratio of distances to sound propagation velocity, refraction at the interface between two media complicates this task. The sound follows the fastest path (Fermat's principle) that cannot be predicted by closed formulae and must be found by iterative procedures [4-5].

In [6] we described a technique that avoids the difficulties associated to refraction. It is based on computing a virtual array (VA) that operates in the second medium only, whose TOFs to foci are approximately equivalent to those obtained from the real array with refraction at the interface.

This work proposes the Total Focus Phased Array (TFPA) technique, which keeps A-scan information as in PA but with emission-reception focusing as in TFM. This is achieved by means a parallel processing hardware based on efficient real-time focusing logic. The virtual array concept is adapted to the TFPA technique for two propagation media applications. Experimental verification is carried out comparing TFPA with TFM and PA images of an aluminum part inspected in water immersion.

II. THE TOTAL FOCUSING PHASED ARRAY TECHNIQUE

A single array element emits and echo signals received by all elements are recorded. This dataset is used to beamform the L scan lines of the image with dynamic focusing in reception. This yields a low-resolution image due to the omnidirectional emission. The acquisition process is repeated changing the position of the emitter and accumulating the low-resolution images, until all array elements have been used as emitters. A final image focused in emission and reception is obtained.

Differently from conventional TFM, beamforming is carried out on samples located along propagation paths at regular intervals $\Delta R = cT_S/2$, where T_S is the sampling period and c the sound speed. Besides preserving beamformed A-scans as in PA, this facilitates an efficient and real-time implementation.

A. Hardware-based TFPA beamforming.

TFPA obtains the final image in real-time with the same acquisition electronics, instead of forwarding the captured data matrix to a separated processing unit. This is achieved using the high processing capabilities of state-of-the-art FPGAs. The possibility of beamforming all image lines in parallel depends on the availability of enough hardware resources.

978-1-4673-9897-8/16/$31.00 ©2016 IEEE

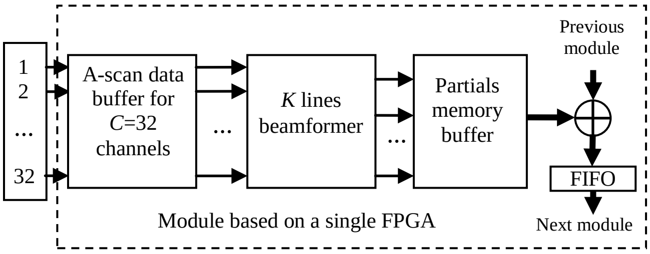

Fig. 1. Module for C channels and L scan lines (C<L, C=32 in this example).

With limited resources, a set of $K<L$ scan lines can be processed in parallel each time. The final image is obtained after [L/K]↑ operations, where [·]↑ represents rounding up. Fig. 1 presents an architecture to perform these operations when there are more ultrasound channels (N) than those (C) fitting in a single FPGA (N=128, C=32 require 4 modules).

After each trigger event, ultrasound data received by the array elements are stored in the A-scan data buffer. From these data, beamforming is carried out for K lines in parallel, storing the results in the partial image memory. Successive blocks of K lines are then beamformed from the same A-scan data set until the whole low-resolution image had been obtained. The process is carried out with a clock frequency typically an order of magnitude faster than the A/D channel sampling rate, which allows completing the image between trigger events.

Besides, as soon as corresponding data are available in the current partial memory buffer and in the previous module, they are coherently added and the result is sent to the next module through a FIFO to compensate time differences and data communication delays. Partial images are added in chain and the final image is accumulated in the last module.

B. *Focusing logic for TFPA automatic beamforming*

Differently from TFM, TFPA does not require computing the TOFs from each transducer element (N) to the S image samples in every one of the L scan lines, with a total of $N{\cdot}L{\cdot}S$ TOF computations (millions of TOFs for typical image and arrays). TFPA is based on a *focusing logic* that obtains TOFs iteratively in real-time for all foci along scan lines, using only 3 initialization parameters, developed by our group [6].

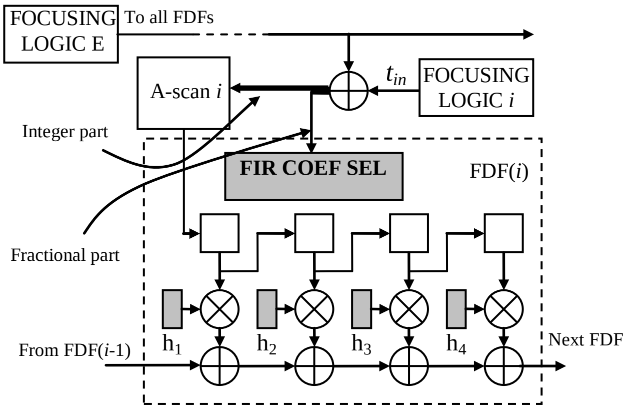

Fig. 2. Beamforming circuit for element i

Figure 2 shows schematically the pipelined TFPA beamforming circuit for element *i*. Each channel has its own focusing logic that calculates TOFs from the element *i* to foci along the scan line. An additional focusing logic E, shared by all channels, provides TOFs from emitter to foci. The sum of both values is the total TOF emitter-focus-receiver. This scheme reduces the amount of $N{\cdot}L{\cdot}S$ TOF computations of TFM to $3{\cdot}N{\cdot}L$ initialization parameters in TFPA.

The integer part of the summation is used to select samples fed to a Fractional Delay Filter (FDF) whose coefficients are selected by the TOF fractional part [7]. FDFs are implemented with Digital Signal Processing (DSP) cells available in state-of-the-art FPGAs. These cells have a multiplier whose output is connected to an adder input. The other adder input is connected to the result of the previous DSP cell, chaining the additions required by the FDF. Logic and connections are hardwired, which are much faster and less power consuming than regular FPGA logic. Furthermore, some key optimizations are performed [8]:

1) All channel FDFs are chained, so that interpolation and coherent sum (interpolation-and-beamforming) is carried out concurrently with the same resources.

2) Several interpolation-and-beamforming operations can be performed in a single sampling period, taking advantage of the high speed of DSP cells. If f_C is the maximum switching rate accounting all the logic involved and f_S is the sampling frequency, up to f_C/f_S scan lines can be simultaneously processed (multi-line beamforming). A conservative figure is f_C=200 MHz, providing simultaneously 4 scan lines for f_S = 50 MHz, a value that would be even higher for lower sampling rates or higher performance FPGAs.

3) A compact physical implementation allows integrating several multi-line beamformers in the same chip. For example, the XC7K325T-2 Kintex FPGA from Xilinx has enough resources to implement 8 multi-line beamformers,generating up to 32 scan lines simultaneously with a sampling rate of 50 MHz.

III. THE VIRTUAL ARRAY CONCEPT FOR TFPA

In [6] we proposed a virtual array that, operating in the second medium only, converts a two propagation media problem in a homogeneous case. TOFs from the virtual array to foci are approximately equal to those computed from the real array with refraction at the interface. One advantage of the virtual array is the possibility of using our focusing logic to provide real-time DDF despite refraction.

TABLE I. ARRAY AND IMAGE PARAMETERS FOR THE EXPERIMENTS

Water speed of sound	1.48 mm/µs
Aluminium speed of sound	6.38 mm/µs
Number of array elements (N)	128
Element pitch	0.65 mm
Array center frequency	5 MHz
Sampling frequency	40 MHz
Sample resolution	16 bits
Image	Angular sweep -50º to 50º
Number of image lines (L)	256
Scan length	45 mm
Number of samples per line (S)	512

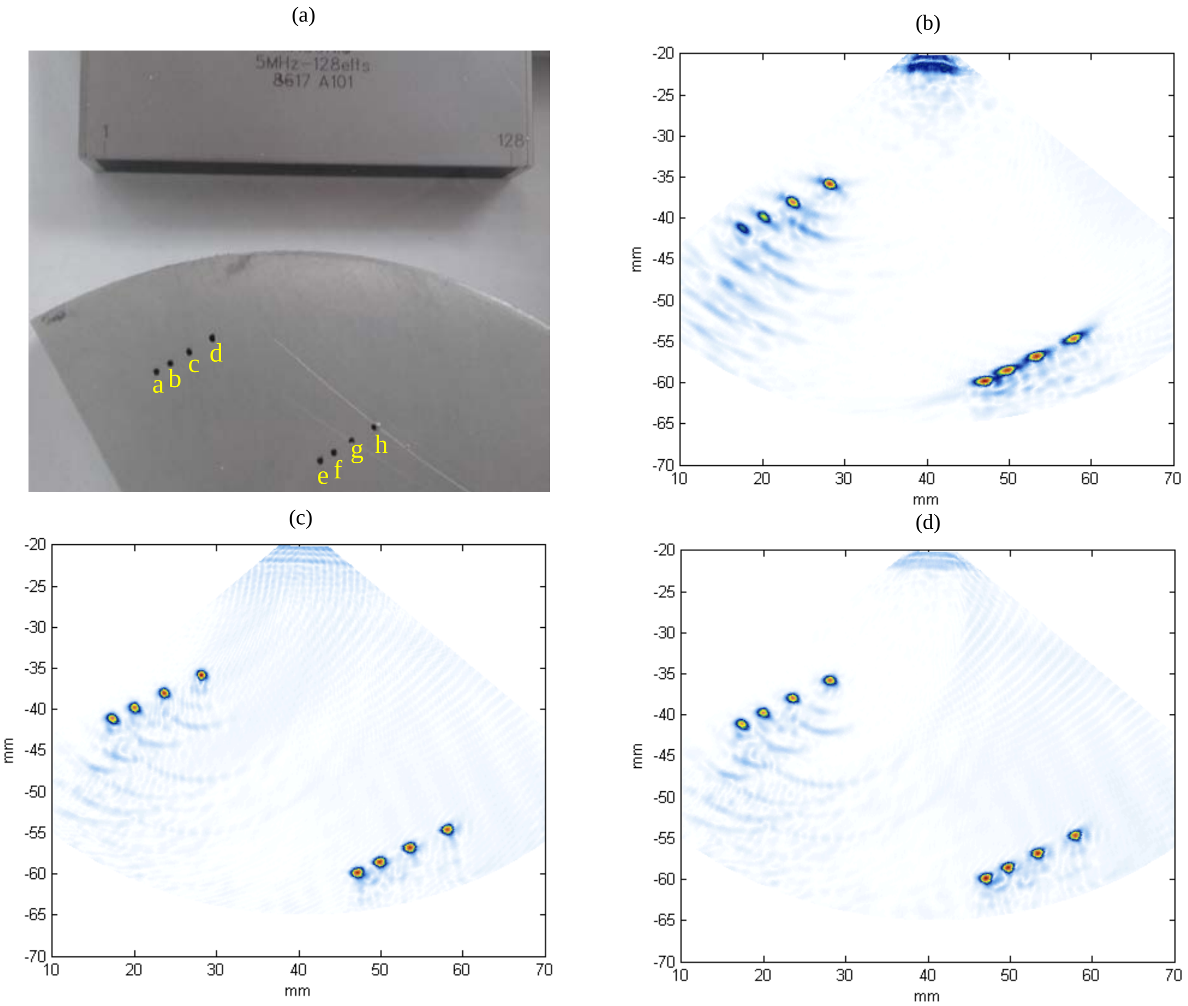

Fig. 3. (a) Inspection set-up, (b) PA image, 12 element emission aperture focused at 22.5 mm from surface, (c) TFM with exact TOFs calculated with Fermat algorithm and (d) TFPA image obtained with the virtual array.

Two virtual elements are involved in TOF computations in TFPA. Since exact TOF values are obtained at two reference foci only, some timing errors are produced in other points. However, as it was demonstrated, these are small errors (below a few tens of ns), whose impact in the image quality is expected to be low. This is verified experimentally by comparing TFM images obtained with exact TOFs computed by application of the Fermat's principle with that provided by TFPA with the virtual array.

IV. EXPERIMENTAL VERIFICATION

To verify and compare the operation of TFPA with regard to PA and TFM, an experiment with a 100-mm-curvature-radius aluminum part with two groups of 1.5-mm diameter side driled holes (SDHs) is inspected in water immersion with the array and image parameters shown on Table I. The array (Imasonic , France) is located approximately 20 mm above the surface of the part (Fig. 3.a).

A SITAU-111 (DASEL SL, Madrid, Spain) phased-array system with 128 active channels was used to acquire the full matrix. All processing was carried out using Matlab (Matworks Inc, USA).

Three images have been generated from the same data set in Matlab. The first one is a PA image with DDF on reception using the virtual array to avoid refraction at the interface (Fig. 3.b). A single focus in emission is set at 22.5 mm from the surface and the emitting aperture is limited to 12 elements to obtain a focal depth of 45 mm (from -20 to -65 mm).

The second image (Fig. 3.c) is a TFM image that can be considered the “gold standard”, where TOFs are obtained by an iterative Fermat algorithm with a timing error below 1ns. The third image (Fig. 3.d) is the image obtained using the virtual array and code that emulates the behavior of the focusing hardware of TFPA.

Since fewer elements are used for emission, the PA image shows lower overall quality, with a loss of resolution more

TABLE II. QUANTITATIVE FWHM MEASUREMENTS

SDH	FWHM (mm) PA	 TFM	 TFPA
a	1.44	1.13	1.20
b	1.36	1.03	1.13
c	1.04	0.91	1.05
d	1.18	0.81	1.07
e	1.75	1.17	1.13
f	1.98	1.12	1.13
g	1.80	1.12	1.14
h	1.86	1.06	1.10
Mean	1.55	1.04	1.12
STD	0.91	0.33	0.12

evident on the **e**, **f**, **g** and **h** holes because they are farther from the emission focus. One of the SDH (**a**) has clearly less amplitude probably caused by the shadowing of **b**, **c** and **d** holes.

TFPA and TFM yield quite similar images. Table II shows quantitative Full Width Half Maximum (FWHM) of all SDHs measured for PA, TFM and TFPA. On average, TFPA has 38% better resolution than PA and about 8% worse than TFM.

V. CONCLUSION

The TFPA technique has been developed to provide dynamic emission and reception focusing in real-time. To this purpose, digital focusing circuits previously developed for PA real time operation have been adapted. Also, the virtual array concept avoids refraction issues at the interface between two propagation media.

A digital architecture that takes advantage of resources and performance of state-of-the-art FPGAs has been developed. The frame rate that will be obtained depends on the FPGA resources spent and the characteristics of the image, but as an example, a system with 4 XC7K325T-2 Kintex FPGAs could generate more than 50 images per second for inspections parameters similar to those shown in Table I.

TFPA keeps whole A-scan information, can be used with wedges or by immersion, performs in real time and has dynamic focus in both, emission and reception, in all image points. We believe that TFPA can be a widely used and appreciated technique in NDE applications.

ACKNOWLEDGMENT

Work funded by project DPI2013-42236-R of the program “Research challenges” of the Spanish Ministry of Economy and Competitiveness.

REFERENCES

[1] K. Jeon, M. H. Bae, S. B. Park, S. D. Kim, "An efficient real time focusing delay calculation in ultrasonic imaging systems", *Ultrasonic Imaging*, 16, pp. 231-248, 1994.

[2] H. T. Feldkämper, R. Schwann, V. Gierenz, T. G. Noll, "Low power delay calculation for digital beamforming in handheld ultrasound systems", *Proc. IEEE Ultrason. Symp.*, 2, pp. 1763-1766, 2000.

[3] M. Suttcliffe, M. Weston, B. Dutton and I. Cooper, “Real-time full matrix capture with auto-focusing of known geometry through dual layered media”, *NDT Conf. of BINDT*, Daventry, UK, 11-13 Sept. 2012.

[4] R. Long, J. Rusell, P. Cawley and N. Habgood, “Ultrasonic phased array inspection of flaws on weld fusion faces using full matrix capture”, *Rev. Progress QNDE*, 28, pp. 848-855, 2009.

[5] L. Le Jeune, S. Robert, P. Dumas, A. Membre, C. Prada, “Adaptive ultrasonic imaging with the total focusing method for inspection of complex components immersed in water”, *Rev. Progress QNDE*, 34, AIP Conf. Proc. 1650, 1037, Boise, Idaho, 2015.

[6] J. F. Cruza, J. Camacho, L. Serrano, C. Fritsch, “New Method for Real-Time Dynamic Focusing Through Interfaces, *IEEE Trans. Ultrason. Ferroelectr. Freq. Control*, 60, 4, pp. 739-751, 2013.

[7] T. I. Laakso, V. Valimaki, M. Karjalainen, U.K.Laine, “Splitting the Unit Delay”, *IEEE Sig. Proc. Magazine*, pp. 30-58, Jan. 1996.

[8] J. F. Cruza, J. Camacho, J.M. Moreno, L. Medina, “A new architecture for fast ultrasound imaging”, *AIP Conf. Proceedings*, 1581, 1, p.1975-1982 , 2014.

MINISTERIO
DE INDUSTRIA, ENERGIA
Y TURISMO

Oficina Española
de Patentes y Marcas

Nº SOLICITUD: **P201230799**
Nº PUBLICACIÓN: **ES2525600**
TITULAR/ES:
CONSEJO SUPERIOR DE INVESTIGACIONES CIENTÍFICAS (CSIC)
UNIVERSIDAD POLITÉCNICA DE MADRID

FECHA EXPEDICIÓN: 09/02/2016

TÍTULO
DE
PATENTE DE INVENCIÓN

Cumplidos los requisitos previstos en la vigente Ley 11/1986, de 20 de marzo, de Patentes, se expide el presente TÍTULO, acreditativo de la concesión de la Patente de Invención. La solicitud ha sido tramitada y concedida con realización del Informe sobre el Estado de la Técnica y **sin examen previo** de los requisitos sustantivos de patentabilidad.

Se otorga al titular un derecho de exclusiva en todo el territorio nacional, bajo las condiciones y con las limitaciones previstas en la Ley de Patentes. La duración de la patente será de **veinte años** contados a partir de la fecha de presentación de la solicitud (25/05/2012).

La patente se concede sin perjuicio de tercero y sin garantía del Estado en cuanto a la validez y a la utilidad del objeto sobre el que recae.

Para mantener en vigor la patente concedida, deberán abonarse las tasas anuales establecidas, que se pagarán por años adelantados. Asimismo, deberá explotarse el objeto de la invención, bien por su titular o por medio de persona autorizada de acuerdo con el sistema de licencias previsto legalmente, dentro del plazo de cuatro años a partir de la fecha presentación de la solicitud de patente, o de tres años desde la publicación de la concesión en el Boletín Oficial de la Propiedad Industrial, aplicándose el plazo que expire más tarde.

Ana R.

Fdo.: Ana María Redondo Mínguez
Jefe/a de Servicio de Actuaciones Administrativas
(P.D. del Director del Departamento de Patentes e I.T., resolución 05/09/2007)

MINISTERIO DE INDUSTRIA, ENERGIA Y TURISMO

Oficina Española de Patentes y Marcas

TASA en materia de Propiedad Industrial
CODIGO 511

Modelo 791

Identificación

Ejercicio: 2016
Nro Justificante: 7915111195792

Sujeto Pasivo

NIF:

Apellidos y Nombre o Razón Social:

Agente o Representante legal (1):

NIF: A28378578

Apellidos y Nombre o Razón Social: Ungria Patentes y Marcas, S.A.

Código de Agente o Representante (2): 0392

Autoliquidación

Titular del expediente si es distinto del pagador: CONSEJO SUPERIOR INV. CIENTIFICAS CSIC

Modalidad Expediente: P Número Expediente: 201230799 Tipo (3): Publicación

Clave: IP00 Año: 2015 Concepto: INVENCIONES: DERECHOS DE CONCESION

Unidades: 1 Importe: 26,46

Referencia OEPM: 88127320629

909992100200188127320629

Declarante

Fecha: 5/02/16 9:45

Firma: Ungria Patentes y Marcas, S.A.

Ingreso

Importe en euros: 26,46 Adeudo en cuenta: ☒

NRC Asignado: 7915111195792000000003

Modelo 791

(1) Solo cuando el pago se realice con cargo a la cuenta corriente del representante o agente.
(2) En el caso de que tenga asignado un número por la OEPM.
(3) En el caso de patentes europeas, se pondrá una P si es el número de publicación o una S si es el número de solicitud.

MINISTERIO DE INDUSTRIA, ENERGIA Y TURISMO

Oficina Española de Patentes y Marcas

TASA en materia de Propiedad Industrial
CODIGO 511

Modelo 791

Identificación

Ejercicio: 2016
Nro Justificante: 7915111195792

Sujeto Pasivo

NIF:

Apellidos y Nombre o Razón Social:

Agente o Representante legal (1):

NIF: A28378578

Apellidos y Nombre o Razón Social: Ungria Patentes y Marcas, S.A.

Código de Agente o Representante (2): 0392

Autoliquidación

Titular del expediente si es distinto del pagador: CONSEJO SUPERIOR INV. CIENTIFICAS CSIC

Modalidad Expediente: P Número Expediente: 201230799 Tipo (3): Publicación

Clave: IP03 Año: 2014 Concepto: INVENCIONES: 3 ANUALIDAD

Unidades: 1 Importe: 18,48

Referencia OEPM: 88127320742

909992100200188127320742

Declarante

Fecha: 5/02/16 9:45

Firma: Ungria Patentes y Marcas, S.A.

Ingreso

Importe en euros: 18,48 Adeudo en cuenta: ☒

NRC Asignado: 7915111195792000000004

Modelo 791

(1) Solo cuando el pago se realice con cargo a la cuenta corriente del representante o agente.
(2) En el caso de que tenga asignado un número por la OEPM.
(3) En el caso de patentes europeas, se pondrá una P si es el número de publicación o una S si es el número de solicitud.

MINISTERIO
DE INDUSTRIA, ENERGIA
Y TURISMO

Oficina Española
de Patentes y Marcas

TASA en materia de Propiedad Industrial
CODIGO 511

Modelo 791

Identificación

Ejercicio: 2016
Nro Justificante: 7915111195792

Sujeto Pasivo

NIF:

Apellidos y Nombre o Razón Social:

Agente o Representante legal (1):

NIF: A28378578

Apellidos y Nombre o Razón Social: Ungria Patentes y Marcas, S.A.

Código de Agente o Representante (2): 0392

Autoliquidación

Titular del expediente si es distinto del pagador: CONSEJO SUPERIOR INV. CIENTIFICAS CSIC

Modalidad Expediente: P Número Expediente: 201230799 Tipo (3): Publicación

Clave: IP04 Año: 2015 Concepto: INVENCIONES: 4 ANUALIDAD

Unidades: 1 Importe: 23,29

Referencia OEPM: 88127320855

90999210020188127320855

Declarante

Fecha: 5/02/16 9:45

Firma: Ungria Patentes y Marcas, S.A.

Ingreso

Importe en euros: 23,29

Adeudo en cuenta: ☒

NRC Asignado: 7915111195792000000005

Modelo 791

(1) Solo cuando el pago se realice con cargo a la cuenta corriente del representante o agente.
(2) En el caso de que tenga asignado un número por la OEPM.
(3) En el caso de patentes europeas, se pondrá una P si es el número de publicación o una S si es el número de solicitud.

(19) OFICINA ESPAÑOLA DE
PATENTES Y MARCAS

ESPAÑA

(11) Número de publicación: **2 525 600**

(21) Número de solicitud: 201230799

(51) Int. Cl.:

G02B 7/40 (2006.01)
A61B 8/00 (2006.01)

(12) PATENTE DE INVENCIÓN B1

(22) Fecha de presentación:

25.05.2012

(43) Fecha de publicación de la solicitud:

26.12.2014

(88) Fecha de publicación diferida del informe sobre el estado de la técnica:
29.01.2015

Fecha de la concesión:

30.10.2015

(45) Fecha de publicación de la concesión:

06.11.2015

(73) Titular/es:

CONSEJO SUPERIOR DE INVESTIGACIONES
CIENTÍFICAS (CSIC) (50.0%)
Serrano, 117
28006 Madrid (Madrid) ES y
UNIVERSIDAD POLITÉCNICA DE MADRID (50.0%)

(72) Inventor/es:

FRITSCH YUSTA, Carlos;
FERNÁNDEZ CRUZA, Jorge;
CAMACHO SOSA-DÍAS, Jorge;
MORENO LLAMAS, José Miguel;
BRIZUELA SÁNCHEZ, José y
MEDINA VALDÉS, Luis

(74) Agente/Representante:

UNGRÍA LÓPEZ, Javier

(54) Título: MÉTODO PARA EL CONTROL EN TIEMPO REAL DEL ENFOQUE DINÁMICO EN SISTEMAS DE IMAGEN ULTRASÓNICA Y DISPOSITIVO CALCULADOR DE ADELANTO DE MUESTREO ASOCIADO AL MISMO

(57) Resumen:

Método para el control en tiempo real del enfoque dinámico en sistemas de imagen ultrasónica y dispositivo calculador de adelanto de muestreo asociado al mismo.

La presente invención divulga un dispositivo y un método que realizan la focalización dinámica en sistemas de imagen ultrasónica, aplicables a inspecciones con presencia de un medio de acoplamiento entre el transductor y la parte inspeccionada. Los sistemas de imagen ultrasónica comprenden un array de N elementos transductores que emiten pulsos ultrasónicos con tiempos de vuelo característicos a puntos focales dentro del objeto a inspeccionar. La presente invención calcula un array virtual equivalente en tiempos de vuelo al array de N elementos, donde cada elemento perteneciente al array de N elementos virtual se calcula a partir de las coordenadas de dos focos F_A y F_B, ambos situados en un rayo principal, y de la ecuación: $t_K = t_{CF} + t_{FA} - t_{BF} - t_{FV}$ donde t_{CF}, t_{FA}, t_{BF}, t_{FV} son los tiempos de vuelo característicos, y t_K es una constante independiente de la posición del punto focal.

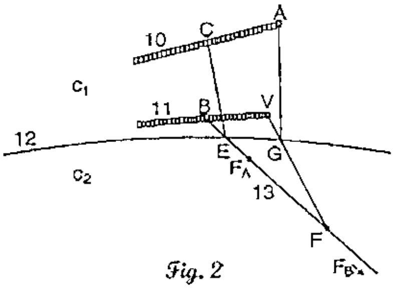

Fig. 2

ES 2 525 600 B1

Aviso: Se puede realizar consulta prevista por el art. 37.3.8 LP.

DESCRIPCIÓN

Método para el control en tiempo real del enfoque dinámico en sistemas de imagen ultrasónica y dispositivo calculador de adelanto de muestreo asociado al mismo

OBJETO DE LA INVENCIÓN

Esta invención descubre un método y un dispositivo para controlar automáticamente y en tiempo real el enfoque a todas las profundidades en sistemas de imagen ultrasónica. La presente invención opera tanto con medios homogéneos como cuando hay un acoplamiento (cuña, agua, etc.) entre el transductor y el medio inspeccionado, es decir, medios heterogéneos.

ANTECEDENTES DE LA INVENCIÓN

Los sistemas de imagen ultrasónica se basan en un conjunto o array de *N* elementos transductores que, al ser excitados eléctricamente, emiten pulsos ultrasónicos en el medio que se desea inspeccionar. El instante de emisión de cada elemento está temporizado para enviar el pulso ultrasónico en una dirección determinada. Se denomina ley focal al conjunto de retardos que deflectan y enfocan dicho pulso en una dirección y rango determinados. Cambiando la ley focal de emisión se modifica la dirección del pulso ultrasónico emitido (deflexión) para realizar un barrido angular de la región de interés.

En recepción, los ecos producidos por discontinuidades en el medio inspeccionado llegan al receptor, el cual, con frecuencia, coincide con el emisor. Las señales recibidas se amplifican y digitalizan. A estas señales también se les aplican leyes focales que hacen una recepción selectiva de los ecos generados por reflectores situados a cierta profundidad en la dirección del haz emitido.

Para ello, hay que compensar las diferencias de tiempo de vuelo en ida y vuelta desde el instante de emisión (que se supone originado en el centro del array) a cada foco y a cada elemento. Esta operación, denominada focalización o enfoque dinámico, requiere modificar dinámicamente el conjunto de retardos aplicados para cada muestra o, alternativamente, capturar selectivamente los ecos en los instantes en que se supone que llegan desde cada foco a cada elemento. Al realizar la suma de las muestras así obtenidas se obtiene una traza enfocada a todas las profundidades.

El proceso se repite para cada ángulo de deflexión del haz, realizando un barrido de la zona inspeccionada. Al visualizar la intensidad de las señales de eco recibidas y enfocadas, la imagen muestra la amplitud de los reflectores en las posiciones que ocupan.

Existe una amplia bibliografía de métodos para realizar la focalización dinámica, como S. C. Miller *et al.*, *Method and apparatus for providing dynamically variable time delays for ultrasound beamformer*, US Pat. 5.844.139, 1 Dic. 1998, y M. D. Poland, *Ultrasonic diagnostic imaging with automatic adjustment of beamforming parameters*, US2007/0088213 A1, Apr. 19, 2007.

Uno de los aspectos claves de este proceso es la determinación y gestión dinámica de los retardos de enfoque a aplicar a las señales recibidas por cada elemento y para cada muestra. Como es bien conocido, tales retardos han de programarse con una resolución del orden de 1/16 a 1/64 el periodo de la señal, y son diferentes para cada canal y para cada muestra de la señal recibida. Como la frecuencia de muestreo de las señales de eco es elevada (típicamente entre 10 y 50 MHz), el volumen de información que supone el conjunto de los retardos de enfoque dinámico es considerable.

En el pasado se han proporcionado métodos que permiten compactar la información requerida por el proceso de enfoque dinámico a un bit por foco y canal (C. Fritsch *et al.*, *Composición coherente de señales por corrección focal progresiva*, Pat. 2004/00203, 30 Ene. 2004). Sin embargo, es preciso calcular todos los retardos de enfoque, codificarlos y almacenarlos en memorias del sistema de imagen como paso previo a su utilización en tiempo real.

Para evitar este proceso, se han propuesto técnicas que calculan los retardos de enfoque en tiempo real o controladores de enfoque. En K. Jeon *et al.*, *An efficient real time focusing delay calculation in ultrasonic imaging systems*, Ultrasonic Imaging, 16, pp. 231-248, 1994, se describe una técnica basada en el algoritmo del punto medio usado en funciones gráficas de computación que evalúa las leyes focales en tiempo real; en R. Beaudin, M. Anthony, *Delay Generator for phased array ultrasound beamformer*, US Pat. 5522391, 4 Jun. 1996, se describe una técnica similar para realizar un generador de retardos en tiempo real; en S. Park *et al.*, *Real-time digital reception focusing method and apparatus adopting the same*, US Pat. 5669384, 23 Sept. 1997, se propone el método del punto medio para realizar un generador de reloj que determina el instante de muestreo en cada canal para realizar la focalización dinámica; en M. Bae, *Focusing delay calculation method for real-time digital focusing and apparatus adopting the same*, US Pat. 5836881, 17 Nov. 1998 se modifica la patente anterior para obtener los retardos de enfoque; en H. T. Feldkämper *et al.*, *Low power delay calculation for digital beamforming in handheld ultrasound systems*, Proc. IEEE Ultrason. Symp., 2, pp. 1763-1766, 2000 se propone otra variante que calcula los retardos de enfoque en tiempo real con menor consumo energético; en R.

Alexandru, *Delay controller for ultrasound receive beamformer*, US Pat. 7804736 B2, 28 Sep. 2010 se propone otro circuito que evalúa los retardos de enfoque con un número limitado de recursos.

Si bien estas técnicas son útiles para operar en medios homogéneos, ninguna de ellas es válida para calcular las leyes focales en tiempo real cuando hay varios medios de propagación, ya que los algoritmos y circuitos descritos en las referencias citadas consideran que el ultrasonido se propaga con velocidad constante por un único medio homogéneo.

Sin embargo, una situación habitual en Ensayos No Destructivos, es la inserción de una "cuña" o una "suela" entre el transductor y la pieza a inspeccionar, o bien la inspección se realiza por inmersión de la pieza en agua. En estos casos existen dos medios de propagación: el del acoplamiento (material de la cuña, suela o agua) y el de la pieza, cada uno de ellos con su propia velocidad de propagación. Por tanto, no son aplicables las técnicas mencionadas, ya que en la interfaz entre ambos materiales han de aplicarse las leyes de refracción, aspecto no considerado por los métodos conocidos para calcular las leyes focales en tiempo real.

En la actualidad, a falta de controladores de enfoque en tiempo real, los cálculos han de realizarse previamente mediante métodos numéricos. Las leyes focales resultantes deben ser programadas en memorias para su utilización posterior en tiempo real. Los requisitos de memoria son elevados y, además, en espacios separados para cada canal.

Además, es bien conocido que, cuando existe una interfaz entre dos medios con velocidades de propagación diferentes, el cálculo de las leyes focales es costoso en tiempo. En primer lugar hay que determinar el punto de entrada en la pieza de un hipotético rayo para cada elemento y cada foco según las leyes de la refracción (aplicación de la ley de Snell o del principio de Fermat), lo cual requiere un proceso de aproximaciones sucesivas para cada foco y cada elemento. Posteriormente, se determinan los tiempos de vuelo en ida y vuelta del ultrasonido en ambos medios siguiendo el rayo así determinado. Finalmente, se obtienen las leyes focales de las diferencias en los tiempos de vuelo y, de éstas, los códigos de enfoque. El proceso requiere un tiempo considerable de cálculo cuando se quiere realizar la focalización dinámica de todas las muestras adquiridas.

Por consiguiente, es muy deseable obtener un dispositivo que evite este proceso previo y facilite el cálculo de las leyes focales en tiempo real dentro del propio sistema de imagen con total generalidad, esto es, tanto para medios homogéneos como para aplicaciones con un medio de acoplamiento interpuesto entre transductor y pieza. Proporcionar tal método y dispositivo es el objeto de la presente invención.

DESCRIPCIÓN DE LA INVENCIÓN

La presente invención divulga un dispositivo calculador de adelanto de muestreo que controla en tiempo real el enfoque dinámico de todas las muestras adquiridas, operando indistintamente en medios homogéneos o en medios heterogéneos, es decir, en aplicaciones donde exista un medio de acoplamiento entre transductor y pieza. . Se entiende por tiempo real el intervalo de tiempo predefinido para que se produzca un acontecimiento.

El problema se aborda en dos pasos:

i) Una fase de preparación o *método* por el cual se obtiene un *array virtual equivalente* en tiempo de vuelo del ultrasonido que opera en un único medio, evitando las complicaciones asociadas al paso de una interfaz (refracción, etc.).

ii) Un controlador o *aparato* que, a partir de parámetros derivados de las posiciones de los elementos del array virtual equivalente, mantiene el enfoque para cada muestra adquirida en cada canal.

Por tanto, en un primer aspecto de la invención se divulga un método para el control en tiempo real del enfoque en sistemas de imagen ultrasónica que opera tanto en un medio homogéneo o cuando existe un acoplamiento interpuesto entre transductor y pieza. Los sistemas de imagen ultrasónica comprenden un array de N elementos transductores que emiten pulsos ultrasónicos con tiempos de vuelo característicos a una diversidad de puntos focales comprendidos dentro de un objeto a inspeccionar. El método para el control en tiempo real del enfoque en sistemas de imagen ultrasónica comprende calcular un array de N elementos virtual equivalente en tiempos de vuelo al array de N elementos comprendido en el sistema de imagen ultrasónica, donde las coordenadas (x_v, z_v) de cada elemento perteneciente al array de N elementos virtual se calculan a partir de las coordenadas de dos focos F_A y F_B, ambos situados en un rayo principal que parte del centro del array de N elementos transductores y el punto focal, y de la ecuación:

$$t_K = t_{CF} + t_{FA} - t_{BF} - t_{FV}$$

donde los t_{CF}, t_{FA}, t_{BF}, t_{FV} son los tiempos de vuelo característicos entre cada dos puntos indicados en los subíndices, siendo "B" el centro del array de N elementos virtual, "A" el transductor del array de N elementos transductores que recibe el eco del rayo principal y "V" el punto del array de N elementos virtual correspondiente al punto "A", y t_K es una constante independiente de la posición del punto focal; y donde el array de N elementos virtual es independiente del tipo de objeto a inspeccionar y del medio de acoplamiento entre el array de N elementos transductores y el objeto inspeccionado. Uno de los focos F_A se ubica en las proximidades de la interfaz que separa los dos medios, uno de los medios alberga al array de N elementos transductores y el otro medio alberga al objeto a inspeccionar, y el otro foco F_B se encuentra en el límite del campo cercano dado por el rango:

$$R_B = \frac{D_A^2}{4\lambda}$$

donde D_A es el tamaño de la apertura y $\lambda=c_2/f$ la longitud de onda en el segundo medio, siendo f la frecuencia fundamental del transductor. El tiempo de vuelo característico t_n de los elementos del array de N elementos virtual a un punto focal n, el cual pertenece a la diversidad de puntos focales, se obtiene en tiempo real mediante el cálculo de una estimación $\hat{t}_n$ tal que:

$$|t_n - \hat{t}_n| \leq 1/v$$

siendo v un valor arbitrario mayor que la unidad. El cálculo de la estimación $\hat{t}_n$ tiene asociado un error acotado obteniendo una variable binaria Q_n, tal que incrementa la estimación $\hat{t}_n$ en 1 o en 1-1/v para determinar la siguiente estimación $\hat{t}_{n+1}$, dependiendo de si la estimación actual es menor o mayor que el valor t_n.

En un segundo aspecto de la invención se divulga un dispositivo calculador de adelanto de muestreo que comprende dos registros, un contador, un multiplicador, cuatro sumadores y un multiplexor que calcula en tiempo real la variable binaria Q_n de un 1 bit definida en el primer aspecto de la invención. Los dos registros son cargados con unos valores iniciales determinados por las posiciones de los elementos del array de N elementos virtual definido en el primer aspecto de la invención y de un tiempo resultado del cálculo de la estimación $\hat{t}_n$ definido en el primer aspecto de la invención.

Dada la naturaleza de la presente invención, es necesario para la comprensión de la misma su apoyo en las figuras adjuntas. Por tanto, los detalles relacionados con los aspectos de la presente invención se encuentran en el apartado de "forma de realización de la invención".

DESCRIPCIÓN DE LAS FIGURAS.

Para complementar la descripción que se está realizando y con objeto de ayudar a una mejor comprensión de las características de la invención, de acuerdo con un ejemplo preferente de realización práctica de la misma, se acompaña como parte integrante de dicha descripción, un juego de dibujos en donde con carácter ilustrativo y no limitativo, se ha representado lo siguiente:

La Fig. 1 muestra una discontinuidad de medios que produce efectos de refracción sobre el ultrasonido emitido por un array y sobre los ecos devueltos por un posible reflector en el foco.

La Fig. 2 muestra la construcción de un array virtual que opera en un único medio y, por tanto, está libre de los problemas debidos a la refracción.

La Fig. 3 muestra el centro del array virtual situado en el origen de coordenadas y los elementos necesarios para el cálculo de leyes focales.

La Fig. 4 muestra una realización preferida de un controlador de enfoque que opera en tiempo real.

La Fig. 5 muestra un esquema de aplicación del controlador de enfoque a un banco de filtros de retardo fraccional.

La Fig. 6 muestra los errores en los tiempos de vuelo en ida y vuelta a todas las muestras de un ejemplo de aplicación del controlador de enfoque que opera sobre el array virtual.

FORMA DE REALIZACIÓN DE LA INVENCIÓN

Respecto del primer aspecto de la invención, la Figura 1 muestra un array (10) y una interfaz (12) que separa dos medios con velocidades de propagación c_1 y c_2 correspondientes al medio de acoplamiento y a la pieza a inspeccionar, respectivamente. Se considera que la emisión se realiza desde el centro C del array en la dirección (13) o rayo principal, en el que se ubican los focos en el interior de la pieza. El tiempo de vuelo de ida y vuelta a un foco en F y al elemento A está dado por:

$$t_{CF} + t_{FA} = \left(\frac{CE}{c_1} + \frac{EF}{c_2}\right) + \left(\frac{FG}{c_2} + \frac{GA}{c_1}\right) \qquad (1)$$

donde E y G son los puntos de cruce de la interfaz del rayo principal y del de retorno.

El cálculo anterior requiere conocer la posición de los puntos E y G. Al no existir formulaciones cerradas generales, este cálculo se realiza por métodos numéricos buscando, para todos los puntos de entrada posibles, aquellos que minimizan t_{CF} y t_{FA} para E y G, respectivamente, por aplicación del conocido principio de Fermat. También puede aplicarse la conocida ley de Snell de la refracción para evaluar las posiciones de estos puntos, conociendo la normal a la interfaz en cada punto. En ambos casos el proceso de cálculo es costoso, pues hay que repetirlo para cada uno de los focos, para todos los elementos del array y para todos los ángulos de deflexión.

Una simplificación, que es un primer objetivo de la presente invención, consiste en obtener un array virtual que, operando únicamente en el segundo medio, proporcione tiempos de vuelo a los focos prácticamente iguales a los del array real. La Figura 2 muestra el array virtual (11) en el que, para el elemento V que corresponde al A del array real, se verifica:

$$t_{BF} + t_{FV} + t_K = \frac{BF + FV}{c_2} + t_K \approx t_{CF} + t_{FA} \tag{2}$$

donde t_K es una constante independiente de la posición del foco. Para su aplicación, es preciso calcular las coordenadas de los elementos del array virtual equivalente y el valor de la constante t_K.

El array virtual evita las complicaciones del paso de la interfaz y, en particular, del cálculo de las posiciones de los puntos E y G para cada uno de los focos. Además, al operar en un único medio homogéneo con velocidad de propagación c_2, se abre la posibilidad de operar con circuitos ya conocidos de cálculo de leyes focales en tiempo real y, preferiblemente, con los que se describen posteriormente en esta memoria.

El centro B del array virtual (11) se sitúa sobre la prolongación del rayo principal, ya que la ecuación (2) se verifica para todos los elementos del array, incluido uno que estuviera ubicado en su centro.

Utilizando la ecuación (2) con el signo de igualdad:

$$t_K = t_{CF} + t_{FA} - t_{BF} - t_{FV} \tag{5}$$

La diferencia de tiempo t_{CF}-t_{BF} es una constante independiente de la posición del foco, igual a la diferencia en los tiempos de vuelo desde los centros de ambos arrays al punto de entrada E del rayo principal:

$$t_{CF} - t_{BF} = t_{CE} - t_{BE} = \Delta t_E \tag{6}$$

Los otros términos son:

$$t_{FA} - t_{FV} = \frac{AG}{c_1} + \frac{GF}{c_2} - \frac{FV}{c_2} \approx \frac{AG}{c_1} + \frac{GF}{c_2} - \left(\frac{VG}{c_2} + \frac{GF}{c_2}\right) \tag{7}$$

donde se ha considerado que el rayo de retorno FV pasa, aproximadamente, por el punto G evaluado para un foco lejano. Sustituyendo (6) y (7) en (5):

$$t_K = \Delta t_E + \frac{AG}{c_1} - \frac{VG}{c_2} \tag{8}$$

En óptica geométrica el invariante de Abbe establece que, para una interfaz de radio de curvatura mucho mayor que la distancia de la fuente a su superficie S_1 y en la región paraxial, la imagen se forma a una distancia S_2 tal que $c_1 S_1 \approx c_2 S_2$. Su aplicación a la geometría actual proporciona:

$$c_1 \cdot AG \approx c_2 \cdot VG \tag{9}$$

Sustituyendo en (8) se obtiene el valor de la constante t_K:

$$t_K = \Delta t_E + \frac{AG}{c_1}\left(1 - \frac{c_1^2}{c_2^2}\right) \tag{10}$$

Las coordenadas (x_V, z_V) de los elementos del array virtual se calculan a partir de dos focos F_A y F_B (Fig. 2) en el rayo principal y resolviendo la ecuación (2) con el signo de igualdad. Preferentemente F_A se ubica en las proximidades de la interfaz y F_B en el límite del campo cercano, dado por el rango:

$$R_B = \frac{D_A^2}{4\lambda} \qquad (11)$$

donde D_A es el tamaño de la apertura y $\lambda = c_2/f$ la longitud de onda en el segundo medio, siendo f la frecuencia fundamental del transductor. No es crítica la posición de F_B, por lo que puede utilizarse para D_A el tamaño de la apertura real, ya que el de la virtual sólo será conocido tras obtener las posiciones de sus elementos. La ubicación de F_A tampoco es crítica, pudiendo situarse dentro de la pieza a una distancia R_A tal que $0.5D_A \le R_A \le 1.5\, D_A$. En los focos F_A y F_B la ecuación (2) se cumplirá exactamente, mientras que en los focos intermedios lo hará de forma aproximada.

Una vez fijadas las coordenadas (x_{FA}, z_{FA}) y (x_{FB}, z_{FB}) de los focos F_A y F_B, se evalúa la ecuación (1) mediante los métodos numéricos descritos anteriormente (aplicación del principio de Fermat o de la ley de Snell), obteniendo los tiempos de vuelo t_A y t_B, respectivamente. Su sustitución en (2) con el signo de igualdad proporciona el par de ecuaciones:

$$\begin{aligned} \frac{\sqrt{(x_V - x_{FA})^2 + (z_V - z_{FA})^2}}{c_2} + t_K = t_A \\ \frac{\sqrt{(x_V - x_{FB})^2 + (z_V - z_{FB})^2}}{c_2} + t_K = t_B \end{aligned} \qquad (12)$$

con incógnitas x_V, z_V y t_K dado por la ecuación (10). Elevando al cuadrado:

$$\begin{aligned} (x_V - x_{FA})^2 + (z_V - z_{FA})^2 = c_2^2 (t_A - t_K)^2 \\ (x_V - x_{FB})^2 + (z_V - z_{FB})^2 = c_2^2 (t_B - t_K)^2 \end{aligned} \qquad (13)$$

Denominando:

$$\begin{aligned} &k_A = c_2(t_A - t_K) \\ &k_B = c_2(t_B - t_K) \\ &K = x_{FA}^2 - x_{FB}^2 + z_{FA}^2 - z_{FB}^2 - k_A^2 + k_B^2 \\ &a = \frac{K}{2(x_{FA} - x_{FB})} \\ &b = \frac{z_{FA} - z_{FB}}{x_{FA} - x_{FB}} \end{aligned} \qquad (14)$$

se llega a la ecuación de 2° grado:

$$A z_V^2 + B z_V + C = 0 \qquad (15)$$

en la que:

$$\begin{aligned} &A = 1 + b^2 \\ &B = 2b x_{FA} - 2ab - 2z_{FA} \\ &C = x_{FA}^2 + z_{FA}^2 + a^2 - 2a x_{FA} - k_A^2 \end{aligned} \qquad (16)$$

Resolviendo (15) se obtienen las soluciones:

$$
\begin{aligned}
z_V &= \frac{-B-\sqrt{B^2-4AC}}{2A} \quad \text{para elementos } i \leq \frac{N}{2} \\
z_V &= \frac{-B+\sqrt{B^2-4AC}}{2A} \quad \text{para elementos } i > \frac{N}{2} \\
x_V &= a - bz_V
\end{aligned}
\qquad (17)
$$

siendo *N* el número de elementos del array e *i* el índice con el rango de variación expresado.

Es importante destacar que los métodos numéricos se utilizan únicamente para dos focos (F_A y F_B) en lugar de los miles de focos que componen una señal. Por consiguiente, el cálculo es cientos de veces más rápido que la aplicación de técnicas convencionales. Además, una vez obtenidas las posiciones de los elementos del array virtual con la ecuación (17), pueden calcularse las leyes focales prescindiendo de la interfaz y, por tanto, de las complicaciones asociadas a la refracción. Esto es también más rápido pero, incluso, es innecesario con los circuitos que se presentan a continuación.

Respecto del segundo aspecto de la invención, la Figura 3 muestra el array virtual calculado según el procedimiento descrito anteriormente, donde las coordenadas de cada elemento (x_V, z_V) se evalúan por medio de la ecuación (17) y el origen de coordenadas se ha situado en el centro del array virtual B en (x_B, z_B) mediante una mera traslación:

$$x'_V = x_V - x_B, \quad z'_V = z_V - z_B \qquad (18)$$

El tiempo de vuelo en ida y vuelta de un elemento del array virtual a un foco F en estas coordenadas locales es:

$$t_F = \frac{R_F + r_F}{c_2} \qquad (19)$$

donde R_F es la distancia del centro del array al foco (camino de ida) y r_F es la distancia del foco al elemento (camino de vuelta), siendo:

$$r_F = \sqrt{R_F^2 + x'^2_V + z'^2_V - 2R_F(x'_V \sin\theta + z'_V \cos\theta)} \qquad (20)$$

El intervalo ΔR entre muestras está determinado por el periodo de muestreo T_S que, en ida y vuelta y en la pieza es:

$$\Delta R = \frac{c_2 T_S}{2} \qquad (21)$$

Tomando ΔR como unidad de medida, las distancias se corresponden con intervalos de tiempo expresados en periodos T_S. En particular, los tiempos asociados a las distancias $R_F = \{\Delta R, 2\Delta R, 3\Delta R, ...\}$ quedan representados por la secuencia de números naturales $n = \{1, 2, 3, ...\}$. Escalando R_F, r_F, x'_V y z'_V por ΔR se obtienen los valores *n*, *r*, *x* y *z*, respectivamente, que representan dichas distancias por el tiempo de vuelo en ida y vuelta en periodos T_S:

$$n = R_F / \Delta R \quad r = r_F / \Delta R \quad x = x_A / \Delta R \quad z = z_A / \Delta R \qquad (22)$$

Con esto,

$$r_n = \sqrt{n^2 + x^2 + z^2 - 2n(x\sin\theta + z\cos\theta)} \qquad (23)$$

Elevando al cuadrado y denominando $\alpha = x\sin\theta + z\cos\theta$, $\beta = x^2 + z^2$, siendo ambas constantes independientes del foco, se obtiene:

$$r_n^2 = n^2 - 2n\alpha + \beta \qquad (24)$$

De (19), el tiempo de vuelo i/v al foco *n* en intervalos T_S es,

$$t_n = \frac{n + r_n}{2} \qquad (25)$$

Esta expresión debe obtener r_n de (23), lo que requeriría circuitos demasiado complicados para operar en tiempo real. Pero, en realidad, basta obtener estimaciones $\hat{t}_n$ de t_n tales que el error sea pequeño, esto es,

$$|t_n - \hat{t}_n| \leq 1/v \qquad (26)$$

donde *v* es un valor arbitrario mayor que la unidad y, además, no es necesario que sea entero ni potencia de 2.

Por ejemplo, eligiendo v=10, el error de la estimación $\hat{t}_n$ respecto al valor real t_n será inferior a 1/10 del periodo de muestreo. Entonces, si la frecuencia de muestreo es 4 veces la del transductor, el error en la estimación del tiempo de vuelo será inferior a 1/40 el periodo de la señal. Como es conocido por los especialistas, los errores comprendidos entre 1/16 y 1/64 el periodo de la señal son aceptables por lo que, típicamente, $4 \leq v \leq 16$.

Para mantener el error acotado según (26), esta invención evalúa una variable binaria Q_n ($Q_n = \{0,1\}$) que incrementa la estimación actual $\hat{t}_n$ en 1 o en $1-1/v$ para obtener la siguiente, $\hat{t}_{n+1}$, dependiendo de si la estimación es menor o mayor que el valor actual t_n, esto es:

$$Q_n = (t_n < \hat{t}_n) \tag{27}$$

$$\hat{t}_{n+1} = \hat{t}_n + 1 - Q_n / v \tag{28}$$

La ecuación (27) determina que si la estimación es inferior al valor actual resulta $Q_n = 0$, y la ecuación (28) indica que, en este caso, para la muestra $n+1$ se mantenga el intervalo de muestreo nominal, T_S. Si, por el contrario, la estimación supera al valor actual, entonces $Q_n = 1$ y para la muestra $n+1$ el instante de muestreo se adelanta una cantidad T_S/v. En definitiva es un sistema de control que procura mantener la estimación $\hat{t}_n$ próxima al valor actual t_n, con un error absoluto inferior a T_S/v.

Las ecuaciones (27) y (28) proporcionan estimaciones con un error inferior a $1/v$ respecto al tiempo de vuelo verdadero a partir de cierto rango R_0 para el que la diferencia de tiempos de vuelo a muestras consecutivas verifica:

$$1 - \frac{1}{v} \leq t_{n+1} - t_n < 1 \tag{29}$$

En efecto, si $|\hat{t}_n - t_n| < 1/v$, la aplicación de (28) producirá $|\hat{t}_{n+1} - t_{n+1}| < 1/v$ en todo el rango en que se verifique (29). El rango mínimo R_0 depende de v y del tamaño de la apertura D y viene dado por:

$$R_0 = \frac{Dv}{4\sqrt{v-1}} \tag{30}$$

Se comprueba que, para $v=8$, la mínima apertura numérica utilizable es $F\#_{min} = R_0/D = 0.76$. Otros calculadores de leyes focales requieren $F\#_{min} > 1$ para operar con la misma precisión ($v=8$), por lo que el método descrito en esta patente opera en regiones más próximas al array con apertura completa.

Un aspecto clave de la presente invención es obtener en tiempo real los valores sucesivos de Q_n para todas las muestras $n > n_0 = [R_0/\Delta R]_{\uparrow}$ mediante un sencillo circuito. Así, el valor obtenido se utiliza para adelantar en T_S/v ($Q_n = 1$) o no adelantar ($Q_n = 0$) el instante de muestreo de la muestra n para mantener enfocada la recepción. Para ello, de (25),

$$t_{n+1} = \frac{n + 1 + r_{n+1}}{2} \tag{31}$$

$$\Delta t_n = t_{n+1} - t_n = \frac{r_{n+1} - r_n + 1}{2} \tag{32}$$

Combinando este resultado con la expresión (29) se obtiene,

$$r_n + 1 - \frac{2}{v} \leq r_{n+1} < r_n + 1 \tag{33}$$

Como en el caso de la ecuación (27), Q_n puede obtenerse de la comparación del valor estimado $\hat{r}_n$ con el actual de r_n:

$$Q_n = (r_n < \hat{r}_n) \tag{34a}$$

$$\hat{r}_{n+1} = \hat{r}_n + 1 - 2Q_n / v \tag{35}$$

Para evaluar (34a) podemos operar con los cuadrados ya que se trata de magnitudes positivas. Esto es, igualmente se puede decir que:

$$Q_n = (r_n^2 < \hat{r}_n^2) \tag{34b}$$

Así, elevando (24) al cuadrado se obtiene:

$$r_{n+1}^2 = n^2 + 2n + 1 - 2n\alpha - 2\alpha + \beta \tag{36}$$

Llamando $A = 1 - 2\alpha = 1 - 2(x\sin\theta + z\cos\theta)$, constante para un elemento y una dirección de deflexión determinados, (36) queda:

$$r_{n+1}^2 = r_n^2 + 2n + A\,, \tag{37}$$

Por otra parte, elevando (35) al cuadrado y denominando P_n=1-2Q_n/v,

$$\hat{r}_{n+1}^2 = \hat{r}_n^2 + 2P_n\hat{r}_n + P_n^2 \tag{38}$$

Restando esta ecuación de la (37),

$$r_{n+1}^2 - \hat{r}_{n+1}^2 = (r_n^2 - \hat{r}_n^2) + 2n + A - 2P_n\hat{r}_n - P_n^2 \tag{39}$$

Denominando,

$$\begin{aligned} B_n &= 2n + A \\ C_n &= P_n(2\hat{r}_n + P_n) \\ D_n &= r_n^2 - \hat{r}_n^2 \end{aligned} \tag{40}$$

se obtienen de (35) y (39) las siguientes fórmulas de cálculo iterativo:

$$\begin{aligned} B_{n+1} &= B_n + 2 \\ D_{n+1} &= D_n + B_n - C_n \\ \hat{r}_{n+1} &= \hat{r}_n + P_n \end{aligned} \tag{41}$$

Por otra parte, teniendo en cuenta (34a) y (34b):

$$Q_n = (r_n < \hat{r}_n) = (r_n^2 < \hat{r}_n^2) = (D_n < 0) \tag{42}$$

esto es, el valor de Q_n es el bit de signo de D_n. Además, como P_n=1-2Q_n/v:

Si $D_n \geq 0$ es Q_n =0 y P_n =1
Si $D_n < 0$ es Q_n =1 y P_n =1-2/v

El proceso de cálculo es aplicable a partir de un primer valor n=n_0 para el cual se establecen los valores iniciales:

$$\begin{aligned} n &= n_0 = [R_0/\Delta R]_\uparrow \\ A &= 1 - 2(x\sin\theta + z\cos\theta) \\ \hat{r}_n &= r_0 = r(n_0) \\ D_n &= D_0 = 0 \\ B_n &= B_0 = 2n_0 + A \end{aligned} \tag{43}$$

donde "↑" en $[x]_\uparrow$ representa el redondeo por exceso del argumento x.

Las variables B_n, D_n y $\hat{r}_n$ se actualizan en tiempo real para cada muestra $n > n_0$ tal y como indica las ecuaciones (41). Los restantes valores son:

$$\begin{aligned} Q_n &= (D_n < 0) \\ P_n &= 1 - 2Q_n / v \\ C_n &= P_n(2\hat{r}_n + P_n) \end{aligned} \tag{44}$$

Con esto se completa el cálculo de la variable binaria Q_n para realizar el enfoque en tiempo real por aplicación de la ecuación (45). El método se basa en evaluar los valores B_{n+1}, C_{n+1} y D_{n+1} a partir de los anteriores B_n, C_n, D_n y Q_n.

La Figura 4 muestra un circuito que realiza los cálculos de las ecuaciones (41) y (44). La lógica evalúa las tres variables registradas D_n, B_n y $\hat{r}_n$ (unidades 21, 22 y 23, respectivamente) mediante sumadores (unidades 24, 25, 26 y 27), un multiplicador (unidad 29) y un multiplexor (unidad 30). El multiplicador x2 (unidad 28) no requiere lógica, es un mero desplazamiento a la izquierda de los bits del registro R (unidad 23), añadiendo un 0 en el bit menos significativo.

Los registros R y D (unidades 21 y 23) actualizan en cada ciclo de reloj los valores $\hat{r}_n$ y D_n con los valores presentes a sus entradas respectivas, que corresponden a los valores $\hat{r}_{n+1}$ y D_{n+1} dados por (41). Por su parte, B (unidad 22) incrementa su valor en 2 unidades en cada ciclo de reloj, como indica la misma ecuación. El reloj para estas unidades es el de muestreo, de modo que la actualización de su contenido se produce en cada muestra, realizando por consiguiente el enfoque dinámico en cada muestra. Por claridad, en este esquema se ha omitido la lógica para la carga de los valores iniciales en estos registros aspecto que, por otra parte, es trivial.

El valor de Q_n está representado por el signo actual de D_n, que es el bit más significativo del registro D (23). Éste se utiliza para controlar el multiplexor (30), de forma que si $Q_n = 0$ se selecciona $P_n = 1$ y si $Q_n = 1$ se obtiene $P_n = 1 - 2/v$, de acuerdo con lo expresado por la teoría desarrollada.

El valor de $\hat{r}_{n+1}$ se obtiene a la entrada del registro R como la suma en la unidad (24) de su contenido actual $\hat{r}_n$ con el valor P_n proporcionado por el multiplexor. El contenido de R será actualizado en el siguiente ciclo de reloj.

El cálculo de C_n requiere el valor $2\hat{r}_n$, que se obtiene en (28) por un simple desplazamiento a la izquierda de la salida de R, operación que se realiza sin coste alguno de lógica. El sumador (25) obtiene $2\hat{r}_n + P_n$, que se proporciona como una de las entradas al multiplicador (29), cuya salida es el valor $C_n = P_n(2\hat{r}_n + P_n)$.

Por su parte, el restador (26) obtiene a su salida B_n-C_n valor que, a su vez, constituye una de las entradas del sumador (27). Éste obtiene la suma final $(B_n - C_n) + D_n$ que es el valor D_{n+1} preparado a la entrada del registro D (23) para ser actualizado en el siguiente ciclo de reloj.

Este circuito presenta diversas ventajas frente a otras realizaciones. En primer lugar, utiliza un multiplicador que le da la versatilidad de poder elegir arbitrariamente la fracción v que controla el error de enfoque. Hasta ahora, se ha tratado de evitar el uso de multiplicadores por el gran número de recursos lógicos que consume esta operación. Sin embargo, los actuales dispositivos de lógica programable contienen decenas a miles de multiplicadores realizados en silicio con alta precisión, velocidad y bajo consumo energético. Por tanto, usar un multiplicador no supone una desventaja en cuanto a consumo de recursos.

Otra ventaja del circuito propuesto es la posibilidad de realizarlo con celdas dedicadas (celdas DSP) disponibles en los modernos dispositivos de lógica programable. Estas celdas no consumen recursos lógicos, tienen bajo consumo y elevada precisión, lo que dota de mayor versatilidad al diseño. Una particularidad del circuito propuesto es que se trata de un diseño en cadena, cuya segmentación es sencilla, lo que facilitaría compartir un único circuito de control de enfoque entre varios canales, con el consiguiente ahorro de recursos.

Una ventaja adicional es que el circuito proporciona una única salida de un bit (la variable Q_n) que marca el instante de muestreo en cada canal para mantener la recepción enfocada en todo el recorrido, evitando la transferencia de palabras multi-bit a otras unidades. En sí mismo el circuito descrito es un generador de reloj de muestreo para cada canal, que sólo requiere la carga de 2 parámetros iniciales (r_0 y B_0). Utilizando la salida Q_n como reloj de muestreo se mantiene la imagen ultrasónica enfocada muestra a muestra.

El circuito es útil también para calcular el tiempo de vuelo array-foco-elemento en tiempo real y, de este resultado, obtener los retardos de enfoque en periodos de muestreo, aunque este modo no sea el preferido por requerir una salida multi-bit. Para ello, basta sumar el contenido del registro R (unidad 21, $\hat{r}_n$) con el de un contador N (no mostrado) que cuenta el número de muestras n desde el disparo; dividiendo el resultado por 2, tal y como expresa la ecuación (25), se obtiene el tiempo de vuelo en ida y vuelta.

En la realización preferida de este circuito, la única salida necesaria es el valor del bit Q_n, siendo las restantes variables instrumentos para su cálculo. Para operar con conversores analógico-digitales que tienen un reloj común en todos los canales, la señal binaria Q_n se utiliza para "adelantar" en $1/v$ la señal adquirida con un reloj de muestreo de frecuencia constante. Para ello se utiliza un banco de v filtros de retardo fraccional como indica la Figura 5 para v=4.

En esta forma de aplicación de la presente invención la señal Q (32) acciona un contador de b bits (40) que selecciona la salida de uno de los v filtros de retardo fraccional mediante el multiplexor 45. Estos filtros interpolan las muestras de la señal de entrada $x_k = x(kT_S)$, con k= entero, y proporcionan a la salida muestras $y_k = x(kT_S + a/vT_S)$, con a/v = fraccionario, esto es retrasadas una fracción a/vT_S. Estos filtros son bien conocidos y su diseño está descrito, por ejemplo, en T. I. Laakso *et al.*, *Splitting the Unit Delay*, IEEE Sig. Proc. Magazine, pp. 30-58, Jan. 1996.

En el ejemplo mostrado en la figura 5, v =4 y cada filtro (unidades 41 a 44) proporciona el valor de la muestra de entrada (50) retrasada una cantidad $(1+1)\cdot T_S$, $(1+1/4)\cdot T_S$, $(1+1/2)\cdot T_S$ y $(1+3/4)\cdot T_S$, respectivamente. Esto es, el intervalo temporal entre las salidas es T_S/v, en este caso $T_S/4$. Para otros valores de v los retardos de los filtros y su número cambian de forma correspondiente.

Cuando la entrada 32 indica $Q = 1$, el contador (40) avanza y hace que el multiplexor (45) seleccione la salida del siguiente filtro de retardo fraccional para producir en la salida (51) muestras con un retardo T_S/v inferior, esto es, se adelanta la señal en T_S/v. Justamente esta es la aplicación de la ecuación 28 que, como se ha demostrado, mantiene las muestras con un error en los retardos inferior a T_S/v (ecuación 26).

El consumo de recursos de los circuitos presentados (Figuras 4 y 5) es limitado, pudiendo integrarse fácilmente en los dispositivos de lógica programable actuales. Puesto que la frecuencia de operación es la de muestreo, no existen problemas críticos para el enrutamiento de las señales.

Finalmente, aplicando la metodología descrita, estos circuitos realizan automáticamente el control del enfoque con independencia de que exista o no una interfaz interpuesta entre el transductor y la región de interés, aspecto que diferencia especialmente a esta invención de otras propuestas con anterioridad.

Ejemplo de realización

A continuación se especifica un ejemplo de realización de la presente invención con valores reales de una posible situación real. En este ejemplo se trata de realizar una imagen ultrasónica por inmersión de una pieza cilíndrica de acero. Las velocidades de propagación del ultrasonido en el agua y en la pieza son $c_1 = 1500$ m/s y $c_2 = 6000$ m/s, respectivamente. Se utiliza un array con N=32 elementos, de frecuencia central f =5 MHz y distancia entre elementos d = 0.6 mm. Todos estos valores son típicos en situaciones reales y la geometría es la mostrada en la Fig. 1, para un rayo con un ángulo de deflexión de 40° respecto a la normal en la superficie de la pieza. Este es uno de los múltiples rayos generados para realizar un barrido sectorial de la pieza.

Se ha evaluado el array virtual para esta situación, obteniéndose el resultado mostrado en la Fig. 2. Con los parámetros calculados de este array virtual, se ha obtenido el rango mínimo R_0 (ecuación 30) y, para este rango, los valores iniciales dados por la ecuación 43.

Se ha simulado la operación del circuito mostrado en la Figura 4 para el elemento 32 en un rango entre 14 mm y 144 mm de la interfaz, donde el valor inferior corresponde a R_0. Se han anotado los tiempos de vuelo en ida y vuelta proporcionados por el circuito a los focos situados a intervalos ΔR =0.075 mm en dicho rango, utilizando un factor v=8 y una frecuencia de muestreo de 40 MHz (periodo T_S = 25 ns).

Por otro lado, para contrastar estos resultados, se han calculado los tiempos de vuelo a cada uno de los focos atravesando la interfaz utilizando métodos numéricos (aplicación del principio de Fermat), esto es, teniendo en cuenta la refracción como hacen los métodos convencionales.

La Fig. 6 muestra el valor absoluto de las diferencias en los tiempos de vuelo entre uno y otro método, las cuales se consideran errores. Como puede observarse, estos son muy limitados (errores inferiores a 9 ns en todo el rango), lo que para este array representa 1/22 el periodo de la señal. Se ha repetido el proceso para todos los demás elementos, encontrándose que los errores son en todos los casos inferiores a los mostrados en la Figura 6.

Se observa que estos errores tienen dos componentes: una única oscilación en todo el rango, responsable de la mayor amplitud del error, a la que se superponen múltiples oscilaciones de pequeña amplitud. La primera componente se debe a las aproximaciones de cálculo realizadas para obtener el array virtual equivalente en un único medio. La componente de menor amplitud y variación más rápida es debida al circuito de control de enfoque, cuyo error teórico es inferior a T_S/v = 3.125 ns en este ejemplo. Se comprueba que, en efecto, las oscilaciones son inferiores a esta cantidad.

El proceso se ha repetido también para otras configuraciones, geometrías, valores de v, ángulos de deflexión, etc., encontrando en todos los casos resultados similares: bajos errores en los tiempos de vuelo que mantendrán un correcto enfoque a todas las profundidades en tiempo real.

Por otra parte, se ha verificado que si el medio es homogéneo (esto es, no existe interfaz), el array virtual coincide con el real y los únicos errores son los debidos al circuito de control del enfoque, que son inferiores a T_S/v.

Por consiguiente, se concluye que el método y circuitos descritos son válidos para mantener el enfoque controlado en toda la profundidad, tanto si se trata de un único medio homogéneo, como cuando existe un acoplamiento interpuesto entre el transductor y la pieza inspeccionada.

REIVINDICACIONES

1. Método para el control en tiempo real del enfoque dinámico en sistemas de imagen ultrasónica, donde los sistemas de imagen ultrasónica comprenden un array de *N* elementos transductores que emiten pulsos ultrasónicos con tiempos de vuelo característicos a una diversidad de puntos focales comprendidos dentro de un objeto a inspeccionar; el método está caracterizado por que comprende:

- calcular un array de *N* elementos virtual equivalente en tiempos de vuelo al array de *N* elementos transductores comprendido en el sistema de imagen ultrasónica, donde las coordenadas (x_v, z_v) de cada elemento perteneciente al array de *N* elementos virtual se calculan a partir de las coordenadas de dos focos F_A y F_B, ambos situados en un rayo principal que parte del centro "C" del array de *N* elementos transductores y el punto focal "F", y de la ecuación:

  $$t_K = t_{CF} + t_{FA} - t_{BF} - t_{FV}$$

  donde los t_{CF}, t_{FA}, t_{BF}, t_{FV} son los tiempos de vuelo característicos entre cada dos puntos indicados en los subíndices, siendo "B" el centro del array de N elementos virtual, "A" el transductor del array de *N* elementos transductores que recibe el eco del rayo principal y "V" el punto del array de *N* elementos virtual correspondiente al punto "A", y t_K es una constante independiente de la posición del punto focal; y,
  donde dicho array de *N* elementos virtual es independiente del tipo de objeto a inspeccionar y del medio de acoplamiento entre el array de *N* elementos transductores y el objeto inspeccionado.

2. Método para el control en tiempo real del enfoque dinámico en sistemas de imagen ultrasónica según la reivindicación 1, caracterizado porque uno de los focos F_A es ubicado en las proximidades de una interfaz que separa dos medios, uno de los medios alberga al array de *N* elementos transductores y el otro medio alberga al objeto a inspeccionar, y el otro foco F_B es ubicado en el límite del campo cercano, dado por el rango:

$$R_B = \frac{D_A^2}{4\lambda}$$

donde D_A es el tamaño de la apertura y $\lambda = c_2/f$ la longitud de onda en el segundo medio, siendo f la frecuencia fundamental del transductor.

3. Método para el control en tiempo real del enfoque dinámico en sistemas de imagen ultrasónica según la reivindicación 1, caracterizado por que el tiempo de vuelo característico t_n de los elementos del array de N elementos virtual a un punto focal *n*, el cual pertenece a la diversidad de puntos focales, se calcula en tiempo real mediante el cálculo de una estimación $\hat{t}_n$ tal que:

$$|t_n - \hat{t}_n| \leq 1/v$$

siendo *v* un valor arbitrario mayor que la unidad.

4. Método para el control en tiempo real del enfoque dinámico en sistemas de imagen ultrasónica según la reivindicación 3, caracterizado por que el cálculo de la estimación $\hat{t}_n$ tiene asociado un error que se encuentra acotado mediante el cálculo de una variable binaria Q_n que incrementa la estimación $\hat{t}_n$ en 1 o en 1-1/*v* para obtener la siguiente estimación $\hat{t}_{n+1}$, dependiendo de si la estimación es menor o mayor que el valor actual t_n.

5. Dispositivo calculador de adelanto de muestreo adecuado para llevar a cabo el método definido en una cualquiera de las reivindicaciones anteriores, que comprende tres registros (21, 22, 23) que cargan sendas variables iniciales, un contador, un primer multiplicador (29), cuatro sumadores (24, 25, 26, 27) y un multiplexor (30) que calcula en tiempo real la variable binaria Q_n de un 1 bit definida en la reivindicación 4; donde un sumador (26) de los cuatro sumadores recibe la señal de un registro (22) a la que le resta la señal de otro registro (21) tras pasar, dicha señal, por un multiplicador (28), otro sumador (25) de los cuatro sumadores y el primer multiplicador (29); la salida de dicho un sumador (26) se conecta a otro sumador (27) y la salida de este se conecta a un registro (23), cuya salida está conectada a la entrada del control del multiplexor (30) que conecta su salida con una de sus entradas de valor 1 y 1-2/v en función del valor de la entrada de control.

6. Dispositivo calculador de adelanto de muestreo, según la reivindicación 5, caracterizado porque los dos registros son cargados con unos valores iniciales que están determinados por las posiciones de los elementos del array de *N* elementos virtual definido en una cualquiera de las reivindicaciones 1 a 4 y de un tiempo resultado del cálculo de la estimación $\hat{t}_n$ definido en una cualquiera de las reivindicaciones 3 a 4.

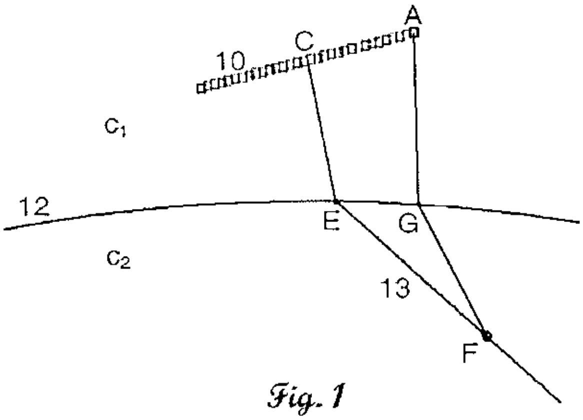

Fig. 1

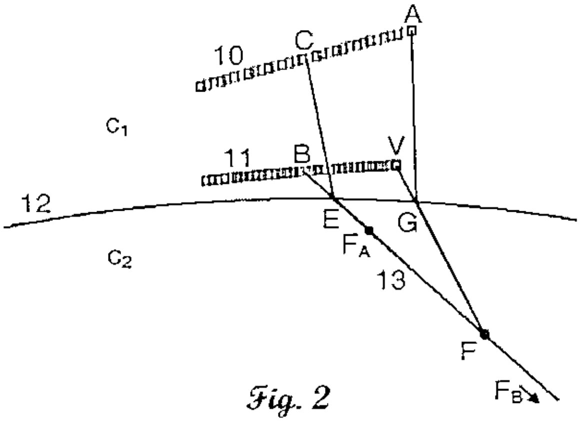

Fig. 2

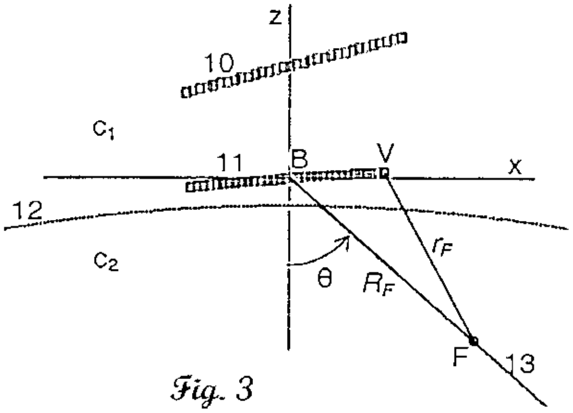

Fig. 3

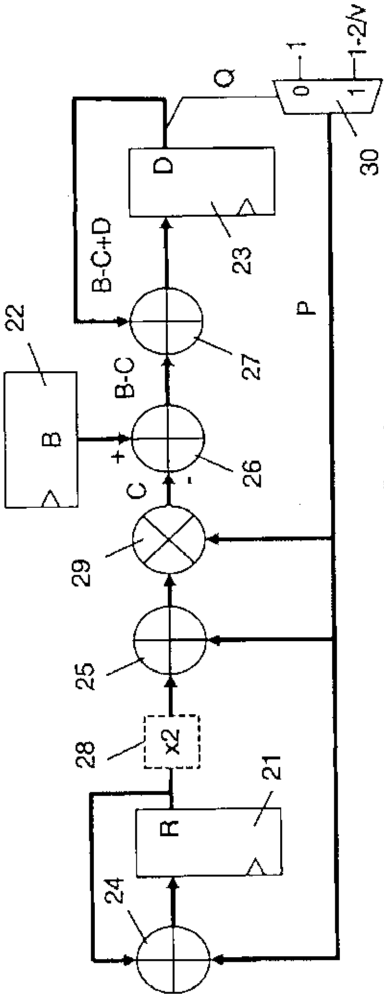

Fig. 4

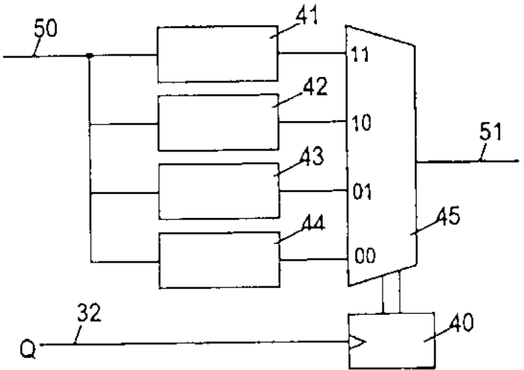
50
41
42
43
44
11
10
01
00
51
45
32
Q
40

Fig. 5

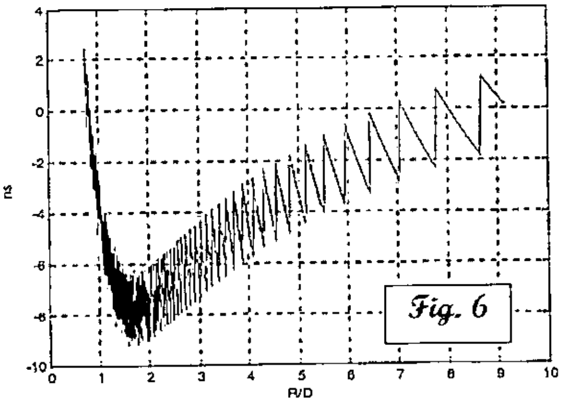
4
2
0
-2
-4
-6
-8
-10
ns
0
1
2
3
4
5
6
7
8
9
10
R/D

Fig. 6

OFICINA ESPAÑOLA
DE PATENTES Y MARCAS

ESPAÑA

㉑ N.º solicitud: 201230799

㉒ Fecha de presentación de la solicitud: 25.05.2012

㉜ Fecha de prioridad:

INFORME SOBRE EL ESTADO DE LA TECNICA

(51) Int. Cl. : *G02B7/40* (2006.01)
A61B8/00 (2006.01)

DOCUMENTOS RELEVANTES

Categoría	(56) Documentos citados	Reivindicaciones afectadas
A	IEEE transactions on ultrasonics, ferroelectrics, and frequency control, vol. 45, no. 4; YOUSSRY Y. BOTROS, EMAD S. EBBINI Y JOHN L. VOLAKIS; "Two-Step Hybrid Virtual Array-Ray (VAR) Technique for Focusing Through the Rib Cage" Documento recuperado de internet <URL: http://ieeexplore.ieee.org/stamp/stamp.jsp?arnumber=710577>, [recuperado el 20.01.2015] fecha 31.07.1998, toda la página web.	1-6
A	WO 2011156624 A2 (UNIV MINNESOTA et al.) 15.12.2011, resumen; figuras, especialmente la 1,4B,7E; párrafos 3,16,188,198,211,212,215.	1-6
A	US 2003149362 A1 (AZUMA TAKASHI et al.) 07.08.2003, resumen; figuras, especialmente la 12; párrafos 4,6,14,15,49.	1-6
A	US 2002145941 A1 (POLAND MCKEE D et al.) 10.10.2002, resumen; figuras; párrafos 3-5,12,43-45.	1-6
A	WO 2007056104 A2 (VISUALSONICS CORP et al.) 18.05.2007, resumen; figuras; párrafos 92,93,141-143,146,160,165.	1-6
A	ES 2046973 T3 (ACUSON) 16.02.1994, resumen; figuras; columnas 1,3.	1-6
A	Xilinx Inc., "Xtreme DSP DSP-48A for Spartan 3A DSP FPGAs," User Guide, ug-431, Documento recuperado de internet <URL: http://www.xilinx.com/support/documentation/user_guides/ug431.pdf>, [recuperado el 20.01.2015] fecha 31.12.2008, toda la página web.	5-6

Categoría de los documentos citados
X: de particular relevancia
Y: de particular relevancia combinado con otro/s de la misma categoría
A: refleja el estado de la técnica
O: referido a divulgación no escrita
P: publicado entre la fecha de prioridad y la de presentación de la solicitud
E: documento anterior, pero publicado después de la fecha de presentación de la solicitud

El presente informe ha sido realizado
☒ para todas las reivindicaciones ☐ para las reivindicaciones nº:

Fecha de realización del informe	Examinador	Página
21.01.2015	A. López Ramiro	1/5

Documentación mínima buscada (sistema de clasificación seguido de los símbolos de clasificación)

G02B, A61B

Bases de datos electrónicas consultadas durante la búsqueda (nombre de la base de datos y, si es posible, términos de búsqueda utilizados)

INVENES, EPODOC

Fecha de Realización de la Opinión Escrita: 21.01.2015

Declaración

Novedad (Art. 6.1 LP 11/1986)	Reivindicaciones	1-6	SI
	Reivindicaciones		NO
Actividad inventiva (Art. 8.1 LP11/1986)	Reivindicaciones	1-6	SI
	Reivindicaciones		NO

Se considera que la solicitud cumple con el requisito de aplicación industrial. Este requisito fue evaluado durante la fase de examen formal y técnico de la solicitud (Artículo 31.2 Ley 11/1986).

Base de la Opinión.-

La presente opinión se ha realizado sobre la base de la solicitud de patente tal y como se publica.

1. Documentos considerados.-

A continuación se relacionan los documentos pertenecientes al estado de la técnica tomados en consideración para la realización de esta opinión.

Documento	Número Publicación o Identificación	Fecha Publicación
D01	IEEE transactions on ultrasonics, ferroelectrics, and frequency control, vol. 45, no. 4; YOUSSRY Y. BOTROS, EMAD S. EBBINI y JOHN L. VOLAKIS; "Two-Step Hybrid Virtual Array-Ray (VAR) Technique for Focusing Through the Rib Cage" Documento recuperado de internet <URL: http://ieeexplore.ieee.org/stamp/stamp.jsp?arnumber=710577>.	31.07.1998
D02	WO 2011156624 A2 (UNIV MINNESOTA et al.)	15.12.2011
D03	US 2003149362 A1 (AZUMA TAKASHI et al.)	07.08.2003
D04	US 2002145941 A1 (POLAND MCKEE D et al.)	10.10.2002
D05	WO 2007056104 A2 (VISUALSONICS CORP et al.)	18.05.2007
D06	ES 2046973 T3 (ACUSON)	16.02.1994
D07	Xilinx Inc., "Xtreme DSP DSP-48A for Spartan 3A DSP FPGAs," User Guide, ug-431, Documento recuperado de internet <URL: http://www.xilinx.com/support/documentation/user_guides/ug431.pdf>.	31.12.2008

2. Declaración motivada según los artículos 29.6 y 29.7 del Reglamento de ejecución de la Ley 11/1986, de 20 de marzo, de Patentes sobre la novedad y la actividad inventiva; citas y explicaciones en apoyo de esta declaración

Reivindicación 1

El documento más próximo es D01, dicho documento presenta (toda la página web) un método para el control en tiempo real del enfoque dinámico en sistemas de imagen ultrasónica, donde los sistemas de imagen ultrasónica comprenden un array de N elementos transductores que emiten pulsos ultrasónicos con tiempos de vuelo característicos a una diversidad de puntos focales comprendidos dentro de un objeto a inspeccionar. El método describe el calcular una array de N elementos virtual.

La diferencia entre el objeto de la presente solicitud y D01 se basa en calcular las coordenadas de cada elemento perteneciente al array de N elementos virtual a partir de las coordenadas de dos focos en un rayo principal que parte del centro del array de N elementos transductores y a partir de una ecuación que tiene en cuenta los tiempos de vuelo característicos. El array virtual es independiente del tipo de objeto a inspeccionar y del medio de acoplamiento entre el array de N elementos transductores y el objeto inspeccionado.

El efecto de dicha diferencia se basa en poder hacer el enfoque dinámico a pesar de los efectos refractivos en el caso de existir un interfaz, con bajo nivel de error, de forma que se convierte el caso de los dos interfaces en un caso de un medio homogéneo.

No se conocen documentos en el estado de la técnica que calculen el array virtual en función de las coordenadas de los focos, del punto focal y del tiempo de vuelo que sea independiente del medio de acoplamiento.
Se considera relevante mencionar los siguientes documentos del mismo campo técnico.

El documento D02 presenta (resumen, figuras, especialmente la 1, 4B, 7E; párrafos 3, 16, 188, 198, 211, 212 y 215) un método para el control en tiempo real del enfoque dinámico en sistemas de imagen ultrasónica, donde los sistemas de imagen ultrasónica comprenden un array de N elementos transductores que emiten pulsos ultrasónicos con tiempos de vuelo característicos a una diversidad de puntos focales comprendidos dentro de un objeto a inspeccionar. El método describe el calcular una array de N elementos virtual.

Se observa en D03 (resumen, figuras, especialmente la 12; párrafos 4, 6, 14, 15, 49) que es conocido en el estado de la técnica el uso de elementos virtuales en la generación de imágenes ultrasónicas, de forma que se realice un enfoque dinámico. En este caso se realiza el uso de una apertura de transmisión virtual.

El documento del mismo campo técnico D04 (resumen, figuras; párrafos 3-5, 12, 43-45) presenta un sistema de imagen ultrasónica con un array de elementos transductores que calcula la imagen en tiempo real.

El documento D05 (resumen, figuras, párrafos 92, 93, 141-143, 146, 160, 165) también presenta un sistema de imagen ultrasónica, con una pluralidad de elementos transductores con capacidad de ajustar dinámicamente el perfil de retrasos de recepción, actualizado según el tiempo de vuelo.

También se considera relevante mencionar el documento D06 (resumen, figuras, columnas 1 y 3), que a su vez presenta un sistema de imagen acústica con una red de transductores.

Por lo mencionado, la reivindicación 1 presenta novedad (Artículo 6 LP) y actividad inventiva (Artículo 8 LP).

Reivindicaciones 2-4

Por su dependencia con la reivindicación 1, las reivindicaciones 2-4 presentan novedad (Artículo 6 LP) y actividad inventiva (Artículo 8 LP).

Reivindicación 5

Se puede observar en D07 (toda la página web) la posibilidad de realizar el circuito mencionado en la reivindicación 5, ya que la presentación de elementos de cálculo en sí, aunque se dispongan en forma novedosa, no supone la existencia de actividad inventiva de por sí. Sin embargo, en la reivindicación 5, la disposición de los elementos tiene el efecto técnico de permitir el cálculo por hardware del adelanto de muestreo en tiempo real, y a su vez, permitir trabajar con arrays de formas arbitrarias, por lo que sí se considera que tiene actividad inventiva, al no conocerse documento del mismo campo técnico que solucione este problema. Los documentos D01-D06 presentan dispositivos de cálculo de adelanto de muestreo, que sin embargo, no hacen uso de un dispositivo que presente el efecto técnico de la reivindicación 5.

Por lo mencionado, la reivindicación 5 presenta novedad (Artículo 6 LP) y actividad inventiva (Artículo 8 LP).

Reivindicación 6

Por su dependencia con la reivindicación 5, la reivindicación 6 presenta novedad (Artículo 6 LP) y actividad inventiva (Artículo 8 LP).

Automatic Dynamic Depth Focusing for NDT

Jorge Camacho, Jorge F. Cruza, Jose Brizuela, and Carlos Fritsch, *Senior Member, IEEE*

***Abstract*—Auto-focusing along with dynamic depth focusing (DDF) would be very valuable to inspect arbitrarily shaped parts when operating with wedges or with other coupling media to avoid the burden of computing and setting the correct focal laws while still getting the best possible resolution at all depths.**

This work proposes a three-step procedure to perform the auto-focusing function with DDF in real time. First, the part geometry is estimated by the first echo time-of-arrival following one of several possible strategies: pulse–echo, pitch–catch, or plane wave. These are analyzed with regard to their performances and acquisition time, giving closed formulae to get the coordinates of interface points. After a curve fitting and extrapolation process, a virtual array that operates in a homogeneous medium is computed, avoiding the complications of refraction at the interface and allowing operation with already known focusing hardware. This hardware is initialized with the set of focusing parameters adapted to the estimated probe–part geometry, and ensures that all received samples are in focus. Using a standard computer, the auto-focusing procedure currently takes about 2 s to perform. Experiments carried out under different conditions validate the proposed technique.

I. Introduction

Phased-array technology applied to nondestructive testing (NDT) provides high-resolution images generated by scanning an inspected part with electronically controlled ultrasonic beams. Dynamic depth focusing provides higher sensitivity and quality by setting a focus at every image sample. However, unlike optical cameras, their acoustic counterparts lack the auto-focusing feature. The availability of such a function in NDT instruments is a dream held by many engineers and operators in the field. Automatic dynamic depth focusing (ADDF) would avoid the complications of computing and setting the correct focal laws, while maintaining the best possible resolution at all depths, without needing computer-aided design (CAD) geometry descriptions or additional software tools.

Currently, planar parts can be inspected with the array probe in contact. This is the simplest scenario, in which the focal laws can be computed using closed formulae from the knowledge of the array geometry and the sound propagation velocity. Furthermore, dynamic depth focusing focal laws can be pre-computed and stored in the equipment, as is usually done in medical echography.

However, for arbitrarily shaped parts or, more generally, when a coupling medium is located between the array probe and the inspected part, refraction effects must be considered. When the geometry is relatively constant, wedges tailored to the surface with motorized means to correct small misalignments have been used [1], [2].

In many situations, however, the probe-part geometry is not sufficiently well known to accurately compute the focal laws. This is a common case when the manufacturing process has no tight tolerances (casting material, molded components, non-rigid parts or parts with varying shape, soft curved plates, weld-caps, etc.) or when the relative positions of the probe and the part change. Merely a tenth of a millimeter of displacement yields timing errors of 130 ns in water immersion, which is more than half the period of a 5 MHz signal; a misalignment of the transducer probe by only 1° may lead to amplitude losses of several decibels and incorrect localization of the indications by some millimeters [3].

Water-filled bags attached to conventional array probes can be useful to adapt the probe to irregularities in the inspected part [4]. However, refraction effects must be again taken into account, unless the propagation velocities of the two media are similar (i.e., biological tissue). Another approach uses flexible array probes, in which individual elements are spring loaded, forcing them to operate in contact [5], [6]. Methods to estimate the position of the array elements with auxiliary devices or from image features have been developed, showing good behavior, although with high computational cost [7]–[9]. Furthermore, these methods demand low-speed scanning to avoid excessive wear of the transducer surface and use nonconventional probes and equipment.

The time reversal mirror technique provides automatic focusing to the strongest reflector [10], [11]. Generalization to multiple reflector detection has been proposed using iterative techniques [12], [13]. These methods demand specialized hardware and have high processing loads, so that their applications have been mostly constrained to the academic field. Furthermore, the state-of-the-art of these methods still requires the geometry description to form an image.

Recently, the self-adaptive ultrasound technique (SAUL) has been proposed as an auto-focusing alternative [14], [15]. Starting with a simultaneous trigger of all the array elements, the two-way time-of-flight to individual elements is used to set the emission focal laws for the next trigger event. After some shots, a wave-front parallel to the interface is produced and the ultrasound penetrates with normal incidence. The technique yields unfocused

Manuscript received November 2, 2013; accepted January 8, 2014. This work has been funded by project DPI 2010-17648 of the Spanish Ministry for Science and Innovation.

J. Camacho, J. F. Cruza, and C. Fritsch are with the Ultrasound Systems and Technology Group (USTG), Spanish National Research Council (CSIC), Madrid, Spain (e-mail: j.camacho@csic.es).

J. Brizuela is with the Comisión Nacional de Energía Atómica (CNEA), Consejo Nacional de Investigaciones Científicas y Técnicas (CONICET), Buenos Aires, Argentina.

DOI http://dx.doi.org/10.1109/TUFFC.2014.2955

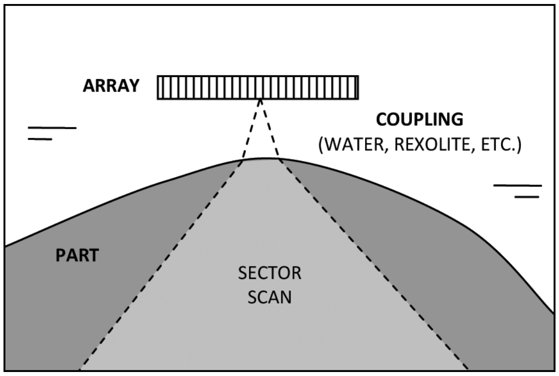

Fig. 1. Sector imaging of an arbitrarily-shaped part with a coupling medium.

images that are useful to inspect laminated structures, and requires a full-parallel ultrasound system with a high channel count to get adequate coverage of the interface.

In addition to the accurate knowledge of the array–part geometry, refraction at the interface complicates the focal law computation task. Unlike the homogeneous case with probe and part in contact, there are no closed formulae to compute the time-of-flight from every array element to every focus. This problem is frequently addressed by simulation tools, using different approaches: spatial impulse response [16], [17], propagation of monochromatic waves [18]–[20], ray-tracing methods [21]–[24], etc. In general, computing time can be an issue for dynamic depth focusing, so that focal laws are frequently obtained for a small set of foci [25].

From a practical point of view, Fermat's principle is frequently applied in searching for the minimum time-of-flight path. In the most general case, without code optimization, the required fine sampling of the interface leads to long searches. In [26], using the total focusing method (TFM), focal law computation took 49 s per image with parallel computing on GPU/CPUs. For a phased array, we proposed a fast focal law calculator (FFLC) based on the Newton–Raphson algorithm [27], which takes 2.6 s for an image of similar size in a standard computer. Real-time processing has been recently achieved for TFM using a top-performance GPU platform, but for small images (30 × 10 mm) and relatively low element count (32 array elements) [28]; the processing time is proportional to the number of image pixels and to the number of array elements.

This work addresses auto-focusing in isotropic media with soft, curved interfaces of arbitrary shape, using standard array probes and equipment. For this purpose, the array–part geometry is estimated by first echo time-of-arrival measurements and curve fitting algorithms. Two more steps follow, computing a virtual array and setting the parameters of a real-time dynamic focusing hardware, as is described in our recent work [29]. Of course, any focal-law computing procedure can be used once the probe–part geometry has been determined, which is the major concern of this paper.

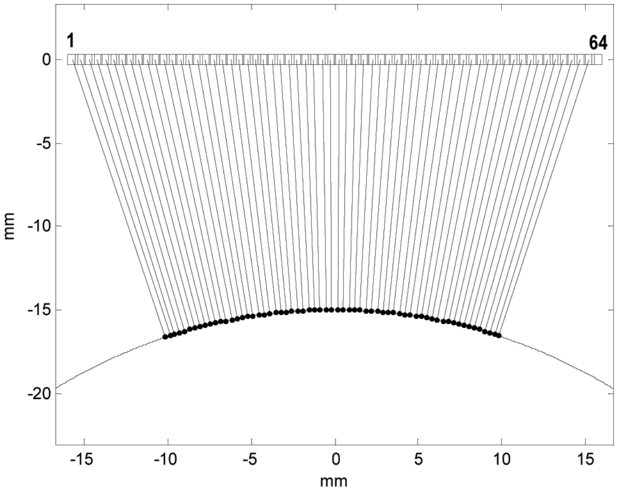

Fig. 2. Detected interface points using the pulse–echo technique.

Special attention is paid to interface geometry estimation, which is a subject poorly covered in ultrasound literature. Although this topic was previously addressed for pulsed radar [30] and ultrasonic range-finders [31], application of these methods in NDT ultrasound is not entirely evident. In this work, three techniques are proposed and analyzed: pulse–echo, pitch–catch, and plane wave. They are also experimentally tested and compared. It is shown that the proposed auto-focusing procedure provides good geometry estimation and image quality comparable to that obtained by conventional methods that require an *a priori* and accurate knowledge of the array–part geometry.

II. Interface Geometry Estimation

The inspection of arbitrarily shaped parts is frequently performed inserting a coupling material (liquid or solid) between the array and the part (Fig. 1) and generating a linear or sector scan. When the geometry is unknown, it must be first estimated. Here, three techniques are proposed to perform this task using first echo time-of-arrival measurements: pulse–echo, pitch–catch, and plane wave.

A. Pulse–Echo Interface Estimation

The interface profile can be obtained with N individual shots by measuring the time-of-flight in pulse–echo from every array element to the interface, T_i, $1 \leq i \leq N$. Fig. 2 shows the points detected in a cylindrical part of radius $R_\mathrm{C} = 32$ mm, in water immersion with a coupling path of 15 mm, by an $N = 64$-element array with $d = 0.5$ mm pitch (sound propagation velocity $c = 1480$ m/s). Only the fraction of the interface where there is normal incidence from the array elements is directly detected.

The distance from array element i to the interface is $R_i = cT_i/2$. This yields a set of N circumferences centered at the array elements and tangent to the interface, as is shown in Fig. 3. Array element i has coordinates $(x_{\mathrm{A}i}, z_{\mathrm{A}i})$,

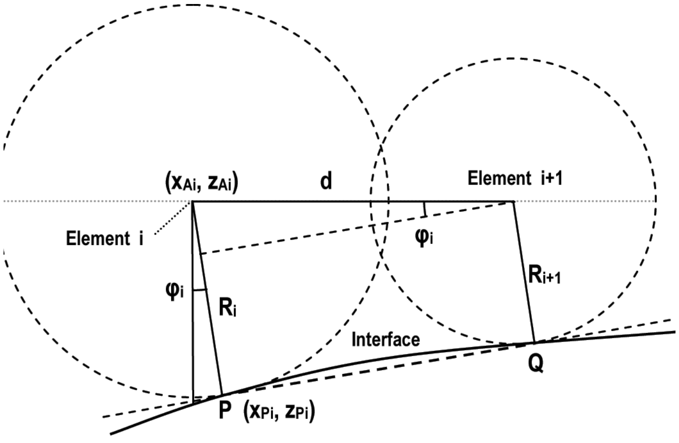

Fig. 3. The interface is defined by the envelope of N circumferences.

the element pitch is d, and the angle to the tangency point is given by:

$$\sin \phi_i = \frac{R_i - R_{i+1}}{d} = \frac{c}{2d}(T_i - T_{i+1}). \qquad (1)$$

Because R_i is normal to the interface, the coordinates of P are

$$\begin{aligned} x_{\mathrm{P}i} &= x_{\mathrm{A}i} + R_i \sin \phi_i \\ z_{\mathrm{P}i} &= z_{\mathrm{A}i} - R_i \cos \phi_i. \end{aligned} \qquad (2)$$

The only assumption made is that segments R_i and R_{i+1} are parallel. As long as d is small in relation with the local curvature radius of the interface, errors produced by this approximation will be low. In fact, for a plane interface ($R_\mathrm{C} = \infty$), this method is free from geometric errors.

The technique uses N trigger events to get $N - 1$ interface points. The acquisition time can be reduced by using one out of $M < N$ elements in pulse–echo, which results in $\sim N/M$ trigger events instead of N with d in (1) changed to $M \cdot d$. For example, for $N = 64$, $M = 8$ yields 7 interface points $\{(x_{\mathrm{P}i}, z_{\mathrm{P}i})\}$ with 8 measurements. However, reducing the acquisition time this way has some effects. The larger the distance $M \cdot d$ is, the greater are the differences in the interface slope at P and at Q, the assumption of parallelism between R_i and R_{i+M} is not as accurate, and geometric errors increase.

B. Pitch–Catch Interface Estimation

In this case, element i is used as emitter–receiver in pulse–echo and a set of M elements at every side are used as receivers in pitch–catch configuration. Fig. 4 shows the same example as in Fig. 2 for pitch–catch mode with $M = 10$ and emitters at elements $\{i\} = \{11, 32, 53\}$. In this case, 60 interface points are detected with just 3 shots.

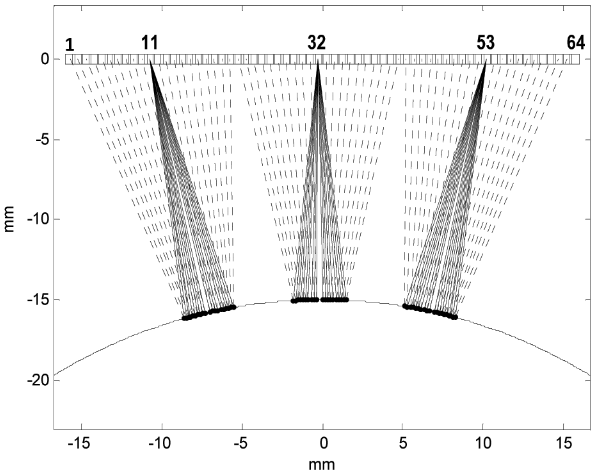

Fig. 4. Detected interface points using three trigger events and multiple receivers in pitch–catch.

Fig. 5 shows the geometry for elements i (emitter) and k (receiver) in the pitch–catch mode. The emitter-to-receiver distance is $D_{ik} = (k - i) \cdot d$. The pulse–echo time-of-flight $T_{\mathrm{A}i}$ to element i at $(x_{\mathrm{A}i}, z_{\mathrm{A}i})$ and the pitch–catch time $T_{\mathrm{AB}ik}$ from element i to the interface and back to element k are, respectively:

$$T_{\mathrm{A}i} = 2R_{\mathrm{A}i}/c, \quad T_{\mathrm{AB}ik} = (R_{1ik} + R_{2ik})/c. \qquad (3)$$

As before, the measured time $T_{\mathrm{A}i}$ determines a circumference of radius $R_{\mathrm{A}i}$, whereas the pitch–catch value $T_{\mathrm{AB}ik}$ defines an ellipse with foci F_i and F_k at elements i and k, respectively, for which

$$R_{\mathrm{A}i} = cT_{\mathrm{A}i}/2, \quad R_{\mathrm{AB}ik} = R_{1ik} + R_{2ik} = cT_{\mathrm{AB}ik}. \qquad (4)$$

Assuming that the normal to the interface has approximately equal slope at P and at E, the angle α_{ik} of the incident ray with the normal at P is equal to the angle of the reflected ray at E. Therefore, triangles PEF_i and PEC are equal and $PC = PF_i = R_{Ai}$ and $EC = EF_i = R_{1ik}$. Now, from the cosine theorem applied to F_iCF_k,

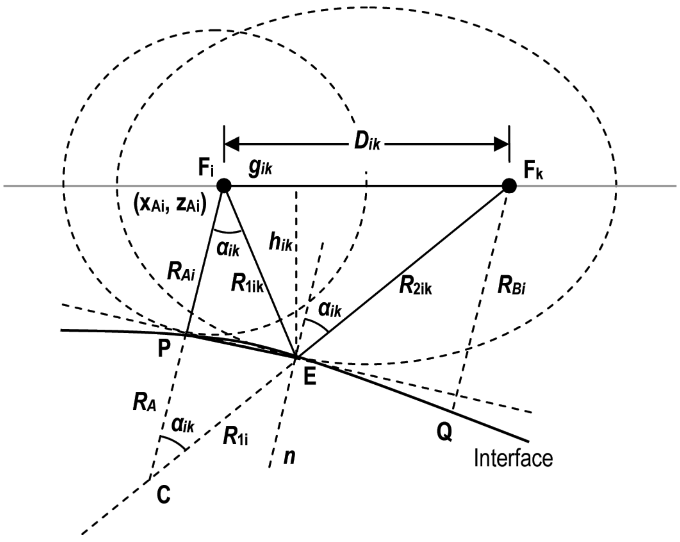

Fig. 5. Geometry of the interface profile estimation by pitch–catch.

$$D_{ik}^2 = 4R_{\mathrm{A}i}^2 + (R_{1ik} + R_{2ik})^2 - 4R_{\mathrm{A}i}(R_{1ik} + R_{2ik})\cos\alpha_{ik} \tag{5}$$

$$\cos\alpha_{ik} = \frac{4R_{\mathrm{A}i}^2 + R_{\mathrm{AB}ik}^2 - D_{ik}^2}{4R_{\mathrm{A}i}R_{\mathrm{AB}ik}}. \tag{6}$$

Substitution in $R_{\mathrm{A}i} = R_{1ik}\cos\alpha_{ik}$ yields

$$R_{1ik} = \frac{4R_{\mathrm{A}i}^2 R_{\mathrm{AB}ik}}{4R_{\mathrm{A}i}^2 + R_{\mathrm{AB}ik}^2 - D_{ik}^2}, \tag{7}$$

where all the terms at the right-hand side are known. Then,

$$R_{2ik} = R_{\mathrm{AB}ik} - R_{1ik}. \tag{8}$$

The segments g_{ik} and h_{ik} in Fig. 5 verify

$$h_{ik}^2 = R_{1ik}^2 - g_{ik}^2 = R_{2ik}^2 - (D_{ik} - g_{ik})^2 \tag{9}$$

$$g_{ik} = \frac{R_{1ik}^2 - R_{2ik}^2 + D_{ik}^2}{2D_{ik}}, \quad h_{ik} = \sqrt{R_{1ik}^2 - g_{ik}^2}, \tag{10}$$

and the coordinates (x_{Eik}, z_{Eik}) of the interface at E_{ik} are

$$x_{Eik} = x_{\mathrm{A}i} + g_{ik}, \quad z_{Eik} = z_{\mathrm{A}i} - h_{ik}. \tag{11}$$

In this way, for every trigger shot with $2M$ receivers surrounding the emitter, a set of $2M$ interface points $E(x_{Eik}, z_{Eik})$ is obtained. Although it would also be possible to compute $R_{\mathrm{B}i} = R_{\mathrm{A}i}R_{2i}/R_{1i}$ because of the similarity of triangles F_iPE and F_kQE, the errors for estimating Q would be rather high because of the departure of the interface from the straight line passing by P and E, so this option is not advisable.

With $M = 1$, two interface points are obtained for every three elements, using the central element as the emitter. In this way, $\sim N/3$ trigger events produce $\sim 2 \cdot N/3$ interface points. The geometric errors will be lower than those found by the pulse–echo technique because the assumption of parallelism of the normal at P and E fits better than at P and Q.

In an extreme case, this technique would yield $N - 2$ interface points with a single trigger from a central element, with $M = N/2 - 1$. However, care must be taken because geometric errors increase with the distance D_{ik} from the emitter to the receivers. Also, the element sensitivity decreases with higher steering angles, making the method less robust because weak interface echoes can be masked by noise. As with the pulse–echo mode, there is a trade-off between interface estimation accuracy and acquisition time.

C. Plane Wave Interface Estimation

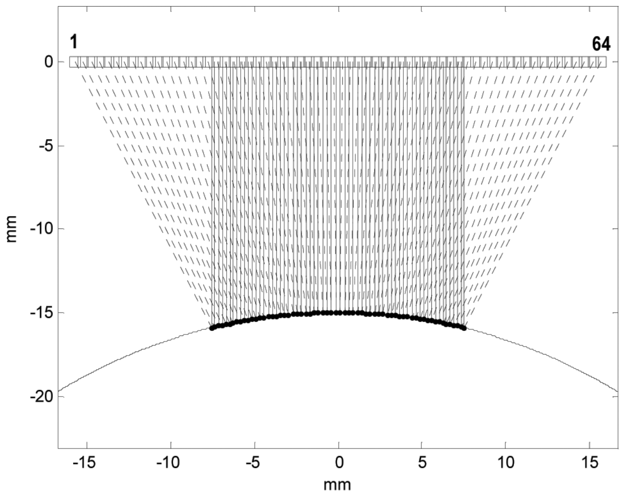

Fig. 6. Detected interface points with plane-wave excitation.

In this method, a plane wave is produced, up to some range within the near field, by simultaneously triggering all the array elements (zero-delay focal law). After emission, all the elements are used as receivers and the individual first echo arrival times are measured. Fig. 6 shows an example of this process, were only part of the plane wave produces reflections at the interface that arrive at some array element. Fig. 7 shows the basic geometry for this acquisition mode. Element i receives the echo from point P at time T_i after the wave has traveled the distances z_i and R_i. Taking into account that $z_i < 0$,

$$R_i - z_i = cT_i. \tag{12}$$

The locus of possible points $P(x, z)$ is given by

$$\sqrt{(x - x_{\mathrm{A}i})^2 + z^2} - z = cT_i \tag{13}$$

$$z = \frac{(x - x_{\mathrm{A}i})^2}{2cT_i} - \frac{cT_i}{2}. \tag{14}$$

This parabola with focus at the receiving element $(x_{\mathrm{A}i}, 0)$ is tangent to the interface at P, so that their slopes are equal:

$$\frac{\mathrm{d}z}{\mathrm{d}x} = \frac{x - x_{\mathrm{A}i}}{cT_i} = \tan\alpha_i. \tag{15}$$

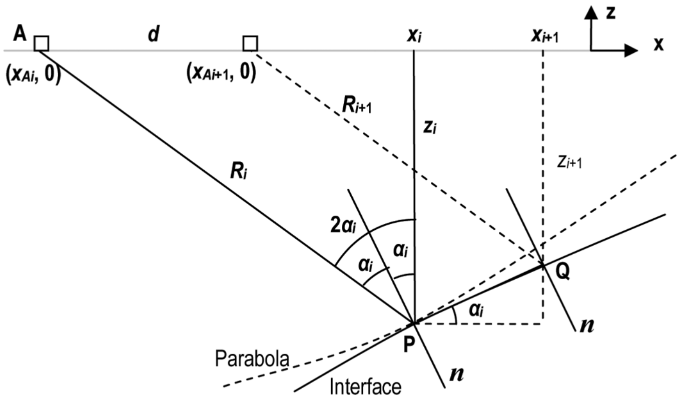

Fig. 7. Geometry for the interface estimation with a plane wave.

From Snell's law at P, the incident and reflected angles are equal to α_i. Then,

$$\begin{aligned} z_i &= -R_i \cos 2\alpha_i \\ x_i &= x_{\mathrm{A}i} + R_i \sin 2\alpha_i. \end{aligned} \tag{16}$$

Substitution into (12) yields

$$R_i = \frac{cT_i}{1 + \cos 2\alpha_i}. \tag{17}$$

Calling $\Delta L_i = c(T_{i+1} - T_i)$ and assuming that normal at P and Q are parallel:

$$R_{i+1} - R_i = \frac{c(T_{i+1} - T_i)}{1 + \cos 2\alpha_i} = \frac{\Delta L_i}{1 + \cos 2\alpha_i}. \tag{18}$$

From (16),

$$\begin{aligned} \Delta z_i &= z_{i+1} - z_i = \frac{-\cos 2\alpha_i}{1 + \cos 2\alpha_i} \Delta L_i \\ \Delta x_i &= x_{i+1} - x_i = d + \frac{\sin 2\alpha_i}{1 + \cos 2\alpha_i} \Delta L_i. \end{aligned} \tag{19}$$

After a few mathematical manipulations, the following equations are obtained:

$$\tan \alpha_i = \frac{\Delta z_i}{\Delta x_i} = \frac{(\tan^2 \alpha_i - 1)\Delta L_i}{2(d + \Delta L_i \tan \alpha_i)} \tag{20}$$

$$\Delta L_i \tan^2 \alpha_i + 2d \tan \alpha_i + \Delta L_i = 0. \tag{21}$$

Solving for $\tan \alpha_i$ and substituting into (15) yields $x = x_i$, whereas $z = z_i$ is obtained from (14), giving the coordinates (x_i, z_i) of P. Applying this procedure to all the elements $1 \leq i \leq N$ provides a set of $N - 1$ interface points with a single simultaneous trigger event.

III. Comparison of the Proposed Techniques

The three methods proposed to estimate the interface geometry have different characteristics. The pulse–echo technique is the simplest one and can be used with standard multiplexed phased-array equipment, where a linear scan with an active aperture of 1 element is performed and the first echo arrival-time is recorded. By contrast, the pitch–catch and plane wave techniques require parallel reception with a high element count, which needs higher cost full-parallel systems. Processing time is not an issue for any of these techniques, because they are based on closed formulae.

On the other hand, for a given number S of estimated interface points, the plane wave technique requires a single simultaneous trigger event, being the faster one. By contrast, the pulse–echo and the pitch–catch methods will require several trigger events, typically around $S/5$ to $S/10$, choosing $M \sim 5$.

After estimation of S interface points, a curve fitting algorithm interpolates and extends the interface beyond the detected region. The robustness of this approach depends on the measurements' accuracy, the absence of outliers, and, to a lesser extent, on the number S of points, as is discussed later.

When the interface has a completely unknown shape, but soft curvature, a second- to fourth-degree polynomial fit can be used. Abrupt changes or discontinuities would require specific fitting algorithms, like piecewise approximations. If the interface is known to be planar, a fit to a first-degree function is advisable. Finally, if the interface is circular, the modified least square algorithm (MLS) described in [32] is quite effective. These procedures are very fast in modern computers and yield an analytical representation of the interface shape.

The geometric errors associated with these techniques are mainly due to the assumption of parallelism among the normals at different points of the interface and will decrease for higher interface curvature radius. Fig. 8 shows the maximum absolute geometric errors as a function of the normalized curvature radius $R_{\mathrm{C}}/D_{\mathrm{A}}$ with $D_{\mathrm{A}} = N \cdot d$ for the three described techniques and the considered example ($N = 64$, $d = 0.6$ mm, water immersion, and cylindrical parts at 15 mm from the array). No other sources of error are considered here. The estimated interface is extrapolated using the MLS method to get enough points for inspection at normal incidence.

The higher errors correspond to the plane wave technique, although these are quite acceptable for most applications (below 2 μm for a curvature radius $R_{\mathrm{C}} = 0.5D_{\mathrm{A}}$, 16 mm in this case). The lowest errors correspond to the pitch–catch technique, where the detected interface points get closer. It is worth noting that, in all cases, the geometric errors become negligible from a practical point of view.

Geometric errors introduce some deviation in the curvature radius estimation, shown in Fig. 9 for the three

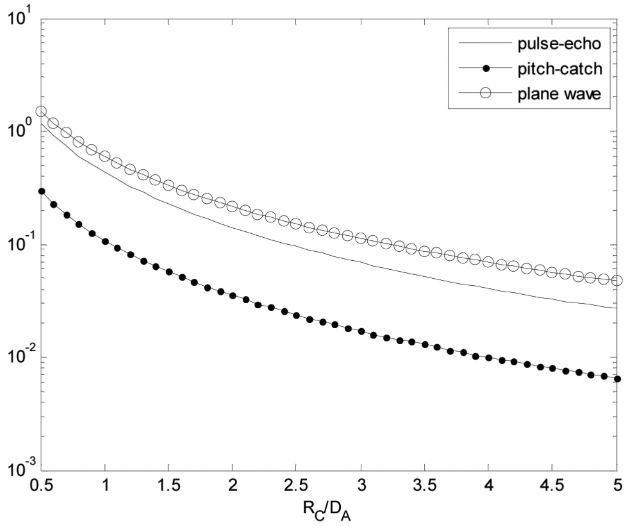

Fig. 8. Maximum geometric errors of the proposed techniques as a function of the normalized curvature radius of the inspected part.

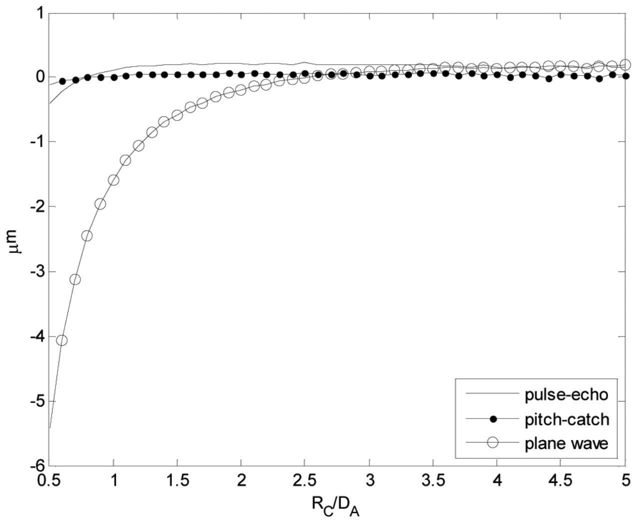

Fig. 9. Absolute errors in the estimation of the curvature radius.

proposed methods. It is higher with the plane wave method and is negligible with the pulse–echo and pitch–catch techniques.

Every technique estimates a different extent of the interface. Fig. 10 shows, in degrees, the angular region of the interface covered by the different techniques as a function of the relative curvature radius. The plane wave procedure yields a smaller range (less than 25° versus more than 40° for the lower radius part), which makes the fitting algorithm less robust. These differences decrease for higher curvature radius.

As has been shown, the intrinsic geometric errors of the proposed techniques are so low that they can be neglected in practice. However, in real applications, there are other sources of error that may be much more significant.

First, the time-of-flight is quantized by the sampling rate, which introduces an uncertainty of at least ±1 sampling period. For example, in water immersion and with a sampling rate of 160 MHz, errors of about ±5 µm in the measurements can be expected. They may become slightly reduced by the curve fitting process as long as the number p of free parameters is well below the number S of data points acquired. This is another reason to use procedures that detect a larger number of interface points. Moreover, sampling errors can be further reduced using correlation or frequency-domain methods to measure the time-of-arrival of echoes.

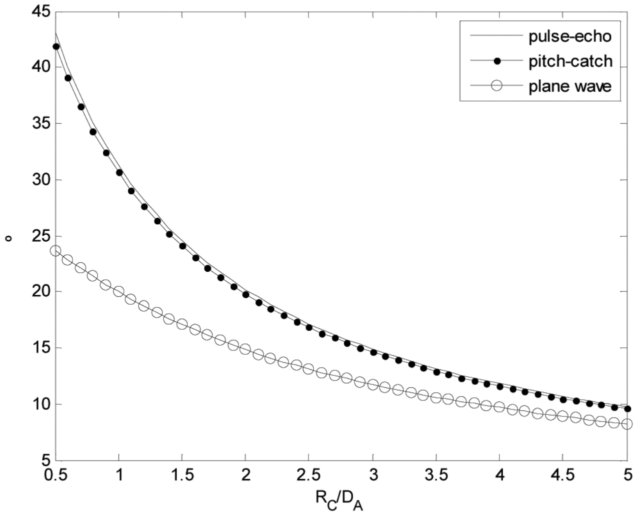

Fig. 10. Interface extent in degrees of the estimated points by the different procedures.

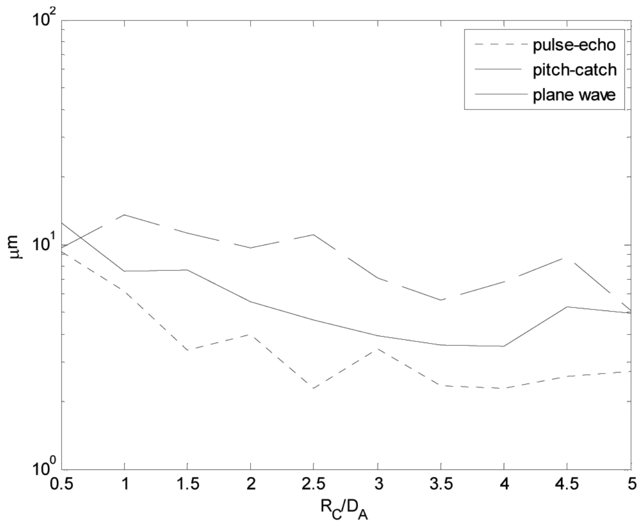

Fig. 11. Geometric errors with a 160 MHz sampling rate and water immersion.

Fig. 11 shows the effect of time quantization using a 160 MHz sampling rate. Geometric errors (around 10 µm) are well above those found before with infinite time resolution (intrinsic geometric errors), but are quite acceptable for estimating the interface shape from a practical point of view.

A different and more dangerous error source is the presence of outliers or time measurements that do not belong to echoes produced by the interface. Because only the time to the first echo is recorded, outliers can be produced by the excitation tail, noise spikes, or weak interface echoes. The estimated interface may be seriously affected by outliers, which should be removed.

Defining a blind region near the array surface will avoid detecting the excitation pulse tail as an echo. Also, keeping only the time-of-flight measurements that lie within a given time window around their neighbors, is an effective way to remove outliers and spurious measurements. Other methods reject those measurements that are some distance apart from the estimated geometry, which can be iteratively evaluated.

Another source of error may be the part geometry itself. The proposed techniques are quite robust for detecting convex shapes, even with relatively small curvature radius. However concave parts must have a large enough curvature radius, especially with the plane wave technique, because of the focusing effect of the interface toward the array center. For concave parts of small curvature radius, the crossing of the returning rays invalidates the plane-wave interface estimation procedure. By contrast, the pulse–echo and pitch–catch techniques are more robust and allow estimating the geometry of concave parts as well.

Finally, further errors can be introduced by uncertainties on the input parameters. Although the array pitch is given with high precision by the manufacturer, sound velocity in the first medium is prone to errors resulting from temperature variations and material composition. To minimize their impact, it is advisable to calibrate the system measuring the sound velocity before interface detection.

IV. Application to Automatic Focusing

After estimation of the interface geometry, focal laws must be computed and programmed to obtain the image. As proposed in [29], this is achieved in two steps: first, the complications of refraction are avoided by obtaining a nearly equivalent virtual array that operates in a single medium (the second one); then, a real-time focusing hardware per element is configured with just a few parameters. Because these procedures were covered in depth in the referred work, only a short presentation will be given here in relation to their application to automatic focusing.

A. Obtaining a Virtual Array Operating in a Single Medium

Focal law computation becomes complicated by refraction at the interface when there are two media with different propagation velocities, c_1 and c_2. The evaluation of an equivalent virtual array that operates only in the second medium completely removes this problem (Fig. 12).

For this purpose, it is postulated that the time-of-flight t_{VF} of echoes from a virtual array element V to a focus F following a straight path at propagation velocity c_2, plus a constant t_K, is approximately equal to the time t_{AF} from the corresponding real element A to focus F following the refraction laws through the entry-point at G. Mathematically,

$$t_{VF} + t_K \approx t_{AF}. \tag{22}$$

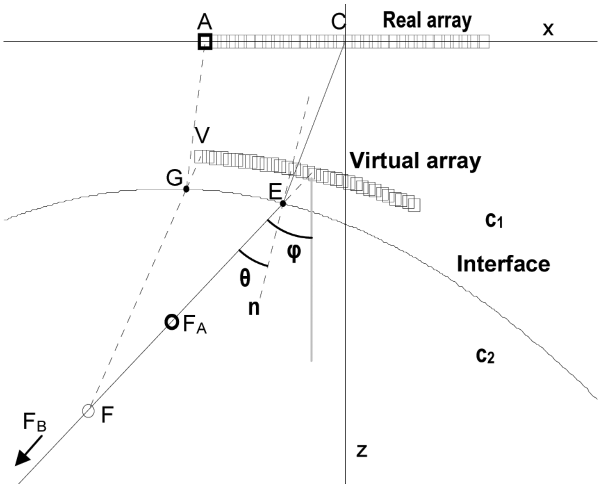

Fig. 12. Geometry of the virtual array that operates in the second medium.

By application of the Abbe's invariant,

$$t_K = t_{AG}\left(1 - \frac{c_1^2}{c_2^2}\right), \tag{23}$$

where t_{AG} is the time-of-flight from A to G, obtained along with the time-of-flight t_{AFB} from element A to focus F_B at (x_{FB}, z_{FB}) by numerical methods (applying Fermat's principle, for example). The time-of-flight t_{AFA} from element A at $(x_A,\ z_A)$ to focus F_A at (x_{FA}, z_{FA}) is also computed and the coordinates (x_V, z_V) of the virtual element at V are obtained by solving the equations

$$\begin{aligned} \frac{\sqrt{(x_V - x_{FA})^2 + (z_V - z_{FA})^2}}{c_2} + t_K &= t_{AFA} \\ \frac{\sqrt{(x_V - x_{FB})^2 + (z_V - z_{FB})^2}}{c_2} + t_K &= t_{AFB}. \end{aligned} \tag{24}$$

The virtual array provides exact time-of-flight to foci F_A and F_B and approximate values to points in between. Properly choosing F_A and F_B yields a good approximation of (22) in the F_A to F_B range. As was shown, the small errors involved in this approximation (a few nanoseconds) have little impact on NDT images.

B. Using a Real-Time Dynamic Depth Focusing Hardware

Over the years, different approaches have been proposed to perform real-time DDF for homogeneous media using specialized hardware [33]–[38]. In general, the focusing circuits iteratively compute the time-of-flight, the focusing delays, or the sampling instants to consecutive foci from a starting point. These circuits require setting some parameters before operation, which are easily computed from known variables (steering angle, element position, start sample, etc.).

However, these approaches do not work when changes of propagation media are involved. However, once the interface has been removed by the virtual array, most of these circuits can be used to perform real-time DDF. In particular, the architecture proposed in [29] offers several advantages for auto-focusing: it requires initialization of only 2 parameters, the array elements can be located anywhere (as required by the virtual array) and it consumes few hardware resources. Furthermore, it provides a timing resolution of T_S/v, where T_S is the sampling period and v is an arbitrary parameter, keeping focusing delay errors within $\pm T_S/v$ at all depths. For a virtual array of size D_V, the minimum range of operation with full aperture is given by

$$R_0 = \frac{v}{4\sqrt{v-1}} D_V. \quad (25)$$

For shorter ranges, dynamic aperture can be used. Operation with numerical apertures of f-number ≥ 1 for values $v \leq 15$ is possible.

The focusing circuit requires initialization of only two registers, whose values are computed using closed formulae from the virtual element position, the steering angle, and the sampling period. Every element requires its own focusing circuit, but its implementation with the DSP cells available in state-of-the art FPGAs allows time-multiplexing of several channels with a single cell.

C. Autofocus Operation

Auto-focusing is a very valuable tool to set up inspections, because it provides a simple and automatic means to free the operator from setting focal laws or concern about CAD-based geometry descriptions. In the current non-optimized experimental implementation, it takes about 2 s to perform the whole process using a standard computer and a Matlab (The MathWorks Inc., Natick, MA) program. When the operator pushes the autofocus button, the following process is run:

1) Estimate the interface geometry using the pulse–echo, pitch–catch, or plane-wave methods as described in Section II. The acquisition time depends on the method used.
2) For every scan-line, compute the corresponding virtual array. Currently, this task consumes about 3/4 of the time used by the auto-focusing function.
3) Compute the focusing parameters and program them in the hardware, which is fast enough to be neglected with regard to the previous tasks.

Upon completion of these steps, the hardware is ready to acquire images with DDF, automatically adapted to the actual array–part geometry and without further operator intervention.

V. Experimental Verification

Several experiments have been carried out to assess the performance of the proposed auto-focusing approach. Although all of them were carried out in water immersion for convenience, it is important to note that the method can be also applied with solid wedges. The first experiment compares the three proposed methods (pulse–echo, pitch–catch, and plane wave) for estimation of the interface geometry.

A 5-MHz, $N = 128$-elements array (Imasonic, Besançon, France) with pitch $d = 0.6$ mm was used to inspect, by water immersion, a 50-mm-radius aluminum ring located at approximately 34 mm from the array surface. A SITAU-112 ultrasound system (Dasel S.L., Madrid, Spain) with 128 active channels was used to generate and receive the ultrasound signals, controlled by a script developed in Matlab. Signals sampled at 40 MHz were upsampled by a factor of 4, giving an equivalent sampling rate of 160 MHz. All processing was carried out on an Asus K53S (AusTek Computer Inc., Fremont, CA) portable computer with an Intel Core i7 (Intel Corp., Santa Clara, CA) 2.2-GHz processor and 4 GB of RAM memory.

In all experiments, time-of-flight measurements were carried out from the trigger instant to the maximum of the envelope by programming a hardware gate with a threshold to avoid detecting noise. Despite emitting with a single element in pulse–echo and pitch–catch modes, a moderate gain was enough and noise was not an issue in either experiment because the coupling medium has low attenuation.

Fig. 13(left) shows the points detected by the pulse–echo, pitch–catch, and plane-wave interface estimation methods using 128 array elements, together with the fitted circles. Maximum part coverage (±24°) is obtained with the pulse–echo technique, whereas pitch–catch and

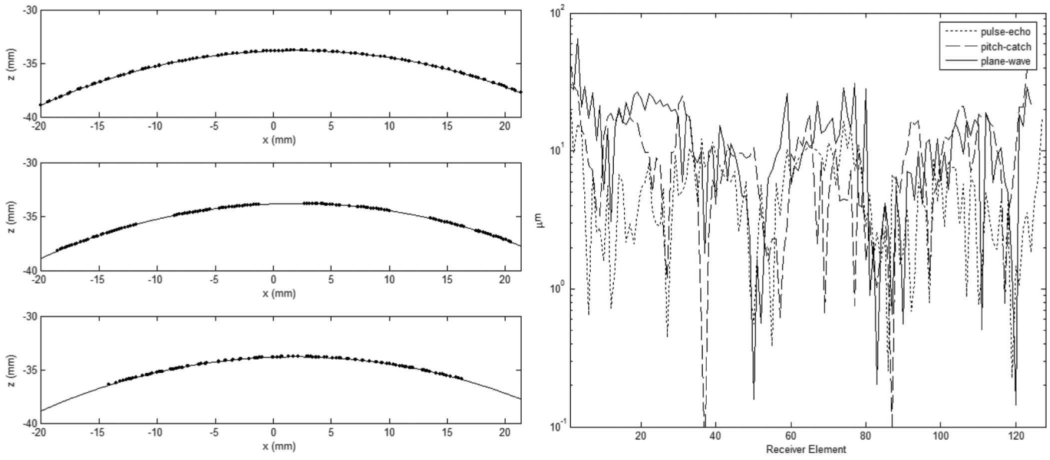

Fig. 13. (left) Estimated interface points (dots) and adjusted circle with (top) pulse–echo method, (center) pitch–catch with $M = 15$ and (bottom) plane-wave emission. (right) Reconstruction errors.

TABLE I. Interface Geometry Estimation Results.

Method	Radius (mm)	Water column (mm)	Coverage (°)	RMS reconstruction error (µm)
Pulse–echo	49.67	33.81	±24	7
Pitch–catch	49.84	33.80	±22	13
Plane-wave	49.85	33.80	±16	16

plane-wave methods obtain ±22° and ±16° respectively. In the pitch–catch method (left, center) it can be appreciated how the detected points become grouped around the four emitting elements.

Reconstruction errors are evaluated as the distances of the detected points to the estimated interface. They are comparable for all methods and do not show any pattern or tendency along the array elements (Fig. 13, right), which confirms a good fitting to a circle. RMS errors were 7, 13, and 16 µm for the pulse–echo, pitch–catch, and plane-wave methods, respectively, being of the same order as those found by simulation (Fig. 11).

Table I summarizes the results for the three acquisition methods. All of them estimate the part radius and the distance to the array with good precision, the maximum difference being 180 µm and 10 µm, respectively.

Fig. 14(left) shows a picture of the experimental arrangement; Fig. 14 (right) shows the image obtained by linear scanning with 48 active elements and normal incidence after applying the proposed auto-focusing method (pulse–echo estimation of the interface was used). The interface, the bottom echo, and the 1.5-mm side-drilled holes (SDHs) are correctly imaged and with the expected lateral resolution according to the aperture size. The amplitude of the leftmost SDH in the second row is lower because of shadowing effects. All images in this section are represented with a linear color scale.

Images obtained with pitch–catch and plane-wave detection methods are not shown because they are indistinguishable from that obtained with the pulse–echo technique, as was expected because of the small differences in the interface estimation (Table I). From here to the end of the document, the detection method used is pulse–echo with 128 elements.

A second experiment was conducted using an aluminum 90° sector located some unknown distance apart from the array probe, which is arbitrarily tilted with regard to the part surface [Fig. 15(a)]. After performing the auto-focusing process fitting of the interface to a third-degree polynomial, a sector image was obtained using an active aperture of 96 elements [Fig. 15(b)]. Fig. 15(c) shows a detail around the two groups of SDHs. The effect of DDF keeping a good lateral resolution and sensitivity at all depths can be appreciated.

In a third experiment, an arbitrarily shaped concave aluminum part with several SDHs was used [Fig. 16(a)]. The water path from the center of the array probe was approximately 35 mm. Fig. 16(b) shows the B-scan obtained by pulse–echo from every array element, with the straight line showing the end of the blind region used to suppress the pulser tail and marks where echoes were detected. Fig. 16(d) shows the calculated interface points and the extrapolated interface, fitting to a third-degree polynomial by the least squares method.

After estimating the interface, virtual array and focusing parameters were computed for a sector scan of ± 45° using 128 active elements. The resulting phased-array image is shown in Fig. 16(c). All the SDHs in the field of view are clearly seen, with the expected lateral resolution according to the aperture size. A slight improvement on the resolution, barely perceptible in the image, was obtained by fitting to a sixth-degree instead of a third-degree polynomial.

Fig. 17(a) shows a final example with the same part but in a region where the surface changes its slope. The interface estimated by fitting a third-degree polynomial is shown in Fig. 17(b). Note that although it does not exactly match the part shape at the left, the detected region

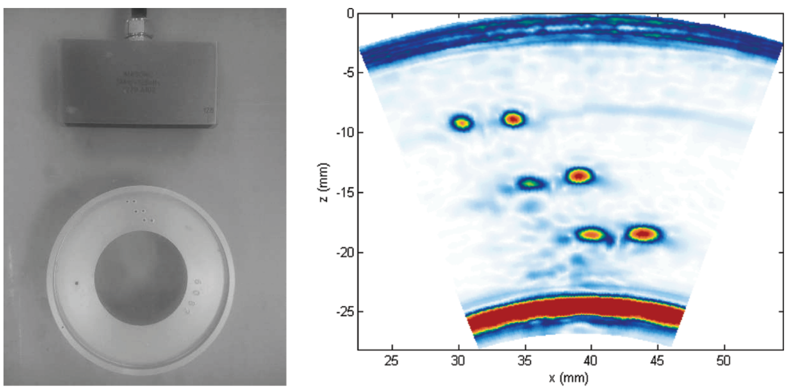

Fig. 14. (left) Experimental arrangement, aluminum ring with 3 rows of pairs of SDHs. (right) Linear scan image following the auto-focusing process with the pulse–echo technique.

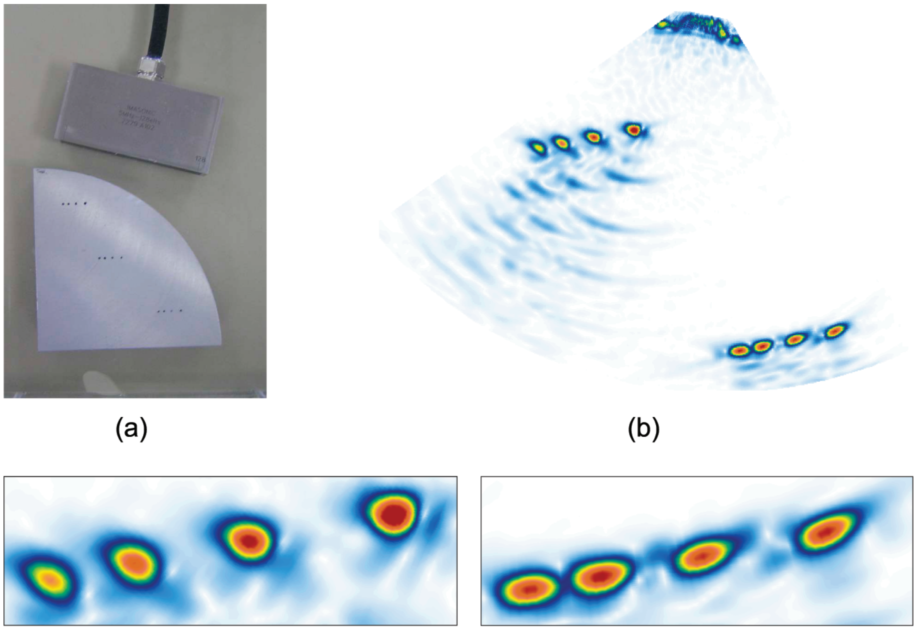

Fig. 15. (a) Probe-part arrangement; (b) phased array sector image; (c) detail of the SDHs.

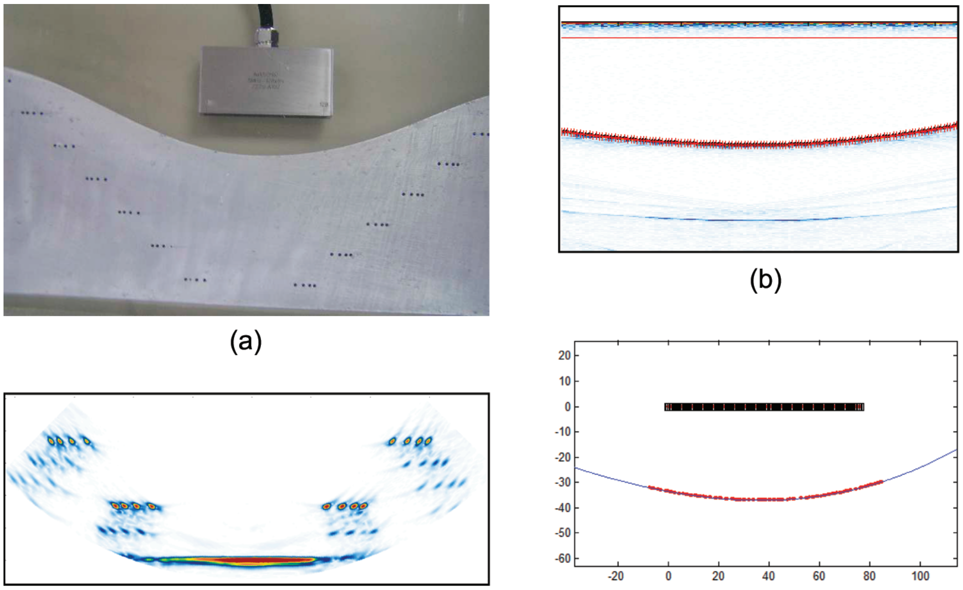

Fig. 16. (a) Inspection of a concave part in water immersion; (b) linear scan with 1 active element to detect the interface; (c) obtained image with 128 active elements and ± 45° steering; (d) representation of the array probe and the calculated interface.

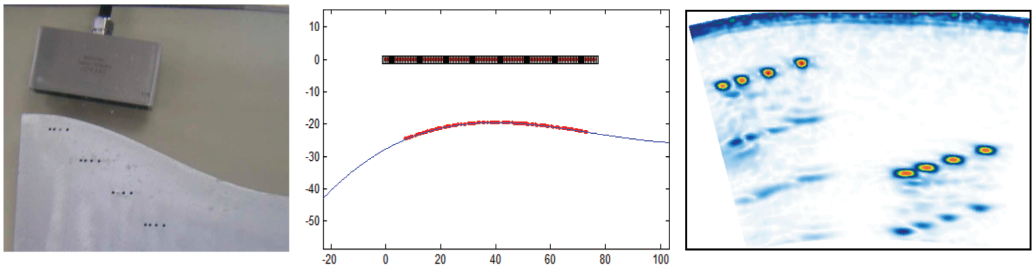

Fig. 17. (a) Probe-part geometry; (b) detected points and extrapolated interface; and (c) linear scan image.

extent is enough to perform a linear scan at 0° and 32 active elements, as shown in Fig. 17(c).

VI. Conclusions

This work proposes an automatic dynamic focusing procedure particularly addressed to applications in which the probe–part geometry is unknown. The auto-focusing function requires knowledge of the propagation velocities in both media and the element pitch of the array. No further information is required. It produces dynamically depth focused images of high quality, competing with those acquired with focal laws computed from a perfectly known geometry using specialized software tools. Furthermore, it can be applied with conventional array probes and equipment.

Auto-focusing avoids the burden of computing and programming focal laws and the complications of CAD-based geometry descriptions, and is an effective tool to adapt to changes in the probe–part geometry during the inspection. It is even faster than conventional procedures based on software tools to compute the focal laws: the current non-optimized implementation (Matlab code), computes and programs the required dynamic depth focusing information in about 2 s using a standard PC for a 128-element array and 100 steering angles.

The auto-focusing procedure is based on three steps: 1) estimation of the array-part geometry, 2) computing a virtual array for every steering angle, and 3) computing the small set of parameters needed by a real-time dynamic focusing circuit. In this work, three methods have been analyzed to perform the first step, based on pulse–echo, pitch–catch, and plane wave measurements of the first echo time-of-arrival.

Theoretically and experimentally, it has been shown that, with regard to accuracy, all of these methods are equivalent for the estimation of the interface geometry. In practice, their main differences reside in the time spent to perform the measurements for a given number of detected interface points. The pulse–echo method is the slower one, requiring N measurements to get $N - 1$ interface points. By contrast, the plane wave technique obtains $N - 1$ interface points with a single simultaneous emission and the pitch–catch one gets about the same number of points with a few shots. However, although the pulse–echo technique can be applied with standard phased array equipment, the pitch–catch and the plane wave methods require full-parallel receiving instruments.

Experimental work is in agreement with theoretical predicted errors, which are of a few micrometers in the estimation of curvature radius and position. These errors may be even lower than those produced in real applications using CAD descriptions of the geometry because of undetected small misalignments between the probe and the part, whereas auto-focusing considers their actual true relative positions.

References

[1] F. Young, C. Uyehara, and H. Bui, “Ultrasonic testing of corner radii having different angles and sizes,” U.S. Patent US2009/02111361 A1, Aug. 27, 2009.

[2] R. Meier, J. Becker, and T. Rehfeldt, “Method for the ultrasound testing of a workpiece within a curved region of its surface and device suitable for the execution of the process,” U.S. Patent 7516664 B2, Apr. 14, 2009.

[3] S. Chatillon, S. Mahaut, and P. Dubois, “Simulation of advanced UT phased array techniques with matrix probes and dynamic settings for complex component inspections,” *Rev. Quant. Nondestruct. Eval.*, vol. 28, pp. 864–871, 2009.

[4] R. Long, J. Rusell, and P. Cawley, “Non-destructive inspection of components with irregular surfaces using a conformable ultrasonic phased array,” in *6th Int. Conf. NDE in Relation to Structural Integrity for Nuclear and Pressurized Components*, 2007, pp. 1–9.

[5] O. Casula, C. Poidevin, G. Cattiaux, and G. Fleury, “A flexible phased array transducer for contact examination of components with complex geometry,” in *16th Conf. Nondestructive Testing*, 2004, art. no. 773.

[6] G. Toullelan, A. Nadim, O. Casula, P. Dumas, E. Abittan, and L. Doudet, “Inspection of complex geometries using flexible phased array transducers,” in *17th World Conf. Nondestructive Testing*, 2008, art. no. 391.

[7] O. Roy, S. Mahaut, and S. Chatillon, “Ultrasonic inspection of complex geometry component specimen with a smart flexible contact phased array transducer: Modeling and applications,” in *Proc. IEEE Ultrasonics Symp.*, 2000, pp. 763–766.

[8] A. Hunter, B. Drinkwater, and P. Wilcox, “Autofocusing ultrasonic imagery for non-destructive testing and evaluation of specimens with complicated geometries,” *NDT Int.*, vol. 43, no. 2, pp. 78–85, 2010.

[9] A. Hunter, B. Drinkwater, and P. Wilcox, “Least-squares estimation of imaging parameters for an ultrasonic array using known geometric image features,” *IEEE Trans. Ultrason. Ferroelectr. Freq. Control*, vol. 58, no. 2, pp. 414–426, 2011.

[10] M. Fink, C. Prada, F. Wu, and D. Cassereau, “Self focusing in inhomogeneous media with ‘time reversal’ acoustic mirrors,” in *Proc. IEEE Ultrasonics Symp.*, 1989, pp. 681–686.

[11] M. Fink, “Time reversal of ultrasonic fields—Part I: Basic principles,” *IEEE Trans. Ultrason. Ferroelectr. Freq. Control*, vol. 39, no. 5, pp. 555–566, 1992.

[12] C. Prada, F. Wu, and M. Fink, “The iterative time reversal mirror: A solution to self-focusing in pulse–echo mode,” *J. Acoust. Soc. Am.*, vol. 90, no. 2, pp. 1119–1129, 1991.

[13] C. Prada, M. Tanter, and M. Fink, “Flaw detection in solid with the DORT method,” in *Proc. IEEE Ultrasonics Symp.*, 1997, pp. 679–683.

[14] S. Robert, O. Casula, O. Roy, and G. Neau, “Real-time inspection of complex composite structures with a self-adaptive ultrasonic technique,” in *18th World Conf. Non Destructive Testing,* 2012, art. no. Tu.4.B.2.

[15] S. Robert, O. Casula, M. Njiki, and O. Roy, “Assessment of real-time techniques for ultrasonic non- destructive testing,” *Rev. Quant. Nondestruct. Eval.*, vol. 31, pp. 1960–1967, 2012.

[16] P. R. Stepanishen, “Transient radiation from pistons in an infinite planar baffle,” *J. Acoust. Soc. Am.*, vol. 49, no. 5B, pp. 1629–1638, 1971.

[17] F. Buiochi, O. Martínez, L. G. Ullate, and F. Montero, “A computational method to calculate the longitudinal wave evolution caused by interfaces between isotropic media,” *IEEE Trans. Ultrason. Ferroelectr. Freq. Control*, vol. 51, no. 2, pp. 181–192, 2004.

[18] T. Huttunen, M. Malinen, J. P. Kaipio, P. J. White, and K. Hynynen, “A full-wave Helmholz model for continuous-wave ultrasound transmission,” *IEEE Trans. Ultrason. Ferroelectr. Freq. Control*, vol. 52, no. 3, pp. 397–409, 2005.

[19] A. Ibañez, M. Parrilla and J. Villazón, “Simulation of ultrasonic continuous wave fields in homogeneous media with soft curved interfaces,” in *9th European Conf. NDT*, 2006, art. no. Th.3.3.1.

[20] A. Ibañez, C. Fritsch, M. Parrilla, and J. Villazón, “Monochromatic transfer matrix method for acoustic field simulation thorough media boundaries,” *Phys. Proc.*, vol. 3, no. 1, pp. 883–890, 2010.

[21] L. Leber, O. Roy, and N. Jazayeri, “Applications of phased array techniques to NDT of industrial structures,” in *2nd Int. Conf. Technical Inspection and NDT*, 2008, art. no. 72.

[22] D. Richard, D. Reilly, J. Berlanger, and G. Maes, (2010, Sep.). "Software tools for the design of phased array UT inspection techniques," in *Simulation in NDT 2010*, [Online]. Available: http://www.ndt.net/article/SimNDT2010/papers/9_Richard.pdf

[23] C. Poidevin, O. Roy, S. Chatillon, and G. Cattiaux, "Simulation tools for ultrasonic testing," in *Proc. 3rd Int. Conf. NDE in Relation to Structural Integrity for Nuclear and Pressurized Component*, 2001, art. no. 105.

[24] P. Calmon, S. Mahaut, S. Chatillon, and O. Roy, "Simulation of phased array techniques for realistic NDE configurations," *Proc. IEEE Ultrasonic Symp.*, 2002, pp. 723–727.

[25] J. Liang, Z. Wang, Y. Shi, "Ultrasonic inspection of thick parts with phased array dynamic focusing," in *European Conf. NDT 2010*, art. no. 1.3.91.

[26] M. Suttcliffe, M. Weston, B. Dutton, and I. Cooper, "Real-time full matrix capture with auto-focusing of known geometry through dual layered media," in *NDT Conf. of the British Institute of Non-Destructive Testing*, 2012, art. no. 3A1.

[27] M. Parrilla, J. Brizuela, J. Camacho, A. Ibaez, P. Nevado, and C. Fritsch, "Dynamic focusing through arbitrary geometry interfaces," *Proc. IEEE Ultrasonics Symp.*, 2008, pp. 1195–1198.

[28] M. Sutcliffe, M. Weston, P. Charlton, K. Donne, B. Wright, and I. Cooper, "Full matrix capture with time-efficient auto-focusing of unknown geometry through dual-layered media," *Insight*, vol. 55, no. 6, pp. 297–301, Jun. 2013.

[29] J. F. Cruza, J. Camacho, L. Serrano-Iribarnegaray, and C. Fritsch, "New method for real-time focusing through interfaces," *IEEE Trans. Ultrason. Ferroelectr. Freq. Control*, vol. 60, no. 4, pp. 739–751, 2013.

[30] T. Sakamoto and T. Sato, "A target shape estimation algorithm for pulse radar systems based on boundary scattering transform," *IEICE Trans. Comm. E*, vol. 87-B, no. 5, pp. 1357–1365, 2004.

[31] B. Barshan, "Ultrasonic surface profile estimation by spatial voting," in *Proc. IEEE Instrum. Meas. Technology Conf.*, 2001, pp. 583–588.

[32] D. Umbach and K. N. Jones, "A few methods for fitting circles to data," *IEEE Trans. Instrum. Meas.*, vol. 52, no. 6, pp. 1881–1885, 2003.

[33] K. Jeon, M. H. Bae, S. B. Park, and S. D. Kim, "An efficient real time focusing delay calculation in ultrasonic imaging systems," *Ultrason. Imaging*, vol. 16, no. 4, pp. 231–248, 1994.

[34] M. Bae, "Focusing delay calculation method for real-time digital focusing and apparatus adopting the same," U.S. Patent 5 836 881, 1998.

[35] H. T. Feldkämper, R. Schwann, V. Gierenz, and T. G. Noll, "Low power delay calculation for digital beamforming in handheld ultrasound systems," in *Proc. IEEE Ultrasonics Symp.*, 2000, vol. 2, pp. 1763–1766.

[36] B. G. Tomov and J. A. Jensen, "Compact implementation of dynamic receive apodization in ultrasound scanners," *Proc. SPIE*, vol. 5373, pp. 260–271, 2004.

[37] I. Lie and M. E. Tanase, "About the possibility to implement a nonuniform oversampling receive beamformer in a FPGA," in *Proc. IEEE Ultrasonics Symp.*, 2005, pp. 1404–1407.

[38] R. Alexandru, "Delay controller for ultrasound receive beamformer," U.S. Patent 7 804 736 B2, 2010.

Jorge Camacho was born in Montevideo, Uruguay, in 1979. He received the B.S degree in electronic engineering from the Universidad de la República, Uruguay (UdeLaR), in 2004. He received the Ph.D. degree in systems and automation engineering from the Universidad Complutense de Madrid (UCM) in 2010. Since 2005, he has been an associate researcher at the Spanish National Research Council (CSIC). His research interests include high-resolution acoustic imaging, real-time beamforming, and new imaging methods for medical and NDT applications.

Jorge F. Cruza was born in Madrid, Spain, in 1983. He obtained the B.S. degree in telecommunication engineering in 2009 and the M.S. degree in electronics in 2011, both from the Universidad de Alcalá (UAH). He is currently Ph.D. student at UAH. Since 2010, he has been an Associate Researcher at the Spanish National Research Council (CSIC). His research interests include high-resolution acoustic imaging, real-time beamforming, and FPGA signal processing.

Jose Brizuela was born in Córdoba, Argentina, in 1977. He received the B.S. degree in electronic engineering from the National Technological University of Argentina (UTN-FRC) in 2002. Then, in 2007, he obtained the M.S. degree in information technology from the Technical University of Madrid, Spain (EUI-UPM). In 2010, he achieved his doctoral degree from the Complutense University of Madrid, Spain (UCM). Since 2005, he has been working on research activities at the Spanish National Research Council (CSIC). In 2012, he moved to Argentina to work as a research scientist for the National Scientific and Technical Research Council (CONICET) and technology consultant for the National Atomic Energy Commission (CNEA). His research interests include nondestructive testing (NDT) by ultrasound techniques (UT) for industrial and medical applications, ultrasonic imaging, beamforming, phased array systems, conventional UT and advanced backscattering UT (AUBT) techniques, embedded and real time systems, FPGA & GPU programming, data processing, and system integration and transfer technology activities.

Carlos Fritsch was born in Madrid, Spain, in 1948. He obtained the M.S. degree in telecommunication engineering and the Ph.D. degree in informatics from the Universidad Politécnica de Madrid, in 1971 and 1988, respectively. Since 1972, he has been a member of the scientific staff at the Spanish National Research Council (CSIC). In the last 22 years, he has headed several research projects in the field of ultrasound technology. His research interests include digital signal processing applied to the field of ultrasound, beamforming and processing architectures, ultrasound imaging, fast focal law computing algorithms, and new methods for NDT and medical applications.

AUTOFOCUS: ENFOQUE AUTOMÁTICO PARA PHASED ARRAYS

J. F. Cruza[1], J. Camacho[1], C. Fritsch[1], R. González-Bueno[2], R. Giacchetta[2]

[1] *ITEFI-CSIC, c/Serrano 144, 28006 Madrid, carlos.f@csic.es*

[2] *DASEL, S.L., Av. Madrid 84, 28500 Arganda, Madrid, ricardo@daselsistemas.com*

RESUMEN

La inspección con phased arrays requiere definir el conjunto de leyes focales en emisión y recepción que dependen de la geometría y de las velocidades de propagación en acoplante y pieza. Para su cálculo suelen utilizarse programas de simulación junto a descripciones CAD de la geometría.

La tecnología AUTOFOCUS aquí presentada estima automáticamente la geometría array-pieza y determina las leyes focales óptimas para enfoque dinámico (DDF). Opera de forma transparente y obtiene imágenes enfocadas a todas las profundidades, optimizadas para la posición actual de transductor y pieza. AUTOFOCUS hace innecesaria la descripción CAD y/o el uso de programas auxiliares de cálculo de leyes focales. También es muy rápido: realiza todo el proceso en apenas 0.2 segundos para arrays de hasta 128 elementos e imágenes con más de 100 líneas. El trabajo describe sus fundamentos y presenta algunos resultados experimentales.

ABSTRACT

Phased array inspections require defining the emission and reception focal laws that are function of geometry and propagation velocities in the coupling and in the component. They are usually computed using simulation software together with CAD descriptions of the geometry.

AUTOFOCUS technology automatically estimates the array-part geometry and computes the optimal focal law set for dynamic depth focusing (DDF). Its operation is transparent and obtains images focused at all depths optimized for the actual transducer-part position. AUTOFOCUS makes CAD descriptions and/or auxiliary focal law computing software unnecessary. It is also very fast: the whole process takes less than 0.2 seconds for 128-element arrays and more than 100 image lines. This work describes its foundations and presents some experimental results.

Palabras clave (keywords): autofocus, dynamic depth focusing, DDF, phased array, leyes focales, NDT, END, autoenfoque.

1. INTRODUCCIÓN

La tecnología *phased array* se ha incorporado con fuerza al ámbito de la Evaluación No Destructiva por ultrasonidos por las importantes ventajas que proporciona: imágenes adquiridas en tiempo real, capacidad de modificar el foco y ángulo de deflexión, operación con ondas transversales o longitudinales, mejoras de resolución y sensibilidad, etc.

Sin embargo, los *phased arrays* también presentan algunas dificultades por las diferencias que existen con la tecnología convencional de palpadores mono-elemento. No tanto en cuanto a interpretación y evaluación de resultados (donde la tecnología *phased array* es claramente superior), como en relación con la preparación de la inspección.

En efecto, los sistemas *phased array* requieren la definición y programación de leyes focales o retardos de enfoque en emisión y recepción. Si se opera con una cuña estándar, el problema se reduce a colocar adecuadamente los focos, pues el propio sistema evalúa las leyes focales, al menos para foco fijo. Pero, con frecuencia, la inspección se realiza por inmersión (local o total) debido a la geometría compleja de la pieza o a la realización de barridos sin contacto transductor-pieza.

En estas condiciones el problema de determinar, no sólo la posición de los focos sino, sobre todo las leyes focales, no es trivial. Requiere evaluar los tiempos de vuelo del ultrasonido desde cada elemento a cada foco en la pieza contando con la refracción en la interfaz. Los programas de cálculo de leyes focales (simuladores, etc.) requieren conocer geometría array-pieza con buena precisión. Un error geométrico de tan sólo 0.1 mm, por ejemplo, produce desfases que pueden arruinar el enfoque; una desviación angular del array de 1º hace que se ubiquen erróneamente los defectos en varios milímetros [1]. Obviamente el problema es mayor con enfoque dinámico (Dynamic Depth Focusing, DDF), que es la técnica que proporciona la mejor imagen, siempre que las leyes focales dinámicas estén correctamente evaluadas (errores inferiores a 1/10 periodos de señal en cada foco).

Este trabajo presenta la tecnología SITAU-AUTOFOCUS, que supera tales inconvenientes mediante la realización automática del siguiente proceso:

1. Estimación automática de la geometría array-pieza actual por medio de algunas medidas ultrasónicas. La pieza puede ser de forma arbitraria y estar ubicada en cualquier posición respecto al array.
2. Determinación de las leyes focales óptimas para realizar el enfoque dinámico DDF estricto (esto es, muestra a muestra). Se calculan y programan automáticamente sin intervención del operador.
3. Generación continua de imágenes con enfoque dinámico hasta que se desee repetir el proceso de autoenfoque (que puede ser periódico).

Con esta estrategia se obtienen numerosas ventajas, destacando:

a) El operador queda liberado de determinar la posición de los focos y de suministrar una descripción geométrica de la pieza y transductor.

b) Se obtiene la imagen óptima para la actual posición array-pieza, lo que maximiza la sensibilidad y ubica correctamente las indicaciones.

c) En inspecciones con barrido, es innecesario pre-calcular y almacenar las leyes focales adaptadas a los cambios geométricos. Basta con ejecutar un autoenfoque cuando se produzcan tales cambios.

d) Es mucho más rápido que el tiempo invertido en calcular y programar las leyes focales mediante programas auxiliares. AUTOFOCUS realiza todo el proceso en apenas 0.2 segundos.

e) Las imágenes generadas están correctamente enfocadas a todas las profundidades, aunque pueden obtenerse también con foco fijo.

f) AUTOFOCUS no requiere sondas especiales. Opera con cualquier array en inmersión o con suelas/cuñas sólidas.

Este trabajo describe los fundamentos y componentes de AUTOFOCUS, así como las estrategias seguidas para calcular las leyes focales adaptadas teniendo en cuenta los efectos de la refracción en la interfaz. Finalizamos mostrando algunos ejemplos experimentales.

2. ESTIMACIÓN AUTOMÁTICA DE LA GEOMETRÍA

La figura 1.a muestra un ejemplo genérico en el que se desea inspeccionar una pieza de geometría desconocida, por inmersión, con un array de N elementos y paso d. Se suponen conocidas las velocidades de propagación en el acoplante (c_1) y en el material de la pieza (c_2). El operador desea adquirir una imagen sectorial entre los ángulos θ_1 y θ_2 con la normal (n) con cierto intervalo angular entre líneas. No es necesario proporcionar ningún otro parámetro. Análogamente, se podría definir un barrido lineal.

Para estimar la geometría se mide la distancia desde cada elemento del array a la superficie por pulso-eco. Considerando emisión omnidireccional dado el pequeño tamaño del elemento, cada medida del tiempo de vuelo T_i define una circunferencia con centro en el elemento i, radio $R_i = c_1 T_i/2$ que es tangente a la interfaz en A (figura 1.b). Se tiene:

$$\sin\varphi_i = \frac{R_i - R_{i+1}}{d} = \frac{c_1}{2d}(T_i - T_{i+1}) \qquad (1)$$

donde se ha supuesto que los segmentos R_i y R_{i+1} son paralelos. Esta hipótesis se cumple si el radio de curvatura de la interfaz es mucho mayor que la distancia entre elementos d, como es habitual.

Si el elemento i del array está en las coordenadas (x_i, z_i), el punto A en la interfaz se ubica en:

$$\begin{aligned} x_{Ai} &= x_i + R_i \sin\varphi_i \\ z_{Ai} &= z_i - R_i \cos\varphi_i \end{aligned} \qquad (2)$$

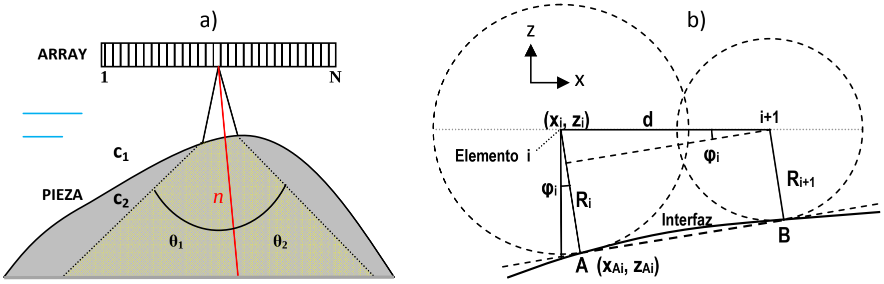

Figura 1. a) Esquema genérico de inspección con barrido sectorial por inmersión de una pieza de geometría arbitraria; b) Medida de la interfaz

De este modo, con cada disparo de un elemento del array en pulso-eco, se obtienen las coordenadas de un punto de la interfaz. En general, con N disparos se obtienen N-1 puntos. Para realizar estas medidas, se programa un barrido lineal con una apertura activa de 1 elemento. Puede acelerarse el proceso con un paso de barrido de varios elementos, reduciendo el número de disparos así como el número de puntos registrados de la interfaz. En [2] describimos también otras alternativas con menor número de disparos.

En general (geometría arbitraria), las N-1 coordenadas obtenidas de (1) y (2) se ajustan por mínimos cuadrados a un polinomio de grado $p < N-1$. En la práctica, para interfaces suavemente curvadas, $1 \le p \le 4$. Por otra parte, si se sabe que la pieza es cilíndrica, el ajuste se realiza a una circunferencia, determinando radio y coordenadas del centro. Si se conoce que la interfaz es plana, se limita el polinomio a uno de primer grado. Con este proceso, desarrollado a partir de las medidas obtenidas, se obtiene una representación analítica de la interfaz en forma de función $z=\mathrm{f}(x)$.

3. EL PROBLEMA DE LA REFRACCIÓN: EL ARRAY VIRTUAL

Pero, incluso conociendo analíticamente la geometría de la interfaz, queda por resolver el problema que plantea la refracción. Convencionalmente se utiliza el principio de Fermat: para cada foco y elemento, hay que determinar el punto de entrada en la interfaz del rayo que presente el menor tiempo de vuelo, considerando los recorridos en cada medio. Salvo para el caso de una interfaz plana (resolver ecuación de 4º grado), no existen fórmulas cerradas y hay que proceder con métodos numéricos iterativos.

Nuestra aproximación al problema es diferente. Encontramos que es posible obtener un *array virtual* casi equivalente al real en tiempos de vuelo, pero que sólo opera en el segundo medio [3]. De este modo, el array virtual obvia por completo los problemas de la refracción pues opera en un medio homogéneo. Cada línea de la imagen tiene su propio array virtual.

La figura 2 muestra los arrays virtuales obtenidos para los ángulos de deflexión extremos en un barrido sectorial de -50º a +50º de una pieza de aluminio (c_2 = 6.2 mm/µs) inspeccionada por inmersión (c_1 = 1.5 mm/µs) y geometría arbitraria.

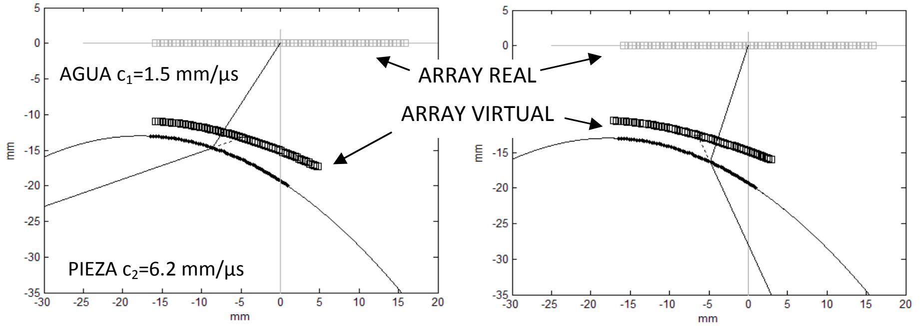

Figura 2. Array virtual para una pieza de geometría arbitraria y dos líneas extremas de un barrido de -50º a +50º respecto a la normal en cada punto.

El array real (5 MHz) tiene 64 elementos con d=0.5 mm. Sobre la interfaz se representan los puntos detectados con la técnica pulso-eco descrita. El array virtual calculado tiene también 64 elementos y el tiempo de vuelo cuasi-equivalente desde cada elemento i a cada foco en (x_F, z_F) se calcula a partir del elemento virtual en (x_{Vi}, z_{Vi}) mediante:

$$t_{iF} = \frac{1}{c_2}\sqrt{(x_{Vi}-x_F)^2+(z_{Vi}-z_F)^2}+t_k \qquad (3)$$

donde t_k es una constante que devuelve el calculador del array virtual. La figura 3 muestra el error absoluto en los tiempos de vuelo calculados con el array virtual respecto a los obtenidos con un proceso iterativo de Fermat. Se observa que son inferiores a 4 ns a partir de los 8 mm de la interfaz.

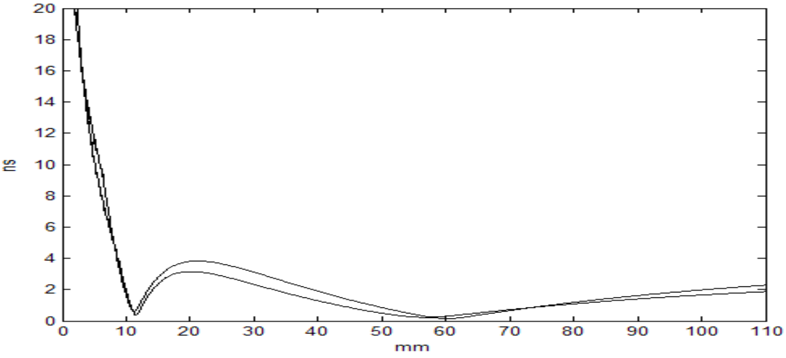

Figura 3. Errores temporales absolutos del array virtual equivalente

4. ENFOQUE DINÁMICO EN TIEMPO REAL POR HARDWARE

El proceso anterior debería repetirse para cada foco en cada línea, con el fin de obtener una imagen con enfoque dinámico en profundidad. Sin embargo, un tercer aspecto de AUTOFOCUS evita estos cálculos mediante un hardware específico que calcula los instantes de adquisición de las señales recibidas por cada elemento para corregir el enfoque muestra a muestra.

La idea deriva de un trabajo nuestro anterior, en el que encontramos que el instante de muestreo siguiente en un determinado canal debe ser un periodo de muestreo (T_S) o algo menor, $T_S(1\text{-}1/v)$ con $v>1$, para mantener enfocado el haz a lo largo de su propagación [4]. El método, llamado "*Corrección Focal Progresiva*", garantiza errores inferiores a T_S/v y fue la base del enfoque dinámico realizado en la primera generación de la tecnología SITAU (la primera comercial en disponer enfoque dinámico para aplicaciones de END).

Extendimos esta idea para operar con el array virtual, desarrollando un circuito que realiza automáticamente la Corrección Focal Progresiva a partir de un par de parámetros de inicialización. Estos circuitos han sido incorporados a la segunda generación de la tecnología phased array SITAU. De este modo se evita calcular las leyes focales para cada muestra: Basta determinar dos parámetros iniciales mediante una formulación cerrada para que el circuito realice el enfoque dinámico con un error temporal inferior a T_S/v. Puesto que la frecuencia de muestreo será, al menos, 4 veces la de la señal (criterio de Nyquist en banda ancha), con v=8 el circuito garantiza errores de enfoque inferiores a 1/32 el periodo de la señal, garantizando un enfoque correcto muestra a muestra (enfoque dinámico estricto). El enfoque dinámico estricto se diferencia de otras aproximaciones que sólo permiten definir un número limitado de focos en cada A-scan.

5. OPERACIÓN Y VERIFICACIÓN

Tras definir los parámetros principales de la inspección (profundidad, ángulos, etc.), al ejecutar "AUTOFOCUS" el sistema desencadena el proceso descrito: estimación de la interfaz, array virtual y programación de los parámetros iniciales de enfoque. A partir de este momento el sistema adquiere la imagen con enfoque dinámico estricto de forma continua hasta que se desee modificar las leyes focales mediante una nueva operación de autoenfoque.

Para la realización de los experimentos se utilizó un array de Imasonic (Besançon, Francia) de 5 MHz, N=128 elementos y paso d=0.6 mm. El sistema utilizado SITAU-FP-AF 128 (Dasel, S.L., Madrid) se configuró para diferentes modalidades de barrido, con una frecuencia de muestreo de 40 MHz y haciéndolo operar en modo AUTOFOCUS. Todos los experimentos se realizaron por inmersión en agua.

La figura 4 muestra un primer ejemplo, obtenido con AUTOFOCUS aplicado a la inspección en inmersión de una pieza cilíndrica de aluminio de 50 mm de diámetro con 3 parejas de taladros laterales, ubicado a una distancia desconocida del array. Se supuso conocida la geometría, pero no así el diámetro ni la posición de la pieza y se configuró el ajuste de la interfaz a una circunferencia. El error geométrico eficaz obtenido de múltiples medidas del diámetro con la técnica pulso-eco fue inferior a 10 µm.

Se programó un barrido angular entre -55º y +55º con un intervalo de 0.5º entre líneas, utilizando 32 elementos en emisión y recepción. Se situó el foco de emisión a 10 mm de la interfaz y se operó con enfoque dinámico (DDF) en recepción.

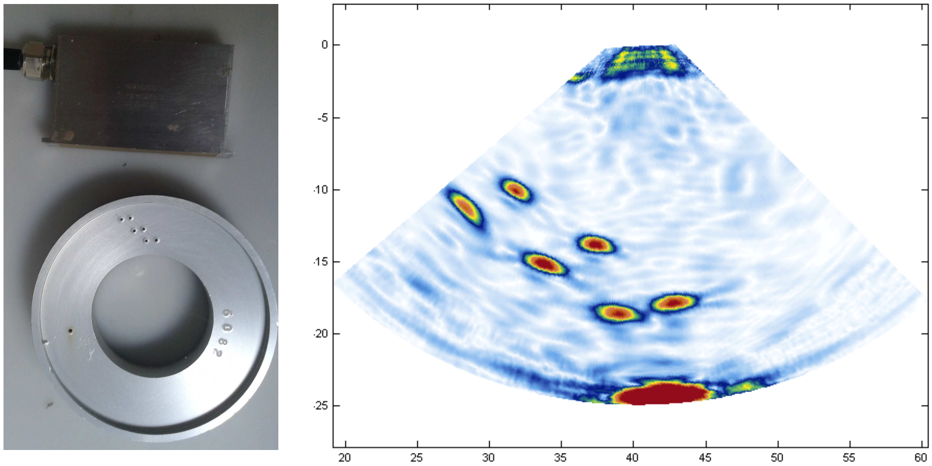

Figura 4. Inspección con AUTOFOCUS de una pieza circular de aluminio con barrido angular entre -55º y +55º. Izquierda: esquema, Derecha: imagen.

La figura 4.derecha muestra la imagen obtenida, donde son claramente visibles los taladros y el eco de fondo. Otras indicaciones residuales de menor amplitud son consecuencia de reverberaciones internas y cambios de modo en la interfaz. La resolución lateral es la esperada con el array descrito a la profundidad de los defectos, lo que indica un correcto enfoque en toda la imagen.

En un segundo ejemplo situamos otra pieza de geometría supuestamente desconocida en una posición aleatoria respecto al array (figura 5). Se programó un barrido entre -45º y +45º con un intervalo angular de 0.5º entre líneas. El foco de emisión se situó a 38 mm y el rango de la inspección se programó en 50 mm. Se utilizaron 48 elementos en emisión y 96 elementos en recepción.

En este caso se aplicó un ajuste genérico de la interfaz detectada por medidas del tiempo de vuelo en pulso-eco (barrido lineal de 1 elemento) a un polinomio de tercer grado.

Se aplicó la función AUTOFOCUS para determinar la geometría array-pieza, evaluar los arrays virtuales de las 181 líneas que componen la imagen y calcular y programar los parámetros iniciales de enfoque en cada canal activo en recepción.

El tiempo de cálculo de todos los parámetros de esta inspección con auto-enfoque fue de 0.2 segundos desde el momento en que se inicia la estimación de la interfaz hasta el que se genera la primera imagen. Se pueden obtener imágenes continuamente auto-enfocadas a una cadencia de 5 imágenes/s, prácticamente en tiempo real. Es decir, la tecnología SITAU-AUTOFOCUS permite mantener constantemente la máxima calidad de imagen ante variaciones geométricas.

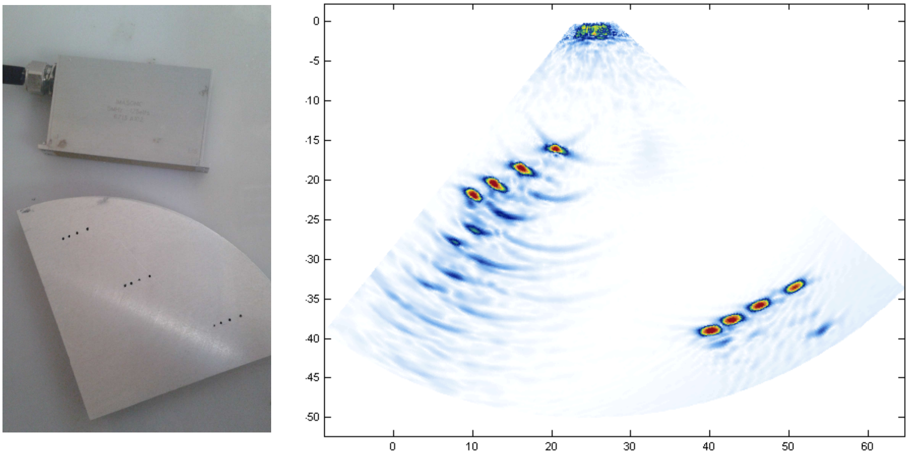

Figura 5. Inspección de una pieza de geometría "desconocida".

La figura 5.derecha muestra la imagen obtenida, en la que se aprecian dos de las tres filas de taladros laterales practicados en la pieza. Se observa que se mantiene la elevada resolución lateral propia del enfoque dinámico estricto a todas las profundidades de la imagen.

En un tercer experimento, se colocó una pieza plana de aluminio con parejas de taladros laterales, con una orientación arbitraria respecto a la del array (figura 6). Se solicitó una imagen de barrido lineal a 0º (incidencia normal), utilizando aperturas activas de 64 elementos en emisión y recepción hasta cubrir todo el array (128 elementos), esto es, 65 líneas de imagen. El foco de emisión se situó a 35 mm de profundidad, próximo al rango máximo solicitado de 40 mm. La figura 6.derecha muestra la imagen obtenida, donde se observan las indicaciones de los taladros con la resolución esperada de un enfoque dinámico correcto.

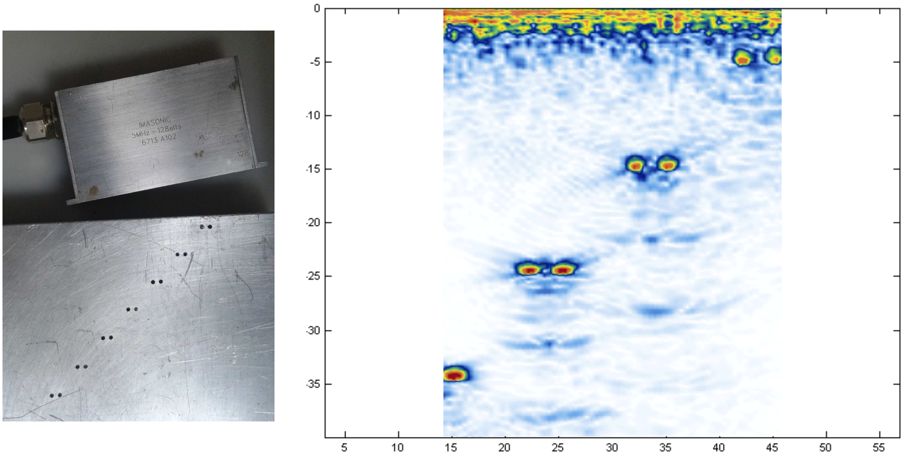

Figura 6. a) Inspección de una pieza plana con el array inclinado un ángulo desconocido.

6. DISCUSIÓN Y CONCLUSIONES

Hasta ahora no se había dotado de una capacidad de autoenfoque a los sistemas de imagen phased array, que contrasta con lo sucedido con las cámaras fotográficas/video. Esta carencia ha dificultado en no pocas ocasiones su aplicación en condiciones reales, especialmente cuando la geometría de los componentes a inspeccionar es compleja, desconocida o variable. Pero, incluso cuando se conoce con precisión, es necesario un proceso de cálculo de leyes focales adaptadas que, inevitablemente, quedan invalidadas ante cualquier desviación de la geometría nominal.

Dado el interés del tema, también se han dado otras aproximaciones notables al problema de autoenfoque con phased arrays. Así, el método SAUL [5] produce una onda de incidencia normal en la superficie tras 3 ó 4 disparos, aunque no realiza ningún tipo de enfoque en el interior de la pieza. Otra alternativa, para TFM, estima la interfaz y evalúa los tiempos de vuelo a los focos mediante una búsqueda iterativa de Fermat, utilizando potentes plataformas CPU/GPUs para limitar el tiempo de cálculo [6].

Por otra parte, nuestro grupo del CSIC desarrolló, conjuntamente con Tecnatom, S.A., una tecnología de corrección de leyes focales en tiempo real para piezas de geometría compleja [7]. La técnica, denominada *Adaptive Beamforming*, evalúa los cambios en la geometría array-pieza durante el barrido a partir de las desviaciones producidas en la imagen anterior, modificando las leyes focales para obtener incidencia normal y mantener el enfoque en la siguiente imagen. No requiere disparos adicionales, aunque sí el conocimiento a priori de la geometría nominal del componente.

Finalmente, la tecnología SITAU-AUTOFOCUS descrita en este trabajo es de propósito general, manteniendo las ventajas del enfoque dinámico y la versatilidad de la técnica phased array. La mayor parte de los cálculos se realizan con fórmulas cerradas que evitan procesos iterativos.

Es suficientemente rápido para muchas aplicaciones (0.2 segundos), aunque tal vez no lo suficiente para compensar imagen a imagen las posibles desviaciones geométricas en barridos a alta velocidad, tema en el que seguimos trabajando.

En cualquier caso, la tecnología SITAU-AUTOFOCUS es la primera disponible comercialmente y de propósito general, que evita los procesos de cálculo y la programación de leyes focales mediante la integración de las funciones necesarias en el hardware-software del sistema. Realiza un enfoque dinámico estricto (todas las muestras) y ha demostrado su robustez en múltiples aplicaciones como las mostradas en este trabajo.

Por otra parte, hace innecesarias las descripciones CAD de la geometría array-pieza, así como el uso de software auxiliar de cálculo de leyes focales. Ello proporciona importantes reducciones de costes y tiempos de preparación de las inspecciones.

7. AGRADECIMIENTOS

Este trabajo ha sido financiado por el proyecto EuroStar E!6771 SAPHARI, financiado por la UE y el CDTI.

REFERENCIAS

[1] S. Chatillon, S. Mahaut, and P. Dubois, "Simulation of advanced UT phased array techniques with matrix probes and dynamic settings for complex component inspections," *Rev. Quant. Nondestruct. Eval.*, vol. 28, pp. 864–871, 2009.

[2] J. Camacho, J. F. Cruza, J. Brizuela and C. Fritsch, "Automatic Dynamic Depth Focusing for NDT", *IEEE Trans. Ultrason. Ferroelectr. Freq. Control*, vol. 61, 4, pp. 673-684, 2014.

[3] J. F. Cruza, J. Camacho, L. Serrano and C. Fritsch, "New Method for Real-Time Dynamic Focusing Through Interfaces", *IEEE Trans. Ultrason. Ferroelectr. Freq. Control*, vol. 60, 4, pp. 739-751, 2013.

[4] C. Fritsch, M. Parrilla, A. Ibáñez, R. Giacchetta and O. Martínez, "The progressive focusing correction technique for ultrasound beamforming", *IEEE Trans. Ultrason. Ferroelectr. Freq. Control*, vol. 53, 10, pp. 1820–1831, 2006.

[5] S. Robert, O. Casula, O. Roy and G. Neau, "Real-time Inspection of Complex Composite Structures with a Self-Adaptive Ultrasonic Technique", *18th World Conf. on Non Destructive Testing,* Durban (South Africa), 2012.

[6] M. Sutcliffe, M. Weston, P. Charlton, K. Donne, B. Wright, and I. Cooper, "Full matrix capture with time-efficient auto-focusing of unknown geometry through *dual*-layered media," *Insight*, vol. 55, no. 6, pp. 297–301, Jun. 2013

[7] E. Cuevas, S. Hernández, J. Camacho, J. F. Cruza, "Fast Scanning and Adaptive Beamforming: two innovative algorithms to improve ultrasonic inspections", 11th. European Conf. on NDT (ECNDT 2014), Oct. 6-10, Prague, Czech Republic, 2014.

NDT&E International 74 (2015) 1–7

Contents lists available at ScienceDirect

NDT&E International

journal homepage: www.elsevier.com/locate/ndteint

Ultrafast hardware-based focal law calculator for automatic focusing

Jorge F. Cruza*, Jorge Camacho, Jose M. Moreno, Carlos Fritsch

Ultrasound Systems and Technology Group (GSTU), Spanish National Research Council (CSIC), Madrid, Spain

ARTICLE INFO

Article history:
Received 11 February 2015
Received in revised form
8 April 2015
Accepted 12 April 2015
Available online 20 April 2015

Keywords:
Autofocus
FPGA
focal law computing
ultrafast adaptive focusing

ABSTRACT

Phased array ultrasonic imaging of arbitrarily shaped components at high scanning speed demands computing an adapted set of focal laws before each new image. This requires computing the individual time-of-flight (TOF) from array elements to foci in a two media scenario. Most precedent approaches to this problem were based on iterative search for the minimum TOF in a sampled interface (Fermat's principle). This work follows a different approach by implementing a specialized processor that performs TOF computations. Several algorithms are implemented using High Level Synthesis (HLS) for state-of-theart FPGAs: Fermat iterative search, Newton–Raphson, Illinois and a combination of the latter.

1. Introduction

Ultrasonic imaging with phased array transducers is routinely used in medicine (echography) and industry (Non-Destructive Testing or NDT). While in the former case the transducer probe operates in contact with the body and focal laws can be pre-computed and stored in the instrument, a coupling medium is frequently inserted between the probe and the inspected component in NDT. Here, specific focal laws must be computed for every geometric probe-part configuration, taking into account refraction and mode conversion effects at the two media interface. When coupling is performed with solid wedges, focal laws can be also pre-computed for a given material since geometry is constant. Changes in the material or in the probe-part geometry demand a different set of focal laws. Such requirement adds a complexity to the preparation of the inspection and supposes a real challenge for geometry changes when scanning large parts at high speed.

Ray-tracing techniques are often incorporated into simulation tools that allow obtaining the focal laws for a general case [1–3]. However, computing time can still be an issue for Dynamic Depth Focusing (DDF) at all the sampled points, so that focal laws are usually obtained only for a small set of foci [4].

Application of Fermat's principle is commonly used, searching the beam axis entry point at the interface with the minimum time-of-flight (TOF) from every array element to every focus or pixel in the imaged region [5–6]. To improve accuracy, a fine quantification of the interface is required, which involves a long search time: there are not closed formulae to solve this problem in the general case. Nevertheless, if focal laws are pre-computed for the different geometries found along the component scan, the frame rate and inspection speed can be improved significantly [7–8].

For planar interfaces, an analytical alternative yields the entry point coordinates by solving a 4th degree polynomial [9]. The exact solution of this equation can be found elsewhere by application of the Ferrari, Cardano and Euler methods [10]. In addition, numerical procedures for non-planar interfaces have been proposed [11]. Using high performance multi CPU/GPU platforms for limited size images, real-time processing has been achieved [12].

Our group proposed another software approach some time ago, the Fast Focal Law Computing (FFLC), which performed DDF computations in a comparatively shorter time [13–14]. Besides, it is valid for known arbitrary geometry interfaces. Though, it is yet not fast enough to deal with real-time changing geometry, where a new set of adapted focal laws must be available before a new image acquisition.

When geometry is not fixed neither perfectly known (immersion inspections, variable shape parts, manufacturing tolerances, part-to-part variability, weld caps, probe misalignments, etc.), the focal laws should be evaluated for the actual probe-part configuration. It must be highlighted that small probe deviations ($\sim 1^\circ$) produce notable amplitude losses and incorrect localization of the indications [15]. Fast inspection of large components (aircraft industry, energy generators, etc.) demands a new set of adapted focal laws before each new image acquisition, which must be computed on-line.

To deal with these problems, flexible arrays that intrinsically operate in contact with arbitrarily shaped parts have been also proposed [16–18]. These devices avoid refraction or mode conversion

---

* Corresponding author. Tel.: +34 915618806.
E-mail addresses: jorge.f.cruza@csic.es (J.F. Cruza), j.camacho@csic.es (J. Camacho), jm.moreno@csic.es (J.M. Moreno), carlos.f@csic.es (C. Fritsch).

http://dx.doi.org/10.1016/j.ndteint.2015.04.003
0963-8695/

problems, but additional means must be provided to get the array elements position to compute the adapted focal laws. To this purpose both, the integration of displacement sensors and indirect techniques based on maximizing image contrast, have been proposed [19]. However, scanning speed is limited by probe wear and focal law computing adapted to the changing element positions.

Another approach, the Self-Adaptive Ultrasound (SAUL), modifies the emission focal law in successive trigger and acquisition steps to produce a wavefront adapted to the interface geometry [20]. This process is typically achieved in 3 to 5 trigger events, although it does not provide focusing. A frame rate of 50 image/s has been reported for a 48-element array [21].

Recently, our group developed a set of techniques that perform auto-focusing with DDF on arbitrary shaped parts following a 3-step procedure:

1) Map the interface by ultrasonic TOF measurements using pulse-echo, pitch-catch or plane wave emission. From these measurements interface points are obtained, which are used by curve fitting algorithms to get its analytical representation [22]. This is a fast procedure since it is based on closed formulae and can be achieved with a single trigger event and simultaneous acquisition in all the channels.
2) Compute the element coordinates of a virtual array that operates in the second medium only, thus avoiding refraction and mode conversion problems. These are obtained by closed formulae from the computed TOF to two reference foci for every scan line [23]. This process takes most of the auto-focusing time, because these TOFs are computed by iterative search algorithms.
3) Evaluate and program a few parameters in a focusing hardware that performs real-time DDF [23]; the process is very fast, since their values are also given by closed formulae.

While such auto-focusing technique provides adaptive DDF, it is yet not fast enough for scanning applications at high speed: programmed in Matlab (The MathWorks Inc., Natick, MA) it takes about 2 s for a 128-element array and 100 image lines of any depth (videos attached in the on-line version of [22]).

In a typical application the array probe scans a component at speeds of 200 mm/s or more with a spatial resolution of one image per mm. This demands computing and programming a full set of DDF adapted focal laws for any image size every 5 ms, approximately, which is much faster than any other auto-focusing implementation reported so far.

We refer to Ultra-Fast Auto-Focusing (UFAF) as a process able to compute and program a new set of adapted focal laws in few milliseconds. As it was identified, the critical point for success is achieving very fast array-to-foci TOF computations for arbitrarily shaped interfaces. Besides, UFAF should be accurate enough to keep the high resolution and image quality provided by DDF.

This work investigates for the first time the possibilities of performing UFAF by hardware to achieve the required high speed. The objective is to obtain a high performance specific processor that performs geometry-adapted focal law computations preceding every image acquisition. To this purpose, several numerical procedures are proposed, taking advantage of High Level Synthesis (HLS) tools and high performance FPGAs with embedded processors currently available at low cost.

2. High Level Synthesis and state-of-the-art FPGAs

In the last years automated tools for software-based hardware design have been developed, known as High Level Synthesis. HLS bridges the gap between software and hardware domains by specifying algorithms in C/C++/SystemC that are mapped to a synthesizable implementation for FPGAs [24]. When appropriately programmed, these tools make a very efficient use of the available resources by pipelining and time-sharing of computing blocks. Optimal resource allocation and concurrency are set after defining the required performance, a process that rivals with hand coding in Hardware Description Languages (HDLs).

The Vivado High Level Synthesis from Xilinx (Xilinx Inc., USA) is an example that allows behavioral specification using a high-level language like C/C++ or SystemC, and produces a Register Transfer Logic (RTL) specification that can be implemented in state-of-the-art FPGAs. This tool performs dataflow analyses to extract parallelism information, to reduce resource requirements by functional block time-sharing and to detect common sub-expressions. From such analysis, it generates the control flow and scheduling of elementary tasks.

Simultaneously, state-of-the-art FPGAs have a large amount of hardware resources and, specifically, Digital Signal Processor (DSP) cells and on-chip RAM blocks (RAMB) that operate at high speed. These capabilities allow the hardware implementation of complex algorithms that were difficult to achieve by hand coding.

Much ultrasound equipment is based on FPGAs that perform the signal acquisition and beamforming processes in real-time. Conventionally, system control is carried out by an external computer, where acquisition parameters, focal laws, etc. are evaluated off-line. Sometimes, images are also built on high-performance external CPU/GPU platforms using the Total Focusing Method (TFM) [25]. In this case raw data transfers from and to the acquisition hardware represent the bottleneck: for a $N=128$ element transducer and 8K samples per A-scan, 256 MB of data must be transferred to build a single image, which limits the frame rate with current technology. Furthermore, latency of transfer protocols, computer busses and software is sometimes more restrictive for real applications that transfer speed.

In fact, it seems more efficient to integrate the focusing, beamforming and other digital signal processing together with the data acquisition functions, instead of relying on an external platform. HLS and state-of-the-art FPGAs provide an opportunity to implement these operations at high frame rates, together with less user requirements (i.e., geometric descriptions and additional tools for focal law computing would be avoided).

This work focuses on the most time consuming task, TOF calculations, using several iterative techniques. These methods provide the significant throughput improvements required to achieve the proposed ultra-fast adaptive focusing paradigm.

3. The Fermat iterative search

From a practical point of view in ultrasound applications, Fermat's principle states that a beam follows the path of minimum time between two points, being directly related with Snell's law. The basic Fermat based iterative search discretizes the interface and compares the TOFs through the set of points until a minimum is found.

Computing burden is directly related with the search step or interface discretization interval. A large step is faster but it might not provide the required time resolution; a short interval defines a higher number of interface points and takes more time to find the minimum TOF, whatever is the search procedure. Noteworthy, the literature has not paid too much attention to optimally set this essential parameter. Here we provide a criterion that yields an upper bound of the maximum horizontal error Δx from the true beam entry point to the nearest interface sample for a given maximum timing error Δt. Then, the interface sampling interval can be simply set to $2\Delta x$ in the x-direction.

For N-element array imaging systems with a ratio μ of the ultrasonic signal period to the focusing delay resolution Δt, the rms amplitude of the sidelobes due to timing errors (delay quantization

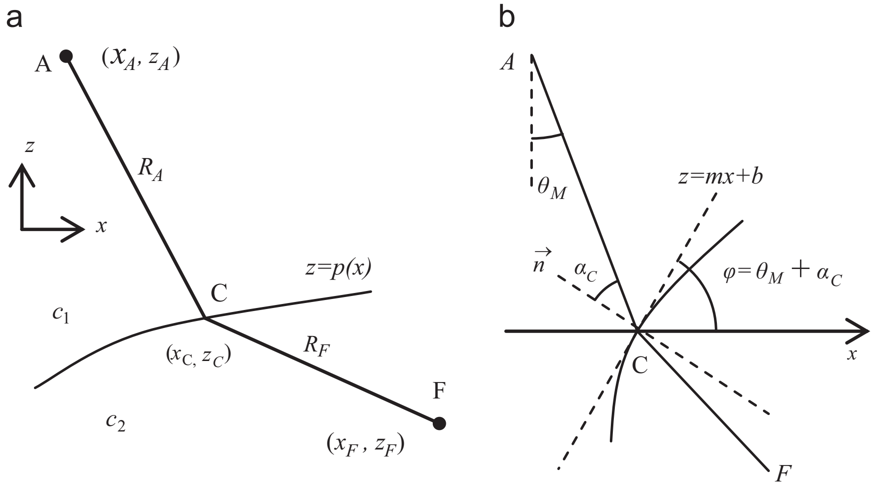

Fig. 1. Geometry: (a) array element A, interface $p(x)$, beam axis crossing point C and focus F; (b) maximum interface slope.

lobes), relative to the main lobe amplitude is [26]

$$\eta = \frac{\pi}{\mu\sqrt{6N}}, \tag{1}$$

To keep its level below half the array noise floor $1/N$,

$$\Delta t \le \frac{1}{2\pi f_R}\sqrt{\frac{6}{N}} \tag{2}$$

This value can be also used to set the limit of the acceptable timing error for TOF computations. Consider the geometry of Fig. 1(a) with an array element at A (x_A, z_A), an interface defined by the function $z=p(x)$ and a focus at (x_F, z_F). The array is assumed horizontal and sound propagation is towards the z-direction. The interface separates two media with propagation velocities c_1 and c_2 and the sound beam crosses the interface (entry-point) at C (x_C, z_C).

TOF from A to F through some point (x, $p(x)$) at the interface is given by

$$t(x) = \frac{R_A(x)}{c_1} + \frac{R_F(x)}{c_2} = \frac{\sqrt{(x-x_A)^2+[p(x)-z_A]^2}}{c_1} + \frac{\sqrt{(x-x_F)^2+[p(x)-z_F]^2}}{c_2} \tag{3}$$

Taking the derivative, with $z=p(x)$

$$\frac{dt}{dx} = \frac{x-x_A+(z-z_A)p'(x)}{c_1 R_A(x)} + \frac{x-x_F+(z-z_F)p'(x)}{c_2 R_F(x)} \tag{4}$$

Defining the slope at the vicinity of the entry point C as $m=p'(x_c)$ and evaluating (4) at $x=x_C+\Delta x$, $z=z_C+m\Delta x$,

$$\frac{dt}{dx} \approx \frac{x_C-x_A+(z_C-z_A)m}{c_1 R_A} + \frac{1+m^2}{c_1 R_A}\Delta x + \frac{x_C-x_F+(z_C-z_F)m}{c_2 R_F} + \frac{1+m^2}{c_2 R_F}\Delta x, \tag{5}$$

where for notation simplicity $R_A \equiv R_A(x_C+\Delta x)$ and $R_F \equiv R_F(x_C+\Delta x)$. On the other hand dt/dx equals zero at point C and hence,

$$\frac{x_C-x_F+(z_C-z_F)m}{c_2 R_F(x_C)} = -\frac{x_C-x_A+(z_C-z_A)m}{c_1 R_A(x_C)} \tag{6}$$

With $R_F(x_C) \approx R_F(x_C+\Delta x)$ and $R_A(x_C) \approx R_A(x_C+\Delta x)$, substitution of (6) in (5) yields

$$\frac{dt}{dx} \approx (1+m^2)\left(\frac{1}{c_1 R_A} + \frac{1}{c_2 R_F}\right)\Delta x \tag{7}$$

$$\Delta t \approx (1+m^2)\left(\frac{1}{c_1 R_A} + \frac{1}{c_2 R_F}\right)\Delta x^2 \tag{8}$$

Given Δt, the optimum Δx can be obtained from (8) for the maximum slope m and minimum R_A and R_F distances. On the other hand, m is bounded by the maximum steering capability of the array elements θ_M and by the critical angle of the inspected material, α_C. From Fig. 1(b),

$$m \le \tan(\theta_M + \alpha_C) \tag{9}$$

and, typically, $|m| \le 1$. The R_A value can be roughly set to the minimum probe-part distance and R_F to the distance of the interface to the nearest focus. This parameter is critical for not over-discretizing the interface, because Eq. (8) rapidly grows for low R_F values. Minimum R_F is obtained when the first focus is on the interface. In the worst case, it is at (x_C, z_C) and halfway between two interface samples at ($x_C \pm \Delta x$, $z_C \pm m\Delta x$):

$$\min(R_F) = \sqrt{[x_C-(x_C+\Delta x)]^2 + [z_C-(z_C+m\Delta x)]^2} = \Delta x\sqrt{1+m^2} \tag{10}$$

Substitution in Eq. (8) yields,

$$\Delta t \le \frac{(1+m^2)}{c_1 R_A}\Delta x^2 + \frac{\sqrt{1+m^2}}{c_2}\Delta x \tag{11}$$

and Δx can be obtained by solving this second degree equation. However, the first term can be neglected for foci close to the interface,

$$\Delta x \le \frac{c_2 \Delta t}{\sqrt{1+m^2}}, \quad \text{if } R_F \to 0 \tag{12}$$

This has been frequently used as the general criterion for setting the interface sampling interval, although it yields a timing resolution that is seldom required. A more practical approach uses Eq. (8) setting the first focus at some minimum distance from the interface. For example, if it is placed at

$$R_F \ge R_A^{\min}\frac{c_1}{c_2} \tag{13}$$

and considering $|m| \le 1$, a simple upper bound for Δx is

$$\Delta x \le \frac{\sqrt{c_1 R_A^{\min}\Delta t}}{2}, \qquad R_F \ge R_A^{\min}\frac{c_1}{c_2} \tag{14}$$

Application of Eqs. (2) and (8) allows a near optimal choice of Δx in a given inspection scenario. For example, a 128-element, 5 MHz array requires $\Delta t \le 7$ ns. In water immersion ($c_1 \approx 1480$ m/s), inspecting an aluminum part ($c_2 \approx 6200$ m/s) with a minimum probe-part distance of 10 mm, from Eq. (14) $\Delta x \leq 0.16$ mm, valid for $R_F \geq 2.4$ mm. If Eq. (12) was applied instead, the result had been $\Delta x \leq 0.03$ mm, a very low value that oversamples the interface. The first choice will affect TOF errors to foci in the 0 to 2.4 mm range only, which usually has no critical consequences due to the presence of the interface echo. Indeed, any special application requiring precise focusing in this range should use Eq. (12).

4. More efficient focal law computing algorithms

We proposed the FFLC technique in [13–14] based on the Newton–Raphson method to get the TOF in a single iteration for successive foci. Implemented in software, it outperformed by an order of magnitude the Fermat iterative search. It was thought that its hardware implementation could provide similar improvements. Another advantage is that, differently from Fermat iterative search, interface discretization is not required. Fig. 2a shows the Newton–Raphson algorithm behavior, which is further analyzed in Section 4.1.

Since we address the general case of unknown interface geometry, alternate procedures must be provided in the case the algorithm fails to converge. The problem is overcome by switching to the Illinois method, whose convergence is guaranteed. Fig. 2b shows graphically the behaviour of this algorithm, which is further addressed in Section 4.2.

This way, the process starts with the Newton–Raphson algorithm, which is faster and requires a single initial point, while the Illinois technique requires two points. The Illinois algorithm is only chosen when convergence fails in the former.

4.1. The Newton–Raphson algorithm

This is one of the countless iterative methods proposed for finding roots of a real-valued function. Given a function $f(x)$, its derivative $f'(x)$ and a starting point x_0, successively better approximations to the solution of $f(x)=0$ are found by [27]

$$x_{k+1} = x_k - \frac{f(x_k)}{f'(x_k)}, \quad k = 0,\ 1,\ 2, \ldots \tag{15}$$

Fig. 2(a) shows the behaviour of the algorithm. The next guess x_{k+1} is obtained as the intersection of the tangent of $f(x)$ at x_k with the x-axis. Here the function to solve is the derivative of the TOF given by (3), for which the second derivative is also required

$$f(x) = \frac{dt}{dx} = \frac{x - x_A + [p(x) - z_A]p'(x)}{c_1 R_A} + \frac{x - x_F + [p(x) - z_F]p'(x)}{c_2 R_F} = 0$$

$$R_A = \sqrt{(x - x_A)^2 + [p(x) - z_A]^2}$$

$$R_F = \sqrt{(x - x_F)^2 + [p(x) - z_F]^2} \tag{16}$$

$$f'(x) = \frac{df}{dx} = \frac{1}{c_1}\frac{A'R_A - A^2/R_A}{R_A^2} + \frac{1}{c_2}\frac{F'R_F - F^2/R_F}{R_F^2}$$

$$A = (x - x_A) + p'(x) \cdot [p(x) - z_A]$$

$$A' = 1 + p''(x) \cdot [p(x) - z_A] + [p'(x)]^2$$

$$F = (x - x_F) + p'(x) \cdot [p(x) - z_F]$$

$$F' = 1 + p''(x) \cdot [p(x) - z_F] + [p'(x)]^2 \tag{17}$$

Decomposing the equations in partial results helps to save hardware resources, since the corresponding computing blocks can be reused by other parts of the process. Identification of these blocks is important to achieve a compact hardware design, which makes a difference with software implemented algorithms. Software executes algorithms sequentially, while well organized hardware can process several processes concurrently. For example, a floating point divider can be used at different times on different operands, concurrently with the evaluation of other partial results.

The algorithm terminates when $|f(x)\Delta x| < \Delta t$, where $\Delta x = x_{k+1} - x_k$ is computed at every iteration. Convergence of the Newton–Raphson algorithm is fast (quadratic) as long as $f'(x) \neq 0$ in an interval around the solution, $f''(x)$ is finite and x_0 is sufficiently close to the solution. These conditions usually apply to ultrasonic inspection with soft curved interfaces, but sometimes the algorithm fails to find a solution due to:

1. Some x_k falls outside the predefined $[x_{min}, x_{max}]$ interval.
2. After certain number of iterations the finishing criterion is not reached. This typically happens when the algorithm gets stuck in a relative minimum of $f(x)$.
3. Second derivative of t is negative, that is $f'(x) < 0$: last guess fell near a relative maximum and the algorithm has high chance to find it instead of a minimum.

When any of the above conditions is met, the hardware automatically switches to the Illinois algorithm described below.

4.2. The Illinois algorithm

Its name derives after being proposed at the Univ. of Illinois in the early 1950's and is a modification of the classic *regula falsi* method [28–29]. It is a “bracketed algorithm”, in the sense that, after iteration k, the root will lie in some interval $U_k = [a_k, b_k]$ for which $f(a_k) \cdot f(b_k) < 0$ that is, $f(a_k)$ and $f(b_k)$ are of opposite sign. A new approximation to the root is found by linear interpolation in the segment between points $[a_k, f(a_k)]$ and $[b_k, f(b_k)]$, as shown

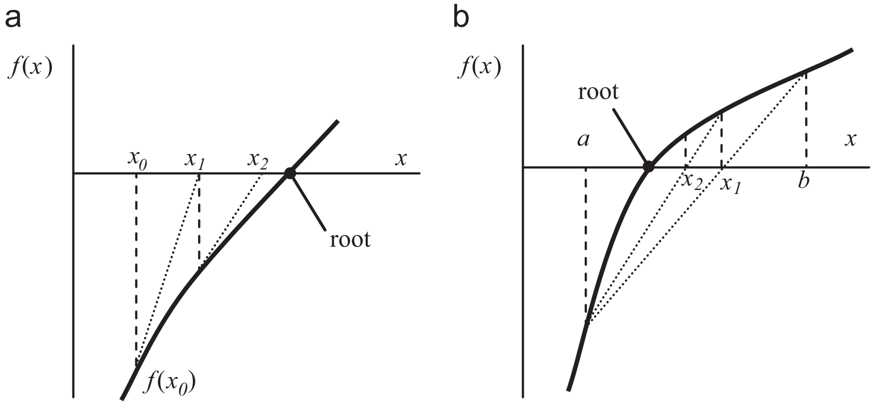

Fig. 2. Behaviour of: (a) the Newton Raphson; (b) Regula falsi or Illinois algorithms.

graphically in Fig. 2(b)

$$x_{k+1} = \frac{b_k f(a_k) - a_k f(b_k)}{f(a_k) - f(b_k)} \tag{18}$$

The next interval is chosen with x_{k+1} and whichever of a_k or $b_k$with a function value of opposite sign to $f(x_{k+1})$. The Illinois algorithm simply introduces a weight w_k that helps to improve the speed of convergence when in successive iterations one of the endpoints is retained. In this case, the function value $f(a_k)$ or $f(b_k)$ of the retained endpoint is halved for the next iteration by setting $w_k = 0.5$. Assuming this happens in the a_k side

$$x_{k+1} = \frac{w_k b_k f(a_k) - a_k f(b_k)}{w_k f(a_k) - f(b_k)} \tag{19}$$

With no endpoint retention, Eq. (18) is point applied, which is equivalent to setting $w_k = 1$ in Eq. (19).

Convergence is guaranteed in both, *regula falsi* and Illinois. The algorithms need two initial values a_0 and b_0 meeting the condition $f(a_0) \cdot f(b_0) < 0$. Since this rule must be verified before starting computations, the search and the process of finding initial values can be a non-trivial issue [30]. It is, thus, advantageous to begin with Newton–Raphson because it is faster and requires a single initial. Moreover, if switching to Illinois is required, it provides one of the bracket terms (the last valid value found); the other is chosen to meet the opposite sign condition.

It must be highlighted that once the Newton–Raphson algorithm has been implemented, most of the computing blocks required by the Illinois are already available, so that mixing both techniques require very few additional resources.

5. Hardware implementation

Hardware implementation of ultrasound TOF finding algorithms have not been attempted before due to the difficulties in integrating floating-point arithmetic with fast response and moderate resource consumption. Floating point arithmetic is required to deal with situations that handle numbers spanning orders of magnitude. Organizing data, sharing resources and extensive use of pipelining is required to pack a fast computing engine in a reasonable volume.

High-Level Synthesis provides an opportunity to translate software methods to high speed hardware. The general architecture is shown schematically in Fig. 3. The interface function $p(x)$ is obtained by an embedded ARM processor from ultrasound measurements [23].

If the representation is an nth order polynomial, its derivatives $p'(x)$ and $p''(x)$ are easily found. These results are stored in a static parameter memory together with element and foci coordinates. In the current implementation, polynomials of up to 4th degree can be accommodated. This parameter has no effect on computing performance, but only in resource consumption.

The central unit is the TOF computing engine. For testing purposes, four variants were implemented: a) Fermat iterative search, b) Newton–Raphson only, c) Illinois only and d) Newton–Raphson with Illinois. It connects to memories that store the successive iteration results. TOF computing is carried out in parallel for 32 array elements. Data in partial results memory is reused to set the starting point of a new computation of the time of flight from the same element to the next focus. This improves significantly the efficiency since precedent result is near the next solution.

Operations are also highly pipelined to improve performance and resource sharing. This involves latency in obtaining the results: new data are feed to the TOF computing engine without waiting for the completion of previous partial results. The cost is that processing of a block of 2 × 16 foci per element is completed when all of the corresponding TOFs have been evaluated. However, overall performance is still higher using this approach, which is not required in a slower software implementation.

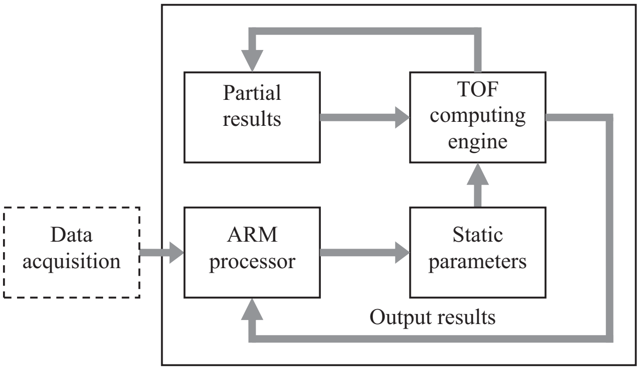

Fig. 3. Architecture for Fast Focal Law Computing.

Table 1
Resources used by algorithms. In parenthesis, percentage of the resources available in a XC7Z020-1C FPGA.

	Fermat search	Newton only	Illinois only	Newton+Illinois
LUTs	5247 (10%)	11603 (22%)	8785 (17%)	10,988 (21%)
Registers	5318 (5%)	11,310 (11%)	11,250 (11%)	12,470 (12%)
RAMB18	44 (16%)	44 (16%)	44 (16%)	44 (16%)
DSP48	20 (9%)	41 (19%)	30 (14%)	43 (20%)

Currently, output results are returned to the ARM processor for verification purposes. In a real implementation, they will be directly used to set the initial parameters of the DDF focusing hardware. In any case, all data traffic is restricted to within the chip.

Table 1 shows the resources used in a XC-7Z020-1C FPGA (Xilinx, Inc.) to implement the different processing algorithms. All of them perform a single iteration every 4 clock cycles.

The simpler Fermat iterative search uses about half the resources required for the higher performance Newton and Illinois algorithms. It may seem surprising that the Newton or the simpler Illinois algorithms use approximately the same resources than the combination of both. Newton uses more resources due to the computation of the second derivative of the TOF. However, higher resource requirements do not follow from the increased complexity, as long as the resources can be shared between algorithms, as it is the case. Decomposition of the procedure in reusable computing blocks is the basis for these savings.

Anyway, it must be highlighted that all algorithms use only a fraction of the resources available in a modest chip. The most complex one (Newton+Illinois) uses about 20% of the available resources in this low-cost chip. This leaves plenty room for other signal processing functions and/or the architecture can be on-chip replicated to increase parallelism and reduce response time.

6. Experimental results

Algorithms were first implemented and validated in Matlab, by comparing their results against those obtained by a conventional iterative Fermat search with $\Delta t = 1$ ns. They were also coded in C++ for three targets: 1) a Core i-7 computer, 2) the ARM embedded processor and, 3) full hardware implementation through HLS using Vivado for the targeted FPGA.

Tests were carried out for the configuration shown in Fig. 4, where two rows of 128 foci each are arbitrarily set at constant depths of 5 and 15 mm from the x-axis. The array has 128

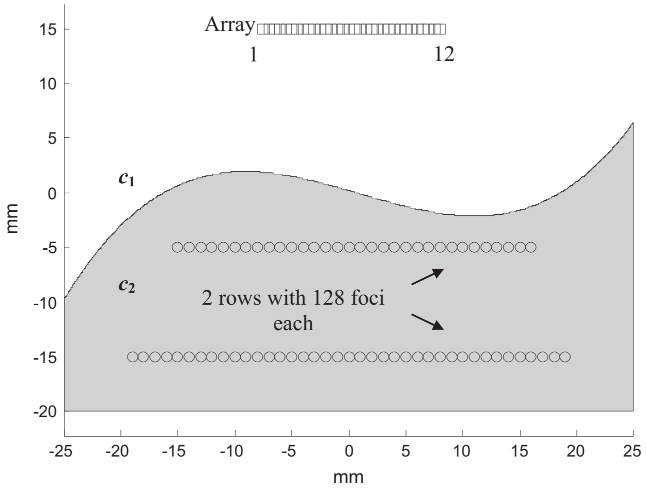

Fig. 4. Example part used for the experimental verification.

Table 2
Algorithm performances ($N=128$, $L=128$, 2 focus/line).

	Fermat	Newton+Illinois
Nr. iterations (average)	8.7	1.8
Total time in Core i-7 software (ms)	50	19
Total time in ARM software (ms)	397	148
Total time in hardware (ms)	21.6	3.3
Maximum timing error (ns)	0.11	0.48
Speed gain HW/SW(ARM)	18 ×	45 ×

elements, and the part has a shape defined by

$$p(x)=0.001x^3-0.003x^2-0.3x-0.2 \tag{20}$$

Table 2 shows the performance of every algorithm for a 128 element array and 2 × 128 = 256 foci, that is, $M=32\text{K}$ TOF calculations per image. Timing was set to $t_i=4$ clock cycles/iteration with a clock period $T_{CLK}=10$ ns.

Hardware implemented Fermat iterative search is considerably faster (18 ×) than the software approach if computed in the integrated ARM processor, but only 2.3 times faster if evaluated in a Core i-7 computer. However, in this case, the time required to transfer A-Scan data between the acquisition subsystem and the computer had to be taken into account. Also the total latency from the acquisition subsystem to the computer processor memory or cache should be considered. This may amount for considerable performance losses, perhaps comparable with that of the embedded ARM processor, which does not require external transfers.

By contrast, the hardware implemented Newton+Illinois processing algorithm is significantly faster than any other approach, an order of magnitude above the software implemented Fermat algorithm in core i-7, even not accounting for the time required to transfer data. It is nearly two orders of magnitude above the performance of the Fermat method in the embedded ARM processor. This is a quite satisfactory result achieved with a moderate resource percentage of a low-end FPGA.

With the hardware implemented Newton+Illinois algorithm, TOFs computing time to 2 foci per element and scan line, as required for auto-focusing with DDF following [23], is 3.3 ms for an extreme case of 128-element arrays and 128 scan lines of any depth, achieving a frame rate of 300 image/s. In summary, this represents 100 ns per element and focus, orders of magnitude faster than any other known implementation. Since processing time is proportional to both, the number of array elements and of the image lines (2 foci/line), frame rates up to 1000 image/s can be achieved in common applications if geometric measurements are carried out in parallel with autofocus processing.

Furthermore, by simple replication of the hardware in the same FPGA, the performance can be multiplied. Even in this case, the hardware requirements would be about 40% of the available chip resources. A faster and/or denser chip could be also used to increase throughput if needed.

It should be highlighted that good data and code organization, well adapted to the supporting architecture, is essential to achieve the reported performance, which requires high skills on parallel hardware design and C/C++ programming.

7. Conclusions

This work attempted to achieve time-of-flight (TOF) computations at very high speed in a two media scenario. The main application would be Ultra-Fast Adaptive Focusing (UFAF), where a new set of focal laws adapted to the actual probe-part geometry is computed before each new image acquisition at high frame rates.

The work has demonstrated this possibility by High Level Synthesis (HLS) coding of different algorithms, including iterative Fermat search, Newton–Raphson and Illinois to solve the non-linear equation representing the derivative of the TOF. A combination of the Newton and Illinois algorithms provides the fastest processing and guarantees convergence with similar resource requirements.

In fact, FPGA resource consumption is limited due to computing block sharing, while high performance is achieved by means of pipelining. Careful description of the algorithms in HLS, adapted to the underlying architecture, is essential.

Experimentally it has been found that time to compute 32K TOF for 128 elements and 128 scan lines with 2 foci/line is 3.3 ms (100 ns per focus and element). This uses only about 20% of the hardware resources available in a low-end FPGA with an embedded ARM processor. This would allow scanning parts with UFAF at speeds of 300 mm/s and 1 mm of spatial resolution without replicating hardware. Higher speeds are achievable with less array elements and/or scan lines, as well as with hardware replication and/or using higher density/performance FPGAs.

This approach opens a new research line, where many of the digital signal processing algorithms currently implemented in software for ultrasound applications and others can be migrated to hardware by means of HLS coding.

Acknowledgments

This work has been supported by project DPI2013-42236-R of the Spanish Ministry of Economy and Competitiveness.

References

[1] Le ber L, Roy O, Jazayeri N. Applications of phased array techniques to NDT of industrial structures. In: Proceedings of the 2nd international conference on Technical inspection and NDT. Tehran, Iran; 2008.

[2] Richard D, Reilly D, Berlanger J, Maes G. Software tools for the design of phased array UT inspection techniques; 2010, Online available: 〈http://www.ndt.net/article/SimNDT2010/papers/9_Richard.pdf〉.

[3] Calmon P, Mahaut S, Chatillon S, Roy O. Simulation of phased array techniques for realistic NDE configurations. In: Proceedings of the IEEE ultrasonic symposium; 2002. p. 723–727.

[4] Liang J, Wang Z, Shi Y. Ultrasonic Inspection of thick parts with phased array dynamic focusing. In: Proceedings of the European conference on NDT; 2010, art. no. 1.3.91.

[5] Long R, Rusell J, Cawley P, Habgood N. Ultrasonic phased array inspection of flaws on weld fusion faces using full matrix capture. Rev Prog Quant Nondestruct Eval 2009;28:848–55.

[6] Drinkwater BW, Bowler AI. Ultrasonic array inspection of the Clifton Suspension Bridge chain-links. Insight 2009;51(9):491–8.

[7] Sutcliffe M, Weston M, Dutton B, Cooper I. Real-time full matrix capture with auto-focusing of known geometry through dual layered media. In: Proceedings of the NDT 2012 conference of the BINDT. Daventry (UK); 2012, 11–13 September.

[8] Sutcliffe M, Weston M, Charlton P, Donne K, Wright B, Cooper I. Full matrix capture with time-efficient auto-focusing of unknown geometry through dual-layered media. Insight 2013;55(6):297–301.

[9] Shin HC, Prager R, Gomersall H, Kinsbury N, Treece G, Gee A. Estimation of speed of sound in dual-layered media using medical ultrasound image deconvolution. Ultrasonics 2010;50(7):716–25.

[10] Nickalls RWD. The quartic equation: invariants and Euler's solution revealed. Math Gaz 2009;93(256):66–75 Online available:.

[11] Weston M. [Ph. D. thesis]. Advanced ultrasonic digital imaging and signal processing for applications in the field of non-destructive testing. UK: University of Manchester; 2011.

[12] Weston M, Mudge P, Davis C, Peyton A. Time efficient auto-focussing algorithms for ultrasonic inspection of dual-layered media using Full Matrix Capture. NDT&E Int 2012;47:43–50.

[13] Parrilla M, Brizuela J, Camacho J, Ibáñez A, Nevado P, Fritsch C. Dynamic focusing through arbitrary geometry interfaces. In: Proceedings of the IEEE ultrasonics symposium; 2008. p. 1195–1198.

[14] Parrilla M, Ibañez A, Camacho J, Fritsch C. Fast Focal law computing for non-destructive testing with phased arrays. In: Proceedings of the international congress on ultrasonics. Vienna ; 2007, paper ID 1228.

[15] Chatillon S, Mahaut S, Dubois P. Simulation of advanced UT phased array techniques with matrix probes and dynamic settings for complex component inspections. Rev Prog Quant Nondestruct Eval 2009;28:864–71.

[16] Casula O, Poidevin C, Cattiaux G, Fleury G. A flexible phased array transducer for contact examination of components with complex geometry. In: Proceedings of the 16th conference on nondestructive testing. Montreal, Canada; 2004.

[17] Toullelan G, Nadim A, Casula O, Dumas P, Abittan E Doudet L. Inspection of complex geometries using flexible phased array transducers. In: Proceedings of the 17th world conference on nondestructive testing. Shangai (China); 2008.

[18] Roy O, Mahaut S, Chatillon S. Ultrasonic inspection of complex geometry component specimen with a smart flexible contact phased array transducer: modeling and applications. In: Proceedings of the IEEE ultrasonics symposium; 2000. p. 763–766.

[19] Hunter A, Drinkwater B, Wilcox P. Autofocusing ultrasonic imagery for non-destructive testing and evaluation of specimens with complicated geometries. NDT&E Int 2010;43:78–85.

[20] Robert S, Casula O, Njiki M, Roy O. Assessment of realtime techniques for ultrasonic non- destructive testing. Rev Prog Quant Nondestruct Eval 2012;31:1960–7.

[21] Robert S, Casula O, Roy O, Neau G. Real-time inspection of complex composite structures with a self-adaptive ultrasonic technique. In: Proceedings of the 18th world conference non-destructive testing; 2012, art. no. Tu.4.B.2.

[22] Camacho J, Cruza JF, Brizuela J, Fritsch C. Automatic dynamic depth focusing for NDT. IEEE Trans Ultrason Ferroelectr Freq Control 2014;61(4):673–84.

[23] Cruza JF, Camacho J, Serrano L, Fritsch C. New method for real-time dynamic focusing through interfaces. IEEE Trans Ultrason Ferroelectr Freq Control 2013;60(4):739–51.

[24] Xilinx, High-Level Synthesis. Vivado Design Suite User Guide. UG-902; 2014.

[25] Lambert J, Pédron A, Gens G, Bimbard F, Lacassagne L, Iakovleva E, et al., Analysis of multicore CPU and GPU toward parallelization of Total Focusing Method ultrasound reconstruction. In: Proceedings of the IEEE international conference on design and architectures for signal and image processing, DASIP-2012. Karlsruhe, Germany; 2012.

[26] Peterson DK, Kino GS. Real-time digital image reconstruction: a description of imaging hardware and an analysis of quantization errors. IEEE Trans Sonics Ultrason 1984;31(4):337–51.

[27] Traub JF. Iterative methods for the solution of equations. American mathematical society. New York: Chelsea Pub. Co.; 1982.

[28] Dowell M, Jarratt P. Modified regula falsi method for computing the root of an equation. BIT 1971;11:168–74.

[29] Ford JA. Improved algorithms of Illinois-type for the numerical solution of nonlinear equations. Technical report CSM-257. Colchester (GB): Department of Computer Science, Essex University; 1995.

[30] Shacham M, Kehat E. Converging interval methods for the iterative solution of a non-linear equation. Chem Eng Sci 1971;28:2187–93.

Auto-Focused Virtual Source Imaging With Arbitrarily Shaped Interfaces

Jorge Camacho and Jorge F. Cruza

Abstract—**This work presents a new method, named auto-focused virtual source imaging (AVSI), for synthetic aperture focusing through arbitrarily shaped interfaces with arrays. First, the shape of the component surface is obtained by time-of-flight (TOF) measurements. Then, a set of virtual source/receivers is created by focusing several array subapertures at the interface normal incidence points. Finally, the synthetic aperture focusing technique (SAFT) is applied to the received signals to generate a high-resolution image. The AVSI method provides several advantages for ultrasonic imaging in a two-media scenario. First, knowledge of the probe–part geometry is not required, because all information needed for image formation is obtained from a set of ultrasonic measurements. Second, refraction complications in TOF calculations are avoided, because foci at the interface can be considered as virtual source/receivers, and SAFT can be performed in the second medium only. Third, the signal-to-noise ratio is higher than with synthetic aperture techniques that use a single element as emitter, and fourth, resolution is higher than that obtained by phased-array imaging with the same number of active elements, which reduces hardware complexity. The theoretical bases of the method are given, and its performance is evaluated by simulation. Finally, experimental results showing good agreement with theory are presented.**

I. INTRODUCTION

SYNTHETIC aperture focusing technique (SAFT) has been used in ultrasound nondestructive testing (NDT) for increasing lateral resolution [1]–[3]. It is based on coherently adding signals acquired from different positions to produce a higher resolution image than that directly obtained from the received signals. Successive positions of the transducer correspond to the elements of a virtual aperture, whose extent determines the achievable lateral resolution.

One of the main requisites of SAFT is to emit and receive wide beams at each transducer position, so that each pixel of the output image receives contributions from many emitter/receivers (ideally from all of them). Wide beams can be generated by using small transducers, as in time-of-flight diffraction technique (TOFD), where SAFT has been used to increase lateral resolution in the movement direction parallel to a weld [4]. However, apart from these applications, using small transducers is not convenient because of their lower signal-to-noise ratio.

Although it seems contradictory at first, focused transducers have been proposed as an alternative for simultaneously increasing SNR and generating wide beams [5]. This approach is based on the fact that a focus behaves approximately like a virtual point source that generates a wave front that can be considered cylindrical in some angular region. The more focused the transducer (lower f-number, the ratio of the focal distance to the aperture size), the wider the beam produced away from the focus and the better suited for SAFT processing. Based on this idea, several applications with focused single-element transducers have been developed in NDT and medicine [6]–[10].

The widespread use of arrays extended the virtual source SAFT concept (VS-SAFT). Using focused subapertures and electronic scanning, signals can be acquired at high speed and without moving the probe. Furthermore, f-number can be electronically changed, controlling the virtual source position and the wave front properties [11], [12]. Several approaches have been followed in which the array is in contact with the inspected part, positioning the virtual source inside the material, behind the array, or a combination of both [13].

VS-SAFT with arrays has been described as a dual beamformer process [14]. First, virtual sources (VSs) are generated by focusing the beam in emission and reception at VS positions; then, a second beamformer obtains the SAFT image from the previously recorded A-scans. For the second beamformer, several approaches exist, some of them based on delay-and-sum (DAS) operations in the time domain [15], [16] and others implemented in the frequency domain [17], [18].

In the medical field, the propagation velocity can be usually considered constant, which simplifies SAFT calculations: VS beam properties are just determined by the f-number and the DAS process is straightforward. However, in the NDT field, a coupling medium with different propagation velocity is commonly used between probe and part to provide beam steering and/or mode conversion, to protect the transducer from frictional wear, or to accommodate component shape variations by water immersion. Beam refraction at the two-media interface complicates the VS-SAFT process because the virtual source beam pattern becomes modified by refraction and no closed formulae exist for time-of-flight calculation for arbitrarily shaped parts.

When using single-element focused transducers, a simple solution is to place the beam focus just at the interface

---

Manuscript received March 30, 2015; accepted August 30, 2015. This work was funded by project DPI2013-42236-R of the program "Research challenges" of the Spanish Ministry of Economy and Competitiveness.

The authors are with the Ultrasound Systems and Technology Group (USTG), Spanish National Research Council (CSIC), 28006 Madrid, Spain (e-mail: j.camacho@csic.es).

DOI http://dx.doi.org/10.1109/TUFFC.2015.007092

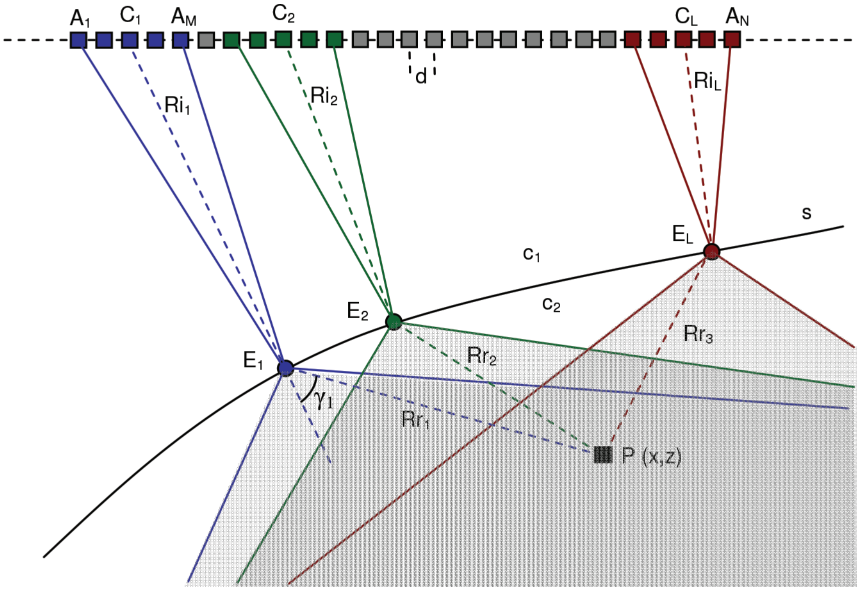

Fig. 1. Schematic representation of the AVSI process. Virtual source/receivers E_i are located by an autofocus algorithm. Shaded areas represent the regions covered by the refracted beams at three different virtual source/receivers generated by three array subapertures, which overlap at point $P(x, z)$.

between the couplant and the component under test [19], [20]. In this way, the virtual foci are located at the component surface, and the SAFT process is carried out only in the second medium with constant velocity. Simple models to find the beam profile taking into account refraction at the interface have been developed and used to calculate the opening angle inside the material and image aberrations caused by positioning errors [21]. To obtain high-quality images, the transducer focus must be accurately positioned at the component surface, and for arbitrarily shaped components this requires complex and high-precision positioning mechanics.

In this regard, immersion inspections are the most challenging ones, especially when component geometry changes during acquisition or the transducer relative position cannot be accurately known. These problems can be overcome by using arrays instead of single-element transducers because of their electronic focusing capability. Several approaches have been followed to automatically detect the component surface and generate the focal laws for phased-array [22] and total focusing method [23], in what are usually called auto-focusing algorithms.

In this work, an auto-focusing process is proposed to accurately position the virtual source/receivers and perform SAFT in presence of interfaces of unknown geometry. A complete methodology is given for detecting the component surface, generating the set of virtual sources, and obtaining the SAFT image considering sound propagation in the second medium only. In this way, SNR is increased with regard to single-element emission and refraction issues in time-of-flight calculations are avoided. The method is named auto-focused virtual source imaging (AVSI).

First, the overall process is described, giving nomenclature and basic equations. Then, each of the partial steps is explained: interface geometry automatic detection, generation of virtual source/receivers, and SAFT image composition. Finally, experimental results are presented with different part geometries and conclusions are extracted.

II. The Auto-Focused Virtual Source Imaging Concept

Fig. 1 depicts the AVSI concept. An array of N elements is used to perform a linear scan of L lines using subapertures of M elements each and with one element step ($L = N - M + 1$), although larger steps can be also used. Subaperture k is focused in emission and in reception with a fixed focus at the interface between the two media, generating the virtual source/receiver E_k. These L virtual source/receivers can be placed at any interface point by beam-steering but, as is shown by later analysis, the point of normal incidence from the center of each subaperture gives the optimum component insonification. A simple auto-focus algorithm finds the coordinates of these points. Theoretically, the distance between virtual sources should be less than quarter a wavelength in the second medium to avoid grating lobes [24].

For a propagation velocity in the component c_2 greater than that in the coupling medium c_1, the divergence angle of an incident focused beam widens within the part, producing a broader insonification or opening angle (Fig. 1). Each pixel P of the output image is obtained by coherently adding the signals acquired from all virtual sources/receivers whose refracted beams include the pixel position. In the case in which the whole set of L signals could be used in the composition and the pitch of the virtual source/receivers is d_v, the lateral resolution of the SAFT image would be equivalent to that provided by an array of aperture $D_v = L \cdot d_v$. This is better than the resolution ob-

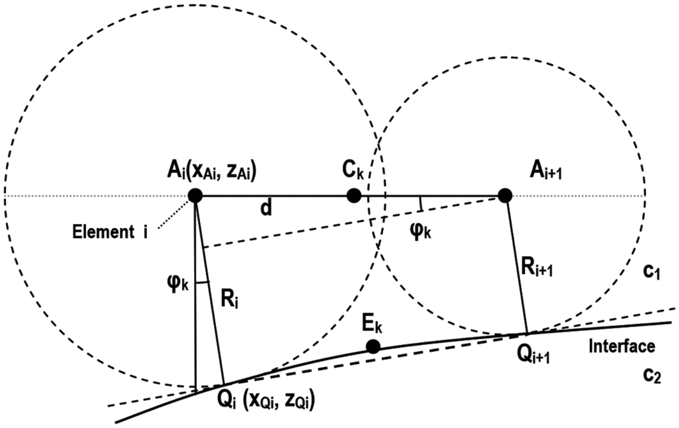

Fig. 2. Schematic representation of the surface estimation process by pulse–echo.

tained with the equivalent phased-array linear scan with subapertures $D_M = M{\cdot}d$ and dynamic depth focusing, because $M < L$ and $D_M < D_\mathrm{v}$. This is the main advantage of AVSI processing: achieving higher lateral resolution than a phased array for the same number of active element/channels and in the presence of interfaces.

With regard to conventional SAFT or other related techniques, the proposed AVSI technique gives three important advantages. First, signal-to-noise ratio is increased by $\sqrt{M}$ with regard to single-element emission because virtual sources are generated by focusing with M active elements [24]. Second, time of flight calculations are performed in the second medium only, which avoids refraction issues and simplifies SAFT image formation for arbitrarily shaped interfaces. Third, it does not require any description of the probe–part geometry because AVSI automatically obtains all the information required to produce an all-point focused image.

An additional advantage is that no complex equipment is needed. In particular, a multiplexed system with few active channels will provide a resolution comparable to that produced by full-parallel instruments operating in phased-array mode.

III. Automatic Virtual Source/Receiver Positioning

The position of the interface with respect to the array must be known to place the virtual source/receivers. In [22], three methods were given for automatic detection of the interface based on time-of-flight measurements from the array elements. Any one of them could be used in the present application, because all give an analytical representation of the interface obtained by curve fitting algorithms, which could be used to place virtual sources anywhere. However, if the virtual sources are placed in the normal incidence points from each subaperture, the pulse–echo method is preferred and the curve fitting processes can be avoided. Furthermore, angular coverage into the part is optimized, as analyzed in Section IV.

Consider the case of two consecutive elements A_i and A_{i+1} around the center C_k of a subaperture with an even number of elements (Fig. 2). Both elements are sequentially excited and first echo time of flight T_i and T_{i+1} to the respectively nearest interface points Q_i and Q_{i+1} are measured. They determine two circumferences of radius R_i and R_{i+1} centered at the emitting elements and tangent to the component surface. If the pitch d is small when compared with the interface curvature radius, segments A_iQ_i and $A_{i+1}Q_{i+1}$ can be considered parallel and the steering angle to reach the virtual source position E_k from the aperture center at C_k is

$$\varphi_k = \sin^{-1}\left(\frac{R_i - R_{i+1}}{d}\right) = \sin^{-1}\left(\frac{c_1}{2d}(T_i - T_{i+1})\right). \quad (1)$$

The coordinates of the virtual source E_k are directly obtained by

$$\begin{aligned} x_{Ek} &= x_{Ck} + R_k \sin\varphi_k \\ z_{Ek} &= z_{Ck} - R_k \cos\varphi_k, \end{aligned} \quad (2)$$

where $R_k \equiv (R_i + R_{i+1})/2$ is the distance from the array center to the virtual source obtained by the time-of-flight measurements T_i and T_{i+1}. In the case of an aperture with an odd number of elements, the aperture center C_k will coincide with element A_i or A_{i+1}, and the virtual source position E_k will coincide with entry point Q_i or Q_{i+1} respectively. No curve fitting procedure is needed at all to get the virtual source/receivers coordinates.

In general, for a set of L virtual source/receivers, a total of $2{\cdot}L$ individual shots would be required. But, if the active subaperture is shifted by one element in successive VS acquisitions, one of the time-of-flight measurements can be shared between consecutive virtual sources and the total number of shots is reduced to $L + 1$.

IV. Virtual Source/Receiver Generation

For the generation of the virtual source/receivers, a conventional fixed-focus emission-reception beamformer is used, with the focus placed at the desired position. From Fig. 1, time of flight from array element A_i to virtual source E_k is

$$T_{ik} = \frac{|\vec{r}_{Ai} - \vec{r}_{Ek}|}{c_1} = \frac{\sqrt{(x_{Ai} - x_{Ek})^2 + (z_{Ai} - z_{Ek})^2}}{c_1}, \quad (3)$$

where $\vec{r}_{Ai}$ and $\vec{r}_{Ek}$ are the vectors from origin to element A_i and virtual source E_k, respectively. Analogously, the time of flight of the main ray-path from the subaperture center C_k to the virtual source is

$$T_{Ck} = \frac{|\vec{r}_{Ck} - \vec{r}_{Ek}|}{c_1} = \frac{\sqrt{(x_{Ck} - x_{Ek})^2 + (z_{Ck} - z_{Ek})^2}}{c_1}. \quad (4)$$

The subaperture focal law is then obtained by

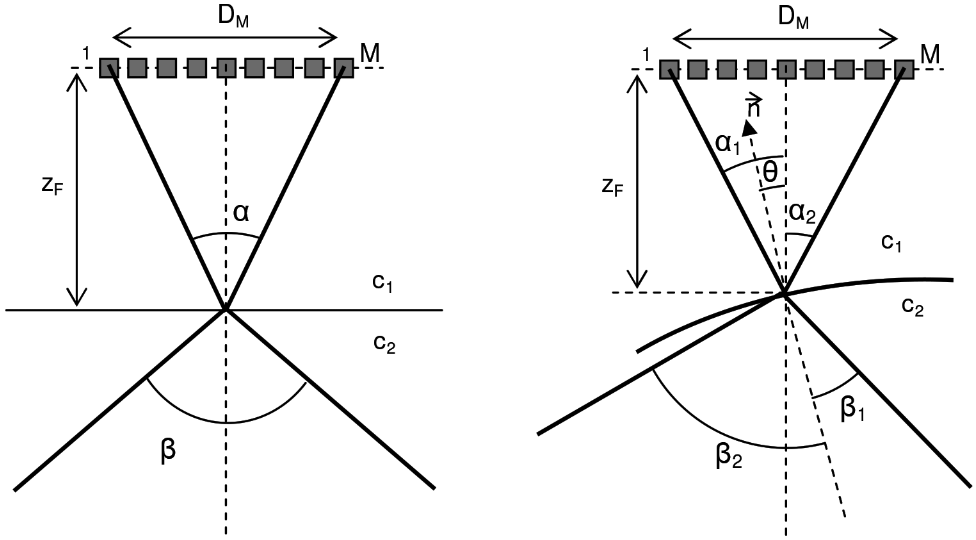

Fig. 3. Schematic representation of a beam focused at flat (left) and curved (right) interfaces.

$$\mathrm{FL}_{ik} = T_{Ck} - T_{ik}. \tag{5}$$

After each focused emission, a single focus A-scan is beamformed in reception by

$$s_k(t) = \sum_{i=1}^{M} s_i(t - \mathrm{FL}_{ik}), \tag{6}$$

where $s_i(t)$ is the signal received by element i. This process requires M active channels and can be carried out in real time by virtually any phased-array equipment. After all subapertures have been excited, a set of L A-scans are ready for SAFT image formation, which can be performed by an external computer or specialized hardware.

An important subject for a correct SAFT reconstruction is virtual source quality. Ideally, the focus at the interface should behave like an omnidirectional source, propagating a cylindrical wave into the second medium; but, because of the finite extension of the emitting subapertures, the generated wave field can be considered cylindrical in a limited angular extent only. The number of active elements and the incidence angle at the interface determines the properties of the beam, and must be wisely selected.

Fig. 3(left) shows the simplest model for a focused beam with normal incidence at a plane interface with $c_2 > c_1$, which is the most common situation in NDT. For an active aperture with size D_M and focused at a distance z_F, the opening angle at −6 dB into the second medium can be approximated by [8]:

$$\begin{aligned}\beta &= 2\sin^{-1}\left(\frac{c_2}{c_1}\sin\left(\tan^{-1}\left(\frac{D_M}{2z_F}\right)\right)\right)\\ &= 2\sin^{-1}\left(\frac{c_2}{c_1}\frac{1}{\sqrt{1+4(\mathrm{f-number})^2}}\right),\end{aligned} \tag{7}$$

Full part coverage requires $\beta = 180°$, for which the f-number must satisfy

$$\text{f-number} \le \frac{1}{2}\sqrt{\left(\frac{c_2}{c_1}\right)^2 - 1}. \tag{8}$$

Considering that in AVSI f-number $= R_k/D_M$, substitution in (8) gives a criterion for the minimum number of active elements required to get full coverage into the part:

$$M \ge \frac{2R_k}{d\sqrt{\left(\frac{c_2}{c_1}\right)^2 - 1}}. \tag{9}$$

This expression is also valid for non-planar interfaces and normal incidence, as long as the focal spot is much smaller than the local curvature radius of the interface, which is usually satisfied. In the case of oblique incidence, refracted angles from extreme elements of the array must be computed separately [see Fig. 3(right)], and the opening angle is

$$\begin{aligned}\beta &= \beta_1 + \beta_2\\ &= \sin^{-1}\left(\frac{c_2}{c_1}\sin(\alpha_1 - \theta)\right) + \sin^{-1}\left(\frac{c_2}{c_1}\sin(\alpha_2 + \theta)\right),\end{aligned} \tag{10}$$

where θ is the surface slope at the virtual source point and α_1 and α_2 the steering angles from the left- and right-most elements of the active aperture to the entry point, respectively. In this case, no closed formulae can be given for the minimum number of active elements required for ±90° opening angle, and (10) must be evaluated numerically. Fig. 4 shows values of β for a water–aluminum interface as a function of f-number for several slope values θ. For a fixed θ, the opening angle is larger for lower f-number values (as a consequence of larger incident angles), until the critical angle is reached and $\beta = 180°$. On the other hand, for a given opening angle, lower f-number values are needed (and hence more active elements) for higher surface slopes. Therefore, placing the virtual source at the normal

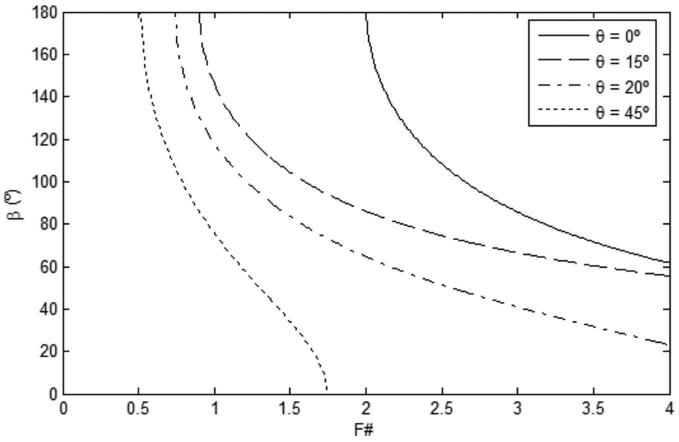

Fig. 4. Divergence angle into the second medium as a function of f-number for different surface slopes in a water-aluminum interface for longitudinal waves.

incidence point from each subaperture minimizes the number M of active channels required to achieve a given opening angle β, which can be considered an optimal choice.

For a given inspection scenario, it seems reasonable to choose the number of active elements M that ensures full part insonification. Fig. 5 shows pulsed wave simulation results with in-house developed software [25] based on the point source model and programmed in Matlab (The MathWorks Inc., Natick, MA, USA). Time of flight from each point source to each image pixel was obtained by solving for the fastest path through the interface according to the Fermat principle. Simulation parameters are $M = 17$ (f-number = 1.96), 5-MHz array with 80% bandwidth and 0.3 mm pitch, inspecting by water immersion a planar surface aluminum part placed at 10 mm distance ($c_1 = 1.5$ mm/μs and $c_2 = 6.2$ mm/μs). The number of elements was selected according to (9) for obtaining full part insonification.

Fig. 5(a) shows the field amplitude (in decibels). A focused beam is observed in water, which diverges on entering the aluminum part, creating the virtual source. This effect is clearer in the time-of-flight (TOF) image [Fig. 5(b)], where the contour plots of constant TOF from the virtual source evidence the creation of a point-like emitter at the focus position. Fig. 5(d) shows that wave front TOF differences with those of a cylindrical waveform, calculated at a constant radius $Rr = 20$ mm, are less than ±10 ns, an order of magnitude below the signal period for the whole angular extent. These TOF variations are due to the phase and amplitude distribution of the incident field along the interface, which is not exactly that of an ideal point source. The presence of side lobes, although of low amplitude, generates a distortion in the refracted beam pattern.

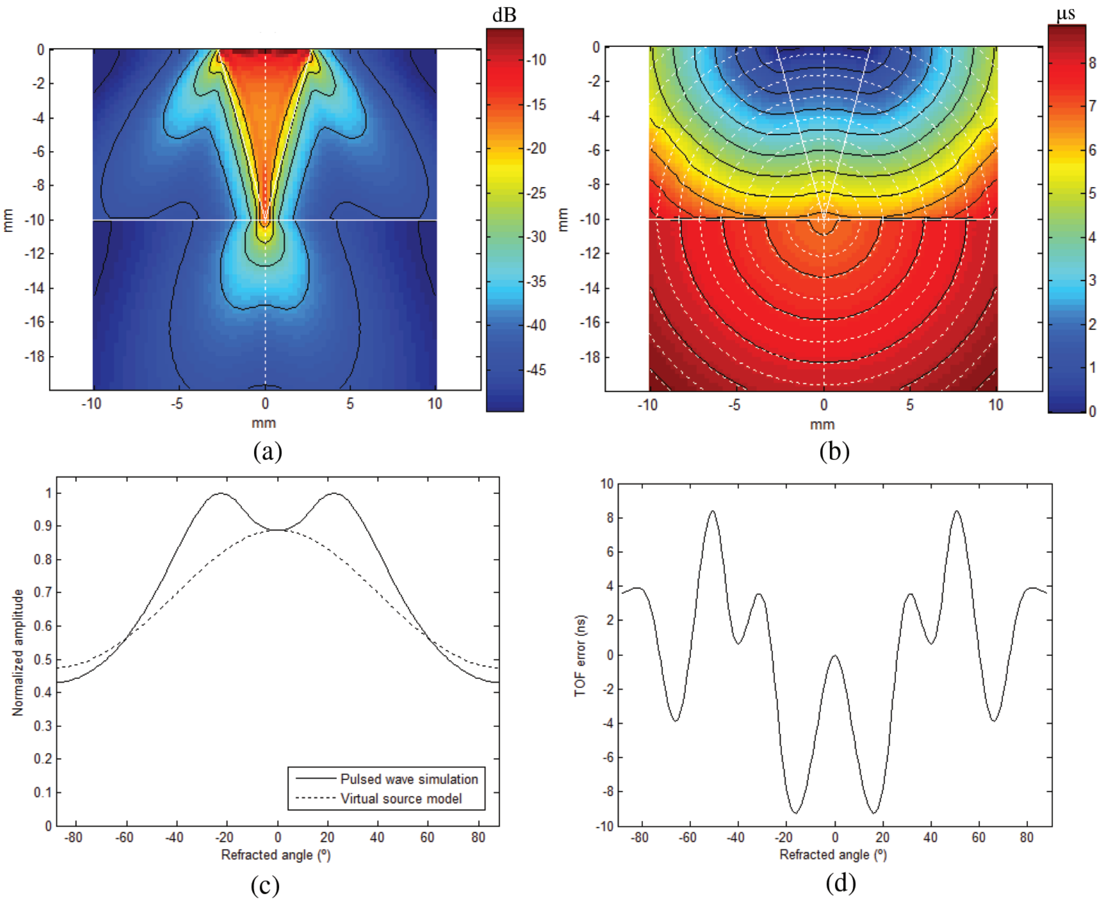

(a) (b)

(c) (d)

Fig. 5. Pulsed wave simulation for $M = 17$ elements of a 5-MHz array with 80% bandwidth and 0.3 mm pitch, inspecting by water immersion a planar surface aluminum part at 10 mm from the array. (a) Amplitude field in decibels, (b) time of flight field in microseconds, (c) lateral beam pattern, and (d) TOF error (in nanoseconds) at $Rr = 20$ mm from the virtual source inside the aluminum.

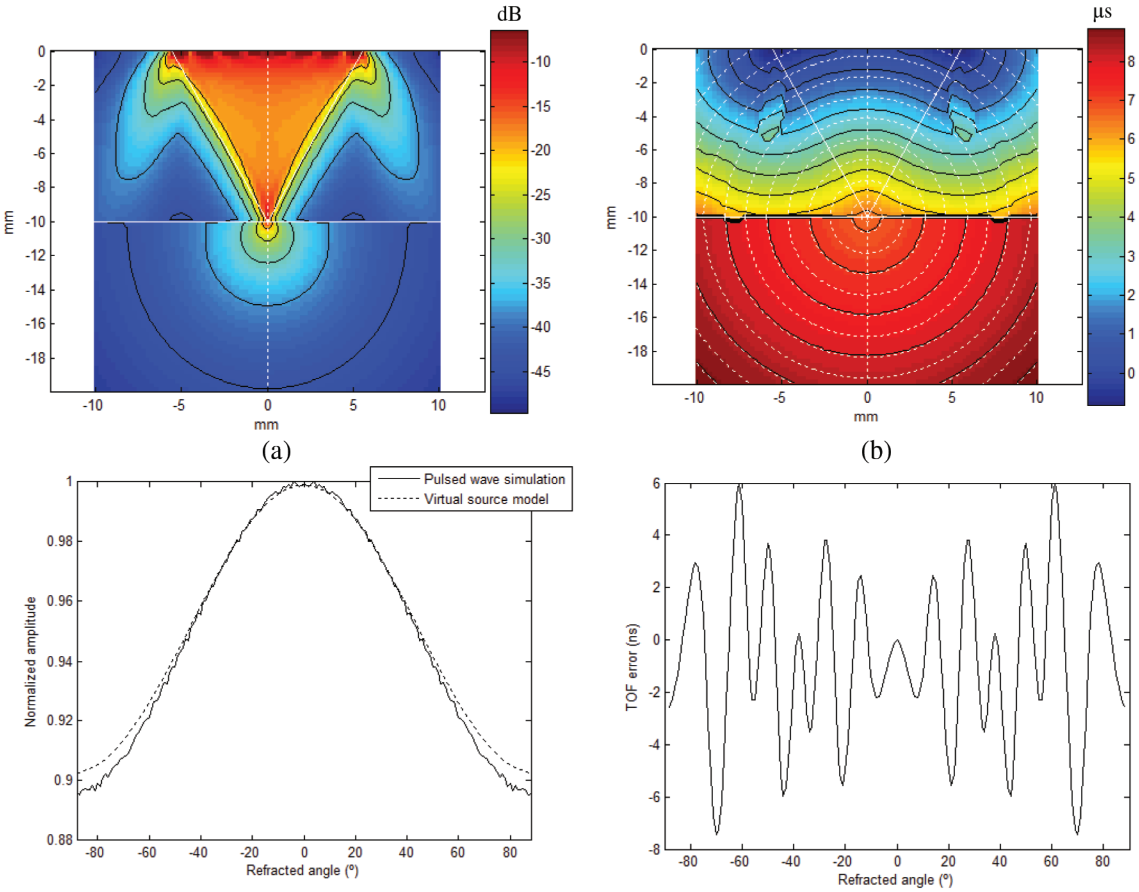

(a) (b) (c) (d)

Fig. 6. Pulsed wave simulation with $M = 40$ and the other parameters same as in Fig. 5. (a) Amplitude field in decibels, (b) time of flight field in microseconds, (c) lateral beam pattern, and (d) TOF error (in nanoseconds) at $Rr = 20$ mm from the virtual source inside the aluminum.

Fig. 5(c) shows the beam amplitude over the same constant radius of 20 mm. Although beam width at −6 dB is ±90° as predicted by (7), lateral profile presents two unexpected local maxima at ±25°. These are again a consequence of the field amplitude and phase distributions on the interface, which cannot be considered exactly equal to those of a point source. However, because the amplitude variation with refracted angle is small, it should have little impact in the final image and, in any case, it could be compensated by an inverse apodization in the SAFT imaging process.

Increasing the number of active elements would increase SNR and improve the beam's lateral profile. Fig. 6 shows simulation results with $M = 40$ (f-number = 0.83). Together with time-of-flight errors being slightly reduced compared with the previous case [compare Fig. 5(d) with Fig. 6(d)], the beam amplitude angular profile at Fig. 6(c) does not present the side lobes of the previous case. Moreover, it is very well approximated by the lateral profile of a single element located at the focus position with a size d_{eff}, equal to the −6-dB lateral extent of the focus:

$$d_{\text{eff}} \approx 1.22 \frac{R_i \cdot c_1}{f \cdot M \cdot d} = 1.22 \cdot \lambda_1 \cdot \text{f-number}, \tag{11}$$

where λ_1 is the wavelength in the first medium. This is a more realistic way of modeling the virtual source, whose lateral profile [dotted line in Figs. 5(c) and 6(c)] can be obtained by

$$A(\gamma) = \left| \operatorname{sinc}\left(\frac{d_{\text{eff}}}{\lambda_2} \sin(\gamma) \right) \times \operatorname{sinc}\left(\frac{d - \text{gap}}{\lambda_1} \sin\left(\theta - \sin^{-1}\left(\frac{c_1}{c_2} \sin(\gamma) \right) \right) \right) \right|, \tag{12}$$

where gap is the inter-element space and γ is the refracted angle into the second medium. The first term in (12) corresponds to the lateral sensitivity of the virtual source model, whereas the second term introduces the angular sensitivity of the array elements in the first medium.

Further increase of the number of active elements should enhance the SNR and, according to (11) and (12), it should also improve the beam angular profile. The limit to both variables is given by the lateral sensitivity of the array elements, which can be rather low in water immersion when using arrays with relatively large elements. For example, maximum steering angle in water for a 5-MHz array with 0.5 mm pitch is about 30°, which gives a minimum f-number = 0.87. For larger active apertures, no

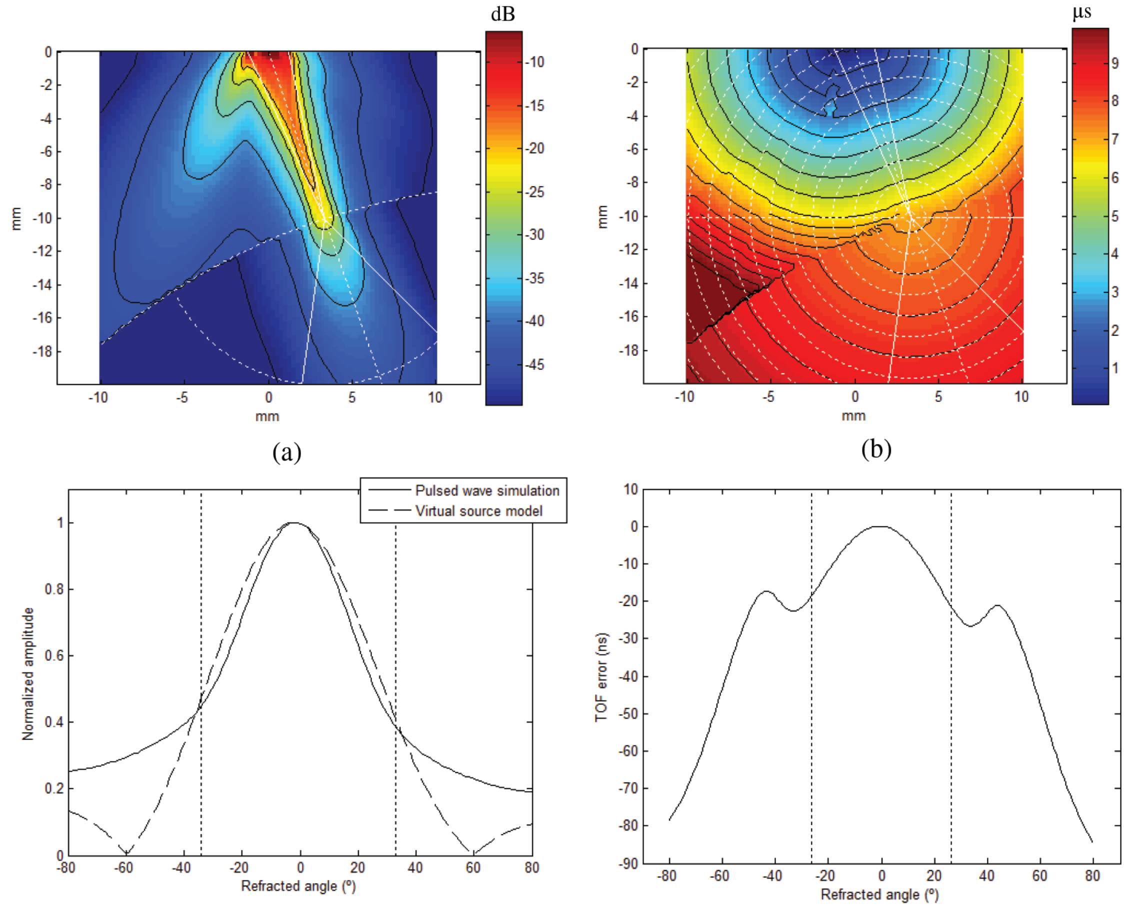

(a) (b)

(c) (d)

Fig. 7. Pulsed wave simulation with $M = 9$ and a cylindrical aluminum part with 40 mm of radius (a) Amplitude field in decibels, (b) time of flight field in microseconds, (c) lateral beam pattern, and (d) TOF errors (in nanoseconds) at $Rr = 10$ mm from the focus inside the aluminum part.

SNR or lateral sensitivity improvement should be expected, because the extra elements will not contribute useful information.

To provide further insight into AVSI performance, a final simulation was performed with a cylindrical surface with 40 mm radius and $M = 9$ elements (f-number = 3.9), which yields a theoretical angular coverage $\beta = 67°$. The virtual source was located at the surface normal incidence point from the aperture center, which requires a beam steering angle of 19°. Fig. 7 shows simulation results, from which it is evident that the generated focus can be approximated by a point-like source only in a limited angular extent, depicted with dashed lines in Figs. 7(c) and 7(d). Outside these limits, amplitude decay below −6 dB and timing errors with respect to a cylindrical wave front increase significantly.

V. SAFT Image Formation Process

The final step of the proposed algorithm is to generate the SAFT image of the inspected part. In the virtual source model, the sound propagation path is assumed to be a straight line from the emitting aperture center C_k to the virtual source E_k and, then, to any point P into the material, also in a straight path (Fig. 8). The last is valid inside the angular extent of the refracted field where the wave front can be considered cylindrical. Thereby, the TOF from the emission with subaperture k centered at C_k to pixel P with coordinates (x, z) is

$$\begin{aligned} t_{k,xz} &= T_{C_kE_k} + T_{E_kP} \\ &= \frac{\sqrt{(x_{Ck} - x_{Ek})^2 + (z_{Ck} - z_{Ek})^2}}{c_1} \\ &\quad + \frac{\sqrt{(x_{Ek} - x)^2 + (z_{Ek} - z)^2}}{c_2}. \end{aligned} \tag{13}$$

It must be pointed out that the first term of (13) is independent of the pixel position, and hence, it is a constant that can be calculated only once for each subaperture. The output sample of the SAFT image is then obtained by summation of all contributing signals by

$$I_{xz} = \left| \frac{1}{B_{xz}} \sum_{k=1}^{L} \alpha_{k,xz} V_{k,xz} S_k(2 \cdot t_{k,xz}) \right|. \tag{14}$$

where $V_{k,xz}$ is an apodization factor for controlling side lobes, $\alpha_{k,xz}$ is a binary coefficient to avoid adding up samples that are outside the opening angle β, B_{xz} is a normal-

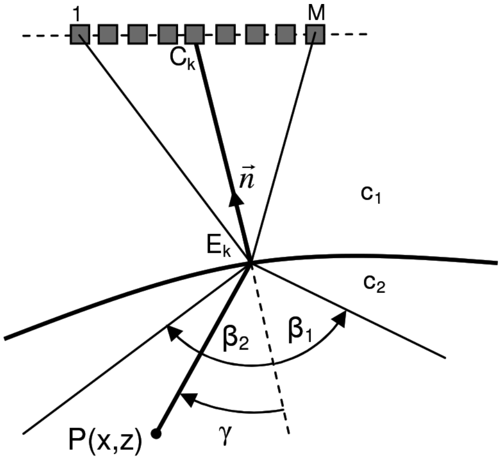

Fig. 8. Geometry for the SAFT image formation showing subaperture k and pixel $P(x, z)$.

ization factor that counts the number of added samples for each image pixel, and $S_k(t)$ is the analytic representation of the beamformed signal $s_k(t)$ obtained with the Hilbert transform $\mathrm{H}(\cdot)$ by

$$S_k(t) = s_k(t) + j\,\mathrm{H}(s_k(t)). \tag{15}$$

From Fig. 8, the coefficient $\alpha_{k,xz}$ can be obtained from the refracted angle γ to P as

$$\alpha_{k,xz} = \begin{cases} 1 & \text{for } \beta_2 \leq \gamma \leq \beta_1 \\ 0 & \text{otherwise,} \end{cases} \tag{16}$$

and the normalization factor B_{xz} is defined as

$$B_{xz} = \sum_{k=1}^{L} \alpha_{k,xz}. \tag{17}$$

Using the analytic representation of $s_k(t)$ instead of the RF received signals is common in synthetic aperture techniques. It allows spacing output samples to satisfy the Nyquist criterion for the signal envelope (instead of the RF signal), reducing data throughput, memory, and computation time. Furthermore, the signal envelope is extracted by simply taking the absolute value of the complex sum and no post-processing filter is required.

The lateral resolution of the SAFT image is dependent of the number of virtual sources B_{xz} used for each pixel calculation. Full-width at half-maximum resolution (FWHM) at depth z from the interface can be obtained by

$$\Delta x_{xz} = \frac{1}{2}\left(1.22\,\frac{\lambda_2}{L_{\mathrm{eff}}}\right) z = \frac{0.61\,\lambda_2\, z}{B_{xz}\, d_v}, \tag{18}$$

where d_{v} is the distance between virtual source/receivers (assumed constant), and L_{eff} is the effective virtual aperture size. Taking into account that

$$\tan\frac{\beta}{2} = \frac{L_{\mathrm{eff}}}{2z}, \tag{19}$$

substitution into (18) yields

$$\Delta x_{xz} = 0.3\lambda_2 \left(\tan\frac{\beta}{2}\right)^{-1}. \tag{20}$$

As expected for a SAFT image when dynamic aperture is applied, lateral resolution is constant and independent of depth [26], up to the distance $z_{\max}$, where the effective aperture equals the total extent of the virtual aperture $D_{\mathrm{v}} = L \cdot d_{\mathrm{v}}$

$$z_{\max} = \frac{L \cdot d_{\mathrm{v}}}{2} \left(\tan\frac{\beta}{2}\right)^{-1}. \tag{21}$$

For example, in the simulation of Fig. 7 with $\beta = 67°$, lateral resolution will be constant and $\Delta x_{\text{-6dB}} = 0.56$ mm up to $z_{\max} = 27$ mm if an array with $N = 128$ elements is used ($L = 120$ and $d_{\mathrm{v}} = 0.3$ mm).

VI. Experimental Results

For experimental verification, an array with $N = 128$ elements, $f = 5$ MHz, and pitch $d = 0.65$ mm (Imasonic SAS, Voray-sur-l'Ognon, France) was used to inspect several components with flat and curved shapes, by water immersion. A SITAU-311 (DASEL SL, Madrid, Spain) phased-array system with 32 active channels multiplexed to 128 elements was used to generate the virtual sources/receivers and record virtual A-scans. Further processing was carried out off-line using Matlab.

In a first experiment, a flat surface aluminum block with a single 1.5-mm-diameter side-drilled hole (SDH) at 30 mm depth was used. The array was placed parallel to the surface at a distance $h \approx 25$ mm in water. The interface was automatically detected by the proposed method and a total number of $L = 96$ virtual sources/receivers were generated at the normal incidence points defined by (2). The selected active aperture was $M = 16$ elements, which gives f-number = 2.4.

Fig. 9(a) shows the image of the raw acquired data. Echoes from the SDH are distributed on a hyperbola with the apex at the reflector position and TOF described by (13). The solid line in Fig. 9(b) shows the expected angular profile of the received echoes following (12), squared to account for pulse–echo operation. Experimental data reasonably matches the theoretical prediction, confirming that the −6-dB opening angle into the part is $\beta \approx 60°$, according to (7), divided by 2 for pulse–echo operation.

Fig. 9(c) shows the AVSI image after SAFT beamforming with $\beta = 60°$. The SDH at $z = 30$ mm is detected with good resolution. Side and grating lobes characteristic of SAFT images are also observed. Fig. 9(d) shows the lateral profile at the depth of the defect, with a FWHM resolution $\Delta x = 0.96$ mm that reasonably matches the expected resolution of 0.65 mm predicted by (20). The difference is mainly caused by the SDH diameter (1.5 mm) that cannot be neglected for the main beam width calculation, as assumed in (20).

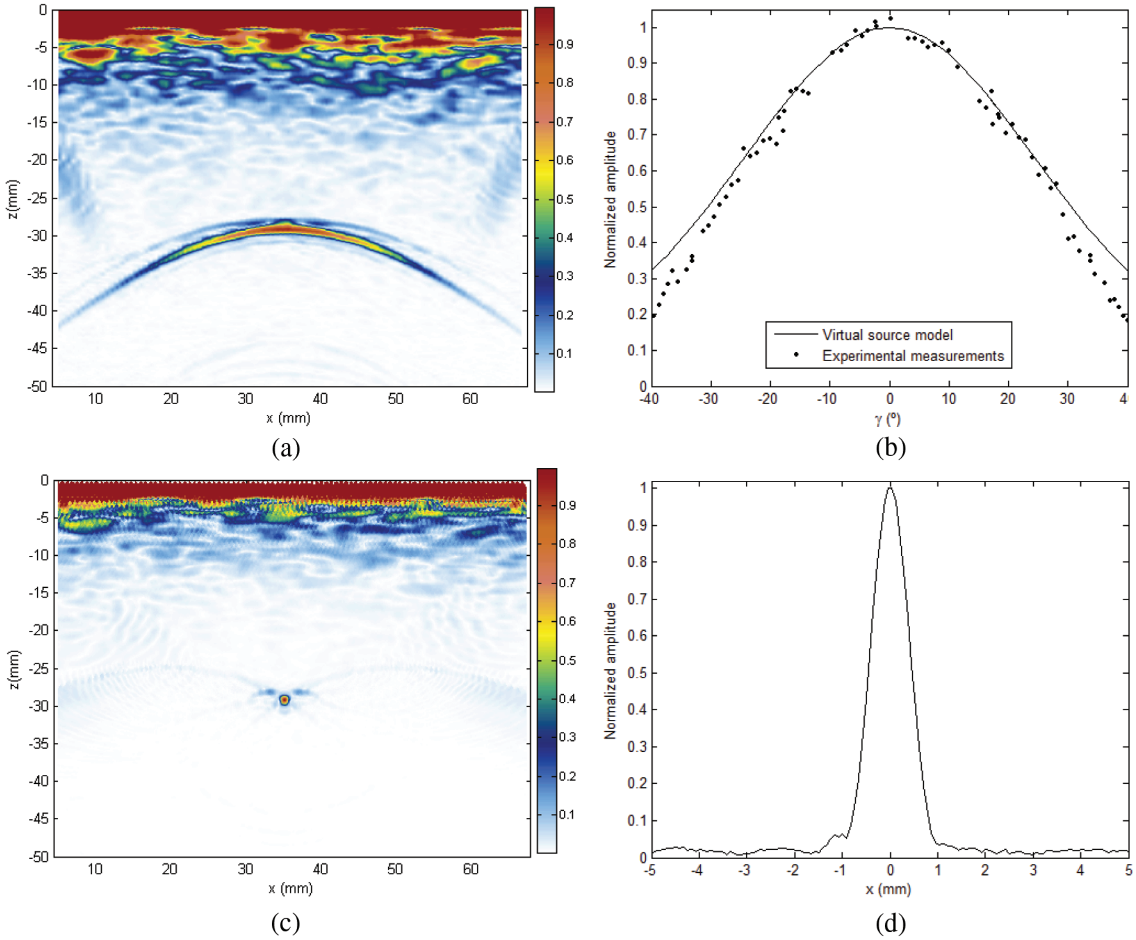

Fig. 9. Images from experiment 1: (a) raw B-scan data, (b) angular profile of SDH echo (solid) analytic model (dots) experimental measurements, (c) AVSI image, and (d) lateral profile at the SDH depth. Color scale is linear.

Figs. 10(a), 10(b), and 10(c) show detail around the SDH position for $M = 12$, 16, and 32 active elements, respectively. As expected, higher M values (lower f-number) yield higher opening angles and, hence, better lateral resolution. Fig. 10(d) shows the lateral profiles at the SDH depth for the three cases. FWHM with $M = 16$ is 1.4 times lower than with $M = 12$, which agrees with an effective aperture increase by a factor of 1.3. On the other hand, doubling the number of active elements from $M = 16$ to $M = 32$ does not double resolution. This is explained by the limited angular sensitivity of the array elements in water ($d \approx 2.2\ \lambda_1$), which limits the effective opening angle into the second medium for large active apertures [second term of (12)].

SNR improvement when increasing M predicted by [24] cannot be evaluated from the present experiments, because the acoustic background noise generated by the side lobes of the SAFT technique is much higher than the electrical white noise at the input of each element amplifier. Because electrical noise is independent between channels it will be reduced by increasing M, but the same will not happen with the side lobe level of the SAFT image, which only depends of the number of virtual sources L. SNR improvements will be investigated in future work with the inspection of highly attenuating materials such as austenitic steel and welds.

A second experiment was conducted with the same array and an aluminum block with 7 pairs of 2.5-mm-diameter SDHs, separated 3 mm in the in x direction and 10 mm in the z direction. The array was placed parallel to the interface at a distance $h \approx 25$ mm in water, and the interface was automatically detected by the proposed method. Again, $L = 96$ virtual sources/receivers were created, with an active aperture of $M = 16$ elements that gives $\beta \approx 60°$.

Fig. 11 shows the raw B-scan data (left) and the AVSI image (right), where all SDHs can be individually resolved. Fig. 12 shows the measured lateral resolution, and as predicted by (20), it is essentially constant with depth up to the maximum range $z_{\max} \approx 54$ mm given by (21). The image was beamformed using lower values of $\beta = \{40°, 30°\}$, verifying the inverse relation between resolution and opening angle also predicted by (20). Note that, in all cases, the resolution of the pair of SDH's at $z = -70$ mm is worse than expected. The reason is that the effective aperture near the lateral image limits is reduced at large depths because fewer virtual source/receivers can be used for each pixel.

The experiment was repeated after tilting the part 5.3° with respect to the array. Fig. 13(a) shows the resultant

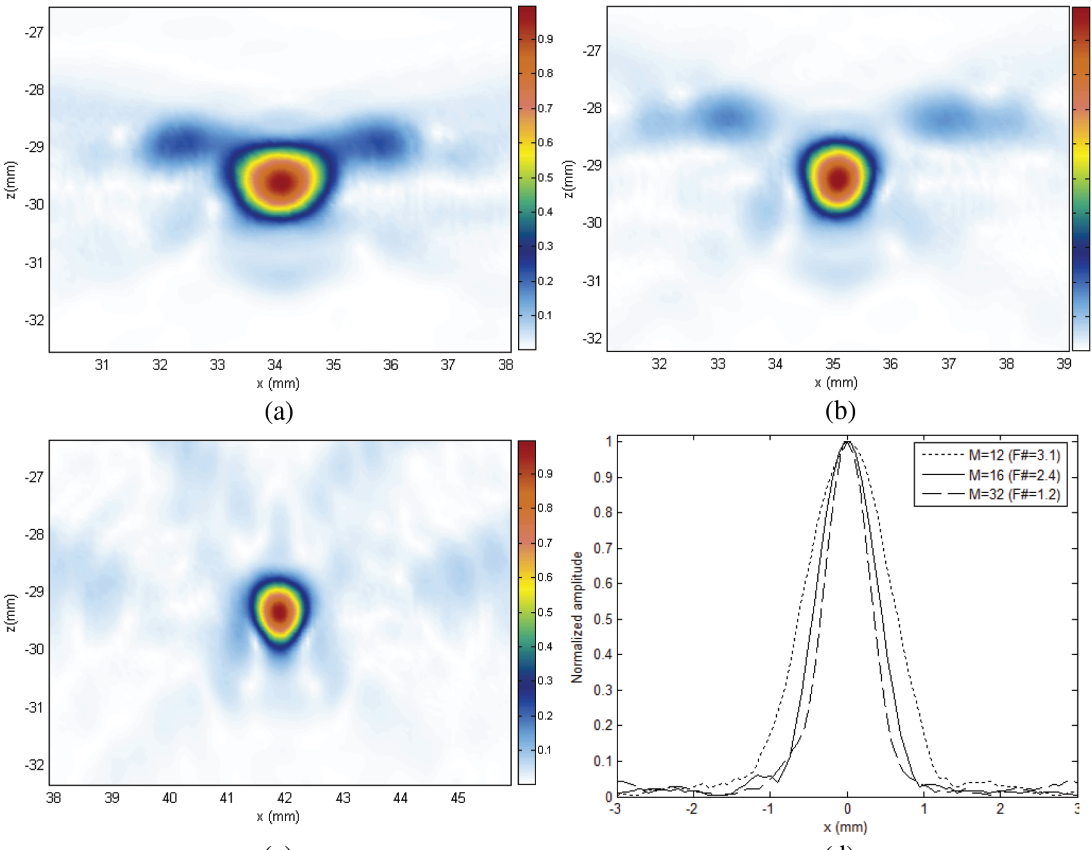

(a) (b)

(c) (d)

Fig. 10. Detail of the AVSI image at SDH position with (a) $M = 12$, (b) $M = 16$, and (c) $M = 32$ active elements for virtual sources/receives. (d) Lateral profiles at the SDH depth. Color scale is linear.

AVSI image, which is equivalent to that obtained with the array at 0° [Fig. 11(b)]. Lateral resolution is kept [Fig. 13(b)] because it depends on the virtual array extension only, which practically does not change for a small tilt. On the other hand, a slight amplitude loss can be appreciated, because of the reduced lateral sensitivity of the array elements in water.

A final experiment was performed with a 100-mm-curvature-radius aluminum part with two groups of 1.5-mm-diameter SDHs. The array was placed at distance $h \approx 20$

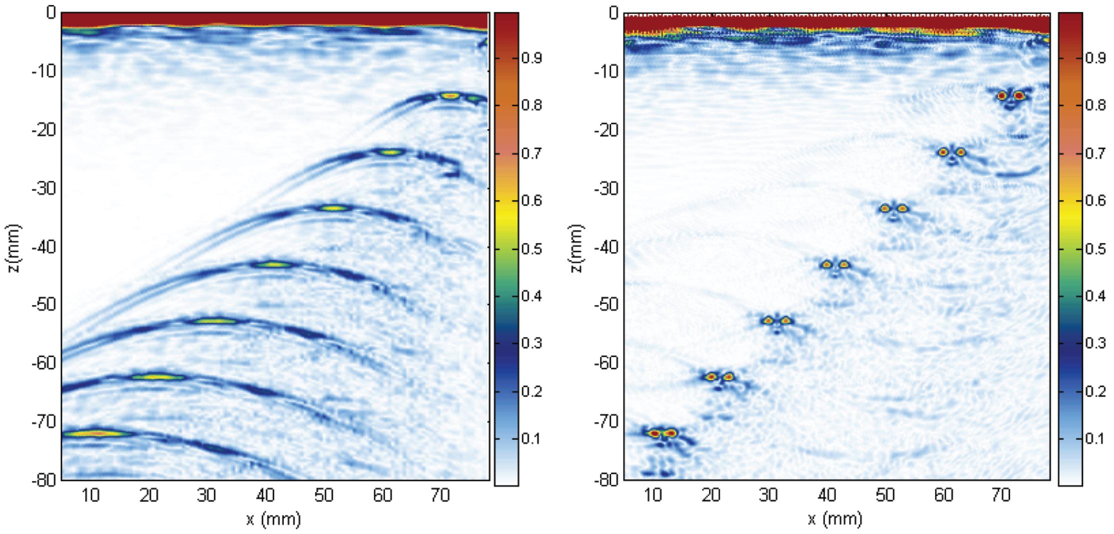

(a) (b)

Fig. 11. Images from experiment 2: (a) raw B-scan data and (b) AVSI image with $M = 16$ active elements for virtual source/receivers creation. Color scale is linear.

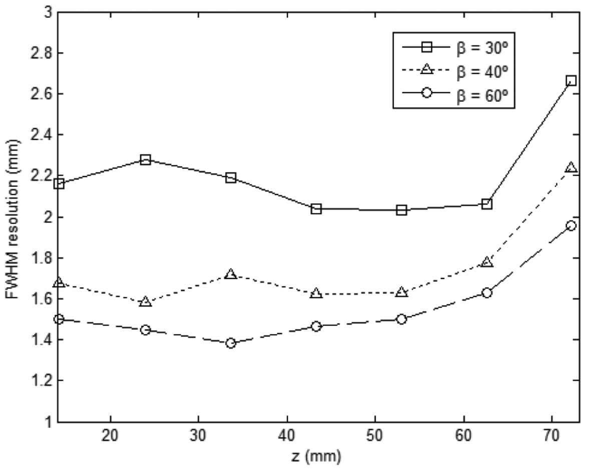

Fig. 12. FWHM lateral resolution as a function of depth for all SDHs in experiment 2 and opening angles β = 30°, 40°, and 60°.

mm from the component surface in water. The interface was automatically detected by the proposed method and a total number of $L = 96$ virtual sources/receivers were generated at the normal incidence points defined by (2) (dots at the interface in Fig. 14(a)]. Active aperture was $M = 16$ elements.

Fig. 14(b) shows the AVSI image, where all SDHs are individually resolved with the expected lateral resolution. For comparison, a conventional phased-array image generated with $M = 16$ active elements, emission focus at $z = -25$ mm and dynamic depth focusing in reception was included in Fig. 14(c). Higher resolution of AVSI processing is evident when comparing Figs. 14(b) and 14(c), both obtained with the same number of active elements, and hence with the same hardware complexity.

Finally, Fig. 14(d) shows the image obtained with a 128-active-element phased-array system (SITAU-111, Dasel, Madrid, Spain) in angular scan configuration with dynamic depth focusing in reception. As expected, lateral resolution in this case is comparable to that obtained with AVSI using only 16 active elements [Fig. 14(b)]. On the other hand, the acoustic noise floor is lower in the 128-element phased-array image because of the lower side lobe level of the phased array with regard to SAFT.

VII. Discussion and Conclusions

In this work, the SAFT approach was followed for image formation, but the AVSI concept can be easily extended to any other synthetic aperture scheme, such as TFM or M-SAFT. A different virtual receiver from the virtual source can be created by activating different subapertures in emission and in reception. In that case, (14) is easily reformulated as

$$I_{xz} = \left| \frac{1}{B_{xz}} \sum_{k=1}^{L} \sum_{j=1}^{P} \alpha_{jk,xz} V_{jk,xz} S_{jk}(t_{k,xz} + t_{j,xz}) \right|, \qquad (28)$$

where P is the number of virtual receivers for each virtual source, S_{jk} is the signal registered with virtual receiver j and virtual source k, $t_{k,xz}$ is the TOF from the emitter aperture center C_k to the pixel at (x, z) and $t_{j,xz}$ is the TOF from the pixel back to the receiver aperture center C_j, each obtained from (13). Evaluation of the performance of different AVSI (L, P) schemes and their implementation requirements are under research and will be presented in a future work. It is expected that image contrast will be improved because of the lower side-lobe level of multi-element synthetic aperture techniques.

Apart from these possible extensions, the concept of AVSI provides several advantages for ultrasonic imaging in a two-media scenario. First, knowledge of the probe–part geometry is not required, because all information needed for focusing into the part can be automatically obtained from a set of ultrasonic measurements. Simple closed for-

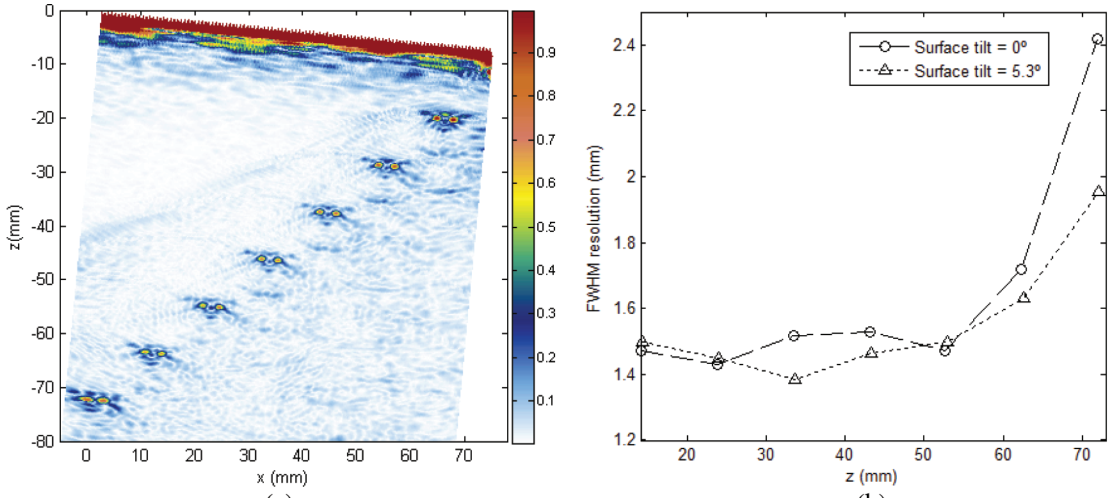

(a) (b)

Fig. 13. (a) AVSI image from experiment 2 after tilting the part 5.3° with respect to the array. (b) FWHM lateral resolution as a function of depth for all SDHs in experiment 2 for 0° and 5.3° tilt angle. Color scale is linear.

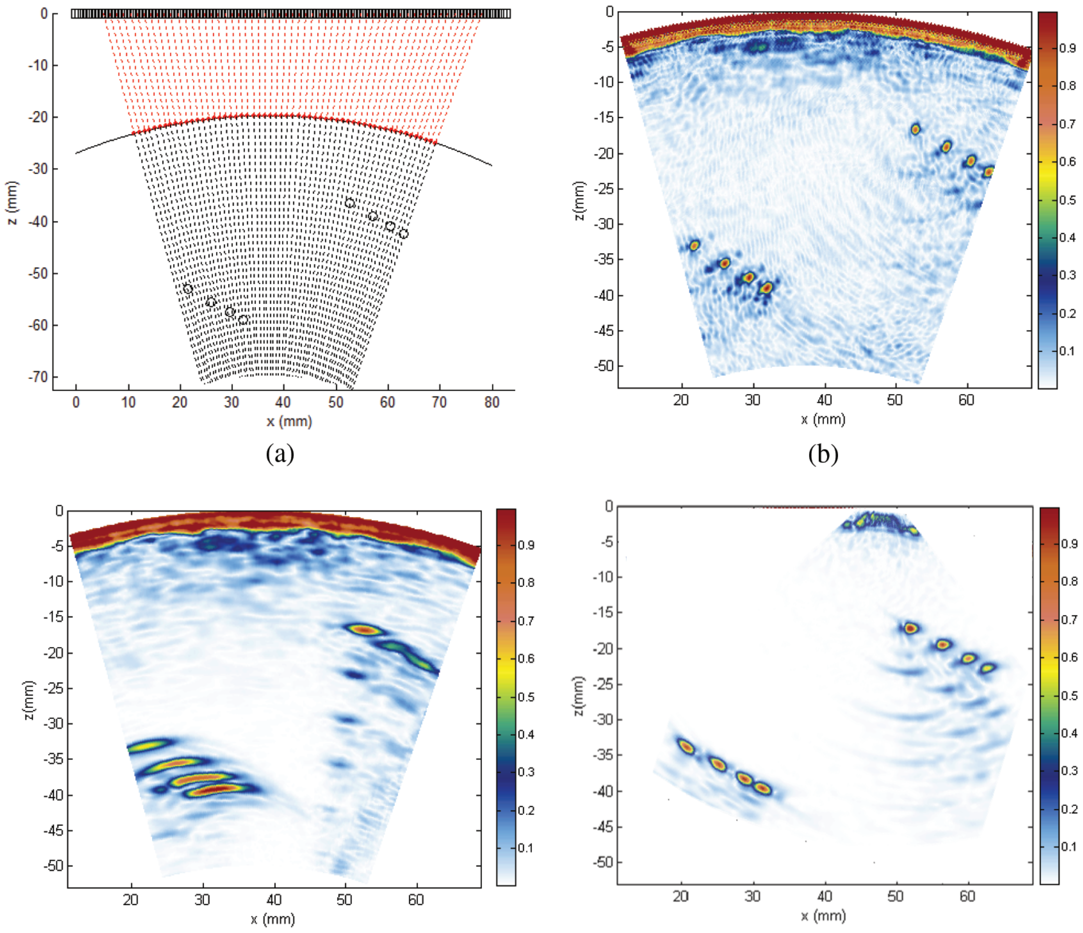

(a) (b) (c) (d)

Fig. 14. (a) Inspection scenario of experiment 3, showing with red dots the location of the virtual sources/receivers, (b) AVSI image with $M = 16$, (c) conventional phased-array linear scan image with 16 active elements, and (d) conventional phased-array sector scan with 128 active elements. Color scale is linear.

mulae locate the focus at the interface for normal incidence and yield the corresponding focal laws. Subaperture size can be chosen to optimize the opening angle in the inspected part to obtain the required lateral resolution. Although $\beta = 180°$ insonification angle would be desirable, it is important to account for the actual lateral sensitivity of the array elements in water, which is sometimes lower than that predicted by the second term of (12).

Second, refraction complications are avoided, and all the required focal laws are computed for a homogeneous constant velocity medium. This is a consequence of setting the virtual source/receiver at the two-media interface.

Third, resolution is quite high, of the order of that obtained with a full parallel phased-array system, but with significant lower system complexity: final images are composed from a set of A-scans obtained with low-channel-count subapertures. Resolution is constant up to a depth determined by the effective virtual aperture. This is achieved with the same number of trigger events as is required for a simple phased-array linear scan.

Fourth, signal-to-noise ratio should be higher than with synthetic aperture techniques that use a single element as emitter, because AVSI always operates with a focused subaperture of M elements. Improvements in SNR of the order of $M^{1/2}$ with regard to SAFT can be expected, which could have significant impact in the inspection of highly attenuating materials.

This work presented the principles of AVSI and its main characteristics. The theory was verified by pulsed wave simulation and experimentally. In short, the AVSI has shown to be a simple and efficient technique for NDT ultrasonic imaging.

REFERENCES

[1] K. J. Langenberg, M. Berger, Th. Kreutter, K. Mayer, and V. Schmitz, "Synthetic aperture focusing technique signal processing," *NDT Int.*, vol. 19, no. 3, pp. 177–189, Jun. 1986.

[2] V. Schmitz, W. Muller, and G. Schafer, "Synthetic aperture focusing technique: State of the art," *Acoust. Imaging*, vol. 19, pp. 545–551, 1992.

[3] V. Schmitz, S. Chalkov, and W. Muller, "Experience with synthetic aperture focusing technique in the field," *Ultrasonics*, vol. 38, pp. 731–738, 2000.

[4] D. MacDonald, "Images of flaws in generator retaining rings using SAFT reconstruction of TOFD data," in *Review of Progress in Quantitative Nondestructive Evaluation*, 1990, pp. 765–772.

[5] C. H. Frazier and W. D. O'Brien Jr., "Synthetic aperture techniques with a virtual source element," *IEEE Trans. Ultrason. Ferroelectr. Freq. Control*, vol. 45, no. 1, pp. 196–207, Jan. 1998.

[6] C. Passmann and H. Ermert, "A 100-MHz ultrasound imaging system for dermatologic and ophthalmologic diagnostics," *IEEE Trans. Ultrason. Ferroelectr. Freq. Control*, vol. 43, no. 4, pp. 545–552, Jul. 1996.

[7] T. Stepinski, "SAFT performance in ultrasonic inspection of coarse grained metals," in *Sixth Int. Conf. NDE in Relation to Structural Integrity for Nuclear and Pressurized Components*, Budapest, Hungary, October 2007, pp. 1–8.

[8] T. Scharrer, A. Koch, K. T. Fendt, S. J. Rupitsch, A. Sutor, H. Ermert, and R. Lerch, "Ultrasonic defect detection in multi-material, axis-symmetric devices with an improved synthetic aperture focusing technique (SAFT)," in *Proc. IEEE Int. Ultrasonics Symp.*, 2012, pp. 1039–1042.

[9] M.H. Skjelvareid, Y. Birkelund, and Y. Larsen, "Internal pipeline inspection using virtual source synthetic aperture ultrasound imaging," *NDT & E Int.*, vol. 54, pp. 151–158, Mar. 2013.

[10] S. J. Rupitsch and B. G. Zagar, "Acoustic microscopy technique to precisely locate layer delamination," *IEEE Trans. Instrum. Meas.*, vol. 56, no. 4, pp. 1429–1434, Aug. 2007.

[11] M. H. Bae and M. K. Jeong, "A study of synthetic-aperture imaging with virtual source elements in B-mode ultrasound imaging systems," *IEEE Trans. Ultrason. Ferroelectr. Freq. Control*, vol. 47, no. 6, pp. 1510–1519, Nov. 2000.

[12] P. Nanekar, A. Kumar, and T. Jayakumar, "SAFT-assisted sound beam focusing using phased arrays (PA-SAFT) for non-destructive evaluation," *Nondestruct. Test. Eval.*, vol. 30, no. 2, pp. 105–123, http://dx.doi.org/10.1080/10589759.2014.1002837, 2015.

[13] M. Sutcliffe, P. Charlton, and M. Weston, "Multiple virtual source aperture imaging for non-destructive testing," *Insight*, vol. 56, no. 2, pp. 75–81, Feb. 2014.

[14] J. Kortbek, J. A. Jensen, and K. L. Gammelmark, "Sequential beamforming for synthetic aperture imaging," *Ultrasonics*, vol. 53, no. 1, pp. 1–16, Jan. 2013.

[15] J. A. Seydel, "Ultrasonic synthetic-aperture focusing techniques in NDT," in *Research Techniques for Nondestructive Testing*, New York, NY, USA: Academic Press, 1982, pp. 1–47.

[16] S. R. Doctor, T. E. Hall, and L. D. Reid, "SAFT—The evolution of a signal processing technology for ultrasonic testing," *NDT Int.*, vol. 38, pp. 165–167, Jun. 1986.

[17] K. Nagai, "A new synthetic-aperture focusing method for ultrasonic B-scan imaging by the Fourier transform," *IEEE Trans. Sonics Ultrason.*, vol. 32, no. 4, pp. 531–536, Jul. 1985.

[18] K. Mayer, R. Marklein, K. Langenberg, and T. Kreutter, "Three-dimensional imaging system based on the Fourier transform synthetic aperture focusing technique," *Ultrasonics*, vol. 28, no. 4, pp. 241–255, 1990.

[19] T. Lukomski, T. Stepinski, and J. Kowal, "Synthetic aperture focusing technique with virtual transducer for immersion inspection of solid objects," *Insight*, vol. 54, no. 11, pp. 623–627, Nov. 2012.

[20] T. Scharrer, M. Schrapp, S. Rupitsch, A. Sutor, and R. Lerch, "Ultrasonic imaging of complex specimens by processing multiple incident angles in full-angle synthetic aperture focusing technique," *IEEE Trans. Ultrason. Ferroelectr. Freq. Control*, vol. 61, no. 5, pp. 830–839, May 2014.

[21] C. H. Chang, Y. F. Chang, Y. Ma, and K. K. Shung, "Reliable estimation of virtual source position for SAFT imaging," *IEEE Trans. Ultrason. Ferroelectr. Freq. Control*, vol. 60, no. 2, pp. 356–363, Feb. 2013.

[22] J. Camacho, J. F. Cruza, J. Brizuela, and C. Fritsch, "Automatic dynamic depth focusing for NDT," *IEEE Trans. Ultrason. Ferroelectr. Freq. Control*, vol. 61, no. 4, pp. 673–684, Apr. 2014.

[23] M. Sutcliffe, M. Weston, P. Charlton, K. Donne, B. Wright, and I. Cooper, "Full matrix capture with time-efficient auto-focusing of unknown geometry through dual-layered media," *Insight*, vol. 55, no. 6, pp. 297–301, Jun. 2013.

[24] M. Karaman, P. Li, and M. O'Donnell, "Synthetic aperture imaging for small scale systems," *IEEE Trans. Ultrason. Ferroelectr. Freq. Control*, vol. 42, no. 3, pp. 429–442, May 1995.

[25] J. L. Ealo, J. J. Camacho, and C. Fritsch, "Airborne ultrasonic phased arrays using ferroelectrets: A new fabrication approach," *IEEE Trans. Ultrason. Ferroelectr. Freq. Control*, vol. 56, no. 4, pp. 848–858, Apr. 2009.

[26] L. J. Cutrona, "Comparison of sonar system performance achievable using synthetic-aperture technique with the performance achievable by more conventional means," *J. Acoust. Soc. Am.*, vol. 58, no. 2, pp. 336–348, 1975.

Jorge Camacho was born in Montevideo, Uruguay, in 1979. He received the B.S. degree in electronic engineering from the Universidad de la República, Uruguay (UdeLaR) in 2004. He received the Ph.D. degree in systems and automation engineering from the Universidad Complutense de Madrid (UCM) in 2010. Since 2005, he has been an associate researcher at the Spanish National Research Council (CSIC). His research interests include high-resolution acoustic imaging, real-time beamforming, and new imaging methods for medical and NDT applications.

Jorge F. Cruza was born in Madrid, Spain, in 1983. He obtained the B.S. degree in telecommunication engineering in 2009 and the M.S. degree in electronics in 2011, both from the Universidad de Alcalá (UAH). He is currently a Ph.D. student at UAH. Since 2010, he has been an Associate Researcher at the Spanish National Research Council (CSIC). His research interests include high-resolution acoustic imaging, real-time beamforming, and FPGA signal processing.

Total Focusing Method With Virtual Sources in the Presence of Unknown Geometry Interfaces

Jorge F. Cruza and Jorge Camacho

Abstract— **Auto-focused virtual source imaging (AVSI) has been recently presented as an alternative method for synthetic aperture focusing through arbitrarily shaped interfaces with arrays. This paper extends the AVSI concept to the case of the total focusing method (TFM-AVSI) using several virtual receivers for each virtual source. This approach overcomes the known contrast limitation of AVSI, while preserving the advantage of performing synthetic focusing in the second medium only [no time-of-flight (TOF) calculations through the interface]. In contrast, equipment with more active channels must be used to digitalize the signals received by all the array elements after each focused emission. When compared with the conventional TFM, the proposed method reduces the processing complexity of the most time consuming task: TOF calculation in the presence of interfaces. This improvement could lead to more efficient real-time implementations of the TFM in non-destructive testing applications where water immersion or flexible wedges are used. In this paper, the mathematical formulation for the new method is given, accounting for the surface slope and the array angular sensitivity. Its performance is evaluated by numerical simulation, experimentally and compared with AVSI and the conventional TFM. It was found that the TFM-AVSI achieves the same resolution and contrast as that of the TFM, although it shows a wider blind zone below the interface due to focusing with normal incidence.**

Index Terms— **Auto-focused virtual source imaging (AVSI), beamforming, total focusing method (TFM).**

I. INTRODUCTION

IN ULTRASOUND non-destructive testing (NDT), a coupling medium is commonly used between the probe and the part to protect the transducer surface from frictional wear, to change the nominal inspection angle, or to accommodate component shape variations by water immersion. Differences in the speed of sound between both media generate refraction and complicate the focal law computation when using arrays. While no closed solution exists for arbitrarily shaped interfaces, the time-of-flight (TOF) from each array element to each image pixel must be obtained by the iterative algorithms, being one of the most time consuming processes in any synthetic focusing algorithm. Furthermore, if the interface shape is not known with enough accuracy, or if it changes during the scanning process, focusing errors will degrade image quality.

To overcome the above limitations, Camacho and Cruza [1] proposed a new method called auto-focused virtual source imaging (AVSI). First, the shape of the component surface is estimated from a set of TOF measurements from the same array used for imaging. Second, a conventional delay and sum beamformer is used to obtain a set of A-Scans focused, in emission and in reception, at several points on the interface. Because these points act as the virtual emitters and receivers, synthetic aperture focusing (SAFT) can be performed in the second medium only, avoiding refraction complications in the image formation process. Besides, AVSI provides better signal-to-noise ratio than the conventional SAFT, because focused beams are used instead of single-array elements. Furthermore, lateral resolution is improved with regard to a conventional phased-array image obtained with the same number of active elements, because the virtual aperture is larger than the active one. Finally, the focusing process is fully automated, because no knowledge of the component surface shape is needed.

The focused transducers and synthetic aperture techniques have been proposed as an alternative for simultaneously increasing SNR and generating wide beams [2], exploiting the fact that a strong focus behaves approximately like a virtual point source. Based on this idea, several applications with focused single-element transducers have been developed before in NDT and medicine [3], [4].

The main limitation of AVSI is its relatively low image contrast because of the large sidelobes level of SAFT. While in a phased-array image obtained with an array of N elements, the sidelobes level is about $1/N^2$ times lower than the main lobe amplitude; in SAFT, this ratio is $1/N$ [5]. This is the main limitation of the SAFT when compared with phased array: a higher acoustic noise level that reduces image contrast and generates unwanted artifacts.

These problems are overcome by simultaneously using several elements in reception for each trigger event [6], [7]. The process of registering the signals received by all the array elements after the individual excitation of each one of them is referred as full matrix capture (FMC) [8]. Once acquired, several imaging methods can be applied off-line to this data set. The total focusing method (TFM) uses all the FMC signals to coherently add the received samples at each pixel, and it is considered the gold standard in NDT ultrasound imaging. Because the N^2 signals are coherently summed at each image pixel, the expected sidelobes level is $1/N^2$, giving the same contrast than the phased-array technique, but with the advantage that all the image samples are

Manuscript received December 23, 2015; accepted July 17, 2016. Date of publication July 28, 2016; date of current version October 1, 2016. This work was supported by the Spanish Ministry of Economy and Competitiveness through the Research Challenges Program under grant DPI2013-42236-R.

The authors are with the Ultrasound Systems and Technology Group, Spanish National Research Council, Madrid 28006, Spain (e-mail: jorge.f.cruza@csic.es; j.camacho@csic.es).

Digital Object Identifier 10.1109/TUFFC.2016.2593439

focused in emission and in reception. Instead, a phased-array image has a unique focus in emission, even though dynamic depth focusing (DDF) is applied in reception. By counterpart, FMC-TFM significantly increases the required bandwidth between the acquisition hardware and the processing computer, because N^2 signals must be transmitted instead of N. Furthermore, signal-to-noise ratio is lower because of single element emission [9].

Several works have addressed the problem of calculating the focusing delays for the TFM in the presence of an interface between two media. Fermat's principle is commonly used to search for the ultrasound entry point at the interface, for each element and image pixel, that minimizes the overall TOF. This process requires performing N TOF calculations per pixel, and given a discrete representation of the interface, it is usually carried out by exhaustive search [10]. To obtain the required accuracy, a fine discretization step is required, which normally gives a long search time. Nevertheless, when using a rigid wedge, the focal laws can be precomputed, which usually gives reasonable inspection speeds [11]. If the component shape changes during the acquisition, a whole set of focal laws can be precomputed if the interface geometry is known, and the correct focal law is applied according to the array position given by an encoder [12].

When the interface shape is unknown, some means of detecting it from the same ultrasonic data is desirable. In [13], the surface profile is mapped using the diagonal signals of the FMC, which represent the pulse-echo signals of each array element. Then, TOFs between each element and pixel are calculated by the application of Fermat's principle, and a TFM image is finally obtained for each array position. Camacho *et al.* [14] proposed an auto-focusing process for phased-array DDF images. The interface shape is also obtained by a set of TOF measures with individual array elements, and then, a virtual array that operates only in the second medium is calculated, allowing the focusing circuits on the phased-array hardware to calculate the DDF laws on the fly. Real-time implementation of this auto-focus method in state-of-the-art programmable devices has been presented in [15].

Several methods for accelerating the calculation of TFM delays in the presence of an unknown interface have been proposed, including numerical procedures for nonplanar interfaces [16] and using high performance CPU/graphics processing units (GPU) platforms for real-time imaging [17]. In any case, the FMC matrix can be acquired at the maximum possible rate, because it does not need the focusing delay information. Then, once the acquired data is available in the processing computer, the interface shape and the final image can be obtained from the FMC data offline, relaxing timing requirements when compared with auto-focus process in the case of real-time phased-array imaging.

In this paper, the AVSI concept is extended to support the TFM imaging modality. While a single virtual focus is generated per trigger event in emission, several virtual receivers are created in reception. This can be done by software after transferring all the received signals to the processing computer or it can be performed in real time if the acquisition hardware supports parallel beamforming. In any case, after this first fixed-focus beamforming process, an FMC data (virtual FMC) is obtained, where each A-scan represents the signal received from each virtual element on the component surface. Finally, the TFM process is carried out only in the second medium, avoiding refraction complications at the interface.

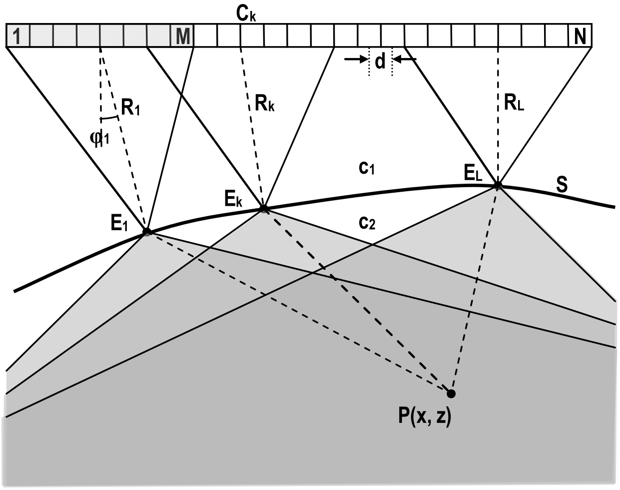

Fig. 1. AVSI concept. A set of L virtual sources $\{E_1, \ldots, E_L\}$ is created with a linear scan by focusing the M-element subapertures at the interface.

While the possibility of combining the AVSI with the TFM was foreseen in our previous work [18], it needed to be studied, implemented, and tested. In this paper, advantages of TFM-AVSI with regard to conventional AVSI are shown, and the image quality differences with the TFM are analyzed and discussed. Furthermore, the case of large slope values is addressed theoretically and by numerical simulation.

II. TOTAL FOCUSING METHOD WITH AVSI

Fig. 1 shows the principle of operation of the AVSI [1], [18]. An N-element array transducer performs a linear scan with M-element subapertures creating emission and reception foci at the interface between the coupling medium and the component under test. This way, a total of $L = N - M + 1$ virtual sources/receivers are created, which act as a virtual array with elements at $\{E_1, \ldots, E_L\}$ in the second medium. Since, commonly, the propagation velocity in the part is higher than in the coupling medium ($c_2 > c_1$), the focused beams widens within the part, which increases sound coverage in the second medium. The image values at pixels $P(x, y)$ within the beam overlapping region can be obtained by coherently adding the signals acquired from all the virtual source/receivers, in a synthetic aperture process (SAFT) computed only in the second medium.

Lateral resolution of AVSI is better than that obtained by a multiplexed phased-array linear scan with an active aperture $D = M \cdot d$, where d is the array element pitch [1], given that the beam spread into the material allow to effectively insonify all the pixels [18]. The AVSI aperture size is $D_V = L \cdot dV$, where dV is the distance between the virtual sources, and $dV \approx d$ if the linear scan is carried out with one element step. Then, $D_V > D$, since $L > M$, and AVSI achieves better lateral resolution than the phased array with the same number of active elements. On the other hand, AVSI does not require complex equipment. A multiplexed system with some active channels can provide a resolution compared with that of a full-parallel system operating in a phased-array mode, since the AVSI virtual aperture size D_V is similar to the aperture size of the N-element array transducer, i.e., $D_V = (N-M) \cdot dV \approx N \cdot d$. Furthermore, data volume generated for each AVSI image is the same that for a phased-array linear scan, so no increase in communications throughput is needed. Finally, SAFT image can be easily obtained in real time using GPU, since the TOF calculations are performed only in the second medium (no refraction issues).

The main limitation of AVSI is the low contrast and relatively high acoustic noise floor produced by the SAFT because of emitting and receiving with the same virtual source [1]. To overcome this limitation, the application TFM with AVSI virtual sources is analyzed in this paper. For each focused emission E_k, all the array elements are used in reception, and an FMC matrix is transferred to the processing computer. Then, the virtual receivers E_1 to E_L are created offline applying focusing delays to the same subapertures used in emission, obtaining a second virtual FMC matrix where the signals correspond to the reception with the virtual elements. Finally, the TFM is performed only in the second medium from the L^2 A-scans of the virtual FMC, avoiding the complication of calculating the TOFs through the interface. The whole process involves the steps addressed in Section II-A.

A. Automatic Surface Detection

Before data acquisition, AVSI requires locating the L emission and receiving foci at the interface. Although any incidence point is valid for creating a virtual source, it is demonstrated in [18] that the normal incidence point at the interface from each subaperture center is the optimum choice. It maximizes the refracted angle, achieving the best possible sound coverage into the second medium, and closed equations were given for the minimum number of active elements to use and the effective size of the generated virtual source.

Consider the two array elements A_i and A_{i+1} at both sides of some subaperture center C_k (Fig. 2). Prior to the virtual FMC capture, they are consecutively excited to get the first echo TOFs T_i and $T_{\mathrm{i}+1}$ that correspond to a normal incidence point. Distances to the interface from the array elements are $R_i = c_1 T_i/2$ and $R_{\mathrm{i}+1} = c_1 T_{\mathrm{i}+1}/2$, respectively.

The steering angle to reach the virtual element position E_k from the aperture center at C_k is [14]

$$\phi_k = \sin^{-1}\left(\frac{R_i - R_{i+1}}{d}\right) = \sin^{-1}\left(\frac{c_1}{2d}(T_i - T_{i+1})\right) \tag{1}$$

and the coordinates of the virtual element E_k are obtained by

$$\begin{aligned} x_{Ek} &= x_{Ck} + R_k \sin\phi_k \\ z_{Ek} &= z_{Ck} - R_k \cos\phi_k \end{aligned} \tag{2}$$

where $R_k \equiv (R_i + R_{\mathrm{i}+1})/2$ is the distance from the subaperture center to the virtual element. This process is simple and fast, and does not require any curve fitting procedure. Furthermore, the virtual element coordinates are obtained from $L+1$ trigger shots if the active subaperture is shifted by one element in successive acquisitions, because the element A_i of the subaperture k coincides with the element $A_{\mathrm{i}+1}$ of the subaperture $k-1$.

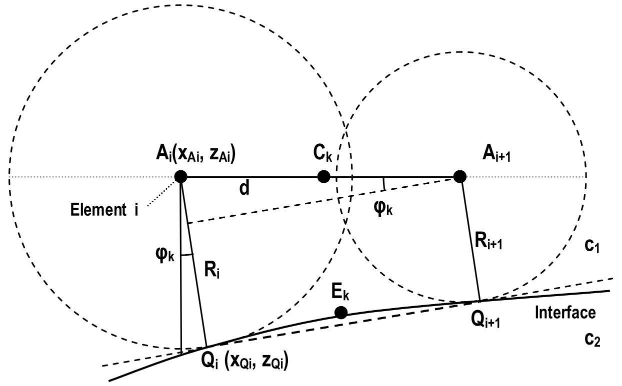

Fig. 2. Schematic representation of the surface estimation process by pulse-echo.

B. Virtual FMC Acquisition

In emission, a fixed-focus beamforming configuration creates the virtual source located at coordinate $\{E_k\}$. TOF from array element A_i in the subaperture k to the virtual source at E_k is given by

$$T_{ik} = \frac{|\vec{r}_{Ai} - \vec{r}_{Ek}|}{c_1} = \frac{\sqrt{(x_{Ai} - x_{Ek})^2 + (z_{Ai} - z_{Ek})^2}}{c_1} \tag{3}$$

where $\vec{r}_{Ai}$ and $\vec{r}_{Ek}$ are the vectors from origin to element A_i and virtual source at E_k, respectively. Analogously TOF of the main ray-path from the subaperture center C_k to the virtual source at E_k is

$$T_{Ck} = \frac{|\vec{r}_{Ck} - \vec{r}_{Ek}|}{c_1} = \frac{\sqrt{(x_{Ck} - x_{Ek})^2 + (z_{Ck} - z_{Ek})^2}}{c_1}. \tag{4}$$

The subaperture emission focal law is then obtained by

$$\tau_{ik} = T_{Ck} - T_{ik}. \tag{5}$$

After each single-focus emission k, the A-scan received by the virtual element E_j is obtained by coherently adding the signals received by the M elements of the j subaperture, discounting the travel time in the coupling medium (see Fig. 3)

$$v_{k,j}(t) = \sum_{i=j}^{i=j+M-1} s_{k,i}\left(t - \tau_{ij} - \frac{R_k + R_j}{c_1}\right) \tag{6}$$

where $s_{k,i}\ (t)$ is the signal received by element A_i when emitting with the virtual source E_k. This way, the set of signals $v_{k,j}(t)$ are the FMC matrix of the virtual array $\{E_1 \ldots E_L\}$.

Computation of the virtual FMC involves applying, for each focused emission, a fixed-focus focal law to each reception subaperture. This can be done in the processing computer if the N signals $s_{k,i}\ (t)$ received by the array elements are transferred, generating the virtual data set $v_{i,j}\ (t)$ offline. Alternatively, if the ultrasound hardware has parallel beamforming capabilities [19], subaperture focusing could be applied in real time, and the reduced set of L virtual A-scans will be transferred after each focused emission.

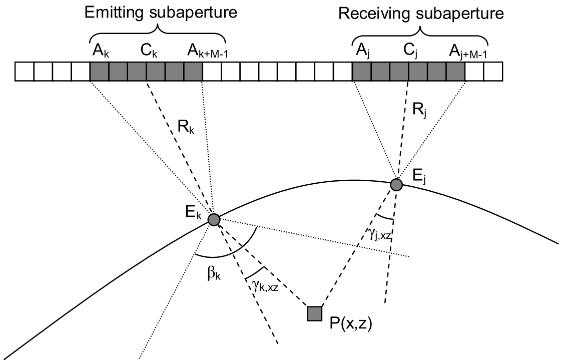

Fig. 3. Schematic representation of the TFM-AVSI image formation process with emitting subaperture k, receiving subaperture j and pixel $P(x, z)$.

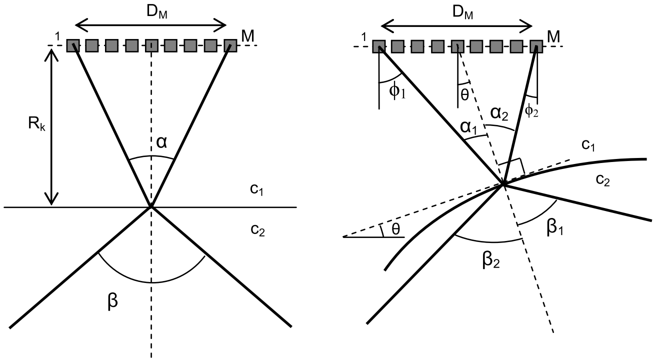

Fig. 4. Schematic representation of a beam focused on (left) a flat horizontal and (right) a curved and inclined surface with normal incidence in both cases.

C. Virtual Source Quality

An important subject for a correct TFM reconstruction is the virtual source quality. Ideally, the focus at the interface should behave like an omnidirectional source, propagating a cylindrical wave into the second medium. However, because of the finite extension of the emitting subapertures, the generated wavefield can be considered cylindrical in a limited angular extent only. Furthermore, the amplitude and phase distribution of the field along the surface will be different from that of a point source or a small piston-like element. Therefore, the number of active elements, the distance to the part, the incidence angle at the interface and its slope determine the properties of the focus at the interface, and must be wisely selected to achieve an acceptable virtual source.

Fig. 4 (left) shows the simplest model for a focused beam with normal incidence at a plane interface with $c_2 > c_1$, which is the most common situation in NDT. For an active aperture with size D_M and focused at a distance R_k, the opening angle at −6 dB into the second medium can be approximated by [20]

$$\begin{aligned}\beta &= 2\sin^{-1}\left(\frac{c_2}{c_1}\sin\left(\tan^{-1}\left(\frac{D_M}{2R_k}\right)\right)\right)\\ &= 2\sin^{-1}\left(\frac{c_2}{c_1}\frac{1}{\sqrt{1+4(F\#)^2}}\right)\end{aligned} \tag{7}$$

with $F\# = R_k/D_M$. Camacho and Cruza [18] analyzed the case of an interface parallel to the array (or slightly tilted), concluding that the minimum number of active elements required in AVSI to get full coverage into the component ($\beta = 180°$) is

$$M \geq \frac{2R_k}{d\sqrt{\left(\frac{c_2}{c_1}\right)^2 - 1}}. \tag{8}$$

It was also verified that for small interface slope values, the focus can be modeled as a small virtual source element with a size half the main-lobe width at the focal distance. Furthermore, it was shown that the approximation is valid for curved parts assuming that the local curvature radius is much larger than the spot size, a condition usually satisfied. However, in this paper, the hypothesis is extended to the higher interface slope values θ, explicitly including it in the virtual source effective size formulation

$$d_{\text{eff}} \approx 1.22\frac{\lambda_1}{D_M\cos(\theta)}R_k. \tag{9}$$

For normal incidence of the main ray and $\theta \neq 0$ [Fig. 4 (right)], the refracted angles from the extreme elements of the array must be computed separately

$$\begin{cases}\beta_1 = \sin^{-1}\left(\dfrac{c_2}{c_1}\sin(\alpha_1)\right)\\ \beta_2 = \sin^{-1}\left(\dfrac{c_2}{c_1}\sin(\alpha_2)\right)\end{cases} \tag{10}$$

being α_1 and α_2 the incident angles from the left and rightmost elements of the active aperture to the entry point, respectively. These angles are given by

$$\begin{cases}\alpha_1 = \sin^{-1}\left(\dfrac{\cos\theta}{\sqrt{4F\#^2 + 4F\#\sin\theta + 1}}\right)\\ \alpha_2 = \sin^{-1}\left(\dfrac{\cos\theta}{\sqrt{4F\#^2 - 4F\#\sin\theta + 1}}\right).\end{cases} \tag{11}$$

The virtual source behavior was analyzed by pulsed wave simulations, carried out with an in-house developed software in MATLAB (Matworks Inc, USA). The TOF from each array element (modeled as an omnidirectional source) to each simulated point in the second medium is obtained by solving for the fastest path through the interface according to the Fermat principle. Then, a set of M broadband complex radio frequency signals are delayed accordingly, weighted by the element directivity function, and added together to obtain the field at each simulated point. The maximum of this signal envelope gives the amplitude field [Fig. 5(a)], and the time-to-peak was used to construct a TOF map [Fig. 5(b)]. The simulation parameters are $M = 35$ ($F\# = 1.9$) active elements of an array with $f = 5$ MHz, an 80% bandwidth, $d = 0.3$-mm pitch, and $g = 0.1$-mm gap between elements, inspecting a plane surface aluminum part located at 20-mm distance and tilted $\theta = 45°$ in water immersion ($c_1 = 1.5$ mm/μs and $c_2 = 6.2$ mm/μs). The number M of the elements was selected according to (8) trying to get full part insonification.

A focused beam is observed in water [Fig. 5(a)], which diverges when entering the aluminum part creating the virtual source. This effect is clearer in the TOF image [Fig. 5(b)], where the contour plots of constant TOF evidence the creation

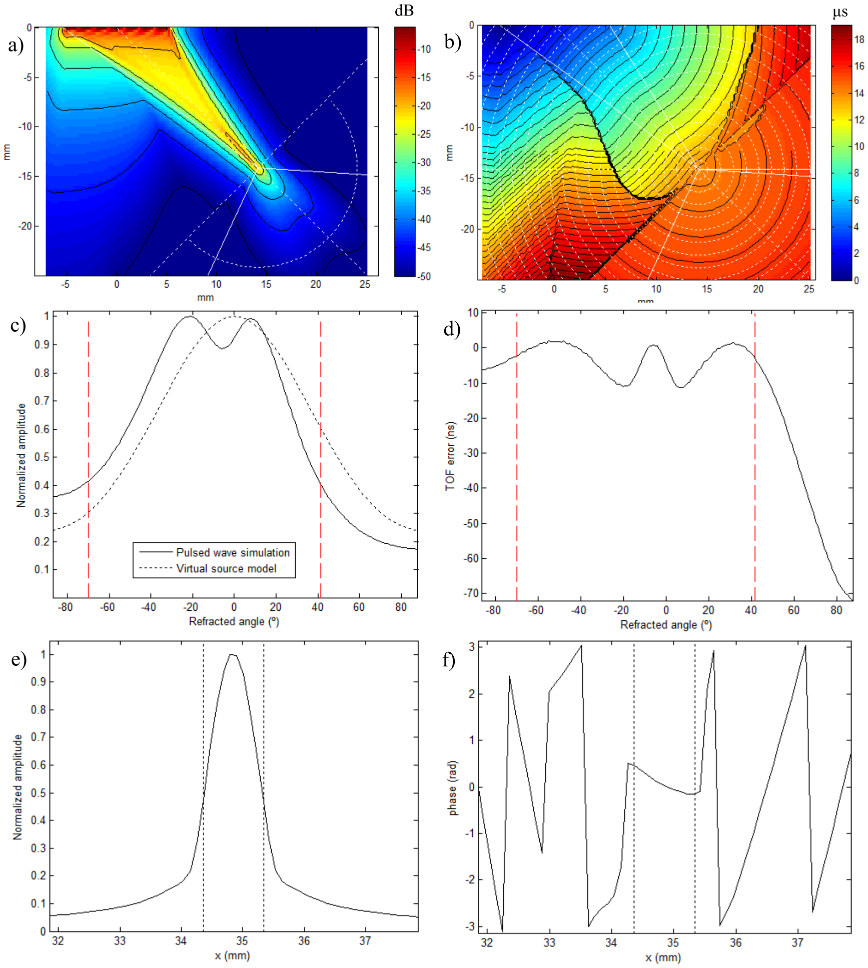

Fig. 5. Pulsed wave simulation for $M = 35$ elements of a 5-MHz array with an 80% bandwidth and a 0.3-mm pitch, inspecting by water immersion a planar surface aluminum part at 20 mm from the array and tilted $\theta = 45°$. (a) Amplitude field in decibel. (b) TOF field in μs. (c) Simulated (solid line) and theoretical (dashed line) lateral beam patterns. (d) TOF error (in ns) at $R = 10$ mm from the virtual source inside the aluminum. (e) Amplitude and (f) phase distribution of the incident field on the interface (solid line) and lateral limits of the virtual source model (dashed line).

of a point-like emitter to the second medium at the focus position.

The first remarkable observation is that full angle insonification into the second medium is not achieved, despite using the number of elements defined by (8), which was derived for an interface parallel to the array. When steering the beam to achieve normal incidence on a tilted surface, the focus width increases, and the refracted angles into the material become reduced with regard to the parallel interface case.

This behavior is predicted by (10) and (11) that estimate the effective refracted angles β_1 and β_2 measured at -6 dB [Fig. 5(c) and (d) (red dotted lines)]. Fig. 5(d) shows the wavefront TOF differences with regard to those of a cylindrical waveform, calculated at a constant radius $R = 10$ mm from the virtual source. Between β_1 and β_2, the time deviations are lower than 10 ns, an order of magnitude below the signal period. Such low timing errors should not have a significant impact in the TFM focusing process if only those virtual elements that reach each pixel with angles within β_1 and β_2 are used for image formation.

Fig. 5(c) shows the beam amplitude over the same constant radius of 10 mm. While beamwidth at -6 dB is well approximated by the difference $\beta_1 - \beta_2$, the angular profile presents two unexpected local maxima when compared with the theoretical angular response of the virtual source modeled by (9) (dashed line). Furthermore, the whole angular pattern seems to be displaced about 5° to the left, evidencing a beam steering effect when entering the component despite of normal incidence.

These irregularities in the angular response are explained by the difference in the field distribution along the interface with regard to that of a piston-like element. In particular, an analysis of the phase distribution around the focal spot [Fig. 5(f)], reveals an almost linear trend within the main-lobe, that reasonably explains the observed steering effect into the second medium. Furthermore, although of low relative amplitude, the sidelobes of the incident field are responsible of the local amplitude variations observed in Fig. 5(c). In any case, the wavefront shape can be still considered cylindrical between β_1 and β_2 [errors below 10 ns in Fig. 5(d)], and local amplitude aberrations (less than 6 dB) should not have a significant impact in the TFM image.

To obtain full angle insonification with inclined parts, (8) should be reformulated to account for the surface slope.

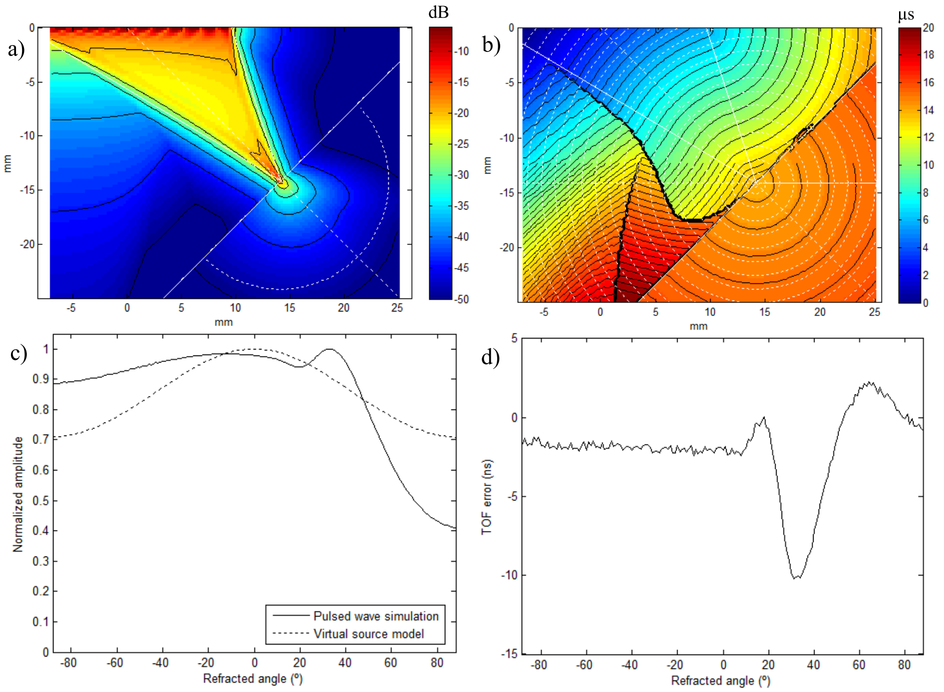

Fig. 6. Pulsed wave simulation with $M = 63$ elements of a 5-MHz array with an 80% bandwidth and a 0.3-mm pitch, inspecting by water immersion a plane surface aluminum part at 20 mm from the array tilted $\theta = 45°$. (a) Amplitude field in decibel. (b) TOF field in μs. (c) Simulated (solid line) and theoretical (dashed line) lateral beam patterns. (d) TOF error (in ns) at $R = 10$ mm from the virtual source inside the aluminum.

Considering $\beta_1 = 90°$ in (10), substituting in (11) and operating gives

$$M \geq \frac{2R_k}{d(\cos\theta\sqrt{(c_2/c_1)^2 - 1} - \sin\theta)}. \tag{12}$$

For the previously simulated case, application of (12) yields $M = 63$ with the results shown in Fig. 6. An almost cylindrical field is now obtained for the whole angular range (±90°), with amplitude variations less than 6 dB and TOF errors below 10 ns, confirming that the virtual source can be modeled by (9) as a flat element of size d_{eff} also for higher slopes.

It is worth to mention that (10), (11), and (12) are only valid when the array elements have enough angular sensitivity to contribute to the focus from the extreme array positions. The steering angles $\phi_1$and ϕ_2 from the left and rightmost elements in Fig. 3 (right) are, respectively

$$\begin{cases} \phi_1 = \alpha_1 + \theta \\ \phi_2 = \alpha_2 - \theta \end{cases} \tag{13}$$

which, for a given element size $e = d - g$ are bounded by (−6-dB signal drop)

$$\phi_1, \phi_2 \leq \sin^{-1}\left(0.61\frac{\lambda_1}{d - g}\right) = \phi_M. \tag{14}$$

Substituting (13) and (14) into (10) gives the maximum refracted angles that can be achieved into the component for a given slope θ with less than 6-dB losses

$$\begin{cases} \beta_1 \leq \sin^{-1}\left(\dfrac{c_2}{c_1}\sin(\phi_M - \theta)\right) \\ \beta_2 \leq \sin^{-1}\left(\dfrac{c_2}{c_1}\sin(\phi_M + \theta)\right). \end{cases} \tag{15}$$

This is an important consideration in TFM-AVSI, because some arrays designed for operation in solids have reduced steering capability when used in immersion because of the large element size with regard to wavelength in water. Therefore, the maximum slope of the inspected part with regard to the array will be limited by the elements angular sensitivity. It is worth to note that (15) is independent of *F#*, that is, increasing the number of active elements or reducing the distance to the part does not help to increase the coverage angle into the material if it is already limited by the angular sensitivity of the array. Furthermore, the angular sensitivity limitation of arrays will also affect the conventional TFM and phased-array inspections for the same reasons than for AVSI and TFM-AVSI.

Fig. 7 shows the simulation results for the array used in the experimental work of this paper, with $f = 5$ MHz, $d = 0.65$ mm, and $g = 0.1$ mm, inspecting a planar aluminum component at $R = 20$-mm distance and tilted $\theta = 15°$. According to (12), using $M = 16$ active elements full angular coverage should be achieved. Instead, and according to (15), angular sensitivity of the array ($\phi_M = 19.4°$ at −6 dB) limits the right-hand refracted angle to $\beta_1 = 18.6°$. Fig. 7(c) (red vertical line) confirms that (15) is an acceptable approximation, where the losses are limited to 6 dB.

Furthermore, deviations from a cylindrical wave are small, with TOF errors below 12 ns within the angular interval $[-90°, \beta_1]$ [Fig. 7(d)], where the wavefront can still be considered cylindrical. Again, the beam amplitude distortion should not have a significant impact in the focusing process if only those virtual elements that reach each pixel with angles within −90° and β_1 are used in this case.

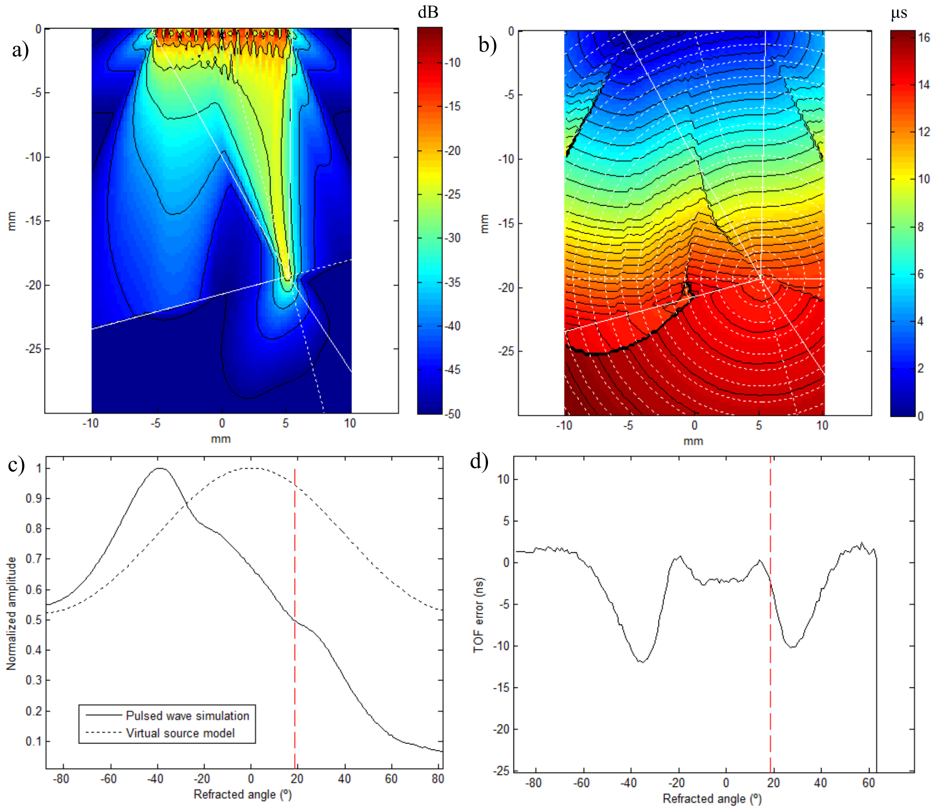

Fig. 7. Pulsed wave simulation for $M = 16$ elements of a 5-MHz array with an 80% bandwidth and a 0.65-mm pitch, inspecting by water immersion a planar surface aluminum part at 20 mm from the array tilted $\theta = 15°$. (a) Amplitude field in decibel. (b) TOF field in μs. (c) Simulated (solid line) and theoretical (dashed line) lateral beam patterns. (d) TOF departure (in ns) at Rr = 10 mm from an ideal cylindrical wavefront.

It is important to remark that full coverage is not necessary for successful application of AVSI or TFM-AVSI. The wider the aperture angle into the component, the better the resolution and contrast, but operating with lower refracted angles and larger slopes is possible if the achieved resolution and sensitivity are within the application requirements.

D. TFM-AVSI Image Formation Process

The final step of the process is to generate the TFM image of the inspected part from the virtual FMC matrix. In the virtual source model, the sound propagation path is assumed to be a straight line from the emitting aperture center C_k to the virtual element E_k, and then, to any point P into the material also in a straight path (Fig. 3). The last is valid inside the angular extent $[\beta_1, \beta_2]$ of the refracted field shown by (10) and (15).

Equivalent assumptions are made for the back-propagation path from pixel P to the virtual receiver E_j. Thereby, the TOF from the virtual source E_k to pixel P with coordinates (x, z) is

$$T_{k,xz} = \frac{\sqrt{(x_{Ek} - x)^2 + (z_{Ek} - z)^2}}{c_2}. \tag{16}$$

The output sample of the TFM-AVSI image is then obtained by the summation of all the contributing signals by

$$I_{xz} = \left| \frac{1}{B_{xz}} \sum_{k=1}^{L} \sum_{j=1}^{L} \alpha_{k,j,xz} V_{k,j}(T_{k,xz} + T_{j,xz}) \right| \tag{17}$$

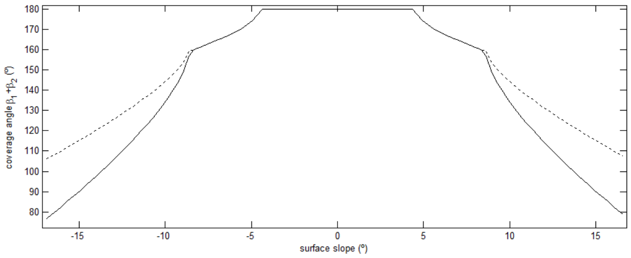

Fig. 8. Coverage angle $\beta 1 + \beta 2$ for the experiment 1 against the surface local slope (dashed line) calculated from (10), and (solid line) including angular sensitivity by (15).

where $\alpha_{k,j,xz}$ is a binary coefficient to only add the samples that are inside the opening angles β_1 and β_2, B_{xz} is the number of added samples for each image pixel, and $V_{k,j}$ (t) is the analytic representation of the virtual FMC matrix $v_{k,j}$ (t) obtained with the Hilbert transform $H(\cdot)$ by

$$V_{k,j}(t) = v_{k,j}(t) + jH(v_{k,j}(t)). \tag{18}$$

From Fig. 3, the coefficient $b_{k,xz}$ can be obtained from the refracted angle γ to P as

$$b_{k,j,xz} = \begin{cases} 1, & \text{for } |\gamma_{k,xz}| \le \beta_1 \text{ and } \beta_2 \\ 0, & \text{otherwise} \end{cases} \tag{19}$$

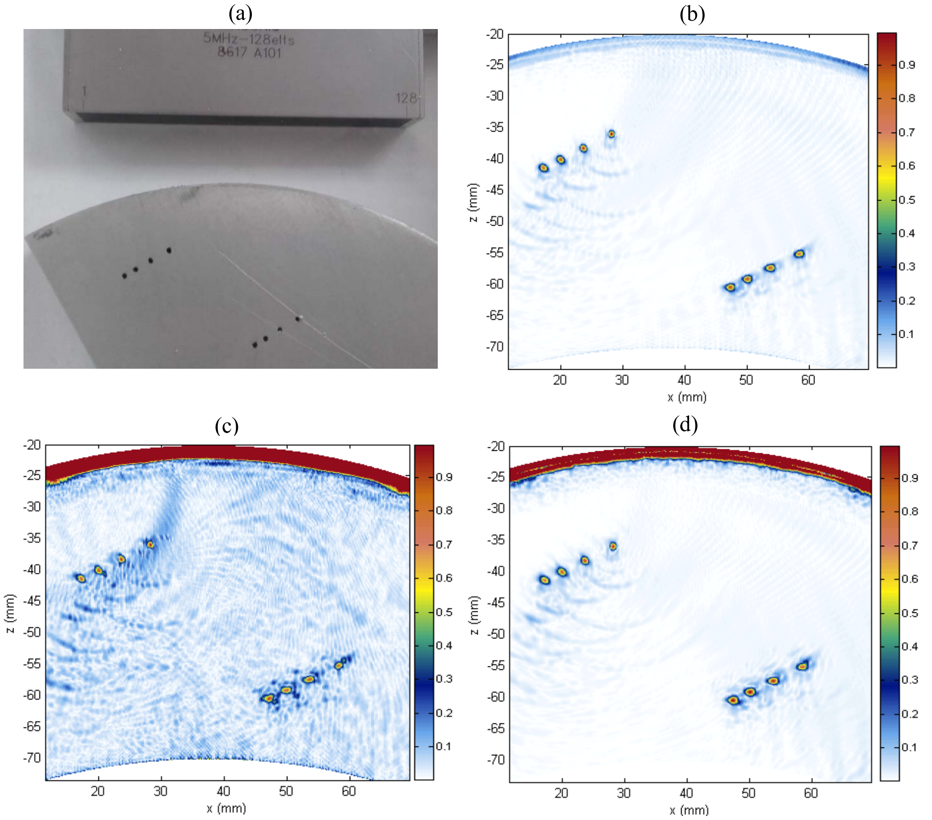

Fig. 9. (a) Picture of the array and component for experiment 1. (b) Conventional TFM image with $N = 128$ elements. (c) AVSI image and (d) TFM-AVSI image, both with $M = 16$ and $L = 113$. Color scale is linear in all cases.

and the normalization factor B_{xz} is defined as

$$B_{xz} = \sum_{k=1}^{L} \sum_{j=1}^{L} b_{k,j,xz}. \tag{20}$$

Opening angles β_1 and β_2 depend on the surface local slope and *F#*, and hence, they should be calculated for each virtual source. Alternatively, the worst case can be assumed (higher slope), and a single pair of values being used for the whole image.

Using the analytic representation of $v_{k,j}(t)$ instead of the radio frequency signal allows the spacing output samples to satisfy Nyquist criterion for signal envelope, reducing data throughput, memory, and computation time. Furthermore, signal envelope is extracted by just taking the absolute value of the complex sum and no postprocessing filter is required.

III. EXPERIMENTAL VERIFICATION

For experimental verification, an array with $N = 128$ elements, $f = 5$ MHz, and pitch $d = 0.65$ mm (Imasonic, France) was used to inspect two parts by water immersion. A SITAU-111 (DASEL SL, Spain) phased-array system with 128 active channels was used to generate the virtual sources and to capture the FMC matrix. Further processing was carried out off-line using MATLAB (Matworks Inc, USA).

Besides TFM-AVSI images, the conventional TFM images were generated for comparison. TOF from each array element to each pixel was calculated by Fermat's principle, looking for the entry point that gives the fastest path. The algorithm described in [21] was used instead of the exhaustive search to reduce calculation time.

First, the experiment was performed with a 100-mm curvature radius aluminum part with two groups of 1.5-mm diameter SDH's. The array was placed at a distance $h \approx 20$ mm from the component surface in water [Fig. 4(a)]. Interface was automatically detected by the proposed method, and a total number of $L = 113$ virtual sources/receivers were generated at the normal incidence points defined by (2). Active subaperture was $M = 16$ elements. Output image was made of 256×256 pixels with a separation of 0.23 mm in both the directions ($\sim$1/5 of the envelope axial resolution). Table I summarizes all the relevant acquisition and processing parameters.

Fig. 8 (dashed line) shows the total coverage angle $\beta = \beta_1 + \beta_2$ into the part against the surface local slope for the 113 virtual sources, obtained from (10). For $M = 16$, full coverage is obtained at the central part of the component only, where the slope is below 5°. In the intermediate region between 5° and 8°, coverage angle is progressively reduced, because the steering angle and the distance to the part increase, while the active aperture is kept constant. Above 8°, the limited angular sensitivity of the array elements further restricts the coverage angle according to (15) (solid line). These theoretical values were used during the AVSI-TFM image formation process.

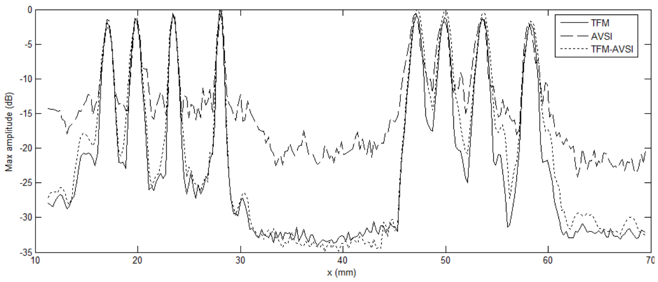

Fig. 10. Maximum amplitude in decibel along z-direction for the TFM (solid line), AVSI (dashed line), and TFM-AVSI (dotted line).

TABLE I

ACQUISITION AND PROCESSING PARAMETERS FOR EXPERIMENT 1

Speed of sound in water	1.48 mm/us	
Speed of sound in aluminium	6.38 mm/us	
Number of array elements (N)	128	
Number of Virtual Elements (L)	113	
Acquisition time per trigger event	58 us	
Sampling frequency	40 MHz	
Sample resolution	16 bits	
Acquired data volume per image	TFM	72 Mb
	AVSI	512 Kb
	TFM-AVSI	67 Mb
Number of image pixels	65536 (256 x 256)	

Fig. 9(b) shows the conventional TFM image that can be considered the gold standard, obtained with all the array elements ($N = 128$). While all SDHs are visible with the expected lateral resolution, some low-level background acoustic noise is seen, which is due to signal reverberations and sidelobes. Meanwhile, AVSI image in Fig. 9(c) achieves the same lateral resolution that TFM, but the acoustic noise increases significantly because of reverberations and higher sidelobes. Finally, TFM-AVSI image is presented in Fig. 9(d), in which background noise and artifacts are reduced when compared with AVSI, reaching similar levels to those observed in TFM.

To better quantify the differences between the images, Fig. 10 shows the maximum amplitude (in decibel) along the z-direction. Lateral resolution, measured as the average −6-dB amplitude drop in all SDHs is practically equivalent in all the cases: 1.04 mm in TFM, 1.18 mm in AVSI, and 1.11 mm in TFM-AVSI. Since the whole array aperture $D = 83.2$ mm is larger than the virtual array aperture $D_v = 58.2$ mm, a better lateral resolution could be expected from TFM, but because of the larger distance to the part due to the water path, resolution is similar in both cases. The slightly wider main lobe in AVSI and TFM-AVSI is explained by the distortion in the field profile radiated by each virtual source with regard to that of an ideal point emitter. As analyzed in Section II-C, the actual amplitude and phase distribution of the incident beam around the focal spot produce an apodization effect in the virtual element response that tends to reduce the lateral resolution of the synthetic aperture image.

Due to reverberations and grating lobes artifacts, the theoretical sidelobe level of $1/N^2$ is not reached in the TFM. Instead, a maximum contrast of 32.5 dB is achieved in the central image region around $x = 40$ mm. While contrast of the AVSI image is 20.5 dB, when applying the proposed TFM-AVSI method, it improves to 33.2 dB, which is equivalent to that obtained with the conventional TFM.

Because of the emission focus and normal incidence at the component surface, AVSI and TFM-AVSI present a stronger interface echo than the TFM, which can generate a saturated blind zone just below the interface depending on the amplifiers gain level [Fig. 9(c) and (d)]. Fig. 11 shows this effect when imaging a 1-mm diameter hole located at 1.2 mm from the surface of (a) an aluminum part, obtained by (b) TFM and (c) TFM-AVSI. In the latter case, the interface echo is stronger than in the TFM and presents a lateral periodic pattern that corresponds with the virtual source positions. The saturated region extension is ~0.6-mm depth, and the lateral resolution at the defect is poorer than in TFM (wider main lobe).

Near the surface and according to (19), only a few virtual sources participate in the TFM-AVSI beamforming process when $\beta < 180°$, which explains the wider blind zone and the resolution loss. If all the virtual sources are used for computing each pixel, the blind zone is reduced, and the resolution is restored when compared with the TFM [Fig. 11(d)]. On the other hand, the noise level increases, and some artifacts appear because of including signals from virtual sources that do not contribute with coherent information.

A final experiment was performed with an aluminum block with eight pairs of 2.5-mm diameter SDH's, separated 3 mm in the in x-direction and 10 mm in the z-direction. The array was placed tilted 15° with respect to the interface at a distance $h \approx 30$ mm in water immersion [see Fig. 12(a)]. For higher slope values, the low angular sensitivity of the array elements and the presence of grating lobes in water precluded obtaining usable images with any imaging method (TFM, AVSI, and TFM-AVSI). The interface was automatically detected by the proposed method, and a total number of $L = 113$ virtual sources/receivers were generated at the normal incidence points defined by (2). The selected active aperture was $M = 16$ elements, which yields a maximum opening angle $\beta = 64°$ considering the array angular sensitivity ($\beta_1 = 18.5°$ and $\beta_2 = 45.5°$). The output image was made of 512×256 pixels with a separation of 0.25 mm in both directions. Fig. 12(b) shows the resultant FMC image, where all SDHs are visible.

Fig. 13 shows the region within the red box in Fig. 12(b). Average main lobe width at −6 dB was 1.23 mm in TFM, 1.52 mm in AVSI, and 1.48 mm in TFM-AVSI. Because the water path is larger than in the first experiment, the refracted angle into the component is lower, and hence, fewer samples are added at each pixel. Consequently, resolution of the AVSI and TFM-AVSI images is slightly worse than with the TFM, where N^2 samples are used in all pixels, added to the angular apodization effect of the virtual source field studied in Section II-C. Again, because of the presence of reverberations, the theoretical sidelobe level of $1/\mathrm{N}^2$ is not reached in the TFM. Instead, a maximum contrast of 42 dB is achieved in TFM, 29.2 dB in AVSI, and 42.8 dB in TFM-AVSI. It is worth to note that an artifact appears between each pair

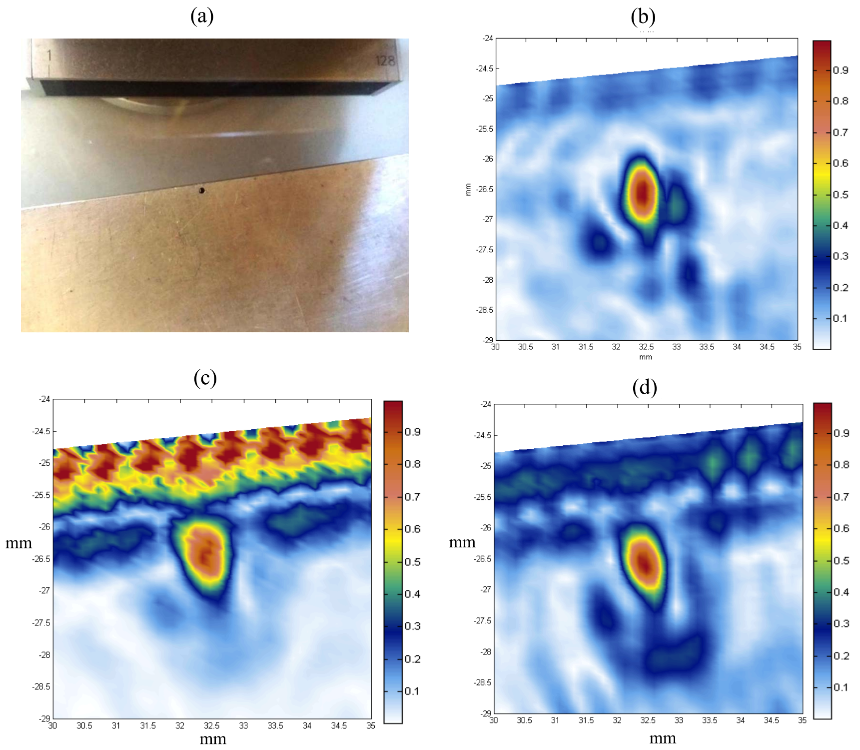
(a) (b) (c) (d)

Fig. 11. 1-mm Ø hole near the interface. (a) Picture of the arrangement. (b) TFM image. (c) TFM-AVSI image. (d) TFM-AVSI image including all virtual sources [$b = 1$ for all k and j in (20)].

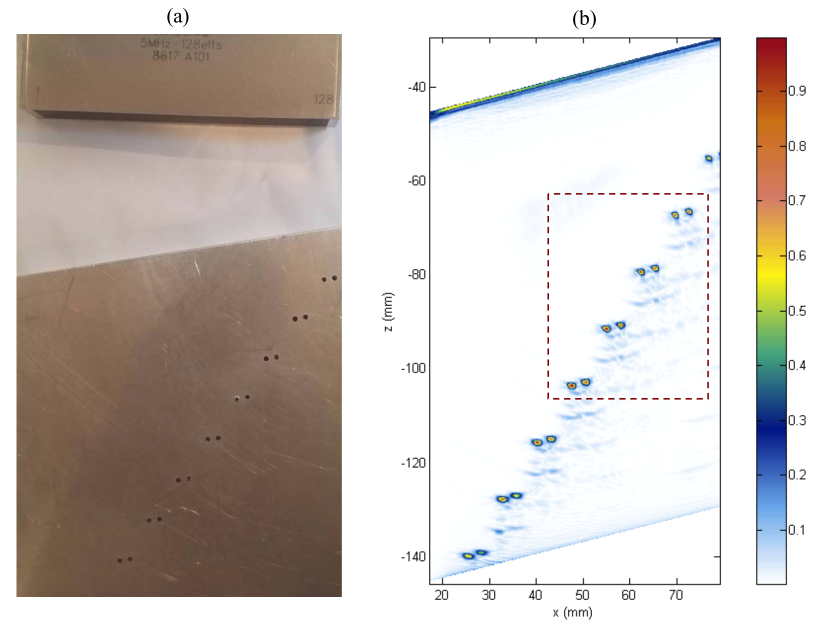
(a) (b)

Fig. 12. (a) Picture of the array and component for experiment 2. (b) Conventional TFM image with $N = 128$ elements.

of SDH echoes in the AVSI image, and not in both the TFM images. It is produced by a constructive interference of the sidelobes generated by the holes that are very close each other. It is a consequence of the SAFT algorithm, and hence, it does not appear in the TFM and TFM-AVSI images, because more signals are added in that point, and destructive interference reduces the artifact amplitude.

With regard to performance, acquisition time is slightly larger in TFM, because it requires N emissions instead of L. On the other hand, transfer time is lower in AVSI, where a set of just L signals per image is sent to the personal computer (PC), instead of $N * N$ in the TFM and $L * N$ in the TFM-AVSI. In all cases, the image formation process was performed in a standard PC, using a custom developed MATLAB code.

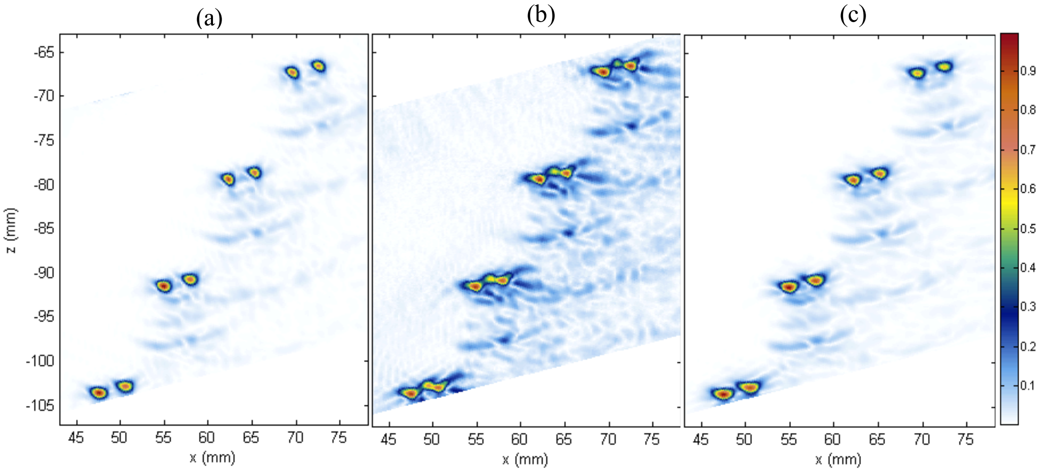

Fig. 13. Detail of Fig. 6 (red rectangle). (a) Conventional TFM image with $N = 128$ elements. (b) AVSI image and (c) TFM-AVSI image, both with $M = 16$ and $L = 113$.

IV. CONCLUSION

The main limitation of AVSI is its relatively low image contrast due to the large sidelobes level and unwanted artifacts of the SAFT. While in a phased-array image obtained with an array of N elements, the sidelobes level is $1/N^2$, in SAFT, this ratio is $1/N$. This limitation can be overcome by using the TFM instead of the SAFT, because N^2 signals are coherently summed at each image pixel, and the expected sidelobes level is $1/N^2$.

In this paper, the AVSI concept was extended to support TFM imaging modality. While in emission a single virtual focus is generated per trigger event, several virtual sources are created in reception. This was done by software after transferring all the received signals to the processing computer, but it could be performed in real time if the acquisition hardware supports parallel beamforming. With this first fixed-focus beamforming process, an FMC data (virtual FMC) is obtained, where each A-scan represents the signal received from each virtual element on the component surface. Then, TFM process is carried out only in the second medium, avoiding refraction complications, while contrast is improved with regard to SAFT. By counterpart, an equipment with more active channels must be used to simultaneously digitalize the signals received by all the array elements after each focused emission. Furthermore, data-transfer time increases, because L^*N signals must be sent instead of L, and also does the image processing time.

When focusing at the interface, the coverage angle into the component depends on the surface slope, and for higher slope values, more active elements are needed for emission. The limit is usually given by the angular sensitivity of the array elements, which in water can be specially compromised because of the relatively large element size of common NDT arrays with regard to wavelength. Closed formulae were given to estimate the effective refracted angles into the component accounting for interface slope and array sensitivity, which were verified by numerical simulation.

It was found that the AVSI and TFM-AVSI images present a stronger interface echo than the TFM, which could difficult the detection of subsurface defects. It is a common problem when inspecting with normal incidence, because interface echo directly returns to the emitting aperture. While averaging a large number of samples at the subsurface pixels in the TFM help to reduce the interface echo, in TFM-AVSI, the same pixels are obtained from less and more coherent samples, because opening angles are calculated from the virtual source at the interface. As demonstrated, a possible work-around would be to include more virtual sources in the beamforming process by relaxing the −6 dB criteria that defines the refracted angle β at the subsurface region. However, a tradeoff must be achieved, because samples from the farthest virtual sources can lead to increased noise and artifacts due to the addition of noncoherent echoes.

The experimental work confirmed that the TFM-AVSI method achieves better contrast that AVSI, producing an image equivalent in resolution and contrast to that obtained by the TFM with less processing complexity (no refraction calculations). This could help to obtain more efficient real-time implementations of the auto-focused TFM systems for NDT applications, currently a research topic of several groups.

REFERENCES

[1] J. Camacho and J. F. Cruza, “High resolution autofocused virtual source imaging (AVSI),” in *Proc. IEEE Int. Ultrason. Symp. (IUS)*, Oct. 2015, pp. 1–4.
[2] C. H. Frazier and W. D. O’Brien, “Synthetic aperture techniques with a virtual source element,” *IEEE Trans. Ultrason., Ferroelectr., Freq. Control*, vol. 45, no. 1, pp. 196–207, Jan. 1998.
[3] C. Passmann and H. Ermert, “A 100-MHz ultrasound imaging system for dermatologic and ophthalmologic diagnostics,” *IEEE Trans. Ultrason., Ferroelectr., Freq. Control*, vol. 43, no. 4, pp. 545–552, Jul. 1996.
[4] T. Stepinski, “SAFT performance in ultrasonic inspection of coarse grained metals,” in *Proc. 6th Int. Conf. NDE Rel. Struct. Integrity Nuclear Pressurized Compon.*, Budapest, Hungary, Oct. 2007, pp. 1–8.
[5] P. D. Corl, P. M. Grant, and G. S. Kino, “A digital synthetic focus acoustic imaging system for NDE,” in *Proc. Ultrason. Symp.*, 1978, pp. 263–268.
[6] M. Nikolov and V. Behar, “Analysis and optimization of synthetic aperture ultrasound imaging using the effective aperture approach,” *Int. J. Inf. Theory Appl.*, vol. 12, no. 3, pp. 257–265, 2005.
[7] J. A. Jensen, S. I. Nikolov, K. L. Gammelmark, and M. H. Pedersen, “Synthetic aperture ultrasound imaging,” *Ultrasonics*, vol. 44, pp. e5–e15, Dec. 2006.

[8] C. Holmes, B. W. Drinkwater, and P. D. Wilcox, "Post-processing of the full matrix of ultrasonic transmit–receive array data for non-destructive evaluation," *NDT E Int.*, vol. 38, no. 8, pp. 701–711, 2005.

[9] R. Y. Chiao, L. J. Thomas, and S. D. Silverstein, "Sparse array imaging with spatially-encoded transmits," in *Proc. IEEE Ultrason. Symp.*, vol. 2. Toronto, ON, Canada, Oct. 1997, pp. 1679–1682.

[10] R. Long, J. Russell, P. Cawley, and N. Habgood, "Ultrasonic phased array inspection of flaws on weld fusion faces using full matrix capture," *Rev. Progress QNDE*, vol. 28, pp. 848–855, 2009.

[11] B. W. Drinkwater and A. I. Bowler, "Ultrasonic array inspection of the Clifton suspension bridge chain-links," *Insight*, vol. 51, no. 9, pp. 491–498, 2009.

[12] M. Sutcliffe, M. Weston, B. Dutton, and I. Cooper, "Real-time full matrix capture with auto-focusing of known geometry through dual layered media," in *Proc. 51st Annual Conf. BINDT*, Daventry, U.K., Sep. 2012.

[13] M. Sutcliffe, M. Weston, P. Charlton, K. Donne, B. Wright, and I. Cooper, "Full matrix capture with time-efficient auto-focusing of unknown geometry through dual-layered media," *Insight*, vol. 55, no. 6, pp. 297–301, 2013.

[14] J. Camacho, J. F. Cruza, J. Brizuela, and C. Fritsch, "Automatic dynamic depth focusing for NDT," *IEEE Trans. Ultrason., Ferroelectr., Freq. Control*, vol. 61, no. 4, pp. 673–684, Apr. 2014.

[15] J. F. Cruza, J. Camacho, J. M. Moreno, and C. Fritsch, "Ultrafast hardware-based focal law calculator for automatic focusing," *NDT E Int.*, vol. 74, pp. 1–7, Sep. 2015.

[16] M. Weston, "Advanced ultrasonic digital imaging and signal processing for applications in the field of non-destructive testing," Ph.D. dissertation, Faculty Eng. Phys. Sci., School Elect. Electron. Eng., Univ. Manchester, Manchester, U.K., 2011.

[17] M. Weston, P. Mudge, C. Davis, and A. Peyton, "Time efficient auto-focussing algorithms for ultrasonic inspection of dual-layered media using full matrix capture," *NDT E Int.*, vol. 47, pp. 43–50, Apr. 2012.

[18] J. Camacho and J. F. Cruza, "Auto-focused virtual source imaging with arbitrarily shaped interfaces," *IEEE Trans. Ultrason., Ferroelectr., Freq. Control*, vol. 62, no. 11, pp. 1944–1956, Nov. 2015.

[19] J. F. Cruza, L. Medina-Valdes, and C. Fritsch, "Real time autofocusing hardware for ultrasonic imaging with interfaces," in *Proc. IEEE Int. Ultrason. Symp. (IUS)*, Oct. 2015, pp. 1–4.

[20] T. Scharrer *et al.*, "Ultrasonic defect detection in multi-material, axis-symmetric devices with an improved synthetic aperture focusing technique (SAFT)," in *Proc. IEEE Int. Ultrason. Symp. (IUS)*, Oct. 2012, pp. 1039–1042.

[21] M. Parrilla, J. Brizuela, J. Camacho, A. Ibañez, P. Nevado, and C. Fritsch, "Dynamic focusing through arbitrary geometry interfaces," in *Proc. IEEE Ultrason. Symp. (IUS)*, Nov. 2008, pp. 1195–1198.

Jorge F. Cruza was born in Madrid, Spain, in 1983. He received the B.S. degree in telecommunication engineering and the M.S. degree in electronics from the Universidad de Alcalá, Madrid, Spain, in 2009 and 2011, respectively, where he is currently pursuing the Ph.D. degree.

He has been an Associate Researcher with the Spanish National Research Council, Madrid, since 2010. His current research interests include high-resolution acoustic imaging, real-time beamforming, and FPGA signal processing.

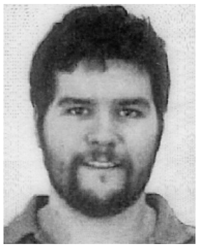

Jorge Camacho was born in Montevideo, Uruguay, in 1979. He received the B.S. degree in electronic engineering from the Universidad de la República, Montevideo, in 2004, and the Ph.D. degree in systems and automation engineering from the Universidad Complutense de Madrid, Madrid, Spain, in 2010.

He has been an Associate Researcher with the Spanish National Research Council, Madrid, since 2005. His current research interests include high-resolution acoustic imaging, real-time beamforming, and new imaging methods for medical and NDT applications.

NDT&E International 87 (2017) 31–37

Contents lists available at ScienceDirect

NDT&E International

journal homepage: www.elsevier.com/locate/ndteint

Plane-wave phase-coherence imaging for NDE

J.F. Cruza*, J. Camacho, C. Fritsch

Ultrasound Systems and Technology Group (GSTU), Spanish National Research Council (CSIC), Madrid, Spain

ARTICLE INFO

Keywords:
Ultrafast imaging
High frame rate
Phase coherence
Plane-wave imaging

ABSTRACT

In ultrasound imaging with arrays the frame rate is limited by the number of insonifications of the inspected medium. In the limit, a single omnidirectional or plane wave insonification (OWI or PWI, respectively) would provide the maximum frame rate. However, since focusing is applied in reception only, this method yields a poor image quality (resolution, SNR, sidelobe levels, etc.). By contrast, multi-insonification techniques, such as the Total Focusing Method (TFM) or Multi-Plane Wave Imaging (M-PWI) provide the highest quality images, although they require more acquisition time.

This work tries to achieve the image quality of TFM and M-PWI with a single plane-wave insonification to provide ultra-fast imaging at frame rates of tens of KHz. This is achieved by weighting the plane wave image with a phase coherence factor that keeps in-focus indications and suppresses spurious signals. The bases of the new Plane Wave with Phase Coherence Imaging (PWPCI) are described. Experimental work is also carried out to contrast the image quality with that provided by the well established gold standard TFM. This work demonstrates that the proposed PWPCI technique provides similar or superior image quality than TFM at significantly higher frame rates.

1. Introduction

Automated ultrasonic Non-Destructive Evaluation (NDE) of large components requires high scanning speed to reduce costs, while keeping inspection reliability. Conventional Phased Array imaging technology (PA) produces a single scan line after emitting with a given delay law, that produces a steered beam focused at a single depth. In reception, state-of-the art phased array instruments implement strict dynamic depth focusing (DDF), which focuses all the acquired samples along the beam propagation path. The process is repeated for certain number of directions to get an image in real-time [1,2].

However, due to the single focus capability of PA in emission, the aperture size must be limited to achieve the required depth of field. This broadens the ultrasonic beam with the corresponding resolution losses, since dynamic focusing is carried out in reception only.

By contrast, the Total Focusing Method (TFM) uses always the full aperture and takes into account the times-of-flight (TOFs) from emitters and receivers to all the image pixels, achieving focusing in emission and in reception. The TFM image results from the coherent addition of individual low-resolution images formed after the omnidirectional wave emission of each array element (an Omnidirectional Wave Image or OWI). In fact, TFM first obtains N OWIs from emissions with different array elements to build the final high resolution image. TFM is considered the “gold standard” that provides the best resolution and the larger dynamic range [3–6].

Most NDE inspections are performed using PA or TFM. In both cases, the scanning speed is related to the number of insonifications required to obtain the image with an N-element array. PA beamforming is achieved line by line concurrently with signal acquisition, typically reaching 20–200 image/s even with strict DDF if the equipment hardware supports it. Basically, the PA frame rate is limited by the number of image lines and the two-way TOF to the maximum depth.

By contrast, TFM requires a more involved beamforming process that limits the frame rate. Currently, it depends on image size, number of elements and processing power much more than on acquisition time. Some approaches try to overcome this problem: the wave-number algorithm produces the image in the Fourier domain with a lower computational cost [7]; multi-CPU/GPU platforms take advantage of the parallelization possibilities of TFM [8]; a recent FPGA implementation of TFM achieves 7 fps for 120×120 pixel images with a 64-element array [9]. Furthermore, from published specifications of a commercially available system (Gekko, M2M, Les Ulis, France), up to 30 fps are obtained with 64-element arrays for 256×256 pixel images [10].

However, even with zero processing time, i.e. beamforming simultaneously with the ultrasound propagation as in PA, acquisition time cannot be ignored. Acquisition time for a single image, either in PA or TFM, is proportional to the number of times the inspected medium is

---

* Corresponding author.
E-mail addresses: jorge.f.cruza@csic.es (J.F. Cruza), j.camacho@csic.es (J. Camacho), carlos.f@csic.es (C. Fritsch).

http://dx.doi.org/10.1016/j.ndteint.2017.01.005
Received 22 September 2016; Received in revised form 23 December 2016; Accepted 4 January 2017

insonified to the full depth. The only way to increase the frame rate above this limit is reducing the number of emissions.

The so called "paintbrush" technique simultaneously emits with all array elements only once, which produces a plane wave. The image is built by averaging the recorded A-scans of elements grouped in sub apertures to speed-up the process. Although it is fast (a single trigger event), the paintbrush technique yields poor resolution due to the lack of focusing and beamforming [11].

A single Plane Wave Imaging method (PWI), based on the parallel beamforming of the A-scans received by individual elements provided higher resolution and SNR at high frame rates, limited by the technology available at that time to ~1000 s^{-1} [12]. On the other hand, multi-plane wave imaging (M-PWI) was proposed for some medical applications requiring high frame rates and good resolution and dynamic range (heart imaging, shear wave elastography, etc.) [13,14].

With M-PWI a set of plane waves with different angles is used to sequentially insonify the inspected medium. Coherent beamforming follows the emission of every plane wave and the final image is formed by compounding all these images. It has been shown that the number of plane wave emissions required by M-PWI is lower than the number of trigger events of optimal multi focus phased-array (analogous to TFM) to get a similar image quality [15]. In fact, the same M-PWI principle has been recently applied to NDE, demonstrating that M-PWI achieves a resolution and SNR similar to that of TFM, but with 3–10 times less insonifications [16].

From these published data, to get the image quality of TFM with 128-element transducer arrays and direct mode image reconstruction, the number of emitted plane waves should be around 40 for both, the medical and NDE cases, while TFM requires 128 insonifications. These results also show that resolution and dynamic range of a single PWI are poor. OWI images obtained with the single emission of an omnidirectional source (TFM partial image) show similar quality losses. In fact TFM can be considered a multi-OWI modality, although we will keep the well established TFM denomination.

Until now the highest image quality of TFM and M-PWI seems not being compatible with the highest frame rate attained with single PWI. TFM and M-PWI require M ultrasound emissions in the inspected medium (typically $M=N$ in TFM and $M \sim N/3$ in M-PWI for direct mode and high resolution image reconstruction), while PWI uses a single emission. However, as PWI lacks emission focusing, it provides a lower image quality.

These observations led to our research work in ultra-fast high resolution imaging, which tries to get similar resolution, SNR and dynamic range than the gold standard TFM, but with a single emission. The conflict between frame rate and image quality is solved by combining Plane Wave (PW) emission with Phase Coherence Imaging (PCI) in reception to get the PWPCI technique that is proposed in this paper.

In contrast with techniques like apodization that reduced sidelobes at expenses of resolution, Phase Coherence Imaging (PCI) was proposed to simultaneously improve resolution and reduce the sidelobes level [17]. Furthermore, it provided suppression of grating lobes, reverberations and grain noise [18,19]. To get these characteristics, the output of a standard beamformer is weighted by a coherence factor that approaches unity when the received signals originate at focus and zero when they come from other regions. This way, on-focus indications are kept while spurious artifacts become reduced or suppressed.

As we shall see, PWPCI yields unprecedented frame rates that can reach tens of thousands of ultrasonic images per second in NDE with a quality comparable to that of TFM. Frame rate is mainly limited by the time required between acquisitions for reverberation vanishing in the coupling medium and in the inspected part, which for some low attenuation media may amount several signal acquisition times. Besides, the beamforming process should be carried out in parallel with high-performance hardware architectures [20] to not limit the ultra-high frame rate provided by PWPCI.

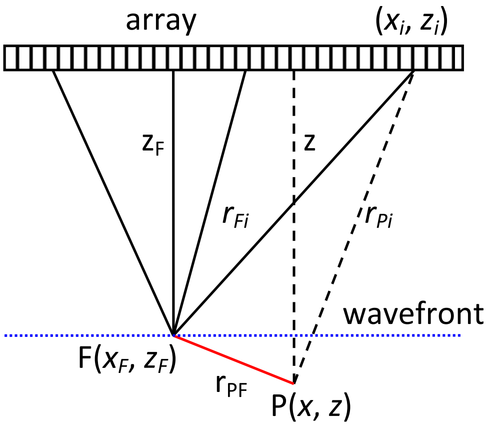

Fig. 1. Reception at array element i of a signal reflected at P when focusing at F with a 0° plane wave.

2. Theoretical PWPCI bases

Since a single PW (or OW) lacks focusing in emission, the image it provides has poor resolution and SNR, high sidelobe levels and spurious indications. Since PCI techniques improve simultaneously these parameters we hypothesized that these can be a good co-processing method to improve the PW image quality. This had not been tested yet and it is one of the aims of the present work.

PCI provides a phase *Coherence Factor CF* in the [0,1] range that depends on the received signals origin: if they come from the focus, *CF* approaches unity; if not, *CF* tends to 0. The computed *CF* is used to weight the output of any conventional beamformer. This is an adaptive process that modifies the beamformer output as a function of the aperture data, hopefully suppressing spurious indications and keeping the information present at focus. Since strict focusing is applied in reception, *CF* can be used to modify every beamformed sample. We describe next the principles of coherence imaging with plane wave insonification.

Fig. 1 shows schematically the reception at the array element i (x_i, z_i) of the echo originated at point P in (x, z) when the reception focus is set to point F at (x_F, z_F). Focusing delay is:

$$T_{Fi} = r_{Fi}/c, \quad r_{Fi} = \sqrt{(x_F - x_i)^2 + (z_F - z_i)^2} \tag{1}$$

and the time of flight T_{Pi} from P to the receiving element i is,

$$T_{Pi} = r_{Pi}/c, \quad r_{Pi} = \sqrt{(x - x_i)^2 + (z - z_i)^2} \tag{2}$$

If the emitted signal is $A(t)\cos(\omega t)$, the echo produced at P and received by element i is:

$$a_i(t) = A_i(t + T_{Pi} + z/c)\cos(\omega(t + T_{Pi} + z/c)), \tag{3}$$

where z/c is the TOF from emission to depth z. The aperture data $s_i(t)$ are delayed versions of $a_i(t)$ by the focusing delay T_{Fi}:

$$s_i(t) = a_i(t - T_{Fi}) = A_i(t + T_{Pi} - T_{Fi} + z/c)\cos(\omega(t + T_{Pi} - T_{Fi} + z/c)) \tag{4}$$

and the aperture data phases are,

$$\varphi_i(t) = \omega(t + z/c) + \omega(T_{Pi} - T_{Fi}) = \varphi_0(t) + \Delta\varphi_i \tag{5}$$

For a given time instant t, the phase variations across the aperture are only due to the second term $\Delta\varphi_i = \omega(T_{Pi} - T_{Fi}) = \omega(r_{Pi} - r_{Fi})/c$. Only if P is located at F is $\Delta\varphi_i$ =0 for all i; in any other case, $r_{Pi} \neq r_{Fi}$ for, at least, some i and the aperture data phase dispersion will not be null. This situation is produced when the signal received by the array originated at some point P different than the focus.

Phase dispersion can be measured with a variety of statistics (standard deviation, variance, etc.). In [17,21,22] we defined the following coherence factors:

1. *Phase coherence factor*. Considers that the aperture data phases are distributed in the (-π, π] interval. Their standard deviation σ is computed and normalized by the standard deviation of a uniform linear distribution of phase, $\sigma_0 = \pi/\sqrt{3}$:

$$PCF = \max\left(0\ ,\ \ 1 - \frac{\sigma}{\sigma_0}\right) \tag{6}$$

2. *Sign coherence factor*. It results from the discretization of the phase with a single bit, the sign of the aperture data b_i. It is computed as:

$$SCF = 1 - \sqrt{1 - \left[\frac{1}{N}\sum_{i=1}^{N} b_i\right]^2} \tag{7}$$

3. *Circular coherence factor*. It was defined in [21,22] to consider the continuous circular distribution of the phase in (0, 2π]. It is computed from the analytical signal s_a=s+jH(s), where s is the aperture data, H[·] represents the Hilbert transform of the argument and j=$(-1)^{1/2}$:

$$CCF = 1 - \sqrt{\mathrm{var}\left(\frac{s_i}{|s_{ai}|}\right) + \mathrm{var}\left(\frac{\mathrm{H}[s_i]}{|s_{ai}|}\right)} \tag{8}$$

PCF requires obtaining the phases as the argument of the analytical signal and their standard deviation σ in the interval (-π, π]. By contrast, *SCF* is obtained from the sum of the sign bits b_i of the aperture data, which has a straightforward implementation. Finally, *CCF* is continuous, but has two drawbacks: a) computing the variance uses many hardware resources for real-time processing and b) it is very sensitive to small phase misalignments.

A midway approach is also possible. Consider N phase samples $\{\varphi_i\}$ expressed as the unit vectors $(\cos\varphi_i,\ \ \sin\varphi_i)$ in the unit circle of the complex plane. The normalized length $|R|$ of the vector resultant of the addition of these vectors is a measure of phase concentration with a maximum value of 1, being computed as [23]:

$$|R| = \frac{\sqrt{(\sum \cos\varphi_i)^2 + (\sum \sin\varphi_i)^2}}{N} \tag{9}$$

The value of $|R|$ can be interpreted as a phase coherence measurement, which we call *vector coherence factor* (*VCF*). *VCF* tends to zero if phases are evenly spread over the unit circle and to unity if they are concentrated around some value. *VCF* is computed from the analytical representation s_a = s+jH(s) of aperture data as:

$$VCF = \frac{\sqrt{(\sum s)^2 + (\sum[\mathrm{H}(s)])^2}}{N|s_a|} \tag{10}$$

In a general comparison between coherence factors, *PCF* does not provide practical advantages over *VCF*, since it requires computing a standard deviation and is not a continuous function of phase. On the other hand, although computing the *VCF* is more complex than obtaining the *SCF*, it is simpler than obtaining the *CCF* that requires variance calculation. Besides, *VCF* is more tolerant to small phase errors than *CCF* and *SCF*, an important aspect that can be present in real-life inspections due to noise, target shading, reverberations and other spurious signals.

It is worth to note that a simple method to soften the correction strength of a given coherence factor is rising its computed value to a power exponent 0≤ p≤1, as described in [17]. In particular, for the sign coherence factor,

$$SCF^p = \left(1 - \sqrt{1 - \left[\frac{1}{N}\sum_{i=1}^{N} b_i\right]^2}\right)^p, \quad 0 \le p \le 1 \tag{11}$$

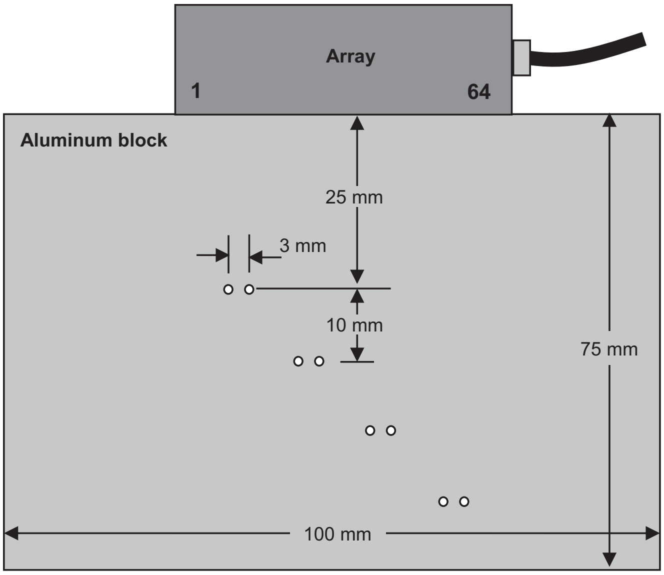

Fig. 2. Array in contact with an aluminum block with pairs of 1.5 mm diameter side drilled holes.

In this work we will use to weight the plane wave images the sign coherence factor SCF^p with p=1 and p=0.5, as well as the vector coherence factor *VCF*. Values $p < 1$ reduce the SCF sensitivity to changes in the aperture data signs, which helps to compensate amplitude losses due to interference, grain noise, focusing errors, etc. as it is shown in the experimental work. On the other hand, image quality improvement provided by *SCF* is reduced, giving the original PW image when *p=0*. In this sense, *p=0.5* is a compromise value between both extreme cases, but any other value could be used as well.

3. Verification of the PWPCI technique

A set of experiments have been carried out to verify the operation of the proposed PWPCI ultrafast imaging technique with regard to TFM and M-PWI. A 5 MHz, 64-elements, 0.65 mm pitch array (Imasonic, France) was used in contact with an aluminum part of measured sound velocity 6.32 mm/μs. Several pairs of 1.5 mm diameter holes, separated 3 mm were drilled at different depths at 10 mm intervals (Fig. 2).

The TFM image results from the coherent addition of individual low-resolution images formed after the omnidirectional emission of a different array element. For PWI, array elements were triggered with a linear delay law to produce a plane wave at a selected angle. In both cases, the Full Matrix Capture (FMC) was carried out with a SITAU 111 instrument (Dasel SL, Spain). TFM required T=64 insonifications and PWI a single simultaneous trigger (T=1). Beamforming was carried out in Matlab (The Mathworks Inc, USA) on a rectangular grid that is common to both techniques. Images are shown in a logarithmic scale with a dynamic range of 60 dB.

Fig. 3left shows the TFM image, where the 4 pairs of holes are clearly seen, besides acoustic noise due to spurious signals: sidelobes, reverberations and mode converted signals, mainly in the region below the holes indications. Maximum dynamic range is approximately 55 dB, which is below the maximum 72 dB theoretically expected for a 64-elements TFM image, due to these spurious signals. Average lateral resolution measured by full width at half maximum (FWHM) at all reflectors is 1.4 ± 0.3 mm.

Fig. 3right shows the image obtained with the same array when emitting a single plane wave (PWI) at 0° without further processing other than reception beamforming. Average lateral resolution and contrast losses are evident when compared with TFM: dynamic range of a single PW image is approximately 35 dB, while average FWHM degrades to 2.0 ± 0.4 mm and sidelobes are quite visible.

Fig. 4left shows the PWPCI single emission image weighted by the

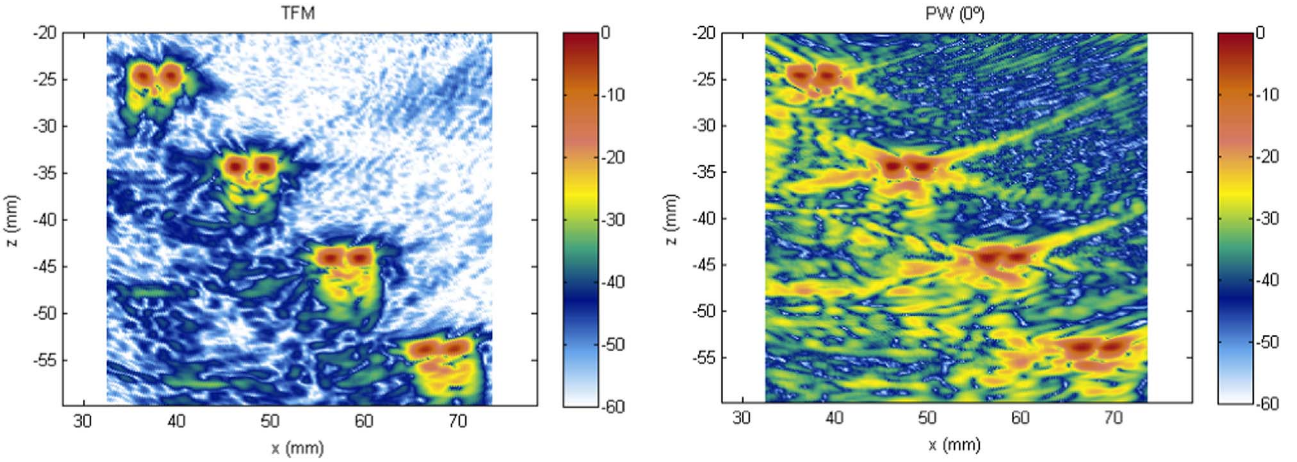

Fig. 3. Imaging with a 64-elements array. Left: TFM image. Right: PWI with single emission at 0°.

sign coherence factor (*SCF*). Dynamic range and resolution improve even with regard to TFM, to 75 dB and 1.3 ± 0.4 mm, respectively, and dramatically with regard to the values obtained with a single PW emission image and focusing in reception only (Fig. 3right).

By counterpart, an average amplitude loss of −2.2 ± 2.1 dB is observed, being maximum at the third pair of holes (−5.1 dB). As explained in [17] these amplitude losses can be reduced by lowering the value of the exponent *p*, at the expenses of reducing somewhat the achieved dynamic range. Fig. 4right shows the PWPCI image weighted by $\mathrm{SCF}^{0.5}$, with resolution and dynamic range equivalent to that of TFM and slight amplitude losses of −1.1 ± 1.0 dB.

There are several causes for a reflector to give a coherence factor less than 1, an effect that produces the amplitude losses above. Noise (electrical and/or acoustic) and reverberations, reduce the coherence value by contaminating the measured phases. Also, the beamforming process assumes ideal point-like reflectors and, hence, their shape and size introduce some phase dispersion, lowering the coherence value. Finally, shadowing effects caused by other reflectors can introduce random phases in several array elements. Although, in general, these effects are limited, they must be taken into account.

Some of these issues can be addressed by increasing the spatial diversity in the beamforming process. For example, by RF compounding several images obtained with plane waves at different propagation angles, following the strategy proposed in [16]. Fig. 5left shows the result of RF compounding three PW images with angles −7°, 0° and 7° and without phase coherence processing. When compared with a single PW emission (Fig. 3right) maximum dynamic range is slightly improved, and further, there is a clear reduction of spurious echoes.

However, for each one of the three emissions a coherence factor matrix is obtained, which can be used to weight each corresponding individual PW image or, alternatively, can be combined and applied to the compounded image. Fig. 5right shows the compounded image weighted by the maximum coherence among the three individual coherence values, following:

$$im(x,\ y) = \left(\sum_{i=1}^{K} PW_k(x,\ y)\right) \cdot \max\left[SCF_1(x,\ y),\quad SCF_2(x,\ y),\quad SCF_3(x,\ y)\right] \tag{12}$$

Taking the maximum coherence value of the three acquisitions minimizes the amplitude losses due to shadowing and interferences. Here, amplitude losses are −0.3 ± 0.5 dB, dynamic range is kept at 73 dB and FWHM is 1.3 ± 0.3 mm. It should be noticed that, with just 3 PWPCI emissions, an image with better quality than TFM with 64 omnidirectional emissions has been obtained.

An alternative way to minimize amplitude variations is weighting with *VCF*, a coherence factor less sensitive to shadowing and reverberations than *SCF*, but with lower capability of reducing side-lobes. Fig. 6left shows the image obtained by weighting the PWPCI single emission image (Fig. 3right) by *VCF*. Dynamic range is 54 dB and FWHM is 1.4 ± 0.3, nearly equivalent to the TFM case. Furthermore, reflector amplitude losses are −1.0 ± 0.4 dB. Although image quality is similar to that obtained with $SCF^{0.5}$ (Fig. 4right) *VCF* avoids the discontinuities in the sign calculation, which yields a more stable image, although with a slightly more complicated computation.

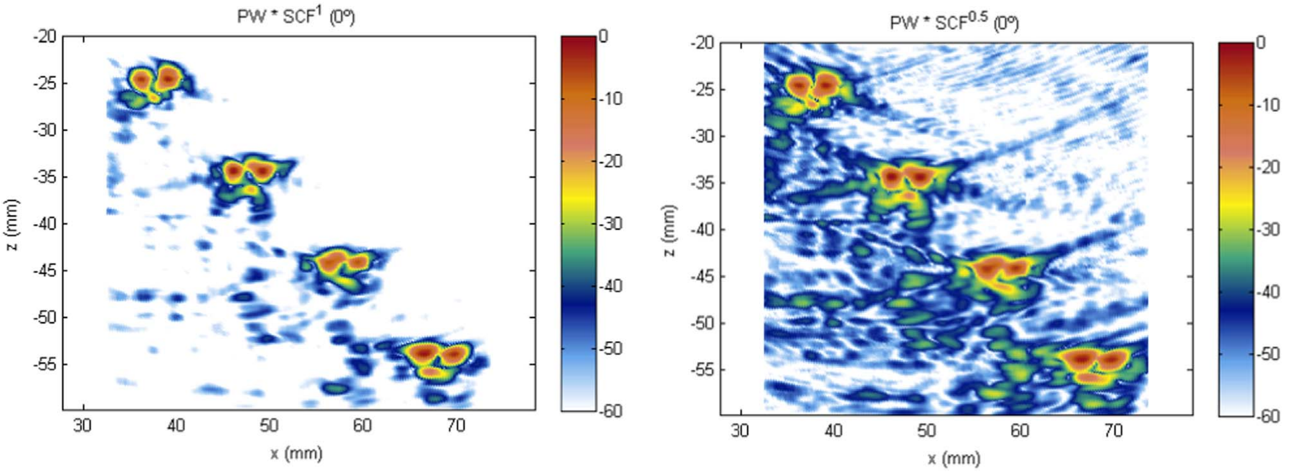

Fig. 4. PWPCI single emission at 0°. Left: weighted by SCF^1. Right weighted by $\mathrm{SCF}^{0.5}$.

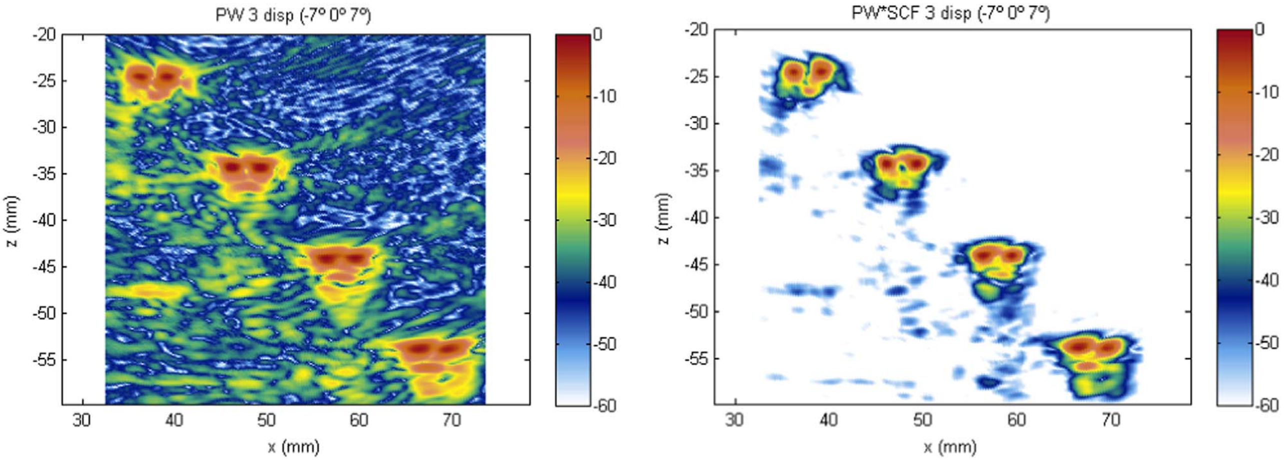

Fig. 5. Image compounding. Left: with 3 PW emissions at −7°, 0° and 7°. Right: further weighted pixel by pixel by the maximum coherence value among the three emissions.

In order to complete the analysis, Fig. 6right shows the image obtained by compounding three plane wave emissions at −7°, 0° and 7° and weighting by maximum VCF. Average FWHM and maximum dynamic range are equivalent to those obtained with single emission, while reflector amplitude losses are slightly reduced to -0.7 ± 0.3 dB. Different from *SCF*, increasing the number of emissions when weighting by *VCF* does not improve significantly the image quality.

In summary, Fig. 7 shows the lateral pattern at the depth of each pair of holes for the three more relevant cases: TFM with 64 emissions, PWPCI with 3 emissions weighted by the maximum *SCF* and PWPCI with 1 emission weighted by *VCF*. While the three methods are nearly equivalent for all reflectors (resolution and amplitude), compounding three PWPCI with *SCF* weighting provides a larger dynamic range than TFM and PWPCI with *VCF* weighting. Tables 1 and 2 summarizes the FWHM and amplitude variations measured at each hole for all the analyzed methods.

4. Discussion

The maximum frame rate theoretically achievable with PWPCI is the inverse of the two-way TOF through the inspected part. For that used in the experiments, the two-way TOF is, approximately, 24 µs and a theoretical maximum above 40,000 frames/s could be achieved if processing were carried out concurrently with the acquisition. However, even so, such figure is difficult to reach. Some time is required to fade away reverberations between emissions, which depends on the attenuation and acoustic impedances of the coupling and the part.

In practice, the frame rate should be related with the scanning speed required. Here, PWPCI can be a good alternative in the aeronautic industry where the inspection time of large parts is important, as well as in the manufacturing processes of laminated materials. In these cases a frame rate of, simply, 1000 s^{-1} is already considered very fast. Another field of application is railways track inspection, which would be carried out at high speed (for example, at more than 100 km/h ≈30 m/s), obtaining high quality images at 10 mm intervals with a frame rate of 3000 s^{-1}. Many other fields can also benefit from ultrafast ultrasonic imaging.

Since the maximum frame rate theoretically achievable with a single PW emission would be seldom required, the multi-angular PWPCI technique can provide fast enough imaging. This way the coherence losses due to shadowing or interferences would be minimized, still achieving the high quality of TFM or better.

With regard to implementation, real-time ultrafast PWPCI requires beamforming the high-resolution image concurrently with the acquisition or, more precisely, in the time interval between two acquisitions. Currently, this is within the reach of state-of-the-art FPGAs, which allow beamforming multiple lines in parallel [20]. However, most reported ultrafast imaging techniques acquire ultrasound data in real time at high frame rates and, then, processes these signals off-line. This allows recording a movie for medical diagnosis, but it is not enough for some NDE applications as the railways case with inspections of tens to hundred of km.

A final word about the possible application of the above concepts to omnidirectional wave emission imaging with phase coherence processing (OWPCI). Along the TFM process, *N* OWs are obtained. The

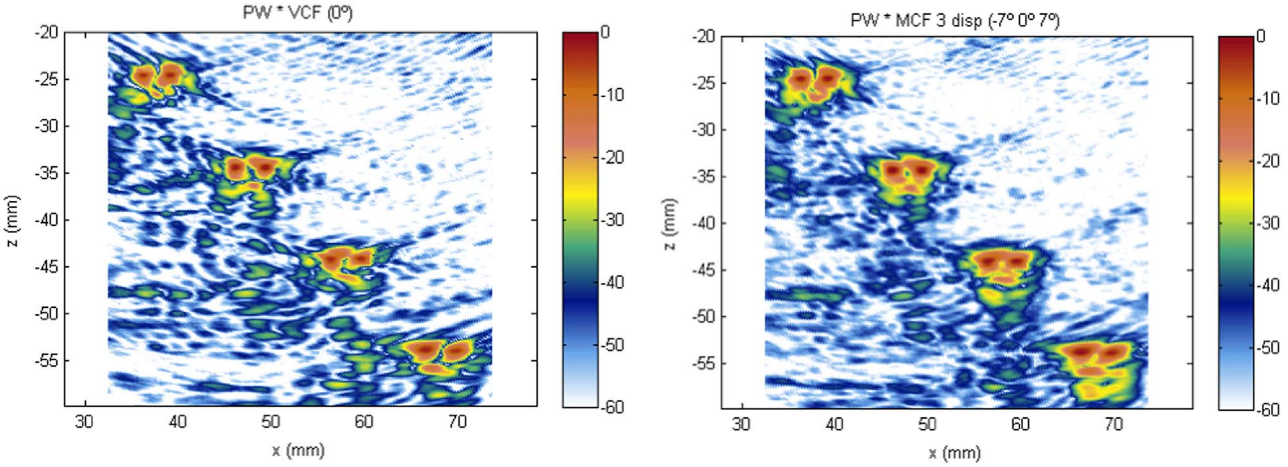

Fig. 6. PWPCI emission image weighted by *VCF*. Left: with single PW emission. Right: with 3 PW emissions at −7°, 0° and 7°.

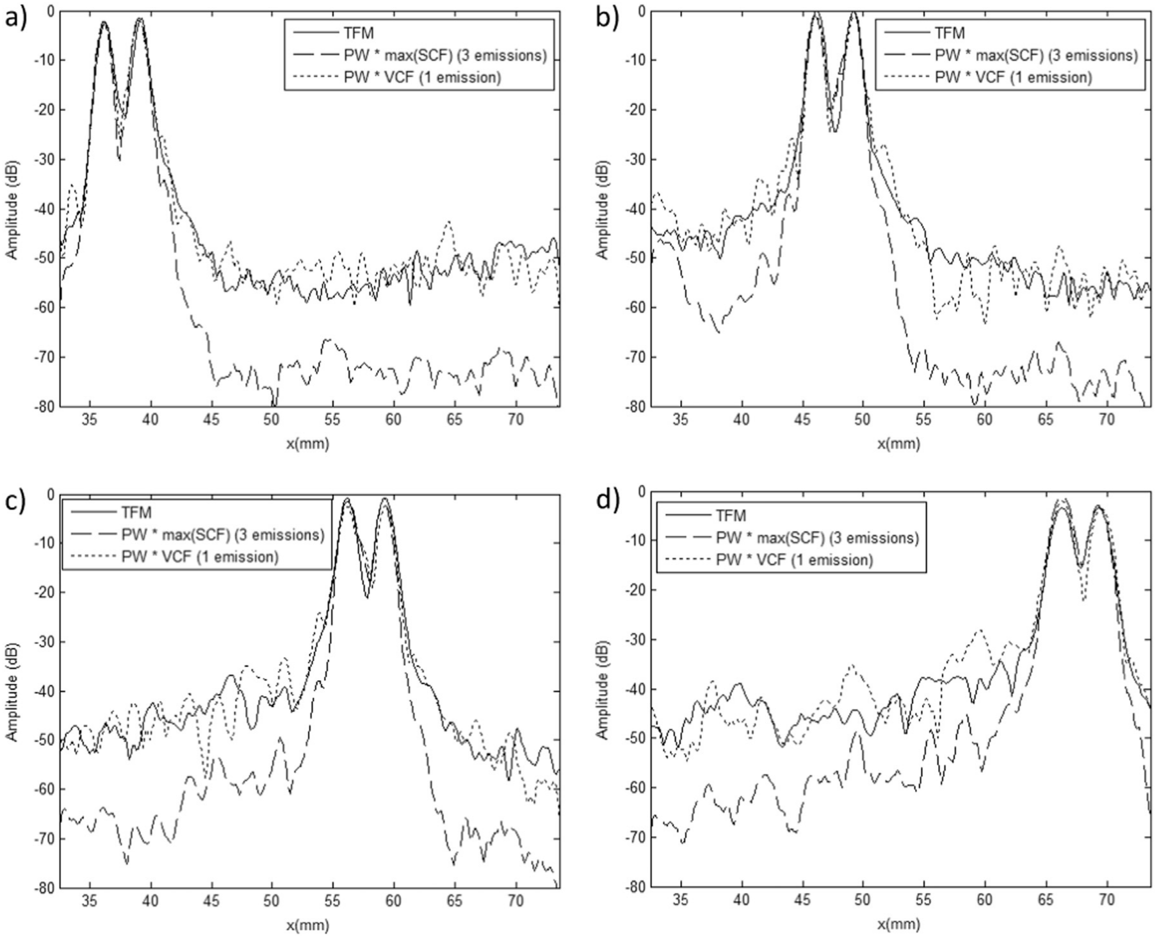

Fig. 7. Lateral profiles of TFM with 64 emissions (solid line), 3 emissions PW weighted by maximum of *SCF* (dashed) and single emission PW weighted by *VCF* (dotted). Depth ranges of each pair of holes: (a) *z*=25 mm (b) *z*=35 mm (c) *z*=45 mm and (d) *z*=55 mm.

Table 1
FWHM at each hole for TFM and single PW emission weighted by *VCF* and SCF, and 3 PW emissions weighted by maximum *SCF* and *VCF*.

	FWHM (mm)							
	z=25 mm		z=35 mm		z=45 mm		z=35 mm	
TFM	1.2	1.1	1.2	1.1	1.4	1.4	1.7	1.7
PW 1 emission	1.6	1.6	1.7	1.8	2.5	2.0	2.3	2.3
PW 1 emission with *VCF*	1.2	1.2	1.2	1.1	1.5	1.3	1.8	1.7
PW 1 emission with SCF	1.0	1.1	1.1	1.1	2.1	1.2	1.7	1.5
PW 3 emissions with max(*SCF*)	1.1	1.2	1.2	1.1	1.4	1.2	1.9	1.6
PW 3 emissions with max(*VCF*)	1.2	1.3	1.3	1.2	1.5	1.3	1.9	1.8

Table 2
Attenuation introduced at different depths by the coherence factors.

	Amplitude loss (dB)							
	z=25 mm		z=35 mm		z=45 mm		z=35 mm	
PW 1 emission with *VCF*	−0.9	−0.6	−1.1	−1.0	−1.4	−1.4	−0.6	−1.8
PW 1 emission with *SCF*	−1.8	−0.5	−1.1	−1.7	−5.8	−5.4	0.0	−1.4
PW 1 emission with $SCF^{0.5}$	−0.9	−0.3	−0.6	−0.9	−2.9	−2.8	0.0	−0.8
PW 3 emissions with max(*SCF*)	−0.5	0.0	−1.0	0.0	0.0	0.0	0.0	−1.2
PW 3 emissions with max(*VCF*)	−0.7	−0.4	−1.0	−1.0	−1.0	−1.1	−0.2	−0.4

OWPCI process, analogous to PWPCI, would weight any one of these OW images with some phase coherence factor. Image quality of OWPCI (Fig. 8right) is significantly improved with regard to that of an OW image (Fig. 8left), although with some differences with PWPCI. First, the SNR of OWPCI is lower than that of PWPCI since a single element is used in emission. Furthermore, sensitivity worsens with depth due to diffraction of the emitted omnidirectional wave, while PWPCI keeps the amplitude of the plane wave constant up to the depth of the near field, approximately $D^2/4\lambda$, where D is aperture size and λ wavelength.

Due to these drawbacks, in general PWPCI will be preferred to OWPCI, unless a sector image is desired, since both of them require, basically, the same acquisition and processing time.

5. Conclusions

This work has demonstrated the possibility of achieving ultrafast imaging with the highest quality by combining Plane Wave emission with Phase Coherence Imaging (PWPCI). Thousands of images per second can be obtained with a single emission and providing the same or better quality that the considered gold standard Total Focusing Method (TFM).

Besides, phase coherence processing suppresses spurious indications (side-lobes, reverberations, etc.). However, the coherence level can be affected by noise or shadowing effects that lower the indications amplitude by some dB. These losses can be limited by raising the coherence factor to a power less than unity, although this reduces somewhat the image dynamic range.

Compounding a few PW images with different angles and using the maximum of the coherence factors avoids these drawbacks. It has been

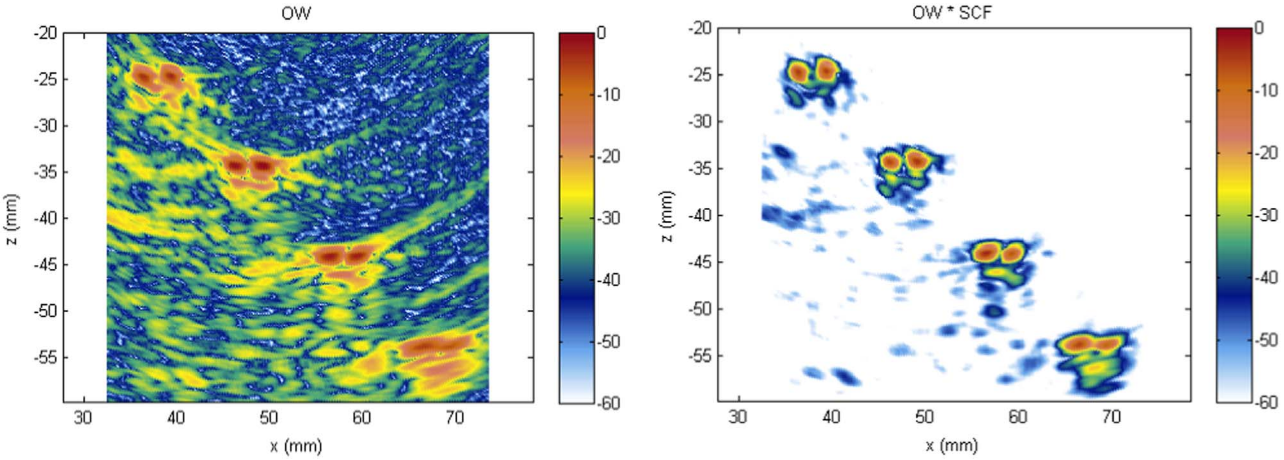

Fig. 8. Omni-directional wave image obtained after emitting with element 32. Left: beamformed in reception only (OWI); Right: weighted by SCF (OWPCI).

shown that this strategy recovers in practice the coherence level with a quite limited number of emissions, achieving a quality similar to that provided by TFM. We have also proposed the vector coherence factor (VCF), less sensitive to these influences. VCF has been also verified to achieve ultrafast high quality imaging.

Acknowledgments

Work funded by project DPI2013-42236-R of the program “Research challenges” of the Spanish Ministry of Economy and Competitiveness (DPI2013-42236-R).

References

[1] Fritsch C, Parrilla M, Ibáñez A, Giacchetta R, Martínez O. The progressive focusing correction technique for ultrasound beamforming. IEEE Trans Ultrason Ferroelectr Freq Control 2006;53(10):1820–31.

[2] Camacho J, Cruza JF, Brizuela J, Fritsch C. Automatic dynamic depth focusing for NDT. IEEE Trans Ultrason Ferroelectr Freq Control 2014;61(4):673–84.

[3] Holmes C, Drinkwater B, Wilcox P. Post-processing of the full matrix of ultrasonic transmit–receive array data for non-destructive evaluation. NDTE Int 2005;38(8):701–11.

[4] Drinkwater BW, Wilcox PD. Ultrasonic arrays for non-destructive evaluation: a review. NDTE Int 2006;39:525–41.

[5] Holmes C, Drinkwater BW, Wilcox PD. Advanced post-processing for scanned ultrasonic phased arrays: application to defect detection and classification in non-destructive evaluation. Ultrasonics 2008;48:636–42.

[6] Zhang J, Drinkwater BW, Wilcox PD, Hunter AJ. Defect detection using ultrasonic arrays: the multi-mode total focusing method. NDTE Int 2010;43(2):123–33.

[7] Hunter A, Drinkwater BW, Wilcox PD. The wavenumber algorithm for full-matrix imaging using an ultrasonic array. IEEE Trans Ultrason Ferroelectr Freq Control 2008;55(11):2450–62.

[8] Lambert J, Pédron A, Gens G, Bimbard F, Lacassagne L, Iakovleva E. Analysis of multicore CPU and GPU toward parallelization of total focusing method ultrasound reconstruction, DASIP 2012 Conference on Design and Architectures for Signal and Image Processing. Karlsruhe, Germany, Oct. Available at: ⟨https://hal.inria.fr/hal-01093274/document⟩; 2012.

[9] Njiki M, Bouaziz S, Elouardi A, Casula O, Roy O. A Multi-FPGA implementation of real-time reconstruction using total focusing method. In: Proceedings of the 2013 IEEE international conference on cyber technology in automation, control and intelligent systems. Nanjing, China, May 26–29; 2013. p. 468–73

[10] M2M, Gekko, Phased-array flaw detector, Available at: ⟨http://www.m2m-ndt.com/products/Spec%20Gekko.pdf⟩

[11] Dominguez N, Ithurralde G. Ultra-fast ultrasonic inspection for aeronautical composites using paintbrush acquisitions and data processing on GPU, European conference on NDT, Moscow. Available at: ⟨http://www.ndt.net/article/ecndt2010/reports/1_10_03.pdf⟩; 2010.

[12] Camacho J, Cruza JF, Cuevas E, Hernández S, Fast Scanning: achieving high scanning velocities in the phased array inspection of aeronautic components. In: Proceedings of the 6th international symposium on NDT in aerospace. 12-14 Nov. 014, Madrid, Spain. Available at: ⟨http://www.ndt.net/events/aeroNDT2014/app/content/Paper/41_Cruza.pdf⟩

[13] Tanter M, Bercoff J, Sandrin L, Fink M. Ultrafast compound imaging for 2-D motion vector estimation: application to transient elastography. IEEE Trans Ultrason Ferroelectr Freq Control 2002;49(10):1363–74.

[14] Tanter M, Fink M. Ultrafast imaging in biomedical ultrasound. IEEE Trans Ultrason Ferroelectr Freq Control 2014;61(1):102–19.

[15] Montaldo G, Tanter M, Bercoff J, Benech N, Fink M. Coherent plane-wave compounding for very high frame rate ultrasonography and transient elastography. IEEE Trans Ultrason Ferroelectr Freq Control 2009;56(3):489–506.

[16] Le Jeune L, Robert S, Lopez Villaverde E, Prada C. Plane Wave Imaging for ultrasonic non-destructive testing: generalization to multimodal Imaging. Ultrasonics 2016;64:128–38.

[17] Camacho J, Parrilla M, Fritsch C. Phase coherence imaging. IEEE Trans Ultrason Ferroelectr Freq Control 2009;56(5):958–74.

[18] Camacho J, Parrilla M, Fritsch C. Grating lobes reduction by application of Phase Coherence Factors. IEEE Int Ultrason Symp Proc 2009:341–4.

[19] Camacho J, Fritsch C. Phase coherence imaging of grained materials. IEEE Trans Ultrason Ferroelectr Freq Control 2011;58(5):1006–15.

[20] Cruza JF, Camacho J, Moreno JM, Medina L. A new architecture for fast ultrasound imaging. AIP conf. proceedings, 1581, 1. 2014:1975–82.

[21] Camacho J. Imagen ultrasónica por coherencia de fase [Ph. D. Thesis]. Univ. Complutense Madrid; 2010 ⟨http://eprints.ucm.es/12317/1/T32771.pdf⟩.

[22] Camacho J, Fritsch C. Adaptive beamforming by phase coherence processing,. Ultrasound Imaging, Chap. 4, Ed InTech, Available from: ⟨http://www.intechopen.com/books/ultrasound-imaging/⟩; 2011.

[23] Jammalamadaka SR, Sen Gupta A. Sen GuptaTopics in circular statistics, 15, Ed.. Singapore: World Scientific; 2001.

6th International Symposium on NDT in Aerospace, 12-14th November 2014, Madrid, Spain - www.ndt.net/app.aeroNDT2014

Fast Scanning: achieving high scanning velocities in the phased array inspection of aeronautic components

Jorge CAMACHO [1], Jorge F. CRUZA [1], Esmeralda CUEVAS [2], Sergio HERNANDEZ [2]

[1] ITEFI-CSIC, c/Serrano, 144, Madrid (Spain), e-mail: j.camacho@csic.es
[2] Tecnatom, S.A., Av. Montes de Oca, 1, San Sebastián de los Reyes, Madrid (Spain)

Abstract
This work proposes a fast inspection method for large planar and soft curved aeronautic components, named Fast Scanning, able to obtain more than 1000 images per second in continuous operation. Using arrays, this method is based on composing every B-scan image in real time with a single trigger event, which reduces the acquisition time by the amount of image lines. Differently from other approaches, Fast Scanning performs real-time parallel beamforming of all the A-scan lines that compose the image with an adaptive control of focal laws. The former provides well focused images, while the latter keeps the optimal focal laws under probe-part geometry variations. Experimental results show that phased array imaging and Fast Scanning yield similar image quality with regard to resolution, sensitivity and signal-to-noise ratio. However, Fast Scanning provides one to two orders of magnitude higher frame rates, opening an opportunity to significantly reduce the inspection time of large aircraft components without compromising the image quality.

Keywords: phased array, parallel beamforming, aerospace, carbon fiber composite

1. Introduction

Inspection time is an important parameter for efficient handling and cost reduction in the aeronautic industry, specifically in the manufacturing process of composites. Automatic phased array imaging improves inspection time and reliability by providing B and C-scan images of the tested part covering the full extent of the transducer array, wider than conventional mono-element based inspections. Furthermore, its beam focusing capabilities yields higher image quality.

However, conventional phased array images are obtained in a line per line basis, usually following a linear scan strategy. This requires multiple trigger events to get the whole set of lines that compose the image. Since the ultrasound transit time is bounded by different parameters, the frame rate becomes limited up to some tens of images per second, which yields a moderate scanning speed (typically bellow 300 mm/s).

Several efforts have been performed to overcome this limitation. The so named *Paintbrush* technique [1] simultaneously excites all the array elements and registers the A-Scans received with each one of them. The B-Scan image is directly formed with these A-Scans, which yields relatively low resolution and signal-to-noise ratio. Some quality improvement techniques have been proposed, but they require the use of parallel processor units (GPUs) for their real time realization.

Another interesting approach is the *SAUL* technique, which performs between 2 and 4 excitation events to iteratively adapt the generated wave-front to the shape of the part, ensuring normal incidence at all surface points. Although it is an excellent technique for the inspection for complex shape components [2], achievable scanning speed is moderate. For example, when acquiring a B-Scan image every 2 mm and using 4 iterations, reported scanning speed is about 100 mm/s [3].

This work proposes an alternative method, named Fast Scanning, able to obtain over 1000 images per second in large and soft curved aeronautic components. It is based on composing every B-scan image in real time with a single trigger event, which reduces the acquisition time by the amount of A-scan lines in the image. For a typical automated inspection with index resolution of 2 mm, scanning speeds above 3 m/s are estimated to be achieved.

Differently from other approaches, Fast Scanning performs real-time parallel beamforming of all the A-scan lines that compose the image with an adaptive control of focal laws. The former provides well focused images, while the latter keeps the optimal focal laws under probe-part geometry variations. Image formation is achieved by switching the acquired data to multiple beamformers, each one with an active aperture up to 16 elements (limited by hardware resources) and their own focal laws. This way, all the image lines are beamformed in parallel. Simultaneously, the ultrasound hardware computes the focal laws for the next acquisition from the acquired data, thus performing adaptive beamforming for planar and soft-curved surfaces.

Experiments were performed to compare the performance of Fast Scanning and conventional phased array imaging. Both yield similar image quality with regard to resolution, sensitivity and signal-to-noise ratio. However, Fast Scanning provides one to two orders of magnitude higher frame rates, opening an opportunity to significantly reduce the inspection time of large aircraft components without compromising the image quality.

2. Fundamentals

Figure 1 shows a schematic representation of a typical phased-array linear scan process. A sub-set of M elements (active aperture) is excited with some emission delays to generate a focused beam into the material. Echoes are registered by the same M elements and individual signals are combined in a reception beamforming process, usually involving apodization, delay and sum operations. The obtained raw A-Scan is usually further processed with band-pass filters, envelope detection algorithms and peak detections gates, to finally get a single image line. The whole process is repeated moving the active aperture between emissions, thus generating a B-Scan image.

In this scenario, scanning speed is limited by image formation time, which is physically limited by the ultrasound time-of-flight (TOF) to the bottom of the component. But besides this upper limit, there are some other technological factors like maximum pulse repetition frequency (PRF), beamforming and digital processing (DSP) time or data transfer rate that usually further reduce inspection speed.

Lets consider a case study of a CFRP component with thickness $E = 40\ mm$ and speed of sound $c_P = 3000\ m/s$. An $f_R = 5\ MHz$ array with $N=128$ elements and pitch $d=1mm$ is used to perform a linear scan with $M = 6$ active elements, resulting in $L=123$ image lines. Scanning resolution in the movement direction (index resolution) is $\Delta y = 2\ mm$ and signal sampling frequency is $f_s = 20\ MHz$. A water column of $H = 30mm$ is assumed between the array and the component surface.

With these numbers, the ultrasound time-of-flight to the back-wall is ($c_W = 1500\ m/s$):

$$T_V = 2E/c_P + 2H/c_W \approx 67\ \mu s \tag{1}$$

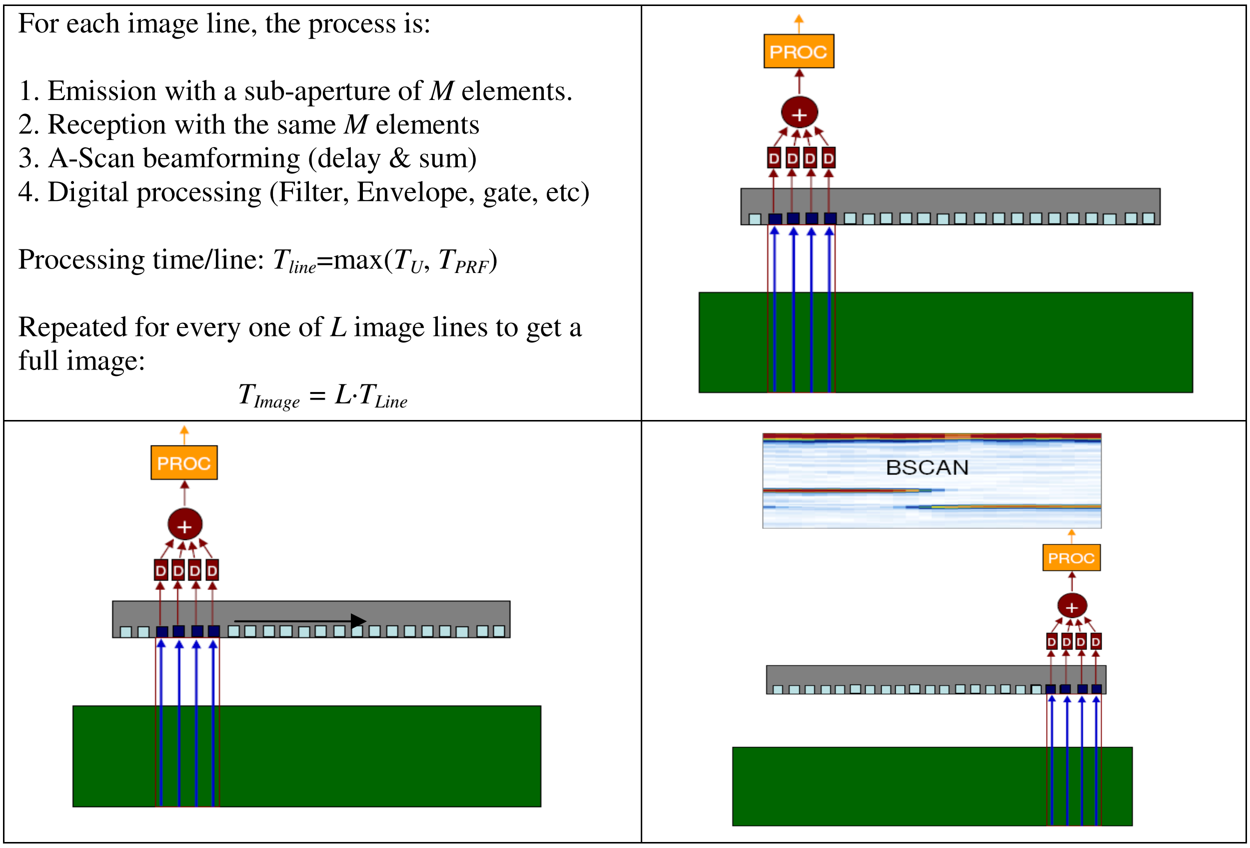

For each image line, the process is:

1. Emission with a sub-aperture of *M* elements.
2. Reception with the same *M* elements
3. A-Scan beamforming (delay & sum)
4. Digital processing (Filter, Envelope, gate, etc)

Processing time/line: $T_{line}=\max(T_U, T_{PRF})$

Repeated for every one of *L* image lines to get a full image:

$$T_{Image} = L \cdot T_{Line}$$

Figure 1 –Schematic representation of the conventional linear scan process.

With conventional phased-array technique, the minimum acquisition time for each B-Scan is (assuming null beamforming and digital processing times)

$$T_{ACQ} = L * T_V = 8.2 \text{ ms} \qquad (2)$$

If data transfer time is neglected, the maximum achievable frame rate is

$$FPS = 1/T_{ADQ} \approx 120 \text{ images/s} \qquad (3)$$

and the maximum scanning speed is

$$v = FPS * \Delta y = 240 \text{ mm/s} \qquad (4)$$

The required system PRF to obtain this inspection speed is

$$PRF = L * FPS = 15 \text{ kHz} \qquad (5)$$

Finally, the required data communication bandwidth between the acquisition system and the evaluation computer for sustained operation is about 16 MB/s, if only the samples inside the component are registered and transferred (540 samples per A-Scan). This throughput can be achieved with conventional links like USB 2.0, but there are other limiting factors like beamforming time, operative system latencies, etc, that usually reduce inspection speed typically bellow 300 mm/s.

The goal of the Fast Scanning method [4] is to increase this figure an order of magnitude, above 2 m/s. If it could be achieved, scanning speed will not be limited by the ultrasound inspection process. Instead, limitations will arrive from mechanical movement and restrictions related with operation safety.

Figure 2 depicts the overall process. After emission of a plane wave with all array elements, individual signals are registered. If the B-Scan image were formed directly from these signals like in the *Paintbrush* method, a low resolution and SNR signal would be obtained (Figure 2.top-right). Instead, in the Fast Scanning method, a set of L hardware implemented beamformers are used to generate L focused scan lines with higher resolution and SNR. Depending of the processing power of the target hardware, this process could be realized in strict real time (same output and input throughput) or with some overhead time for internal signal transfer and processing.

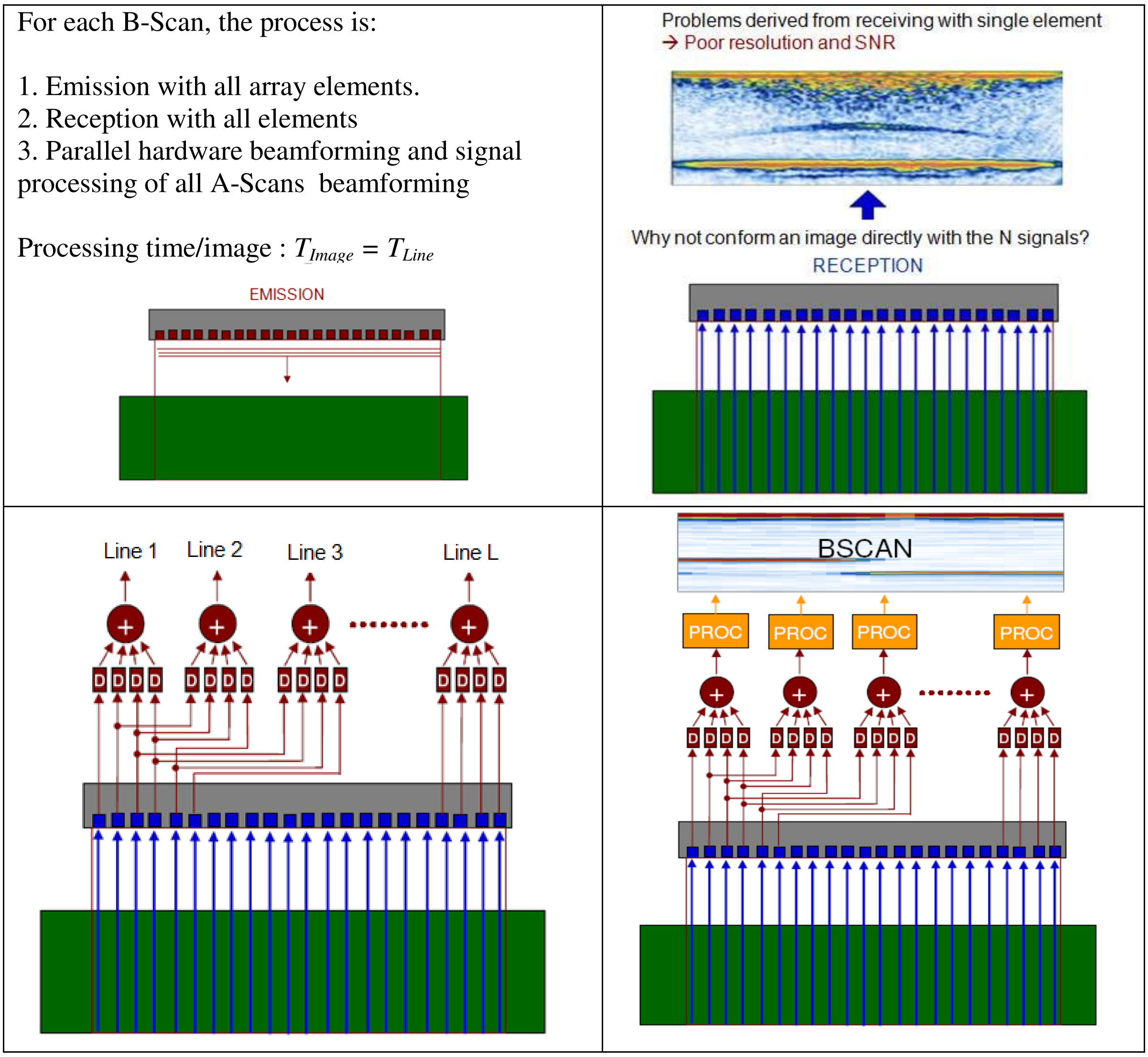

For each B-Scan, the process is:

1. Emission with all array elements.
2. Reception with all elements
3. Parallel hardware beamforming and signal processing of all A-Scans beamforming

Processing time/image : $T_{Image} = T_{Line}$

Figure 2 – Schematic representation of the Fast-Scanning method

Besides increasing resolution and contrast, the beamforming process allows to correct probe-part misalignments by electronic beam steering. Signal loss because of array misalignment is a quite severe problem in this kind of inspections, mainly because of the high directivity of the generated beams. A slight inclination of 3º can produce more than 12 dB of signal loss in the interface echo. Moreover, refraction at the interface because of the large impedance mismatch between water and composite deflects the beam and further reduces defects and back-wall echo amplitudes.

To overcome this limitation, a focal-law correction algorithm was developed. Based on the echo-start information of each acquired image, surface inclination angle is estimated and a new set of emission and reception delays are calculated. This ensures normal incidence for both the emitted plane-wave and generated reception beams. The algorithm was optimized for being implemented in the acquisition hardware. Parallelizing the angle correction and the image formation processes, a negligible overhead is ensured. Moreover, because correction information is obtained directly from each B-Scan data, no extra emission events are required like in other approaches.

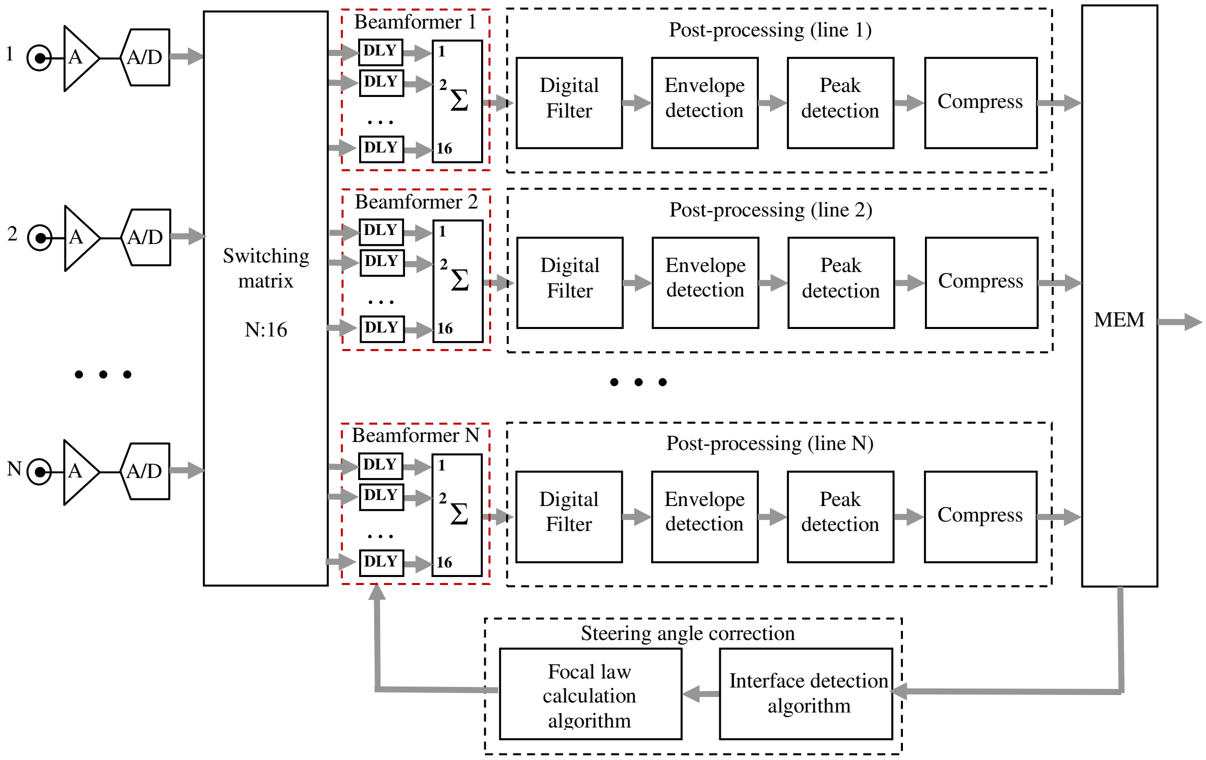

Figure 3 – Schematic representation of the Fast Scanning hardware implementation.

Table I summarizes the expectable maximum inspection speed depending of the active aperture size, for a 5 MHz array with 128 elements, pitch 1 mm and a component of 50 mm thickness. Scan resolution is 2 mm in both C-Scan directions, and all frame rate restrictions were considered (TOF, PRF, beamforming time, DSP, etc.). Calculations were performed for the available hardware platform based on Xilinc Spartan 3 FPGAs.

Highlighted in green is a common configuration used in aerospace industry to ensure detection of 6x6 mm defects. In this case, Fast scanning method is 11 times faster than conventional phased-array linear scan, and a theoretical scanning speed of 5.5 m/s could be achieved.

Active elements (M)	**Image lines (L)**	**Inspection speed increase factor (K)**	**Maximum inspection speed (m/s)**
1	64	13	5.5
4	60	12	5.5
6	**56**	**11**	**5.5**
8	52	10	5.5
10	48	8	4.6
12	44	6	3.4
14	40	4	2.7
16	36	3	2.3

Table I – Maximum inspection speed for several active apertures with 2 mm resolution scan

3. Image quality

The proposed method can be valid for industrial applications only if image quality is comparable to that obtained with the conventional phased-array method. Emitting a plane wave with all array elements instead of a narrower beam will produce a broader main lobe and higher side-lobe levels, reducing resolution and contrast. In any case, because of the high directivity of array elements typically used in this kind of inspections (d > 3λ), image quality losses are not expected to be high.

Figure 4 shows a continuous-wave simulation of the two-way lateral beam pattern of an active aperture of 6 elements with *1 mm* pitch, at *30 mm* away from the probe surface, with phased-array (blue) and fast scanning (red) techniques. Main lobe at -6dB is 25% wider and side lobes about 5 times higher with fast scanning method than with phased-array. Because of the large refraction index of the water-CFRP interface, it is expected that side-lobes level increase have low impact in image quality.

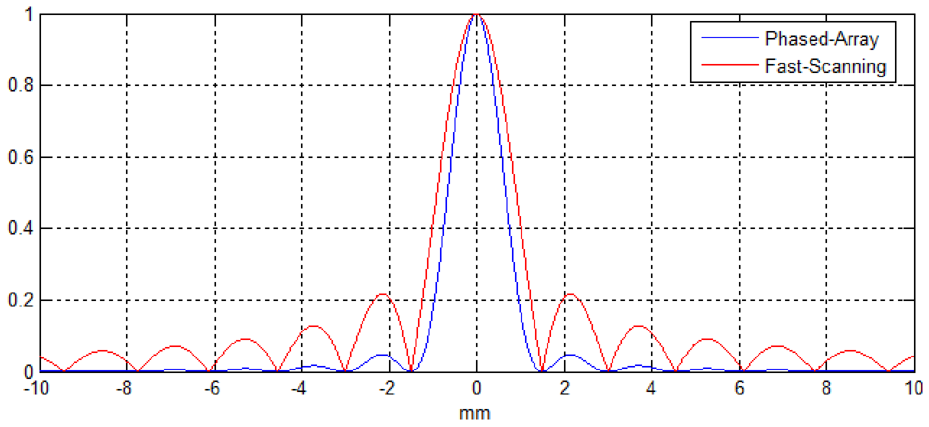

Figure 4 – Simulation of the continuous wave lateral wave pattern of a 6 elements 1 mm pitch aperture with conventional phased-array (blue) and fast scanning method (red).

Figure 5 shows experimental results with a 12 mm thick CFRP with artificial defects at different depths, inspected with a 5 MHz array of 1 mm pitch. On the left column are images obtained with conventional phased-array linear scan, and on the right column the corresponding Fast Scanning images. In all cases images are equivalent, with just a slight increase in lateral defect size for the Fast Scanning method. Side-lobe level increase of Figure 4 is not noticeable, mainly because continuous-wave simulation is a worst-case scenario when compared with pulse-echo broadband acquisitions.

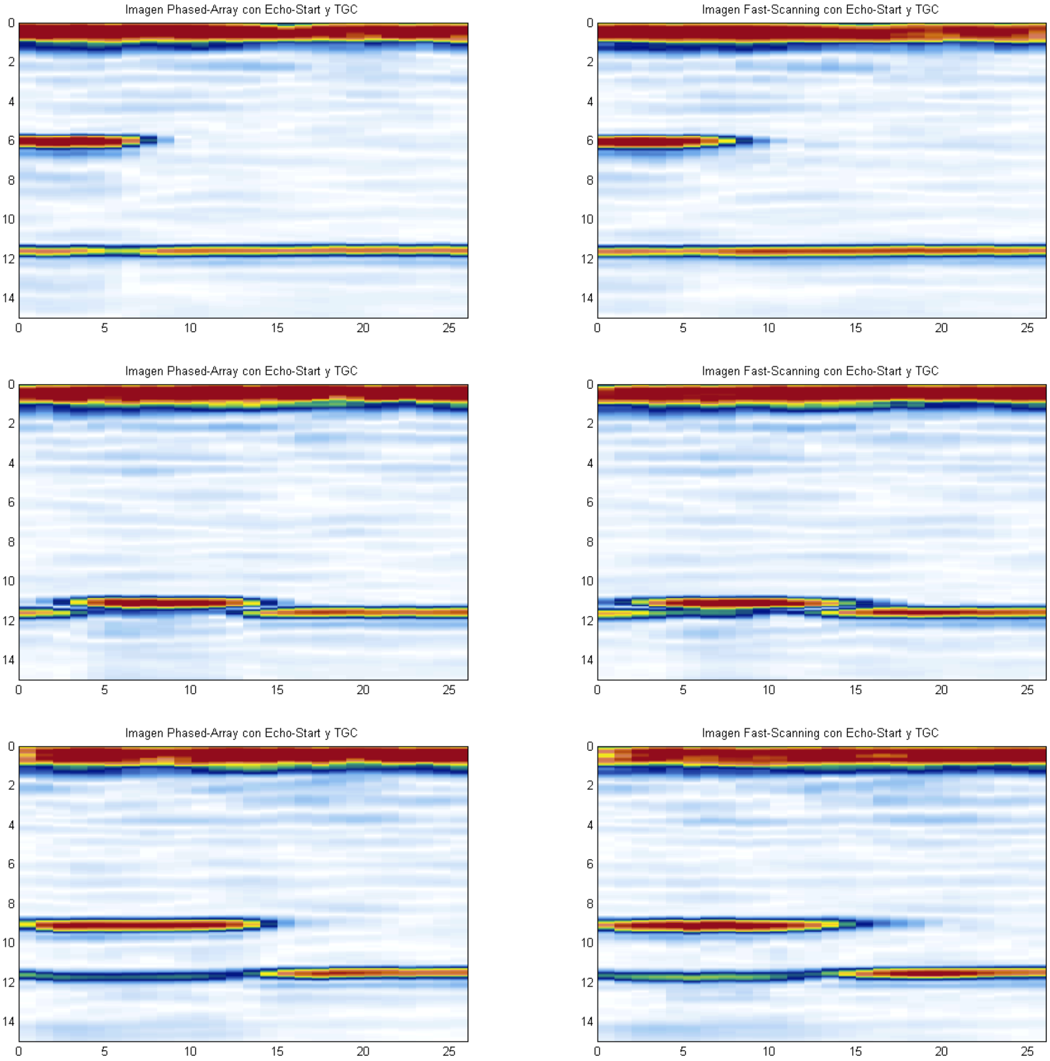

Figure 5 – Images of defects at different depths obtained with conventional phased-array (left) and with fast scanning method (right). Active aperture of 6 elements and 1 mm scan resolution.

Figure 6 shows the lateral profile at the depth of the shallowest defect (*z* = *6 mm*) for both methods. Fast Scanning (green) produces 13% more amplitude at the defect because of the emission with a larger number of elements, with the counterpart of increasing the defect size in 1 mm in the lateral direction when measured at -6 dB. This value is bellow the theoretically expected value of 1.5 mm predicted by continuous wave simulation.

Considering that the minimum defect size for aerospace industry is 6x6 mm and that typical inspection step is 2 mm, the increase of 1 mm in defect size will not be noticed in practice because it is below the measurement grid resolution. In any case, if focusing is used, active aperture size could be slightly increased to compensate this lateral resolution loss, ensuring the same detection capabilities than with the phased-array inspection.

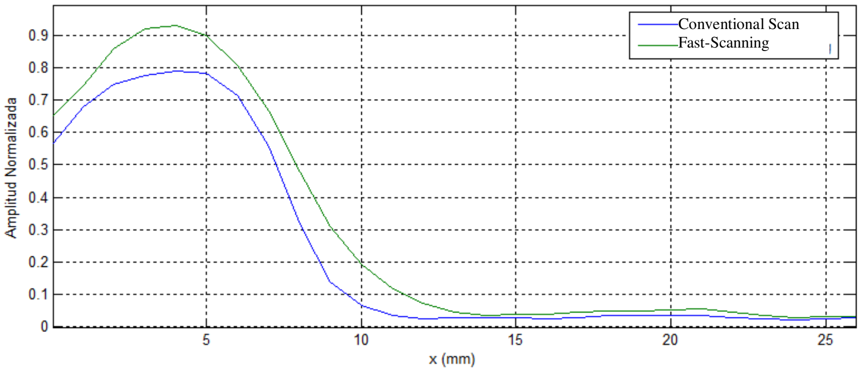

Figure 6 – Lateral profile of the flaw at 6 mm depth with Phased Array (blue) and Fast Scanning (green)

4. Experimental results

As a proof of concept, the whole algorithm was software implemented in Matlab, working in real-time with a full parallel 128 channel ultrasound system. A 5 MHz array with 128 elements and 1mm pitch was used to acquire images of a 12 mm thick CFRP with planar surface and several artificial defects. A mechanical device was added to change the angle between the part and the probe to emulate misalignment errors. Figure 7 shows the user interface that allows setting the acquisition and processing parameters.

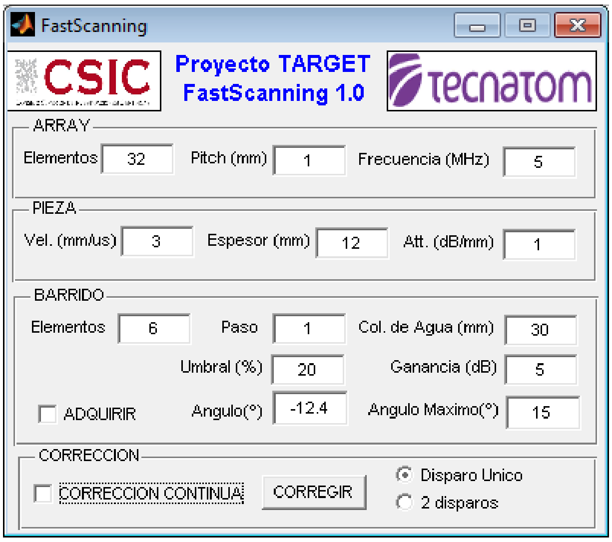

Elementos 32
Pitch (mm) 1
Frecuencia (MHz) 5

Vel. (mm/us) 3
Espesor (mm) 12
Att. (dB/mm) 1

Elementos 6
Paso 1
Col. de Agua (mm) 30
Umbral (%) 20
Ganancia (dB) 5
☐ ADQUIRIR
Angulo(°) -12.4
Angulo Maximo(°) 15

☐ CORRECCION CONTINUA
● Disparo Unico
○ 2 disparos

Figure 7 – User interface of the developed testing software.

Figure 8 shows the image obtained with conventional phased-array technique when the probe and part surface are tilted 0º (ideal case), 2º and 4º. As expected, amplitude of the surface echo is significantly reduced even for a low tilt angle, which could easily break in the inspection if the echo-start gate loses its reference. Furthermore, because of large refraction index between water and CFRP, normal incidence is lost into the material, which significantly reduces echo amplitude from delaminations and back-wall.

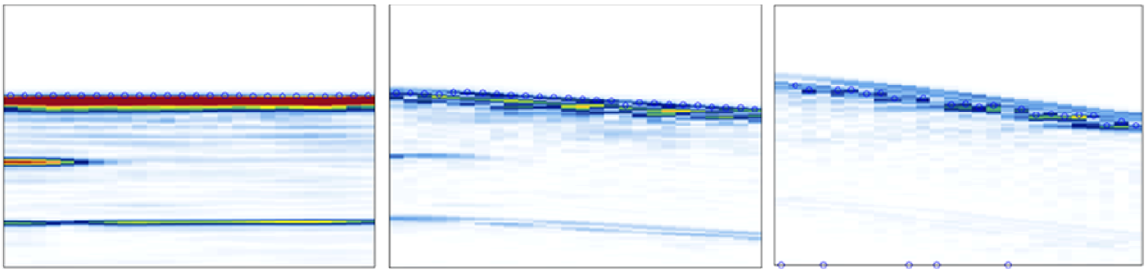

Figure 8 - Effects of slight probe-part misalignment on the image: 0º, 2º and 4º from left to right. Defect detection degradation is evident.

With Fast Scanning, each image is used to find the steering angle for the next trigger event to produce a plane wave with normal incidence on the component surface. Simultaneously, the corresponding receiving focal laws are computed for the tilted surface and loaded into the focusing circuits.

Figure 9 shows the effect of this steering and focal law correction algorithm. At the left, the ideal image acquired with 0º incidence and, at the right, the image obtained after automatic correction of a 4º misalignment (see Figure 8-right for the uncorrected image). Although there are small differences with the ideal image, the corrected one still allows detection and evaluation of the flaw and bottom echo.

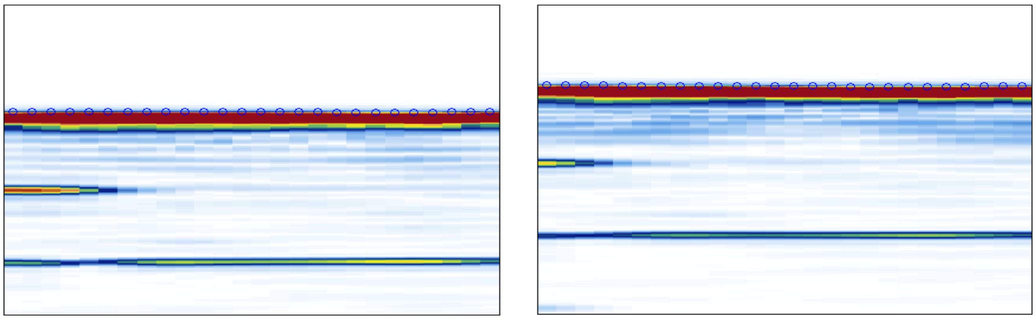

Figure 9 – Comparison between the original image at 0º (left) and that with the probe tilted 4º and automatic steering correction (right).

5. Conclusions

Main conclusion of this work is that it is possible to inspect planar CFRP components at speeds above 1 m/s without significant losses in resolution and contrast when compared with conventional phased-aray linear scan. Developed algorithm, named Fast Scanning, can be implemented in the current hardware platform to obtain more than 2500 images per second, achieving a scanning speed of 5 m/s in a typical configuration of 6 active elements with 2 mm resolution. Furthermore, a full automated tilt angle correction algorithm was developed to minimize the adverse effects of misalignment between the probe and the component surface. Because it can be implemented in the acquisition hardware, it does not degrade inspection speed and it is independent of the evaluation computer.

Algorithms were software implemented and validated by experimental trials with a CFRP planar component with artificial defects. Results were satisfactory and encourage continuing with the hardware implementation process of the technique.

6. Acknowledge

This project was partially founded by the project “CENIT TARGET: Intelligent and environmental sustainable technologies for composite materials generation” from the Spanish Ministry of Economy and Competitiveness.

References

1. N. Dominguez, G. Ithurralde, “Ultra-fast ultrasonic inspection for aeronautical composites using paintbrush acquisitions and data processing on GPU”, European Conf. on NDT, Moscow, 2010.
2. S. Robert, O. Casula, M. Njiki and O. Roy, “Assessment of real-time techniques for ultrasonic non- destructive testing”, Rev. Progress in Quantitative Nondestructive Evaluation, 31, pp. 1960-1967, 2012.
3. S. Robert, O. Casula, O. Roy and G. Neau, “Real-time Inspection of Complex Composite Structures with a Self-Adaptive Ultrasonic Technique”, 18th World Conf. on Non Destructive Testing, Durban (South Africa), 2012.
4. J. Camacho, C. Fritsch, J.F. Cruza, 'Documentación de Algoritmos de procesado de señal para la inspección de componentes con curvatura y requisitos HW para su aplicación en tiempo real', Target Project deliverable, June 2013.

10.1109/ULTSYM.2015.0544

Real time autofocusing hardware for ultrasonic imaging with interfaces

Jorge F. Cruza, Luis Medina-Valdes, Carlos Fritsch
Instituto de Tecnologías Físicas y de la Información (ITEFI) Torres Quevedo
Consejo Superior de Investigaciones Científicas (CSIC)
c/ Serrano 144, 28006 Madrid
jorge.f.cruza@csic.es

***Abstract*—A hardware architecture for fast imaging (multi-beamforming) with auto-focusing capabilities is presented. Auto-focusing is carried out without the knowledge of probe-part geometry, which is obtained by ultrasound measurements. The proposed technique and hardware achieves a high throughput that allows autofocus in real-time (for instance, in part scanning applications). The paper yields some figures of performance and other preliminary results.**

Keywords—autofocusing; DDF; NDT; scanning; focal laws

I. INTRODUCTION

Imaging of arbitrarily shaped components demands a new set of focal laws for every change in the array-part geometry. The process is currently carried out off-line and requires an accurate description of geometry. However, along a scan, geometry may change in an uncontrolled way and the nominal focal laws become not optimal. The main objective of this research is to find new techniques to obtain the set of focal laws adapted to unknown probe-part geometry in real-time at high frame rates.

Some interesting approaches have been addressed in the past to inspect irregular parts. Flexible array probes have been designed to adapt the part surface shape with some means to estimate the position of the elements to compute the adapted focal laws [1-2]. This contact technique is useful for low-speed scan of the tested part.

For faster scanning some coupling medium is required and inspections are frequently carried out by local immersion. In these cases a second problem arises: with two propagation media the focal law computing task becomes much more complicated. The problem can be addressed applying the Fermat principle [3] or using a Fast Focal Law Calculator [4] if the geometry is known and constant. However, these procedures are too slow to be carried out by software in real time under geometry changes along the scan, which requires a response in the millisecond range.

An adaptive technique to produce a wavefront parallel to the surface of the inspected part has been also proposed, which is more useful to inspect laminated structures [5]. This method does not require prior knowledge of the geometry and performs at moderate scanning rates, although no focusing is carried out and full-parallel equipment is required.

We have also developed several techniques that provide automatic Dynamic Depth Focusing (DDF) through interfaces of unknown geometry. In [6] we described a technique to convert a two-media propagation scenario into a single medium, thus avoiding the difficulties arising from refraction at the interface. It is achieved by computing a virtual array that operates in the second medium only that is approximately equivalent to the actual one with refraction at the interface.

Besides, we proposed a simple circuit that performs focusing at every acquired sample in reception (DDF) and requires only 3 initialization parameters for any array geometry and, in particular, for the virtual array [6].

Then, in [7], we described several methods to estimate the actual probe-part geometry by ultrasonic measurements: pulse-echo, pitch-catch and plane wave. These techniques provide the coordinates of a set of interface points, which are used to obtain an analytical representation of the interface by curve fitting procedures.

Auto-focusing for a single image is achieved in 3 steps:

1. Estimation of actual probe-part geometry by ultrasonic measurements.

2. Compute a virtual array operating in the second medium and adapted to the geometry.

3. Compute the initialization parameters of DDF hardware for all scan lines and array elements.

These procedures were software implemented, requiring about 2 seconds to get an auto-focused phased array image of L=100 lines of any depth with an N=128-element array. Although this time is acceptable for laboratory or manual inspections, it is not fast enough to adapt to unexpected geometric changes in real-time while scanning the part at high speed (above 100-200 mm/s).

This work presents the underlying architecture to achieve such high frame rate, while automatically adapting the focal laws for the current probe-part geometry to perform the autofocus function.

Work supported by project DPI2013-42236-R of the Spanish MINECO.

978-1-4799-8182-3/15/$31.00 ©2015 IEEE

II. ARCHITECTURE LAYOUT

Our approach is a distributed architecture with modules built around XC7K160T, XC7K325T or XC7K410T Kintex FPGAs, all of them pin-compatible (Fig. 1). Each module handles 32 ultrasound channels in emission and reception with pulsers (± 90V) and analog front-ends (variable gain, 60-dB ultralow noise amplifiers, 50 MHz, 14-bit ADCs). Any number of modules can be configured in a system.

Every module has DDR3 chips for 1 GB local storage at 6.4 GB/s. Eight full-duplex 10 Gb/s transceivers provide high-speed links with adjacent modules, which configure a two-way ring-shaped architecture (Fig.2). They allow to transmit and share partially beamformed A-scans with adjacent modules at 40 Gb/s. Due to the high communications throughput, in most cases, the overall system behaves as a single device beamformer, while performance remains independent of the number of modules configured in the system.

Fig. 1. The 32 ultrasound channel module in 150 x 60 mm.

On the other hand, a single SoC module (AVNET's Zynq AP SoC Mini-Module Plus) acts as the Interface and Control Unit (ICU). The ICU performs system control through separate LVDS links running at 800 Mb/s and external communications through 1 Gbps Ethernet. The Ethernet is used to receive general configuration parameters and send processed data from and to an external computer, which is not involved in real-time control operations. For real-time software processing, the ICU includes a two core 800 MHz ARM processor.

Processing required to obtain auto-focused images is performed in a distributed way between the ARM processor in the ICU, FPGA hardware in the ICU and module FPGAs. Some of these functions are executed by software, while the most critical ones have been hardware implemented. This achieves a trade-off among circuit complexity, resource usage and response time, as it is presented in the next Sections.

III. BEAMFORMER DESIGN

Our beamformer architecture takes advantage of the available resources in state-of-the-art FPGAs, mainly the so-called DSP-cells. They have a multiplier with dynamically changing coefficients connected to one of the two inputs of an adder; the other receives the result of the previous DSP cell, so they are chained in large rows. Specific logic and connections are hard wired, which are much faster and less power consuming than regular FPGA logic.

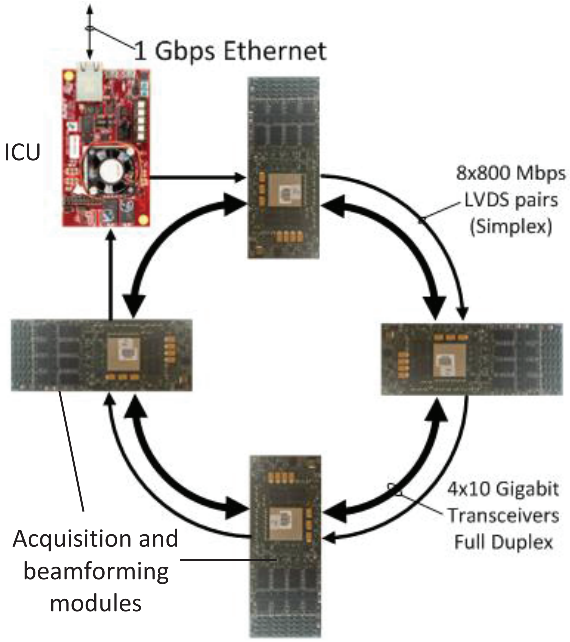

Fig. 2. Architecture layout.

Beamforming is a delay-and-sum operation. The integer part of the delay in sampling clock period is achieved by selection of the corresponding sample from a RING BUFFER. A sub-sampling period resolution is obtained by fractional delay filters [9]. The DSP-cell structure is well adapted to perform the fractional delay and the beamforming sum.

Fig. 3 shows the cell arrangement as a cascade of systolic filters. Filtering (fractional delay) and coherent sum of the delayed samples are carried out simultaneously (in pipeline). A time-resolution of ¼ the sampling period is achieved with a set of 4 coefficients, chosen from a LUT in the block DELAY CALC, which also extracts samples from the RING BUFFER to perform the coarse delay. The DELAY CALC block is highly pipelined and use 4 adders based on the circuit presented in [6], which require 3 parameters per scan line to initialize. These parameters are provided by the autofocusing hardware presented afterwards.

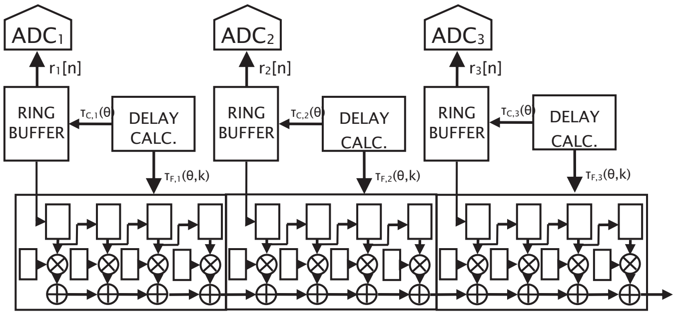

Fig. 3. Beamformer simplified architecture.

The beamformer performs at the sampling rate. Memory buffers have storage just to accommodate time of flight differences between different channels to the same image focus. Moreover, since high performance components are used

(Block RAMs and DSP cells), and the delay calculators are carefully designed, the beamformer working frequency is above 200MHz. This allows sharing the same hardware among 4 scan lines for a 50 MHz sampling frequency by time multiplexing, thus saving valuable resources.

The design allows time multiplexing for up to 32 scan lines with the output stream of beamformed samples at the working frequency (200 MHz) with interleaved scan lines. Requirements shown in TABLE I. show that 8 beamformers fit well in a single, moderately sized FPGA, leaving many resources for other subsystems and functions. Thus, up to 256 scan lines can be simultaneously beamformed, two orders of magnitude higher performance than other approaches.

TABLE I. RESOURCE REQUIREMENTS FOR A 32-CHANNEL BEAMFORMER IN A XC7K325T-2 FPGA

	Slices	*Flip-Flop*	*LUT*	*DSP48*	*BRAM*
Used	4629	11632	11554	64	32
Available[a]	50950	407600	203200	840	890
	9.09%	2.85%	5.67%	7.62%	3.60%

a. Available resources depend on target FPGA.

Fig. 4 shows the internal structure of the module. Raw data from the 32 ADCs goes to 4 beamformers or to dynamic RAM for off-line beamforming or other purposes (i.e. ultra fast imaging). An arbiter takes care of data traffic among these resources.

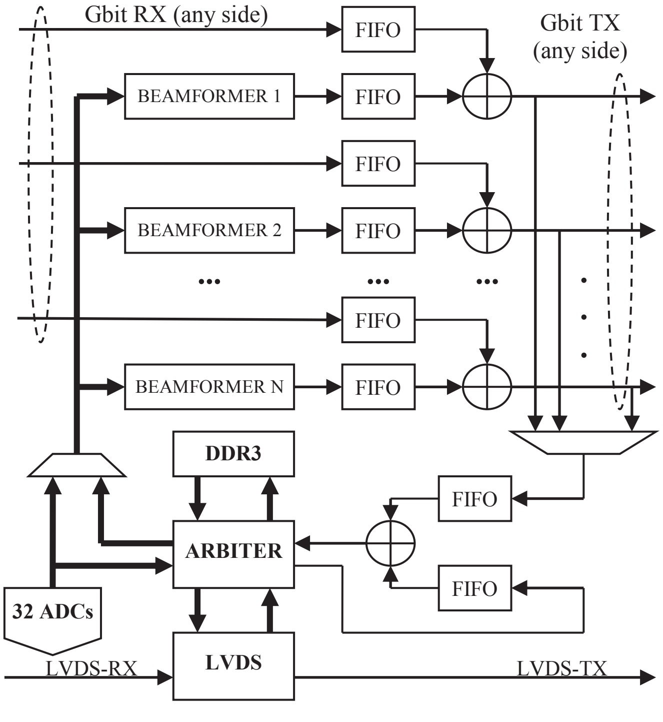

Fig. 4. Architecture of the multi-beamformer module

The LVDS block decodes commands issued by the ICU to LVDS-RX and forwards them through TX to the next module. Beamformer outputs are added to results of the precedent module received by the Gbit RX ports. Final results are then forwarded through Gbit TX ports to the next module. FIFOs compensate time differences between incoming and generated data. Both side links are available for sending and receiving scan lines so the ring architecture can support the traffic of 12 beamformers per FPGA (32-bits word width). Final result is sent to the ICU through the lower speed LVDS links.

IV. AUTOFOCUSING HARDWARE AND SOFTWARE

The most critical task is obtaining the time-of-flight (TOF) from every array element and scan line to two foci, taking into account refraction [6]. This is required to compute the virtual array in a single medium. Since there are not closed formulae to compute TOFs through an arbitrarily shaped interface, quite time-consuming iterative procedures must be used. In general, the problem is addressed by application of the Fermat's principle, searching the ray path for the minimum TOF.

To reduce the computing burden, we developed hardware in the ICU that performs this task at high speed. However, instead of applying the Fermat's principle, we implemented a combination of Newton-Raphson with Illinois algorithms search for the minimum TOF. The search engine is hardware implemented using High Level Synthesis (HLS) tools [8].

In all cases the minimum TOF is found when the derivative of the TOF from a given array element to interface points and to the focus taking into account the respective propagation velocities, equals zero.

The Newton-Raphson technique finds the root of an equation of the form $f(x)=0$, starting with a x_0 guess by iteratively computing:

$$x_{k+1} = x_k - \frac{f(x_k)}{f'(x_k)}, \quad k = 0, 1, ... \tag{1}$$

On the other hand, the Illinois algorithm is a modification of the *regula falsi* method: the root lies within an interval $U_k=[a_k , b_k]$ for which $f(a_k)\cdot f(b_k) <0$, that is, $f(a_k)$ and $f(b_k)$ are of opposite sign.

Starting with a given interval U_0 a new approximation to the root is found by linear interpolation in the segment between points $[a_k , f(a_k)]$ and $[b_k , f(b_k)]$, being w_k a weighting coefficient to accelerate convergence (typically $w_k = 0.5$):

$$x_{k+1} = \frac{w_k b_k f(a_k) - a_k f(b_k)}{w_k f(a_k) - f(b_k)} \tag{2}$$

The next interval is chosen with x_{k+1} and whichever of a_k or b_k has a function value $f(a_k)$ or $f(b_k)$ of opposite sign to $f(x_{k+1})$.

The advantage of using both algorithms is that Illinois convergence is guaranteed, while the Newton-Raphson is faster. The implemented hardware switches to the Illinois technique when the Newton-Raphson fails to converge.

The implementation of these algorithms was highly parallelized, computing simultaneously TOFs for 32 array elements. This yields a very high throughput, of about 100 ns/focus/element in current implementation. However, in spite of this and the use of floating point arithmetic, resource consumption is moderate, using about 20% of the available resources in the FPGA that implements the ICU.

V. OVERALL PROCESS

The overall process is schematically shown in Fig. 5. The ARM processor in the ICU receives TOF measurements from the data acquisition and beamforming modules. It uses such data to estimate a function $z=p(x)$ for the interface by curve fitting, where (x,z) represent Cartesian coordinates. Currently $p(x)$ is a polynomial of programmable degree between 1 and 8.

The ARM feeds this function to the minimum TOF search engine. This unit performs iteratively up to differences in TOF are smaller than $\varepsilon=1$ ns, which is the finishing condition. Simultaneously, in a pipelined process, another HW module uses the minimums TOFs found to compute the virtual array and the DDF focusing parameters. This process loops once per image to keep it focused in spite of geometric changes.

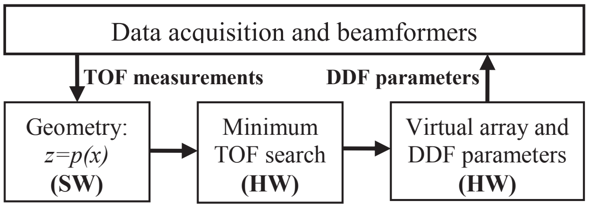

Fig. 5. Autofocusing hardware (HW) and software (SW) operation.

VI. EXPERIMENTAL RESULTS

TABLE II shows the estimated performance for a case example with N=128-element array, L=96 scan lines, water column = 15 mm, steel part depth = 50 mm.

TABLE II. PERFORMANCE OF THE AUTOFOCUSING HARDWARE

Function	Time (ms)
Interface geometry estimation	5.2
Virtual array + focusing parameters	1.1
All imaging parameters set-up	0.3
TOTAL	6.6

A frame rate above 150 images/s can be achieved with auto-focusing. If spatial resolution is one image every 2 mm, scanning speed can reach 300 mm/s. Furthermore, the computed focal laws can be reused for some images if abrupt changes in geometry are not expected.

To show the operation of auto-focusing, a 50 mm diameter aluminum part with several side drilled holes was inspected in water immersion with a 5 MHz, 128-element array, 0.6 mm pitch (Imasonic, Besançon, France). Measurements were made with a Sitau-112 equipment (Dasel, Madrid, Spain), since at the time of this writing the autofocus system was not yet fully operative. Processing was carried out by software.

Fig. 6 (left) shows the arrangement and the image obtained after auto-focusing, where all the indications are clearly seen. At the right, upper panel, the part has been slightly moved generating a meaningless image. Running the autofocusing process produces again a sharp image.

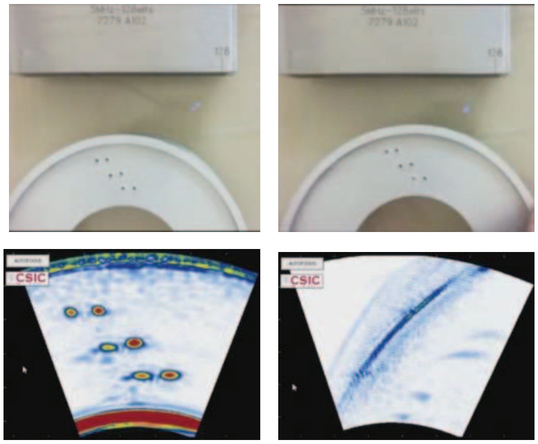

Fig. 6. Left: Autofocused image; Right: if part is slightly deviated and focal laws are kept, the resulting image is meaningless.

VII. CONCLUSIONS

Autofocusing is a very useful function that adapts the focal laws to current probe-part geometry. We have presented a hardware architecture that provides fast response to perform auto-focusing in real-time. Besides, the devised architecture allows beamforming multiple scan lines in parallel.

ACKNOWLEDGMENT

This work was supported by project DPI2013-42236-R of the Spanish Ministry of Economy and Competitiveness.

REFERENCES

[1] O. Casula, C. Poidevin, G. Cattiaux and G. Fleury, "A flexible phased array transducer for contact examination of components with complex geometry", *16th Conf. on Nondestructive Testing*, Montreal, Canada, 2004.

[2] A. Hunter, B. Drinkwater and P. Wilcox, "Autofocusing ultrasonic imagery for non-destructive testing and evaluation of specimens with complicated geometries", *NDT&E International*, 43, pp. 78-85, 2010.

[3] M. Suttcliffe, M. Weston, B. Dutton and I. Cooper, "Real-time full matrix capture with auto-focusing of known geometry through dual layered media", NDT Conf. of BINDT, Daventry, UK, 11-13 Sept. 2012.

[4] M. Parrilla et al., "Dynamic focusing through arbitrary geometry interfaces", *Proc. IEEE Ultrason. Symp.,* pp. 1195-1198, 2008.

[5] S. Robert, O. Casula, M. Njiki and O. Roy, "Assessment of real-time techniques for ultrasonic non- destructive testing", *Rev. Progress in Quantitative Nondestructive Evaluation*, 31, pp. 1960-1967, 2012.

[6] J. F. Cruza, J. Camacho, L. Serrano and C. Fritsch, "New Method for Real-Time Dynamic Focusing Through Interfaces, *IEEE Trans. UFFC*, 60, 4, pp. 739-751, 2013.

[7] J. Camacho, J. F. Cruza, J. Brizuela and C. Fritsch, "Automatic Dynamic Depth Focusing for NDT", *IEEE Trans. UFFC*, 61, 4, pp. 673-684, 2014.

[8] J. F. Cruza, J. Camacho, J.M. Moreno and C. Fritsch, "Ultrafast hardware-based focal law calculator for automatic focusing", NDT&E International, 74, pp. 1-7, 2015.

[9] T. I. Laakso, V. Valimaki, M. Karjalainen, U.K.Laine, "Splitting the Unit Delay", IEEE Sig. Proc. Magazine, pp. 30-58, Jan. 1996.

AIP Conference Proceedings, Volume 1581, Issue 1, pp.1975-1982, 2014
doi: http://dx.doi.org/10.1063/1.4865066

A New Architecture for Fast Ultrasound Imaging

J. F. Cruza, J. Camacho, J. M. Moreno, L. Medina

Instituto de Tecnologías Físicas y de la Información "Torres Quevedo"
Consejo Superior de Investigaciones Científicas (CSIC), Serrano 144, 28006 Madrid, Spain
e-mail: jorge.f.cruza@csic.es

Abstract. Some ultrasound imaging applications require high frame rate, for example 3D imaging and automated inspections of large components. Being the signal-processing throughput of the system the main bottleneck, parallel beamforming is required to achieve hundreds to thousands of images per second.

Simultaneous A-scan line beamforming in all active channels is required to reach the intended high frame rate. To this purpose, a new parallel beamforming architecture that exploits the currently available processing resources available in state-of-the-art FPGAs is proposed. The work aims to get the optimal resource usage, high scalability and flexibility for different applications.

To achieve these goals, the basic beamforming function is reformulated to be adapted to the DSP-cell architecture of state-of-the-art FPGAs. This allows performing simultaneous dynamic focusing on multiple A-scan lines.

Some realistic examples are analyzed, evaluating resource requirements and maximum operating frequency. For example, a 128-channel system, with 128 scan lines and acquiring at 20 MSPS, can be built with 4 mid-range FPGAs, achieving up to 18000 frames per second, just limited by the maximum PRF. The gold standard Synthetic Transmit Aperture method (also called Total Focusing Method) can be carried out in real time at a processing rate of 140 high-resolution images per second (16 cm depth on steel).

Keywords: fast ultrasound imaging, FPGA, plane wave imaging.
PACS: ultrasonographic imaging, 87.63.dh

INTRODUCTION

Phased Array (PA) imaging technique has been widely used in NDT. This technique uses individual delays in emission to get a focus at a given steering angle (scan line). The echoes produced in the insonified material are registered by all the array elements. These signals are delayed to compensate the differences in the time-of-arrival to each element (focusing in reception). By using different delays for every point of the scan line Dynamic Depth Focusing (DDF) is performed, which achieves a focused image in reception at all ranges and in real-time. Currently, only some ultrasound Phased Array NDT equipment implements DDF. For PA, the maximum image rate that can be achieved with S scan lines per image is:

$$FPS_{PA} = \frac{PRF_{\max}}{S} \tag{1}$$

Where $PRF_{\max}$ is the pulse repetition frequency and depends on acquisition length (depth of the image). So that, for an image of 200 mm on steel (propagation velocity c≈6 mm/μs) and S=150:

$$FPS_{PA} = \frac{PRF_{\max}}{S} = \frac{\left(2\cdot 200mm \big/ 6\,mm/\mu s\right)^{-1}}{150} = \frac{15000}{150} = 100FPS \tag{2}$$

Since just one line is beamformed, the required hardware is affordable and provides a frame rate sufficient for most applications.

Total Focusing Method (TFM) proceeds in a different way. In this case, each element of the array is triggered separately, and a complete sub-image is composed using all the array elements. Since the emission is unfocused (ideally omnidirectional), the sub-image quality is poor. But by repeating this process for all the array elements as emitters and averaging the sub-images, a highest resolution is achieved. The advantage of this technique is that it considers the focusing delays from the emitter to every focus and back to the receiving elements, thus achieving dynamic depth focusing in emission and in reception. By contrast, PA produces emission focusing at a single depth only.

With the TFM mode for the above example and non-parallel PA hardware, the maximum image rate for a N=128 channel system, is:

$$FPS_{TFM} = \frac{PRF_{\max}}{S \cdot N} = \frac{15000}{150 \cdot 128} = 0.78125 FPS \tag{3}$$

However, since a single element is used for emission, all the region of interest is insonified and more than a single scan line can be simultaneously beamformed in reception. If P=50 lines are simultaneously beamfomed the image rate can be improved by such factor:

$$FPS_{TFM} = \frac{PRF_{\max}}{\frac{S}{P} \cdot N} = \frac{15000}{150/_{50} \cdot 128} = 39.0625 FPS \tag{4}$$

In an optimal case where S=P, a sub-image can be obtained with a single trigger event. In that case:

$$FPS_{TFM} = \frac{PRF_{\max}}{N} = 117.1875\,\mathrm{FPS} \tag{5}$$

Another kind of ultrasonic image technique that can take advantage of parallel beamforming is Plane Wave Image Compounding, where a plane wave is emitted using all the elements of the array. Also, several lines can be simultaneously beamformed to get, in the upper limit, one image per trigger event. As in the above case, since there is no focusing in emission, low quality images are obtained at rates of:

$$FPS_{PWIC} = PRF_{\max} = 15000 FPS \tag{6}$$

To improve the image quality certain number C of images with different plane wave angles can be compounded [1]. For C=60,

$$FPS_{PWIC} = \frac{PRF_{\max}}{C} = 250 FPS \tag{7}$$

Also, 3D UT imaging with 2D matrix arrays requires a large number of scan lines. For example, for an image with S by S scan lines (S=150), the maximum frame rate is:

$$FPS_{PWIC} = \frac{PRF_{\max}}{S \cdot S} = \frac{15000}{150 * 150} = 0.666 FPS \tag{8}$$

However, if the emitting beam is broad enough [2], a number of P lines can be simultaneously beamformed, increasing the frame rate by this factor. If P=50:

$$FPS_{PWIC} = \frac{PRF_{\max}}{\frac{S \cdot S}{P}} = 33.333 FPS \tag{9}$$

However, since 2D matrix arrays have a large number of channels and beamformer complexity increases linearly with the number of channels, the problem of parallel beamforming is even more challenging.

Summarizing, several imaging modes can take advantage of parallel beamforming to improve the image rate and/or quality. In this work we present a FPGA-based architecture aimed to achieve high performance parallel beamforming. The architecture is highly scalable to fit different applications of advanced imaging techniques in real time.

PARALLEL BEAMFORMING HARDWARE

Classic Fractional Delay Filter Based Beamformer

The conventional delay-and-sum beamformer with dynamic focus introduces time-varying delays to the signals received by every array element to compensate the time-of-flight differences from every focus, usually located along a steering direction or scan line, to every array element. This operation produces the aperture data, which are added together (coherent sum) to provide an output sample of the focused A-scan along the steering direction. Focusing delays must be changed for every output sample to get strict DDF.

High timing resolution is required to reduce the level of the delay quantization lobes [3]. However, the high channel count of the system makes it very expensive in terms of power, space and required bandwidth sampling at very high rates. Instead, it is preferred sampling at the Nyquist's frequency and then perform interpolation to achieve the required timing resolution [4].

One way to get high time resolution is using fractional delay filters, which allow splitting the sampling period in an integer number of sub-sampling intervals [5]. Here, a bank of L fractional delay filters allow to chose the equivalent sampling instant at $1/L$, $2/L$, ..., 1 the sampling period. L is closely related to the delay resolution and usually ranges from 4 to 16. On the other hand, every filter in the bank requires a number F of coefficients large enough to achieve the required accuracy ($F \sim L$).

Every filter in the bank provides a sample delayed an amount τ_{Fn} (k, θ) that compensates the differences in the two-way time-of-flight to focus F located at sample k of steering angle θ.

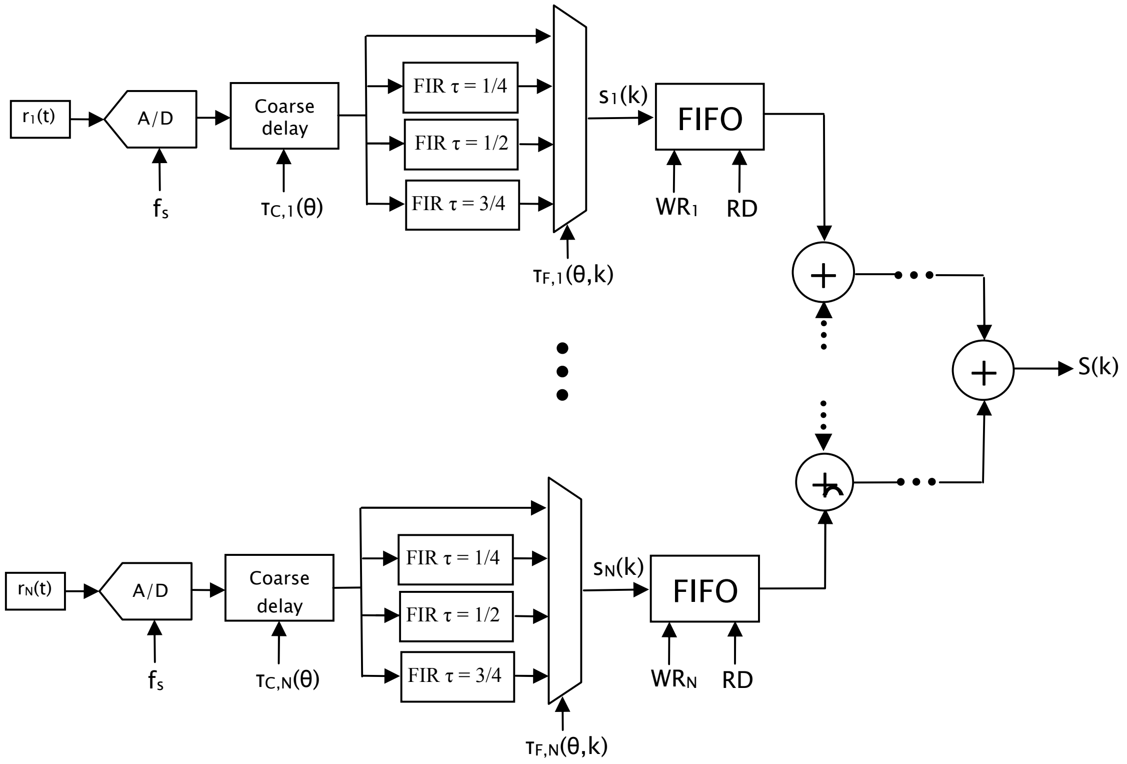

FIGURE 1. Classic architecture of FIR fractional delay filters beamformer.

If $\tau_{F,n}(\theta,k)$ is calculated for increasing values of k (sample index), it performs dynamic depth focusing along a single scan line. The first approach to perform parallel beamforming would be to replicate this structure to beamform many scan lines simultaneously. However, such approach has some important drawbacks:

- First, it uses many *arithmetic resources* to implement fractional delay filters and adder trees. It needs L-1 FIR filters with F coefficients each (at least, F=L=4) for every channel and every parallel beamformed scan line. The adder tree requires N-1 adders, being N the number of active channels in reception. For S=30 simultaneous scan lines and N=128 channels, the number of necessary adders and multipliers are:

$$\begin{aligned} &S\cdot N\cdot(L-1)\cdot F = 46080 \text{ multipliers} \\ &S\cdot[N\cdot(L-1)\cdot(F-1)+N-1] = 38370 \text{ adders} \end{aligned} \tag{10}$$

- The second drawback is the *memory resources* consumption. The depth of the FIFOs has to be large enough to compensate the differences in the time-of-arrival of echoes to different channels. An upper limit can be calculated considering that the maximum distance between elements is the aperture size D=N·d, where d is the array pitch (typically $\lambda/2 \le d \le 2\lambda$).. For example, an array with N=128 elements, with a pitch of two wavelengths (D=N·d=256λ) and a sampling frequency four times the center frequency of the array (f_S=4f_C), the depth of the FIFOs that guarantee that no samples are lost is:

$$D_{MEM} = \frac{D}{c} f_S = \frac{256\lambda}{c} 4 f_C = 1024 \text{ samples} \tag{11}$$

Therefore, this architecture would need one 1024-sample FIFO for every channel (N=128) and every scan line (S=30). In terms of FPGA resource consumption, a 16 bit width, 1024 depth FIFO can be implemented with a single Block RAM. Then, the number of Block RAMs required is:

$$S\cdot N = 3840 \text{ Block RAMs} \tag{12}$$

Additionally, fine delays $\tau_{F,n}(\theta,k)$ must be obtained for every sample, channel and scan line This can be carried out from values stored on memories or circuits that perform the *delay calculation* dynamically. Our group developed an optimized method that achieves dynamic focusing with just 1 memory bit per focus and channel [6]. However, even with this optimized technique the number of necessary Block RAMs (18Kbit each) for a N=128 channels system, a scan length of 4096 samples and S=30 scan lines is given by (13):

$$\frac{S\cdot N\cdot 4096}{18Kbit} \approx 853 \text{ Block RAMs} \tag{13}$$

On the other hand, dynamic delay calculators do not consume memory resources but use regular FPGA logic resources that are difficult to quantify. Anyway, the problem of obtaining $S\cdot N$ delays still remains.

Our Parallel Beamforming Architecture

DSP Processing Optimization

Equation (10) revealed that parallel beamforming demands a large amount of DSP resources (adders and multipliers). Current FPGAs have dedicated hardware elements for DSP processing, called *DSP cells*. These cells have a multiplier with dynamically changing coefficients connected to one of the inputs of an adder. The other adder input is connected to the result of the previous DSP cell, so they are arranged in large rows. Specific logic and connections are hard wired, which are much faster and less power consuming than regular FPGA logic. Three key optimizations can be performed using these elements:

1. Since coefficients can be dynamically changed and just one fractional delay is applied every sampling period, the same hardware can be used for every L fractional delay filters by time-multiplexing. Instead of selecting which output sample of the L filters goes into the output FIFO, $\tau_{F,n}(\theta,k)$ will select which set of coefficients are used by the multipliers.
2. As shown in **FIGURE 2**, fractional delay filters from different channels can be chained. In this situation, the result of the filtering of channel n is passed to the filter of channel n+1 and added to the result of the first multiplication of the filter. This way, filtering and coherent sum are carried out simultaneously with the same set of resources.
3. The high DSP cell commutation frequency range can be exploited by doing several operations per sampling period. So, if R is the relation between FIR filter maximum commutation frequency (f_{FIR}) and sampling frequency (f_S), R scan lines can be beamformed simultaneously sharing the same hardware:

$$R_{FIR} = \left\lfloor \frac{f_{FIR}}{f_S} \right\rfloor \tag{14}$$

The switching frequency for Xilinx mid-range and high-range FPGAs is, at least, 400MHz. Then, in case of arrays of up to 10MHz and a sampling frequency of 40MHz, R_{FIR} is 10, so that, ten scan lines can be simultaneously beamformed. For an array of 2.5 MHz with signals sampled at 10MHz, up to R_{FIR}=40 scan lines can be simultaneously beamformed.

With these 3 optimizations, the number of FPGA DSP cells needed for a system of N=128 active channels, sampling at f_S=40MHz, FIR filters working at f_{FIR}=400MHz and F=4 coefficients per fractional delay filters, is affordable for currently available commercial FPGAs:

$$\left\lceil \frac{S}{R_{FIR}} \right\rceil \cdot N \cdot F = 1536 \text{ DSP blocks} \tag{15}$$

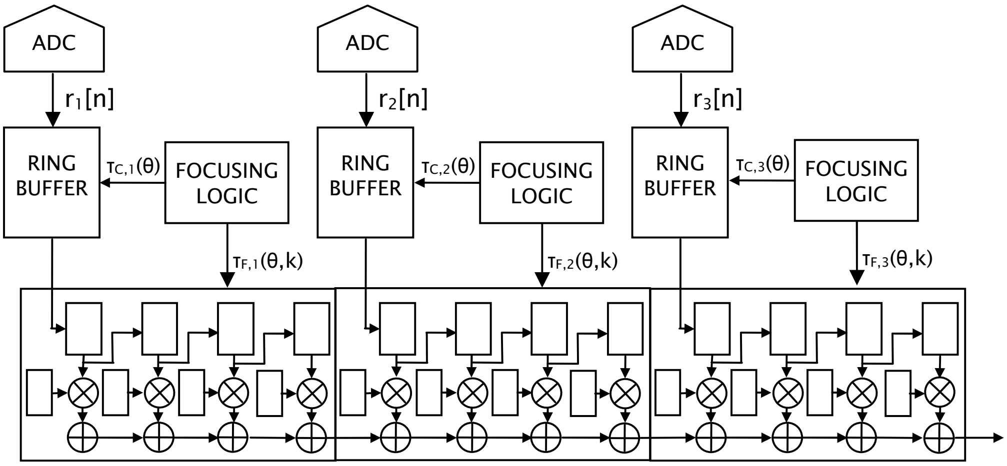

FIGURE 2. Proposed beamformer architecture.

Memory Optimization

Equations (11) and (12) show the large memory requirements for parallel beamforming. The problem is that different samples are needed for each scan line at each time. However, with a ring buffer instead of a FIFO, it is possible to access any sample taken D_{MEM} sample periods before the last acquired sample. Since memory size is a fixed design parameter and have to be sized for the worst case, the ring buffer will always hold the required sample for every scan line.

Accordingly, just one memory per channel would be necessary no matter how many scan lines the image has. However, the block RAM bandwidth (f_{RAM}) allows producing a limited number of samples R_{RAM} related with the sampling frequency (f_S) by:

$$R_{RAM} = \left\lfloor \frac{f_{RAM}}{f_S} \right\rfloor \tag{16}$$

From (11), (12) and (15) , with f_{RAM}=200MHz, f_S=40MHz, 1024 samples per ring buffer and N=128 channels, the total number of required block-RAMs is:

$$\left\lceil \frac{S}{R_{RAM}} \right\rceil \cdot N = 768 \text{ Block RAMs} \tag{17}$$

Focusing Delay Calculation Optimizations

For delay calculation, our approach is based on a circuit that performs dynamic focusing in real time as presented in [7]. The circuit just needs setting up 2 parameters per line and the focusing range is just limited by the width of some registers. A new highly pipelined version of this circuit that allows time multiplexing has been developed. This circuit uses regular FPGA logic that is slower than DSP cells and block RAMs. However it has been carefully designed to have just one logic level between registers, getting a maximum switching frequency of 250 MHz. For every channel and scan line its necessary to get a delay value at every sample period, so, each circuit can be multiplexed R_{FOC} times:

$$R_{FOC} = \left\lfloor \frac{f_{foc}}{f_S} \right\rfloor \tag{18}$$

The number of focusing circuits needed for a N=128 channels system and S=30 simultaneous scan lines is:

$$\left\lceil \frac{S}{R_{FOC}} \right\rceil \cdot N = 768 \text{ focusing circuits} \tag{19}$$

This focusing circuit allows dynamic focusing up to 32768 samples (5 meters on steel at 40 MSPS) and consumes 215 flip-flops and 193 Look-Up Tables, occupying 100 slices in a XC7K325T-2 FPGA.

Implementation and Validation

The architecture of **FIGURE 2** has been coded on VHDL. In order to get maximum performance for different applications and on different devices, some parameters of the architecture are user defined: Number of channels, number of filter coefficients, ring buffer depth and circuit working frequency. Furthermore, there are other parameters that can be dynamically changed like the sampling frequency (it will define multiplexing ratios R_{DSP}, R_{RAM}, R_{FOC}).

A 32 channel beamformer has been validated with synthetic signals. Results from Matlab® simulation, hardware simulation (Modelsim®) and experimental tests on a Xilinx KC705 (XC7K325T-2 FPGA) evaluation board via JTAG probe, have been compared obtaining exactly the same image, thus validating the design.

The architecture of **FIGURE 2** has been adapted to XC7K325T-2. To take advantage of DSP cell switching frequency, two ring buffers and two focusing circuits have been attached to each filter. With this configuration, filters can work at 480MHz and buffers and focusing circuits at 240MHz. Thus, a single beamformer can simultaneously beamform 5 scan lines for a 10MHz array or 20 scan lines for a 2.5MHz array.

TABLE 1). Resource usage for a 32-channel beamformer in a XC7K325T-2.

	Slices	**Flip-Flop**	**LUT**	**DSP48**	**BRAM**
Used	4629	11632	11554	64	32
Available	50950	407600	203200	840	890
	9.09%	2.85%	5.67%	7.62%	3.60%

Depending on the specific FPGA available resources, different number of beamformers can be configured into a single FPGA. As shown in **TABLE 1**, at least 10 beamformers of 32 channels can be fitted on a single XC7K325T, allowing to simultaneously beamform 50 scan lines for a 10MHz array or 200 scan lines for a 2.5MHz array.

THE SYSTEM ARCHITECTURE

Once we have a good estimation of the necessary hardware for a given performance, it is possible to select which FPGA is more suitable in terms of processing resources. However, there are many other factors that affect system architecture. Number of user configurable Input/Output pins limits the number of channels and of DDR3 memory chips that can be handled by a single FPGA. Also, if more than one FPGA is used, it is important to consider the chip to chip communication bandwidth.

The first approach can be to integrate 128 channels into a single FPGA to beamform all channels avoiding chip to chip communications. **TABLE 2** shows that a system with 4 mid range XC7K160T676-2C FPGAs can simultaneously beamform the same number of scan lines than a single XC7VX690T1936-2C, but the system cost is significantly higher in the second case. Also, if no high bandwidth communication is provided, the system would not be scalable; it could not handle more than 128 channels.

TABLE 2). Performance of systems based on different FPGAs.

Device	**Package**	**Channels per FPGA**	**Price each**	**Price 128 CH system**	**Beamformers**	**Scan Lines (2 MHz Array)**	**Scan Lines (10MHz Array)**
XC7K160T676-2C	676	32	$358	$1435	5	120	30
XC7K325T676-2C	676	32	$1347	$5388	10	240	40
XC7K410T676-2C	676	32	$2362	$9450	12	288	72
XC7VX690T1152-2C	1152	64	$6814	$13629	10	240	40
XC7VX690T1936-2C	1936	128	$7836	$7836	5	120	30

Our approach is a distributed architecture where each node can be any FPGA of the first 3 rows on **TABLE 2,** that are full pin-compatible (676 terminals). Each FPGA controls 32 channels and have two DDR chips attached. These FPGAs have 8x10Gbit full-duplex integrated transceivers that are used to configure two links. Each link communicates with another node, forming a ring-shaped distributed architecture. The scan lines samples pass through each FPGA, where the results of its own partial coherent sum are added. Once a FPGA has processed a scan line, it is stored in memory. To optimize memory bandwidth and size, the scan lines of the whole image can be split among all nodes.

This ring-shaped distributed architecture has the following advantages:

- A closed ring takes benefit of full duplex transceivers, getting a total bandwidth of 80Gb/s. This is enough to simultaneously circulate 125 scan lines at 40 MSPS and 16 bit per sample.

- The architecture is fully scalable in terms of number of channels, because the ring size has no limit, as long as its bandwidth is kept. Also, the more nodes, the more memory and processing resources the system has.
- A system is made by sseveral 32 channel modules. This leads to lower engineering costs and also allows developing both, higher performance large systems and small lower cost instruments.

CONCLUSIONS

A FPGA-based digital beamformer architecture for high performance parallel beamforming has been presented. The design optimizes DSP, memory and regular logic resources. Also, a focusing circuit operating at over 250MHz switching frequency allows time multiplexing between image lines. Some cases of complex imaging techniques are analyzed, realizing that hundreds of scan lines can be beamformed in parallel to perform these techniques in real-time. A high performance system can be built with 4 mid-range FPGAs and the proposed architecture. For 120 scan line images up to a depth of 20cm on steel, using a 2.5 MHz and 128-elements array it achieves:

- Total Focusing Method: 117 FPS
- Coherent Plane Wave Image Compounding (1 angle, poor quality): 15000 FPS
- Coherent Plane Wave Image Compounding (70 angles, good quality): 250 FPS

Proposed architecture is also highly scalable. Systems of arbitrary number of channels can be made without any performance loss. Another advantage compared with other systems is that scan lines are beamformed at the same rate that ultrasound wave is sampled, instead of storing the acquisition and performing processing afterwards. Another key difference is that there is no acquisition length limit.

Finally, the digital hardware can be reconfigured for implementing new imaging techniques.

ACKNOWLEDGMENTS

This work has been funded by project DPI 2010-17648 of the Spanish Ministry for Science and Innovation.

REFERENCES

1. Gabriel Montaldo, Mickaël Tanter, Jérémy Bercoff, Nicolas Benech, and Mathias Fink, “Coherent Plane-Wave Compounding for Very High Frame Rate Ultrasonography and Transient Elastography”, IEEE Transactions on Ultrasonics, Ferroelectrics, and Frequency Control, vol. 56, no. 3, March 2009.
2. T. Hergum, T. Bjastad and H. Torp, “Parallel Beamforming using Synthetic Transmit Beams”, IEEE Transactions on Ultrasonics, Ferroelectrics and Frequency Control, 54(2007)2, 271–279.
3. D. K. Peterson, G. S. Kino, “Real-Time Digital Image Reconstruction: A Description of Imaging Hardware and an Analysis of Quantization Errors”, IEEE Trans. Sonics Ultrason., 31, 4, pp. 337-351, 1984.
4. J.-Y. Lee, H. S. Kim, J. H. Song, J. Cho, T. K. Song, “A hardware efficient beamformer for small ultrasound scanners”, Proc. IEEE Ultrason. Symp., 2, pp. 1396-1399, 2005.
5. T. I. Laakso, V. Valimaki, M. Karjalainen, U.K.Laine, “Splitting the Unit Delay”, IEEE Sig. Proc. Magazine, pp. 30-58, Jan. 1996.
6. C. Fritsch, M. Parrilla, A. Ibáñez, R. Giacchetta, O. Martínez, “The Progressive Focusing Correction Technique for Ultrasound Beamforming”, IEEE Trans. UFFC, 53, 10, pp. 1820-1831, 2006.
7. J. F. Cruza, J. Camacho, L. Serrano-Iribarnegaray, C. Fritsch, “New Method for Real-Time Focusing through Interfaces”, IEEE Trans. on UFFC, , 2013.

Available online at www.sciencedirect.com

SciVerse ScienceDirect

Physics Procedia (2014) 000–000

Physics Procedia

www.elsevier.com/locate/procedia

43rd Annual Symposium of the Ultrasonic Industry Association

Real Time Fast Ultrasound Imaging Technology and Possible Applications

J. F. Cruza[a] *, M. Perez[a], J. M. Moreno[a], C. Fritsch[a]
Instituto de Tecnologías Físicas y de la Información "Torres Quevedo"
c/ Serrano, 144, 28006 Madrid (Spain)

Abstract

In this work a novel hardware architecture for fast ultrasound imaging based on FPGA devices is proposed. A key difference over other approaches is the unlimited scalability in terms of active channels without performance losses. Acquisition and processing tasks share the same hardware, eliminating communication bottlenecks with smaller size and power losses. These features makes this system suitable to implement the most demanding imaging applications, like 3D Phased Array, Total Focusing Method, Vector Doppler, Image Compounding, High Speed Part Scanning and advanced elastographic techniques. A single medium sized FPGA allows beamforming up to 200 scan lines simultaneously, which is enough to perform most of the above mentioned applications in strict real time.

Selection and peer-review under responsibility of Department of Physics, Indian Institute of Technology Guwahati.

Keywords: Fast ultrasound imaging; High frame rate; Beamformer Architecture; Image Compounding; TFM; 3D Phased Array

---

1. Introduction

Ultrafast ultrasonic imaging is nowadays receiving increased attention due to the large number of new applications that could be addressed. Ultrafast imaging assumes operation at rates above one thousand frames per second. Since the sound propagation velocity sets a physical limit to the frame rate, new imaging algorithms and hardware architectures with real-time parallel processing capabilities are required.

---

* Corresponding author. Tel.: +3491 561 88 06; fax: +3491 411 76 51.
E-mail address: jorge.f.cruza@csic.es

Selection and peer-review under responsibility of Department of Physics, Indian Institute of Technology Guwahati.

The widely used phased array technique builds the image in a line-per-line basis, generating a single beam, single focus in emission, with dynamic focusing in reception for improved image quality. A single image line is obtained in the two-way transit time of the ultrasound pulse up to the desired depth. For example, if depth is 60 mm in biological tissue (propagation speed $c \approx 1500$ m·s^{-1}), acquiring a single image line takes 80 µs; for an N=128-element array with linear scan, the time to acquire the image is over 10 ms, limiting the maximum frame rate to less than 100 images/s. However, several emissions (F) with focus at different depths, followed by reception beamforming, are commonly used, which further reduce the imaging frame rate.

Ultrafast ultrasonic imaging opens opportunities to new applications. In the medical field, high frame rates are required for 3D/4D imaging (Wygant et al., 2006). It will also improve the evaluation of the myocardial function by allowing real-time accurate imaging of the heart movements (Hasegawa and Kanai, 2011). New diagnosis tools linked to the viscoelastic properties of tissue, like Transient Elastography and Supersonic Shear Imaging, require also very high frame rate imaging, typically around 5 Kframes/s (Tanter, 2002; Bercoff, 2004). A single reflection tomogram for breast cancer diagnosis by incoherent circular image compounding can be achieved in few milliseconds; this allows taking hundreds of tomograms to image the full breast volume in a short time, which could be an alternative to mammography for breast cancer screening (Camacho et al., 2012). Automated Ductal Echography (Teboul, 2010), could be also achieved in few seconds, thus improving medical practices.

For Non Destructive Testing (NDT) ultrafast ultrasonic imaging will allow scanning parts at high speed with high spatial resolution. For example, to obtain one image per mm scanning at 1 m/s, a frame rate of 1000 images/s is required. Scanning speed with this tight resolution is currently limited to less than 0.07 m/s (Smith et al., 2003).

Achieving high frame rates requires new image formation algorithms linked to new processing architectures. The explososcan technique composed several image lines in parallel by adding small individual delays to every scan line (Shattuck et al., 1984). Simultaneous beamforming of four to sixteen lines have been reported using 2D arrays (von Ramm et al., 1991; Rasmussen, 2012) and the frame rate is increased by a factor of x4 to x16.

Another technique reported to increase the frame rate is Synthetic Aperture Imaging (SAI), also called Total Focusing Method (TFM). In this case, a single array element or a small de-focused aperture is used in emission to illuminate the whole region of interest, obtaining a low-resolution partial image with a larger aperture. After averaging K images taken from a set of different emitter positions, a high quality image is formed (Nikolov et al., 2005). Assuming that the hardware resources are fast enough, the frame rate increases with regard to a multi-focal phased array by about N/K. SAI or TFM image formation is usually carried out by software following the acquisition phase. Some recent implementations based on GPUs achieve this task in real time (Yiu et al., 2011), but without considering the time involved in transferring the acquired data, which is currently the bottleneck of the procedure.

However the improvements in frame rate given by these techniques are insufficient for the requirements of ultra-fast imaging applications. Other recent ideas allowed reaching rates of thousands of images/s. One is based on plane wave emission (simultaneous triggering of all array elements) followed by RF echo data recording for post-processing (Bercoff, 2004). Frame rates of 6000 images/s along a time limited by the available memory resources have been reported, although with a limited image quality due to the lack of emission focusing.

Plane wave emission has been also used for coherent image compounding (Montaldo et al., 2009). In this case the image is formed by superposition of RF images acquired with plane waves propagating with different angles. In this aspect is a technique analogous to SAI, producing well focused images in emission and reception at all depths with frame rates above 1000 images/s.

These new concepts require the development of a very fast performing hardware to achieve these ultrafast imaging rates, which is the main objective of this work, where we propose a new architecture that exploits the possibilities offered by state-of-the-art FPGAs.

2. Parallel beamforming for ultrafast imaging.

Conventional phased array beamforming introduces time-varying delays to the signals received by array elements that compensate the two-way time-of-flight differences from every focus to every array element. This operation produces the aperture data, which are coherently added together (in RF) to provide the focused A-scan along the steering direction. The focusing delay T_i for element *i* must be modified for every output sample *k* to get strict Dynamic Depth Focusing (DDF, all samples in focus). Expressing T_i in sampling periods, the involved operation is:

$$s(k) = \sum_{i=1}^{N} r_i[k - T_i(k)], \tag{1}$$

where r_i is the signal received by element *i* (perhaps after multiplication by an apodization coefficient) and *N* is the number of elements of the active aperture. High timing resolution is required to keep low delay resolution lobes (Peterson and Kino, 1984). The delay T_i contains an integer and a fractional part. The latter can be conveniently obtained by means of a fractional delay filter, which splits the sampling period in an integer number *L* of sub-sampling intervals (Laakso et al., 1996). The interpolated sample is obtained by means of a FIR filter of *P* coefficients $h_m(j)$, $1 \le j \le P$, that change with sample *k* for every element *i* and fraction *m*(*k*):

$$r_i[k - T_i(k)] = r_i[k - Z_{ik} - \frac{m_i(k)}{L}] \approx \sum_{j=1}^{P} h_{m_{i,k}}(j) r_i[n_{ik} - j] \tag{2}$$

where *Z* represents the integer part and *m/L* is the fractional part of the delay. Inserting (2) in (1),

$$s(k) = \sum_{i=1}^{N} \sum_{j=1}^{P} h_{m_{i,k}}(j) r_i(n_{ik} - j) = \sum_{i=1}^{N} \sum_{j=1}^{P} h_{m_{i,k}}(j) r_i(n_{ik} - j) \tag{3}$$

Changing the order of the summations:

$$s(k) = \sum_{j=1}^{P} \sum_{i=1}^{N} h_{m_{i,k}}(j) r_i(n_{ik} - j) \tag{4}$$

Interpolation and the *N*-channel beamforming processes can be interspersed. In a simple implementation, every *P* cycles of a clock *P* times faster than the sampling frequency, an output sample is obtained with the coherent sum of *N* signals. But multiple image lines can be simultaneously obtained with the same hardware.

Figure 1 shows a simple architecture that obtains the interpolated data s_k from the received samples r_k for one of the *N* channels. Four DSP-cells are used to this purpose (*P*=4) and coefficients *h* are chosen from a local memory in every cell. The number *L* of coefficients provides the timing resolution but, in practice, *L* is chosen of the same order than *P*. Once the latency period has elapsed (9 cycles), an interpolated sample is obtained at every sampling clock cycle. Focusing hardware chooses one among the set of *L* coefficients at every clock cycle, common to all the cells for the same sample, which is easily achieved by shifting the *h*-value used in one cell to the next one.

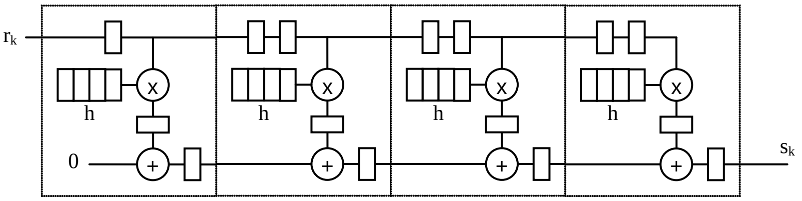

Fig. 1. Implementation of the interpolation filter with DSP cells.

The chain in Fig. 1 is extended to include other channels, as in Fig. 2. This architecture does not require logic resources external to the DSP-cells other than the memories to store the set of coefficients and the small delays required to compensate latency. Given the high operating frequency of the DSP-cells, which is several times the sampling frequency, several scan lines can be simultaneously beamformed with the same hardware by time-multiplexing. If the switching frequency of the DSP-cells is f_{DSP} and the sampling rate is f_S, the ratio $R=f_{DSP}/f_S$ yields the number of lines than can be beamformed concurrently. Since the switching frequency for Xilinx mid-range and high-end FPGAs is, at least, 400 MHz. Then, in case of arrays of up to 10 MHz and a sampling frequency of 40 MHz, *R*=10 and ten scan lines can be simultaneously beamformed with the hardware shown in Fig. 2.

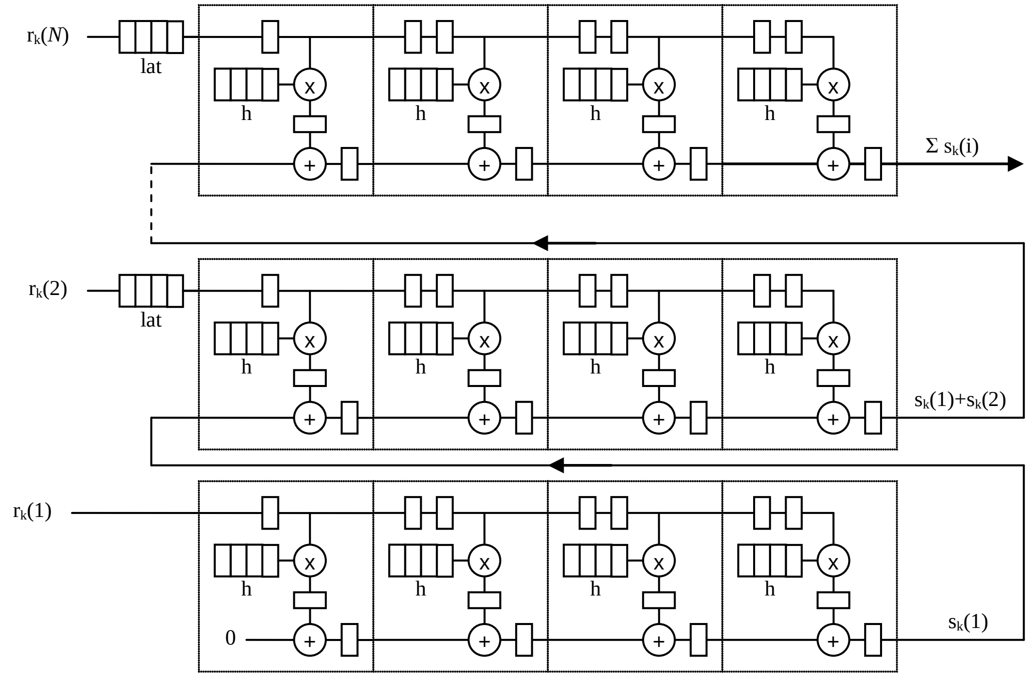

Fig. 2. A systolic architecture for interpolation and beamforming on N-channels based on DSP-cells.

3. Memory resources

Every channel must have a memory to compensate the differences in focusing delays, usually implemented as a FIFO. For an aperture D, the maximum time difference is $2D/c$ and the FIFO depth is given by:

$$M = \frac{2D}{c} f_S \tag{6}$$

The sampling rate f_S must meet the Nyquist criterion with regard to the signal frequency f_R and, typically, $f_S = 4f_R$. With $\lambda=c/f_R=4c/f_S$ it results $M=8D/\lambda$.

For a maximum aperture $D=128\lambda$, $M = 1$ K samples. This memory can be implemented in FPGA using a single Block-RAM. Thus, a single beamformer would require N Block-RAMs and the simultaneous composition of R scan lines would demand $N\cdot R$ Block-RAMs. For example, beamforming $R=32$ lines for an $N=128$ element array would require 4096 Block-RAMs, a figure too high even for high density FPGAs.

A different approach is followed in the proposed architecture taking into account that the time-distance between the input samples that compose a given output sample in different lines is lower than the maximum delay, so that they will be into the delay compensating memory. In other words, the beamformer has access to any sample taken up to M sampling clock periods before the current one for any scan line.

To this purpose, instead of having a FIFO for every scan line, a single ring buffer with M positions is assigned to every channel. The contents of this memory are provided to every beamformer input $r(i)$ on Fig. 3 as required for the current sample and scan line under control of the focusing logic. This approach requires, theoretically, N instead of $N\cdot R$ Block-RAMs to beamform simultaneously any number R of scan lines. However, the Block-RAM bandwidth (f_{RAM}) limits the number of data samples provided every sampling period to $S = f_{RAM}/f_S$. Since the multi-beamformer requires R samples per sampling clock period, a number $B=[R/S]$ of Block-RAMs per channel achieves the required throughput. Typically Xilinx Block-RAMs in current FPGAs operate over 200 MHz. Thus, for the example above (f_S= 40 MHz, R=10) results in S=5 and B=2, that is, two Block-RAMs are required per channel, increasing the theoretical number of required Block-RAMs to $B\cdot N = 256$, a number that fits well in medium sized FPGAs.

Figure 3 summarizes these results and shows the proposed architecture. Data from the A/D converters included in the Analog Front End (AFE) are temporally stored in a ring buffer (~ 2 BRAMs) addressed by the focusing logic to provide the samples required by every scan line. This logic selects also the set of coefficients for the beamformer cell of the current channel. Every beamformer cell has the structure shown in Figs. 1 and 2, where the pipeline registers are replaced by small buffers.

With this architecture the same hardware can be used for different applications, with a range of parallel beamforming capabilities given by the ratio *R* as long as the ring buffer is given the same bandwidth by using multiple Block-RAMs. Furthermore, mid-range and high-end FPGAs can integrate several parallel beamformers of this kind. This naturally multiplies the number of lines simultaneously beamformed. For example, if the application parameters yield *R*=32 and the FPGAs available resources fit 4 beamformers (mid-range FPGA), 128 scan lines can be built simultaneously at the sampling rate. This allows performing TFM in real-time.

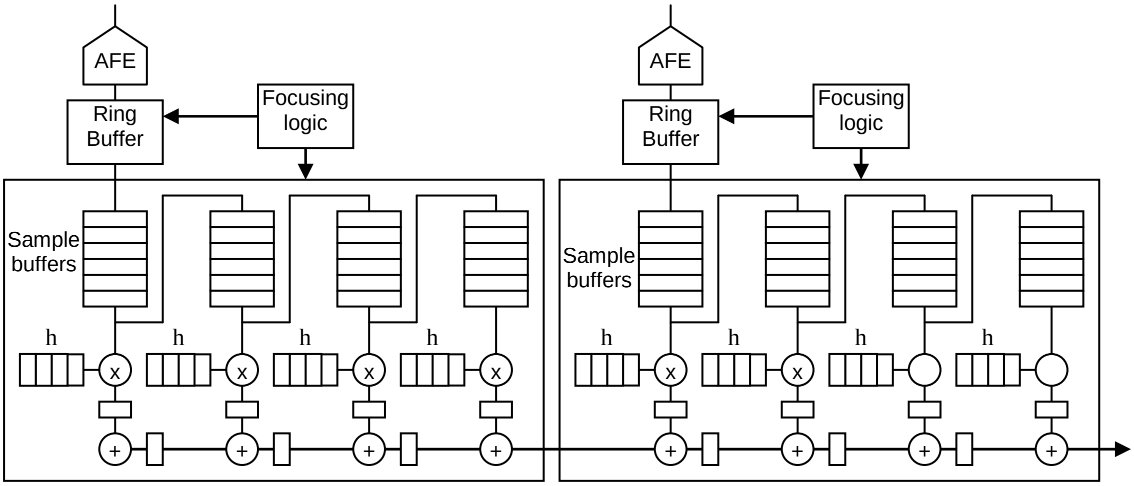

Fig. 3. Structure of the DSP-cells based parallel beamforming architecture.

4. Implementation and validation

The parallel beamforming architecture has been coded in VHDL. In order to get maximum performance for different applications and on different devices some parameters of the architecture are user defined: channel number, filter order, ring buffer depth and working frequency. There are other parameters that can be dynamically changed like the sampling rate that defines the ratio *R* with regard to the device performance.

A 32 channel beamformer has been implemented in a Xilinx XC7K325T-2 FPGA. To take advantage of the high DSP-cell switching frequency, two ring buffers and two focusing circuits have been attached to each filter to adapt their bandwidths. With this configuration, filters work at 400 MHz, while ring buffers and focusing circuits operate at 200 MHz. A single beamformer builds simultaneously 5 scan lines for a 10 MHz array, or 20 scan lines for a 2.5 MHz array. Resource utilization in this device for this implementation is as shown in Table 1.

Table 1. Resource utilization for a 32-channel beamformer in a XC7K325T-2

	Slices	Registers	LUTs	DSP-cells	Block-RAMs
Used	4629	11632	11554	64	32
Available	50950	407600	203200	840	890
% Used	9.1%	2.9%	5.7%	7.6%	3.6%

Certain number of parallel beamformers can be integrated in a single device as a function of the available resources. In this case, the XC7K325T-2 FPGA can accommodate up to 10 parallel beamformers of 32 channels for signals up to 10 MHz, getting up to 50 scan lines in real time. For signals up to 2.5 MHz, 200 scan lines can be obtained in parallel, which allows implementing TFM in real time. The implementation was validated with synthetic signals on a Xilinx KC705 (XC7K325T-2 FPGA) evaluation board via JTAG probe by comparison with results provided by software in Matlab® that yield exactly the same image.

It must be highlighted that the proposed architecture is fully scalable by increasing the number of FPGAs and analog front-ends. To this purpose the communication bandwidth among FPGAs should be equal to that of the DSP-cells on a bus wide enough to accommodate partial results (typically, 20 bits). This calls for communication bandwidths of 480x20 = 9.6 Gb/s. Such high rate can be attained using one or more of the available GTX pairs on the same FPGA, which can run up to 10 Gb/s each.

5. Conclusions

A new beamforming architecture that takes advantage of the availability of high-performance DSP-cells in state-of the art FPGAs has been proposed. It performs focusing delay interpolation and beamforming simultaneously in a chain of DSP-cells, using the high switching speed of the DSP-cells for parallel beamforming by time-multiplexing the same resources. Multiple parallel beamformers fit in medium sized FPGAs, their number being given by the ratio of the DSP-cell bandwidth to the sampling frequency. The architecture is fully scalable to deal with different demands and applications. A full DDF image can be obtained in real time, providing a good alternative to software-based TFM by avoiding the bottleneck of data transfer from the analog front-end to the processing platform.

Acknowledgements

Work carried out within the project EuroStar E!6771 funded by the UE, MINECO and DASEL, S.L.

References

Bercoff, J., Tanter, M., Fink, M., 2004. Supersonic Shear Imaging: A New Technique for Soft Tissue Elasticity Mapping, IEEE Trans. UFFC, 51, 4, 396-409.

Camacho, J., Medina, L., Cruza, J.F., Moreno, J.M., Fritsch, C., 2012. Multimodal Ultrasonic Imaging for Breast Cancer Detection, Archives of Acoustics, 37, 3, 253-260.

Hasegawa, H., Kanai, H, 2011. High-frame rate echocardiography using diverging transmit beams and parallel receive beamforming, J. of Medical Ultrasonics, May, 1-12.

Laakso, T. I., Valimaki, V., Karjalainen, M., Laine, U.K., 1996. Splitting the Unit Delay", *IEEE Signal Processing Magazine*, Jan., 30-58.

Montaldo G. Tanter, M. Bercoff, N., Benech, N. Fink, M, 2009. Coherent Plane-Wave Compounding for Very High Frame Rate Ultrasonography and Transient Elastography, IEEE Trans. UFFC, 56, 3, 489-506.

Nikolov M., Behar, V., 2005. Analysis and optimization of synthetic aperture ultrasound imaging using the effective aperture approach, Int. J. Information Theory & Applications, 12, 257-265.

Peterson D.K., Kino, G.S., 1984. Real-Time Digital Image Reconstruction: A Description of Imaging Hardware and an Analysis of Quantization Errors, IEEE Trans. Sonics Ultrason., 31, 4, 337-351.

Rasmussen, M. F., Férin, G., Dufait, R., Jensen, J.A., 2012. Comparison of 3D Synthetic Aperture Imaging and Explososcan using Phantom Measurements, IEEE Int. Ultrasonics Symp. Proc., 113-116.

Shattuck D. P, Weinshenker, M.D., Smith, S. W., von Ramm, O. T., 1984. Explososcan: a parallel processing technique for high speed ultrasound imaging with linear phased arrays.

Smith R. A., Bending, J. M., Jones, L. D., Harman, T. R. C., Lines, D. I. A., 2003. Rapid ultrasonic scan of ageing aircraft, Insight-Non Destructive Testing and Condition Monitoring, 45, 3, 174-177.

Tanter, M., Bercoff, J., Sandrin, L., Fink, M., 2002. Ultrafast Compound Imaging for 2-D Vector Estimation: Application to Transient Elastography. IEEE Trans. UFFC, 49, 10, 1363-1374.

Teboul, M., 2010. Advantages of Ductal Echography (DE) over Conventional Breast Investigation in the diagnosis of breast malignancies", Medical Ultrasonography, 12, 1, 32-42.

von Ramm, O. T., Smith, S. W., Pavy, H. G., 1991. High-Speed Ultrasound Volumetric Imaging System. Part II: Parallel Processing and Image Display. IEEE Trans. UFFC., 38, 2, 109-115.

Wygant, I.O., Karaman, M., Oralkan, O., Khuri-Yakub, B., 2006. Beamforming and hardware design for a multichannel front-end integrated circuit for real-time 3D catheter-based ultrasonic imaging", in Medical Imaging, Proc. Spie, 6147, 61470A-1.

Yiu B. Y. S., Tsang, I. K. H., Yu, A. C. H, 2011. GPU-Based Beamformer: Fast Realization of Plane Wave Compounding and Synthetic Aperture Imaging, IEEE Trans. UFFC, 58, 8, 1698-1705.

AIP | Conference Proceedings

Modular architecture for ultrasound beamforming with FPGAs

J. F. Cruza, J. Camacho, J. Brizuela, J. M. Moreno, and C. Fritsch

Citation: AIP Conf. Proc. **1433**, 181 (2012); doi: 10.1063/1.3703166
View online: http://dx.doi.org/10.1063/1.3703166
View Table of Contents: http://proceedings.aip.org/dbt/dbt.jsp?KEY=APCPCS&Volume=1433&Issue=1
Published by the American Institute of Physics.

Modular Architecture for Ultrasound Beamforming with FPGAs

J. F. Cruza, J. Camacho, J. Brizuela, J.M. Moreno, C. Fritsch

Consejo Superior de Investigaciones Científicas (CSIC)
UMEDIA Group, La Poveda (Arganda), 28500 Madrid, Spain

Abstract. Reception beamforming requires a high-resolution time base to keep low delay quantization lobes. Usually signals acquired at the Nyquist sampling rate are up-sampled by a factor of 4 to 16 to achieve the required time-resolution. Although this has been carried out for decades using fractional delay interpolating filters, the interpolation and coherent addition processes use a large silicon area and consume power, mainly when implemented in FPGAs. These drawbacks are reduced if the beamformer is implemented in ASICs, but this precludes any retro-fitting operation.

This work presents a beamfoming architecture to overcome these shortcomings, based on the DSP cells incorporated into state-of-the art FPGAs. Since the manufacturing process is similar to that of ASIC, these cells consume low power and processing speed is high. The proposed beamformer interleaves the interpolation and the coherent sum. Besides reducing hardware resources, the design is modular and scalable, which allows to trade off among the number of channels per device, time resolution and resource requirements. It can be easily tailored to very different applications, from the low-channel count systems to the more demanding ones with multi-beamforming capabilities.

Keywords: Beamforming, dynamic focusing, interpolation, real-time imaging, parallel beamforming.
PACS: 43.58-e, 43.35.Yb, 43.60-Lq

INTRODUCTION

The conventional delay-and-sum beamformer with dynamic focus introduces time-varying delays to the signals received by every array element to compensate the time-of-flight differences from every focus, usually located along a steering direction. This operation produces the *aperture data*, which are added together (*coherent sum*) to provide an output sample of the focused A-scan along the steering direction.

High timing resolution is required to reduce the level of the delay quantization lobes [1]. To this purpose, several methods have been proposed, usually falling in one of the following categories:

a) *Dynamic interpolation* techniques, where signals are up-sampled by a factor large enough to achieve the required time resolution and operate with a uniform sampling clock at the Nyquist rate. For this purpose, an interpolating filter for every channel is required before the coherent sum [2-3]. Since the operation is linear, it was suggested to use a single reconstruction filter at the beamformer output [4], but it fails for dynamic focusing because this function is not time-invariant.

b) *Oversampling $\Delta\Sigma$* techniques, which use low bit count sigma-delta A/Ds operated at a high sampling rate that provide the required time resolution and avoids interpolating hardware [5-6]. However, the availability of multi-channel, high-performance front-end analog processors in a single chip [7] makes this approach less attractive, since they use a similar number of interfacing lines, are less sensitive to digital noise, provide high resolution (up to 14 bits) and can operate with higher frequency transducers.

c) *Selective sampling* techniques, which acquire the signals at the instant they arrive to the array element. These use a separate high resolution clock generator for every channel [8-10] and do not require any interpolation process. However, to take advantage of the new analog front-end processors that share the same clock for several channels, these techniques needs to be combined with an interpolation scheme [11].

So that, with the exception of $\Delta\Sigma$ beamformers, some interpolation process must be carried out. Many approaches are based on fractional delay filters, which allow splitting the sampling period in an integer number of sub-sampling intervals [12]. Here, a bank of L fractional delay filters allow to chose the equivalent sampling instant at $1/L$, $2/L$, ..., 1 the sampling period. L is closely related to the delay resolution and usually ranges from 4 to 16. On the other hand, every filter in the bank requires a number F of coefficients large enough to achieve the required accuracy ($F \sim L$). A common variant is to switch the coefficient set to that required for a given fractional delay.

International Congress on Ultrasonics
AIP Conf. Proc. 1433, 181-184 (2012); doi: 10.1063/1.3703166

The interpolation and coherent sum processes require a large silicon area. For example, a parallel implementation demands $L{\cdot}F$ multiply-and-add operations per channel. Thus, only a moderate number of channels can be integrated into a single FPGA [13] and the power consumption is relatively high. The alternative is to switch to an ASIC design [14], but this precludes ulterior hardware updates and greatly reduces system flexibility.

However, state-of-the art FPGAs include DSP cells intended to implement FIR filters. The DSP cells operate at high speed (above 350 MHz) and include, basically, a multiplier and adder with several possible configurations. The manufacturing process is similar to that used for ASICs, so their power consumption is rather low.

This work addresses the design of a beamformer based on the DSP cells currently available in FPGAs. This yields the flexibility of upgrading and low cost of FPGAs together with the low power consumption of ASICs. Furthermore, the design is modular and scalable. The proposed approach allows implementing a complete 128-channel beamformer in a single, moderately sized FPGA.

A SYSTOLIC BEAMFORMING ARCHITECTURE

The beamforming process for an N-element array performs the following operation:

$$S(t)=\sum_{i=1}^{N} w_i r_i[t-\tau_i(t)] \tag{1}$$

where $r_i(t)$ is the signal acquired by channel i, w_i is a weighting function (apodization) and $\tau_i(t)$ is the dynamically changing focusing delay for channel i. In the discrete time domain, the variable t is substituted by the index k to samples with $t=kT_S$, where T_S is the sampling period:

$$S(k)=\sum_{i=1}^{N} w_i r_i[k-T_i(k)] \tag{2}$$

The value $T_i(k)$ represents the delay, in sampling periods, that must be applied to obtain the k-th *output* sample $S(k)$ from the sequence of input samples $\{r_i\}$. Unless $T_i(k)$ is an integer, the value of $r_i[k- T_i(k)]$ is not available from the set $\{r_i\}$, so that it must be estimated by an interpolation process. The interpolation can be performed for band-limited signals by means some kind of FIR or IIR filter or other functions (splines, polynomials, etc.) [12].

To obtain a resolution L times higher than the sampling period, the delay $T_i(k)$ is rounded to the nearest multiple of $1/L$, which yields an integer part $M_i(k)$ and a fractional part $m_i(k)/L$. The set of L possible fractional delays is $\{1/L, 2/L, ...(L-1)/L, 1\}$. The interpolated sample for a given delay $T_i(k) = M_i(k)+m_i(k)/L$ can be approximated by using a $(P-1)$ order FIR filter (P coefficients) as:

$$r_i[k-T_i(k)]=r_i[k-M_i(k)-\frac{m_i(k)}{L}]\approx\sum_{j=1}^{P} h_{m_{i,k}}(j)r_i[k-M_i(k)-j] \tag{3}$$

The filter is applied to the P samples in the set $\{r_i\}$ ahead the $n_{ik} = k-M_i(k)$ sample, which changes dynamically and is handled by the focusing logic. Then,

$$r_i[k-T_i(k)]\approx\sum_{j=1}^{P} h_{m_{i,k}}(j)r_i(n_{ik}-j) \tag{4}$$

Substitution in (2) yields,

$$S(k)=\sum_{i=1}^{N} w_i\sum_{j=1}^{P} h_{m_{i,k}}(j)r_i(n_{ik}-j)=\sum_{i=1}^{N}\sum_{j=1}^{P} h_{m_{i,k}}(j)w_i r_i(n_{ik}-j) \tag{5}$$

Changing the addition order and including the weight w_i in the coefficients for channel i,

$$S(k)=\sum_{j=1}^{P}\sum_{i=1}^{N} h_{m_{i,k}}(j)r_i(n_{ik}-j) \tag{6}$$

Note that the coherent sum can be performed simultaneously with the filtering function in different channels. In a single cycle, a partial result for sample $S(k)$ is obtained as the sum of partial results of the interpolation. After P cycles, the full result for $S(k)$ is obtained.

This mechanism allows the construction of an efficient systolic architecture for beamforming, based on the DSP cells included into state-of-the-art FPGAs. Figure 1 shows schematically the processing element for a single channel based on the DSP-48 cells of Xilinx FPGAs [15]. A small FIFO (1Kx18) adjusts the differences on the time of arrival of echoes to the array elements. Writing samples to the FIFO is carried out at the sampling rate clock CKS and is enabled once the integer delay M_i has elapsed. A/D converters of up to 18 bits can be used.

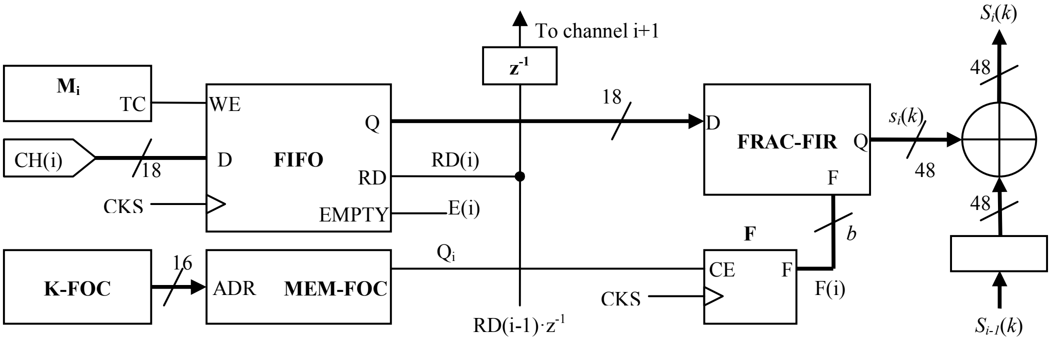

FIGURE 1. Processing element for a systolic beamformer

The focusing logic must provide the integer part n_{ik} as well as the fractional delay for every focus k. Here it is based on the *Progressive Focusing Correction* (PFC) technique described in [10], where a single bit $Q_i(k)$ codes the focusing delay: when $Q_i(k)=0$, the fractional delay remains unchanged; when $Q_i(k)=1$, the next fractional delay is advanced by a quantum $1/L$. From some minimum range that sets the delay n_{i1}, the successive delays are defined incrementally as $T_k = T_{k-1} + (1-Q_k)T_S$, which provides implicitly the n_{ik} value.

The counter F of $b=\log_2 L$ bits selects the set of filter coefficients for the current fractional delay in the FRAC-FIR filter. Data read from the FIFO pass through this filter, producing the aperture data $s_i(k)$ that is added to the partial result from the precedent processing element. Note that F is incremented every time $Q_i = 1$ to select the next fractional delay. This way, a round-robin sequence of fractional delays is produced.

It is worth to note that, when the fractional delay is ‘1’, the sample at the FIFO passes to the filter output without interpolation. If, in this situation, a focusing code $Q_i=1$ is produced, the next delay will be $L-1/L$, which is obtained by interpolation of the preceding P samples in the same cycle. In this case, the FIFO read is disabled since the required data is already available in the FIR filter. This exception is easily implemented (not shown).

The adders are 48-bits wide, which avoids saturation effects (up to thousand of channels). On the other hand, new data samples are read on FIFO(i) when a read is performed in FIFO(i-1) after a pipeline delay and E(i)=0 (not empty). If the first FIFO read is enabled once the maximum initial delay max(M_i) has elapsed, there is no need to care about the FIFO empty flags, since all of them will have stored one or more samples.

An important aspect is the system modularity. An N-channel system is implemented by simply pipelining N processing elements. No logic dependant on system size is required. Therefore, this approach allows using a larger FPGA to integrate more channels or to break the design in several devices for lower cost or other reasons.

Figure 2 shows the overall beamformer architecture. In this case it uses a single DSP48 cell per channel, but the actual implementation code allows using D cells per channel. Note that another cell is used as the final accumulator.

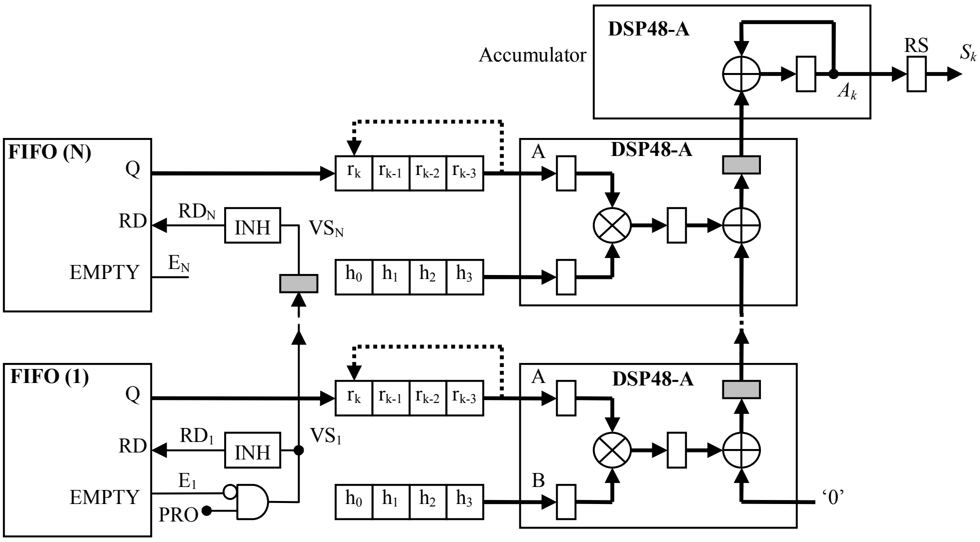

FIGURE 2. A modular, systolic beamforming architecture

In the example shown, for a given set of coefficients selected by the focusing logic ($\{h_0, ..., h_3\}$), partial results for sample k are obtained in P steps (P=4 in this case) as:

Step j: cell i output= $h_{i,j} \cdot r_{i,\,k-j},\ 1 \le i \le N \quad \longrightarrow \quad$ In the accumulator: $A_k(j) = A_k(j-1) + \sum_{i=1}^{N} h_{i,j} r_{i,k-j}$ (7)

Following the P-th step the value A_k is transferred to register RS that stores the final result S_k. Thus, P processing cycles are required for every output sample. DSP cells operate with clocks above 320 MHz, while ultrasound signals are acquired at a much lower rate, typically below 40 MHz. This 8:1 ratio R on speed can be used to get the output samples at the same rate they are acquired using FIR filters with up to 8 coefficients (order 7 or below). Usually this is enough to yield accurate results using, for instance, Lagrange interpolators with $L \le 8$ [12]. If higher filter orders were required, a number $D>1$ cells DSP-48 per channel should be used, but this is usually not required since the delay resolution obtained with these figures will be better than 1/32 the signal fundamental period.

RESULTS

Current VHDL description allows setting, for every processing element, the number D of DSP-48 cells, the number P of filter coefficients and the speed ratio R, where $D=P/R$. This way, the number of DSP-48 cells required for an N-element implementation, taking into account the final accumulator, is:

$$NC = N\frac{P}{R} + 1 \tag{8}$$

Setting N=128 elements, P=8 coefficients and R=8, yields a total NC=129 DSP-48 cells. Other required resources are BRAMs for FIFOs (128) and distributed memory for coefficient and data storage. All this logic fits in a low-cost, moderately sized FPGA of the Xilinx Spartan-6 family XC6SLX75, which has 172 BRAMs and 132 cells DSP-48, leaving room for other processing functions.

CONCLUSION

A systolic beamformer has been described. It efficiently uses the new hardware Digital Signal Processing (DSP) cells available in state-of-the-art FPGAs, which basically provide a multiplier and adder per cell and operate at high speed. The beamformer interleaves the coherent summation with the sample interpolation process required to achieve a high focusing delay resolution. This allows reducing the resource requirements; in particular, only one accumulator is required for all the process. The high-speed of DSP cells are advantageously used to perform several processing cycles in a single sampling period for real-time operation. Furthermore, every cell is time-multiplexed to perform the fractional filtering function, thus reducing the number of required cells.

ACKNOWLEDGMENTS

Work supported by project DPI2010-17648 of the Spanish Ministry for Science and Innovation.

REFERENCES

1. D. K. Peterson and G. S. Kino, *IEEE Trans. on Sonics and Ultrasonics*, **31**, 4, 337-351, (1984).
2. J.-Y. Lee, H. S. Kim, J. H. Song, J. Cho, T. K. Song, *Proc. IEEE Ultrason. Symp.*, 2, 1396-1399, (2005).
3. C. H. Hu, X. C. Xu, J. M. Cannata, J. T. Yen, K. K. Shung, , *IEEE Trans. UFFC*, **53**, 2, pp. 317-323, (2006).
4. R. A. Mucci, *IEEE Trans. Acoust., Speech and Signal Proc.*, **32**, 3, 548-558, (1984).
5. S. R. Freeman et al., *IEEE Trans. UFFC*, **46**, 2, 320-332, (1999).
6. M. Kozak and M. Karaman, *IEEE Trans. UFFC*, **48**, 4, 922–930, (2001).
7. B. Reeder, Analog Dialogue, 41-07, 2007
8. M. O'Donnell and M. G. Magrane, US. Patent No. 4.809.184, (28 Feb. 1989).
9. T. K. Song and J. F. Greenleaf, *IEEE Trans. UFFC*, **41**, 3, 326-332, (1994).
10. C. Fritsch, M. Parrilla, A. Ibáñez, R. Giacchetta and O. Martínez, *IEEE Trans. UFFC*, **53**, 10, 1820-1831, (2006)
11. J. Camacho, A. Ibáñez, M. Parrilla and C. Fritsch, *Proc. IEEE Ultrason. Symp*, 1631-1634, (2006).
12. T. I. Laakso, V. Valimaki, M. Karjalainen and U.K.Laine, *IEEE Sig. Proc. Magazine*, 30-58, Jan. 1996.
13. J. Camacho, M. Parrilla and C. Fritsch, *ICU'2007*, #1229, Vienna, April 9 - 13, (2007).
14. M. Karaman, A. Atalar and H. Köymen, *IEEE Trans. Medical Imaging*, **12**, 4, 711-720, (1993).
15. Xilinx Inc., "XtremeDSP for Virtex-4 FPGAs", UG 073, 2008.

Available online at www.sciencedirect.com

ScienceDirect

Physics Procedia 63 (2015) 134 – 140

Physics Procedia

43rd Annual Symposium of the Ultrasonic Industry Association, UIA Symposium 2014

Multi-modal ultrasound imaging for breast cancer detection

L. Medina-Valdés[a], M. Pérez-Liva[b], J. Camacho[a], J.M. Udías[b], J.L. Herraiz[c], N. González-Salido[a]

[a] *ITEFI , Spanish National Research Council (CSIC), Madrid, Spain.*
[b] *Grupo de Física Nuclear, Dpto. Física Atómica, Molecular Nuclear, Universidad Complutense, CEI Moncloa, Madrid, Spain.*
[c] *Madrid-MIT M+VISION Consortium, Massachusetts Institute of Technology (MIT), Boston, USA.*

Abstract

This work describes preliminary results of a two-modality imaging system aimed at the early detection of breast cancer. The first technique is based on compounding conventional echographic images taken at regular angular intervals around the imaged breast. The other modality obtains tomographic images of propagation velocity using the same circular geometry. For this study, a low-cost prototype has been built. It is based on a pair of opposed 128-element, 3.2 MHz array transducers that are mechanically moved around tissue mimicking phantoms. Compounded images around 360º provide improved resolution, clutter reduction, artifact suppression and reinforce the visualization of internal structures. However, refraction at the skin interface must be corrected for an accurate image compounding process. This is achieved by estimation of the interface geometry followed by computing the internal ray paths. On the other hand, sound velocity tomographic images from time of flight projections have been also obtained. Two reconstruction methods, Filtered Back Projection (FBP) and 2D Ordered Subset Expectation Maximization (2D OSEM), were used as a first attempt towards tomographic reconstruction. These methods yield useable images in short computational times that can be considered as initial estimates in subsequent more complex methods of ultrasound image reconstruction. These images may be effective to differentiate malignant and benign masses and are very promising for breast cancer screening.

PACS: 43.35 Wa; 43.35.Bf

Keywords: image compounding, ultrasound tomography, breast cancer screening, CT, PET

---

doi:10.1016/j.phpro.2015.03.022

1. Introduction

Breast Cancer is the malignant tumor with highest incidence in women and one of highest mortality rates, with 8 million new cases in the world each year (Jemal et al., 2011). However, survival rates are nearly 100% if detected at early stages (Breast cancer, 2014). In this context, mammogram screening programs were developed. However, mammography presents radiation risk and moderate sensitivity, especially in dense breast tissue, which is more likely to develop cancer (Ursin et al., 2005). Promising alternatives are the tomographic ultrasound imaging systems.

The potential of ultrasound computer tomography (USCT) potentials has been known since the 1970s (Schomberg, 1978). Those systems generate different image modalities, providing a performance comparable to Magnetic Resonance Imaging (Ranger et al., 2012), considered the gold standard. Furthermore, scanning is completely automated, so repetitive images are produced, allowing patient follow-up. USCT provides a full perspective of the mamma, so potential lesions can be located accurately. Ultrasound tomography also minimizes some drawbacks of conventional echography. As all insonification angles can be covered, biological structures are fully depicted, image noise due to speckle is reduced and spatial resolution is isotropic. However, the huge data volume involved and the time required to reconstruct images make ultrasound tomography unaffordable for clinical applications. Recently, first models have become available, even though, they still require high performance processing (Roy et al., 2013; Wiskin et al., 2010).

The USCT prototype developed in ARTEMIS project claims to offer automated and multi-modal ultrasonic imaging at reasonable cost. On one hand, Full Angle Spatial Compounding (FASC) is provided during scanning process in real time. This reflectivity image is the outcome of the average of conventional sector echographic images acquired 360º around the breast. FASC imaging reduces speckle and improves contrast to noise ratio. At the same time, angle-dependent artifacts are avoided, so biological structures are fully depicted.

On the other hand, ultrasound computer tomography may offer post-processing high quality reflectivity speed-of-sound images. In this work, we present a straight ray approximation to reconstruct real data from our experimental system. These kinds of approximations are very common in geometrical acoustics to easily obtain images with restriction of the maximum achievable resolution of $\lambda/2$. Two commonly used ray-tracing methods for CT and PET reconstruction (FBP and 2D OSEM) were implemented in order to obtain first attempt tomographic images, which not only give general information about structures under study but also can be usable as input to guide convergence of full wave algorithms.

The USCT system is based on conventional medical grade probes, arranged around the region of interest, configuring a ring aperture. Several 2D slices can be acquired by shifting the ring array along the coronal axis, which allows a complete 3D reconstruction of the breast, from nipple to armpit.

2. Materials and Methods

2.1. The USCT prototype

The experimental arrangement consists of 2 coplanar medical, 128-element, linear array transducers, of 3.2 MHz and 50% of bandwidth (Prosonic, Korea). These can be independently and accurately positioned around a breast phantom by means of a stepper motor with high mechanical resolution (0.1º). The array probes and the breast phantom are arranged inside a water tank to have good ultrasound coupling. The stepper motors are individually controlled by our own designed drivers with a USB interface. Beam steering and dynamic depth focusing are performed by ultrasonic equipment, SITAU 112 (Dasel, Spain). Data are transferred through another USB interface to a computer that performs post-processing and motor control in MATLAB (The Mathworks, USA).

FASC requires that the intersection of all sector images include the whole breast. Moreover, ACT algorithms require insonification of all imaged points for all transmitter positions in the ring aperture. To this purpose, the medical grade array probes have good lateral sensitivity (-6dB @ 45º).

A calibration process is performed prior to data acquisition to deal with mechanical inaccuracies in turning radius (R), angular deviation of the array transducers (β) and actual speed of sound in the coupling medium (water). As a result, array elements are accurately positioned in a global coordinate system.

2.2. Full Angle Spatial Compounding

Full Angle Spatial Compounding (FASC) is the reflectivity image from the average of sector images acquired from several angular positions around the breast. B-Mode images are acquired at regular angles around the region of interest (ROI) of 60 mm of radius, where all images overlap, with one probe in phased-array mode.

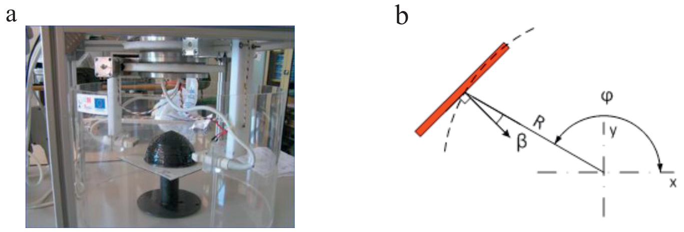

Fig. 1. (a) Experimental arrangement; (b) Reference coordinates and nomenclature

The sampling frequency is 20 MHz, the depth range is within 5 to 180 mm, and the lines are spaced 0.46º in the interval -55º to 55º. B-Mode images are scan converted and averaged on a rectangular pixel matrix. Pixel resolution is 0.15 mm for an estimated spatial resolution of 0.6 mm, which meets the Nyquist criterion in terms of spatial frequency.

In conventional echography, homogeneous speed of sound is assumed. However, the different breast tissues compose a heterogeneous medium. This leads to refraction and double structure artifacts in conventional image compounding. These effects may be avoided if a correction process is carried out for each partial image before composition. Ray tracing algorithms can be used to allocate refracted samples of A-Scans based on a speed of sound map obtained with transmission tomography. However, correction may be also achieved extracting information directly from partial images (Bartelt, 1988). In this work, the imaged object was assumed to be homogeneous, although with a speed of sound different from that of the coupling medium (water), namely c_1. To obtain a speed of sound map, since the A-Scans acquired from opposite directions insonify the same scatterers, the maximum of their cross correlation provides an estimation of the speed of sound in the imaged object.

Let $r_l(t)$ and $r_r(t)$ two A-Scans acquired from opposed angular positions, and T_{TNK} the time of flight between them in water. The correlation between $r_l(t)$ and the inverted version $r_r(T_{TNK}-t)$ peaks at Δt, which is the difference of times of flight (TOF_l and TOF_r) to a virtual scatterer observed from two opposed directions.

$$\Delta t = \left(TOF_l + TOF_r\right) - T_{TNK} \tag{5}$$

When the times of flight are decomposed depending on the propagation media, the speed of sound of the imaged object c_2 is obtained.

$$c_2 = \left(\frac{\Delta t}{2W_{ph}} + \frac{1}{c_1}\right)^{-1} \tag{6}$$

where W_{ph} is the imaged object width, obtained after estimating the interface between the two media. For each angular position of the array probe, the interface is detected by applying a threshold to the A-Scan at 0º steering angle after a moving average filtering. A smooth and closed curve is interpolated with the collected samples. The refraction of incident rays (A-Scans) is computed applying the Snell law. Then, each sample is allocated according to the corresponding time-of-flight and speed of sound.

2.3. Transmission tomography

2.3.1. Time-of-flight sinograms

In ultrasound tomography, the time-of-flight (TOF) is known as the elapsed time since the signal emerges from the emitter transducer until the first reflected signal arrives to the receiver transducer. It can be calculated as follows:

$$TOF = \int \frac{1}{c^2} dl = \int s^2 dl \tag{7}$$

where c is the sound speed, s is the slowness and l is the path length of the wave front.

If straight trajectories are assumed, once the object is scanned from different angles covering projections between 0-360º and TOF values are recorded for all emitter-receiver pairs, we will have a suitable data set to be reconstructed by using inverse radon transform. For this purpose, we stored the entire data into sonograms (Fahei, 2002).

2.3.2. FBP and 2D OSEM methods

The FBP algorithm (Herman, 1980) is a commonly used technique in medical image reconstruction (CT, PET and SPECT). In FBP, the Fourier transform of each projection is multiplied by a ramp filter in the frequency domain. Then, the inverse Fourier transform is applied and the resulting data are back-projected to form the image. It is a very fast technique but it has major disadvantages like poor resolution and low signal to noise ratio. This process can be easily implemented in MATLAB once the data are stored in form of sinograms.

Iterative solutions for image reconstruction are often considered much better quality. Calculations are repeated, and hence, the following iteration is always slightly better than the previous one. The iteration continues until errors reach a prescribed limit. In this sense, the Order Subset Expectation Maximization algorithm (Hudson and Larkin, 1994) is one of the most used methods when working with rectilinear trajectories, basically because of its fast performance and high quality results. This algorithm is based in ML-EM (Shepp and Vardin, 1982). Here the projection data are grouped into ordered subsets, where each subset contains a set of regularly spaced projections. The subset number is the speed-up factor and the sum of counts in projections forming the subsets is equal for all subsets. It is also very easy to implement in Matlab by means of the straight forward and inverse Radon transform.

2.3.3. Experimental setup and phantom description

All the experimental measurements in tomographic mode were performed with the same system described in section 2.1. In this case, 23 fan-beams were employed with step angles of 15 degrees between them. A total of 128 elements per fan-beam were employed to emit and receive, and each emitter element was made to correspond with 10 receiver elements. The total measurement time for this initial prototype was 3 hours.

We also developed an agar-glycerine-gelatine phantom to test our system. Its major characteristics can be seen in Figure 2 and Table 1. Three holes were formed inside the phantom and filled with water.

Fig 2. (a) Front view of the phantom, (b) top view and (c) scheme of the top view

Table 1. Composition and size of the phantom

Water (ml)	Glycerin (ml)	Gelatine (g)	Agar (g)	Height (mm)	External diameter (mm)	Expected sound speed (m/s)
720	180	50	20	98	102	1560

3. Results

3.1. FASC images

Figure 3a shows a conventional sector image, taken when the array probe is at $\varphi = 180^\circ$. Image quality deteriorates at the rightmost part of the image due to worse resolution with depth and to refraction effects. Figure 3b shows the FASC of 36 conventional reflection images, taken at regular-angle positions. As all insonification angles are covered, biological structures are fully depicted and spatial resolution is homogeneous. Moreover, speckle variance is reduced by the spatial compounding. Figure 3c shows the result when refraction is corrected. This yielded a correction of double structures and shape distortions. Some relevant biological structures are depicted in Fig. 4, for which Contrast Ratio (CR) and Noise to Contrast Ratio (CNR) were evaluated. CNR improves with compounding (e.g. 14 dB to 19 dB in the hyperechoic cyst, fig. 4a), while CR remains practically unchanged.

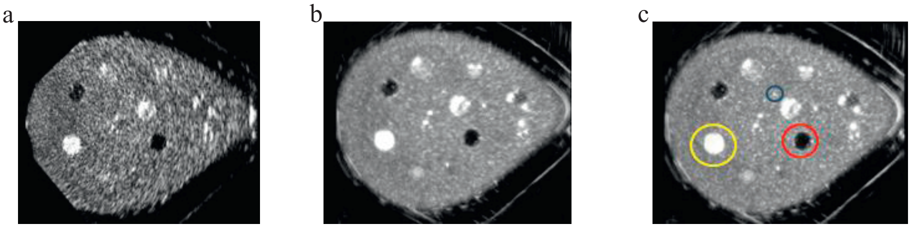

Fig 3. (a) Sectorial B-Mode image acquired at 180º; (b) Spatial compounding of 36 sectorial images without refraction correction; (c) FASC of 36 sectorial images after refraction correction

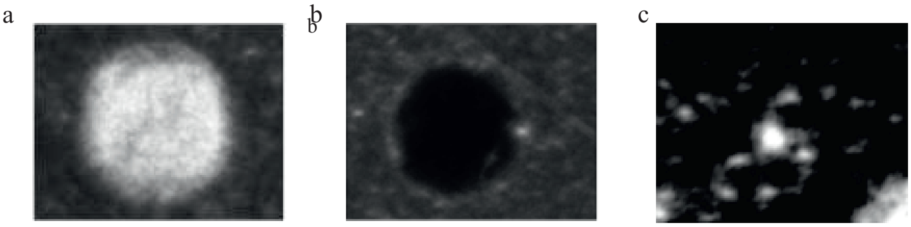

Fig 4 (a) Hiperechoic cyst detail(yellow circle in Fig5c); (b) Anechoic cyst detail (red); (c) Microcalcification detail (blue)

3.2. *Tomographic images.*

The TOF data was arranged into a 2-D sinogram with 600 radial bins and 600 angular bins. With this configuration, the expected maximun resolution achievable is 0.33 mm, which is worse than $\lambda/2$ expected due to the use of ray tracing algorithms. Nevertheless, it is good enough to see major lesions presented in the phantom except the needle with 0.2 mm of diameter. The sinogram and reconstructed images can be seen in Fig. 5 a, b and c respectively.

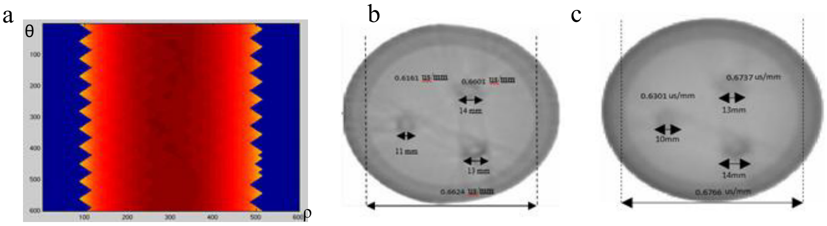

Fig 5. (a) Sinogram of the acquired data (b) reconstructed image with FBP algorithm (c) reconstruction image with OSEM algorithm.

These images were reconstructed in 0.3 and 30 seconds for FBP and OSEM respectively, using one single core of an 8 core, 2.2 GHz CPU. For both cases, adequate values of slowness and a correct location of lesions were achieved. It can be noticed the better image quality obtained with the OSEM algorithm, as the FBP image shows some artefacts at the edges of the cylindrical holes. This demonstrates than even when a less than realistic model is employed (i.e. ray-tracing), the iterative method is capable of recovering most of the information present in these data.

4. Conclusions

An improved parametric spectral procedure applied in laboratory, to estimate shifts in PSD of ultrasonic echoes from an arterial phantom with a 10-MHz transducer, shows promising responses for a non-invasive measurement of small thicknesses alterations in the walls of arterial phantoms. Good spatial resolutions can be potentially attained: of an order of micron, which are clearly better than those attained in walls with non-parametric spectral techniques or using conventional time cross-correlation. The reason is that our parametric spectral procedure presents frequency lobes narrower than other spectral options, in the overtones of the resonant echoes returning from an arterial wall.

For instance, by using the 10th overtone of the resonant wall echo, a reasonable frequency definition of 19.5 kHz is obtained, which represents a excellent spatial resolution of (± 0.9 μm), clearly improving the spatial performance of the methods based on the periodogram or on cross-correlation operators, which provide resolutions around 20-30 μm, ±11 μm in the best scenario of signal to noise ratio.

New experimental efforts and additional analyses with complex ultrasonic echoes, acquired from well-controlled sanguineous tissues patterns, are still needed, to select the best spectral algorithm for distinct cases and optimize the potential resolution of this recent approach. In addition, possible clinical limitations must be evaluated.

Acknowledgements

Luis Medina wishes to acknowledge the Spanish Ministry of Economy and Competitiveness for the financial support (grant BES-2011-048124).

References

Bartelt H. Computation of local directivity, speed of sound and attenuation from ultrasonic reflection tomography data. *Ultrasonic Imaging* 1988; 10:110-120

Breast cancer. (2014). Retrieved May 20, 2014, from http://www.cancer.org/cancer/breastcancer.

Fahei F. Data Acquisition in PET Imaging. *Journal Of Nuclear Medicine Technology* 2002; 30(2):39-49

Herman G. Image reconstruction from projections: the fundamentals of computerized tomography, Academic Press 1980.

Hudson H. and Larkin R. Accelerated image reconstruction using ordered subsets of projection data. Medical *Imaging, IEEE Transactions on,* 1994;13, 601-609.

Jemal A, Bray F, Center MM, Ferlay J, Ward E, Forman D. Global cancer statistics. *CA Cancer J Clin* 2011; 61:69-90.

Ranger B, Littrup PJ, Duric N, Chandiwala-Mody P, Li C. Schmidt S, Lupinacci J. Breast ultrasound tomography versus magnetic resonance imaging for clinical display of anatomy and tumor rendering: Preliminary results. *AJR Am J Roentgenol* 2012; 198(1):233-239

Roy O, Schmidt S, Li C, Allada V, West E, Kunz D, Duric N. Breast imaging using ultrasound tomography: From clinical requirements to system design. *Joint UFFC, EFTF and PFM Symposium* 2013; 1174-1177.

Schomberg H. An improved approach to reconstructive ultrasound tomography. *J. Phys. D: Appl. Phys*. 1978; 11:L181-L186.

Shepp L and Vardi Y. Maximum Likelihood Reconstruction for Emission Tomography. *Medical Imaging, IEEE Transactions on*, 1982; 1, 113-122

Ursin G, Hovanessian-Larsen L, Parisky YR, Pike MC, Wu AH. Greatly increased occurrence of breast cancers in areas of mammographically dense tissue. *Breast Cancer Research* 2005; 7:R605-R608

Wiskin J, Borup D, Johnson S, Berggren M, Robinson D, Smith J, Chen J, Parisky Y, Klock J. Inverse scattering and refraction corrected reflection for breast cancer imaging. *Proc. SPIE Medical Imaging* 2010; 7629:76290K